www.ann-phys.org

SEP | 2013

annalen der physik

Precision Experiments and Fundamental Physics at Low Energies – Part II

Edited by Klaus Blaum, Holger Müller and Nathal Severijns

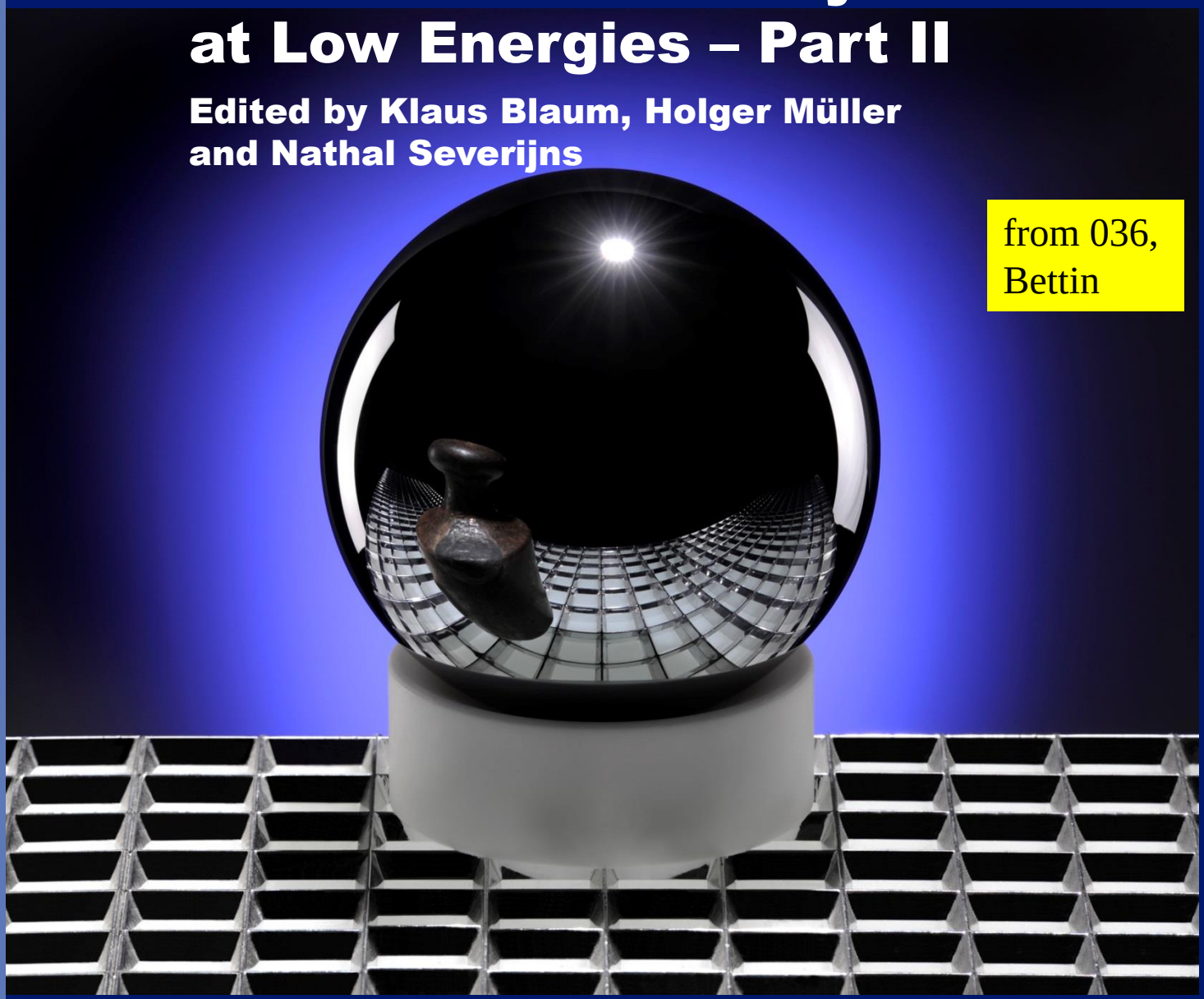

from 036, Bettin

WILEY-VCH

ISSN 0003-3804 • Ann. Phys. (Berlin), Vol. 525 • No. 8-9 (September), 443-538 (2013)

Annalen der Physik • Volume 525 • 2013 • Number 8-9

WILEY ONLINE LIBRARY

Early View publication on wileyonlinelibrary.com
(issue and page numbers not yet assigned;
citable using Digital Object Identifier – DOI)

Ann. Phys. (Berlin), A1–A2 (2013) / DOI 10.1002/andp.201300731

annalen der physik

Editorial

Precision experiments and fundamental physics at low energies – Part II

Klaus Blaum, Holger Müller, and Nathal Severijns

While the Standard Model of particle physics and general relativity has been extremely successful, there is strong observational evidence that they are incomplete. They are unable to explain, *e.g.*, dark energy or why the universe is dominated by matter when the theory exhibits perfect matter-antimatter (CPT-) symmetry, as any Lorentz-invariant, local field theory must. It is hoped that these theories can be unified and completed, perhaps by a version of string theory or loop quantum gravity. The natural energy scale for such theories is the Planck scale, where deviations from relativity and the Standard Model are expected to appear but where direct experimentation is impossible. One may, however, search for suppressed effects at lower energy scales in experiments of extreme precision. These effects will be minuscule and hard to discriminate against signals from conventional physics, except where the signals from standard physics are zero by an exact symmetry of the Standard Model, such as Lorentz and CPT symmetry.

Tests of fundamental symmetries often involve a clever combination of methods to suppress systematic influences. Heil *et al.* (p. 539), for example, report a sensitive test of Lorentz and CPT symmetry based on observing the frequencies of ^{3}He/^{129}Xe masers. While each of these masers is limited in stability by its sensitivity to magnetic field, a particular weighted average of their frequencies is insensitive to magnetic fields. Wilschut *et al.* (p. 652) extend the scope of tests of Lorentz symmetry to the weak interaction based on beta decay. Jungman (p. 550) describes experiments to find a permanent electric dipole moment of fundamental particles. Some of these experiments have already reported upper limits that rule out certain versions of supersymmetric theories beyond the Standard Model. Pustelny *et al.* (p. 659) describe a creative new way to seek for new interactions through a worldwide network of magnetometers. The exploration of the Standard Model through precision experiments is, of course, not restricted to the protons, neutrons and electrons making up the matter of everyday life, as evidenced by Weinheimer *et al.*'s study of neutrino masses (p. 565) and Volpe's study of neutrinos in astrophysics (p. 588). Precision studies of beta decay offered one of the first opportunities to learn about neutrinos, and are still among the best. Ban *et al.* (p. 576) offer a state of the art discussion. Naviliat-Cuncic and González-Alonso (p. 600) describe beta-decay searches for new interactions.

Measuring fundamental constants to high precision is interesting because these constants are often used in a wide range of applications, in the context of testing the accepted laws of physics, and for defining the international system of units (SI). Because of known relationships between fundamental constants there are usually many ways to do so. For example, Sturm *et al.* (p. 620) study the electron's gyromagnetic ratio g_e. Another way to measure the same quantity is through spectroscopy highly charged ions; the link is provided by the theory of quantum electrodynamics (Volotka *et al.*, p. 636). The fine structure constant, in turn, can be expressed as $\alpha^2 = 2(R_\infty/c)(h/m_e)$ by the velocity of light c, the Planck constant h, the electron mass m_e, and the Rydberg constant R_∞, a central quantity obtained by spectroscopy of hydrogen (see Beyer *et al.*, p. 671). One of the largest contributions to the uncertainty in hydrogen physics is the proton's charge radius. The experiments of Pohl *et al.* (p. 647) provided major new insights into this. The relation $\alpha^2 = 2(R_\infty/c)(h/m_e)$ can also be solved for the electron mass. In a future version of the international system of units, the Planck constant will have a defined value, so measurements of α and R_∞ become measurements of m_e, which can then be compared to atomic masses. The link to macroscopic mass measurement can be provided by Avogadro spheres (Bettin *et al.*,

p. 680). Penning traps are central tools in such experiments; some of their intricate properties are discussed by Kretzschmar (p. 688). Penning-trap mass spectroscopy provides opportunities to search for neutrinoless double-electron capture, closing the circle to neutrino physics (Eliseev *et al.*, p. 705).

The fact that gravity is not integrated into the Standard Model of particle physics makes gravitational experiments an exception to the rule: there are no known exact relations between the gravitational constant and other constants of nature. Thus, gravitational experiments form an interesting cosmos of their own. Such experiments operate on all scales from large, like Hagedorn *et al.*'s presentation of the Microscope satellite, a test of the equivalence principle in Earth orbit (p. 718), to small, e.g., Nesterov's paper on a nanonewton force sensor to study gravity at short distances (p. 726).

These papers describe a number of cutting-edge studies that are all interesting by themselves; we hope that by uniting them in one volume, the reader will be offered a view of their relationships, which give us some of our best opportunities for testing the overall consistency of our fundamental theories and experimental methods.

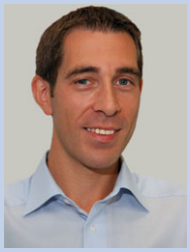

Klaus Blaum graduated in 2000 at the University in Mainz. After a postdoctoral position at GSI, Darmstadt, he went to CERN to lead the ISOLTRAP experiment. In 2004 he became head of a Helmholtz Research Group in Mainz. Since 2007 he is director at the Max-Planck Institute for Nuclear Physics in Heidelberg and head of the Cooled and Stored Ions Division. His main research focus is on precision measurements of atomic and nuclear ground state properties as well as tests of fundamental symmetries using Penning traps.

Holger Müller graduated in 2004 at Humboldt-University, Berlin and was a postdoc with Steven Chu at Stanford. Since July 2009, he has been assistant professor of physics at the University of California, Berkeley. His work is focused on atom interferometers and precision measurements, for example determining the fine structure constant, inertial sensing, and testing general relativity.

Nathal Severijns graduated in 1989 at the Katholieke Universiteit Leuven (KU Leuven). After two years of postdoctoral studies at the Université Catholique de Louvain-la-Neuve (U.C.L.) he became an assistant professor and later full professor of physics at KU Leuven. His work focuses on low energy weak interaction studies, testing symmetries of the standard model and searching for new physics beyond this model in nuclear beta decay and neutron decay, and the search for an electric dipole moment of the neutron.

Klaus Blaum
Max-Planck-Institute for Nuclear Physics,
Stored and Cooled Ions Devision,
Heidelberg, Germany
E-mail: klaus.blaum@mpi-hd.mpg.de

Holger Müller
Department of Physics,
University of California,
Berkeley, CA, USA
E-mail: hm@berkeley.edu

Nathal Severijns
Nuclear and Radiation Physics Section,
University of California,
Leuven, Belgium
E-mail: Nathal.Severijns@fys.kuleuven.be

Ann. Phys. (Berlin) **525**, No. 8–9, A118–A124 (2013) / DOI 10.1002/andp.201370083

annalen der physik

Contents

Full text on our homepage at www.ann-phys.org

WILEY ONLINE LIBRARY

COVER PICTURE

Volume 525 | 2013 | No. 8–9

SPECIAL ISSUE

Precision Experiments and Fundamental Physics at Low Energies – Part II

edited by Klaus Blaum, Holger Müller and Nathal Severijns

Fundamental constants link seemingly different fields of physics and seemingly different quantities and measurement units. Consequently, they are of the utmost interest in metrology and it has been planned to redefine the kilogram by fixing the numerical value of the Planck constant. The paper by H. Bettin et al. (pp. 680-687) summarises the methods to measure the ratio between the Planck constant and a mass and reviews the determination of the Avogadro constant by counting the atoms in a silicon crystal highly enriched by the ^{28}Si isotope.

PHYSICS FORUM

Volume 525 | 2013 | No. 8–9

annalen der physik

REVIEW ARTICLES

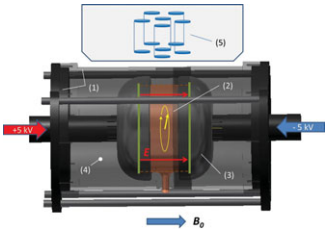

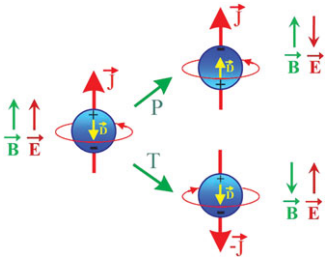

annalen der physik

Full text on our homepage at www.ann-phys.org

The various experiments on neutrino oscillation evidenced that neutrinos have indeed non-zero masses but cannot tell us the absolute neutrino mass scale. This scale of neutrino masses is very important for understanding the evolution and the structure formation of the universe as well as for nuclear and particle physics beyond the present Standard Model. The principle methods and experiments will be discussed in this short review.

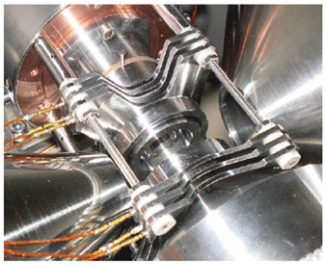

The experimental achievements and the current program with the LPCTrap device installed at the LIRAT beam line of the SPIRAL1-GANIL facility are presented. The device is dedicated to the study of the weak interaction at low energy by means of precise measurements of the β-ν angular correlation parameter. Technical aspects as well as the main results are reviewed.

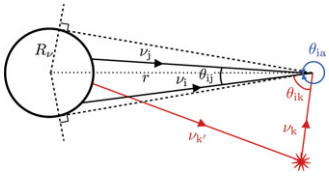

The current understanding of neutrino flavour conversion in media is summarized. The importance of this domain for astrophysical observations is emphasized. Examples are given of the fundamental properties that astrophysical neutrinos have uncovered, or might reveal in the future.

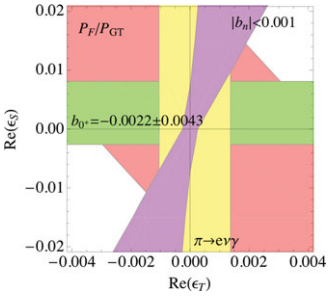

Precision measurements in nuclear β decay offer a sensitive window to search for new physics beyond the standard electroweak model. Experimental developments in nuclear and neutron β decay are discussed with emphasis on their projected goals to improve the limits on exotic weak couplings.

Volume 525 | 2013 | No. 8–9

annalen der physik

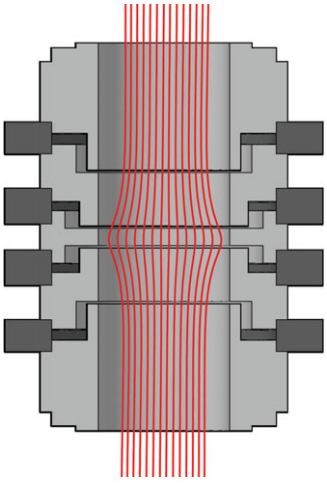

The magnetic moment of the electron, expressed by the *g*-factor in units of the Bohr magneton, is a key quantity in the theory of quantum electrodynamics (QED). Experiments using single particles confined in Penning traps have provided very precise values of the *g*-factor for the free electron as well as the electron bound in hydrogen-like ions. In this paper the status of these experiments is reviewed.

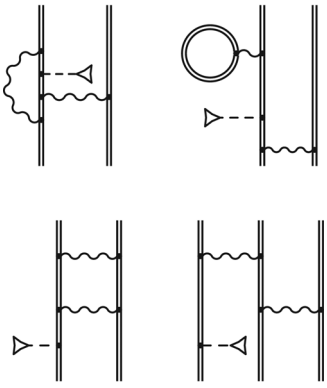

High-precision relativistic evaluations of various properties of tightly bound electrons in highly charged ions represent one of the challenging tasks in modern theoretical atomic physics. This review describes state of the art quantum electrodynamics (QED) calculations for highly charged ions, with a particular emphasis on tests of bound-state QED in the strong field regime.

FEATURE ARTICLE

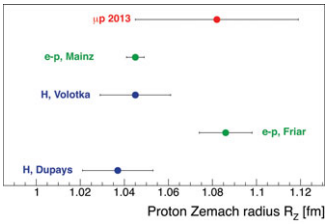

Muonic hydrogen (μp) is a very sensitive probe of the proton structure. Laser spectroscopy of two 2S-2P transitions in μp was used to determine both the Lamb shift and the hyperfine splitting of the 2S state in μp. The rms charge radius of the proton, $R_{ch} = 0.84087(39)$ fm, was extracted from the Lamb shift. The Zemach radius of the proton, $R_Z = 1.082(37)$ fm, was obtained from the 2S-hyperfine splitting.

annalen der physik

Full text on our homepage at www.ann-phys.org

ORIGINAL PAPERS

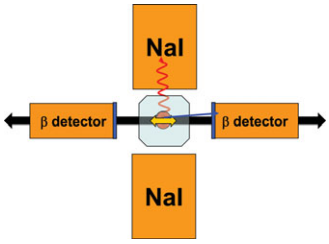

Lorentz invariance has been tested rather poorly in the weak interaction in comparison to the electromagnetic interaction. This work discusses which tests on the weak interaction may be relevant. In particular, it considers exploiting the spin degrees of freedom in β decay for testing rotational invariance.

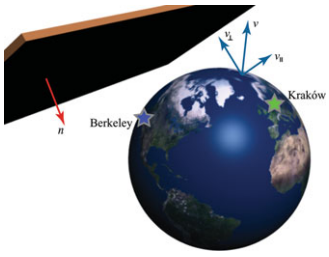

A novel experimental scheme enabling the investigation of transient exotic spin couplings is discussed. The scheme is based on synchronous measurements of optical-magnetometer signals from several devices operating in magnetically shielded environments in distant locations ($\gtrsim$100 km).

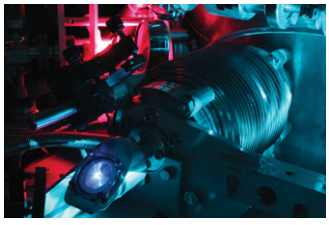

A precision spectroscopy of the 2S-4P transition in atomic hydrogen with a reproducibility of a few parts in 10^{12} is performed. This experiment should contribute to an improved determination of the Rydberg constant and the proton r.m.s. charge radius.

Volume 525 | 2013 | No. 8–9

annalen der physik

Contents

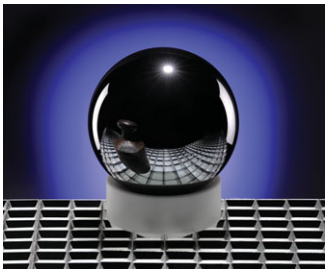

Fundamental constants link seemingly different fields of physics and seemingly different quantities and measurement units. They are of the utmost interest in metrology and it has been planned to redefine the kilogram by fixing the numerical value of the Planck constant. The paper summarises the methods to measure the ratio between the Planck constant and a mass and reviews the determination of the Avogadro constant.

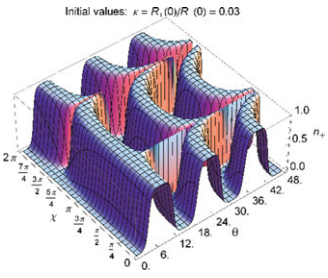

In Penning trap mass spectrometry the masses of stable or radioactive nuclides are determined by measuring their free cyclotron frequency via the resonant conversion of the magnetron into the cyclotron motional mode, which is induced by the interaction with some external radio-frequency field. In this paper we generalize the successful theoretical models describing the interconversion of the radial modes by quadrupolar and octupolar rf-fields to models for general 4*n*-polar fields.

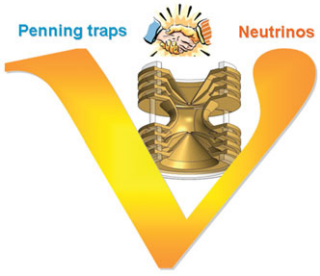

Rapidly developing neutrino physics has found in Penning-trap mass spectrometry a staunch ally in investigating a variety of fundamental problems. The most familiar are the absolute neutrino mass, possible existence of resonant neutrinoless double-electron capture and of keV-sterile neutrinos, and investigation of neutrino oscillations.

annalen der physik

Full text on our homepage at www.ann-phys.org

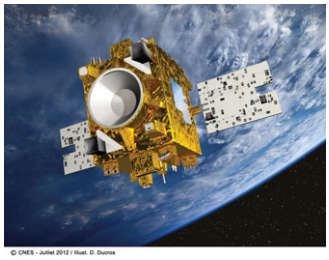

In 2016 the MICROSCOPE space mission is to test the Weak Equivalence Principle (WEP) with an accuracy of 10^{-15}. This paper addresses the scientific objective of the space mission and describes how the performance drives the specification.

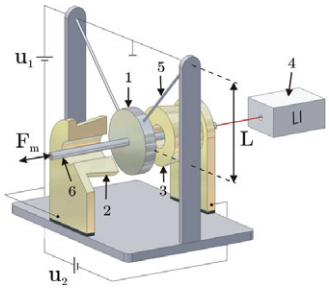

An experiment to test Newton's law of gravity at micro- and submicrometer distances using a nanonewton force facility at PTB and modern microtechnologies is proposed. It is anticipated that the proposed method can advance the search for non-Newtonian gravity forces via an enhanced sensitivity of 10^3 to 10^4 in comparison to current experiments at the micrometer length scale.

Annalen der Physik is indexed in Chemical Abstracts Service/SciFinder, COMPENDEX, Current Contents®/Physical, Chemical & Earth Sciences, FIZ Karlsruhe Databases, INIS: International Nuclear Information System Database, INSPEC, Journal Citation Reports/Science Edition, Science Citation Index Expanded™, Science Citation Index®, SCOPUS, Statistical Theory & Method Abstracts, VINITI, Web of Science® , Zentralblatt MATH/Mathematics Abstracts

Recognized by the European Physical Society

WILEY ONLINE LIBRARY
Early View publication on wileyonlinelibrary.com
(issue and page numbers not yet assigned;
citable using Digital Object Identifier – DOI)

Ann. Phys. (Berlin), 1–11 (2013) / DOI 10.1002/andp.201300048

annalen der physik

Review Article

Spin clocks: Probing fundamental symmetries in nature

Werner Heil[1,], Claudia Gemmel[1], Sergei Karpuk[1], Yuri Sobolev[1], Kathlynne Tullney[1], Fabian Allmendinger[2], Ulrich Schmidt[2], Martin Burghoff[3], Wolfgang Kilian[3], Silvia Knappe-Grüneberg[3], Allard Schnabel[3], Frank Seifert[3], and Lutz Trahms[3]*

Received 8 March 2013, revised 25 April 2013, accepted 2 May 2013
Published online 21 June 2013

The detection of the free precession of co-located ^{3}He/^{129}Xe nuclear spins (clock comparison) is used as ultra-sensitive probe for non-magnetic spin interactions, since the magnetic dipole interaction (Zeeman-term) drops out in the weighted frequency difference, i.e., $\Delta\omega = \omega_{\mathrm{He}} - \gamma_{\mathrm{He}}/\gamma_{\mathrm{Xe}} \cdot \omega_{\mathrm{Xe}}$ of the respective Larmor frequencies. Recent results are reported on searches for (i) short-range P- and T-violating interactions between nucleons, and (ii) Lorentz violating signatures by monitoring the Larmor frequencies as the laboratory reference frame rotates with respect to distant stars (sidereal modulation). Finally, a new experimental initiative to search for an electric dipole moment of ^{129}Xe (CP-violation) is discussed, which strongly benefits from the long spin-coherence times obtained, reaching $T^*_{2,He} >$ 100 h and $T^*_{2,Xe} >$ 8 h in case of ^{3}He and ^{129}Xe, respectively.

1 Features of frequency standards and clocks

Since Galileo Galilei and Christiaan Huygens invented the pendulum clock, time and frequency have been the quantities that we can measure with the highest precision. Since 1967 the Cs atomic clock defines our unit of time, the second, as the period during which a cesium-133 atom oscillates 9,192,631,770 number of cycles on the hyperfine clock transition $|F = 4, m_F = 0\rangle \rightarrow |F = 3, m_F = 0\rangle$ in the $6^2S_{1/2}$ atomic ground state. Cesium atomic clocks have been gradually improved to the point where modern cesium-fountain clocks realize the definition of the second with a relative uncertainty of about 4×10^{-16} [1]. In the near future, the cesium clock defining the fundamental timing reference will be replaced with an optical clock, since suppression of systematic effects shifting the frequency of a standard is greatly facilitated by the use of higher frequencies. Thanks to the incredible high relative accuracy of frequency determination, atomic clocks may touch the μHz range on an absolute scale, but will essentially not go far below.

To address fundamental questions in physics often associated with the experimental search for violation of fundamental symmetries in nature, much smaller frequencies or frequency shifts as a result of tiny changes in the clock transition must be tracked. From that point of view it is more appropriate to develop a "clock" that oscillates at low frequencies (∼10 Hz), but shows the same relative accuracy as a Cs atomic clock. Thus, frequency shifts in the pHz range caused by hypothetical interaction potentials might be accessible.

"Spin clocks" which are based on nuclear spin precession are the most promising approach to reach such sensitivity limits. The ,,spin clock" described here is based on the detection of free spin-precession of gaseous, nuclear spin-polarized ^{3}He or ^{129}Xe samples [2]. Like in a free induction decay (FID) measurement, the decay of the transverse magnetization is monitored and the Larmor frequency ω of the precessing sample magnetization is related to the magnetic field B_0 through $\omega = \gamma \cdot B_0$, where γ is the gyromagnetic ratio of the corresponding nucleus. Since this type of clock will preferably operate at low magnetic fields and thus at low frequencies, using a SQUID as magnetic field detector is appropriate due to its high sensitivity in that spectral range. The ^{3}He/^{129}Xe nuclear spins are polarized by means of optical pumping. Thus, the nuclear polarization obtained exceeds the Boltzmann polarization as used in typical NMR experiments by four to five orders of magnitude.

* Corresponding author E-mail: wheil@uni-mainz.de
[1] Johannes Gutenberg-Universität, Mainz, Germany
[2] Universität Heidelberg, Germany
[3] Physikalisch-Technische Bundesanstalt, Berlin, Germany

2 Co-located ^{3}He/^{129}Xe spin samples

Precision measurement of the Zeeman splitting in a two state system is important for magnetometry, as well as the search for physics beyond the standard model [3–11]. The most precise tests of new physics are often realized in differential experiments that compare the transition frequencies of two co-located clocks, typically radiating on their Zeeman or hyperfine transitions. The advantage of differential measurements is that they render the experiment insensitive to common systematic effects, such as uniform magnetic field fluctuations [8, 11]. That's why clock comparison experiments are often used to study fundamental symmetries of nature. In clock-comparison experiments, the Zeeman-term and thus any dependence on magnetic field fluctuations should drop out for the given combination of Larmor frequencies, i.e.,

$$\Delta\omega = \omega_{He} - \frac{\gamma_{He}}{\gamma_{Xe}} \cdot \omega_{Xe} \stackrel{!}{=} 0 \tag{1}$$

For the ^{3}He/^{129}Xe gyromagnetic ratios we take the literature values [12,13] given by $\gamma_{He}/\gamma_{Xe} = 2.75408159(20)$. The weighted frequency difference $\Delta\omega$ or its equivalent, the weighted phase difference $\Delta\Phi = \Phi_{He} - (\gamma_{He}/\gamma_{Xe}) \cdot \Phi_{Xe}$ is sensitive to anomalous frequency shifts due to non-magnetic spin interactions of type

$$V_{non-magn.} = \vec{a} \cdot \vec{\sigma} \equiv -\vec{\mu}_{PM} \cdot \vec{B}_{PM}, \tag{2}$$

where the interaction can formally be written like the magnetic potential energy $-\mu \cdot B$. Examples of non-magnetic spin interactions that can be addressed by clock-comparison experiments are:

- Search for spin-dependent short-range interactions [14]: $\Delta\omega_{sp} = V(r)/\hbar = c\vec{\sigma} \cdot \hat{r}/\hbar$
- Search for a Lorentz violating (LV) sidereal modulation of the Larmor frequency [15]: $\Delta\omega_{LV} = V/\hbar = \langle\tilde{b}\rangle \hat{\varepsilon} \cdot \vec{\sigma}/\hbar$
- Search for electric dipole moment (EDM) of Xenon [8]: $\Delta\omega_{EDM} = V/\hbar = -|d_{Xe}|\,\vec{\sigma} \cdot \vec{E}/\hbar$
- Search for a gravitoelectric dipole moment [16]: $\Delta\omega_{GDM} = V/\hbar = A\hat{g} \cdot \vec{\sigma}$

On a closer look, the effect of Earth's rotation is not compensated by co-magnetometry as well as frequency shifts due to the Ramsey-Bloch-Siegert shift [2]. The latter ones include "self shift", i.e., coupling of the precessing magnetic moments of the same spin species, as well as "cross talk", i.e., coupling of the ^{3}He and ^{129}Xe magnetic moments among each other. The time dependences of these frequency drifts, however, are well known. For example, the "self shift" induced frequency shift is directly proportional to the particular net magnetization, i.e., the signal amplitude given by $A_{He(Xe)} \cdot \exp(-t/T^*_{2,He(Xe)})$, and will show up in the weighted frequency and/or phase difference.

Thus, non-magnetic spin interactions can be extracted reasonably well from the measured weighted frequency difference $\Delta\omega$(t) if their preset time dependences (if possible) are almost orthogonal, such that the correlated error approaches the uncorrelated one.

According to the Cramer-Rao Lower Bound (CRLB) [2, 17], the accuracy by which the frequency of a damped sinusoidal signal can be determined is given by

$$\sigma_\nu \geq \frac{\sqrt{12}}{(2\pi) \cdot SNR_0 \cdot \sqrt{f_{BW}} \cdot T^{3/2}} \cdot \sqrt{C\left(T,\, T_2^*\right)} \tag{3}$$

SNR_0 denotes the initial signal-to-noise ratio, f_{BW} the bandwidth, and $C(T,T_2^*)$ describes the effect of exponential damping of the signal amplitude with the transverse relaxation time T_2^*. For observation times $T \leq T_2^*$, $C(T,\, T_2^*)$ is of order one. Thus, the sensitivity of a co-located ^{3}He/^{129}Xe spin clock strongly depends on the observation time T. Deviations from the CRLB power-law ($\sim T^{-3/2}$), due to noise sources inherent in the co-magnetometer have to be tested in Allan standard deviation plots [18] used to identify the power-law model for the phase noise spectrum. We could show, that the phase noise of our ^{3}He/^{129}Xe spin clock is Gaussian distributed (after subtraction of the frequency- or phase drifts, mentioned above) at least up to observation times of T≈50000s (see Fig. 1) – one essential requirement the derivation of CRLB is based on. Long spin coherence times T_2^* of macroscopic samples are therefore essential to reach the *pHz* sensitivity range. As an example: Let the initial signal-to-noise ratio be $\mathrm{SNR}_0 = 10000{:}1$ in a bandwidth of 1 Hz, we obtain by use of Eq. (3) a measurement sensitivity of $(\sigma_f)_0 \approx 2\,pHz$ for an observation time of $T = 1$ day ($T \leq T_2^*$). These values can easily be achieved for helium. However, practical constraints in sensitivity of our co-located ^{3}He/^{129}Xe spin sample are presently set by the spin-polarized xenon, where we measure a signal-to-noise ratio of $\mathrm{SNR}_0 \approx 2500{:}1$ and a T_2^* of $T_2^* \approx 7h$, typically. According to Eq. (3), that results in a reduced sensitivity of $\sigma_f \approx (10000/2500) \cdot \sqrt{C\,(24h,\, 7h)} \cdot (\sigma_f)_0 = 40\,pHz$. The measurement sensitivity can be further reduced if correlated errors dominate the statistical one (see section 4 and 5).

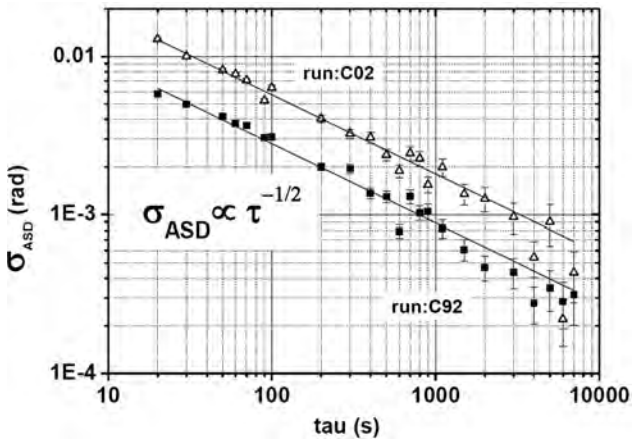

Figure 1 Allan standard deviations (ASD) of the residual phase noise measured in runs called C92 and C02 using nuclear spin precession of co-located ^{3}He and ^{129}Xe gas. In both runs the total observation time was $T = 52\,000$ s. For integration times τ beyond 4 s ($f_{BW} = 0.125$ Hz) the observed fluctuations decrease as $\propto \tau^{-1/2}$ indicating the presence of white phase noise. To fulfill the ASD statistics criteria $(N-1) >> 1$, only data for integration times $\tau \leq 7000$ s are shown, where we have $N-1 \geq 6$ with $N = T/\tau$.

3 Basic layout of experimental setup and principle of measurement

The instrumental setup is sketched in Figure 2 and discussed in detail in ref. [2]. Thus, only a rough description is given here: In our measurements, we use a SQUID vector magnetometer system, which was originally designed for biomagnetic applications inside the strongly magnetically shielded room BMSR-2 at PTB [19]. In all experiments reported below, the glass vessels containing the spin samples are placed directly below the dewar as close as possible to a SQUID sensor, which detects a sinusoidal B field change due to the spin precession of the gas atoms. Inside the μ-metal shielded room, a homogeneous magnetic field of about 400 nT was provided by two square coil pairs (B_x-coil and B_y-coil) which were arranged perpendicular to each other (see Fig. 2). The use of two coil pairs was chosen in order to manipulate the sample spins, e.g., $\pi/2$ spin-flip. The longitudinal relaxation times of helium and xenon in cells made from low-relaxation GE180 glass [20–22] have been measured before in a conventional NMR setup. For our uncoated glass cells, T_1-values were found reaching $T_{1,He} \approx 160$ h and $T_{1,Xe} \approx 11$ h, respectively.

Figure 3 shows the measured signal amplitude of the precessing co-located ^{3}He/^{129}Xe spins. The transverse relaxation times are extracted from the envelope of the decaying signal amplitudes for ^{3}He and ^{129}Xe with $T^*_{2,He} \approx 50 - 100$ h and $T^*_{2,Xe} \approx 5 - 8$ h at gas mixtures with pressures of ^{3}He : ^{129}Xe : N_2 $\approx$ (2 : 8 : 35) mbar, typically. Nitrogen had to be added to suppress ^{129}Xe relaxation due to the formation of long lived Xe-Xe van der Waals molecules [23]. At present, the relatively short $T_{1,Xe}$ wall relaxation time of ^{129}Xe limits the total observation time T of free spin-precession in our ^{3}He/^{129}Xe clock comparison experiments. Efforts to decrease considerably the ^{129}Xe wall-relaxation times are therefore essential.

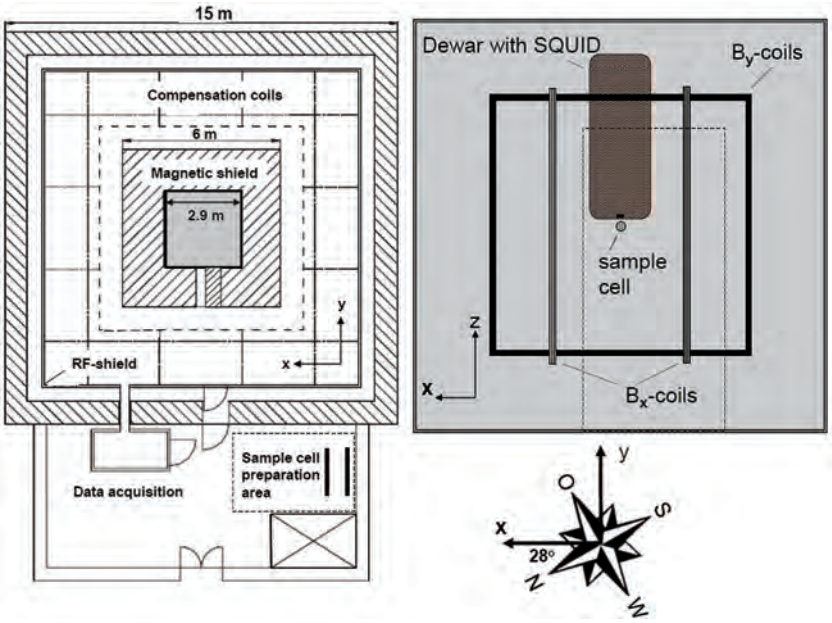

Figure 2 (Left) Horizontal cut view through building, shielded room and annex with data acquisition chamber and sample cell preparation area. The passive shielding factor of the BMSR-2 exceeds 10^8 above 6 Hz. With additional active shielding the room has a shielding factor of more than 7×10^6 down to 0.01 Hz. (Right): side view of inner room ($2.9 \times 2.9 \times 2.9$ m^3) seen from the door opening. The pneumatically driven sliding door is indicated by a rectangle with thin dashed lines. The black rectangle is the Dewar housing the SQUIDs. The big open rectangles are the B_x- and B_y-coil pairs. The small circle below the Dewar represents the sample cell (fixation not shown). The (−x)-axis of the chosen coordinate system points at an angle of $\rho = 28^0$ to the north-south direction.

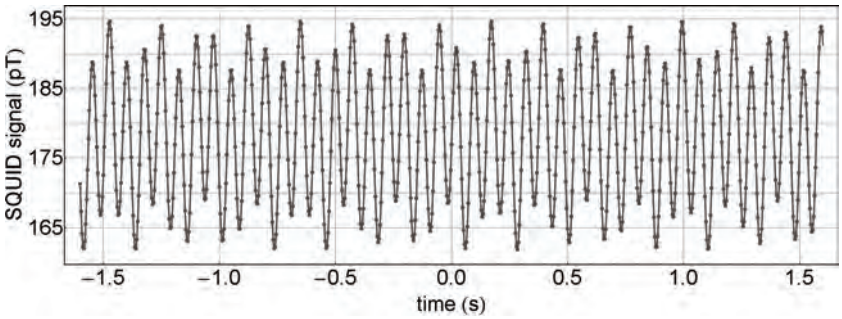

Figure 3 Typical sub-data set of 3.2 s length showing the recorded SQUID gradiometer signal of the precessing ^{3}He/^{129}Xe sample spins (sampling rate: $r_s = 250$ Hz). The uncertainty at each data point is ± 34 fT and therefore less than the symbol size. The signal amplitudes at the beginning of each run were typically $A_{He} \approx 13$ pT and $A_{Xe} \approx 4$ pT.

4 Constraints on spin-dependent short-range interaction between nucleons

Axions are light, pseudoscalar particles that arise in theories in which the Peccei-Quinn U(1) symmetry has been introduced to solve the strong CP problem [24]. They could have been produced in early stages of the Universe being attractive candidates to the cold dark matter that could compose up to ∼1/3 of the ingredients of the Universe [25]. Several constraints from astrophysics, cosmology, and laboratory experiments have been applied in order to prove or rule out the existence of the axion, i.e., constrain the axions mass m_a and/or its couplings. The mass range, in which axions are still likely to exist, could thus be narrowed down to a window reaching from μeV [26] up to some meV [27] (axion window). Most axion searches look for the conversion of a galactic [28], solar [29], or laboratory [30] origin axion into a photon in the presence of a static magnetic field. However, any axion or axion-like particle that couples with both scalar and pseudoscalar vertices to fundamental fermions would also mediate a parity and time-reversal symmetry violating force between a fermion f and the spin of another fermion f_σ, which is parameterized by a Yukawa-type potential with range λ and a monopole-dipole coupling given by [31]:

$$V_{sp}(\vec{r}) = \frac{\hbar^2 g_s^f g_p^{f_\sigma}}{8\pi m_{f_\sigma}} (\vec{\sigma} \cdot \hat{r}) \left(\frac{1}{\lambda r} + \frac{1}{r^2}\right) e^{-r/\lambda} \tag{4}$$

$\vec{\sigma}$ is the spin vector and λ is the range of the Yukawa-force with $\lambda = \hbar/(m_a \cdot c)$. Thus the entire axion window can be probed by searching for spin-dependent short-range forces in the range between 20μm and 0.1 m. g_s^f and $g_p^{f_\sigma}$ are dimensionless scalar and pseudoscalar coupling constants which in our case correspond to the scalar coupling of an axion-like particle to a nucleon ($g_s^f = g_s^N$) and its pseudoscalar coupling to a polarized bound neutron ($g_p^{f_\sigma} = g_p^n$). $\hat{r}$ is the unit distance vector from the bound neutron to the nucleon. The potential given by Eq. 4 effectively acts near the surface of a massive unpolarized sample („close" position) as a pseudomagnetic field and gives rise to a shift $\Delta\upsilon_{sp} = 2 \cdot V_\Sigma / h$ in the precession frequency of nuclear spin-polarized gases (^{3}He and ^{129}Xe), which according to the Schmidt model [32] can be regarded as an effective probe of spin-polarized bound neutrons. The potential V_Σ is obtained by integration of $V_{sp}(\vec{r})$ from Eq. (4) over the volume of the massive unpolarized sample averaged over the volume of the polarized spin-sample. Based on the analytical derivation of $V_{\Sigma,\infty}$ for disc-shaped spin- and matter samples with respective thicknesses D and d [33], we can derive the following expression for V_Σ given by

$$V_\Sigma = V_{\Sigma,\infty} \cdot \eta(\lambda) = \frac{N\hbar^2 g_s^N g_p^n \cdot \lambda^2}{4 \cdot m_n \cdot D} \cdot e^{-\Delta x/\lambda} \cdot \left(1 - e^{-D/\lambda}\right) \cdot \left(1 - e^{-d/\lambda}\right) \cdot \eta(\lambda) \tag{5}$$

$\eta(\lambda)$ takes account for the finite size in transverse direction of our cylindrical samples and Δx represents the finite gap between them. $\eta(\lambda)$ is determined numerically for our cylindrically shaped spin- and matter samples (D = 60 mm, $\varnothing_D$ = 58 mm; d = 70 mm, $\varnothing_d$ = 60 mm) at "close"-position (Δx = 2.2 mm). As unpolarized matter sample, a cylindrical BGO crystal ($Bi_4Ge_3O_{12}$, $\rho_{BGO} = 7.13$ g/cm^3) was used, which has a high nucleon number density, is a non-conductive material that shows low Johnson-Nyquist noise and is said to have an unusual magnetism-related behaviour in weak constant magnetic fields ($\chi_{mag} \approx 0$) [34]. In case of a non-zero spin-dependent axion fermion interaction, a shift $\Delta\nu_{sp}^w$ in the weighted frequency difference (Eq. 1) can be extracted from respective frequency measurements with the BGO in "close" and "distant" position given by

$$\Delta\upsilon_{sp}^w = \frac{2 \cdot V_\Sigma}{h} \cdot \left(1 - \frac{\gamma_{He}}{\gamma_{Xe}}\right) \tag{6}$$

Our result gives $\Delta\upsilon_{sp} = (-2.9 \pm 6.9 \pm 0.4)$ nHz (95% C.L.) for the measured pseudoscalar frequency shift. More details on data analysis and estimation of systematic errors can be found in ref. [35]. From the total

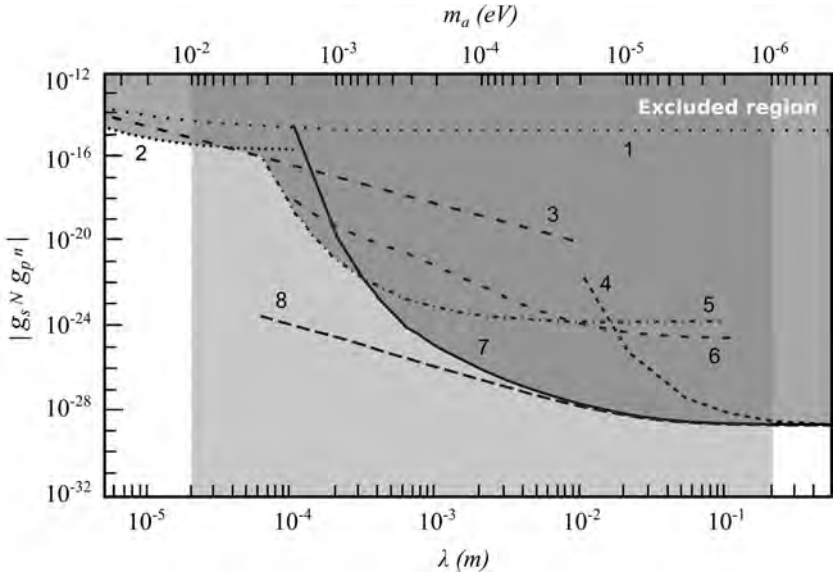

Figure 4 The experimental 95% confidence upper limit on $\left|g_s^N g_p^n\right|$plotted versus λ, the range of the Yukawa-force with $\lambda = \hbar/(m_a c)$. The axion window is indicated by the light grey area. (1): result of [36], (2): result of [37], (3): result of [38], (4): result of [39], (5): result of [40], (6): result of [41], (7): this experiment [35]. The expected results for $\Delta x \approx$ 0 mm (8) using the same data set demonstrates the gain in measurement sensitivity for $\lambda \leq 10^{-3}$ m by reducing the minimal gap between the polarized and unpolarized matter sample (see Eq. (5)). See [14] for bounds on the pseudoscalar short-range force between polarized electrons and unpolarized nucleons. In (4), the relative precession frequency of Hg and Cs magnetometers were measured as a function of the position of two lead masses with respect to an applied magnetic field. Similar to our experiment, a magnetically shielded co-magnetometer cell containing spin-polarized ^{129}Xe and ^{131}Xe was used in (5), measuring the frequency ratio of the two species by recording their FID. (2) uses polarized ultracold neutrons and could improve the limits at the λ length scale of $\lambda \approx 20$ μm.

error $\delta(\Delta\nu_{\rm sp}) = \pm 7.3$ nHz we can derive exclusion bounds for $\left|g_s^N g_p^n\right|$using Eq. 2 and $\left|\delta\left(\Delta\upsilon_{sp}\right)\right| \geq 2 \cdot V_\Sigma / h$ which are shown in Fig. 4. We have substantially improved the bounds on a spin-dependent short-range interaction between polarized (bound) neutrons and unpolarized nucleons over most of the axion window, tightening existing constrains on axion-like particles heavier than 20 μeV by up to four orders of magnitudes. And there are clear strategies on how to improve our experimental sensitivity: For $\Delta x \approx 0$ mm, i.e., direct contact of the ^{3}He/^{129}Xe spin sample with the unpolarized mass (BGO), our present measurement sensitivity will significantly increase for $\lambda \leq 10^{-3}$ m (see Fig. 4). This can be accomplished by rotating the whole arrangement with respect to the applied magnetic field or vice versa. Since $V_{sp}(\vec{r}) \propto \vec{\sigma} \cdot \hat{r}$, the effect changes its sign (rotation by π) for the different orientations. Possible changes of magnetic field gradients which may mimic a pseudoscalar frequency shift or even compensate the effect we are looking for drop out to first order due to co-magnetometry. The same is true for field-gradient induced changes of the T_2^*-times , provided the effect one is looking for leads to an additional *linear* phase drift, such as $\Delta\Phi_{sp} = 2\pi\nu_{sp}^w \cdot t$ [35] or $\Delta\Phi_{GDM} = 2\pi\nu_{GDM}^w \cdot t$ as it is the case with the search for a gravitoelectric dipole moment (see section 7).

5 Limit on Lorentz and CPT violation of the bound neutron using a free precession ^{3}He/^{129}Xe co-magnetometer

A great number of laboratory experiments have been designed to detect diminutive violations of Lorentz invariance. Among others, the Hughes-Drever-like experiments [42, 43], have been performed to search for anomalous spin coupling to an anisotropy in space using electron and nuclear spins with steadily increasing sensitivity [44,45]. Lorentz violating theories should generally predict the existence of privileged reference systems. In contrast with the situation at the end of the 19th century, we have a rather unique choice nowadays for such a "preferred inertial frame", i.e., the frame where the dipole anisotropy of the Cosmic Microwave Background (CMB) vanishes. Trying to measure an anomalous coupling of spins to a relic background field which permeates the Universe and points in a preferred direction in

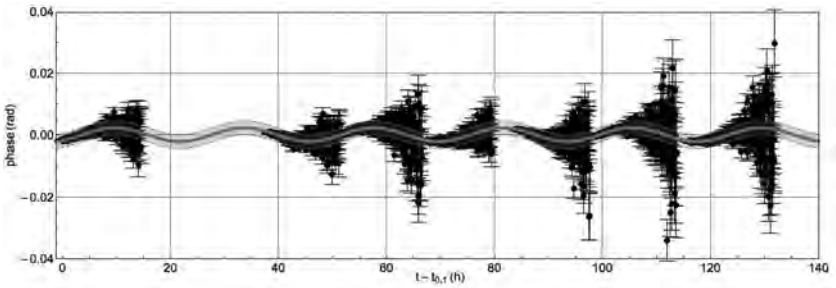

Figure 5 Sequence of phase residuals (j = 1,..,7) with fit results for the sidereal phase modulation (see Eq. 8). The RMS magnitude of the extracted sidereal phase amplitude $\Phi_{SD} = \sqrt{a_s^2 + a_c^2}$ is Φ_{SD} = (2.25 ± 2.29) mrad (95% CL).

space as a sort of New Aether wind is a modern analogue of the original Michelson-Morley experiment. The theoretical framework presented by A. Kostelecky and colleagues parameterizes the general treatment of CPT- and Lorentz violating effects in a Standard-Model extension (SME) [46].

To determine the leading-order effects of a Lorentz violating potential *V*, it suffices to use a non-relativistic description for the particles involved given by [47]

$$V = -\tilde{b}_J^w \cdot \sigma_J^w \quad (\text{with : J = X, Y, Z; w = e, p, n}) \tag{7}$$

Like in [15,45], we search for sidereal variations of the frequency of co-located spin species while the Earth and hence the laboratory reference-frame rotates with respect to a relic background field. The observable to trace possible tiny sidereal frequency modulations is the combination of measured Larmor frequencies (see Eq. 1) and the weighted phase differences, respectively. In March 2009, we performed a measurement consisting of 7 runs in series, each with duration of 13 hours at least.

LV spin interactions – if they exist – would result in a temporal change of the phase residuals after subtraction of the general phase drifts ($\sum_{j=1}^{7} \Phi_{fit}^{(j)}(t)$). For that, a piecewise fit function was defined, which is a combined fit to all seven runs, now including the parameterization of the hypothetic sidereal phase modulation

$$\Delta\Phi_{fit}^{SD}(t) = \sum_{j=1}^{7} \Phi_{fit}^{(j)}(t) + \{a_s \cdot \sin\left(\Omega_{SD}\left(t - t_{0,1}\right) + \varphi_{SD}\right) - a_c \cdot \cos\left(\Omega_{SD}\left(t - t_{0,1}\right) + \varphi_{SD}\right)\} \tag{8}$$

Ω_{SD} is the angular frequency of the sidereal day and φ_{SD} represents the phase offset of the sidereal modulation at the local sidereal time $t_{SD} = 0.4053$ (units of sidereal day) at the beginning $t_{0,1}$ of the first run with $\varphi_{SD} = 2\pi \cdot t_{SD}$. From that, the RMS magnitude of the sidereal phase amplitude $\Phi_{SD} = \sqrt{a_s^2 + a_c^2}$, yielding Φ_{SD} = (2.25 ± 2.29) mrad (95% CL) could be extracted [48] (see Fig. 5). This result is consistent with no Lorentz- and CPT-violating effects. In terms of the SME [47] we can express Φ_{SD} according to

$$\Phi_{SD} = \frac{2\pi}{\Omega_{SD}} \cdot \delta v_\perp \quad with \quad 2\pi\,|\delta v_\perp| \cdot \hbar = \left|2 \cdot (1 - \gamma_{He}/\gamma_{Xe}) \cdot \sin\chi \cdot \tilde{b}_\perp^n\right| \tag{9}$$

χ is the angle between the Earth's rotation axis and the quantization axis of the spins ($\chi = 57^0$). Within the Schmidt model, the valence neutron of ^{3}He and ^{129}Xe determines the spin and the magnetic moment of the nucleus. Thus, ^{3}He/^{129}Xe co-magnetometer is sensitive to the bound neutron parameter $\tilde{b}_\perp^n$. With $\left|\tilde{b}_\perp^n\right| < 3.7 \times 10^{-32}$ GeV (95% CL) we deduced an upper limit on neutron spin coupling to possible Lorentz and CPT violating background tensor fields. Together with the recent result from [45] using a K-^{3}He co-magnetometer, where one could further increase the sensitivity by a factor of 5 (95% CL), the tightest constrains on the SME parameters are presently set on the neutron sector.

The present sensitivity of our ^{3}He/^{129}Xe co-magnetometer is limited by the correlated error, which is about a factor of 50 bigger than the uncorrelated error on a_s and a_c. This is caused by a piecewise similar time structure of $\Phi_{fit}^{(j)}(t)$ and the sidereal phase modulation in the fit function of Eq. 8. In order to overcome this obvious limitation, the relatively short transversal relaxation time of ^{129}Xe has to be increased. In March 2012 a new LV-run was performed (data analysis ongoing). This time the measurement periods of coherent spin precession could be extended up to 26 h, i.e., covering the full period of a possible sidereal phase modulation. In addition, the SNR_0 of xenon could be improved thanks to the higher degrees of polarization ($P_{Xe} \approx 40\%$).

6 Search for an electric dipole moment of ^{129}Xe

The existence of electric dipole moments (EDMs) of atoms or the neutron would imply a breakdown of both parity P and time-reversal symmetry T and, through the CPT theorem, a breakdown in CP, the combined symmetries of charge conjugation C and parity P. P

violation is a well-known feature of the weak interaction. The only known example of CP (and hence T) violation, discovered more than 30 years ago [49], has been found in the decay of the neutral K_o meson and, recently, in heavier neutral B-meson decay channels [50]. The Standard Model (SM) of weak interactions gives the basis for describing the observed CP violation [51], in which CP violation occurs as a phase factor δ_{KM}, being one of the free parameters of the weak quark-mixing matrix (CKM-matrix). In the leading order, δ_{KM} only causes CP violation in flavor changing processes. Since this complex phase factor only enters in matrix elements where heavier quarks are involved, SM contributions to particle EDMs in particular the neutron EDM are of second order in the weak interaction coupling constants and hence are very small being of order 10^{-31} to 10^{-33} e cm. SM contributions to the electron EDM occur at the three loop level and are $d_e \approx 10^{-37} - 10^{-40}$ e cm [52]. Thus, the predicted EDMs are at least four orders of magnitude below the present experimentally established limits and a search for a permanent EDM is still hailed as an unambiguous test of CP violation beyond the SM. Extensions to the SM, such as additional Higgs fields, right handed currents, or super symmetric partners, give rise to dipole contributions which are of first order. These are necessarily much larger and for the neutron EDM typically of the order 10^{-27} to 10^{-26} e cm [53].

EDMs are also connected with another fundamental puzzle: the Baryon Asymmetry of the universe. The asymmetry is generally described by the ratio r_B, between the number of baryons and the number of photons in the universe today. This ratio can be related to the number of baryons and antibaryons at the time of baryon freeze-out in baryogenesis models [54]. The observations indicate that $r_B \sim 6 \times 10^{-10}$, which is about 9 orders of magnitude larger than expected in baryogenesis models based on the SM. A possible explanation for this huge discrepancy was suggested by Sakharov [55]. As a consequence, it is expected that observations and theory could be reconciled if additional sources of CP violation are at work.

Historically, the non-observation of particle EDM has ruled out more speculative models than any other single experimental approach in particle physics. At present, and in future, EDM precision measurements will continue to constrain severely proposed models of new physics. In principal there is no preferred system to search for an EDM. Investigation of different systems is required to discriminate between various EDM sources: intrinsic leptonic, intrinsic hadronic, those resulting from interactions in composite particles, or, possible CP-odd forces between constituents in, e.g., atoms. In composite systems, such as molecules and atoms, the coupling to, and hence the visibility of, constituent EDMs may be significantly enhanced due to internal fields. The highest sensitivity to fundamental CP-violation today comes from measurements on the neutron [56], the diamagnetic ^{199}Hg atom [57] (predominantly sensitive to the nuclear EDM (η)) and the paramagnetic ^{205}Tl atom [58] or YbF-molecule [59] (predominantly sensitive to the electron EDM (d_e)). All of the effects mentioned above become much more prominent for heavy atoms, and so an atomic EDM tends to scale as Z^2 or Z^3. For this reason atomic EDM measurements can set much more stringent limits on certain CP violating processes than neutron EDM measurements can. The most precise EDM limit was measured in the diamagnetic atom ^{199}Hg ($d_{Hg} < 3.1 \times 10^{-29}$ ecm).

Several different theorists [60, 61] have gone beyond this order of magnitude estimate and predicted quantitative values for these CP-violating coefficients (d_e, C_T,C_S,C_{PS}, and η). From these, an expression for d_{Xe} can be found

$$d_{Xe} = 10^{-3} d_e + 5.2 \times 10^{-21} C_T + 5.6 \times 10^{-23} C_S + 1.2 \times 10^{-23} C_{PS} + 6.7 \times 10^{-26} \eta \quad (10)$$

Such coefficients are generally determined to perhaps 30%, given the complicated theory involved. With our initiative to search for a Xe-EDM using co-located ^{3}He/^{129}Xe spin clocks, we want to get more stringent limits than the ^{199}Hg experiment. The key issue for a high-sensitivity EDM detection are the long spin-coherence times: Let T_m be the measurement time. A repetition (n) of short measurements of free spin precession (T) with $T_m = n \cdot T$ results in a final accuracy of frequency determination of (see Eq. 3)

$$\delta\nu_{final} = \frac{\sigma_\nu}{\sqrt{n}} \propto \frac{1}{T^{3/2}} \cdot \frac{1}{\sqrt{n}} = \frac{n}{T_m^{3/2}}, \quad (11)$$

whereas a measurement of uninterrupted precession gives $\delta\nu_{final} \propto 1/T_m^{3/2}$. Hence, the gain in sensitivity is $g = T_m/T$. In the ^{199}Hg-Experiment [57], the possible EDM frequency shift was extracted from the decay of free spin precession of the Hg-atoms using an optical detection method with $T = T_2^* \approx 180s$ being the characteristic time constant for the exponential damping of the signal amplitude, there. Since the limiting time constant for coherent spin-precession of our ^{3}He/^{129}Xe comagnetometer is presently set by $T_2^*$of xenon with $T \equiv T_m = T_{2,Xe}^* \approx 8h$, our gain in EDM sensitivity is $g \approx 160$ over a measurement period of $T_m \approx 8$h. Then, like in the

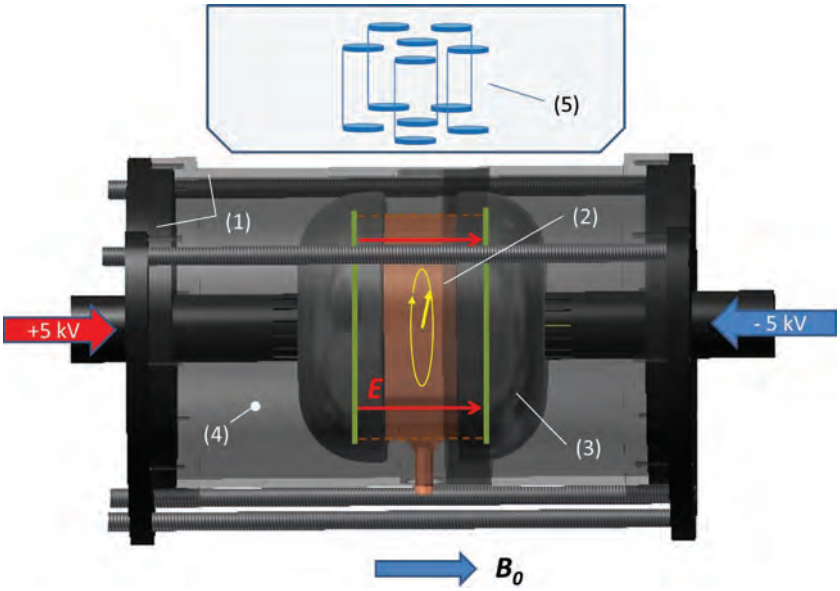

Figure 6 Sketch of experimental setup to measure the EDM of ^{129}Xe. (1) cylindrical container made out of conducting plastic which is at ground potential, (2) ^{3}He/^{129}Xe gas container made out of a cylindrical glass tube (ø = 10 cm, l = 5 cm) with silicon discs used as lids. Not shown, stem with glass valve to fill in the polarized gases together with SF_6 which is used as buffer gas (^{3}He:^{129}Xe:SF_6 ≈ (2:8:50) mbar), (3) HV-feedthrough and electrodes (conducting plastic), (4) SF_6 gas at ∼ 1 bar to minimize leakage currents, (5) dewar housing low-temperature SQUIDs; gradiometric sensor combinations (6 in total) are used in order to suppress environmental disturbance fields like vibrational modes.

^{199}Hg-Experiment, the measurement sensitivity will only scale with $1/\sqrt{n}$.

Fig. 6 shows the sketch of the experimental setup. Again, the weighted frequency difference (Eq. 1) is measured both for electric field parallel and antiparallel to the applied B_0-field, i.e., $\Delta\upsilon^w_{\uparrow\uparrow}$ and $\Delta\upsilon^w_{\uparrow\downarrow}$ with

$$\begin{aligned}\Delta\upsilon^w_{\uparrow\uparrow} &= \Delta\upsilon^{d_{He}}_{\uparrow\uparrow} - (\gamma_{He}/\gamma_{Xe})\cdot\Delta\upsilon^{d_{Xe}}_{\uparrow\uparrow} \approx -(\gamma_{He}/\gamma_{Xe})\cdot\Delta\upsilon^{d_{Xe}}_{\uparrow\uparrow}\\ \Delta\upsilon^w_{\uparrow\downarrow} &= \Delta\upsilon^{d_{He}}_{\uparrow\downarrow} - (\gamma_{He}/\gamma_{Xe})\cdot\Delta\upsilon^{d_{Xe}}_{\uparrow\downarrow} \approx -(\gamma_{He}/\gamma_{Xe})\cdot\Delta\upsilon^{d_{Xe}}_{\uparrow\downarrow}.\end{aligned} \tag{12}$$

Using $h\cdot\left(\Delta\upsilon^{d_{Xe}}_{\uparrow\uparrow} - \Delta\upsilon^{d_{Xe}}_{\uparrow\downarrow}\right) = 4\cdot E\cdot d_{Xe}$, the sensitivity limit on d_{Xe} can be extracted to be

$$|d_{Xe}| \le \frac{h\cdot\left(\Delta\nu^w_{\uparrow\uparrow} - \Delta\nu^w_{\uparrow\downarrow}\right)}{4\cdot E\cdot(\gamma_{He}/\gamma_{Xe})}. \tag{13}$$

A first analysis of our March 2012 run shows, that we can measure the spin precession frequencies with an accuracy of $\Delta\nu \approx 0.1$ nHz per day. Even for a moderate electrical field of E = 2kV/cm applied between the lids (silicon semiconductors) of a cylindrical glass vessel containing the ^{3}He/^{129}Xe spin sample, we will reach a xenon EDM sensitivity of $|d_{Xe}| \le 1.8\times10^{-29} ecm/\sqrt{day}$. Thus, an overall sensitivity of $|d_{Xe}| \approx 10^{-30}$ ecm is envisaged, after accumulation of sufficient statistics corresponding to ∼100 days of data acquisition, typical for EDM-type experiments.

Because the intrinsic sensitivity of ^{129}Xe to underlying physics of CP-violation is less than for ^{199}Hg, this experiment must in fact have much better rejection of systematics than the ^{199}Hg experiment has now, in order to get a better ultimate sensitivity. A worrisome source of magnetic fields correlated with the high voltage are steady state leakage currents flowing between the electrodes of the cell. Using a co-magnetometer (absent in the ^{199}Hg experiment) leakage currents can be suppressed much more efficient than in spatially separated cell geometries, in particular if higher magnetic multipoles are involved. Nonetheless, we have independent measures to monitor the leakage currents. Our SQUID gradiometers (6 in total) are very sensitive devices and only react on magnetic field changes. Thus, we will use them to monitor the leakage currents, too. The ^{199}Hg-experiment has some potential systematic effects which are absent in our experiment. For example light induced false EDM effects: DC and AC stark shift, gradient in light intensity coupled to a magnetic field gradient [57]. Furthermore, possible problems with geometric phases due to motional magnetic fields and applied field gradients [62] have to be considered. ^{3}He is most sensitive to false EDM effects due to geometric phases, but these effects can be kept low ($d^{geo}_{f,He} \approx 3\times10^{-31}$ ecm), since SF_6 (∼50 mbar) is used as buffer gas. We even have the flexibility to vary the buffer-gas pressure, the cell radius, and the magnetic field B_0. To summarize: We do see much less potential systematic effects with our ^{3}He/^{129}Xe-comagnetometer arrangement.

7 Search for a coupling of the Earth's gravitational field to nuclear spins

The equivalence between the gravitational and inertial masses of unpolarized matter has been verified to high

precision. Very little is known, however, about the microscopic properties of gravity, and there remains the possibility that sensitive experiments will uncover evidence for symmetry violations or other new phenomena associated with this interaction. In particular, the notion that polarized objects may violate the equivalence principle through a coupling of intrinsic spin to gravity has been considered by a number of authors [63–68]. An interaction of type $V_{GDM}/\hbar = A \cdot \hat{g} \cdot \vec{\sigma}$, where $\vec{\sigma}$ is the spin operator of the nucleus, $\hat{g}$ is the unit vector pointing towards the center of the Earth, and $A' = A \cdot \hbar$ is the spin-dependent component of the gravitational energy , violates both parity and time-reversal symmetry and could result, for example, from a breakdown of the equivalence principle for spin-polarized matter. In [16], an upper limit on A′ with $A' < 2.2 \cdot 10^{-21}$ eV corresponding to $\Delta\upsilon_{GDM} < 0.53\,\mu Hz$ was obtained by measuring the ratio of nuclear spin-precession frequencies of ^{199}Hg and ^{201}Hg atoms for two orientations of magnetic field relative to the Earth's gravitational field. The same measuring principle is applicable to the co-located ^{3}He/^{129}Xe spin-sample, where we expect a considerably higher measurement sensitivity of ∼0.1 nHz/day (see section 6). The essential requirement is that the change of magnetic field doesn't induce false effects. That mainly concerns field gradient dependent correlated changes of the T_2^*-times of ^{3}He and ^{129}Xe, discussed already in section 3. Although the linear phase drift $\Delta\Phi_{GDM} = 2\pi\nu^{w}_{GDM} \cdot t$ is insensitive to possible changes of T_2^*, the impact of the T_2^*-dependence of higher order terms on $\Delta\Phi_{GDM}$ has to be taken into account above a certain sensitivity level.

In order to collect first experiences, feasibility studies were performed by adjusting the currents in the twin coil set shown in Fig. 1. The direction of the static field could be oriented in any direction within the horizontal plane, while its strength was left unchanged. With this set-up, the precession decay of hyperpolarized ^{3}He gas was measured for various field orientations α. Fig. 7 shows the variation of the T_2^*-relaxation times that were obtained from these measurements when the field orientation was varied in steps of 45°. The data show a clear and reproducible periodicity with 2π that is emphasized by fitting a function with a circular periodicity to the data. At $\alpha = 70°$, both ^{3}He and ^{129}Xe exhibit the longest $T_2{}^*$, indicating that with this orientation of the instrumental field, the gradient of the applied field compensates best the gradient of the residual field inside BMSR-2. There are several strategies on how to reduce the "strong" T_2^*variation: a) use field orientations, even if they are not exactly opposed, where the T_2^*-values are equal (see Fig. 7) and/or b) use additional field-gradient coils to match the field gradients across the sample cell for the selected field orientations.

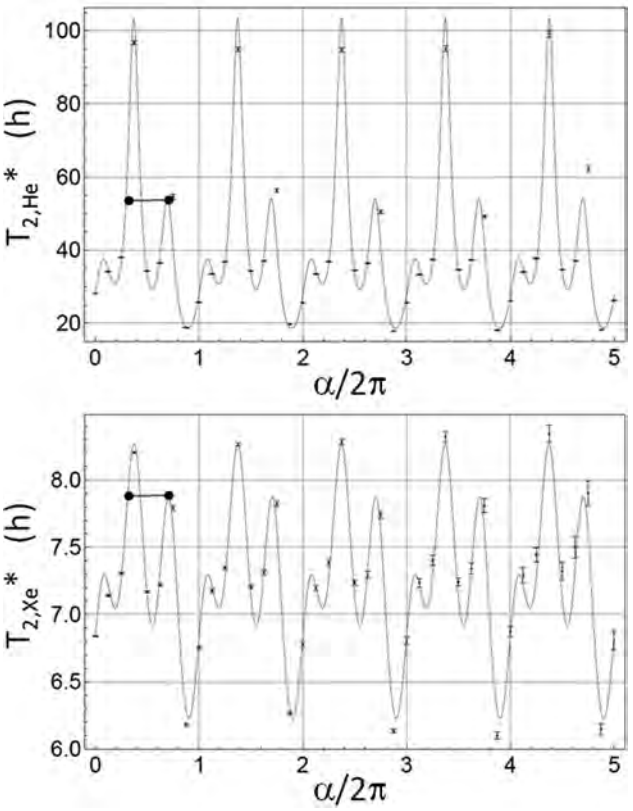

Figure 7 Dependence of the measured transversal relaxation time $T_2{}^*$ of ^{3}He and ^{129}Xe on the orientation of the applied field. The solid line is a fit-function with circular periodicity to guide the eyes. The field was slowly rotated ($d\alpha/dt << \omega_{He(Xe)}$) in steps of 45° that took about 1 min. Then $T_2{}^*$ was measured by monitoring the exponential decay of the precessing spins. During the $T_2{}^*$ measurements (∼15 min), the direction of the field has not changed. The drawn bar indicates field orientations which differ by $\Delta\alpha = 145°$ and provide the same $T_2{}^*$ values.

8 Conclusion

Nuclear spin clocks, based on the detection of free spin precession of gaseous, nuclear polarized ^{3}He or ^{129}Xe samples with a SQUID as magnetic flux detector can be used as ultra-sensitive probe for non-magnetic spin interactions, since the magnetic dipole interaction (Zeeman-term) drops out in case of co-located spin samples. With the long spin-coherence times, measurements of uninterrupted precession of T ∼ 1 day can be achieved at the present stage of

investigation. Together with a signal-to-noise ratio which by far exceeds 1000:1 in a bandwidth of 1 Hz, thanks to an exceptional low system noise inside BMSR-2, the sensitivity to trace tiny frequency changes reaches ~ 0.1 nHz/day.

We reported on recent results on the search for a new spin-dependent P- and T-violating interaction between nucleons mediated by light, pseudoscalar bosons (exclusion plot) and the search for a LV sidereal modulation of the Larmor precession (upper limit) that sets the tightest constrains on the SME parameters of the bound neutron. Finally, our challenging project to measure the EDM of ^{129}Xe down to a sensitivity limit of $|d_{Xe}| \approx 10^{-30}$ ecm was presented. All experimental investigations will benefit considerably by the increase of the still moderate longitudinal wall relaxation time T_1 of xenon ($\sim$ 11h), which is the bottleneck to reach T_2^*-times $>$ 100 h as it is the case for ^{3}He, already.

References

[1] T. E. Parker, Metrologia **47**, 1 (2010).
[2] C. Gemmel, W. Heil, S. Karpuk et al., Eur. Phys. J. D **57**, 303 (2010) and references therein.
[3] V. W. Hughes, H. G. Robinson, and V. Beltran-Lopez, Phys. Rev. Lett. **4**, 342 (1960).
[4] J. D. Prestage, J. J. Bollinger, W. M. Itano et al., Phys. Rev. Lett. **54**, 2387 (1985).
[5] S. K. Lamoreaux, J. P. Jacobs, B. R. Heckel et al., Phys. Rev. Lett. **57**, 3125 (1986).
[6] T. E. Chupp, R. J. Hoare, R. A. Loveman et al., Phys. Rev. Lett. **63**, 1541 (1989).
[7] C. J. Berglund, L. R. Hunter, D. Krause et al., Phys. Rev. Lett. **75**, 1879 (1995).
[8] M. A. Rosenberry, T. E. Chupp, Phys. Rev. Lett. **86**, 22 (2001).
[9] M. V. Romalis, W. C. Griffith, J. P. Jacobs et al., Phys. Rev. Lett. **86**, 2505 (2001).
[10] A. G. Glenday, C. E.Cramer, D. F. Phillips et al., Phys. Rev. Lett. **101**, 261801 (2008).
[11] G. Vasilakis, J. M. Brown, T. W.Kornack et al., Phys. Rev. Lett. **103**, 261801 (2009).
[12] International council for Science: Committee on Data for Science and Technology (CODATA). www.codata.org (2007).
[13] M. Pfeffer and O. Lutz, J. Magn. Res. A **108**, 106 (2005).
[14] S. A. Hoedl, F. Fleischer, E. G. Adelberger et al., Phys. Rev. Lett. **106**, 041801 (2011).
[15] D. Bear, R. E. Stoner, R. L. Walsworth et al., Phys. Rev. Lett. **85**, 5038 (2000).
[16] B. J. Venema, P. K. Majumber, S. K. Lamoreaux et al., Phys. Rev. Lett. **68**, 135 (1992).
[17] S. M. Kay, Fundamentals of Statistical Signal Processing: Estimation Theory (Prentice Hall, New Jersey, 1993), Vol. **I**.
[18] J. A. Barnes, A. R. Chi, L. S. Cutler et al., IEEE Trans. Instrum. Meas. **20**, 105 (1971).
[19] J. Bork, H.-D. Hahlbohm, R. Klein, A. Schnabel, Proc. Biomag 2000, 970 (2000).
[20] J. Schmiedeskamp, W. Heil, E. W. Otten et al., Eur. Phys. J. D **38**, 427 (2006).
[21] A. Deninger, W. Heil, E. W. Otten et al., Eur. Phys. J. D **38**, 439 (2006).
[22] J. Schmiedeskamp, H.-J. Elmers, W. Heil et al., Eur. Phys. J. D **38**, 445 (2006).
[23] B. C. Anger, G. Schrank, A. Schoeck et al., Phys. Rev. A **78**, 043406 (2008).
[24] C. D. Peccei and H. R. Quinn, Phys. Rev. Lett. **38**, 1440 (1977).
[25] J. Jaeckel and A. Ringwald, Annu. Rev. Nucl. Part. Sci. **60**, 405 (2010).
[26] S. J. Asztalos, R. F. Bradley, L. Duffy et al., Phys. Rev. D **69**, 011101(R) (2004).
[27] G. Raelt, Annu. Rev. Nucl. Part. Sci. **49**, 163 (1999).
[28] S. Asztalos, G. Carosi, C. Hagmann et al., Phys. Rev. Lett. **104**, 041301 (2010).
[29] E. Arik, S. Aune, D. Autiero et al., J. Cosmol. Astropart. Phys. **02**, 008 (2009).
[30] K. Ehret, M. Frede, S. Ghazaryan et al., Phys. Lett. B **689**, 149 (2010).
[31] J. E. Moody and F. Wilczek, Phys. Rev. D **30**, 130 (1984).
[32] Th. Schmidt, Zeitschrift für Physik A, Hadrons and Nuclei **106**, 358 (1937).
[33] O. Zimmer, Phys. Lett. B **38**, 685 (2010).
[34] S. Yamamoto, K. Kuroda, and M. Senda, IEEE Transactions On Nuclear Science, **50**, 1683 (2003).
[35] K. Tullney, F. Allmendinger, M. Burghoff et al., arXiv: 1303.6612 (2013).
[36] S. Baeßler, V. V. Nesvizhevsky, K. V. Protasov, and A. Yu. Voronin, Phys. Rev. D **75**, 075006 (2007).
[37] T. Jenke, G. Cronenberg, P. Geltenbort et al., arXiv: 1208:3875v1 (2012).
[38] A. P. Serebrov, O. Zimmer, P. Geltenbort et al., JETP Letters **91**, 6 (2010).
[39] A. N. Youdin, D. Krause, Jr., K. Jagannathan et al., Phys. Rev. Lett. **77**, 2170 (1996).
[40] M. Bulatowicz, R. Griffith, M. Larsen et al., arXiv: 1301.5224v1 (2013).
[41] P.-H. Chu, A. Dennis, C. B. Fu et al., Phys. Rev. D **87**, 011105(R) (2013).
[42] V. W. Hughes, H. G. Robinson, and V. Beltran-Lopez, Phys. Rev. Lett. **4**, 342 (1960).
[43] R. W. P. Drever, Philosophical Magazine **6**, 683 (1961).
[44] S. K. Lamoreaux, J. P. Jacobs, B. R. Heckel et al., Phys. Rev. Lett. **57**, 3125 (1986).
[45] J. M. Brown, S. J. Smullin, T. W. Kornack, and M. V. Romalis, Phys. Rev. Lett. **105**, 151604 (2010).
[46] D. Colladay and V. A. Kostelecký, Phys. Rev. D. **58**, 116002 (1998).
[47] V. A. Kostelecký and C. D. Lane, Phys. Rev. D. **60**, 116010 (1999).
[48] C. Gemmel, W. Heil, S. Karpuk et al., Phys. Rev. D **82**, 111901 (2010).

[49] C. J. Christenson, J. W. Cronin, V. L. Fitch, and R. Turlay, Phys. Rev. Lett. **13**, 138 (1964).
[50] J. Charles, A. Höcker, H. Lacker et al., Eur. Phys. Journal C **41**, 1–131 (2005).
[51] S. M. Barr, Int. J. Mod. Phys. A **8**, 209 (1993).
[52] CP Violation Without Strangeness, S. K. Lamoreaux and I. B. Khriplovich, (Springer, 1997).
[53] J. Ellis, Nucl. Instr. Methods Phys. Res., Sect. A **284**, 33 (1989).
[54] See, e.g., A. Riotto and M. Trodden, Ann. Rev. Nucl. Sci. **49**, 35 (1999).
[55] A. D. Sakharov, JETP Lett. **5**, 24 (1967).
[56] C. A. Baker, D. D. Doyle, P. Geltenbort et al., Phys. Rev. Lett. **97**, 131801 (2006).
[57] W. C. Griffith, M. D. Swallows, T. H. Loftus et al., Phys. Rev. Lett. **102**, 101601 (2009).
[58] B. C. Regan, E. D. Commins, Ch.J. Schmidt et al., Phys. Rev. Lett. **88**, 071805 (2002).
[59] D. M. Kara, I. J. Smallman, J. J. Hudson et al., New Journal of Physics **14**, 103051 (2012).
[60] V. A. Dzuba, V. V. Flambaum et al., Phys. Rev. A **66**, 012111 (2002).
[61] J. S. M. Ginges and V. V. Flambaum, Phys. Rep. **397** , 63 (2004).
[62] J. M. Pendlebury, W. Heil, Yu. Sobolev et al., Phys. Rev.A **70**, 032102 (2004).
[63] I. Yu. Kobzarev and L. B. Okun, JETP **16**, 1343 (1963).
[64] J. Leitner and S. Okubo, Phys. Rev. **136**, B1542 (1964).
[65] N. D. Hari Dass, Phys. Rev. Lett. **36**, 393 (1976).
[66] W. T. Ni, Phys. Rev. Lett. **38**, 301 (1977).
[67] K. Lamoreaux, NIM A **284**, 43 (1989).
[68] B. Mashhoon, Lect. Notes Phys. **702**, 112 (2006).

WILEY ONLINE LIBRARY

Early View publication on wileyonlinelibrary.com
(issue and page numbers not yet assigned;
citable using Digital Object Identifier – DOI)

Ann. Phys. (Berlin), 1–15 (2013) / DOI 10.1002/andp.201300071

annalen der physik

Review Article

Searching for electric dipole moments

*Klaus Jungmann**

Received 24 March 2013, revised 20 May 2013, accepted 26 June 2013
Published online DD MM YYYY

Searches for a permanent Electric Dipole Moment (EDM) of a fundamental particle provide a wide window for the discovery of potential New Physics. Within todays Standard Model in particle physics the well established violation of CP symmetry gives rise to EDMs which are several orders of magnitude below the present experimentally established upper bounds. On the other hand, EDMs appear quite naturally within many modern speculative theories, which have been suggested to improve the known shortcomings of the present Standard Model, e.g., the lack of giving reasons for certain established facts such as the mass hierarchy of the fundamental fermions or the number of three particle generations. They could be almost as large as the present experimental bounds. The speculative models provide for EDMs of different fundamental particles in specific ways. As there is no convincing indication, yet, which of the various extensions to the present standard theory may be more successful, a larger number of EDM searches is very well motivated. Still, even with the discovery of an EDM in one system several experiments will be required to pin down the precise nature and the underlying processes. Therefore searches are going on presently in a variety of systems, ranging from free leptons to complex condensed matter samples. These experiments utilize typically state of the art precision measurements which are often based on forefront technological developments. The experimental efforts are complemented and guided by the further development and refinement of particle theory. Here a few aspects of recent developments in this exciting field are summarized.

1 Introduction

A permanent electric dipole moment (EDM) of a fundamental particle violates both the discrete symmetries parity (P) and time-reversal (T). The combined CPT symmetry [1–3], where C is charge conjugation, relates deeply to our basic understanding of physics through, e.g., spin-statistics. CPT is generally assumed to be unbroken. It has been thoroughly investigated and precisely tested [4]. With CPT valid a permanent Electric Dipole Moment also violates the CP symmetry (see Fig. 1 and, e.g., [5] for a comprehensive introduction and [6–8] for an overview and a more detailed compilation of the background to the subject of permanent EDMs).

We know from experiments and direct observations that the discrete symmetries C, P and T as well as the combined CP symmetry are all broken in weak interactions. Until the 1950ies it had been generally and strongly assumed that these symmetries would be generally valid. Therefore, early search experiments [9–11] for an EDM in neutrons were not considered to have realistic chances.

In 1957 the violation of parity has been discovered in the weak interaction process of nuclear β-decay in ^{60}Co [12]. Shortly thereafter this was confirmed in the decay of pions [13] and muons [14]. In 1964 the violation of the CP symmetry was measured in the weak decay of neutral kaons (K^0) [15].

Only after these facts had been undoubtedly established EDM searches were re-introduced into the spectrum of scientific urgent topics. Today searches for permanent EDMs of fundamental particles are considered to have a large potential to shape significantly our understanding of the fundamental laws of physics. On the path to find New Physics EDMs offer an approach which is complementary to that possible with experiments at the highest in accelerator achievable energies. EDM experiments can probe New Physics at energy scales which are far beyond the reach of present accelerator technology. In certain supersymmetric scenarios, e.g., present established EDM limits provide information about physics at the TeV or even PeV scale [16]. They are competitive or even more sensitive to New Physics than observables connected to hadron and lepton flavour.

* Corresponding author E-mail: jungmann@kvi.nl
Kernfysisch Versneller Instituut, University of Groningen, Zernikelaan 25, NL 9747, AA Groningen

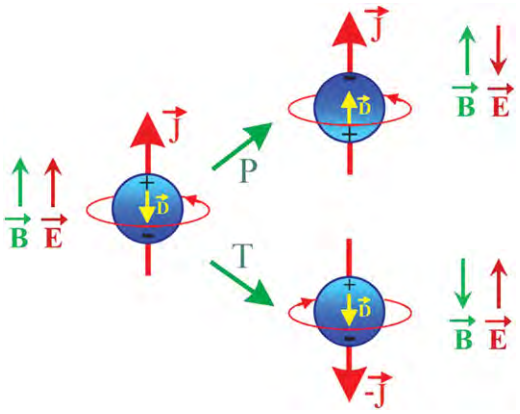

Figure 1 A permanent electric dipole moment $\vec{D}$ of a fundamental particle is proportional to its angular momentum $\vec{J}$, as there can be only one vector in a quantum system. The energy H of a dipole $\vec{D}$ in an external electric field $\vec{E}$ is $H_E = \vec{D} \cdot \vec{E}$, the observable quantity. The electric field $\vec{E}$ also changes sign in a P transformation. Further under a C transformation both $\vec{D}$ and $\vec{E}$ change sign. A permanent Electric Dipole Moment (EDM) violates P, T and CP symmetry. A magnetic dipole moment $\vec{M}$ of a particle stays always aligned with $\vec{J}$ which itself transforms under P,T, and CP like a magnetic field $\vec{B}$. This leaves $H_M = \vec{D} \cdot \vec{E}$ unaltered and magnetic moments can exist.

CP violation as observed first in the neutral Kaon decays can be described with a single phase factor in the Cabbibbo-Kobayashi-Maskawa formalism [17, 18]. CP violation has attracted a lot of attention, because of its possible relation to the observed matter-antimatter-asymmetry in the universe. It has been suggested [19, 20] to explain the observed dominance of matter over antimatter in our world via CP-violation in the early universe in a state of thermal non-equilibrium and with baryon number violating processes. (Additional sources of CP-violation – other than those well established to date – are necessarily required to explain the presently known matter-antimatter asymmetry. CPT violation on the other hand could also be sufficient and even without the need of thermal non-equilibrium [21]. Therefore this opens an alternative route for an explanation). Because CP violation as described in the SM is not sufficient to explain the excess of baryons, a strong motivation is provided to search for yet unknown sources which cause violation of CP symmetry. This is a major driving force behind the ongoing EDM searches.

Electric dipole moments are well known and observed in, e.g., polar molecules. This simple fact is often a source of confusion [6]. Such dipole moments appear in strong external electric fields, where the system needs to be described by a superposition of pure (eigen)states. However, the structural eigenstates of a polar molecule do not give rise to permanent EDMs such as those we are concerned with here. Eigenstates of shape in any quantum system are not energy eigenstates. We are here concerned with the pure energy eigenstates of the systems of interest. They cannot have any dipole moments other than such of tiny strength which arise from the known sources of CP violation [15] within the Standard

Table 1 Several actual limits on EDMs and the improvement factors necessary in experiments to reach Standard Model predictions. It is assumed here that the QCD Θ parameter does not contribute, athough for hadrons it might contribute up to the present bounds. For electrons, neutrons and muons speculative models have predicted a finite value for an EDM that could be reached with presently ongoing or proposed experiments in the near future. There is a number of further, new and ongoing activities, e.g. in neutral and charged molecules or in radioactive atoms, which have no reported limit yet. However, they are similarly promising.

Particle	Limit/Measurement [e cm]	Confidence Level [%]	Reference	SM limit [factor to go]
e	$<1.05 \times 10^{-27}$	90	[101, 102]	10^{11}
μ	$<1.8 \times 10^{-19}$	95	[103]	10^{8}
τ	$(-2.2 < d_\tau < 4.5) \times 10^{-17}$	95	[104]	10^{7}
n	$<2.9 \times 10^{-26}$	90	[67]	10^{4}
p	$<0.54 \times 10^{-23}$	95	[105]	10^{6}
Λ^0	$(-3.0 \pm 7.4) \times 10^{-17}$	95	[106]	10^{11}
$\nu_{e,\mu}$	$<2 \times 10^{-21}$	95	[107]	
ν_τ	$<5.2 \times 10^{-17}$	95	[108, 109]	
Hg-atom	$<3.1 \times 10^{-29}$	95	[110]	$\leq 10^{4}$

Model. Such EDMs are at least 4 orders of magnitude below the present established bounds (see Table 1 below). Therefore, an undisputed future observation of an EDM of a pure state will be a clear and convincing sign of New Physics which is not covered yet by the established Standard Model in particle physics.

Many models beyond the present Standard Model predict often EDMs for fundamental systems which are significantly larger than the values which are calculated using the already known CP-violation. The values of EDMs in speculative models can in many cases be almost as large as the present experimental upper bounds. Since the first experiments to search for EDMs in the 1950ies numerous speculative possibilities, which could provide EDMs, have been suggested and thoroughly discussed. Many of them have been ruled out in the course of the evolution of our physical understanding and many of them do not satisfy any longer the constraints set by present experimental bounds on EDMs. Based on experimental facts, no suggested extension to the Standard Model can be favoured over another or stronger motivated than any other. It will be up to experiments to decide whether there are EDMs from Physics beyond the Standard Model and what the underlying mechanisms are which produce them. Even through the non-observation of a finite EDM value up to now, the searches for them have ruled out so far many speculative models. EDMs have a largely model independent discriminative power. On the other hand, an established EDM would be a clear sign of new physics beyond the Standard Model.[1]

Because of this very high importance of permanent Electric Dipole Moments and because of their very robust discovery potential for New Physics, there have been a number of recent original articles and extensive reviews of the field. They cover the discovery potential and possible implications of possible finite search results [8,22–35], various aspects of theoretical approaches [36–39, 41–46] and the numerous ideas and improvements concerning actual and future experiments searching for permanent EDMs of particles and composed systems [47–52] with the highest reachable experimental sensitivities. The ongoing and upcoming projects have stimulated technological developments and generated quite some activities [53–58]. We do not aim here to expand on this, but rather sketch the present status. We restrict ourselves to aspects of some most recent developments and the realistic chances for a discovery from an intermediate term perspective.

[1] An all encompassing discussion of all the theoretical models which provide for EDMs would exceed the scope of this article.

2 Searches for an EDM – general aspects

From an unbiased point of view there is no preferred system to search for an EDM. In fact, many different systems need to be examined in order to be able to extract unambiguous information on the nature of EDMs, because depending on the underlying, yet unknown processes different systems have in general quite significantly different susceptibility to acquire an EDM through a particular mechanism (see Fig. 2). As a first approach an EDM may be considered an "intrinsic property" of an elementary particle as we know them, because the mechanism causing an EDM is not accessible at present. However, an EDM can also arise from CP-odd forces between the constituents forming a more complex particle with substructure, e.g. such as forces between the quarks in a nucleon, between the nucleons in nuclei or between nuclei and electrons in atoms. Such EDMs could be much larger [59] than such expected for elementary particles and which originate in the presently popular New Physics models.

Distinctively different precision experiments to search for an EDM are under way in a variety of different systems. A large number of ideas for significant improvements have been made public. Still, the electron and the neutron get the largest attention of experimental groups and theorists, although besides tradition there is little which singles out these systems. Nevertheless, there is a considerable number of efforts in the United States, Japan and in Europe which employ different approaches all of which have unique and promising features.

The methods to find an EDM which are presently pursued can be distinguished in three groups:

- Classical approaches which use optical spectroscopy of atoms and molecules in cells, as well as atomic and molecular beams or contained cold neutrons;
- Modern atomic physics techniques such as atomic and ion traps, fountains and interference techniques;
- Innovative approaches involving radioactive species, storage rings, particles in condensed matter (garnets [60], liquid Xe [61]), nuclear spin masers [62], and a few more have been proposed.

2.1 Sensitivity

The statistical limit achievable in an EDM experiment can be generically described by

$$\delta d = \frac{\hbar}{P\varepsilon\sqrt{N\tau}\,TE}. \qquad (1)$$

Here P is the polarization, ε is the efficiency which can vary significantly depending on the experimental setup

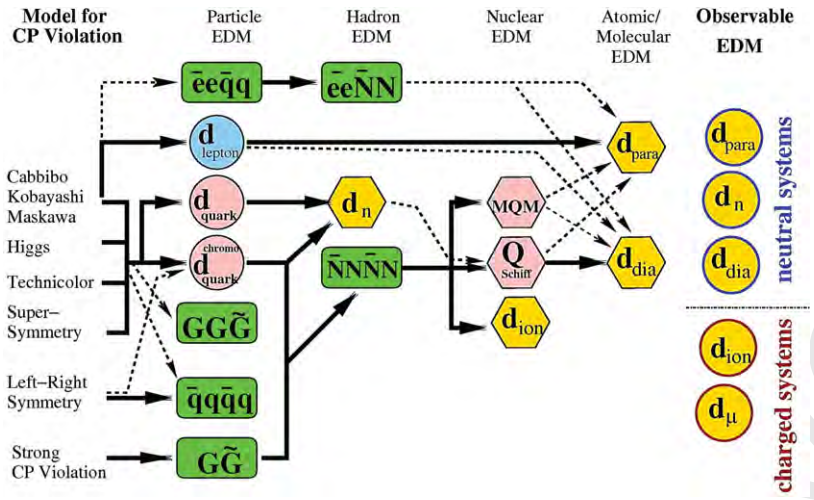

Figure 2 New Physics beyond the present standard theory can induce permanent EDMs through various mechanisms into particles and composed systems. An undisputed observation of an EDM in one system alone would therefore not provide sufficient information to unravel the underlying processes. Further, as of today there is no indication, yet, which of the potential mechanisms would be more favoured than any other. Therefore the results of several experiments – with either a positive signal or with further stringent upper limits – are indispensable for the identification of the nature of the process generating an EDM.

and the system under observation, T the measurement time, N is the number of particles in the observation volume, τ is the spin coherence time and E is the applied electric field. With typical values achievable in realistic experiments ($P \approx 1, \varepsilon \approx 0.1, N = 10^6, \tau \approx 1s, E = 10^5\, V/cm$) one gets $\delta d \approx 10^{-27}$ e cm in one day ($T = 10^5 s$) of measurement time. We note here that among the successfully completed experiments there were large differences in the achieved characteristic numbers due to experimental details. (The neutron experiments so far had the highest efficiency of $\varepsilon \approx 0.5$ and the latest Xe experiment had $\varepsilon < 10^{-7}$. Whereas there were $N < 10^7$ neutrons per day available, for Xe the low efficiency could be compensated by the large number of $N > 10^{21}$ atoms [63].) In general, statistics is not a serious problem, even for experiments which exploit exotic or radioactive systems.

However, systematic effects are known to provide more severe limitations. Therefore their rigorous control needs to be in the very center of attention in the necessary high precision experiments. A recently compiled and updated table of experiments searching for permanent Electric Dipole Moments is given in [64].

2.2 Spin Precession

An EDM d_X of a fundamental particle X is connected with the spin σ_X of the system. It is proportional to the spin and the magneton of the particle μ_{0X}, with a constant of proportionality η_X. We have

$$\mu_{0X} = \frac{e\hbar}{m_X c}, \tag{2}$$

where m_X is the particle mass, e is the elementary unit of charge, $\hbar$ is Planck's constant and c is the speed of light. With this the EDM is

$$d_X = \eta_X \cdot \mu_{0X} \cdot \sigma_X. \tag{3}$$

The constant η_X contains all the relevant information about the physical origin of the processes which cause an EDM. The magnetic moment of an investigated fermionic particle is

$$\mu_X = g_X \cdot \mu_{0X} = 2 \cdot (1 + a_X) \cdot \mu_{0X}, \tag{4}$$

where a_X is the particles magnetic anomaly, i.e. the fractional deviation of the g-factor which has a value of exactly 2 for spin 1/2 fermions in Dirac theory.

Many EDM searches have been performed in experiments where spin precession of a polarized sample was measured. For this the samples are polarized and reside in a weak magnetic field B which is oriented orthogonal to the polarization. The polarization which is proportional to the particle spins precesses with the frequency

$$\omega_B = g_X \cdot \mu_{0X} \cdot B \tag{5}$$

around the magnetic field vector. In an additional electric field $+E$, which is aligned parallel to B, or an electric field $-E$, which is aligned anti-parallel to B, the precession frequency is increased or decreased by

$$\omega_E = \eta_X \cdot \mu_{0X} \cdot E. \tag{6}$$

For an EDM of order 10^{-28} e cm and a typical electric field of order 10^5 V/m this corresponds to a spin

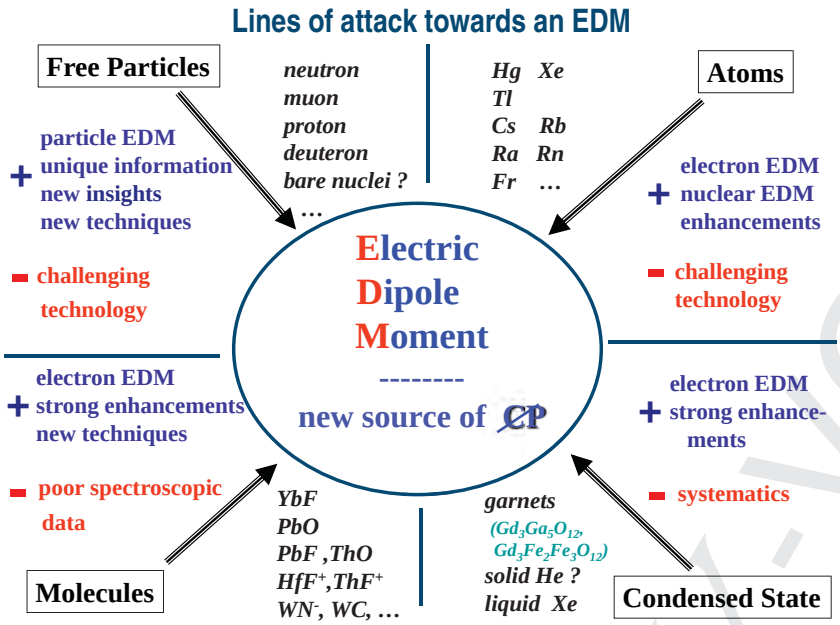

Figure 3 We distinguish four categories of EDM search experiments depending on properties of the system under investigation: single fundamental particles, atoms, molecules and condensed matter. In composed systems amplification mechanisms can significantly enhance the EDMs of fundamental particles. In each category examples are given of systems is which permanent electric dipole moments are searched for. Those where the final decision over the suitability has not been reached are marked '?'. Yet, no single system can be singled out as being more promising than any other. Every line of approach has its characteristic advantages (symbolized by '+') and challenges (symbolized by '-'). The common goal of all these efforts is the identification of new sources of CP violation.

precession frequency of $\approx 1.5\,\mu Hz$. In the combined magnetic and electric fields the spin precesses with the frequencies

$$\omega_L^{\pm} = \omega_B \pm \omega_E, \tag{7}$$

depending on the relative orientation of E and B. For a finite value of the EDM the difference in the frequencies ω_L^+ and ω_L^- yields the EDM as

$$d_X = \frac{\omega_E \cdot \sigma_X}{E} \tag{8}$$

and the parameter of primary interest, η_X, becomes

$$\eta_X = \frac{\omega_E}{\mu_{0X} \cdot E}. \tag{9}$$

Since the magneton μ_{0X} depends on the mass of particle, the limits on EDMs of particles, usually quoted in CGS units, must be compared with each other only with caution. η_X appears to be a more powerful parameter for the purpose of comparisons.

3 Systems to search for EDMs

There are four distinguishable lines of experimental approach towards observing an EDM. They differ concerning the type of system under investigation (see Fig. 3):

- Single *free* Elementary Particles and Atomic Nuclei (electron (e), muon (μ), tauon (τ), neutron (n), proton p, ^{223}Fr, …);
- Atoms and Ions (mercury (Hg), xenon (Xe), thallium (Tl), cesium (Cs), radon (Rn), francium (Fr), radium (Ra), …);
- Molecules and Molecular Ions (thallium fluoride (TlF), ytterbium fluoride (YbF), lead oxide (PbO), hafnium fluoride ion (HfF^+), thorium fluoride ion (ThF^+), …);
- Condensed Matter (ferroelectric materials, liquid Xe, …).

Each of these lines has its own strong advantages. Single particles are the cleanest systems in terms of interpretation of a possible observed EDM. Atoms and ions show often quite strong enhancement factors for the EDMs of their constituents. Depending on the electronic configuration the observation of either the EDM of the electron or the one of the nucleus can be strongly favoured. This depends on whether the atomic system is paramagnetic or diamagnetic. In molecules, particularly the polarizable ones, the enhancement factors can be very large due to a large number of close lying states of opposite parity. In condensed matter samples enhancements can be large as well where each investigated object has its own particular advantages.

A selection of present limits that have been established is listed in Table 1. The confidence levels of the published experimental values reported are 90% and 95% respectively, i.e. some 2σ. In order to be capable to rigorously proof the existence of an EDM with a confidence level of 5σ or more, new experiments must have significantly higher sensitivity than those in which the present limits were found. A significant leap is apparently

needed on the experimental side. On the other hand various speculative models exist which would provide for EDMs up to these limits. Except for being compatible with all other real facts established in physics, they do not at all belong (yet) to the physical theory that describes our world. Unless there will be undoubted and clear experimentally established facts (including maybe the observation of an EDM) which confirm one or the other possible model, such theories have no status in physics, whatsoever.

Unlike for the leptons, for hadronic particles already the Standard Model has provision for EDMs through the so-called QCD Θ-term. Θ is a purely topological parameter, i.e. it arises from boundary conditions, and is associated with P and CP, respectively T, violation (for a more thorough discussion see see e.g. [8, 65]). According to our present knowledge θ needs to be experimentally determined and it is compatible with zero. It could have a finite value. To present knowledge the smallness of the value of Θ has to be considered accidental. Although, models involving hypothetical axions could explain a zero value for Θ. The limit on the neutron EDM provides the present best bound $\Theta \leq 2.4 \cdot 10^{-10}$ [66, 67] and an about twice as large limit has been extracted recently from a search for an EDM in ^{199}Hg [48].

The necessary improvements over present limits in order to reach the Standard Model values (other than those possibly arising from the QCD Θ parameter) are also given in Table 1. Although, at this point the theoretical predictions for the Standard Model values have not been worked out in full detail, yet. The community relies on the validity of the present more general estimates and a number of worked out details. It has been common knowledge that within the Standard Model EDMs cannot appear in first order [68–70]. They are rather expected to arise in higher order loops and are therefore very small in the systems of present major interest [31]. For the neutron there are some 4 orders of magnitude to go, for other systems the room for discovery of non Standard Model CP violation through EDMs is even significantly larger [6].

Very recently, however, the loop-less generation of a nucleon EDM within the Standard Model has been pointed out [71]. EDMs are generated at tree level to second order in the weak interactions through bound state effects. For the neutron this yields a predicted EDM of about 10^{-31} e cm [71]. Concerning the Standard Model values of EDMs there exists some room for an improvement of the situation. More solid numbers would be appreciated when choices for new experiments are discussed.

3.1 Single Elementary Particles and Atomic Nuclei

Single particle EDMs are the simplest systems because there is no theory involved to evaluate, e.g., shielding or enhancement on an EDM by any internal structure of the investigated system. Any measured EDM can be directly attributed to the fundamental particle itself. Within the group of single particle experiments we can distinguish between to our present knowledge 'point' particles such as the leptons electron (e), muon (μ) or tauon (τ) and particles that have known substructure such as the neutron (n) or the proton (p).

These leptonic particles are the cleanest objects to investigate, because they have no known internal structure. An observed particle EDM would be an undoubted property of the particle itself. Among the elementary particles with an established quark substructure are the nucleons p and n and atomic nuclei consisting of them. In these composed systems an EDM can arise in addition to the intrinsic EDMs of the constituents from properties of the interaction between the constituents. As an example, in the deuteron an EDM can arise not only from constituent EDMS, but also from CP-odd parts in the interaction between the proton and the neutron [59].

3.1.1 Neutron

Among the presently ongoing EDM searches there are several independent projects aiming towards the discovery of an EDM of the neutron from sources outside of the Standard model (see e.g. [72, 73]). The modern ones exploit the fluxes available for ultra-cold neutrons at various reactors or accelerators worldwide. These competing projects try to achieve improvements over the presently best result [67, 74] largely through the implementation of sophisticated technical developments in their challenging setups.

The latest completed neutron EDM measurement has yielded a precision result in a spin precession experiment [67]. The neutron EDM searches show that now the experiments have reached a level of accuracy where subtle effects can mimic a *false* EDM, because such effects may be coupled to the electric field and, e.g., reverse if the field is reversed. The final limit in the latest experiment had therefore a need for correction even after publication. It concerns the systematic effects which are caused by the particles moving in the apparatus, in particular also in a partly inhomogeneous magnetic field. The static field in the laboratory is experienced by the moving

particle not as a static one. This time dependent field in the eigenframe of the particles can have large consequences, if its frequency comes close to the frequencies of the neglected terms in rotating wave approximation (Bloch-Siegert term). In particular a false EDM can be simulated by Larmor frequency shifts which are introduced by geometric phases [74,75], as such effects can be proportional to the electric field. At present the bound on the neutron EDM is $d_n < 2.9 \cdot 10^{-26}$ e cm (90% C.L.).

The neutron experiments show very visibly the sensitivity of precision EDM searches to systematics caused by the environment. At first glance such may not be obvious in precision experiments at the forefront of possibilities. Major improvements of the apparatuses in the ongoing set of many independent experiments concern control of the magnetic field via co-magnetometry by exploiting, e.g., Hg magnetometers or squids which are installed close to the actual measurement volume or a buffer gas co-magnetometer which is discussed [76]. It is considered essential that a co-magnetometer really senses the magnetic field in the fiducial volume, at best it measures simultaneously with the EDM search experiment and it co-exists within the the same volume under observation. This condition can be met, e.g., with two mixed gases one of which serves as a co-magnetometer and the second one is searched for an EDM. Such a setup is possible with ^{3}He as magnetometer with known much lower sensitivity to an EDM and ^{129}Xe as a candidate atom for an atomic EDM (see e.g. [77]).

The neutron EDM has at present the attention of a number of independent experimental projects which are actively pursued at different laboratories worldwide. This includes experiments which follow the more traditional routes and implement significant refinement, where neutron flux is a central issue. Such projects are under way at the Institute Laue Langevain in Grenoble, France [78], at the Paul Scherrer Institute (PSI) in Villigen, Switzerland [79], at the Technical University München, Germany [80], at the Spallation Neutron Source in Oak Ridge, USA [81], and a joint project of RCNP KEK and TRIUMF [82]. At the future European Spallation Source in Lund, Sweden, also crystal-diffraction promises to yield competitive limits [83]. These remarkable experimental efforts are accompanied by theoretical activities among which [84, 85].

3.1.2 Charged Particles

In the past a few EDM search experiments have been performed on charged particles exploiting just the properties of these systems themselves directly and without using external electric fields that are applied to the systems in the laboratory. These projects have produced respectable limits.

As an example of the possibilities, already in 1971, a lifetime measurement of the $2^2S_{1/2}$ state in the muonic helium ion $(^4\mathrm{He}\mu^-)^+$ was carried out. This corresponds to a limit on the muon EDM of $d_\mu < 10^{-15}$ e cm [86].[2] A finite EDM would have shortened in that experiment the $1.8(4) \sim \mu s$ lifetime of the metastable state. Further, also the good agreement between theory and experiment for the transition frequency of the $2^2S_{1/2}$-$2^2P_{3/2}$ transition in $(^4\mathrm{He}\mu^-)^+$ had been interpreted in the 1970ies in terms of a limit for the muon EDM of order $d_\mu < 3 \cdot 10^{-12}$ e cm [87]. The discussion in the following decades on the validity of the reported lifetime of the 2s state of $(^4\mathrm{He}\mu^-)^+$ under the high pressure conditions (40 bar)in the experiment [88–90] has primarily been crucial for the interpretation of the laser spectroscopy result in terms of the mean square charge radius of the α-particle the value of which must be still viewed with caution, therefore.

However, this issue is less relevant for pointing out a method to search for an EDM which is different from spin precession experiments. Also, at no time the best limit on the muon EDM has been affected, because of two main reasons: (i) The longevity of the 2s state in $(^4\mathrm{He}\mu^-)^+$ has been measured independently [88]. The lifetime of the $2^2S_{1/2}$state has been determined to be $\tau_{2s} = 960(150)$ ns at a pressure of 200 mbar. This experimental result provides for an independent extraction of a limit on the muon EDM also in the range of 10^{-15} e cm and demonstrates the feasibility of the method. (ii) A limit on the muon EDM of $d_\mu < 2 \cdot 10^{-16}$ e cm [91,92] had been reported already in 1960 from a muon beam experiment at the Nevis cyclotron facility, New York, USA.

This remarkable limit on the muon EDM at the time had been reached by searching for a spin rotation in the motional electric field which muons experience when they pass through a magnetic field. Furthermore, already in 1961 the first muon g-2 experiment at CERN had been modified to establish an even more stringent limit of $d_\mu < 2 \cdot 10^{-17}$ e cm [93] by looking for a precession of the muon spin out of the plane of orbit in a magnetic field, which would have been caused by a finite muon EDM interacting with the motional electric field.

[2] We mention this experimental method other than spin precession in an external field here, because with the significant progress in the production of particles, in spectroscopy and in measurement technology similar approaches could still be competitive today.

The majority of searches for EDMs in charged particles to date have been performed using neutral systems such as atoms, molecules or condensed matter, which contains the objects of interest, such as electrons or nuclei, as constituents. The choices for approaches in experiments are a consequence of the fact that most of the attempted measurements of an EDM require an electric field E. All presently known and ongoing projects follow that route. A charged particle experiences in a static electric field of trivial geometry (such as, e.g., a constant homogeneous field) an acceleration. This has been considered a severe limitation by the majority in the community, because the particle would be expelled from the fiducial volume rather rapidly. However, this argument is only valid for rather straightforward, such as homogeneous, electric field geometries (see e.g. [5]). There are, however, field topologies in which this argument does not hold. and this fact had been demonstrated already in the early 1960ies in muon experiments (see above).

EDM searches do not necessarily require an external homogeneous electric field at all. This fact had apparently not been recognized widely in the atomic physics based community which has been concerned primarily with low energy high precision experiments to search for an EDM until the late 1990ies. Therefore searches for charged particle EDMs such as the electron or of nucleons and nuclei had been performed exclusively in neutral atoms. This has prohibited setting up dedicated high precision EDM searches which can investigate *free* charged particles directly. Geometries for experiments where this is possible are, e.g., magnetic storage rings with a radial electric field in the storage region.

The muon has been the first particle that was investigated in a non-trivial field topology, i.e. a limit has been established for the muon EDM d_μ parasitically with precise measurements of the muon magnetic anomaly a_μ. One example, where this method has been exploited successfully to obtain higher precision already in the 1970ies, is the search for an EDM of the muon d_μ in a storage ring [94] which has been conducted parasitically to the precise measurement of the muon magnetic anomaly [95]. An out of orbit plane precession of the muon spin was searched for along with the data taking for the muon g-2 value; the underlying measurement principle(concerning the origin of the electric field and the detection of the muon spin direction) was the same as the one that been employed already in 1961 [93].

The most recent muon g-2 experiment at the Brookhaven National Laboratory (BNL), Upton, New York, United States, searched also for a muon EDM in a parasitic measurement along the main data taking [96, 97]. An EDM would have manifested itself in an oscillation of the the decay electron distribution around the muon orbit plane. The so far best limit on the muon EDM has been established to be $d_\mu < 1.8 \cdot 10^{-19}$ e cm (90% C.L.). Because the measurement of the muon magnetic anomaly a_μ has yielded a manifest some 3.5 standard deviation difference between experiment and theory [46] a new g-2 experiment will be set up at Fermilab, Batavia, United States, to verify or refute a discrepancy, which would be a sign of New Physics [98]. This new experiment aims for an improvement in a_μ by a factor of 5. At the same time it has a potential to improve the present bound on d_μ by one order of magnitude.

Since the wider recognition of the possibility to exploit charged particles directly a number of further systems has been thoroughly considered. Precision experiments both with trapped cold molecular ions in Paul traps [99] and at high energies using dedicated storage rings muons and nuclei, such as proton, deuteron, triton and others [59, 96, 111–118] are presently under way and aim for most competitive results, i.e. limits on the respective EDMs of order 10^{-29} e cm or better. The projects include such with a stepwise approach with intermediate accuracy of order 10^{-24} e cm to 10^{-25} e cm using to a large part existing storage ring devices such as COSY in Jülich, Germany [112,114], and such that want to reach the most stringent bounds in one go such as an at the BNL based initiative [57, 115].

As far as the experimental approaches are concerned the situation is characterized by a rapid sequence of proposed concepts which range from primarily magnetic storage to primarily electrostatic storage. Which of the concepts is better suited for a real experiment in future will depend on the system under investigation, where its magnetic anomaly plays a major role for the choice of the type of storage ring and technique, as well as resources and the actual collaboration performing a real experiment at a future time. For magnetic storage experiments with sensitivity at the 10^{-24}e cm level major equipment exists already with a moderate pole diameter (order 1 m) magnet at PSI [112] and the COSY storage ring at FZ Jülich [114].

A dedicated storage ring for an EDM experiment was first considered for muons [115]. Longitudinally polarized particles are injected into a magnetic storage ring with a suited radially directed electric field to compensate a spin precession in the plane of orbit which originates from the muon magnetic moment. In such a situation a muon EDM would express itself as a spin rotation around the radius of the particle orbit. This can be

observed as a time dependent change of the above/below the plane of orbit counting rate ratio. The time dependence is to first order linear for all realistic achievable fields and experimental geometries) Different from most other EDM searches, in such an experiment the possible muon flux is a major limitation.

For models with nonlinear mass scaling of EDM's such a muon EDM experiment would already be more sensitive to certain New Physics models than the present limit on the electron EDM (see [119–121]). Note, in certain Left-Right or supersymmetric symmetric models a value of d_μ as high as 10^{-22} e cm is possible.

For the muon in particular a limit of 10^{-24}e cm can be potentially reached with a relative moderate cost project that exploits largely existing key equipment and existing surface muon (about 28 MeV/c momentum) facilities for a first dedicated ring EDM experiment [112] with discovery potential. This value is in the range of a proposed experiment using an existing magnet system at the Paul Scherrer Institut in Villigen, Switzerland [112]. An experiment carried out at a more intense muon source could provide a probe to CP violation for particles in the second generation with correspondingly higher sensitivity. The muon as a particle from the second generation may have different routes to an EDM than the mostly investigated first generation particles. However, the community has not yet really started to exploit this open window of opportunity.[3]

The deuteron is the simplest known nucleus. Here an EDM could arise not only from a proton or a neutron EDM, but also from CP-odd nuclear forces between the two particles [122]. It has been shown recently [59] that in certain scenarios the deuteron can be significantly more sensitive than the neutron. The situation is evident for the case of quark chromo-EDMs, where the EDMs induced into deuteron (d_D) and neutron(d_n), respectively, are

$$d_D = -4.67\, d_d^c + 5.22\, d_u^c \quad \text{and}$$
$$d_n = -0.01\, d_d^c + 0.49\, d_u^c, \tag{10}$$

where d_d^c and d_u^c are the chrom -EDM of the down quark and the up quark, respectively. This implies that the deuteron could have a much higher sensitivity to quark chromo-EDMs which arises from the proton-neutron interaction within the deuteron. Because of its rather small magnetic anomaly the deuteron is a particularly interesting candidate for a magnetic ring EDM experiment, as it provides for the possibility to compensate in a magnetic storage ring the magnetic spin precession [113] with a suited electric field. In such an experiment scattering off a target can be used to observe spin precession, for example. Deuteron polarimeter studies turned out to be very encouraging [123].

Also heavier nuclei in atomic systems with partly filled electronic shells have been considered [124–127]. Because of its rather low magnetic anomaly the ^{223}Fr nucleus is a particularly interesting further candidate for a ring EDM experiment with sensitivity to a nuclear EDM.

Possible ring EDM experiments are presently being intensively discussed and the favoured approaches are subject to frequent changes, yet. A thorough comparison of the various ambitious approaches, which often aim for many orders of magnitude improvements over presently established EDM limits, is not possible unless experimentally the viability of any of the possible paths will have been demonstrated.

3.2 Atoms and atomic Ions

Atoms and atomic ions each consist of a nucleus and one or more electrons. Depending on details of the atomic structure we can have enhancement or suppression of fundamental particle EDMs. Diamagnetic atoms such as Hg, Xe, Rn, Fr and Ra render the possibility to search for nuclear EDMs in experiments which employ the atomic ground state. Excited states may provide for the possibility for searching an electron EDM, if the angular momentum of the state is finite. Paramagnetic atoms such as Tl or Cs provide for electron EDM searches.

In diamagnetic atoms the *Schiff theorem* governs the behaviour of the system. Instead of the complete suppression of an EDM which is expected in non-relativistic approximation for an atom consisting of point-like constituents, we can have substantial enhancements, depending on the details of the atomic system (see Table 2). Different calculations have led to only slightly different enhancement factors K. For the Ra atom $K = 1150$ is found in [42] whereas in [128] $K = 895$ is reported. Given that no EDM has been seen yet, the present

[3] A New Physics (non-SM) contribution a_μ^{NP} to the muon magnetic anomaly and a muon EDM d_μ are real and imaginary part of a single complex quantity related through $d_\mu = 3 \times 10^{-22} \times (a_\mu^{NP}/(3 \times 10^{-9})) \times \tan \Phi_{CP}$ e cm with a yet unknown CP violating phase Φ_{CP}. This provides a further strong motivation to search for a moun EDM d_μ already with values well larger than the search limits for the neutron or the electron.

Table 2 Enhancement factors for an electron EDM d_e in several atoms and diatomic molecules have been calculated [42]. They vary strongly and are generally highest for systems composed of several atoms, in particular if the internal field in the molecule is largely due to difference in the electronegativity of the atoms.

Particle	Rb	Cs	Th	Fr	Ra	PbO	YbF
Enhancement	24	125	585	1 150	40 000	60 000	1 600 000

level of agreement therefore suffices to judge the potential of experiments.

Recently the question was posed whether the *Schiff theorem* would be complete [129]. It has been shown that in each case a more careful analysis of this issue is required. In an atom, to first order the nucleon EDMs can be completely shielded by the electrons [127, 129, 130]. However, in general the rather significant enhancement of the electron EDM due to relativistic electron motion has been found to survive.

The search for an EDM in the diamagnetic ^{199}Hg atom has yielded the numerically best upper limit of all the EDM searches so far [100, 110]. It is $d_{^{199}\mathrm{Hg}} < 3.1 \cdot 10^{-29}$ e cm at 95% C.L. This latest result constitutes an improvement by a factor of 7 over the previous experiment [131] by the same group at the University of Washington, Seattle, USA. It had used the same isotpe ^{199}Hg in an earlier version of the apparatus. This achievement was possible primarily by better control of systematic effects by conceptual and technical improvements. This process is being continued through, e.g., investigations of linear Stark interferences, which can produce energy shifts similar to those expected from an EDM [132]. The further improvements include a better control of the magnetic field in a multi-cell arrangement and longer spin coherence times [48]. The experiment has been analyzed to set numerous new constraints on a variety of CP violating processes of interest for New Physics beyond the Standard Model [110].

Recently spin coherence times of 60 h for ^{3}He and of some 6 h for ^{129}Xe could be achieved. This has already been exploited to limit Lorentz- and CPT- violation for the bound neutron through the observation of free spin precession in a ^{3}He-^{129}Xe gas mixture [133]. The measurement took place in a magnetically well shielded environment at the Physikalisch Technische Bundesanstalt (PTB) in Berlin, Germany. The experiment had already many major ingredients of relevance for a significant improvement of the limit on the EDM in a ^{129}Xe atom. A corresponding experiment with a potential for observing or limiting the EDM in the 10^{-30} e cm range [77] is underway. Significant improvements over the last successful EDM search in ^{129}Xe [134] are expected by some 3 orders of magnitude.

In the recent years it became apparent that several radioactive isotopes of Rn, Fr and Ra in particular offer excellent opportunities for EDM searches due to atomic or nuclear enhancement mechanisms. They are present and pronounced in these system. The availability of intense radioactive sources of Ra as well as the advances at dedicated radioactive beam facilities that can deliver typically 10^5 to 10^6 Fr or Ra ions/s during sufficiently long (typically several weeks) beam times to experimental stations makes new experiments with such species possible. Nevertheless, it is a characteristic feature of experiments with radioactive samples that they have to perform with very low quantities of atoms.

In the Ra atom an accidental close proximity of the $7s7p\,^3P_1$ and the $7s6d\,^3D_2$ levels causes a significant enhancement of a potential electron EDM by a factor of about 40 000 (see Table 2) [135, 136]. For certain isotopes such as ^{225}Ra and ^{223}Ra an enhancement factor of several 100 for a nucleon EDM has been calculated which is due to the octupole deformation in these nuclei [137, 138]. For ^{225}Ra the EDM could be even as large as 6 to $50{\cdot}10^{-27}$ e cm [139]. The enhancement is associated with the close proximity of nuclear states of opposite parity. On the experimental side two programmes are ongoing at Argonne National Laboratory, United States, and at KVI Groningen, The Netherlands. Measurements of relevant optical wavelengths and excited state lifetimes as well as the development of efficient ($\approx 1\%$ level) magneto-optical trapping of heavy alkali earth elements Ba [140] and also Ra [141, 142] have already been achieved as major milestones in precursor experiments. Also the production of several Ra isotopes of interest has been successfully demonstrated already [143] and spectroscopy of their ions has been successfully conducted [144–146].

At TRIUMF, Vancouver, Canada, an experimental programme has been started to exploit in particular nuclear octupole deformations and the associated potential enhancement of an EDM of the radon (Rn) atom in its ground state [147]. Unlike in Ra there is no similar possibility for an enhancement of the electron EDM in Rn an Fr. A similar enhancement exists for Fr (see Table 2) and a corresponding experiment is underway at the Tohoku University, Japan [148]. The experiment uses already successfully an ^{18}O beam directed onto a ^{197}Au target to produce $^{215-x}$Fr isotopes (and x neutrons).

For the EDM experiment magneto-optical trapping of Fr atoms is foreseen. Stable Rb is used as a precursor to set up the experiment.

3.3 Molecules and Molecular Ions

The strong enhancement of a potential electron EDM in polar molecules is also being exploited for EDM searches. In such molecules internal very strong electric fields exist which can significantly enhance the possibility to observe an EDM of the constituent particles.

The best bound on an electron EDM d_e comes form a search experiment that uses YbF [101]. The experiment in London, United Kingdom, uses a beam of cold polar YbF molecules in an interferometric apparatus. A limit of $d_e < 1.05 \cdot 10^{-27}$ e cm (at 90% C.L.) could be established. It improves the previous limit [102] that had been posted in a beam of atomic ^{205}Tl by a factor of 1.5 and thereby further pushes the constraints on speculative extensions to the Standard Model. The experimenters are confident that d_e can be eventually probed at a level of at least $2 \cdot 10^{-28}$ e cm using YbF, where no potential systematics down to $6 \cdot 10^{-29}$ e cm could be identified [149] up to now.

Projects with molecules have been started in PbO [150, 151], ThO [152] and WC [153], because of the very large predicted enhancement factors in these polar systems. Besides PbO and ThO, neutral systems such as TlF and YbF and the ions HfF^+ and ThF^+ are employed in electron EDM searches [154]. As a recent novelty among the approaches to search for an electron EDM, the possibility to exploit charged molecular ions such as HfF^+ and ThF^+ has been recognized and a corresponding experiment has been started [99]. A primary advantage is that trapping of ions in an ion trap is rather straightforward. This provides a basis for the exploitation of the strong enhancement factors for electron EDMs in polar molecules [99]. In the RaO molecule the (T,P)-odd spin axis interaction is even 500 times larger than in TlF [155]. However, no concrete plans are known to take advantage of this fact in an experiment.

The ongoing EDM experiments which use charged molecular systems directly are still in the exploratory and feasibility study phase. The reports on progress are very promising and encouraging.

3.4 Condensed Matter

In condensed matter large fields may exist or such fields can be more conveniently handled than in vacuo or in gaseous samples. This can be advantageously exploited in EDM searches. It will be of crucial importance for any EDM experiment using condensed matter as a sample that they verify and show unambiguously whether any possible positive EDM signal is a true feature of the sample of interest rather than an artifact of an asymmetric behaviour of the condensed matter environment.

Although not yet competitive, an electron EDM search in gadolinium-iron garnet yielded $d_e < 5 \cdot 10^{-24}$ e cm as an intermediate result with a potential to challenge present best electron EDM results. The experiment uses a solid sample and measures a voltage across it. The voltage is induced by the alignment of magnetic dipoles in an external magnetic field [156]. The experimental programme shows that careful and extensive systematic studies are indispensable to understand all details of such an experiment [157, 158].

A novelty has been introduced recently with the idea to search for an EDM in liquid Xe droplets [61]. The experiment uses a technique where several microscopic hyper-polarized liquid ^{129}Xe droplets are placed in a matrix inside a low-field NMR apparatus. The spin precession in external fields is observed with superconducting pick-up coils and SQUID technology. The experiment is in a research and development phase and promises an improvement for d_e by some 3 orders of magnitude over the presently best limit from ^{129}Xe [134].

Among the condensed matter samples which are presently investigated concerning their suitability for EDM experiments garnets [60] and liquid droplets of Xe [61] are both very promising. Considerable effort has been spend to verify that a future result will be not subject to uncontrolled systematic effects with so far very encouraging results.

4 T-violation searches other than EDMs

There are many more possibilities in physics to find T-violation besides through searches for EDMs, in particular also in low energy experiments. Searches for permanent EDMs and searches for T-violation, respectively CP- violation, in other systems are closely related. Examples with comparable discovery potential are the precision studies of neutron and nuclear β-decays (see e.g. [159–162]).

Among the presently ongoing activities certain correlation observables in nuclear β-decays provide excellent opportunities to find new sources of CP violation [163–165]. In β-neutrino correlations the 'D'-coefficient [166] (for spin polarized nuclei) offer a high potential to

observe new interactions in a region of potential New Physics which is less accessible by EDM searches. The coefficient D describes the correlation of the momenta of the β-particle and the neutrino in the decay of polarized nuclei. D has been determined from the decay of polarized cold neutrons by detecting electron-proton coincidences to $D = (-0.94 \pm 1.89 \pm 0.97) \cdot 10^{-4}$ [167, 168], where the first uncertainty is of statistical origin and the second one is systematic. Note that final state interactions contribute at the level of 10^{-5} and can be calculated at the level of 10^{-7} [169].

The 'R'-coefficient [166], which has a similarly low Standard Model value [169] can be measured via the observation of β-particle polarization. It explores the same areas as present EDM searches or β-decay asymmetry measurements. Such challenging experiments are underway (see e.g. [161]). The Standard Model values for the D and R are small. The Standard Model CP violation yields for the neutron the tiny values $D_{SM} \leq 10^{-12}$ and $R_{SM} \leq 10^{-12}$ [169]. This is well out of reach for experiments in the near and not so near future such that for practical purposes the Standard Model expectation for the T-violating coefficients D and R can be considered to be zero. All experiments to date have been in agreement with the Standard Model prediction. Thereby bounds on New Physics models could be set (see e.g. [170]).

As a further example of the obtainable results, recently final results became available from an experiment at the SINQ facility of the PSI where both components of the transverse polarization of β-decay electrons from the decay of polarized unbound 25 K cold neutrons were measured. For the first time the R-coefficient in β-decay was determined as $R = +0.004 \pm 0.012 \pm 0.005$ [171]. This result provides significantly tighter constraints for scalar and tensor couplings in weak interactions as well as for models with leptoquarks and R-parity violating minimal supersymmetry.

5 Conclusions

There is a large number of searches for EDMs on a variety of systems. They all are very well motivated and no best system with highest chances for success can be singled out. The experiments all have unique and robust discovery potential. Furthermore, novel ideas have emerged in the recent past to use yet not studied systems where significant enhancements of particle EDMs are predicted, beyond what was known until recently. New experimental approaches have emerged in the recent past to exploit such new opportunities. They provide excellent opportunities which complement the more traditional experimental approaches on neutron-, atom- and electron-EDMs. The field is characterized and largely benefits from the fruitful interplay between theory and experiment, in exploring the landscape beyond the Standard Model, in identifying new possibilities for experiments and in solidifying the results reached in experiments. Any successful future EDM search experiment in one system needs to be complemented by experiments on other systems in order to pin down eventually the mechanisms which cause the observed EDMs.

The highest values predicted in theoretical work in beyond the Standard Model speculative theories are well within reach of presently ongoing and planned experiments. This makes this field most exciting as a major discovery may be just around the corner.

It requires a case by case detailed analysis in order to identify the highest chances for speedy progress in the search race for additional sources of CP violation. Here technical feasibility is a crucial factor.The presently ongoing and partly very advanced projects each are well motivated as none of them can be considered more promising than any other on the basis of secure knowledge. They have a significant potential for a breakthrough discovery.

Acknowledgments. This work has been supported by the Dutch Stichting voor Fundamenteel Onderzoek der Materie (FOM) in the framework of the research programmes 114 (TRIμP) and 125 (Broken Mirrors and Drifting Constants).

Key words. permanent electric dipole moment, edm, standard model, new physics, precision measurement.

Klaus Jungmann studied Physics at the University of Heidelberg, Germany. He received a Ph.D. degree in 1985 for laser spectroscopy on positronium. Until 1987 he was postdoctoral fellow at the IBM Almaden Research Laboratory in San Jose, USA. Until 2000 he spent extended research periods at the Paul Scherrer Institut, Switzerland, the Rutherford Appleton Laboratory, UK, the Los Alamos National Laboratory, USA, and the Brookhaven National Laboratory, USA. He is now Professor at the Kernfysisch Versneller Instituut of the University of Groningen, Netherlands, with a focus on high precision experiments at low energies and at the interface of atomic, nuclear and particle physics.

References

[1] J. Schwinger, Phys. Rev. **82**, 914 (1951) and Phys. Rev. **91**, 713 (1953).
[2] G. Lüders, Z. Physik **133**, 325 (1952) and Ann. Phys. **2**, 1 (1957).
[3] W. Pauli, Niles Bohr and the Development of Physics McGraw-Hill, New York, (1955).
[4] V. A. Kostelecky and N. Russell, Rev. Mod. Phys. **83**, 1 (2011).
[5] P. G. H. Sandars, Contemp. Phys. **42**, 97 (2001).
[6] I. B. Khriplovich and S. K. Lamoreaux, CP Violation Without Strangeness, Electric Dipole Moments of Particles, Atoms, and Molecules, Springer, Berlin, Heidelberg, New York, (1997).
[7] W. Bernreuther and M. Suzuki, Rev. Mod. Phys. **63**, 313 (1991).
[8] M. Pospelov and A. Ritz, Ann. Phys. **318**, 119 (2005).
[9] N. F. Ramsey and E. M. Purcell, Phys. Rev. **78**, 807 (1950).
[10] N. F. Ramsey and E. M. Purcell, Phys. Rev. **85**, 143 (1952).
[11] N. F. Ramsey and E. M. Purcell, Phys. Rev. **108**, 120 (1957).
[12] C. S. Wu et al., Phys. Rev. **105**, 1413 (1957).
[13] J. I. Friedman and V.Ł. Telegdi, Phys. Rev. **105**, 1681 (1957).
[14] R. L. Garwin, L. M. Lederman, and W. Weinrich, Phys. Rev. **105**, 1415 (1957).
[15] J. W. Cronin, V. Ł. Fitch, and R. Turlay, Phys. Rev. Lett. **13**, 138 (1964).
[16] D. McKeen, M. Pospelov, and A. Ritz, arXiv:1303.1172 (2013).
[17] J. W. Cronin, Rev. Mod. Phys. **53**, 373 (1981).
[18] M. Neubert, Int. J. Mod. Phys. **A11**, 4173 (1996).
[19] A. Sakharov, JETP **5**, 32 (1967).
[20] M. Trodden, Rev. Mod. Phys. **71**, 1643 (1999).
[21] O. Bertolami et al., Phys. Lett. B **395**, 178 (1997).
[22] M. L. Dall and A. Ritz, Hyperfine Inteactions **214**, 87 (2013).
[23] E. D. Commins, Ann. Rev. Nucl. Part. Science **62**, 133 (2012).
[24] B. F. Gibson and I. R. Afnan, Few Body Systems **54**, 191 (2013).
[25] A. Hoecker, Pramana Jour. Phys. **79**, 1141 (2012).
[26] D. E. Morissey and M. J. Ramsey-Musolf, New Jour. Phys. **14**, 125003 (2012).
[27] D. McKeen, M. Pospelov and A. Ritz, Phys. Rev. D **86**, 113004 (2012).
[28] B. Batell, Eur. Phys. Jour. C **72**, 2127 (2012).
[29] O. Naviliat-Cuncic and R. G. E. Timmermans, Comp. Rend. Phys. **13**, 168 (2012).
[30] A. Guiterrez-Rodriguez, Pramana Jour. Phys. **79**, 903 (2012).
[31] T. Fukuyama, Int. Jour. Mod. Phys. A **27**, 1230015 (2012).
[32] M. G. Schmidt, Prog. Part. Nucl. Phys. **66**, 249 (2011).
[33] A. Derevian and M. G. Kozlov, Adv. At. Mol. Opt. Phys. **58**, 77 (2010).
[34] J. A. Behr and G. Gwinner, Jour. Phys. G **36**, 033101 (2009).
[35] H. Abele, Prog. Part. Nucl. Phys. **60**, 1 (2007).
[36] A. P. Balachantran, T. R. Govindarajan, and T. R. Queiroz, Eur. Phys. Jour. Plus **127**, 118 (2012).
[37] F. K. Guo and U. G. Meissner, Jour. High Energy Phys. **12**, 097 (2012).
[38] Y. H. Song, R. Lazauskas and V. Gudkov, Phys. Rev. C **87**, 015501 (2013).
[39] N. Yamanaka, Phys. Rev. D **87**, 011702 (2013).
[40] G. F. Giudice, P. Paradisi and A. Strumia, Phys. Lett. B **694**, 26 (2010).
[41] V. A. Dzuba, V. V. Flambaum and B. Roberts, Phys. Rev. A **86**, 062512 (2012).
[42] V. A. Dzuba and V. V. Flambaum, Int. Jour. Mod. Phys. E **21**, 1230010 (2012).
[43] N. Yamanaka, Phys. Rev. D **86**, 075029 (2012).
[44] J. de Vries et al., Phys. Lett. B **695**, 268 (2011).
[45] N. Auerbach and V. Zelevinsky, Jour. Phys. G **35**, 093101 (2008).
[46] G. F. Giudice, P. Paradisi and M. Passera, J. High Energy Physics **11**, 113 (2012).
[47] M. Pitschmann et al., Phys. Rev. C **87**, 015205 (2013).
[48] M. D. Swallows et al., Phys. Rev. A **87**, 012102 (2013).
[49] C. Orzel, Physica Scripta **86**, 068101 (2012).
[50] B. J. Wundt, C. T. Munger and U. D. Jentschura, Phys. Rev. X **2**, 041009 (2012).
[51] T. Chupp, Adv. At. Mol. Opt. Phys. **59**, 129 (2010).
[52] H. L. Bethlem et al., Jour. Phys. B **39**, R263 (2006).
[53] T. G. Tenev et al., Phys. Rev. A **87**, 022103 (2013).
[54] J. Y. Kim and S. M. Clayton, IEEE Trans. Appl. Superconductivity **23**, 2500104 (2013).
[55] O. Bourrion et al., Nucl. Instr. Meth. A **701**, 278 (2013).
[56] J. P. Miller, E. de Rafael and B. L. Roberts, Ann. Rev. Nucl. Part. Science **62**, 237 (2012).
[57] Y. Orlov, E. Flanagan and Y. Semertzidis, Phys. Lett. A **376**, 2811 (2012).
[58] D. M. Kara et al., New Jour. Phys. **14**, 103051 (2012).
[59] C. P. Liu and R. G. E. Timmermans, Phys. Rev. C **70**, 055501 (2004).
[60] A. O. Sushkov et al., Phys. Rev. A **79**, 022118 (2009).
[61] F. Kuchler et al., Verhandlungen der DPG, Dresden HK, 28.4 (2013).
[62] A. Yoshimi et al., Hyperfine Int. **159**, 401 (2005).
[63] B. Santra, Precision Spectroscopy of Neutral Radium: Towards Searches for Permanent Electric Dipole Moments, PhD thesis, University of Groningen (2012)
[64] K. Kirch, nedm.web.psi.ch/EDM-world-wide (2013).
[65] M. Pospelov and A. Ritz, in: B. L. Roberts and W. J. Marciano, Lepton Dipole Moments, World Scientific, New Jersey, (2010), pp. 439.
[66] M. Pospelov and A. Ritz, Phys. Rev. Lett. **83**, 2526 (1999).
[67] C. A. Baker, Phys. Rev. Lett. **97**, 131801 (2006).
[68] L. Maiani, Phys. Lett. **B62**, 183 (1976).
[69] J. Ellis, Nucl. Phys. **B 109**, 23 (1976).

[70] B. Lee, Phys. Rev. **D 15**, 3394 (1977).
[71] Th. Mannel and N. Uraltsev, Phys. Rev. **D 85**, 096002 (2012).
[72] S. K. Lamoreaux and R. Golub, J. Phys. G **36**, 104002 (2009).
[73] S. K. Lamoreaux and R. Golub, in: B. L. Roberts and W. J. Marciano, Lepton Dipole Moments, World Scientific, New Jersey, (2010), pp. 583.
[74] S. K. Lamoreaux and R. Golub, Phys. Rev. Lett. **98**, 149101 (2007).
[75] J. M. Penedleburry et al., Phys. Rev. A **70**, 032102 (2004).
[76] Y. Masuda et al., Phys. Lett. A **376**, 1347 (2012).
[77] A. Scharth et al., Verhandlungen der DPG, Dresden, HK, 28.6 (2013).
[78] A. P. Serebrov et al., Nucl. Instr. Meas. A **611**, 124 (2009).
[79] G. Ban et al., Hyperf. Interact. **172**, 41 (2006).
[80] I. Altarev et al., II Nuovo Cimento **35 C**, 122 (2012).
[81] S. K. Lamoreaux et al., J. Phys. G. **36**, 104002 (2009).
[82] Y. Masuda et al., Phys. Rev. Lett. **108**, 134801 (2012).
[83] V. V. Fedorov et al., Physica B **406**, 2370 (2011).
[84] R. Kuchimanchi, Phys. Rev. D **86**, 036002 (2012).
[85] S. A. Blundell et al., Phys. Rev. D **86**, 025023 (2012).
[86] A. Placci et al., Nuovo Cimento **1A**, 445 (1971).
[87] V. W. Hughes and T. Kinoshita, in: V. W. Hughes and C. S. Wu, Muon Physics I, Academic Press, New York, 1977), pp. 11.
[88] H. P. van Arp et al., Phys. Lett. **136 B**, 232 (1984).
[89] M. Eckhause et al., Phys. Rev. **A 33**,1743 (1986).
[90] J. Rosenkranz et al., Ann. Phys. **47**, 667 (1990).
[91] D. Berley et al., Phys. Rev. Lett. **1**, 144 (1958).
[92] D. Berley and G. Gidal, Phys. Rev. **118**, 1086 (1960).
[93] G. Charpak et al., Phys. Rev. Lett. **6**,128 (1961), and Nuovo Cimento **22**, 1043 (1961).
[94] J. Bailey et al., J. Phys. G **4**, 345 (1978).
[95] J. Bailey et al., Phys. Lett. B **68**, 191 (1977) and Phys. Lett. B **67**, 225 (1977).
[96] G. W. Bennett et al., Phys. Rev. D **80**, 052008 (2009).
[97] J. P. Miller, B. L. Roberts, and K. Jungmann, in: B. L. Roberts and W. J. Marciano, Lepton Dipole Moments, World Scientific, New Jersey, (2010), pp. 333.
[98] K. Jungmann, Hyperfine Interact. **210** (2012).
[99] M. Grau et al., Jour. Mol. Spectr. **272**, 32 (2012).
[100] W. Clark et al., in: B. L. Roberts and W. J. Marciano, Lepton Dipole Moments, World Scientific, New Jersey, (2010), pp. 635.
[101] J. J. Hudson et al., Nature **473**, 493 (2011).
[102] B. C. Regan et al., Phys. Rev. Lett. **88**, 071805 (2002).
[103] G. W. Bennett et al., Phys. Rev. D **80**, 052008 (2009).
[104] K. Inami et al., Phys. Lett. B **551**, 16 (2002).
[105] V. F. Dmitiev et al., Phys. Rev. Lett. **91**, 212303 (2003).
[106] L. Pondrom et al., Phys. Rev. D **23**, 814 (1981).
[107] F. del Aguila and M. Sher, Phys. Lett. B **252**, 116 (1990).
[108] R. Escribano and E. Masso, Phys. Lett. B **395**, 369 (1997).
[109] T. Ibrahim and P. Nath, Phys. Rev. D **81**, 033007 (2010).
[110] W. C. Griffith et al., Phys. Rev. Lett. **102**, 101601 (2009).
[111] F. Farley et al., Phys. Rev. Lett. **93**, 052001 (2004).
[112] A. Adelmann et al., Jour. Phys. G **37**, 085001 (2010).
[113] C. J. G. Onderwater, Hyperfine Interact., **172**. 1 (2006).
[114] J. Pretz, Hyperfine Interact., DOI 10.1007s10751-013-0799-4 (2013).
[115] Y. K. Semertzidis, Int. J. Mod. Phys. **16**, 690 (2001).
[116] B. L. Roberts, J. P. Miller, and Y. K. Semertzidis, in: B. L. Roberts and W. J. Marciano, Lepton Dipole Moments, World Scientific, New Jersey, (2010), pp. 655.
[117] C. J. G. Onderwater, Nucl. Phys. B **155**, 375 (2006).
[118] K. Jungmann, H. J. Kluge, I. B. Khriplovich, Proceedings Workshop on Nuclear Electric Dipole Moments, GSI, Darmstadt, (1999), pp. 1.
[119] G. Hiller, K. Huitu and T. Rüppell, Phys. Rev. D **82**, 093015 (2010).
[120] K. S. Babu et al., Phys. Rev. Lett. **85**, 5064 (2000).
[121] B. Dutta et al., Phys. Rev. D **68**, 113008 (2003).
[122] J. Hisano and Y. Shimizu, Phys. Rev. D **70**, 093001 (2004).
[123] N. P. Brantjes et al., Nucl. Instr. Meas. **A 664**, 49 (2012).
[124] I. B. Khriplovich, Nucl. Phys. A **147C**, 98 (2000).
[125] I. B. Khriplovich, Hyperfine Interact. **127**, 365 (2000).
[126] I. B. Khriplovich, Phys. Lett. B **444**, 98 (1998).
[127] C. P. Liu, Nucl. Phys. **844**, 250c (2010).
[128] D. Mukherjee et al., J. Phys. Chem. A **113**, 12549 (2009).
[129] C. P. Liu et al., Phys. Rev. C **76**, 035503 (2007).
[130] C. P. Liu and J. Engel, Phys. Rev. C **76**, 028501 (2007).
[131] M. Romalis, W. Griffith and N. Fortson, Phys. Rev. Lett. **86**, 2505 (2001).
[132] T. H. Loftus et al., Phys. Rev. Lett. **106**, 253002 (2011).
[133] C. Gemmel et al., Phys. Rev. D **82**,111901 (2010).
[134] M. A. Rosenberry, T. E. Chupp, Phys. Rev. Lett. **86**, 22 (2001).
[135] V. A. Dzuba et al., Phys. Rev. A **61**, 0622509 (2000).
[136] S. G. Porsev J. S. M. Ginges and V. V. Flambaum, Phys. Rev. A **83**, 042507 (2011).
[137] J. Dobaczewski and J. Engel, Phys. Rev. Lett. **94**, 232502 (2005).
[138] L. P. Gaffney et al., Nature **497**, 199 (2013).
[139] J. Ellis et al., J. High Energy Phys. **2**, 045 (2011).
[140] L. Willmann et al., Phys. Rev. A **79**, 041402 (2009).
[141] R. J. Holt et al., Nucl. Phys. A **844**, 53C (2010).
[142] R. H. Parker et al., Phys. Rev. C **86**, 065503 (2012).
[143] P. D. Schidling et al., Nucl. Instr. Meth. **606**, 305 (2009).
[144] G. S. Giri et al., Phys. Rev. A **84**, 020503 (2011).
[145] O. O. Versolato et al., Phys. Lett. A **375**, 3130 (2011).
[146] M. Nunez Portela et al., Hyperfine Interactions **214**, 157 (2013).
[147] E. R. Tardiff et al., Nucl. Instr. Meas. **579**, 472 (2007).
[148] H. Kawamura et al., Hyperfine Interactions **214**, 133 (2013).
[149] B. E. Sauer et al. Hyperfine Interactions **214**, 119 (2013).

[150] S. Bickman et al., Phs. Rev. A **80**, (2009).
[151] A. N. Petrov et al., Phys. Rev. A **72**, (2005).
[152] A. C. Vutha et al., Phys. Rev. A **84**, 034502 (2011).
[153] J. Lee et al., Phys. Rev. A **87**, 022516 (2013).
[154] E. D. Commins and D. DeMille, in: B. L. Roberts and W. J. Marciano, Lepton Dipole Moments, World Scientific, New Jersey, (2010), pp. 519.
[155] V. V. Flambaum, Phys. Rev. A **77**, 024501 (2008).
[156] B. J. Heidenreich et al., Phys. Rev. Lett. **95**, 253004 (2005).
[157] S. Eckel et al., Phys. Rev. B **79**, 014422 (2009).
[158] S. Eckel et al. Phys. Rev. Lett. **109**, 193003 (2012).
[159] D. Dubbers and M. G. Schmidt, Rev. Mod. Phys. **83**, 11111171 (2011).
[160] H. W. Wilschut et al., Pramana Jour. Phys. **75**, 163 (2010).
[161] N. Severijns and O. Naviliat-Cuncic, Ann. Rev. Nucl. Part. Phys. **61**, 23 (2011).
[162] T. E. Chupp et al., Hyperf. interact. **214**, 97 (2013).
[163] NuPECC Long Range Plan 2010, edited by A. Bracco, J. J. Gaardhoje, P. H. Henen, G. Rosner, E. Widmann, G. E. Körner, http://www.nupecc.org/lrp2010/Documents/lrp2010_final_hires.pdf (2010).
[164] T. Akesson et al., Eur. Phys. J. C **51**, 421 (2007).
[165] P. Herczeg, J. Res. Nat. Inst. Stand. Tech. **110**, 453 (2005).
[166] P. Herczeg, Prog. Part. Nucl. Phys. **46**, 413 (2001).
[167] H. P. Mumm et al., Phys. Rev. Lett. **107**, 102301 (2011).
[168] T. E. Chupp et al., Phys. Rev. C **86**, 035505 (2012).
[169] P. Herczeg and I. B. Khriplovich, Phys. Rev. D **56**, 80 (1997).
[170] N. Severijns and O. Naviliat-Cuncic, Physica Scripta **T152**, 014018 (2013)
[171] A. Kozela et al., Phys. Rev. C **85**, 045501 (2012).

Query

Q1: Author: **Citation of Ref. 40 is missing. Please check and provide its right location.**

WILEY-BLACKWELL

USING e-ANNOTATION TOOLS FOR ELECTRONIC PROOF CORRECTION

Required software to e-Annotate PDFs: Adobe Acrobat Professional or Adobe Reader (version 8.0 or above). (Note that this document uses screenshots from Adobe Reader X)
The latest version of Acrobat Reader can be downloaded for free at: http://get.adobe.com/reader/

Once you have Acrobat Reader open on your computer, click on the Comment tab at the right of the toolbar:

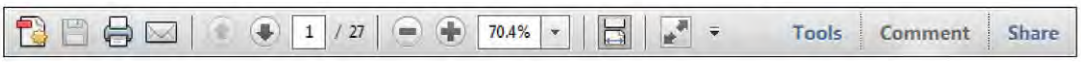

This will open up a panel down the right side of the document. The majority of tools you will use for annotating your proof will be in the Annotations section, pictured opposite. We've picked out some of these tools below:

1. Replace (Ins) Tool – for replacing text.

Strikes a line through text and opens up a text box where replacement text can be entered.

How to use it

- Highlight a word or sentence.
- Click on the Replace (Ins) icon in the Annotations section.
- Type the replacement text into the blue box that appears.

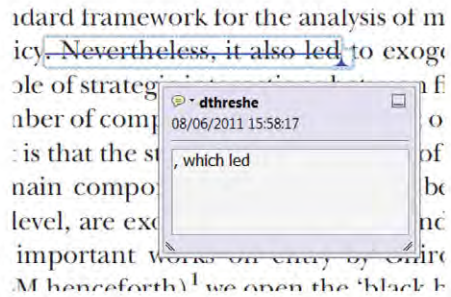

2. Strikethrough (Del) Tool – for deleting text.

Strikes a red line through text that is to be deleted.

How to use it

- Highlight a word or sentence.
- Click on the Strikethrough (Del) icon in the Annotations section.

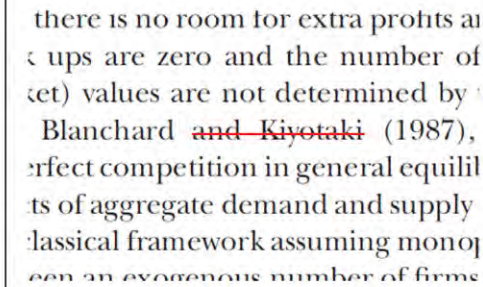

3. Add note to text Tool – for highlighting a section to be changed to bold or italic.

Highlights text in yellow and opens up a text box where comments can be entered.

How to use it

- Highlight the relevant section of text.
- Click on the Add note to text icon in the Annotations section.
- Type instruction on what should be changed regarding the text into the yellow box that appears.

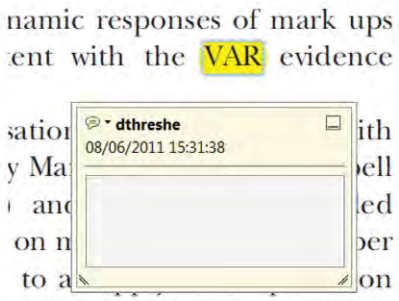

4. Add sticky note Tool – for making notes at specific points in the text.

Marks a point in the proof where a comment needs to be highlighted.

How to use it

- Click on the Add sticky note icon in the Annotations section.
- Click at the point in the proof where the comment should be inserted.
- Type the comment into the yellow box that appears.

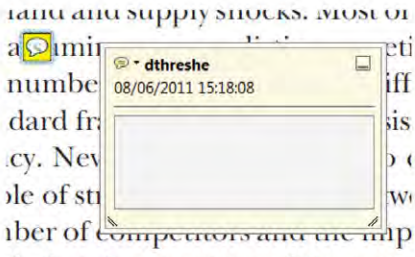

WILEY-BLACKWELL

USING e-ANNOTATION TOOLS FOR ELECTRONIC PROOF CORRECTION

5. Attach File Tool – for inserting large amounts of text or replacement figures.

Inserts an icon linking to the attached file in the appropriate pace in the text.

How to use it

- Click on the Attach File icon in the Annotations section.
- Click on the proof to where you'd like the attached file to be linked.
- Select the file to be attached from your computer or network.
- Select the colour and type of icon that will appear in the proof. Click OK.

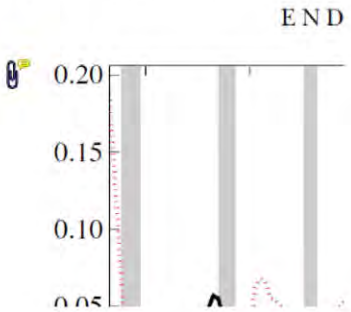

6. Add stamp Tool – for approving a proof if no corrections are required.

Inserts a selected stamp onto an appropriate place in the proof.

How to use it

- Click on the Add stamp icon in the Annotations section.
- Select the stamp you want to use. (The Approved stamp is usually available directly in the menu that appears).
- Click on the proof where you'd like the stamp to appear. (Where a proof is to be approved as it is, this would normally be on the first page).

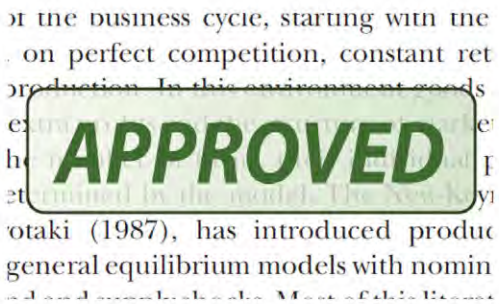

7. Drawing Markups Tools – for drawing shapes, lines and freeform annotations on proofs and commenting on these marks.

Allows shapes, lines and freeform annotations to be drawn on proofs and for comment to be made on these marks..

How to use it

- Click on one of the shapes in the Drawing Markups section.
- Click on the proof at the relevant point and draw the selected shape with the cursor.
- To add a comment to the drawn shape, move the cursor over the shape until an arrowhead appears.
- Double click on the shape and type any text in the red box that appears.

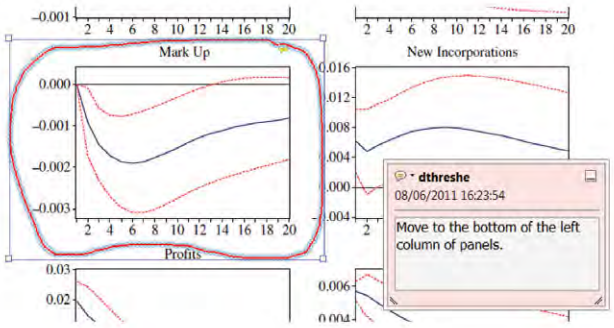

For further information on how to annotate proofs, click on the Help menu to reveal a list of further options:

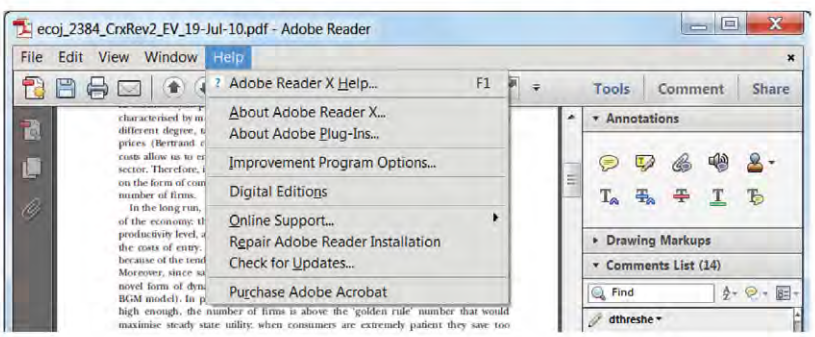

Instructions for Proof Corrections and Orders

annalen der physik

2013

WILEY-VCH Verlag GmbH
& Co. KGaA
Annalen der Physik
Rotherstrasse 21
10245 Berlin
Germany
TEL +49 (0) 30–47 03 13 21
FAX +49 (0) 30–47 03 13 99
E-MAIL ann-phys@wiley.com

WILEY
Publishers Since 1807

Please correct your proofs and return them within 5 days together with the completed reprint order form. The editors reserve the right to publish your article with editors' corrections if your proofs do not arrive in time.

After having received your corrections, your paper will be published online soon in the Wiley Online Library (wileyonlinelibrary.com).
Please keep in mind that reading proofs is your responsibility. Corrections should therefore be clear. We prefer the corrections be made directly within the PDF file (see E-annotations instructions). Alternatively, you may provide us with a list of corrections by e-mail, with the corrections referring to their line number.
Manuscript files are sometimes slightly modified by the production department to follow general presentation rules of the journal.

Note that the quality of the halftone figures is not as high as the final version that will appear in the issue.

Check the enclosed proofs very carefully, paying particular attention to the formulas (including line breakings introduced in production), figures, numerical values, tabulated data and layout of the pages.

A black box (■) or a question at the end of the paper (after the references) signals unclear or missing information that specifically requires **your attention.** Note that the author is liable for damages arising from incorrect statements, including misprints.

The main aim of proofreading is to correct errors that may have occurred during the production process, **and not to modify the content of the paper**. Corrections that may lead to a change in the page layout should be avoided.

Note that sending back a corrected **manuscript** file **is of no use**.

Return the corrected proofs within 5 days by e-mail.

Please do not send your corrections to the typesetter but to the Editorial Office:

E-MAIL ann-phys@wiley.com

Please limit corrections to errors in the text; cost incurred for any further changes or additions will be charged to the author, unless such changes have been agreed upon by the editor.

If your paper contains **color figures**, please fill in the Color Print Authorization and note the further information given on the following pages.

Full color reprints, Customized PDF files, Printed Issues, Color Print, and Cover Posters may be ordered by filling in the accompanying form.

Order Form

annalen der physik

2013

WILEY-VCH Verlag GmbH
& Co. KGaA
AdP Editorial Office
Rotherstrasse 21
10245 Berlin
Germany
TEL +49 (0) 30-47 03 13 21
FAX +49 (0) 30-47 03 13 99
E-MAIL ann-phys@wiley.com

WILEY
Publishers Since 1807

Please complete this form and return it by e-mail or FAX.

Article No.

Author/Title

e-mail address

Required Fields may be filled in using Adobe Reader

Color Print Authorization

Please bill me for

☐ color print figures (total number of color figures)

❒ YES, please print Figs. No. ☐ in color.

❒ NO, please print all color figures in black/white.

Reprints/Issues/PDF Files/Posters

Whole issues, reprints and PDF files (300 dpi) for an unlimited number of printouts are available at the rates given on the next page. Reprints and PDF files can be ordered before *and after* publication of an article. All reprints will be delivered in full color, regardless of black/white printing in the journal.

Reprints

Please send me and bill me for

☐ full color reprints with color cover

☐ full color reprints with personalized color cover

Issues

Please send me and bill me for

☐ entire issues

Customized PDF-Reprint

Please send me and bill me for

❒ a PDF file (300 dpi) for an unlimited number of printouts **with customized color cover sheet.**

The PDF file will be sent to your e-mail address.

Send PDF file to:

Please note that posting of the final published version on the open internet is not permitted. For author rights and re-use options, see the Copyright Transfer Agreement at http://www.wiley.com/go/ctavchglobal.

Cover Posters

Posters are available of all the published covers in two sizes (see attached price list). **Please send me and bill me for**

☐ A2 (42 × 60 cm/17 × 24in) posters

☐ A1 (60 × 84 cm/24 × 33in) posters

Mail reprints and/or issues and/or posters to (no P.O. Boxes):

VAT number:

Information regarding VAT

Please note that from German sales tax point of view, the charge for **Reprints, Issues or Posters** is considered as **"supply of goods"** and therefore, in general, such delivery is a subject to German sales tax. However, this regulation has no impact on customers located outside of the European Union. Deliveries to customers outside the Community are automatically tax-exempt. Deliveries within the Community to institutional customers outside of Germany are exempted from the German tax (VAT) only if the customer provides the supplier with his/her VAT number.

The VAT number (value added tax identification number) is a tax registration number used in the countries of the European Union to identify corporate entities doing business there. It starts with a country code (e.g. FR for France, GB for Great Britain) and follows by numbers.

The charge for **front cover/back cover/inside cover pictures, color figures or frontispieces publications** is considered as **"supply of services"** and therefore it is a subject to German sales tax. However, in case you are an institutional customer outside of Germany, the tax can be waived if you provide us with the VAT number of your company.

Customers outside of the EU may have a VAT number starting with "EU" instead of the country code if they are registered by the EU's tax authorities. In case you do not have a VAT number of EU and you are a taxable person doing business in a country outside EU, then please provide us with a certification from your local tax authorities confirming that you are a taxable person under the local tax law. Please note that the certification needs to confirm that you are a taxable person and you are conducting an economic activity in your country. Certifications which confirm that you are tax-exempt legal body (non-profit organization, public body, school, political party, etc.) in your country cannot be accepted for the German VAT purposes.

Purchase Order No.:

Terms of payment:

❒ Please send an invoice ❒ Cheque is enclosed

❒ **VISA, MasterCard and AMERICAN EXPRESS.**

Please use this link (Credit Card Token Generator) to create a secure Credit Card Token and include this number in the form instead of the credit card data.

https://www.wiley-vch.de/editorial_production/index.php

CREDIT CARD TOKEN NUMBER:

Send invoice to:

Signature _____

Date _____

Please use this form to confirm that you are prepared to pay your contribution.

Please sign and return this page.

You will receive an invoice following the publication of your article in the journal issue.

Price List – Annalen der Physik 2013

Reprints/Issues/PDF-Files/Posters

The prices listed below are valid only for orders received in the course of 2013. Minimum order for reprints is 50 copies. **Reprints can be ordered before *and after* publication of an article. All reprints are delivered with color cover and color figures.** If more than 500 copies are ordered, special prices are available upon request.

Single issues are available to authors at a reduced price.

The prices include mailing and handling charges. All prices are subject to local VAT/sales tax.

Reprints with color cover	Price for orders of (in Euro)					
Size (pages)	50 copies	100 copies	150 copies	200 copies	300 copies	500 copies*
1–4	345	395	425	445	548	752
5–8	490	573	608	636	784	1077
9–12	640	739	786	824	1016	1396
13–16	780	900	958	1004	1237	1701
17–20	930	1070	1138	1196	1489	2022
for every additional 4 pages	147	169	175	188	231	315
for personalized color cover	**190**	**340**	**440**	**650**	**840**	**990**

PDF file (300 dpi, unlimited number of printouts, customized cover sheet)	€ 330
Issues	€ 48 per copy for up to 10 copies.*
Cover Posters • A2 (42 × 60 cm/17 × 24in)	€ 49
• A1 (60 × 84 cm/24 × 33in)	€ 69

*Prices for more copies available on request.

Special offer: If you order 100 or more reprints you will receive a pdf file (300 dpi, unlimited number of printouts, color figures) and an issue for free.

Color figures

If your paper contains **color figures**, please notice that, generally, these figures will appear in color in the online PDF version and all reprints of your article at no cost. This will be indicated by a note "(online color at: www.ann-phys.org)" in the caption. The print version of the figures in the journal hardcopy will be black/white unless the author explicitely requests a color print publication and contributes to the additional printing costs.

	Approximate color print figure charges
First figure	€ 495
Each additional figure	€ 395 Special prices for more color print figures on request

If you wish color figures in print, please answer the **color print authorization** questions on the order form.

Neutrino Masses

Christian Weinheimer[*1] **and Kai Zuber**[**2]

[1] Institut für Kernphysik, Westfälische Wilhelms-Universität Münster, Wilhelm-Klemm-Str. 9, D-48149 Münster, Germany

[2] Institut für Kern- und Teilchenphysik, Technische Universität Dresden, Zellescher Weg 19, D-01069 Dresden, Germany

Received 15 November 1900, accepted 2 December 1900

Key words Neutrino mass, double β-decay, Majorana-type of neutrinos, direct neutrino mass determination.

The various experiments on neutrino oscillation evidenced that neutrinos have indeed non-zero masses but cannot tell us the absolute neutrino mass scale. This scale of neutrino masses is very important for understanding the evolution and the structure formation of the universe as well as for nuclear and particle physics beyond the present Standard Model. Complementary to deducing constraints on the sum of all neutrino masses from cosmological observations two different methods to determine the neutrino mass scale in the laboratory are pursued: the search for neutrinoless double β-decay and the direct neutrino mass search by investigating single β-decays or electron captures. The former method is not only sensitive to neutrino masses but also probes the Majorana character of neutrinos and thus lepton number violation with high sensitivity. Currently quite a few experiments with different techniques are being constructed, commissioned or are even running, which aim for a sensitivity on the neutrino mass of O(100) meV. The principle methods and these experiments will be discussed in this short review.

1 Introduction

The various experiments with atmospheric, solar, accelerator and reactor neutrinos provide compelling evidence that neutrino flavor states are non-trivial superpositions of neutrino mass eigenstates and that neutrinos oscillate from one flavor state into another during flight. By these neutrino oscillation experiments the neutrino mixing matrix U containing the mixing angles as well as the differences between the squares of neutrino masses can be determined [1].

The value of the neutrino masses are very important for astrophysics and cosmology to describe the role of neutrinos in the evolution of the universe. Although neutrinos are very light they may contribute significantly to the mass density of the universe: With 336 neutrinos per cm^3 left over from the big bang they are about a billion times more abundant than atoms. On the other hand the values and the pattern of the neutrino masses are very important for nuclear and particle physics, since they are a very sensitive probe for physics beyond the Standard Model of particle physics at large scales: Since neutrinos are neutral there is the possibility that neutrinos are their own antiparticles and, additionally, so-called Majorana mass terms originating from large scales could play the dominant role in describing neutrino masses [2].

Clearly, neutrino oscillation experiments prove that neutrinos have non-zero masses, but they – being a kind of *interference experiment* – cannot determine absolute masses. Therefore, we need other ways to determine the absolute value of the neutrino masses. Three methods are sensitive to the values of the neutrino mass eigenstates and their mixing angles in different ways:

* Corresponding authors E-mail: weinheimer@uni-muenster.de, Phone: +49 251 83 34971, Fax: +49 251 83 34962
** E-mail:zuber@physik.tu-dresden.de, Phone: +49 351 463 42250, Fax: +49 351 463 37292

1.1 Neutrino mass from cosmology

The relic neutrinos would have smeared out fluctuation on small scales, depending on their mass. By analysing the power spectrum of the universe limits on the sum of the three neutrino mass states, e.g. $\sum m(\nu_i) < 0.5$ eV [3], have been obtained which are to some extent model and analysis dependent.

1.2 Neutrino mass from neutrinoless double β-decay ($0\nu\beta\beta$)

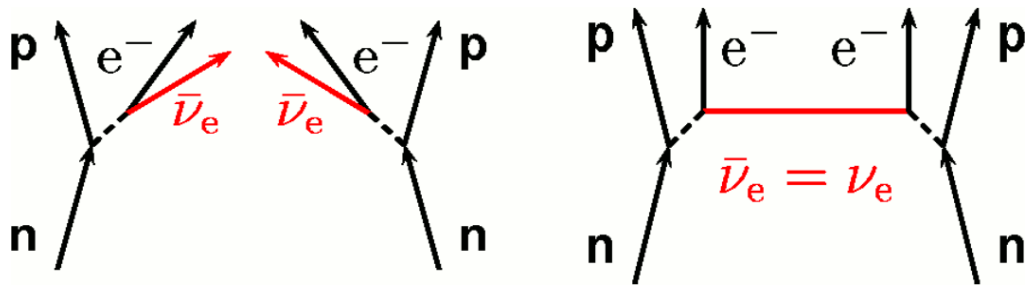

Fig. 1 Normal double β-decay with the emission of two antineutrinos (left) and neutrinoless double β-decay (right). The diagrams are shown for the case of a $\beta^-\beta^-$ decay.

Some even-even nuclei can only decay via double β-decay into a nucleus with higher binding energy. This 2^{nd} order week process has been proposed more than 70 years ago [4] and has been experimentally confirmed for around a dozen of nuclei since more than 20 years (see figure 1 left). If – in the case of a $\beta^-\beta^-$-decay – the electron antineutrino going out at one vertex is absorbed at the other vertex as neutrino (see figure 1 right) the double β-decay will be neutrinoless. It would violate lepton number conservation by two units. Therefore, neutrinoless double β-decay is forbidden in the Standard Model of particle physics. It could exist only, if the neutrino is its own antiparticle ("Majorana-neutrino" in contrast to "Dirac-neutrino"). Secondly, the left-handedness of neutrinos and the right-handedness of antineutrino in charge current weak interactions provide a 2^{nd} obstacle for neutrinoless double β-decay. A finite neutrino mass is the most natural explanation to produce in the chirality-selective weak interaction a neutrino with a small component of opposite handedness on which this neutrino exchange subsists. Then the decay rate will scale with the absolute square of the so called effective neutrino mass, which takes into account the neutrino mixing matrix U:

$$\Gamma_{0\nu\beta\beta} \propto \left|\sum U_{ei}^2 m(\nu_i)\right|^2 := {m_{ee}}^2 \tag{1}$$

In case of neutrinoless double β-decay the neutrino mixing matrix U also contains 2 so-called Majorana-phases in addition to the normal CP-violating phase δ. The latter is important for neutrino oscillation whereas the former do not influence neutrino oscillation but m_{ee}. A significant additional uncertainty entering the relation of m_{ee} and the decay rate comes from the uncertainties of the nuclear matrix elements of the neutrinoless double β-decay [5].

In case of $\beta^+\beta^+$ decays there are two alternative processes including one or two electron capture (EC) processes: β^+EC and ECEC. However, the modes involving positrons are phase-space suppressed and only six possible $\beta^+\beta^+$ emitters are known. Since in case of neutrinoless double β-decay the inner neutrino propagator is not observable the exchange could subsists on a completely different particle allowing this lepton number violating process, e.g. a particle from theories beyond the Standard Model, which leads to a very interesting interplay with new LHC data [6], because at the TeV scale their contribution to double beta decay can have a similar amplitude then the light neutrino exchange. Among others there are heavy Majorana neutrinos, right-hand W-bosons and double charged higgs boson, which are getting constrained by measurements of ATLAS and CMS [7, 8, 9, 10]. But there is a general theorem, that there will be always a Majorana neutrino mass term in case neutrinoless double β-decay will observed [11]. Diagrams

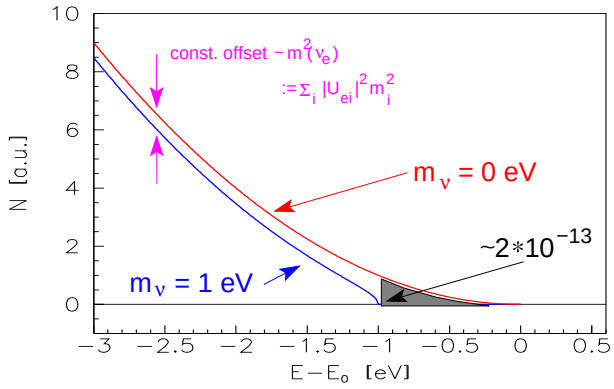

Fig. 2 Expanded β-spectrum of an allowed or super-allowed β-decay around its endpoint E_0 for $m(\nu_e) = 0$ (red line) and for an arbitrarily chosen neutrino mass of 1 eV (blue line). In the case of tritium β-decay, the gray-shaded area corresponds to a fraction of $2 \cdot 10^{-13}$ of all tritium β-decays.

like the one shown in fig. 1 right can also occur for other out-going leptons in theories beyond the Standard Model [12].

There are many recent reviews on neutrinoless double β-decay and neutrinoless double β-decay searches, e.g. [6, 13].

1.3 Neutrino mass from direct neutrino mass determination

The direct neutrino mass determination is based purely on kinematics or energy and momentum conservation without further assumptions. In principle there are two methods: time-of-flight measurements and precision investigations of weak decays. The former requires very long baselines and therefore very strong sources, which only cataclysmic astrophysical events like a core-collapse supernova could provide. From the supernova SN1987a in the Large Magellanic Cloud upper limits of 5.7 $\mathrm{eV/c^2}$ (95 % C.L.) [14] or of 5.8 $\mathrm{eV/c^2}$ (95 % C.L.)[15] on the neutrino mass have been deduced, which depend somewhat on the underlying supernova model. Unfortunately nearby supernova explosions are too rare and seem to be not well enough understood to compete with the laboratory direct neutrino mass experiments.

Therefore, the investigation of the kinematics of weak decays and more explicitly the investigation of the endpoint region of a β-decay spectrum (or an electron capture) is still the most sensitive model-independent and direct method to determine the neutrino mass. Here the neutrino is not observed but the charged decay products are precisely measured. Using energy and momentum conservation the neutrino mass can be obtained. In the case of the investigation of a β-spectrum usually the "average electron neutrino mass squared" $m^2(\nu_e)$ is determined [16]:

$$m^2(\nu_e) := \sum |U_{ei}^2| m^2(\nu_i) \tag{2}$$

This incoherent sum is not sensitive to phases of the neutrino mixing matrix in contrast to neutrinoless double β-decay.

In β-decay e.g. $(A, Z) \rightarrow (A, Z') + e^- + \bar{\nu}_e$ the outgoing electron is sharing the decay energy with the outgoing electron antineutrino. Therefore the shape of the β-spectrum near its endpoint E_0, i.e. the maximum energy of the electron in case of zero neutrino mass, is sensitive to the neutrino mass as shown in figure 2. A recent review about this topic is reference [17].

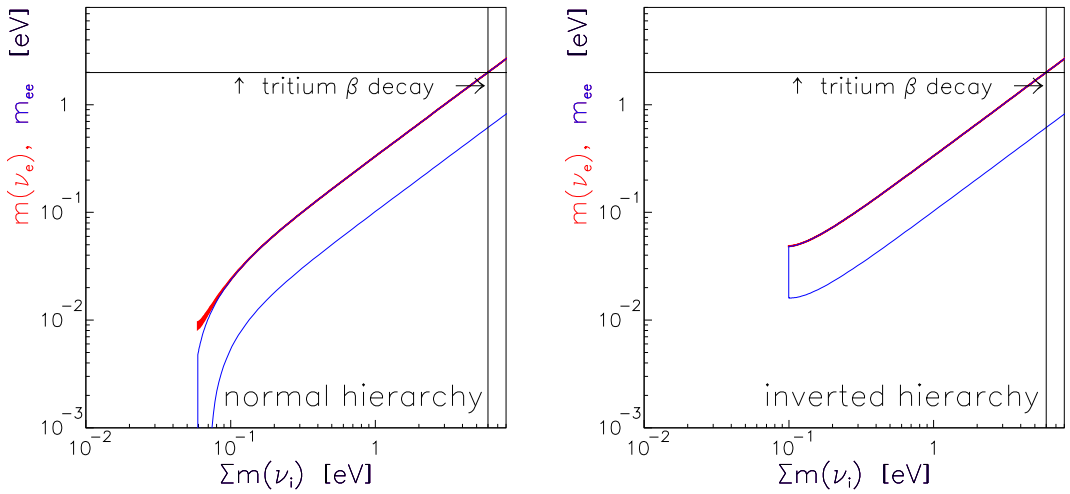

Fig. 3 Observables of neutrinoless double β-decay $m_{\rm ee}$ (open blue band) and of direct neutrino mass determination by single β-decay $m(\nu_{\rm e})$ (red) versus the cosmologically relevant sum of neutrino mass eigenvalues $\sum m(\nu_{\rm i})$ for the case of normal hierarchy (left) and of inverted hierarchy (right). The width of the bands/areas is caused by the experimental uncertainties (2σ) of the neutrino mixing angles [1] and in the case of $m_{\rm ee}$ also by the completely unknown Majorana-CP-phases. Uncertainties of the nuclear matrix elements, which enter the determination of $m_{\rm ee}$ from the measured values of half-lives or of half-live limits of neutrinoless double β-decay, are not considered.

1.4 Comparison of the different neutrino mass methods

Figure 3 demonstrates that the different methods are complementary to each other and compares them. It shows, that the cosmological relevant neutrino mass scale $\sum m(\nu_{\rm i})$ has a nearly full correlation to $m(\nu_{\rm e})$ determined by direct neutrino mass experiments. The observable of neutrinoless double β-decay, the effective neutrino mass $m_{\rm ee}$, does not allow a very precise neutrino mass determination, *e.g.* to determine $\sum m(\nu_{\rm i})$, due to the unknown CP and Majorana phases and the uncertainties of the nuclear matrix elements [5]. In the case of normal hierarchy and small neutrino masses the effective neutrino mass $m_{\rm ee}$ even can vanish (see figure 3 left), which is not possible in the case of inverted hierarchy (see 3 right). On the other hand the combination of all three methods gives an experimental handle on the Majorana phases. As already mentioned in addition the exchange of SUSY particles may be the dominant process of neutrinoless double β-decay, which would spoil the whole information on the neutrino mass. Nevertheless, the search for the neutrinoless double β-decay is the only way to prove the Majorana character of neutrinos and one of the most promising ways to search for lepton number violation.

This article is structures as follows: Section 2 reports on the various searches for neutrinoless double β-decay. In section 3 the neutrino mass determination from tritium and ^{187}Re β-decay as well as from ^{163}Ho electron capture are presented. The conclusions are given in section 4.

2 Search for neutrinoless double β decay

There are 35 double β-decay isotopes with the emission of two electrons, the strong dependence of the phase space with the Q-value only makes 11 of them (Q-value larger than 2 MeV) good candidates. For most of them the normal double β-decay with neutrino emission has been observed. For neutrinoless double β-decay there is only one claim for evidence at $m_{\rm ee} \approx 0.3$ eV/c^2 by part of the Heidelberg-Moscow collaboration [18, 19], all other experiments so far set upper limits. A couple of experiments with sensitivity O(100) meV are being set up to check this claim or started data taking recently. Common to all these experiments is the use of ultrapure materials with very little radioactivity embedded in a passive and

an active shield placed in an underground laboratory. Most of them are using isotopical enriched material as well.

The most important signature of neutrinoless double β-decay is, that the sum of the energy of both decay electrons (in case of double β^- decay, positrons for double β^+ decay) is equal to the Q-value of the nuclear transition. The current proposed or running double beta search experiments are given in Table. 1.

Neutrinoless double β-decay is also sensitive to different scenarios with sterile neutrinos [20]. The sum in equation (1) will then run over more than 4 neutrino mass states and the corresponding mixing matrix elements. The experimental approaches can be classified into two methods (see Figure 4) [21]:

Isotope	nat. abund. (%)	Q-value (keV)	Experiment
^{48}Ca	0.187	4262 $\pm$ 0.84	CANDLES
^{76}Ge	7.8	2039.006 $\pm$ 0.050	GERDA, MAJORANA
^{82}Se	9.2	2997.9 $\pm$ 0.3	SuperNEMO, LUCIFER
^{96}Zr	2.8	3347.7 $\pm$ 2.2	-
^{100}Mo	9.6	3034.40 $\pm$ 0.17	AMoRE, LUMINEU, MOON
^{110}Pd	11.8	2017.85 $\pm$ 0.64	-
^{116}Cd	7.5	2813.50 $\pm$ 0.13	COBRA, $CdWO_4$
^{124}Sn	5.64	2292.64 $\pm$ 0.39	-
^{130}Te	34.5	2527.518 $\pm$ 0.013	CUORE
^{136}Xe	8.9	2457.83 $\pm$ 0.37	EXO, KamLAND-Zen, NEXT
^{150}Nd	5.6	3371.38 $\pm$ 0.20	SNO+, MCT

Table 1 The table shows the eleven candidate isotopes with a Q-value larger than 2 MeV. Given are the natural abundances and Q-values as determined from precise Penning trap measurements. The last column shows the experiments addressing the measurement of the corresponding isotope. For some experiments only the "default" isotope is mentioned as they have the option of exploring several ones. Several additional research and development projects are ongoing.

2.1 "Source=detector" configuration

In the "source=detector" configuration the double β-decay nuclei are part of the detector, which measures the sum of the energy of both β-electrons. The experimental implementation of these calorimeters are semiconductors (*e.g.* isotopes: ^{76}Ge, ^{116}Cd, experiments: GERDA, MAJORANA, COBRA), cryobolometers (*e.g.* isotope: ^{130}Te, ^{82}Se, experiments: CUORE, LUCIFER) and liquid scintillators (*e.g.*

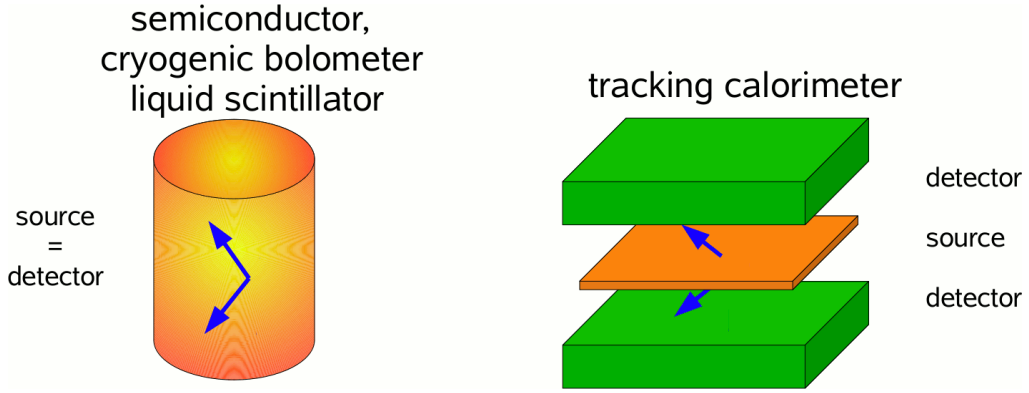

Fig. 4 Two different experimental configurations in search for the neutrinoless double β-decay.

isotope: ^{48}Ca, ^{136}Xe, ^{150}Nd, experiments: EXO-200, SNO+, NEXT, KamLAND-Zen, CANDLES). In general, this method allows more easily to install a large target mass.

Currently the most sensitive limits come from the EXO-200 and KamLAND-Zen experiment using a large amount of enriched ^{136}Xe. EXO-200 is a liquid Xenon TPC with a fiducial target mass of 80 kg installed at the WIPP in New Mexico, USA. Coincident drifted charge and scintillation light read-out allows to improve the energy resolution and to reduce the background. EX0-200 gave a half-life limit on neutrinoless double β-decay [22] of

$$t_{1/2}(^{136}\mathrm{Xe}) > 1.6 \cdot 10^{25}\ \mathrm{y} \tag{3}$$

The KamLAND-Zen-experiment uses the KamLAND-detector, which was built for long baseline reactor neutrino oscillation measurements, in which a nylon-based inner balloon of 3 m diameter was inserted. This balloon is filled with 13 t of Xenon-loaded liquid scintillator. The scintillation light coming from decays in this balloon is detected by the photomultipliers surrounding the KamLAND-detector. For the neutrinoless double β-decay search a fidcuial volume with 2.70 diameter containing 179 kg of ^{136}Xe was used yielding a half-life limit [23] of

$$t_{1/2}(^{136}\mathrm{Xe}) > 1.9 \cdot 10^{25}\ \mathrm{y} \tag{4}$$

Both the EXO-200 and the KamLAND-Zen results exclude the claimed evidence of part of the Heidelberg-Moscow collaboration for a large part of matrix element calculations.

The GERDA experiment [24] at the Gran Sasso underground laboratory is being proceeded in two phases with the option of a third phase together with the MAJORANA experiment [25]. GERDA uses enriched Germanium[1] embedded in a shielding cryostat filled with liquid argon, which itself sits in a water veto tank (see figure 5). This new shielding technique allowed to improve the background rate compared to the Heidelberg Moscow experiment by an order of magnitude. For a second phase point contact BEGe detectors for optimized pulse shape analysis are currently produced aiming for another factor 10 in background reduction. The GERDA experiment has started data taking in November 2011 and first new results in form of a new 2ν double β-decay half-life have been obtained [26]. The unblinding of the first data with a measurement time of 21 kg y is expected for summer 2013. These data should allow to give an answer on the claim by part of the Heidelberg-Moscow collaboration.

Recently a revived interest for neutrino less double electron capture [27] has been grown due to potential resonance enhancement with an excited state of the daughter nucleus [28, 29]. Due to the sharpness of the resonance a major action was taken with Penning traps to provide better atomic masses and indeed some systems like ^{152}Gd seem to fulfill the requirement for resonance enhancement (f.e. [30]). There is still a lack of understanding what the signal of neutrino less double EC to the ground state could be.

2.2 "Source≠detector" configuration

In the this configuration the double β-decay source is separated from two tracking calorimeters, which determine direction and energy of both β-electrons separately (*e.g.* isotope ^{82}Se, ^{100}Mo, experiments: NEMO3 and its much larger successor SuperNEMO, ELEGANT, MOON).

By this method the most sensitive limit comes from the NEMO3 experiment [31] in the Modane underground laboratory LSM. NEMO3 was using thin source foils of a total area of 20 m^2. These foils contained 7 kg of the double β-decay isotope ^{100}Mo and 1 kg of the double β-decay isotope ^{82}Se. The foils were surrounded by a tracking chamber in a magnetic field composed of 6400 drift cells working in Geiger mode and calorimeter made out of 1940 plastic scintillators. The recent upper limits on neutrinoless double β-decay from NEMO3 are [31]:

$$\begin{aligned} t_{1/2}(^{100}\mathrm{Mo}) &> 1.0 \cdot 10^{24}\ \mathrm{y} \quad \text{and} \quad m_{\mathrm{ee}} < 0.31 - 0.96\ \mathrm{eV} \\ t_{1/2}(^{82}\mathrm{Se}) &> 3.2 \cdot 10^{23}\ \mathrm{y} \quad \text{and} \quad m_{\mathrm{ee}} < 0.94 - 2.6\ \mathrm{eV} \end{aligned}$$

[1] The enrichment of the double β-decay isotope ^{76}Ge is about 86 %. The total mass of the phase 1 detectors amounts to 18 kg.

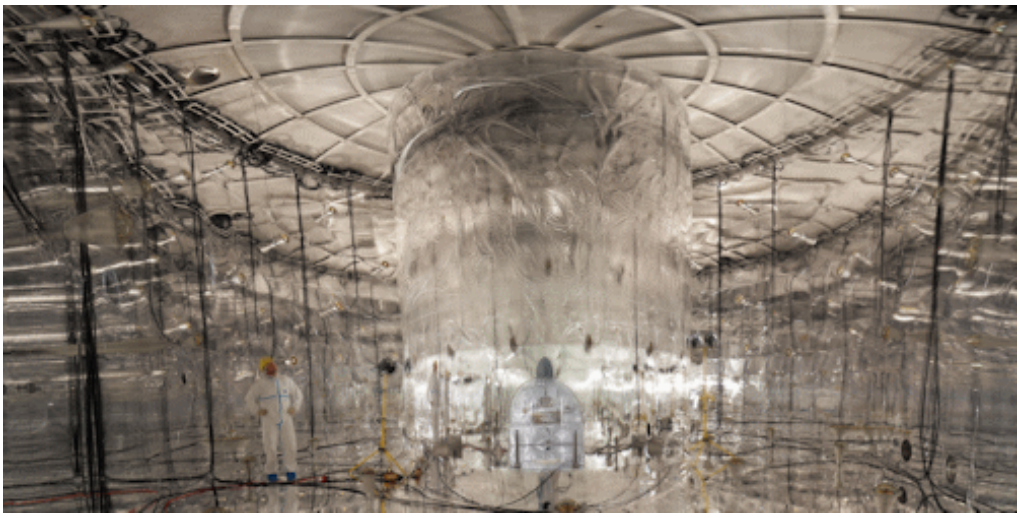

Fig. 5 View of the GERDA LAr cryostat within the water shielding which is instrumented as muon veto (Courtesy of the GERDA collaboration).

Although it requires much larger detectors to accumulate similar large target masses as in the "source=detector" case, there is the advantage, that the independent information of both electrons allows to study double β-decay processes with 2 neutrinos in detail. In case neutrinoless double β-decay would be detected, the angular correlation of both electrons will allow to draw some conclusion on the underlying process [2].

3 Direct neutrino mass experiments

The signature of a non-zero neutrino mass is a tiny modification of the spectrum of the β-electrons near its endpoint (see Figure 2), which has to be measured with very high precision. To maximize this effect, β emitters with low endpoint energy (e.g. $E_0(^{187}\mathrm{Re}) = 2.47$ keV, $E_0(^{3}\mathrm{H}) = 18.57$ keV) are favored [32].

3.1 "Source≠detector" configuration: Tritium β decay experiments

Tritium is the standard isotope for this kind of study due to its low endpoint of 18.6 keV, its rather short half-life of 12.3 y, its super-allowed shape of the β-spectrum, and its simple electronic structure. Tritium β-decay experiments using a tritium source and a separated electron spectrometer have been performed in search for the neutrino mass for more than 60 years [16, 17] yielding a sensitivity of 2 eV by the experiments at Mainz [33] and Troitsk [34]. The huge improvement of these experiments in the final sensitivity as well as in solving the former "negative $m^2(\nu_\mathrm{e})$" problem with respect to previous experiments is mainly caused by the new spectrometers of MAC-E Filter type and by careful studies of the systematics.

To further increase the sensitivity to the neutrino mass down to 200 meV by a direct measurement the KArlsruhe TRItium Neutrino experiment KATRIN [35, 36] is currently being set up at the Karlsruhe Institute of Technology KIT. Since $m^2(\nu_\mathrm{e})$ is the observable, this requires an improvement by two orders magnitude compared to the previous tritium β-decay experiments at Mainz and Troitsk. The KATRIN design is based on the successful MAC-E-Filter spectrometer technique combined with a very strong windowless gaseous molecular tritium source [36]. Figure 6 illustrates the whole 70 m long setup.

[2] A theorem by Schechter and Valle [11] requests the neutrinos to have non-zero Majorana masses, if neutrinoless double β-decay is proven to exist, but the dominant process could still be different, *e.g.* based on other BSM physics like right-handed weak charged currents, which would show a completely different angular distribution of the two electrons with respect to a neutrino mass term.

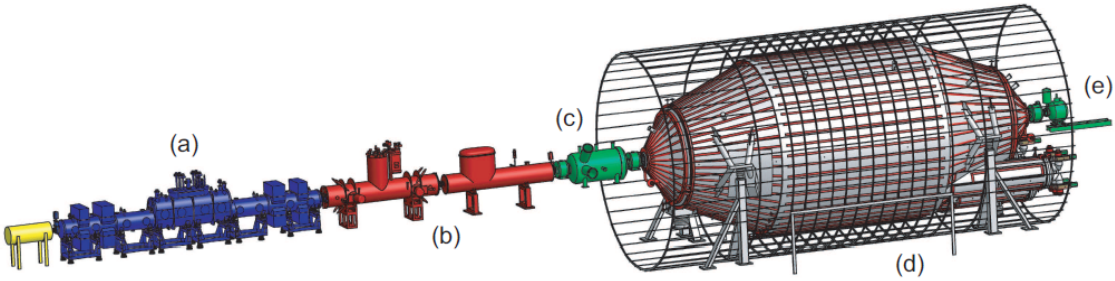

Fig. 6 Schematic view of the 70 m long KATRIN experiment consisting of calibration and monitor rear system (yellow), windowless gaseous T_2-source (a), differential pumping and cryo-trapping section (b), small pre-spectrometer (c) and large main spectrometer (d) and segmented PIN-diode detector (e). Not shown is the separate monitor spectrometer (Courtesy of the KATRIN collaboration).

The windowless gaseous molecular tritium source (WGTS) essentially consists of a 10 m long tube of 9 cm diameter kept at 30 K. Molecular tritium gas injected in the middle of this tube is freely streaming to both ends of the beam tube. The tritium gas is pumped back by huge turbo-molecular pumps placed at pump ports intersected with straight sections. The β-electrons are guided by superconducting solenoids housing the beam tubes. A so-called WGTS demonstrator has been set up to prove that the new concept of the ultra-stable beam-pipe cooling works: gaseous and liquid neon is sent through two tubes welded onto the beam tube. By stabilizing the pressure of this two-phase neon the temperature of the beam tube can be stabilized well below the requirement of 10^{-3} [37]. The input pressure is chosen to obtain a total column density of $5 \cdot 10^{17}$ molecules/cm^2 allowing a near maximum count rate at moderate systematic uncertainties [38]. Currently the WGTS demonstrator is being upgraded into the full WGTS.

The electron guiding and tritium retention system consists of a differential and a cryogenic pumping unit. It has been demonstrated that the tritium flow reduction by the differential pumping is about as large as expected by Monte Carlo simulations [39]. Inside the differential pumping sections Fourier transform ion cyclotron resonance Penning traps will be installed to measure the ion flux from the tritium source [40]. Ions will be ejected from the beam by a transverse electric field. The principle of the cryogenic pumping section based on argon frost at $3 - 4.5$ K has been demonstrated in a test experiment [41]. The overall tritium reduction amounts to 10^{-14}.

A pre-spectrometer will transmit only the interesting high energy part of the β-spectrum close to the endpoint into the main spectrometer [42], in order to reduce the rate of background-producing ionization events therein. The big main spectrometer is of MAC-E-Filter type as the pre spectrometer. It is essentially an electric retarding spectrometer with a magnetic guiding and collimating field [43]. In order to achieve the strong energy resolution of 1:20,000 the magnetic field in the analyzing plane in the centre of the spectrometer has to be 20,000 times smaller than the maximum magnetic field of 6 T provided by the pinch magnet. Due to conservation of the magnetic flux from the WGTS to the spectrometer it needs to have a diameter of 10 m in the analyzing plane. To avoid background by scattering of β-electrons inside the spectrometer extreme requirements for the vacuum pressure of $p \approx 10^{-11}$ mbar are necessary [44]. The β-electrons which have enough energy to pass the MAC-E-Filter are counted with a state-of-the-art segmented PIN detector. The spatial information provided by the 148 pixels allow to correct for the residual inhomogeneities of the electric retarding potential and the magnetic fields in the analyzing plane. Active and passive shields minimize the background rate at the detector.

Of crucial importance is the stability of the retarding potential. KATRIN is using a twofold way to achieve the necessary redundancy: A custom-made ultra-high precision HV divider [45] developed together with the PTB Braunschweig and a state-of-the-art 8.5 digit digital voltmeter measure directly the retarding voltage. In addition the retarding voltage is applied to a third MAC-E-Filter, the so-called monitor spectrometer reusing the former MAC-E-Filter at Mainz. The line position of ultra-stable electron

Fig. 7 Wire electrode system inside the KATRIN main spectrometer during installation, photo: M. Zacher.

sources based on the isotope ^{83m}Kr [46] is continuously compared to the retarding voltage of the main spectrometer. Both methods reach the required ppm precision.

The sensitivity limit of 200 meV on the neutrino mass for the KATRIN experiment is based on a background rate of 10^{-2} cts/s, observed under optimal conditions at the experiments at Mainz and Troitsk using similar MAC-E-Filters. To reach this low background rate with the so much larger KATRIN instrument requires new methods. At Mainz the main residual background originated from secondary electrons ejected from the walls/electrodes on high potential by passing cosmic muons or by γs from radioactive impurities. Although there is a very effective magnetic shielding by the conservation of the magnetic flux, small violations of the axial symmetry or other inhomogeneities allowed a fraction of about 10^{-5} of these secondary electrons to reach the detector and to be counted as background. A new method to reject these secondary electrons from the electrodes has been developed and successfully tested at the Mainz spectrometer [47]: nearly mass-less wires are installed in front of these electrodes, which are put on a more negative electrical potential than the electrode potential by -100 V to -200 V. For KATRIN a double layer wire electrode system consisting of 248 modules with 23440 wires in total has been developed, which should reduce the secondary electron background by a factor 100 [54]. Its installation (fig. 7) has been completed in early 2012.

Other relevant background sources are decays of radioactive atoms in the spectrometer volumes, e.g. the fast decaying radon isotope ^{219}Rn from emanation out of the non-evaporable getter pumps [49] or small amounts of tritium originating from the WGTS [50]. They create electrons, which might be stored by the magnetic mirror effect and/or by the negative potentials of the two MAC-E-Filters or within the non-avoidable Penning trap between the pre and the main spectrometers. For these backgrounds new methods have been developed to avoid storage of electrons or to eject them [51, 52, 53].

Since the KATRIN experiment will investigate only the very upper end of the β-spectrum, quite a few systematic uncertainties will become negligible because of excitation thresholds. Others systematics like the inelastic scattering fraction or the source intensity will be controlled very precisely by measuring the column density online by an angular-selective electron gun [54, 55], by keeping the temperature and pressure within the tritium source at the per mille level constant [38] and by determining the tritium fraction of the gas in the source by laser Raman spectroscopy to the sub per mille level [56]. An important consistency check of the correct systematic corrections will be comparison of the endpoint energy E_0 fitted from the β-spectrum with a precision value derived from ultra-high precision ion cyclotron resonance mass spectroscopy in a multi-Penning trap setup measuring the ^{3}He-^{3}H mass difference [57] with the final goal

to use the measured Q-value in the neutrino mass fit. KATRIN's sensitivity will allow to fully investigate the *quasi-degenerate neutrino mass* regime to distinguish between different neutrino mass models as well as to fully investigate the cosmological relevant neutrino mass range, where neutrino masses would shape significantly structure formation. In addition, the KATRIN experiment will be sensitive to contributions to sterile neutrinos [58, 59, 60] as suggested by the so-called reactor anomaly.

The commissioning of the KATRIN spectrometer and detector system has started in May 2013. The tritium source as well as the electron transport and tritium elimination section will be put into operation in 2014. First tritium data with the full KATRIN setup are expected for 2015.

There is also R&D on rather different approaches, like Project-8, which wants to measure the endpoint spectrum of tritium β-decay by detecting the radio emission of coherent cyclotron radiation from a KATRIN-like tritium source [61, 62]. Its main idea is that the cyclotron frequency $\omega = (eB)(\gamma m_e)$ scales inversely with γ, only the radiated power but not the frequency depends on the angle of the emitted β-electron w.r.t. the magnetic field. Measuring the β-spectrum by synchrotron radiation has the principle advantage that the radiofrequency photons can leave a tritium source, which is already opaque for electrons thus allowing much larger source strengths. Currently the Project-8 collaboration is investigating, whether this very low intensity coherent cyclotron radiation can be detected.

3.2 "Source=detector" configuration: ^{187}Re β-decay and ^{163}Ho electron capture experiments

3.2.1 ^{187}Re β-decay experiments

Compared to tritium the isotope $^{187}\mathrm{Re}$ has a 7 times lower endpoint energy of 2.47 keV resulting in a 350 times higher relative fraction of the β-spectrum in the interesting endpoint region. Unfortunately $^{187}\mathrm{Re}$ exhibits a very complicated electronic structure and a very long half life of $4.3 \cdot 10^{10}$ y. This disadvantage can be compensated by using it as β-emitter in cryo-bolometers, which measure the entirely energy released in the absorber, except that of the neutrino.

A cryo-bolometer is not an integral spectrometer like the MAC-E-Filter but measures always the entire β-spectrum. Pile-up of two random events may pollute the endpoint region of a β-decay on which the neutrino mass is imprinted. Therefore cryo-bolometers with mg masses are required to suppress pile-up by 4 or more orders of magnitude. Unfortunately large arrays of cryo-bolometers are then required to reach the necessary sensitivity to the neutrino mass. Another technical challenge is the energy resolution of the cryo-bolometers. Although cryo-bolometers with an energy resolution of a few eV have been produced with other absorbers, this resolution has not yet been achieved with rhenium.

Two groups have started the field of $^{187}\mathrm{Re}$ β-decay experiments: The MANU experiment at Genoa was using one metallic rhenium crystal of 1.6 mg working at a temperature of 100 mK and read out by Germanium doped thermistor. The β environmental fine structure was observed for the first time giving rise to a modulation of the shape of the β-spectrum by the interference of the out-going β-electron wave with the rhenium crystal [63]. The spectrum near the endpoint allowed to set an upper limit on the neutrino mass of $m(\nu_\mathrm{e}) < 26$ eV [64]. The MiBeta collaboration at Milano was using 10 crystals of $AgReO_4$ with a mass of about 0.25 mg each [65]. The energy resolution of a single bolometer was about 30 eV. One year of data taking resulted in an upper limit of $m(\nu_\mathrm{e}) < 15$ eV [65].

Both groups are now working together with additional groups in the MARE project [66] to further the development of sensitive micro-calorimeters investigating the $^{187}\mathrm{Re}$ β-decay. MARE consists of two phases [67]: MARE-1 aims to investigate alternative micro-calorimeter concepts to improve the energy resolution, to shorten the rise time of the signals and to develop possibly a multi-plexing read-out. A summary of the sensitivity reach dependent on these detector properties can be found in [68]. Among these possible technologies for MARE are transition edge and neutron-doped thermistors for the temperature read-out, but also new technologies based on magnetic micro-calorimeters [69]. These new dectectors are being tested in medium-size arrays with up to 300 cryo-bolometers enabling MARE-1 to reach a sensitivity to the neutrino mass of a few $\mathrm{eV/c^2}$. After selection of the most successful technique a full scale experiment with sub-eV/c^2 sensitivity to the neutrino mass will then be set up in MARE phase 2 comprising about 50000 detectors.

3.2.2 ^{163}Ho electron capture experiments

MARE is not only aiming at the ^{187}Re β-decay but also wants to investigate the electron capture of ^{163}Ho, triggered by the persisting difficulties with superconducting metallic rhenium absorbers coupled to the sensors [70]. The isotope ^{163}Ho could be implanted into well-suited cryo-bolometers. The very upper end of the electromagnetic de-excitation spectrum of the ^{163}Ho daughter ^{163}Dy looks similar to the endpoint spectrum of a β-decay and is sensitive to the neutrino mass [71]. Additionally, the ECHO collaboration has been set up to investigate the direct neutrino mass search with ^{163}Ho implanted in magnetic micro-calorimeters [72]. In these detectors, the temperature change following an energy absorption is measured by the change of magnetization of a paramagnetic sensor material (Au : Er) sitting in an external magnetic field. This change of magnetization is read out by a SQUID. A first ^{163}Ho spectrum has been presented [69]. Again large efforts are been undertaken to develop a multi-plexing read-out technology to allow the run large arrays of these magnetic micro-calorimeters.

4 Conclusions

The absolute neutrino mass scale is addressed by three different methods. The analysis of large scale structure data and the anisotropies of the cosmic microwave background radiation are very sensitive but model dependent. The search for neutrinoless double β-decay requires neutrinos to be their own antiparticles (Majorana neutrinos) and is measuring a coherent sum over all neutrino masses contributing to the electron neutrino with unknown phases. Therefore – even without the contribution of other beyond the Standard Model physics processes – the value of the neutrino mass cannot be determined very precisely. On the other hand the discovery of neutrinoless double β-decay would be the detection of lepton number violation, which would be an extraordinary important discovery. A few double β-decay experiments of the second generation like EXO-200 and KamLAND-Zen have already delivered exciting new data, much more, e.g. given from the GERDA-experiment, will come in the near future. Among the various ways to address the absolute neutrino mass scale the investigation of the shape of β-decay spectra around the endpoint is the only real model-independent method, independently of other beyond the Standard Model physics processes. The KATRIN experiment is being setup at Karlsruhe and will start data taking in 2015, whereas the MARE experiment is commissioning a small array of detectors starting MARE phase 1 and ECHO is developing a new technology of electron capture experiments. The latter field of cryogenic calorimeters is also driven by the field of astronomy, where arrays of cryogenic bolometers with O(1000) pixels have been established already. From both laboratory approaches, the search for neutrinoless double β-decay and the direct neutrino mass determination, we expect in the coming years sensitivities on the neutrino mass of O(100) meV.

5 Acknowledgments

The work of the authors is supported by the German Ministery for Education and Research BMBF and the German Research Society DFG.

6 Bibliography

References

[1] G.L. Fogli *et al.*, *"Global analysis of neutrino masses, mixings and phases: entering the era of leptonic CP violation searches"*, arXiv:1205.5254v3
[2] R. N. Mohapatra, A. Y. Smirnov, *"Neutrino Mass and New Physics"*, Ann. Rev. Nucl. Part. Sci. 56 (2006) 569
[3] K.N. Abazajian *et al.*, *"Cosmological and Astrophysical Neutrino Mass Measurements"*, Astropart. Phys. 35 (2011) 177
[4] M. Goeppert-Mayer, *Phys. Rev.* 48 (1935) 512
[5] F. Simkovic *et al.*, Phys. Rev. **C79** 055501 (2009)

[6] W. Rodejohann, Int. J. Mod. Phys. E **20** 1833 (2011)
[7] ATLAS-collaboration, ATLAS-CONF-2011-115 (2011)
[8] G. Aad et al., ATLAS-collaboration, Eur. Phys. J. C **72** 2244 (2012)
[9] S. Chatrchyan et al., CMS-collaboration, Eur. Phys. J. C **72** 2189 (2012)
[10] S. Chatrchyan et al., CMS-collaboration, Phys. Lett. B **717** 109 (2012)
[11] J. Schechter and J.W.F. Valle, Phys. Rev. **D25**, 2951 (1982)
[12] K. Zuber, Prog. Part. Nucl. Phys **48**, 223 (2002)
[13] B. Schwingenheuer, *"Status and prospects of searches for neutrinoless double beta decay"*, Annalen d. Physik, (2013)
[14] T.J. Loredo and D.Q. Lamb, *"Bayesian analysis of neutrinos observed from supernova SN 1987A"*, Phys. Rev. D65 (2002) 063002
[15] G. Pagliarolia, F. Rossi-Torresa and F. Vissania, *"Neutrino mass bound in the standard scenario for supernova electronic antineutrino emission"*, Astropart. Phys. 33 (2010) 287
[16] E.W. Otten and C. Weinheimer, *"Neutrino mass limit from tritium beta decay"*, Rep. Prog. Phys. 71 (2008) 086201
[17] G. Drexlin, V. Hannen, S. Mertens, C. Weinheimer, *'Current Direct Neutrino Mass Experiments"*, Advances in High Energy Physics 2013, 293986 (2013)
[18] H.V. Klapdor-Kleingrothaus *et al.*, Phys. Lett. **B 586**, 198 (2004)
[19] H.V. Klapdor-Kleingrothaus *et al.*, Mod. Phys. Lett. A 21 (2006) 1547
[20] J. Barry, W. Rodejohann, H. Zhang, JHEP 1107, 091 (2011)
[21] A. Guiliani, Acta Phys. Polnica **41** Issue 7, 1447 (2010)
[22] M. Auger *et al.*, Phys. Rev. Lett.**109**, 032505 (2012)
[23] A. Gando *et al.*, Phys. Rev. Lett.**110**, 062502 (2013)
[24] K.-H. Ackermann *et al.*, Eur. Phys. J. C **73** 2330 (2013)
[25] C. E. Aalseth *et al.* [MAJORANA Collaboration], J. Phys. Conf. Ser. **203**, 012057 (2010) [arXiv:0910.4598 [nucl-ex]].
[26] M. Agostini *et al.*, J. Phys. G**40**, 035110 (2013)
[27] J. Bernabeu, A. De Rujula, C. Jarlskog, *"Neutrinoless double electron capture as a tool to measure the electron neutrino mass"*, Nucl. Phys. B **223**(1983) 15
[28] Z. Sujkowski, S. Wycech, Phys. Rev. C **70** 052501 (2004)
[29] M. I. Krivoruchenko, F. Simkovic, D. Frekers and A. Faessler, *"Resonance enhancement of neutrinoless double electron capture"*, Nucl. Phys. A **859** (2011) 140
[30] S. Eliseev *et al.*, Phys. Rev. Lett.**106**, 052504 (2011)
[31] L. Simard, J. Phys. Conf. Ser. **375**, 042011 (2012)
[32] C. Weinheimer,*"Direct neutrino mass measurements"*, Hyperfine Interactions, DOI 10.1007/s10751-013-0808-7
[33] C. Kraus *et al.*, Eur. Phys. J. **C40**, 447 (2005)
[34] V.N. Aseev *et al.*, *"Upper limit on the electron antineutrino mass from the Troitsk experiment"*, Phys. Rev. D 84 (2011) 112003
[35] A. Osipowicz *et al.* (KATRIN Collaboration), arXiv:hep-ex/0109033
[36] J. Angrik *et al.* (KATRIN Collaboration), KATRIN Design Report 2004, Wissenschaftliche Berichte FZ Karlsruhe 7090, http://bibliothek.fzk.de/zb/berichte/FZKA7090.pdf
[37] S. Grohmann *et al.*, *"Precise temperature measurement at 30 K in the KATRIN source cryostat"*, Cryogenics 51, 8 (2011) 438-445
[38] M. Babutzka *et al.*, *"Monitoring of the operating parameters of the KATRIN Windowless Gaseous Tritium Source"*, New Journal of Physics 14 (2012) 103046
[39] S. Lukic *et al.*, *"Measurement of the gas-flow reduction factor of the KATRIN DPS2-F differential pumping section"*, Vacuum 86 (8)(2012) 1126–1133.
[40] M. Ubieto-Díaz *et al.*, *"A broad-band FT-ICR Penning trap system for KATRIN"*, Int. J. of Mass Spect. 288 (2009) 1–5
[41] O. Kazachenko *et al.*, *"TRAP - a cryo-pump for pumping tritium on pre-condensed argon"*, Nucl. Instrum. Meth. A 587 (2008) 136
[42] M. Prall *et al.*, *"The KATRIN Pre-Spectrometer at reduced Filter Energy"*, New J. Phys. 14 (2012) 073054
[43] A. Picard *et al.*, *"A solenoid retarding spectrometer with high resolution and transmission for keV electrons"*, Nucl. Instrum. Meth. B 63 (1992) 345
[44] X. Luo, L. Bornschein, C. Day, J. Wolf, *"KATRIN NEG pumping concept investigation"*, Vacuum 81 (2007) 777
[45] T. Thümmler *et al.*, *"Precision high voltage divider for the KATRIN experiment"*, New J. Phys. 11 (2009) 103007
[46] D. Venos *et al.*, *Development of a super-stable standard for monitoring the energy scale of electron spectrometers in the energy range up to 20 keV*, Measurement Techniques 53 (2010) 573

[47] B. Flatt, *Voruntersuchungen zu den Spektrometern des KATRIN-Experiments*, PhD Thesis in German language, Mainz University, 2005
[48] K. Valerius, *"The wire electrode system for the KATRIN main spectrometer"*, Progr. Part. and Nucl. Phys. 64(2) (2010) 291–293
[49] F.M. Fränkle *et al.*, *"Radon induced background processes in the KATRIN pre-spectrometer"*, Astropart. Phys. 35 (2011) 128-134
[50] S. Mertens *et al.*, *"Background due to stored electrons following nuclear decays in the KATRIN spectrometers and its impact on the neutrino mass sensitivity"*, acc. for publ. in Astropart. Phys. (2012)
[51] M. Beck *et al.*, *"Effect of a sweeping conductive wire on electrons stored in a Penning-like trap between the KATRIN spectrometers"*, Eur. Phys. J. A 44 (2010) 499
[52] B. Hillen , *Untersuchung von Methoden zur Unterdruckung des Spektrometeruntergrunds beim KATRIN Experiment*, PhD thesis in German language, University of Münster, 2011
[53] S. Mertens *et al.*, *"Stochastic Heating by ECR as a Novel Means of Background Reduction in the KATRIN Spectrometers"*, acc. for publ. in J. of Instr. (2012)
[54] K. Valerius *et al.*, *"Prototype of an angular-selective photoelectron calibration source for the KATRIN experiment"*, J. of Instr. 6 (2011) P01002
[55] K. Hugenberg [KATRIN Collaboration], *An Angular Resolved Pulsed Uv Led Photoelectron Source For Katrin*, Prog. Part. Nucl. Phys. 64 (2010) 288
[56] M. Sturm *et al.*, *"Monitoring of all hydrogen isotopologues at tritium laboratory Karlsruhe using Raman spectroscopy"*, Laser Phys. 20 (2010) 493-507
[57] K. Blaum, Novikov Yu. N. and G. Werth, *"Penning traps as a versatile tool for precise experiments in fundamental physics"*, Contemp. Phys., 51: 2 (2010) 149 175
[58] A. Sejersen-Riis and S. Hannestad, *"Detecting sterile neutrinos with KATRIN like experiments"*, JCAP (2011) 1475
[59] J. A. Formaggio and J. Barrett, *"Resolving the Reactor Neutrino Anomaly with the KATRIN Neutrino Experiment"*, Phys. Lett. B 706 1 (2011) 68–71
[60] A. Esmaili and Orlando L. G. Peres, *"KATRIN Sensitivity to Sterile Neutrino Mass in the Shadow of Lightest Neutrino Mass"*, arXiv:1203.2632 [hep-ph]
[61] B. Monreal and J. Formaggio, *"Relativistic cyclotron radiation detection of tritium decay electrons as a new technique for measuring the neutrino mass"*, Phys. Rev. D 80 (2009) 051301(R)
[62] J. Formaggio, *"Project 8: Using Radio-Frequency Techniques to Measure Neutrino Mass"*, arXiv:1101.6077v1 [nucl-ex] (2011)
[63] F. Gatti *et al.*, *"Detection of environmental fine structure in the low-energy beta-decay spectrum of Re-187"*, Nature 397 (1999) 137
[64] F. Gatti, *"Microcalorimeter measurements"*, Nucl. Phys. B - Proc. Supp. 91 (2001) 293
[65] M. Sisti *et al.*, *"New limits from the Milano neutrino mass experiment with thermal microcalorimeters"*, Nucl. Inst. and Meth. A 520 (2004) 125-131
[66] A. Monfardini *et al.*, *"The microcalorimeter arrays for a rhenium experiment (MARE): A next-generation calorimetric neutrino mass experiment*, Nucl. Instr. Meth. A 559 (2006) 346
[67] A. Nucciotti, *"The MARE Project"*, J. of Low Temp. Phys. 151 (2008) 597–602
[68] A. Nucciotti, E. Ferri, O. Cremonesi, *'Expectations for a new calorimetric neutrino mass experiment"*, Astropart. Phys. 34 (2010) 80
[69] P.C.-O. Ranitzsch *et al.*, *"Development of metallic magnetic calorimeters for high precision measurements of calorimetric ^{187}Re and ^{163}Ho spectra"*, J. of Low Temp. Phys. 167 (2012) 1004
[70] E. Ferri, *"MARE-1 in Milan: Status and Perspectives"*, J. of Low Temp. Phys. 167 (2012) 1035
[71] A. De Rujula, *A new way to measure neutrino masses"*, Nuclear Physics B, vol. 188, no 3. (1981) 414
[72] L. Gastaldo *et al.*, *"Characterization of low temperature metallic magnetic calorimeters having gold absorbers with implanted ^{163}Ho ions"*, arXiv:1206.5647

WILEY ONLINE LIBRARY
Early View publication on wileyonlinelibrary.com
(issue and page numbers not yet assigned;
citable using Digital Object Identifier – DOI)

Ann. Phys. (Berlin), 1–12 (2013) / DOI 10.1002/andp.201300043

annalen der physik

Review Article

Precision measurements in nuclear β-decay with LPCTrap

G. Ban[1], D. Durand[1], X. Fléchard[1], E. Liénard[1,], and O. Naviliat-Cuncic[2]*

Received 1 March 2013, revised 12 April 2013, accepted 24 April 2013
Published online 31 May 2013

The experimental achievements and the current program with the LPCTrap device installed at the LIRAT beam line of the SPIRAL1-GANIL facility are presented. The device is dedicated to the study of the weak interaction at low energy by means of precise measurements of the $\beta-\nu$ angular correlation parameter. Technical aspects as well as the main results are reviewed. The future program with new available beams is briefly discussed.

1 The $\beta-\nu$ angular correlation

The structure of the weak interaction remains an important topic in the area of fundamental interaction physics. In particular, at low energies, there are nowadays ambitious experimental programs to search for "exotic" currents beyond the *V–A* theory [1, 2]. Such studies have recently made significant progress with the advent of improved trapping techniques [3, 4]. These sophisticated setups allow the production of β-decay sources almost at rest and confined in small volumes that can be surrounded by suitable detectors [5, 6]. We describe here the achievements made with the LPCTrap setup installed at GANIL[1]. The experimental program is dedicated to precision measurements of the $\beta-\nu$ angular correlation parameter.

From a theoretical point of view, the generalization of Fermi's theory leads to consideration of five different Lorentz invariant contributions in the transition amplitude describing nuclear beta decay, which are referred to as *scalar* (*S*), *vector* (*V*), *tensor* (*T*), *axial-vector* (*A*) and *pseudoscalar* (*P*). The search for *S* and *T* exotic contributions can be performed through a precise measurement of the $\beta-\nu$ angular correlation parameter, $a_{\beta\nu}$. For allowed transitions and nonoriented nuclei, this parameter can be directly inferred from an events distribution linked to the angular correlation between the leptons [7].

[1] GANIL: Grand Accélérateur National d'Ions Lourds

Since neutrinos are difficult to detect, a sensitive observable for a $\beta-\nu$ angular correlation measurement is a kinematic parameter of the recoiling daughter nucleus. If the β particles and the recoil ions are detected in coincidence and the relative time of flight (ToF) is measured between the two particles, the expected distribution of events in the electron energy and recoil ion time of flight, *t*, is for all solid angles detected:

$$N(T_e, t)\mathrm{d}T_e\mathrm{d}t = KF(\pm Z, E_e)(T_e + mc^2)(r(t))^3(Q - T_e)\xi \times \left(1 + a\beta\nu\frac{(r(t))^2c^2 - 2T_eE_e - Q(Q - 2T_e)}{2E_e(Q - T_e)} + b\frac{mc^2}{E_e}\right)\mathrm{d}T_e\mathrm{d}t, \quad (1)$$

where T_e, E_e and $r(t)$ denote the kinetic and total energies of the β particle and the recoil ion momentum, respectively. Q is the energy available in the transition, K is a constant and $F(\pm Z, E_e)$ is the Fermi function (β^- and β^+ decays). The parameter $a_{\beta\nu}$ and the Fierz interference term b depend on the coupling constants, C_i and C_i' ($i = S, V, T, A$), associated to the different contributions [7]:

$$a_{\beta\nu}\,\xi = |M_F|^2\ [(-|C_S|^2 - |C_S'|^2 + |C_V|^2 + |C_V'|^2) \mp 2\frac{\alpha Zm}{p_e}\,\mathrm{Im}(C_SC_V^* + C_S'C_V'^*)] + \frac{|M_{GT}|}{3}\ [(|C_T|^2 + |C_T'|^2 - |C_A|^2 - |C_A'|^2) \pm 2\frac{\alpha Zm}{p_e}\mathrm{Im}(C_TC_A* + C_T'C_A'*)] \quad (2)$$

$$b\xi = \pm 2\sqrt{1-\alpha^2Z^2}\ \mathrm{Re}[|M_F|^2\ (C_SC_V^* + C_S'C_V'*) + |M_{GT}|^2(C_TC_A^* + C_T'C_A'*)], \quad (3)$$

* Corresponding author E-mail: lienard@lpccaen.in2p3.fr
[1] LPC Caen, ENSICAEN, Université de Caen, CNRS/IN2P3, Caen, France
[2] NSCL and Department of Physics and Astronomy, Michigan State University, East-Lansing, MI, USA

where

$$\xi = |M_F|^2(|C_S|^2 + |C_S'|^2 + |C_V|^2 + |C_V'|^2) + |M_{GT}|^2(|C_T|^2 + |C_T'|^2 + |C_A|^2 + |C_A'|^2). \quad (4)$$

M_F and M_{GT} are the Fermi (F) and Gamow–Teller (GT) nuclear matrix elements, α is the fine structure constant, Z is the atomic number of the daughter nucleus and m and p_e are the mass and momentum of the β particle, respectively. The P contribution is neglected in a nonrelativistic description of the nucleons. The existence of both coupling constants, C_i and C_i', is related to the transformation properties under parity. The Standard Model (SM) assumes maximal parity violation ($|C_i| = |C_i^{'}|$), time reversal invariance (C_i, C_i' real) and pure vector and axial-vector interactions (V–A theory). The $\beta-\nu$ angular correlation parameter is then given by:

$$a_{\beta\nu} = \frac{1-\rho^2/3}{1+\rho^2}, \quad (5)$$

where $\rho = \frac{C_A M_{GT}}{C_V M_F}$ is the mixing ratio of the transition, leading to $a_{\beta\nu} = 1$ for a pure F transition and $a_{\beta\nu} = -1/3$ for a pure GT transition.

Under the conditions of the present experiment, the parameter that is determined experimentally is actually:

$$\tilde{a}_{\beta\nu} = a_{\beta\nu} / \left(1 + \left\langle b\frac{mc^2}{E_e}\right\rangle\right), \quad (6)$$

where the brackets $< >$ mean a weighted average over the measured part of the β spectrum.

For mirror transitions, the measurement of $a_{\beta\nu}$ also allows for a precise determination of the mixing ratio ρ. If the half-life, the branching ratio (BR) and the masses involved in the transition are well known, this ratio can be used to deduce the first element of the Cabbibo–Kobayashi–Maskawa (CKM) quark mixing matrix, V_{ud} [8]:

$$V_{ud}^2 = \frac{4.794 \times 10^{-5}}{(Ft_{1/2})G_F^2 |M_F|^2 (1+\Delta_R)(1+\frac{f_A}{f_V}\rho^2)}, \quad (7)$$

where $Ft_{1/2}$ is the corrected ft-value of the transition, G_F is the weak interaction fundamental constant, Δ_R is a common radiative correction and f_A (f_V) is the rate statistical function computed for the GT (F) component. Many interesting mirror transitions exist [9], which could form an additional database to test the conserved vector current (CVC) hypothesis in nuclei and to determine V_{ud}.

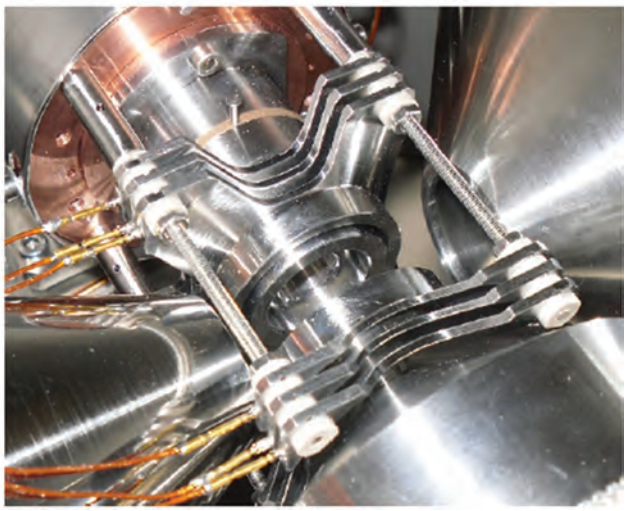

Figure 1 Picture of the transparent Paul trap of the LPCTrap setup.

2 The LPCTrap setup

The experimental setup is installed at the low-energy beam line LIRAT[2] of the SPIRAL1-GANIL[3] facility. Technical details of the setup are described elsewhere [5, 10–12]. The central element of the device is a transparent Paul trap (Fig. 1) constructed to confine singly charged radioactive ions, almost at rest, in a small volume, allowing the detection in coincidence of the β particles and of the recoiling ions. The trap consists of 6 concentric rings with an open geometry, allowing easy injection and extraction as well as an efficient detection of the decay products.

Upstream of the trap, the installation is equipped with a radio-frequency quadrupole cooler-buncher (RFQCB) for the preparation of the beam by reducing the emittance and the production of ion bunches. The low-energy radioactive beam is provided by the ECR source of the SPIRAL facility with a typical energy dispersion of about 20 eV at 10 keV total kinetic energy. The RFQCB is connected to the Paul trap by a short transport line with dedicated beam optics and diagnostics. The offline tuning of the ensemble is made possible by the coupling of an ion source at the entrance of the setup. There, a Faraday cup and a retractable silicon detector provide efficient beam diagnostics. A layout of the equipment is shown in Fig. 2.

[2] LIRAT: Ligne d'Ions RAdioactifs à Très basse énergie

[3] SPIRAL: Système de Production d'Ions Radioactifs Accélérés en Ligne

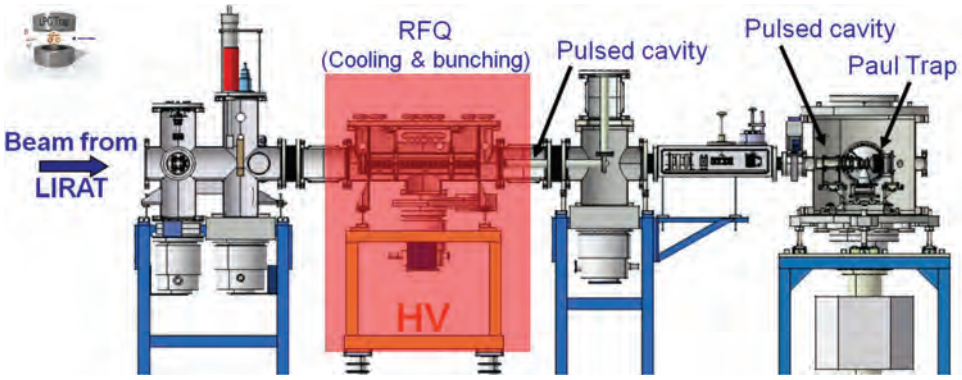

Figure 2 Scheme of the full LPCTrap setup.

The incident beam is first decelerated below a few tens eV by the H.V. applied to the RFQCB platform. This enables the cooling of the ions by collisions with a buffer gas (H_2 or ^{4}He) at a pressure of the order of 10^{-2} mbar. Beam bunches are produced near the exit of the quadrupole at a repetition rate of the order of 10 Hz (cycle). A first pulse cavity is used to transport the bunches at 1 keV downstream from the RFQCB. A second pulse cavity reduces the kinetic energy of the ions at 100 eV for an efficient injection into the Paul trap. There, the ions are once again cooled by elastic collisions with an inert gas injected at very low pressure (10^{-6}–10^{-5} mbar). At equilibrium, the thermalized ions have energies of about 0.1 eV and the diameter of the ion cloud located at the center of the trap is of the order of 2.5 mm (see Fig. 7 in the next section).

Two different detection setups, shown in Fig. 3, have been used in the experiments. In both setups, a telescope and a microchannel plate position sensitive detector (MCPPSD) detect the β particles and the recoil ions, respectively. In the first setup, both detectors are located 10 cm away from the center of the trap in a back-to-back configuration. The β telescope is made of a 60×60 mm^2 300-μm thick double-sided silicon strip detector (DSSSD) for position readout, followed by a 7-cm thick plastic scintillator coupled to a photomultiplier to measure the β particle kinetic energy and to deliver the start signal for the recoil ion time-of-flight measurement. The

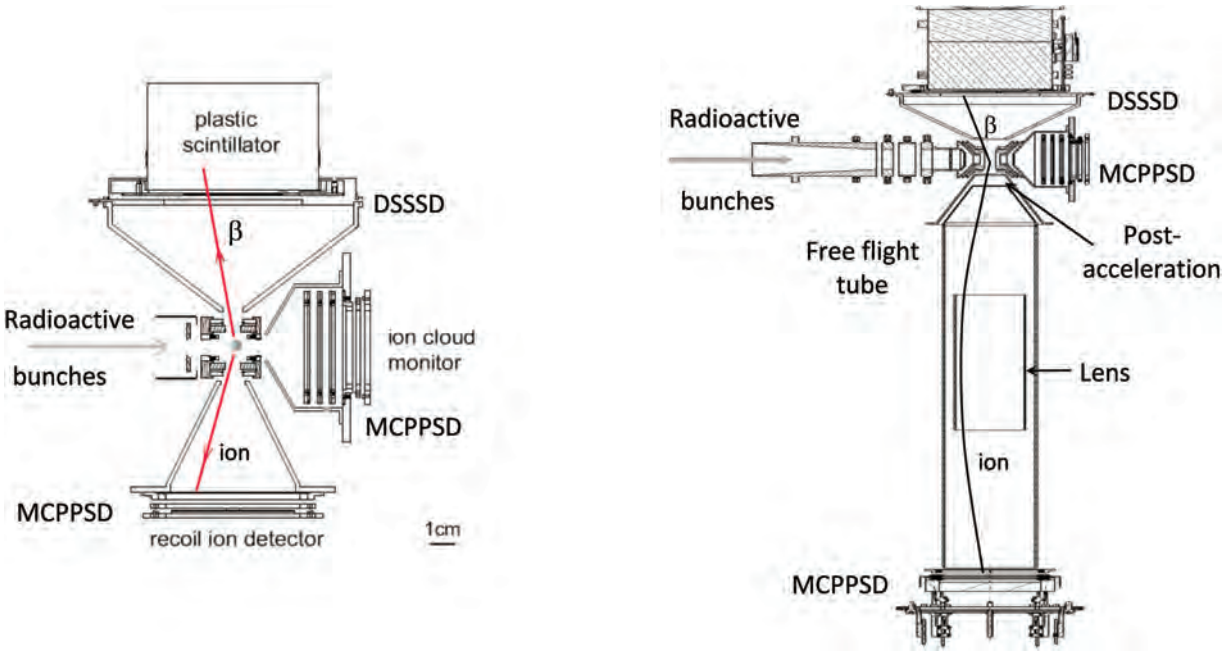

Figure 3 Top view of the detection chamber of LPCTrap. Left panel: First detection setup used in the commissioning phase. Right panel: Improved detection setup allowing the separation of the charge states of the recoil ions.

stop signal is delivered by the MCPPSD whose performances are detailed in Ref. [13]. For each coincidence event, the positions of both particles, the recoil ion ToF, the β particle kinetic energy, the time stamp of the decay within the cycle and the RF phase of the trap are recorded. This set of measured parameters is useful to control systematic effects and to check the consistency of the results.

In the second setup implemented in 2010 (Fig. 3, right panel), a spectrometer has been added to separate the charge states of the recoil ions. The ions emitted towards the spectrometer are accelerated by a –2 kV potential after they cross the collimator located in front of a 50-cm long free-flight tube. An electrostatic lens set at −250 V allows the collection of all the ions on the MCPPSD located at the end of the tube. The front plate of the detector is set at –4 kV to ensure a maximum detection efficiency for all charge states, independently of the ion kinetic energy. This spectrometer makes LPCTrap a unique and unprecedented setup for the measurement of charge-state distributions of ions associated with the β decay of singly charged radioactive ions.

3 Measurements in the decay of ^{6}He

The first nucleus of interest that has been considered is ^{6}He, which decays via a pure GT transition. For such transitions, the experiment described here was the first performed after decades following the last measurements of the beta-neutrino angular correlation in the β decay of ^{6}He [14–16] and ^{23}Ne [17, 18]. Another new experiment, measuring the $\beta-\alpha-\alpha$ correlation from trapped ^{8}Li ions, has recently reported the first results [19]. Among these experiments, only one measurement in the decay of ^{6}He [14] was performed with a relative precision at the level of 1%, yielding $a_{\beta\nu} = -0.3308(30)$ after inclusion of radiative and recoil-order currents corrections [20].

At GANIL, the $^6He^{1+}$ beam is produced by the fragmentation of a primary ^{13}C beam at 75 MeV/u on a graphite target coupled with an ECR source. The low-energy beam is delivered at 10 keV through the LIRAT beam line with a maximum intensity of about 1.5×10^8 pps. The resolving power ($M/\Delta M \sim 250$) of the dipole magnet located at the entrance of the low-energy beam line is not sufficient to eliminate the 10 nA of a stable beam containing mainly $^{12}C^{2+}$, but this contamination is drastically reduced in the RFQ.

A first experiment was performed using the initial setup (Fig. 3, left panel) with a measurement cycle of 100 ms. This experiment is described in details in [21]. The ToF spectrum of the recoil ions is fitted to extract $a_{\beta\nu}$. The analysis is based on the comparison between the experimental ToF spectrum and those obtained for two sets of realistic Monte Carlo (MC) simulations considering pure axial ($a_{\beta\nu} = -1/3$) and pure tensor ($a_{\beta\nu} = +1/3$) couplings. In a first step, the experimental data are calibrated and corrected for the identified sources of unwanted events (background). Then, $a_{\beta\nu}$ is deduced from a fit of the experimental ToF spectrum with a linear combination between the two sets of simulated decays obtained for axial and tensor couplings. Among the many instrumental effects, the detectors response function and geometry, the trap RF field influence, the ion cloud characteristics inside the trap, the shake-off ionization of the recoil ion, and the scattering of the β particles are implemented in the simulations.

The calculation of the expected value of the angular correlation parameter in the SM includes radiative corrections [20, 22]. We have used the formalism described by Glück [20], based on the work of Sirlin [23] to calculate, to first order in α and on an event-by-event basis, the change in the kinematics due to the virtual and real photon emission during the decay process. It turns out that such corrections are at the 1% level of the value of the correlation parameter.

The shake-off ionization of the recoil ion due to the sudden change of the electric charge of the nucleus following β decay is also taken into account. For the present analysis, the shake-off ionization probability of $^6Li^{2+}$ ions has been calculated in the sudden approximation, and found to be $0.02334 + 0.00004E_{\rm RI}$, where $E_{\rm RI}$ is the ion recoil energy in keV. Since the maximum recoil energy is 1.4 keV, the energy-dependent term can be neglected. This ionization probability is in perfect agreement with previous calculations of Wauters and Vaeck [24]. In a second experiment performed with the improved setup of Fig. 3, the shake-off probability was experimentally measured and was found to be in very good agreement with the theoretical value [12].

The characteristics of the ion cloud inside the trap have a strong influence on the ToF spectrum. Simulations of the trapped ions trajectories in the Paul trap have thus been performed using the SIMION8 software package [25]. The geometry of the electrodes of the surrounding elements was included as well as the experimental RF trapping voltages. The collisions between the trapped ions and the H_2 buffer gas molecules were described at the microscopic level using realistic interaction potentials [26]. The position and velocity distributions at thermal equilibrium as a function of the RF phase can be obtained from such simulations. Based on these calculations, the mean thermal energy of the ion cloud is expected to be $kT_{\rm sim} = 0.09$ eV. This is smaller than the

value obtained in offline measurements, $kT_{exp} = 0.107(7)$ eV [27]. A small correction (scaling) factor was thus applied to the cloud characteristics in the simulations. Measurements performed at different ion cloud densities have shown that space-charge effects are negligible under the adopted measuring conditions. The response functions of the detectors dedicated to the detection of the electron and the recoil ion were simulated with particular emphasis on the influence of the backscattering of β particles on the detectors and on other structures inside the detection chamber.

An important source that affects the shape of the ToF spectrum is the backscattering of electrons since, in this case, the kinematics of the decay is biased. The ToF distribution associated with such events ("scattered") is obtained by massive simulations using the GEANT4 software code.

False coincidences ("accidentals"), corresponding to the detection of uncorrelated particles on the β telescope and on the microchannel plate, also contribute to the ToF spectrum and introduce a flat distribution that is easily subtracted. It appears that most such accidentals events originate from (i) the decaying neutralized ^{6}He species that are present inside the whole volume of the chamber and trigger the β telescope, and (ii) H_2 molecules leaking from the RFQCB that trigger the MCPPSD detector.

For a small fraction of the ^{6}He atoms decaying in the chamber volume, the recoil ion can be detected on the MCPPSD, in coincidence with its associated β particle. This constitutes another source of physical events labelled "out-trap" events. Their contribution to the ToF spectrum in the region of the fit can bias the measurement. They are included in the simulation, assuming a decay process with pure axial coupling.

The ToF spectrum obtained for validated coincidences is displayed in Fig. 4. The selected events are conditioned by: a 500 keV energy threshold on the energy deposited in the scintillator, a time within the trapping cycle between 25 and 95 ms (cloud at thermal equilibrium), and a valid reconstruction of the positions in both the DSSSD and the MCPPSD. The "scattered", "out-trap", and "accidentals" events represent, respectively, 4.5%, 2.6%, and 7.3% of the total number of events. These contributions and the ToF obtained for $a_{\beta\nu} = -1/3$ are summed and compared to the experimental spectrum in Fig. 4.

By considering the β decay vertex as a point-like source at the center of the Paul trap, the recoil ion ToF and position can be used to determine the three components of the recoil ion momentum. In a similar way, the full momentum vector of the β particle can be deduced

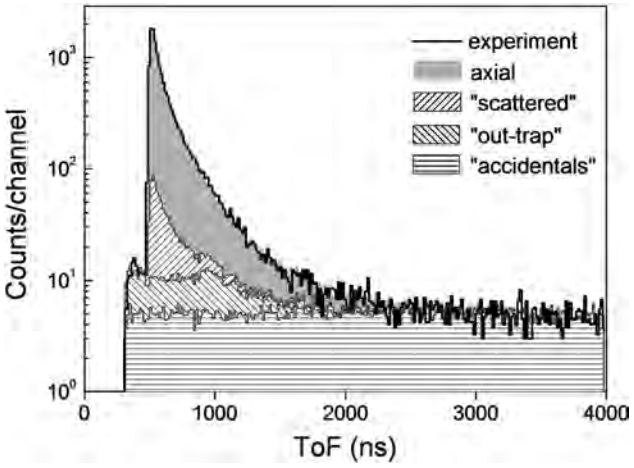

Figure 4 Experimental time-of-flight spectrum (black line) compared to the simulated one (gray area) in the pure axial case, including the different simulated contributions of background, after normalization (see text for details).

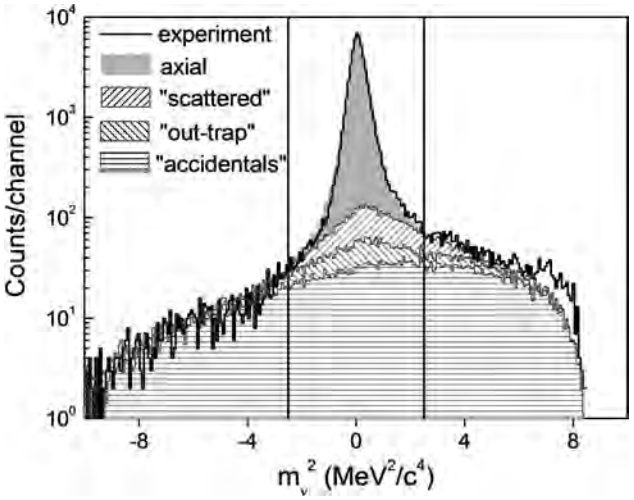

Figure 5 Antineutrino invariant mass spectra for the experimental data, the simulation in the pure axial case, and the simulation of background events. Vertical lines indicate the selection window used in the analysis to reduce background contribution.

from the energy deposited in the β telescope and the position on the DSSSD. This provides the possibility to reconstruct the antineutrino invariant mass:

$$m_\upsilon^2 = E_\upsilon^2 - p_\upsilon^2.$$

This variable is useful to validate in a global manner the quality of the simulations with a small influence of the value of the correlation parameter. Fig. 5 shows the antineutrino invariant mass spectra obtained for the experimental and simulated events. The main peak is well reproduced by the simulations. The shape and position

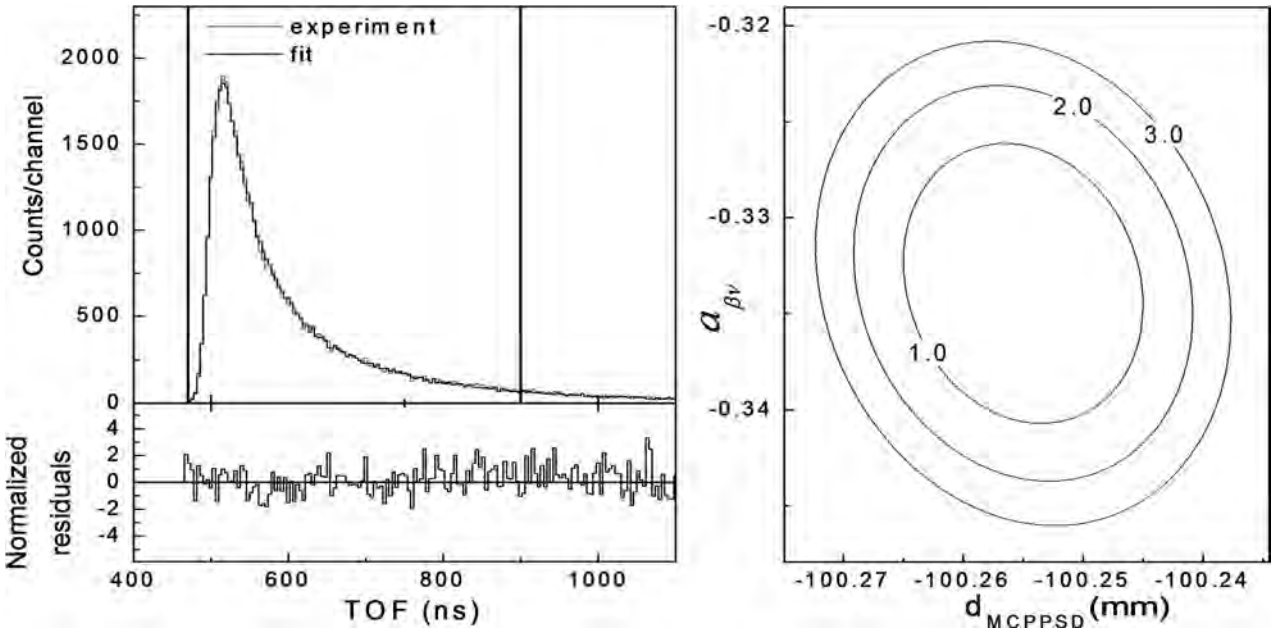

Figure 6 Left panel: Fit of the experimental spectrum (upper panel). The range of the fitted function is indicated by vertical lines. The normalized residuals are plotted in the lower panel. Right panel: projection on the plane of parameters d_{MCPPSD} and $a_{\beta\nu}$ of the computed contours for $(\chi^2 - \chi^2{}_{\mathrm{min}})$ values = 1, 2, and 3.

of this peak depend on all the inputs of the simulations (background, detector response functions, geometries, size of the ion cloud, trap RF field, etc.). The agreement between the experimental and simulated data provides an additional test of the inputs used in the analysis.

After applying a window cut in the antineutrino invariant mass spectrum and after background subtraction, the experimental ToF spectrum is adjusted with a linear combination of the time-of-flight spectra simulated using pure axial and pure tensor couplings (Fig. 6, left panel). Three parameters were left free in the fit: the value of $a_{\beta\nu}$, the total number of events, and the distance d_{MCPPSD} between the MCPPSD detection plane and the center of the Paul trap. Such a distance cannot be measured with better accuracy than a fraction of a mm and is therefore a degree of freedom to be taken into account in the analysis. The range in ToF selected for the fit is indicated by the vertical lines. The experimental data have first been split randomly in four independent sets, and the corresponding ToF spectra were fitted by changing the upper limit of the fitting range. No significant dependency has been found. Contours of constant χ^2 in the plane of parameters d_{MCPPSD} and $a_{\beta\nu}$ are shown on the right panel in Fig. 6. The result from the fit leads to $a_{\beta\nu} = -0.3335 \pm 0.0073$, and $d_{\mathrm{MCPPSD}} = 100.255 \pm 0.011$ mm. The nominal value for this distance is 100.0 mm with a positioning uncertainty of 0.5 mm. The minimum chi-square $\chi^2{}_{\mathrm{min}} = 96.6$ for 105 degrees of freedom corresponds to a P-value of 0.71, which indicates a very good agreement between the data and the fitted function. The quoted error is purely statistical.

The contributions of the main sources of systematic uncertainty are listed in Table 1. The label "present data" in the column "Method" of Table 1 indicates that the parameters and their uncertainties were determined by fitting the experimental data with the MC simulation (assuming a pure axial coupling). In each case, it was verified that the sensitivities of these parameters to the value of $a_{\beta\nu}$ taken as input were negligible at the current level of precision. The associated uncertainties on $a_{\beta\nu}$ were then deduced from the changes in the $a_{\beta\nu}$ values resulting

Table 1 Main sources of systematic error, systematic uncertainties, and impact on the error of $a_{\beta\nu}$ that are discussed in the text. The total uncertainty quoted corresponds to the sum of all effects taken into account in the analysis for which some of them are not discussed here.

Source	Uncertainty	$\Delta a_{\beta\nu}$ ($\times 10^{-3}$)	Method
Cloud temperature	6.5%	6.8	offline measurement
"accidentals" and "out trap'	see text	0.9	present data
β Scattering	10%	1.9	GEANT4
Total (see [21])		7.5	

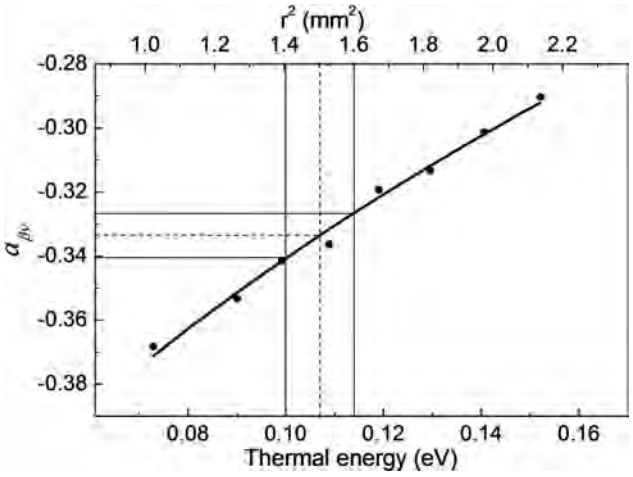

Figure 7 Values of the correlation coefficient resulting from the fit procedure as a function of the ion cloud thermal energy, kT, and of the ion cloud square radius, r^2, where r is the RMS of the spatial distribution in the Paul trap radial plane. The dashed and solid lines correspond, respectively, to the central value and the 1σ uncertainty of the offline temperature measurement.

from the fit of the experimental ToF spectrum while varying the parameters in the MC simulation.

It has been found that the $a_{\beta\nu}$ value resulting from the fit strongly depends on the trapped ion cloud size and on the temperature used in the MC simulation (Fig. 7). This motivated an independent measurement of the ion temperature using an offline source of $^6Li^+$ [27], performed under identical running conditions to those in the $^6He^+$ experiment in terms of trap RF voltage, gas pressure in the trap chamber and number of trapped ions. A relative precision of 6.5% was obtained that constitutes the dominant contribution to the systematic error on the value of $a_{\beta\nu}$.

The uncertainties due to "accidentals" and "out-trap" event subtractions are only statistical. They are limited by the statistics of experimental events that serve as normalization for the MC results. The uncertainty due to the "scattered" events was estimated by considering a 10% relative error on the β scattering yield provided by the GEANT4 simulations. This 10% relative error is based on the work of Hoedl [28], which compares a compilation of published electron scattering experimental data to several MC codes.

Combining all systematic errors quadratically, the final result is:

$$a_{\beta\nu} = -0.3335(73)(75),$$

where the first uncertainty is statistical and the second systematic.

Figure 8 shows the first result obtained with LPCTrap compared with other measurements of the $\beta-\nu$ angular correlation coefficient in pure GT transitions. The values from Carlson and from Allen et al. were obtained in ^{23}Ne decay, the value of Li et al. was obtained in ^{8}Li decay and the others in ^{6}He decay. Our result and the one of Li et al. are the most accurate among the experiments performed using the detection of the recoil ions and β particles in coincidence. The measurement presented here, performed with a different and independent method, confirms the result of Johnson et al. It is to be recalled that the reduced chi-square $\chi^2/\nu = 0.92$ for 105 degrees of freedom obtained in the present work corresponds to a P-value of 0.71. This is to be compared to a P-value of 0.055 for the Johnson et al. experiment, with

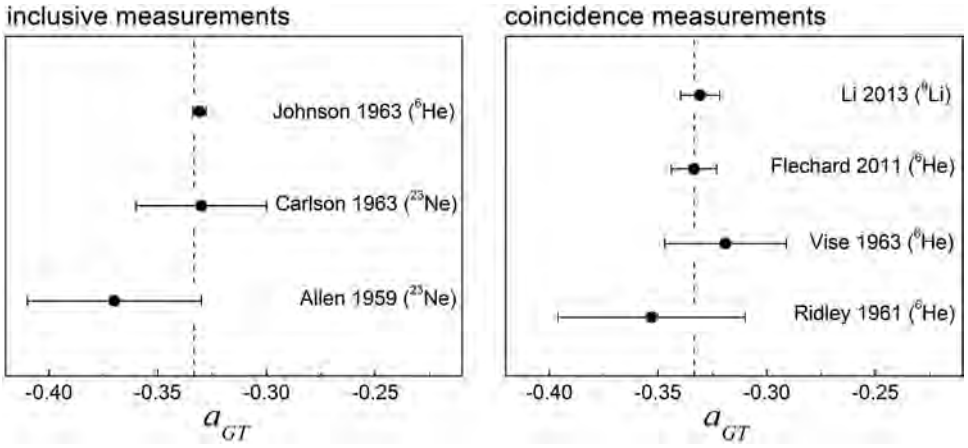

Figure 8 From top to bottom: $a_{\beta\nu}$ experimental values in pure GT transitions from [14, 17, 18] (left panel), [19], present work, [15], and [16] (right panel). The error bars show the quadratic sums of statistical and systematic uncertainties. The dashed lines indicate the value predicted by the SM.

a reduced chi-square $\chi^2/\nu = 1.69$ for 13 degrees of freedom [20].

The techniques used in the two experiments differ in a number of other aspects. First, the use of trapping techniques and the detection in coincidence of two decay products resulted in a larger signal to background ratio, by more than a factor of two compared to the Johnson et al. experiment. Furthermore, the measurement in an event-by-event mode of additional parameters (particle positions, energy of the β particle, RF phase, and time within the trapping cycle) allows a better control of possible systematic effects. With the efficiencies achieved for beam preparation and trapping and for the detection of coincidence events, the average counting rates in the present experiment was about 1 coincidence per second and about 100 single triggers per second. This is, respectively, three and one orders of magnitude lower than in the Johnson et al. experiment. Thus, possible systematic effects due to the counting rate are expected here to have a smaller impact. The dominant contribution to the uncertainty in the Johnson et al. experiment was due to random variations of recoil-energy spectra in a number of sequential data acquisitions, while in the present work, the precision limitation is mainly statistics. Both techniques are thus complementary.

From Eq. (6) and using the value $<mc^2/E_e> = 0.2$ deduced from the β particle energy spectrum [21], the result from the first experiment with LPCTrap corresponds to a limit on the tensor coupling

$$\left|C_T/C_A\right| < 0.13 \quad (90\%\text{C.L.}),$$

assuming $C_T = C_T'$.

A second experiment has been performed with the setup involving the recoil ion spectrometer (Fig. 3, right panel) [12]. A major improvement in the efficiency was reached resulting from several modifications of the setup. First, the injection inside the RFQ was optimized as well as the transmission between the RFQ and the trap. This led to the following efficiencies for a measurement cycle of 200 ms: 0.6% through the RFQ, 40% downstream up to the trap, 20% inside the trap. With an initial intensity of 10^8 pps, this corresponds to about 10^4 ions/bunch inside the Paul trap. The efficiency of detection was also increased by modifying the geometry of the setup. A total of about 1.2×10^6 true coincidences were collected during four days of data taking.

In addition, the understanding of the systematic effect associated with the cloud temperature has been improved by studying in further details the behavior of the leading edge of the ToF distribution [29]. The high statistic of the experiment also enables to improve the subtraction of background by carefully considering the different contributions of such events as a function of time inside the measurement cycle. In the second run, the ions were ejected from the trap after 150 ms trapping duration to detect "out-trap" events during the 50 ms left.

As already stated above, an experimental determination of the shake-off probability was made possible with a very high accuracy. Fig. 9 shows the experimental ToF distribution for the recoil ions detected in coincidence with the electron following the beta decay of $^6He^{1+}$ with the background subtraction described previously. In the present case, only two charge states are possible (Fig. 9, left). The fit, which takes into account all the effects mentioned above, is in perfect agreement with the experimental data. The value obtained for the shake-off probability is:

$$P_{shake-off} = 0.02339(35)_{stat}(07)_{syst}.$$

The main sources of systematic effects have been investigated (Fig. 9, right), and the total systematic uncertainty is very small compared to the statistical error. The experimental value of $P_{\text{shake-off}}$ is in excellent agreement with the theoretical prediction based on the sudden approximation.

As far as the angular correlation parameter is concerned, a preliminary value has been estimated from another analysis: $a_{\beta\nu} = -0.3338(26)_{\text{stat}}$. The error on this value is dominated by the statistics used for the number of events in the simulation. The value is consistent with our previous result and the value obtained by Johnson et al.

The analysis of the experimental data is about to be finalized and the statistics gathered during the experiment should allow us to reach an unprecedented statistical accuracy of 0.0015.

4 Measurements in the decay of ^{35}Ar

The ^{35}Ar nucleus decays through a mirror transition with a large Fermi fraction $x = 92\%$. The basic parameters ($T_{1/2}$, BR, masses) involved in the decay being well known [9], a value of $a_{\beta\nu}$ with sufficient precision can be determined in the framework of the SM. The precise measurement of $a_{\beta\nu}$ in this transition can then be interpreted either to constrain scalar currents, or to determine V_{ud}. In a previous measurement, performed decades ago [17], the recoil ions after beta decay were detected in singles, leading to the value $a_{\beta\nu} = 0.97(14)$.

At the SPIRAL1-GANIL facility, the $^{35}Ar^{1+}$ ions are produced by a primary ^{36}Ar beam at 80 MeV A^{-1} impinging

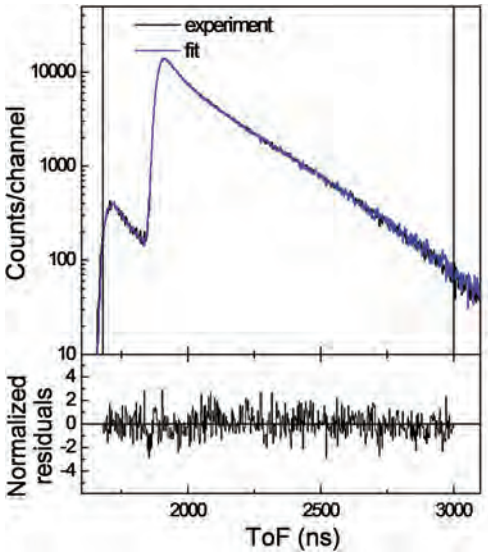

Source	ΔP(10^{-5})	Method
$a_{\beta\nu}$	4.0	[19]
β scattering	4.0	GEANT4
Background	3.5	present data
E_β calibration	1.7	present data
MCP efficiency	1.2	present data
Total	7.0	

Figure 9 Left panel: Fit of the experimental spectrum to deduce the charge-state distribution. Right panel: Dominant source of systematic effects.

on a graphite target coupled to an ECR source. The radioactive beam is delivered to the LPCTrap at 10 keV with a typical intensity of 3.5×10^7 s^{-1} ($\sim$ 5.5 pA), measured by the retractable silicon detector. The dipole magnet located at the entrance of the low-energy beam line is again not sufficient to eliminate the 40 pA of a stable beam containing mainly molecules that have not been fully identified.

The tuning of the RFQ has been adapted to the $^{35}Ar^{1+}$ ions that are cooled with He buffer gas at a 1.6×10^{-2} mbar pressure. To prepare the experiments, tests were first carried out with different stable beams produced either by a surface ionization source or the ECR source of SPIRAL. Typical performances reached with the different beams are given in Table 2 for two values of the cycle (20 ms and 200 ms).

Due to space-charge effects, the transmission, and consequently the lifetimes of the ions in the buncher and in the Paul trap, can be limited by the number of ions per bunch. For the values given in Table 2, the beam current at the entrance of LPCTrap was adjusted in each case to keep this number below 10^7 ions per bunch in order not to saturate the RFQ. For a cycle of 200 ms, this number is reached with a typical beam intensity of 50 pA at the entrance of LPCTrap. A maximum of 2.5×10^5 ions can then be confined in the Paul trap. In the RFQ, the measured efficiencies are mainly defined by the losses at beam injection in the setup (the hole at the entrance has a 6 mm diameter) and by the losses due to charge exchange. A short cycle gives access to the first factor: roughly 70% of the beam is lost at 20 ms. The values obtained for a longer cycle enable determination of the lifetime of the ions in the buncher due to trapping losses. This is of the order of 100 ms for the Ar^+ species and 250 ms for K^+ ions, which is consistent with a lower charge exchange expected with alkali ions. In the measurement Paul trap, the lifetime of confined ions has also been determined and is close to 500 ms for all species, with buffer He gas being injected in the chamber at a very low pressure.

Table 2 Efficiencies of the three main sections of LPCTrap obtained with different stable and radioactive ions around mass 35, for two values of the cycle (20 ms and 200 ms).

		ε (RFQ)				ε (total)	
Species	Source	20 ms	200 ms	ε (transfer line)	ε (trap)	20 ms	200 ms
$^{39}K^{1+}$	Offline	0.27	0.17	0.43	0.2	0.023	0.015
$^{36,40}Ar^{1+}$	ECR/SPIRAL	0.32	0.12	0.22	0.15	0.01	0.0037
$^{35}Ar^{1+}$	ECR/SPIRAL	/	0.15	0.25	0.10	/	0.0038

During the last run performed with $^{35}Ar^{1+}$, an average of 2.5×10^4 radioactive ions were confined for each bunch injection, every 200 ms. Even if the total efficiency of LPCTrap is lower for the stable contaminant, the number of ions counted in the ion cloud monitor revealed that a total of 1.5×10^5 ions were actually confined in the Paul trap at each cycle. This does not jeopardize the experiment, but space-charge effects should be considered in the data analysis. The trapped ions reached their thermal equilibrium about 20 ms after injection in the He buffer

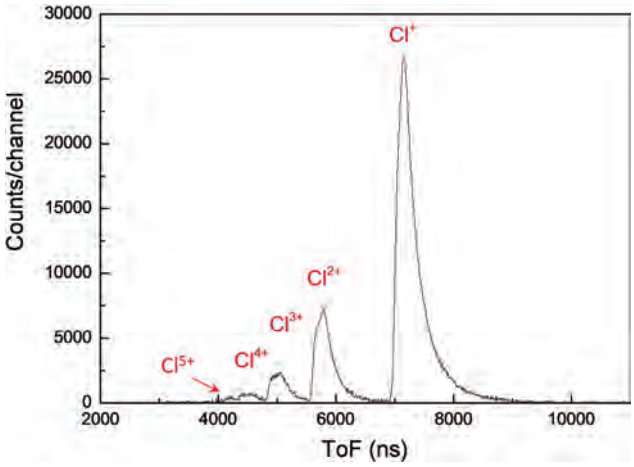

Figure 10 Experimental ToF spectrum obtained during the run with ^{35}Ar, for about 1.5×10^6 coincidence events.

gas at a pressure of 1.5×10^{-5} mbar. After 160 ms trapping duration dedicated to the correlation measurement, the ions were extracted towards the ion cloud monitor and "out-trap" events detected during the 40 ms left. The second detection setup involving the recoil ion spectrometer (Fig. 3, right panel) was used to measure the decay products and a total of 1.5×10^6 real coincidences were recorded. The ToF spectrum obtained during this run is shown in Fig. 10.

The different charge states of the ^{35}Cl daughter ions are well separated by the recoil ion spectrometer. The charge-state distribution had already been estimated from the commissioning run [30]. The preliminary values are:

$$1+ : 75(1)\% \quad 2+ : 17(0.5)\% \quad 3+ : 6(0.5)\%$$
$$4+ : 1.5(0.5)\% \quad 5+ :\sim 0.5\%$$

The study of systematic effects is currently ongoing. Among these effects, the probability of charge-exchange collisions in the ambient gas, which was negligible in the case of ^{6}Li in H_2 [12], has to be estimated in the present case involving many electrons.

The number of neutral recoil ^{35}Cl atoms, which are not detected by the MCPPSD, can be deduced from the comparison between the number of expected coincidences (including neutrals) and the effective number of measured coincidences. The number of expected coincidences is simply computed using the number of β particles detected in singles and the overall ion detection efficiency. This estimate leads to 72(10)% of neutral ^{35}Cl recoils. Beyond the prototypical $^6He^{1+}$ case, this heavier system can reveal the role of more subtle shake-off dynamics involving many electrons as, for instance, the Auger processes [31].

The number of coincidences measured during the last run corresponds to a statistical uncertainty of 0.002 on $a_{\beta\nu}$. In the study of the systematic effects, particular attention will also be devoted to the trap RF influence on the recoil motion. In the ^{35}Ar decay, the recoil kinetic energy reaches at most 452 eV, which is about a factor of 3 lower than in the case of ^{6}He. The RF effect could then become a dominant source of the systematic uncertainty. Moreover, as the total number of ions in the trap nearly reaches the trap capacity, the space-charge effect has to be taken into account in the analysis. Finally, the second main branch of the decay with γ emission (BR = 1.23%) has also to be considered. Such systematic contributions should be properly managed and, assuming a systematic uncertainty of the same order as the statistical one, the final result would constitute the most precise value ever obtained in a $\beta-\nu$ angular correlation measurement. On the one hand, this would add a relevant contribution to better constrain the scalar interaction. On the other hand, in the framework of the SM, this result would improve by a factor of 2 the precision on V_{ud} determined from the study of mirror transitions.

5 Summary and perspectives

The status of the first precision experiments in nuclear β decay performed with LPCTrap at GANIL has been described. Such studies are based on the use of a Paul trap to confine the radioactive ions and on the detection in coincidence of the β particles and the recoil ions. Significant results, especially the most precise value of $a_{\beta\nu}$ ever determined for a pure GT transition using a coincidence method, have been obtained. The last data are very promising and they should deliver the most precise absolute results on both the tensor and scalar sectors. A significant improvement of V_{ud} extracted from the mirror transitions also seems reachable in an alternative interpretation of the ^{35}Ar data. Moreover, an original recoil ion spectrometer enabled measurement of, for the first time, the charge-state distributions of recoiling ions produced by the decay of 1+ ions. The use of the sudden approximation in the theoretical approach has definitively been validated with the result obtained with the 'ideal' $^6He^{1+}$ system, allowing unambiguous tests of the role of other processes in systems involving many electrons as in $^{35}Ar^{1+}$ decay.

A new project involving ^{19}Ne is now underway. This nucleus decays mainly through a mirror transition to the ground state of ^{19}F (BR = 99.9858(20)%). The basic

parameters ($T_{1/2}$, BR, masses) involved in the decay being well known [9, 32], a value of $a_{\beta\nu}$ can be determined in the framework of the SM with sufficient precision. The precise measurement of $a_{\beta\nu}$ in this transition can again be interpreted either to constrain the exotic currents, C_S and C_T, in a global way, or to determine V_{ud}. This experiment is a new challenge for LPCTrap. The half-life of ^{19}Ne is indeed ten times larger than in the case of ^{35}Ar and the recoil maximum kinetic energy is only 203 eV. These are extreme conditions that will push the limits of the device to new levels of sensitivity.

Very exciting opportunities will emerge in the coming years at GANIL with the development of new radioactive beams in an upgrade of SPIRAL [33] and in the forthcoming DESIR[4] hall at SPIRAL2 [34]. The intensities reached during the first production tests for nuclei such as ^{23}Mg, ^{25}Al, ^{33}Cl and ^{37}K, which decay through mirror transitions, are encouraging and these beams should be available at GANIL in 2015.

Key words. $\beta-\nu$ angular correlation, low-energy precision measurements, weak interaction, paul trap.

Gilles Ban is presently Professor at Ecole Nationale Supérieure d'Ingénieurs de Caen and Laboratoire de Physique Corpusculaire de Caen. He got his PhD at the University of Paris in atomic physics and ion sources, he then worked with synchrotron light and X-ray optics. Since joining LPC Caen he has contributed to precision experiments at low energy such as correlations measurements or electric dipole moment searches with neutrons. Other interests are nuclear energy and medical applications.

Dominique Durand is researcher at CNRS-IN2P3, and currently head of the Laboratoire de Physique Corpusculaire at Caen, France. He has obtained the Thibaud prize award (1997). His research interests have focused on nuclear collisions at intermediate energies (INDRA collaboration), double-beta decay experiments (NEMO-3 and SuperNEMO collaborations) and tests of the weak interaction through precision measurements at low energies.

Xavier Fléchard is currently working at the LPC CAEN, France, as a CNRS researcher in the AMO division. After a PhD in atomic Physics at the University of Caen in the field of ion-atom collisions, he first worked at Kansas State University as a research associate on the development of the MOTRIMS technique to provide optically cooled and trapped atomic targets. His main research activities focus today on the use of atom and ion traps in specific fields of atomic and nuclear physics. They are shared between the study of ion-atom/molecules collisions, and precision measurements in nuclear beta decay to search for exotic interactions.

Etienne Liénard is presently Associate Professor at the University of Caen and LPC Caen, France. He got his PhD at the Catholic University of Louvain, Belgium, in the field of nuclear reactions, using the first radioactive beam post-accelerated in the world. He held a first position as a research associate at GANIL, France, where he focused on neutron detection and halo nuclei studies. At LPC Caen, his main research activities concern precision measurements in nuclear beta decay to search for new physics beyond the Standard Model, and he is presently responsible of the LPCTrap setup installed at GANIL

Oscar Naviliat-Cuncic is currently a faculty member at NSCL, Michigan State University. He held previously positions as Professor at the University of Caen, France, and as research associate at the Swiss Federal Institute of Technology in Zurich. After earning a PhD in nuclear spectroscopy at the Catholic University of Louvain, Belgium, his research interests have focused on tests of discrete symmetries and searches for new interactions through precision measurements at low energies. He has been involved in experiments measuring correlations using muons, neutrons and nuclei, some of which required the use traps for the confinement of particles.

4 DESIR: Décroissance Excitation et Stockage d'Ions Radioactifs

References

[1] N. Severijns, M. Beck, and O. Naviliat-Cuncic, Rev. Mod. Phys. **78**, 991 (2006).
[2] N. Severijns and O. Naviliat-Cuncic, Ann. Rev. Nucl. Part. Sci. **61**, 23 (2011).
[3] A. Gorelov, D. Melconian, W. P. Alford, D. Ashery, G. Ball, J. A. Behr, P. G. Bricault, J. M. D'Auria, J. Deutsch, J. Dilling, M. Dombsky, P. Dubé, J. Fingler, U. Giesen, F. Glück, S. Gu, O. Häusser, K. P. Jackson, B. K. Jennings, M. R. Pearson, T. J. Stocki, T. B. Swanson, and M. Trinczek, Phys. Rev. Lett. **94**, 142501 (2005).
[4] P. A. Vetter, J. R. Abo-Shaeer, S. J. Freedman, and R. Maruyama, Phys. Rev. C **77**, 035502 (2008).
[5] X. Fléchard, E. Liénard, A. Méry, D. Rodríguez, G. Ban, D. Durand, F. Duval, M. Herbane, M. Labalme, F. Mauger, O. Naviliat-Cuncic, J. C. Thomas, and Ph. Velten, Phys. Rev. Lett. **101**, 212504 (2008).
[6] V. Yu. Kozlov, M. Beck, S. Coeck, P. Delahaye, P. Friedag, M. Herbane, A. Herlert, I. S. Kraev, M. Tandecki, S. Van Gorp, F. Wauters, Ch. Weinheimer, F. Wenander, S. Zákoucký, and N. Severijns, Nucl. Instrum. Methods Phys. Res. B **266**, 4515 (2008).
[7] J. D. Jackson, S. B. Treiman, and H. W. Wyld Jr, Nucl. Phys. **4**, 206 (1957).
[8] O. Naviliat-Cuncic and N. Severijns, Phys. Rev. Lett. **102**, 142302 (2009).
[9] N. Severijns, M. Tandecki, T. Phalet, and I. S. Towner, Phys. Rev. C **78**, 055501 (2008).
[10] D. Rodríguez, A. Méry, G. Ban, J. Brégeault, G. Darius, D. Durand, X. Fléchard, M. Herbane, M. Labalme, E. Liénard, F. Mauger, Y. Merrer, O. Naviliat-Cuncic, J.-C. Thomas, and C. Vandamme, Nucl. Instrum. Methods Phys. Res. A **565**, 876 (2006).
[11] F. Duval, A. Méry, G. Ban, D. Durand, X. Fléchard, M. Labalme, E. Liénard, F. Mauger, O. Naviliat-Cuncic, D. Rodríguez, and J.-C. Thomas, Nucl. Instrum. Methods Phys. Res. B **266**, 4537 (2008).
[12] C. Couratin, Ph. Velten, X. Fléchard, E. Liénard, G. Ban, A. Cassimi, P. Delahaye, D. Durand, D. Hennecart, F. Mauger, A. Méry, O. Naviliat-Cuncic, Z. Patyk, D. Rodríguez, K. Siegien-Iwaniuk, and J.-C. Thomas, Phys. Rev. Lett. **108**, 243201 (2012).
[13] E. Liénard, M. Herbane, G. Ban, G. Darius, P. Delahaye, D. Durand, X. Fléchard, M. Labalme, F. Mauger, A. Mery, O. Naviliat-Cuncic, and D. Rodríguez, Nucl. Instrum. Methods Phys. Res. A **551**, 375 (2005).
[14] C. H. Johnson, F. Pleasonton, and T. A. Carlson, Phys. Rev. **132**, 1149 (1963).
[15] J. B. Vise and B. M. Rustad, Phys. Rev. **132**, 2573 (1963).
[16] B. W. Ridley, Nucl. Phys. **25**, 483 (1961).
[17] J. S. Allen, R. L. Burman, W. B. Herrmannsfeldt, P. Stähelin, and T. H. Braid, Phys. Rev. **116**, 134 (1959).
[18] T. A. Carlson, Phys. Rev. **132**, 2239 (1963).
[19] G. Li, R. Segel, N. D. Scielzo, P. F. Bertone, F. Buchinger, S. Caldwell, A. Chaudhuri, J. A. Clark, J. E. Crawford, C. M. Deibel, J. Fallis, S. Gulick, G. Gwinner, D. Lascar, A. F. Levand, M. Pedretti, G. Savard, K. S. Sharma, M. G. Sternberg, T. Sun, J. Van Schelt, R. M. Yee, and B. J. Zabransky, Phys. Rev. Lett. **110**, 092502 (2013).
[20] F. Glück, Nucl. Phys. A **628**, 493 (1998).
[21] X. Fléchard, Ph. Velten, E. Liénard, A. Méry, D. Rodríguez, G. Ban, D. Durand, F. Mauger, O. Naviliat-Cuncic, and J.-C. Thomas, J. Phys. G: Nucl. Part. Phys. **38**, 055101 (2011).
[22] F. Glück, Comput. Phys. Commun. **101**, 223 (1997).
[23] A. Sirlin, Phys. Rev. **164**, 1767 (1967).
[24] L. Wauters and N. Vaeck, Phys. Rev. C **53**, 497 (1996).
[25] http://simion.com/info/SIMION_8.html.
[26] G. Ban, G. Darius, D. Durand, X. Fléchard, M. Herbane, M. Labalme, E. Liénard, F. Mauger, O. Naviliat-Cuncic, C. Guénaut, C. Bachelet, P. Delahaye, A. Kellerbauer, L. Maunoury, and J. Y. Pacquet, Nucl. Instrum. Methods Phys. Res. A **518**, 712 (2004).
[27] X. Fléchard, G. Ban, D. Durand, E. Liénard, F. Mauger, A. Méry, O. Naviliat-Cuncic, D. Rodríguez, and P. Velten, Hyperfine Interact. **199**, 21 (2011).
[28] S. A. Hoedl, PhD Thesis, Princeton University (USA), 2003.
[29] Ph. Velten, G. Ban, D. Durand, X. Fléchard, E. Liénard, F. Mauger, A. Méry, O. Naviliat-Cuncic, D. Rodríguez, and J. C. Thomas, Hyperfine Interact. **199**, 29 (2011).
[30] X. Fléchard et al., in preparation.
[31] B. Pons, private communication.
[32] S. Triambak, P. Finlay, C. S. Sumithrarachchi, G. Hackman, G. C. Ball, P. E. Garrett, C. E. Svensson, D. S. Cross, A. B. Garnsworthy, R. Kshetri, J. N. Orce, M. R. Pearson, E. R. Tardiff, H. Al-Falou, R. A. E. Austin, R. Churchman, M. K. Djongolov, R. D'Entremont, C. Kierans, L. Milovanovic, S. O'Hagan, S. Reeve, S. K. L. Sjue, and S. J. Williams, Phys. Rev. Lett. **109**, 042301 (2012).
[33] P. Delahaye, C. Couratin, E. Liénard, O. Bajeat, G. Ban, D. Durand, X. Fléchard, O. Naviliat-Cuncic, M. G. Saint Laurent, T. Stora, J.-C. Thomas, E. Traykov, and the GANISOL group, AIP Conf. Proc. **1409**, 165 (2011).
[34] http://www.cenbg.in2p3.fr/desir/.

Open issues in neutrino astrophysics

C. Volpe[1,*]

Neutrinos of astrophysical origin are messengers produced in stars, in explosive phenomena like core-collapse supernovae, in the accretion disks around black holes, or in the Earth's atmosphere. Their fluxes and spectra encode information on the environments that produce them. Such fluxes are modified in characteristic ways when neutrinos traverse a medium. Here our current understanding of neutrino flavour conversion in media is summarized. The importance of this domain for astrophysical observations is emphasized. Examples are given of the fundamental properties that astrophysical neutrinos have uncovered, or might reveal in the future.

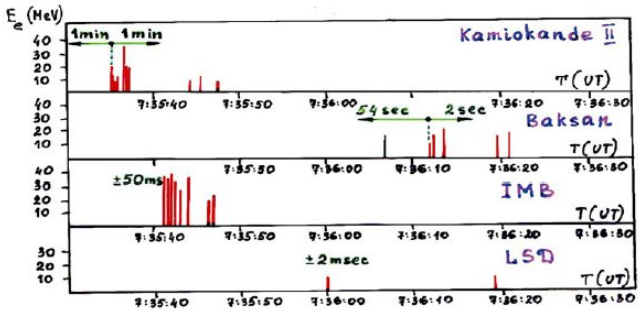

Figure 1 (online color at: www.ann-phys.org) Electron antineutrino events measured by the Kamiokande, Baksan, IMB and LSD experiments during the supernova 1987A, in the Large Magellanic Cloud [11].

1 Introduction

R. Davis' pioneering measurement of electron neutrinos emitted by the sun has opened the era of neutrino astronomy [1]. A significant deficit, compared to the standard solar model predictions, was rapidly measured, triggering several decades of experiments of solar neutrino experiments [2–6] to investigate, if unknown neutrino properties, or solar model uncertainties [7–10], were at its origin. Electron antineutrinos produced by a massive star were first detected during the SN1987A explosion. A burst was first seen in Kamiokande, the electron direction pointing to the Large Magellanic Cloud at 50 kpc from the Milky Way. The occurrence probability of having 9 events per 10 seconds was determined to be less than 5.7×10^{-8} [11]. Altogether the Kamiokande, IMB, Baksan and Mont Blanc detectors observed about twenty events [12–15], in the 40 MeV energy range during 13 seconds (Figure 1). Their angular dependence and energy distribution are reasonably consistent with expectations from core-collapse supernova simulations (see e.g. [16] for a recent analysis). The detection of these events constitute the first experimental confirmation of the predictions from supernova simulation. In 2002, R. Davis and M. Koshiba were awarded the Nobel Prize, for "pioneering contributions to astrophysics, in particular for the detection of cosmic neutrinos". The prize was shared with R. Giacconi for "for pioneering contributions to astrophysics, which have led to the discovery of cosmic X-ray sources". At the same epoch of the solar puzzle, experiments searching for proton decay were measuring an anomaly in the atmospheric neutrino background [17–22]. In 1998 the discovery of neutrino oscillations by the Super-Kamiokande experiment solved the atmospheric anomaly and brought a milestone in the solution of the "solar neutrino deficit" problem [23]. In fact, a deficit of upgoing atmospheric muon neutrinos traversing the Earth was observed, compared to down-going ones, that was shown to be consistent with the hypothesis that up-going muon neutrinos convert into tau neutrinos (Figure 2). This discovery has fundamental implications for high-energy physics, astrophysics and cosmology. For example, neutrinos from the sun give us direct confirmation of the energy production mechanisms in stars (see the seminal works [24, 25]).

The neutrino oscillation phenomenon occurs if neutrinos have non-zero masses and mixings. The possibility

* E-mail: volpe@apc.univ-paris7.fr
1 AstroParticule et Cosmologie (APC), CNRS/Université de Paris 7, 10, rue Alice Domon et Léonie Duquet, 75205 Paris cedex 13, France

to have ν-$\bar{\nu}$ oscillations was first pointed out by B. Pontecorvo in analogy with $K_0 - \bar{K}_0$ mesons [26]. Neutrino oscillations require that the flavour ν_α and the mass ν_i basis are related by $\nu_\alpha = U^*_{\alpha i}\nu_i$ with U being the Pontecorvo-Maki-Nakagawa-Sakata (PMSN) unitary matrix [27]. In the three-flavour framework the U matrix reads

$$U = VD \tag{1}$$

with a possible parametrization given by [28] :

$$V = \begin{pmatrix} c_{12}c_{13} & s_{12}c_{13} & s_{13}e^{-i\delta} \\ -s_{12}c_{23} - c_{12}s_{23}s_{13}e^{i\delta} & c_{12}c_{23} - s_{12}s_{23}s_{13}e^{i\delta} & s_{23}c_{13} \\ s_{12}s_{23} - c_{12}c_{23}s_{13}e^{i\delta} & -c_{12}s_{23} - s_{12}c_{23}s_{13}e^{i\delta} & c_{23}c_{13} \end{pmatrix} \tag{2}$$

where $c_{ij} = \cos\theta_{ij}$ and $s_{ij} = \sin\theta_{ij}$ and

$$D = \begin{pmatrix} e^{-i\phi_1} & 0 & 0 \\ 0 & 1 & 0 \\ 0 & 0 & e^{-i\phi_2} \end{pmatrix} \tag{3}$$

The V matrix is analogous to the Cabibbo-Kobayashi-Maskawa matrix, in the quark sector, although the mixing angles are there measured to be small. The ϕ_1, ϕ_2 are two extra phases that appear in case neutrinos are Majorana particles. Therefore the PMNS matrix depends on three mixing angles, two Majorana-type and one Dirac-type phases. (Here we will not discuss the Majorana phases, since they do not influence neutrino oscillations in vacuum and in matter.) If the Dirac-type phase is non-zero, the PMNS matrix is complex, introducing a difference between the neutrino oscillation probability, and the corresponding ones for antineutrinos, implying CP violation in the lepton sector (for a neutrino physics' overview, see the recent comprehensive book [29]).

Oscillations in vacuum is an interference phenomenon among the matter eigenstates, which is sensitive to their mass-squared differences and to the mixing angles. In the two-flavour framework, the oscillation appearance probability for relativistic neutrinos is given by

$$P(\nu_\alpha \to \nu_\beta) = \sin^2(2\theta)\sin^2(\Delta m^2_{12} L/4E), \tag{4}$$

E being the neutrino energy, L the source-detector distance and $\Delta m^2_{21} = m^2_2 - m^2_1$. While the oscillation amplitude depends on the mixing angle, the squared-mass differences determine the oscillation frequency[1]. In the last decade, reactor, accelerator and solar experiments have precisely measured the two mass-squared differences to be $\Delta m^2_{21} = (7.50 \pm 0.20)\,10^{-5}\mathrm{eV}^2$, $|\Delta m^2_{32}| = (2.32 + 0.12)\,10^{-3}$ eV^2, as well as the mixing angles $\sin^2(2\theta_{12}) = 0.857 \pm 0.024$, $sin^2(2\theta_{23}) > 0.95$ [28]. An indication for a nonzero third neutrino mixing angle has been found by the T2K [30] and the Double-Chooz collaborations [31]; while RENO [32] and Daya-Bay have measured θ_{13} to be $\sin^2(2\theta_{13}) = 0.092 \pm 0.016(stat) \pm 0.005(syst)$ [33].

While the experimental progress is impressive, numerous features remain unrevealed. First, the mechanism that gives a mass to the neutrino is unknown. Depending on the neutrino nature, introducing a neutrino mass might require a right-handed neutrino singlet (that does not couple to the gauge bosons) or, for example, more complex mechanisms of the see-saw type(s) which need significant extensions of the Standard Model. There is the mass hierarchy problem. In fact, there are two ways to order the mass eigenstates since one of the Δm^2 signs is unknown. The case $\Delta m^2_{13} > 0$ corresponds to the normal hierarchy, while $\Delta m^2_{13} < 0$ corresponds to the inverted. Tritium beta-decay experiments give information on the absolute mass scale. The current upper limit is of about 2 eV for the electron neutrino effective mass [28]. This will be significantly improved by the KATRIN experiment that has a discovery potential for a neutrino mass of 0.35 eV at 5 σ [34]. Moreover, key open issues are the existence of leptonic CP violation, of sterile neutrinos and the identification of the ν Dirac versus Majorana nature.

Interestingly, the ensemble of experimental data present a few anomalies that cannot be cast in the three-active neutrino framework. The neutrino flux measurement from intense static ^{37}Ar and ^{51}Cr sources in the GALLEX and SAGE experiments present an anomalous deficit of electron neutrinos (the "Gallium anomaly"). A recent analysis finds a statistical significance at 3 σ [35]. The LSND collaboration has found evidence for oscillations at $\delta m^2 = 1\ eV^2$ (for small mixing angles) using decay-at-rest muons [36] and decay-in-flight pions [37]. Most of the parameter regions identified by LSND have been excluded by the KARMEN experiment based on the same method [38]. The MiniBooNE experiment has been built to clarify the controversial LNSD results. However, at present, MiniBooNE anti-neutrino and neutrino oscillation data combined show an excess of events at 3.8 σ [39, 40]. Besides a recent re-evaluation of the electron anti-neutrino flux from reactors has shown a shift in the flux renormalization by 3 % compared to previous predictions. The re-analysis of all reactor experiments using this new flux has shown a 3 σ inconsistency with the standard oscillation framework (the "reactor anomaly") [41]. These unexplained features might point to new physics and require one or more ster-

[1] For three flavours only two independent Δm^2 can be built. Any extra Δm^2 requires the addition of more mass eigenstates.

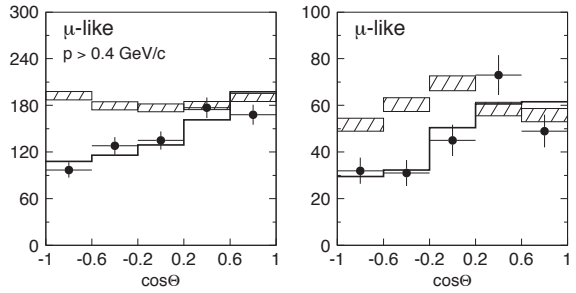

Figure 2 (online color at: www.ann-phys.org) Zenith angle distribution of (a subset of) the sub-GeV and multi-GeV μ-like events observed by Super-Kamiokande in 1998. Upward-going particles have $\cos\Theta < 0$ and downward-going particles have $\cos\Theta > 0$. The hatched region shows the Monte Carlo expectation for no oscillations normalized to the data live-time with statistical errors. The bold line is the best-fit expectation for $\nu_\mu \to \nu_\tau$ oscillations [23].

ile neutrinos, non-standard interactions or CPT violation. However, at present, none of the proposed explanations is capable of providing a comprehensive understanding.

Future experiments using man-controlled sources will address unknown neutrino properties and try to identify the possible explanations of the anomalies. Exploring the Dirac CP violating phase requires long-term accelerator measurements employing either established or novel techniques, such as super-beams, beta-beams [42], neutrino factories (see e.g. [43,44]), or projects like the decay-at-rest based DAEDALUS [45]. The upgrades of T2K and NOνA experiments can also investigate a small fraction of the δ values at 3 σ level [46]. Majorana-type phases and the neutrino nature can be determined by searches for the lepton-number violating neutrino-less double-beta decay. Earth matter effects in long-baseline experiments can be exploited to identify the hierarchy, as in e.g. [44]. Numerous projects are being conceived to test the hypothesis of the existence of sterile neutrinos based e.g. on the use of intense radioactive sources inside spherical detectors such as ^{144}Ce in Ref. [47] or ^{8}Li in Ref. [48] (see [49] for a review).

Astrophysical and cosmological observations offer complementary strategies in these fundamental searches. Cosmological data will reach an unprecedented sensitivity on the sum of the neutrino masses [50, 51] and maybe be sensitive to the hierarchy, although this information is indirect. Experiments measuring atmospheric neutrinos, like PINGU [52] in IceCube or ORCA [53] in ANTARES, might reach the required sensitivity to determine the mass hierarchy. If an (extra)galactic supernova explosion occurs, the time and energy signals of supernova neutrinos will have characteristic imprints from the mass ordering. This would be seen by a network of detectors, such as Super-Kamiokande, KamLAND [54], Borexino [5], or by dedicated supernova observatories like HALO [55–58] and LVD [59]; while some constitute the "SNEWS: SuperNova Early Warning System" aiming at alerting observers if a galactic supernova occurs [60]. About a thousand events can be collected if an explosion happens in our galaxy. Such phenomena are rare (1-3 expected events/century). On the other hand there is the yet unobserved diffuse supernova neutrino background due to supernova explosions at different cosmological redshifts. The sensitivity for its discovery could be reached with improved technologies [61] or with large-size detectors[3] like MEMPHYS or Hyper-K (440 or 770 kton water Cherenkov) and GLACIER (100 kton liquid Argon) [62] that would collect about 350 and 60 events over 10 years, respectively [63]. From the detection of the diffuse supernova background, key information could be extracted on the supernova dynamics, on the star formation rate and on unknown neutrino properties (for a review see [64, 65]).

2 Neutrino flavour conversion in media : status and open questions

It is now established that the deficit of high energy solar neutrinos is due to the Mikheev-Smirnov-Wolfenstein (MSW) effect [66,67], a resonant conversion phenomenon occurring when neutrinos interact with the matter composing a medium. In two-flavours, the MSW resonance location is identified by the relation[4]

$$\sqrt{2} G_F n_e = (\Delta m^2 \cos 2\theta)/2E, \tag{5}$$

with G_F the Fermi coupling constant, n_e the electron number density (see also the early works [68–70], [29] or the recent review [10]). At such a location, a conversion from the electron to the muon (and tau) flavours can take place. Its efficiency (or adiabaticity) depends on the one hand on the mixing angles, on the mass-squared difference values and signs, and on the matter number density profile on

[3] Such detectors are about 20 times larger than Super-Kamiokande. Their goal is to cover an interdisciplinary program including the detection of supernova neutrinos, leptonic CP violation and proton decay searches.

[4] For antineutrinos the *r.h.s.* of the relation has a minus sign.

the other (see Figure 3). In particular, the evolution is little sensitive to the profile details as far as its smooth enough that the adiabatic condition is met. Moreover, depending on the squared-mass difference sign, the MSW effect can occur in the electron neutrino or anti-neutrino channels. Since R. Davis' experiment, numerous solar experiments mainly sensitive to the electron flavour have precisely measured the solar neutrino flux. These experiments also had some sensitivity to the other flavours. Using elastic scattering, charged- and neutral-current neutrino interactions on heavy water, the SNO experiment has showed that the measurement of the total ^{8}B solar neutrino flux is consistent with the predictions of the standard solar model : solar electron neutrinos convert into the other active flavours. In particular, the muon and tau neutrino components of the solar flux has been measured at 5 σ [6]. Moreover the reactor experiment KamLAND has definitely identified the Large Mixing Angle (LMA) solution, by observing reactor electron anti-neutrino disappearance at an average distance of 200 km. The ensemble of these observations shows that averaged vacuum oscillations giving

$$P(\nu_e \to \nu_e) \approx 1 - \frac{1}{2}\sin^2\theta_{12} \approx 0.57 \quad (6)$$

(with $\theta_{12} = 34°$) account for the deficit of low energies (< 2 MeV) solar neutrinos; while the deficit of the high energy portion of the ^{8}B spectrum is due to the MSW effect. For the latter, the matter-dominated survival probability is

$$P(\nu_e \to \nu_e)^{high\ density} \to \sin^2\theta_{12} \approx 0.31 \quad (7)$$

for neutrinos above the critical energy of about 2 MeV Eq.(5) (see e.g. [10, 29]). More recently, the Borexino experiment has measured the low energy portion of the solar neutrino spectrum (pep and ^{7}Be ν) [72]. Figure 4 shows the results from solar experiments [10]. Nowadays the MSW effect constitutes a reference mechanism in the study of neutrino flavour conversion in media.

Another interesting case is represented by neutrinos traversing the Earth. Its matter density profile undergoes a rapid change from the mantle to the core at higher density [73]. It was first pointed out in [74] and in [75] that atmospheric neutrinos traversing the Earth would change in flavour. Besides the MSW effect, another neutrino flavour conversion mechanism can occur, named "parametric resonance" [76] or "neutrino oscillation length resonance" [77]. This effect is an interference effect due to the mantle-core-mantle change in the Earth matter density profile, that can enhance the oscillation probabilities. For example, depending on the trajectory (or azimuthal angle) and energy, atmospheric neutrinos in the few GeV energy

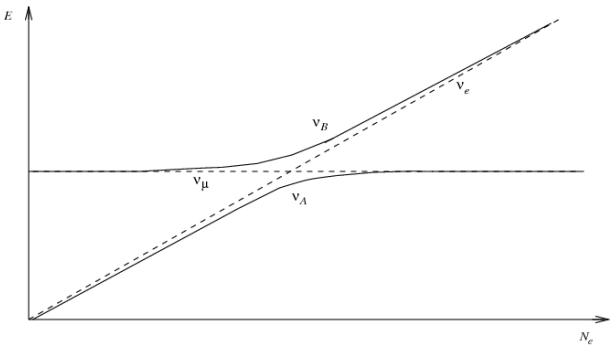

Figure 3 (online color at: www.ann-phys.org) The MSW effect : Schematic behavior of the neutrino matter eigenvalues (solid lines) as a function of the matter number density of a medium. The eigenvalues are pushed far apart because of the presence of mixings, at the MSW resonance location. (The dashed lines shows the eigenvalues in absence of mixings.) In the case of an adiabatic evolution the matter eigenstate ν_B does not mix with the ν_A at the resonance and stays on the higher branch up to the surface of the star. In this case an electron neutrino born as ν_B emerges as ν_B. This produces an electron neutrino deficit in a ν_e sensitive detector on Earth.

range can have an MSW resonant conversion in the core, or in the mantle and in the core. Neutrinos having core-crossing trajectories can also experience the parametric resonance. The MSW and parametric resonance effects have been investigated e.g. in [78] in the subdominant atmospheric $\nu_e \to \nu_\mu$ in Super-Kamiokande. An extended literature concerns matter effects in atmospheric neutrinos (see e.g. [79] and references therein).

A variety of novel flavour conversion mechanisms has been identified in stars with more than 6-8 solar masses - the O-Ne-Mg and iron core-collapse supernovae. Their evolution ends with an explosion where 99 % of the gravitational energy is released as neutrinos of all flavours, in the 100 MeV energy range, during a burst lasting about ten seconds. The explosion leaves either a neutron star or a black hole. Since the matter number density of these stars is very large, the MSW effect occurs at two different locations[5], usually referred to as the High (H) and the Low (L) resonances. The evolution at the H-resonance depends on

[5] Note that there is also a third resonance named $V_{\mu\tau}$, associated to the $(\theta_{23}, \Delta m^2_{23})$ oscillation parameters. It occurs at higher density than the H-resonance. Since, in general, the $V_{\mu\tau}$ resonance has a small effect on observations, it will not be discussed further here.

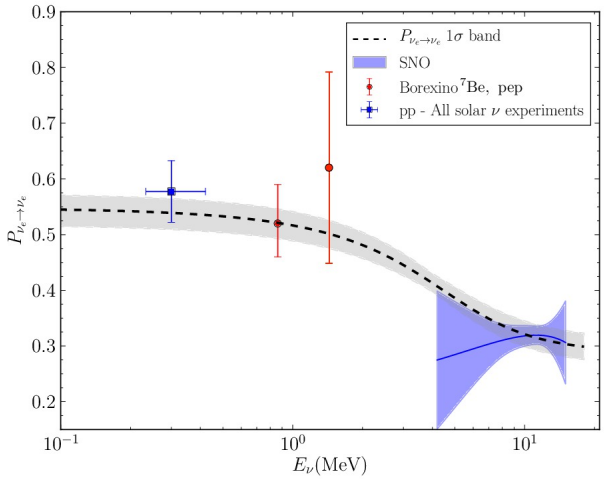

Figure 4 (online color at: www.ann-phys.org) Solar neutrinos : Electron neutrino survival probability, as a function of the neutrino energy, for the pp, pep, ^{7}Be, ^{8}B neutrinos from global solar neutrinos analyses, Borexino, and the SNO combined analysis. The results are compared to the MSW predictions, taking into account present uncertainties on mixing angles. The SNO results are from [71] and the ones on pep are from [72]. Figure from [10].

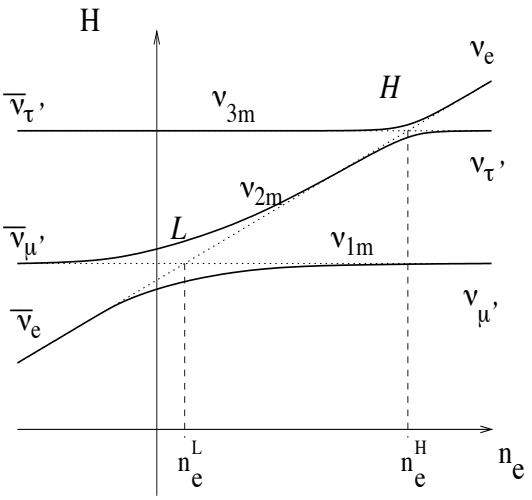

Figure 5 (online color at: www.ann-phys.org) MSW effect in supernovae : Level crossing diagram for the neutrino mass eigenstates in a supernova for the case of normal mass hierarchy. The figure shows the matter eigenvalues evolution associated with the matter eigenstates $\nu_{1m}, \nu_{2m}, \nu_{3m}$, as a function of the electron number density n_e. The two crossings correspond to the high-resonance (H) and the low-resonance (L) associated with the mixing parameters $(\theta_{13}, \Delta m^2_{13})$ and $(\theta_{12}, \Delta m^2_{12})$, respectively [80].

the $(\theta_{13}, \Delta m^2_{13})$ oscillation parameters, while the flavour evolution at the L-resonance (L) depends on $(\theta_{12}, \Delta m^2_{12})$ (see Figure 5) [80]. For example, a 40 MeV neutrino sees the H-resonance at a density of about 10^3 g/cm^3. The identification of the solar LMA solution tells us the value and the sign of Δm^2_{12}. The three neutrino mixing angles are also now precisely determined. For typical supernova matter density profiles, the neutrino passage in the L-resonance region is adiabatic. On the other hand the neutrino flavour content after the H-resonance encodes interesting information on the mass hierarchy. Therefore matter effects on the supernova neutrino spectra can tell us about the hierarchy from signals of future explosions. However, theoretical investigations of the last ten years have shown that the situation is more complex than what shown in Figure 5 of Ref. [80]. This is because one is facing an explosive phenomenon with shock wave(s) and turbulence, with 10^{58} MeV released as neutrinos.

Ref. [81] first pointed out that the shock wave passage in the MSW resonance region would leave an imprint on the time signal of the positrons emitted in inverse beta-decay, i.e. $\bar{\nu}_e + p \to n + e^+$. This is the main detection channel in Cherenkov and scintillator detectors. Ref. [82] has emphasized the effects from the presence of not only a front but also a reverse shock, which are apparent in supernova simulations. The presence of shock waves engenders two important effects. First it makes the H-resonance temporarily non-adiabatic because of the steepness of the shock wave fronts (the adiabaticity depends on the derivative of the density profile). Second, multiple H-resonances appear, since a neutrino of a given energy can meet the resonance condition several times. For example, in presence of two resonances, the electron neutrino survival probability reads [83]

$$P_{\nu_e\nu_e} = \cos^2(\chi_1 - \chi_2) - \sin 2\chi_1 \sin 2\chi_2 \sin^2\left(\int_{x2}^{x1} \frac{\Delta\tilde{m}^2}{4E}\right) dx \tag{8}$$

with χ_1 and χ_2 the matter angles mixing the two matter eigenstates at the resonance locations x_1 and x_2, and $\Delta\tilde{m}^2$ the matter squared-mass difference. The interference term oscillates with the neutrino energy and the resonance locations. Since the shock wave is moving, it will change the resonance locations modifying the phase in such a term. This produces rapid oscillations in the

survival probability for a neutrino of a given energy. The conditions for such oscillations termed "phase effects" are that the flavour evolution is semi-adiabatic at the resonances and that the matter eigenstates stay coherent at the resonances [83].

Turbulence is another characteristic of these explosive environments. Its effects are studied e.g. in [84–86]. The presence of matter density fluctuations can introduce numerous locations where the resonance density is met. Their effect on flavour conversion is therefore of the same kind as of shock waves. In fact turbulence produces phase effects, averaging the neutrino oscillation probability between the adiabatic and non-adiabatic solution [87] (see also [88], and [89] for a review). Still, extensive calculations remain to be done, where one implements matter density fluctuations extracted from multi-dimensional supernova simulations (instead of more schematic prescriptions). Clearly, to fully capture several flavour conversion features in media, that are interference effects, one has to evolve the neutrino amplitudes and not the neutrino probabilities. The latter procedure was often followed in the past, e. g. in predictions with the factorisation hypothesis where one factorizes the probabilities for flavour conversion at the H- and L-resonances.

The implementation of the neutral-current ν-ν interaction constitutes another important progress in simulations of flavour conversions in supernovae. Such contributions are small in the sun, whereas the large neutrino number density renders them important in these environments. Ref. [90] first pointed out that the neutrino self-interaction would introduce a non-linear refractive index. The first numerical simulations showed the appearance of new phenomena [91]. Ref. [92] pointed out a significant impact on the r-process nucleosynthesis. Ref. [93] showed the important effects on the neutrino fluxes with phenomenological implications. This triggered intensive investigations (see [94] for a review). The inclusion of ν self-interaction makes predictions demanding since a system of coupled stiff non-linear equations needs to be solved. Three new conversion regimes near the neutrino-sphere are identified. The first is the "synchronisation" where neutrino flavour conversion is frozen. The second regime consists in bipolar oscillations that can be understood as a "flavour" [95] or a "gyroscopic" pendulum [96]. In the last phase, full or no flavour conversion occurs depending on the neutrino energy. The underlying mechanism producing this abrupt change corresponds to an MSW-like behaviour in the co-moving frame [97], which can be interpreted as a "magnetic resonance" phenomenon [98]. This mechanism produces sharp changes of the neutrino fluxes that appear around 200 km from the neutrino-sphere. The electron and muon (or tau) neutrino fluxes swap above a critical energy called the "split" energy. All these effects are also termed "collective" effects because many of their features can be captured by following the neutrino ensemble (instead of a neutrino at a time). These mechanisms explain the novel flavour modifications appearing in simulations with neutrino self-interactions. However the picture becomes more complex depending on the neutrino luminosity ratios at the neutrino-sphere[7], on the neutrino properties and on the detailed implementation of the geometry of the neutrino emission. For example, large matter densities can decohere collective effects [99]. Recent calculations based on realistic matter density profiles from one-dimensional supernova simulations show that indeed such effects might be suppressed during the accretion phase of the supernova explosion [100]. If so, the situation becomes simpler theoretically because the flavour change is only due to the MSW effect. Nevertheless further modifications can be present due to the shock waves and turbulence, depending on the considered phase of the explosion (neutronization burst, accretion, or cooling phase).

Impressive progress has been achieved in unravelling mechanisms and conditions for flavour conversion of core-collapse supernova neutrinos. Still, serious work is needed to come to a definite and comprehensive understanding and to establish the impact on observations. Current supernova simulations are based on a detailed treatment of the neutrino transport in the dense supernova region inside the neutrino-sphere. They typically account for a good angular, or energy neutrino distribution (but not both), and do not include mixings [101]. Such simulations provide the neutrino energy spectra and fluxes at the neutrino-sphere that are the initial conditions for the flavour evolution studies. These then evolve the ν up to the star surface in order to predict the associated signals in observatories on Earth (in the case of an explosion). The evolution equations used are based on the mean-field approximation. This means that one neutrino (or anti-neutrino) is evolved at a time in a background of matter, of ν and of $\bar{\nu}$ that acts on the "test" particle through a mean-field. It is still an open question if and under which conditions the present treatments describe in an appropriate way the transition between the region that is Boltzmann treated to the one that is mean-field described. In fact more realistic geometrical descriptions or extended equations implementing many-body corrections might be needed. Works along this line of research are just appear-

[7] The neutrino-sphere is the region in the supernova where neutrinos start free streaming (Figure 6).

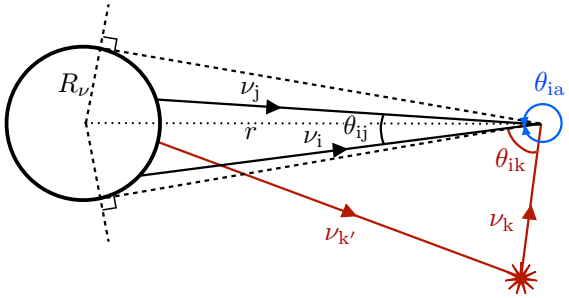

Figure 6 (online color at: www.ann-phys.org) Cartoon picture of neutrinos emitted at the neutrino-sphere of a supernova and interacting with each other. The neutrino-sphere is taken to be a sharp sphere [102].

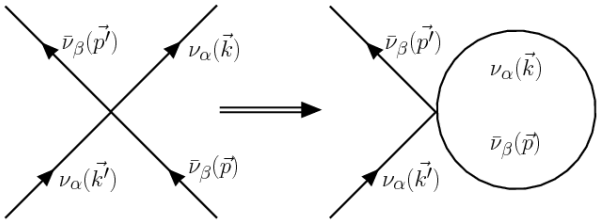

Figure 7 (online color at: www.ann-phys.org) The (low energy) neutrino-antineutrino interaction (left figure) and the associated pairing mean-field (right figure) obtained by summing over the background particles states. These contributions appear in an extended mean-field description that goes beyond the usual mean-field assumption made in the simulations of flavour conversion in core-collapse supernovae [104].

ing. For example, Ref. [102] has pointed out the need for a more realistic geometrical description of the neutrino emission at the neutrino-sphere (Figure 6). Ref. [103] has derived corrections beyond the mean-field approximation using a coherent-state path integral approach. Ref. [104] has used the general many-body framework offered by the Bogoliubov-Born-Green-Kirkwood-Yvon hierarchy to derive both the mean-field and extended mean-field equations. The latter introduce for the first time the abnormal mean-field corresponding to neutrino-antineutrino pairing correlations (Figure 7). So far neglected, these two-body correlations might impact flavour conversion and supernova observations.

The theoretical developments described above also apply to the study of the low energy neutrinos from the accretion disks surrounding black holes (AD-BH). In fact the conditions in the disks are very similar to the core-collapse supernova ones, so that such sites also offer conditions for example for r-process and νp element nucleosynthesis (see e.g. [105, 106]). Refs. [92, 107] have studied e.g. the effect of the neutrino-neutrino interaction in these sites.

Finally, neutrino flavour conversion phenomena are also important in the Early Universe, in particular at the epoch of Big-bang nucleosynthesis. Their description is based on the resolution of a Boltzmann equation for particles with mixings since collisions need to be implemented, as well as neutrino mixings, the coupling to the relativistic plasma and neutrino self-interaction. Note that the importance of the neutrino self-interaction was first pointed out in this context. A key parameter for primordial nucleosynthesis (as for the r-process) is the proton-to-neutron ratio. This is determined by the electron neutrinos and antineutrinos interactions with protons and neutrons and by neutron decay. The build up of the light elements starts at about 1 s after the Big-bang when the plasma temperature is around 1 MeV. The final primordial abundances are very sensitive to neutrino properties (see [108, 109] for a review). Just to give an example, cosmological observations from primordial nucleosynthesis and the matter power spectrum are compatible with about one sterile neutrino (see e.g. [110]). The PLANCK experiment has recently measured $N_{eff} = 3.36 \pm 0.66$ at 95%C.L. (CMB alone) for the effective number of neutrino species [111]. The direct observation of the cosmological neutrino background remains a challenge. Its detection demands novel approaches since such νs are very cold. Attempts are still off from the required sensitivity by several order of magnitudes. The approach which appears as the "closest" is the detection of cosmological neutrinos through their capture by radioactive nuclei, a process without threshold. First proposed by Weinberg [112], this idea has been applied in realistic extensive calculations in [113] (see also Ref. [114]).

3 Open issues and astrophysical ν

One of the crucial open issues is the possible breaking of CP invariance. The recent precise measurement of the third neutrino mixing angle by the RENO [32] and the Daya-Bay collaborations [33] brings a much awaited result for CP searches. In fact CP violation from a non-zero Dirac phase affects oscillations only in the case of three families. The discovery of leptonic CP violation and of neutrino-less double-beta decay would give important clues for the understanding of matter-antimatter asymmetry in the universe (see e.g. [115]). An interesting re-

lated question to explore is the possibility to have indirect manifestations of a non-zero Dirac-type phase in astrophysical environments. The authors of Ref. [116] have first investigated this question in the solar neutrino context showing that there are no CP violating effects in the ν_e survival probability in matter to the leading order in electroweak interaction. Effects from next-to-leading order are estimated to be extremely small. Ref. [117] has first pointed out possible effects in core-collapse supernovae coming to the conclusion that there are no CP violation effects in such environments. Ref. [118] has come to a result at variance with Ref. [117] demonstrating that there can be CP violating effects in supernovae. By using general arguments, the factorisation condition

$$H(\delta) = S^{\dagger} H(\delta = 0) S \tag{9}$$

is obtained[9] with $S = diag(1, 1, e^{i\delta})$. This relation gives a procedure to identify under which conditions such effects can arise : contributions to the neutrino Hamiltonian that break the factorization condition engender CP violating effects. For example, these arise because of radiative corrections in the Standard Model, or of non-standard interactions like flavour-changing interactions that differentiate muon from tau neutrino interactions with matter. This finding has been subsequently independently confirmed by Ref. [119]. A quantitative evaluation of the modifications introduced by a non-zero Dirac phase shows variations at the level of a few percent both of the supernova signal in an observatory on Earth or of the neutron-to-proton ratio relevant for r-process nucleosynthesis [118]. An improved numerical simulation with the neutrino self-interaction has shown that the non-linearity of the equations amplifies the CP violating effects from radiative corrections by several order of magnitudes [120]. While flux modifications are still at the level of about 5-10 %, future improvements of the simulations might introduce further amplification of such effects. Ref. [121] has studied the size of CP violating effects in presence of non-zero neutrino magnetic moments, reaching the same conclusions as previous works [118, 120] concerning the size of CP effects. In the Early universe context Ref. [122] has performed the first investigation of the effects of a non-zero Dirac-type phase on the primordial light elements abundances. Within three-active neutrinos it is shown that the phase modifies the primordial Helium-4 abundance at most by 1%, which is within current systematic uncertainties.

[9] H being in the so-called T_{23} basis

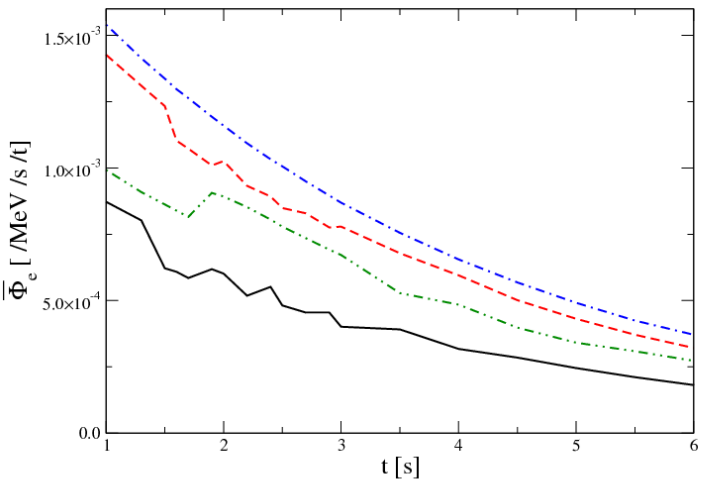

Figure 8 (online color at: www.ann-phys.org) Positron time signal associated with inverse beta-decay for a galactic explosion at 10 kpc per unit tonne in a detector. The different curves are for 10 (solid), 15 (dashed), 19 (dash-dotted) and 29 (dot-dot-dashed line) MeV positron energies. The dips or bumps correspond to the passage of the shock wave in the MSW resonance region. They are present in the case of inverted mass hierarchy [128].

The detection of neutrinos from a future (extra)galactic explosion constitutes one of the strategies to identify the mass hierarchy. Available studies are roughly of three types. The first kind exploits Earth matter effects of supernova neutrinos that traverse the Earth before being detected [80]. This produces a modulation of the neutrino events distribution that gives peaks in the distribution Fourier transform [123]. However such effects are very small making this option hardly feasible [124]. A second option consists in exploiting the early time signal of the supernova explosion either from the neutronization burst [125] or from the accretion phase. In Ref. [126] the signal of the first 200 ms (accretion phase) of the explosion is investigated. This time window has the advantage of being simpler than the late explosion stages since the signal is not affected by the neutrino-self-interaction, the shock-waves (and turbulence). The authors show that in IceCube one could distinguish the normal from the inverted hierarchy. The third type of studies look for effects in the time signal due to the shock waves since their presence depends on the hierarchy [82, 127]. Early works show

features without the $\nu - \nu$ interaction. This improvement is performed in Ref. [128]. The calculation treats neutrino self-interactions and shock-wave effects in a consistent way, using realistic supernova density profiles and propagating neutrino amplitudes (phase effects are properly taken into account). Figure 8 shows the results for the positron time signal associated with inverse beta-decay in water Cherenkov and scintillator detectors. At early times, when the shock wave has not yet reached the MSW resonance region, the neutrino conversion is expected to be adiabatic. As the shock wave reaches this region, the flux becomes the non-adiabatic one, producing either a dip or a bump, depending on the neutrino energy. For electron anti-neutrinos, the resonance condition is met for inverted hierarchy. If the hierarchy is normal, no resonant conversion occurs and the positron time signal presents an exponential behaviour. Such a signature could already be seen in Super-Kamiokande if a galactic supernova happens tomorrow, and be distinguished by the exponential at 3.5 σ (1 σ) for the bump (dip). Note that this signature holds in the electron neutrino channel as well, if the mass hierarchy is normal. This could be seen in a liquid argon detector mainly sensitive to ν_e or in water Cherenkov and in scintillator detectors through scattering on oxygen and carbon respectively.

Complementary information would be obtained by the observation of (extra)galactic supernova explosion(s) and the detection of the diffuse supernova neutrino background. While some of the uncertainties are still large, one can pin down interesting information by combining data from different detectors. Having different technologies sensitive to ν and $\bar{\nu}$ with various energy thresholds is a key aspect to be sensitive to different parts of the neutrino spectra. Figure 9 shows the example of the interest of having one- and two-neutron detection channels in a lead-based detector like HALO [58]. Note that a software - SNOwGLoBES - is now available to compute interaction rates for supernova neutrinos in common detector materials [129, 130].

Observations using the ν_e detection channel would benefit from precise measurements of neutrino-nucleus scattering. Only for deuteron the cross section is known at the level of few percent, while for heavier nuclei uncertainties are typically at the level of few tens of percent. In the future, facilities producing neutrinos in the 100 MeV energy range such as low energy beta-beams [131] or spallation sources [132], could offer a unique opportunity to precisely measure such cross sections and also realise fundamental interaction studies, like measurements of the Weinberg angle at low momentum transfer, a test of the Conserved-Vector-Current hypothesis (see [43] for a review), or of the hypothesis of the existence of sterile

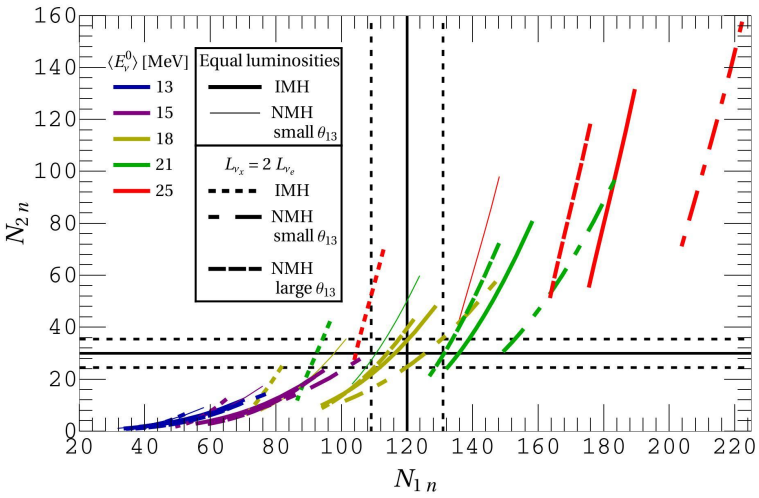

Figure 9 (online color at: www.ann-phys.org) One- and two-neutron emission event rates for a supernova at 10 kpc in the HALO phase-II detector (1 kton of ^{208}Pb). The different curves take into account the uncertainties in the supernova muon (tau) neutrino fluxes at the neutrino-sphere as well as the possible hierarchy (θ_{13} is now measured) [58].

neutrinos [48]. Note that improving the knowledge of the isospin and spin-isospin nuclear response involved in neutrino-nucleus interactions is of importance also for searches on the neutrino nature, since this constitutes a key ingredient of neutrino-less double-beta decay predictions [133].

Observing a supernova luminosity curve is of great astrophysical value besides being of interest for the fundamental particle or interaction properties it encodes. In fact, the ν time signal closely follows the different phases of the explosion, from the collapse to the accretion phase and to the cooling of the remaining proto-neutron star. This measurement would provide key information for the longstanding open problem of the explosion mechanism of iron-core supernovae. Currently, 2- and 3-dimensional simulations are being developed that realistically include the neutrino transport, convection and hydrodynamical instabilities (the Standing-Accretion-Shock o SASI mode). Several groups are obtaining successful explosions for different progenitor masses, while reaching a consensus on the mechanism requires further studies (see e.g. [101, 134, 135]). Using 3D models based on a simplified neutrino transport scheme, Ref. [136] has showed for example that the SASI mode could be tracked in IceCube for a supernova within 2 kpc. These massive stars are also candidate sites for the r-process, whose identification is still

an open issue; while several sites might contribute, such as the accretion disks around black holes [31]. The impact of neutrino properties on the r-process is the object of numerous studies. For example Ref. [137] points out the possible role of sterile neutrinos in getting a successful nucleosynthesis in supernovae. An intriguing question is also the possible impact of flavour conversion on the explosion itself. MSW effects occur in the outer star layers and have no impact on the shock. The collective effects from the neutrino-neutrino interaction take place deep in the star and might have an impact. The first investigations seem to indicate that they are still far out to affect the shock waves [138], although it might still be too early to draw conclusions.

A new window on the universe is opened by high-energy neutrino telescopes like ANTARES, the first undersea in the Mediterranean [139], and IceCube, buried in deep ice at the South Pole [140]. The main mission is to search for galactic and extra-galactic sources of high-energy neutrinos to elucidate the source of cosmic rays and the astrophysical mechanisms that produce them. These telescopes also investigate neutrino oscillations, dark matter and supernova neutrinos (for IceCube). At present, the IceCube collected data on ultra-high-energy neutrinos (above 10^{19} eV) from active galactic nuclei (AGN) and gamma-ray-bursts (GRB) show no significant deviation from background in the number of observed events, although uncertainties in the models are still quite large. Interestingly two 1 PeV events at threshold of GZK searches have been recently identified with a significance of 2.8 σ of not being a background [140]. A follow-up analysis of contained vertex event search has just found 26 more events at lower energy (3.6 σ). There is now evidence for a high-energy neutrino component inconsistent at 4.3 σ with standard atmospheric backgrounds [141]. A future larger data set with increased statistical significance might confirm the discovery of high energy astrophysical neutrinos.

High-energy neutrino telescopes are currently also providing data on neutrino oscillations measuring atmospheric neutrinos, commonly a background for astrophysical neutrino searches. Using low energy samples, both ANTARES [142] and IceCube/DeepCore [143] have measured the parameters θ_{23} and Δm^2_{23} in good agreement with existing data. Crucial information can be extracted from such telescopes in the future from low energy (below 40 GeV) atmospheric neutrinos. Predictions show that from the measurement of flavour conversion effects in the Earth in IceCube/DeepCore can provide a precise measurement of oscillation parameters (see e.g. [144, 145]). PINGU, IceCube extension in the 10 GeV energy range, could measure the mass hierarchy and be sensitive to the Dirac phase [146]. Feasibility studies are currently ongoing both for PINGU and for ORCA to establish if the energy and angular resolution required for the mass hierarchy search can be achieved. Information on the phase could also be extracted by a precise measurement of high-energy neutrino flux ratios [147–149]. Ref. [149] gets a 2 σ coverage of about 10 % of the CP values, if uncertainties on the flux ratios are kept below 7 %. As for a fourth sterile neutrino, its existence might lead to a distortion of the zenith angle distribution of high-energy atmospheric neutrinos through the MSW active-sterile resonance inside the Earth. An analysis of data from Amanda and (incomplete) IceCube as well as the prospects for the completed IceCube give limits that for some of the sterile oscillation parameters are stronger than all combined experiments [150]. Ref. [151] shows that low energy events in DeepCore can substantially constrain the mixing of sterile neutrinos in the eV mass scale. The effect found is different for normal or inverted hierarchy of active neutrinos, so that if such ν_ss exist the hierarchy can also be identified. Finally both terrestrial experiments and neutrino telescopes [152] set tight limits on Lorentz and CPT violation. A constraint also comes from the SN1987A from the nearly simultaneous arrival of the photons and the neutrinos [153]. Interestingly, models based on Lorentz and CPT violation are developed to interpret oscillation data from all experiments (see [154] and the nice summary in Ref. [155]).

In conclusion, neutrinos are messengers having a wide energy range, capable of covering cosmological distances and telling us about quiet and violent phenomena. Neutrino physics is a domain rich of interdisciplinary aspects and approaches. The measurement of these elusive particles requires inventive detectors of huge sizes. Sometimes slow on a man-scale, the progress continues steadily, while the last decade has been rich of exciting observations. Neutrinos have brought milestones in our understanding of fundamental issues in high-energy physics and astrophysics, and will likely bring more in the future.

Key words. Neutrino masses and mixings, flavour conversion in media, solar and supernova neutrinos, mass hierarchy, sterile neutrinos, leptonic CP violation, CPT and Lorentz violation.

References

[1] R. Davis, Phys. Rev. Lett. **12**, 303 (1964).
[2] K. S. Hirata et al., J Phys. Rev. Lett. **63**, 16 (1989).
[3] J. N. Abdurashitov et al., J Phys. Rev. C **60**, 055801 (1999).
[4] P. Anselmannet al. Phys. Lett. BÊ **327**, 377 (1994).

[5] C. Arpesella et al., Phys. Rev. Lett. **101**, 091302 (2008).
[6] Q. R. Ahmad et al., Phys. Rev. Lett. **89**, 011301 (2002).
[7] J. N. Bahcall, and R. K. Ulrich, Rev. Mod. Phys. **60**, 297 (1988).
[8] S. Turck-Chieze , and I. Lopes, Astrophys. J. **408**, 347 (1993).
[9] E. G. Adelberger et al., Rev. Mod. Phys. **70**, 1265 (1998).
[10] W. C. Haxton, R. G. Hamish Robertson, and A. M. Serenelli, arXiv:1208.5723.
[11] A. Suzuki, J. Phys. Conf. Ser. **120**, 072001 (2008).
[12] K. Hirata et al., Phys. Rev. Lett. **58**, 1490 (1987).
[13] R. M. Bionta et al., Phys. Rev. Lett. **58**, 1494 (1987).
[14] Alexeyev, E.N. et al. , Proc. of the Leptonic Session of the 22nd Rencontre de Moriond (1987) 739.
[15] M. Aglietta et al. , Europhys. Lett. **3**, 1315 (1987).
[16] G. Pagliaroli, F. Vissani, M. L. Costantini, and A. Ianni, Astropart. Phys. **31**, 163 (2009).
[17] K. S. Hirata et al., Phys. Lett. B **205**, 416 (1988).
[18] Y. Fukuda et al., Phys. Lett. B **335**, 237 (1994).
[19] D. Casper et al., Phys. Rev. Lett. **66**, 2561 (1991).
[20] C. Berger et al., Phys. Lett. B **245**, 305 (1990).
[21] M. Aglietta et al., Europhys. Lett. **8**, 611 (1989).
[22] G. L. Fogli, E. Lisi, D. Montanino, and G. Scioscia, Phys. Rev. D **55**, 4385 (1997).
[23] Y. Fukuda et al., Phys. Rev. Lett. **81**, 1562 (1998).
[24] H.A. Bethe, Phys. Rev. **55**, 1562 (1939).
[25] G. Gamow, and M. Schoenberg, Phys. Rev. **58**, 1117 (1940).
[26] B. Pontecorvo„ Sov. Phys. JETP **6**, 429 (1957) [Zh. Eksp. Teor. Fiz. **33**, 549 (1957)].
[27] Z. Maki, M. Nakagawa, and S. Sakata, Prog. Theor. Phys. **28**, 870 (1962).
[28] J. Beringer et al., Phys. Rev. D **86**, 010001 (2012).
[29] C. Giunti, and C. W. Kim, "Fundamentals of Neutrino Physics and Astrophysics," (Univ. Pr., Oxford, 2007), p. 710.
[30] K. Abe et al., Phys. Rev. Lett. **107**, 041801 (2011).
[31] Y. Abe et al., Phys. Rev. Lett. **108**, 131801 (2012).
[32] J. K. Ahn et al., arXiv:1204.0626.
[33] F. P. An et al., Phys. Rev. Lett. **108**, 171803 (2012).
[34] A. Osipowicz et al., hep-ex/0109033.
[35] C. Giunti and M. Laveder, Phys. Rev. C **83**, 065504 (2011).
[36] C. Athanassopoulos et al., Phys. Rev. Lett. **77**, 3082 (1996).
[37] C. Athanassopoulos et al., Phys. Rev. Lett. **81**, 1774 (1998).
[38] B. Zeitnitz et al., Prog. Part. Nucl. Phys. **40**, 169 (1998).
[39] A. A. Aguilar-Arevalo et al., Phys. Rev. Lett. **102**, (2009) 101802.
[40] A. A. Aguilar-Arevalo et al., arXiv:1207.4809 [hep-ex].
[41] G. Mention et al., Phys. Rev. D **83**, 073006 (2011).
[42] P. Zucchelli, Phys. Lett. B **532**, 166 (2002).
[43] C. Volpe, J. Phys. G **34**, R1 (2007).
[44] A. Bandyopadhyay et al., Rept. Prog. Phys. **72**, 106201 (2009).
[45] J. Alonso et al., arXiv:1006.0260.
[46] P. Huber et al., JHEP **0911**, 044 (2009).
[47] M. Cribier et al., Phys. Rev. Lett. **83**, 201801 (2011).
[48] C. Espinoza, R. Lazauskas, and C. Volpe, Phys. Rev. D **1986**, , 113016 (2012).
[49] K. N. Abazajian et al., arXiv:1204.5379.
[50] J. Lesgourgues and S. Pastor, Adv. High Energy Phys. **2012**, 608515 (2012).
[51] K. N. Abazajian et al., Astropart. Phys. **35**, 177 (2011).
[52] D. J. Koskinen, Mod. Phys. Lett. A **26**, 2899 (2011).
[53] see http://agenda.infn.it/conferenceDisplay.py?confId=5510
[54] K. Eguchi et al., Phys. Rev. Lett. **90**, 021802 (2003).
[55] see http://www.snolab.ca/halo/
[56] G. M. Fuller, W. C. Haxton, and G. C. McLaughlin, Phys. Rev. D **59**, 085005 (1999).
[57] J. Engel, G. C. McLaughlin, and C. Volpe, Phys. Rev. D **67**, 013005 (2003).
[58] D. Väänänen, and C. Volpe, JCAP **1110**, 019 (2011).
[59] N. Y. .Agafonova t et al., J Astropart. Phys. **28**, 516 (2008).
[60] see http://snews.bnl.gov/
[61] J. F. Beacom, and M. R. Vagins, Phys. Rev. Lett. **93**, 171101 (2004).
[62] D. Autiero et al., JCAP **0711**, 011 (2007).
[63] S. Galais, J. Kneller, C. Volpe, and J. Gava, Phys. Rev. D **81**, 053002 (2010).
[64] J. F. Beacom, Ann. Rev. Nucl. Part. Sci. **60**, 439 (2010).
[65] C. Lunardini, arXiv:1007.3252.
[66] L. Wolfenstein, Phys. Rev. D **17**, 2369 (1978).
[67] S. P. Mikheev, and A. Y. Smirnov, Sov. J. Nucl. Phys. **42**, 913 (1985).
[68] H. A. Bethe, Phys. Rev. Lett. **56**, 1305 (1986).
[69] W. C. Haxton, Phys. Rev. Lett. **57**, 1271 (1986).
[70] J. Bouchez et al., Z. Phys. C **32**, 499 (1986).
[71] B. Aharmim et al., arXiv:1109.0763 .
[72] G. Bellini et al., Phys. Rev. Lett. **108**, 051302 (2012).
[73] A. M. Dziewonski, and D. L. Anderson, Phys. Earth Planet. Interiors **25**, 297 (1981).
[74] V. K. Ermilova, V. A. Tsarev, and V. A. Chechin, JETP Lett. **43**, 453 (1986) [Pisma Zh. Eksp. Teor. Fiz. **43**, 353 (1986)].
[75] E. Kh. Akhmedov, Yad. Fiz. **47**, (1988) 475 [Sov. J. Nucl. Phys. **47** (1988) 301].
[76] E. Kh. Akhmedov, Nucl. Phys. B **538**, 25 (1999).
[77] S. T. Petcov, Phys. Lett. B **434**, 321 (1998).
[78] E. K. Akhmedov et al., Nucl. Phys. B **542**, 3 (1999).
[79] E. K. Akhmedov, M. Maltoni, and A. Y. Smirnov, JHEP **0806**, 072 (2008).
[80] A. S. Dighe, and A. Y. Smirnov, Phys. Rev. D **62**, 033007 (2000).
[81] R. C. Schirato, and G. M. Fuller, astro-ph/0205390 .
[82] R. Tomas et al., JCAP **0409**, 015 (2004).
[83] B. Dasgupta, and A. Dighe, Phys. Rev. D **75**, 093002 (2007).

[84] F. N. Loreti et al., Phys. Rev. D **52**, 6664 (1995).
[85] G. L. Fogli, E. Lisi, A. Mirizzi, and D. Montanino, JCAP **0606**, 012 (2006).
[86] A. Friedland, and A. Gruzinov, astro-ph/0607244.
[87] J. P. Kneller, and C. Volpe, Phys. Rev. D **82**, 123004 (2010).
[88] T. Lund and J. P. Kneller, arXiv:1304.6372.
[89] H. Duan, and J. P. Kneller, J. Phys. G **36**, , 113201 (2009).
[90] J. T. Pantaleone, Phys. Lett. B **287**, 128 (1992).
[91] S. Samuel, Phys. Rev. D **48**, 1462 (1993).
[92] A. B. Balantekin, and H. Yuksel, New J. Phys. **7**, 51 (2005).
[93] H. Duan, G. M. Fuller, J. Carlson, Y.-Z. Qian, Phys. Rev. D **74**, 105014 (2006).
[94] H. Duan, and G. M. Fuller, and Y. -Z. Qian, Ann. Rev. Nucl. Part. Sci. **60**, 569 (2010).
[95] H. Duan, G. M. Fuller, J. Carlson, and Y. -Z. Qian, Phys. Rev. D **75**, .125005 (2007).
[96] S. Hannestad, G. G. Raffelt, G. Sigl , and Y. Y. Y. Wong, Phys. Rev. D **74**, 105010 (2006) [Erratum-ibid. Phys. Rev. D **76**, 029901 (2007)].
[97] G. G. Raffelt, and A. Y. Smirnov, Phys. Rev. D **76**, 081301 (2007) [Erratum-ibid. Phys. Rev. D **77**, 029903 (2008)].
[98] S. Galais, and C. Volpe, Phys. Rev. D **84**, 085005 (2011).
[99] A. Esteban-Pretel et al., Phys. Rev. D **78**, 085012 (2008).
[100] S. Chakraborty et al., Phys. Rev. Lett. **107**, 151101 (2011).
[101] H. -T. Janka, Ann. Rev. Nucl. Part. Sci. **62**, 407 (2012).
[102] J. F. Cherry et al., Phys. Rev. Lett. **108**, 261104 (2012).
[103] A. B. Balantekin, and Y. Pehlivan, J. Phys. G **34**, 47 (2007).
[104] C. Volpe, D. Väänänen, and C. Espinoza, arXiv:1302.2374.
[105] R. Surman, G. C. McLaughlin, and W. R. Hix, Astrophys. J. **643**, 1057 (2006).
[106] L. -T. Kizivat et al., Phys. Rev. C **81**, 25802 (2010).
[107] A. Malkus et al., Phys. Rev. D **86**, 085015 (2012).
[108] A. D. Dolgov, Phys. Rept. **370**, 333 (2002).
[109] F. Iocco et al., Phys. Rept. **472**, 1 (2009).
[110] J. Hamann et al., Phys. Rev. Lett. **105**, 181301 (2010).
[111] P. A. R. Ade et al. , arXiv:1303.5062.
[112] S. Weinberg Phys. Rev. **128**, 1457 (1962).
[113] A. G. Cocco, G. Mangano, and M. Messina, JCAP **0706**, 015 (2007).
[114] R. Lazauskas, P. Vogel, and C. Volpe, J. Phys. G **35**, 025001 (2008).
[115] S. Davidson et al., Phys. Rept. **466**, 105 (2008).
[116] H. Minakata, and S. Watanabe, Phys. Lett. B **468**, 256 (1999).
[117] E. K. Akhmedov, C. Lunardini, and A. Y. Smirnov, Nucl. Phys. B **643**, 339 (2002).
[118] A. B. Balantekin, J. Gava, and C. Volpe, Phys. Lett. B **662**, 396 (2008).
[119] J. P. Kneller, and G. C. McLaughlin, Phys. Rev. D **80**, 053002 (2009).
[120] J. Gava, and C. Volpe, Phys. Rev. D **78**, 083007 (2008).
[121] A. de Gouvea, and S. Shalgar, JCAP **1304**, 018 (2013)].
[122] J. Gava, and C. Volpe, Nucl. Phys. B **837**, 50 (2010).
[123] A. S. Dighe, M. T. Keil, and G. G. Raffelt, JCAP **0306**, 005 (2003).
[124] E. Borriello et al. Phys. Rev. D **86**, 083004 (2012).
[125] JM. Kachelriess et al., Phys. Rev. D **71**, 063003 (2005).
[126] P. D. Serpico et al., Phys. Rev. D **85**, 085031 (2012)
[127] V. Barger, P. Huber, and D. Marfatia, Phys. Lett. B **617**, 167 (2005).
[128] J. Gava, J. Kneller, C. Volpe, and G. C. McLaughlin Phys. Rev. Lett. **103**, 071101 (2009).
[129] http://www.phy.duke.edu/ schol/snowglobes/
[130] K. Scholberg, Ann. Rev. Nucl. Part. Sci. **62**, 81 (2012).
[131] C. Volpe, J. Phys. G **30**, L1 (2004).
[132] F. T. Avignone, and Y. .V. Efremenko, J. Phys. G **29**, 2615 (2003).
[133] C. Volpe, J. Phys. G **31**, 903 (2005).
[134] A. Mezzacappa, Ann. Rev. Nucl. Part. Sci. **55**, 467 (2005).
[135] K. Kotake, K. Sato and K. Takahashi, Rept. Prog. Phys. **69**, 971 (2006).
[136] T. Lund et al., Phys. Rev. D **86**, 105031 (2012).
[137] G. C. McLaughlin, J. M. Fetter, A. B. Balantekin, and G. M. Fuller, Phys. Rev. C **59**, 2873 (1999).
[138] B. Dasgupta, E. P. O'Connor and C. D. Ott, Phys. Rev. D **85**, 065008 (2012) [arXiv:1106.1167 [astro-ph.SR]].
[139] M. Ageron et al., Nucl. Instrum. Meth. A **656**, 11 (2011).
[140] A. Kappes, Phys. Conf. Ser. **09**, 012014 (2013).
[141] see the talk by N. WHITEHORN (Icecube collaboration) at "The IceCube Particle Astrophysics Symposium", May 13th-15th, Wisconsin-Madison.
[142] S. Adrian-Martinez et al., Phys. Lett. B **714**, 224 (2012).
[143] A. Gross, arXiv:1301.4339 [hep-ex].
[144] E. Fernandez-Martinez, G. Giordano, O. Mena, and I. Mocioiu, Phys. Rev. D **82**, 093011 (2010).
[145] O. Mena, I. Mocioiu, and S. Razzaque, Phys. Rev. D **78**, 093003 (2008).
[146] E. K. Akhmedov, S. Razzaque, and A. Y. Smirnov, JHEP **02**, 082 (2013) [JHEP **1302**, 082 (2013)]
[147] P. D. Serpico, and M. Kachelriess, Phys. Rev. Lett. **94**, 211102 (2005).
[148] W. Winter, Phys. Rev. D **74**, 033015 (2006).
[149] D. Meloni, and T. Ohlsson , Phys. Rev. D **86**, 067701 (2012).
[150] A. Esmaili et al., JCAP **1211**, 041 (2012).
[151] S. Razzaque, and A. Y. Smirnov, Phys. Rev. D **85**, 093010 (2012).
[152] R. Abbasi et al., Phys. Rev. D **82**, 112003 (2010).
[153] M. J. Longo, Phys. Rev. D **36**, 3276 (1987).
[154] T. Katori, arXiv:1211.7129.
[155] J. S. Diaz, arXiv:1109.4620.

Prospects for precision measurements in nuclear β decay in the LHC era

Oscar Naviliat-Cuncic[1]* *and Martín González-Alonso*[2]**

Precision measurements in nuclear β decay offer a sensitive window to search for new physics beyond the standard electroweak model. Searches for new physics are also a strong motivation for experiments carried out at the high energy frontier. It is instructive to confront results from the low energy and the high energy frontiers in order to look for possible complementarities. This paper reviews the constraints on new physics obtained from nuclear and neutron decays and compares them to those from other semi-leptonic processes and from the LHC. The sensitivity requirements of new precision experiments in β decay, to impact the search for new physics at the light of current and projected LHC results, are updated. Experimental developments in nuclear and neutron β decay are discussed with emphasis on their projected goals to improve the limits on exotic weak couplings.

1 Introduction

Searches for physics beyond the Standard electroweak Model (SM) are carried out both at the high energy frontier, attained at the most powerful particle colliders, as well as at the high precision frontier, looking for deviations from SM predictions in low background environments, where high sensitivities to small effects can often be achieved.

Nuclear β decay and neutron decay have played a crucial role in the development of the "$V-A$" theory of the weak interaction, which was eventually embedded in the wider framework of the SM [1, 2]. Today, one of the main motivations for improving the experimental sensitivities of precision experiments in nuclear and neutron decays is the search for possible non-SM or "exotic" interactions that would manifest themselves through genuine scalar or tensor terms in semi-leptonic weak processes.

The tests of the SM and the searches for New Physics (NP) in nuclear and neutron decays have been the subject of several recent reviews, with focus either on experiments in nuclear β decay [2–5] or on experiments using cold or ultra-cold neutrons [6–8].

A recurrent question addressed to precision measurements carried out at low energies concerns their sensitivity to NP as compared with results obtained at high energy, and currently at the Large Hadron Collider (LHC).

In this paper we review first the status of constraints on scalar and tensor couplings obtained from precision measurements in nuclear and neutron decays. We stress the observation that, for the most precise measurements, the only relevant parameter providing stringent constraints on exotic interactions is the Fierz interference term, through its contribution to other correlation coefficients.

We confront next the most precise results obtained in β decay with constraints obtained from other semi-leptonic processes and also with results from the LHC [9–11], paying special attention to those observables that are linear on the exotic couplings. The use of an Effective Field Theory (EFT) framework allows us to bridge through the low energy and the high energy searches and to compare their sensitivities to new physics.

Considerable experimental effort using neutrons and nuclei are underway worldwide with the aim to improve

* E-mail: naviliat@nscl.msu.edu
** E-mail: gonzalezalon@wisc.edu
[1] National Superconducting Cyclotron Laboratory and Department of Physics and Astronomy, Michigan State University, 640 South Shaw Lane, East Lansing, MI 48824, USA
[2] Department of Physics, University of Wisconsin-Madison, 1150 University Avenue, WI 53706, USA

the precision on decay observables. We describe recent experimental results and current developments in nuclear and neutron decays, and discuss their precision goals and sensitivities to exotic weak couplings.

2 Theoretical description

In the SM, semi-leptonic processes at the quark-lepton level are described by the exchange of the charged vector bosons, $W^{\pm}$. Since the mass of the bosons are significantly larger than the energies involved in nuclear and neutron β decays, the interaction Lagrangian for these processes takes the usual $(V-A)\times(V-A)$ form

$$\mathscr{L}_{\rm SM} = -\frac{G_F V_{ud}}{\sqrt{2}}\, \bar{e}\gamma_\mu(1-\gamma_5)\nu_e\cdot\bar{u}\gamma^\mu(1-\gamma_5)d\,, \qquad (1)$$

where G_F is the Fermi coupling and V_{ud} is the element of the Cabibbo-Kobayashi-Maskawa (CKM) matrix involved in the weak coupling of the lightest quarks. This Lagrangian provides the framework for the calculations of observables to leading order, that will be compared with experimental results. However, due to the precision of current experiments, the calculation of SM predictions requires to take into account corrections to this contact form arising from the finiteness of the W mass and from electroweak radiative corrections [12, 13].

For the inclusion of NP effects in nuclear and neutron β decays, it is very useful to follow an EFT approach. This model-independent framework allows us to compare the sensitivity of these processes with other low-energy charged-current observables and also with measurements carried out at high energy colliders.

2.1 Quark-level Effective Lagrangian

Assuming that the particles not included in the SM are much heavier than the energy scales relevant for nuclear and neutron β decay, they can again be integrated out along with the W boson and the rest of heavy SM particles. The low-scale $O(1\ \text{GeV})$ effective Lagrangian for semi-leptonic transitions is then given by [9, 10][1].

$$\begin{aligned}\mathscr{L}_{\rm eff} = -\frac{G_F V_{ud}}{\sqrt{2}}\Big[\,&(1+\epsilon_L)\ \bar{e}\gamma_\mu(1-\gamma_5)\nu_e\cdot\bar{u}\gamma^\mu(1-\gamma_5)d\\
&+\tilde{\epsilon}_L\ \bar{e}\gamma_\mu(1+\gamma_5)\nu_e\cdot\bar{u}\gamma^\mu(1-\gamma_5)d\\
&+\epsilon_R\ \bar{e}\gamma_\mu(1-\gamma_5)\nu_e\cdot\bar{u}\gamma^\mu(1+\gamma_5)d\\
&+\tilde{\epsilon}_R\ \bar{e}\gamma_\mu(1+\gamma_5)\nu_e\cdot\bar{u}\gamma^\mu(1+\gamma_5)d\\
&+\epsilon_S\ \bar{e}(1-\gamma_5)\nu_e\cdot\bar{u}d\ +\ \tilde{\epsilon}_S\ \bar{e}(1+\gamma_5)\nu_e\cdot\bar{u}d\\
&-\epsilon_P\ \bar{e}(1-\gamma_5)\nu_e\cdot\bar{u}\gamma_5 d\ -\ \tilde{\epsilon}_P\ \bar{e}(1+\gamma_5)\nu_e\cdot\bar{u}\gamma_5 d\\
&+\epsilon_T\ \bar{e}\sigma_{\mu\nu}(1-\gamma_5)\nu_e\cdot\bar{u}\sigma^{\mu\nu}(1-\gamma_5)d\\
&+\tilde{\epsilon}_T\ \bar{e}\sigma_{\mu\nu}(1+\gamma_5)\nu_e\cdot\bar{u}\sigma^{\mu\nu}(1+\gamma_5)d\Big]+\text{h.c.}\,. \qquad (2)\end{aligned}$$

The ϵ_i and $\tilde{\epsilon}_i$ complex coefficients are functions of the masses and couplings of the new particles, in the same way that the Fermi constant G_F is a function of the weak coupling and the W mass. The specific expressions of these coefficients within the minimal supersymmetric standard model can be found in e.g. Ref. [14].

For the sake of generality we have included right-handed (RH) neutrinos in the low-energy particle content, but they can easily be removed setting $\tilde{\epsilon}_{L,R,S,P,T}=0$. It is worth noticing that operators involving RH neutrinos contribute quadratically to the observables, which makes their effect on the experiments much smaller.

The effective Lagrangian in Eq. (2) describes the effect of NP not only in nuclear and neutron β decay, but also in other processes like for example $\pi^{\pm}\to\pi^0 e^{\pm}\nu$. The details of the hadronization are obviously different, with different form factors needed in each process, but the underlying dynamics is the same.

After removing an overall phase, we have ten real couplings and nine phases that can be probed comparing precise low-energy experiments and accurate SM calculations. Given the smallness of these couplings it is useful to work at linear order in them to identify their main effect on the different observables. As explained above, in this approximation we can neglect the $\tilde{\epsilon}_i$ couplings, since they involve RH neutrinos. Moreover, in nuclear and neutron decays the pseudo-scalar coupling ϵ_P can also be neglected since the associated hadronic bilinear vanishes in the non-relativistic approximation. In this approximation the low-energy effective Lagrangian can be written

[1] For the sake of simplicity we do not considered operators involving ν_μ or ν_τ. The generalization is straightforward and the general formulae can be found in Ref. [10].

as

$$\begin{aligned}\mathscr{L}_{\rm eff} = -\frac{G_F V_{ud}}{\sqrt{2}}\,[1+{\rm Re}\,(\epsilon_L+\epsilon_R)]\times \\ \times\left\{\bar{e}\gamma_\mu(1-\gamma_5)\nu_e\cdot\bar{u}\gamma^\mu\left[1-(1-2\epsilon_R)\gamma_5\right]d\right. \\ +\,\epsilon_S\;\bar{e}(1-\gamma_5)\nu_e\cdot\bar{u}d \\ \left.+\;\epsilon_T\;\bar{e}\sigma_{\mu\nu}(1-\gamma_5)\nu_e\cdot\bar{u}\sigma^{\mu\nu}(1-\gamma_5)d\right\}+{\rm h.c.}\,,\end{aligned} \tag{3}$$

where an overall phase has been omitted.

Furthermore, in neutron decay it is usual to extract the axial-vector form factor g_A (or the so-called mixing ratio in the case of nuclear decays) from experiments. The extracted quantity contains an unobservable NP contribution [9, 15]

$$g_A \to g_A\,{\rm Re}\left[\frac{1+\epsilon_L-\epsilon_R}{1+\epsilon_L+\epsilon_R}\right]\approx g_A\,[1-2{\rm Re}(\epsilon_R)]+\mathscr{O}\left(\epsilon_i^2\right)\,, \tag{4}$$

that can only be probed if a precise lattice calculation of g_A becomes available.

All in all, we see that there are six couplings left in this approximation:

- The real part of $\epsilon_L+\epsilon_R$ that produces a shift in the overall normalization and can be absorbed in a redefinition of V_{ud}, with the only consequence being the violation of the unitarity condition of the first raw of the CKM quark mixing matrix, $|V_{ud}|^2+|V_{us}|^2+|V_{ub}|^2\neq 1$.
- The real parts of the scalar ϵ_S and tensor ϵ_T couplings that modify the energy distributions and CP-even correlation coefficients.
- The imaginary parts of the axial-vector ϵ_R, scalar ϵ_S and tensor ϵ_T couplings that modify CP-odd correlation coefficients.

These six couplings represent the only linear NP effects in nuclear and neutron β decay. Consequently we expect strong bounds on them, whereas weak bounds are expected to be obtained for the rest of the couplings.

2.2 Nucleon-level effective couplings

The next step in the theoretical description is matching the quark-level effective Lagrangian, Eq. (2), onto a nucleon-level effective Lagrangian. Working at leading order in momentum transfer, the neutron-to-proton matrix elements can be written as

$$\langle p|\bar{u}\Gamma d|n\rangle = g_\Gamma\,\bar{\psi}_p\Gamma\psi_n\,, \tag{5}$$

with $\Gamma=1,\gamma_5,\gamma_\mu,\gamma_\mu\gamma_5,\sigma_{\mu\nu}$. Proceedings in this way, the Lee-Yang effective Lagrangian is obtained [16, 17][2]

$$\begin{aligned}-\mathscr{L}_{n\to pe^-\bar{\nu}_e} = \;& \bar{p}\;n\;\left(C_S\bar{e}\nu_e - C_S'\bar{e}\gamma_5\nu_e\right) \\ & +\,\bar{p}\gamma^\mu n\left(C_V\bar{e}\gamma_\mu\nu_e - C_V'\bar{e}\gamma_\mu\gamma_5\nu_e\right) \\ & +\,\bar{p}\sigma^{\mu\nu}n\left(C_T\bar{e}\sigma_{\mu\nu_e}\nu_e - C_T'\bar{e}\sigma_{\mu\nu}\gamma_5\nu_e\right) \\ & -\,\bar{p}\gamma^\mu\gamma_5 n\left(C_A\bar{e}\gamma_\mu\gamma_5\nu_e - C_A'\bar{e}\gamma_\mu\nu_e\right) \\ & +\,\bar{p}\gamma_5 n\;\left(C_P\bar{e}\gamma_5\nu_e - C_P'\bar{e}\nu_e\right)+{\rm h.c.}\,.\end{aligned} \tag{6}$$

The effective couplings C_i, C_i' ($i\in\{V,A,S,T\}$) can be expressed in terms of the parton-level parameters as

$$C_i = \frac{G_F}{\sqrt{2}}\,V_{ud}\,\overline{C}_i \tag{7a}$$

$$\overline{C}_V = g_V\,(1+\epsilon_L+\epsilon_R+\tilde{\epsilon}_L+\tilde{\epsilon}_R) \tag{7b}$$

$$\overline{C}_V' = g_V\,(1+\epsilon_L+\epsilon_R-\tilde{\epsilon}_L-\tilde{\epsilon}_R) \tag{7c}$$

$$\overline{C}_A = -g_A\,(1+\epsilon_L-\epsilon_R-\tilde{\epsilon}_L+\tilde{\epsilon}_R) \tag{7d}$$

$$\overline{C}_A' = -g_A\,(1+\epsilon_L-\epsilon_R+\tilde{\epsilon}_L-\tilde{\epsilon}_R) \tag{7e}$$

$$\overline{C}_S = g_S\,(\epsilon_S+\tilde{\epsilon}_S) \tag{7f}$$

$$\overline{C}_S' = g_S\,(\epsilon_S-\tilde{\epsilon}_S) \tag{7g}$$

$$\overline{C}_P = g_P\,(\epsilon_P-\tilde{\epsilon}_P) \tag{7h}$$

$$\overline{C}_P' = g_P\,(\epsilon_P+\tilde{\epsilon}_P) \tag{7i}$$

$$\overline{C}_T = 4\,g_T\,(\epsilon_T+\tilde{\epsilon}_T) \tag{7j}$$

$$\overline{C}_T' = 4\,g_T\,(\epsilon_T-\tilde{\epsilon}_T)\,. \tag{7k}$$

The use of this Lagrangian to study NP effects is fully justified due to the small magnitude of such effects. On the other hand, in order to have a precise determination of the SM contributions one has, again, to take into account higher order terms in the momentum transfer expansion, like weak-magnetism, as well as other sub-leading corrections like electromagnetic effects [12, 13, 18, 19].

Using these relations and the results of Ref. [20] one can work out the dependence of neutron and nuclear β decay observables on the short-distance parameters ϵ_i and $\tilde{\epsilon}_i$.

For the hadron-level coefficients, the results of Sec. 2.1 indicate that the only quantities that can affect linearly the observables are (i) the real part of (C_V+C_V') that shifts the value of V_{ud}, (ii) the real and imaginary parts of the

[2] Notice that the original paper of Lee and Yang [16] uses a different definition of γ_5 that we do not follow here. The definitions of all the couplings, $C_i^{(\prime)}$ used here and in Refs. [16, 17] are however the same.

combinations $(C_S+C'_S)/C_V$ and $(C_T+C'_T)/C_A$ and (iii) the relative phase between C_V and C_A.

The precise knowledge of both vector and axial-vector charges $g_{V,A}$ is needed to accurately calculate the SM contribution. The vector charge is $g_V = 1$ up to second-order isospin symmetry breaking corrections that can be safely neglected. The axial-vector charge g_A cannot be accurately calculated from first principles, and the usual strategy is to keep it as an independent parameter that can be extracted from experiments with high precision.

The presence of exotic scalar and tensor interactions introduces two additional form factors $g_{S,T}$ that we need to know in order to convert the measured quantities into the quark-level parameters $\epsilon_{S,T}$. In the rest of this article we will use the recent lattice QCD determinations $g_S = 0.8 \pm 0.4$ and $g_T = 1.05 \pm 0.35$ in the $\overline{MS}$ scheme and at the renormalization scale $\mu = 2$ GeV [9]. Notice that, given the smallness of the scalar and tensor couplings $\epsilon_{S,T}$, it is not necessary to have such a precise determination of $g_{S,T}$ as for the $g_{V,A}$ couplings.

The bounds derived for $\epsilon_{S,T}$ depend both on our ability to accurately calculate the $g_{S,T}$ form factors and to perform precise experiments that can put strong constraints on the hadronic couplings C_i. The level of precision needed in the lattice determination so that the final bounds on $\epsilon_{S,T}$ would be dominated by experimental errors has been studied in Ref. [9], assuming a determination of the Fierz term b (see below) at the 10^{-3} level in future neutron decay experiments. That study concluded that an improvement by a factor of two in the current lattice error will be necessary[3], what has motivated a renewed effort in the lattice QCD community to improve the present results [9, 21].

2.3 Nuclear matrix elements

An additional step is necessary for nuclear decays to connect the hadron-level effective Lagrangian, Eq.(6), with the nuclei involved in the transition.

Working at leading order in the non-relativistic approximation, this step can be done in a simple way and only two new quantities are needed: (i) the Fermi nuclear matrix element, M_F, that encodes the nuclear effects in the vector- and scalar-mediated transitions, and (ii) the Gamow-Teller nuclear matrix element, M_{GT}, that plays the same role in transitions mediated by tensor and axial-vector interactions. In this same limit the pseudo-scalar nuclear matrix element vanishes. Moreover M_F (and other terms in the momentum transfer expansion, like weak-magnetism) can be calculated exactly in the isospin symmetry limit.

Once again the use of this approximation is justified to study the effect of NP at the current level of precision, whereas sub-leading corrections have to be taken into account in the calculation of the SM contribution. This includes higher order terms in the momentum transfer expansion like weak-magnetism [22], electromagnetic effects or nuclear structure dependences [13, 23, 24]. Forbidden effects in allowed transitions, associated with an orbital angular momentum of the lepton pair $\ell \neq 0$, are in principle negligible at the current level of precision due to the $(qR)^\ell$ suppression, where R is the nucleus radius. However if the allowed matrix elements M_F or M_{GT} happen to be suppressed, the forbidden effects could become significant what could be the case for nuclear decays with large ft-values.

2.4 Weak-scale operator basis

The effective Lagrangian given in Eq.(2) allows us to compare the NP sensitivity of different low-energy experiments, even when the hadrons involved are different, like pion decay and neutron decay. Under some reasonable assumptions such a comparison can be done also with experiments performed at much higher energies and with some processes involving neutral currents, due to the $SU(2)$ gauge invariance.

Indeed, if we assume that the new fields introduced by the theory that supersedes the SM are not only heavier than the scales relevant for β decay experiments but also heavier than the energy scale of current collider experiments, we can then describe the physics at that scale also through an effective Lagrangian. This high-energy effective Lagrangian includes all SM fields as active degrees of freedom and has the following structure [10, 25]

$$\mathscr{L}_{eff} = \mathscr{L}_{SM} + \frac{1}{\Lambda^2}\sum_i \alpha_i \mathscr{O}_i^{(6)} + \dots , \tag{8}$$

where $\mathscr{O}_i^{(6)}$ are $SU(2)_L \times U(1)_Y$-invariant dimension-six effective operators generated by the exchange of the new fields that we integrated out, α_i are the associated Wilson coefficients and Λ is the characteristic NP scale.

[3] Given the R-fit method used in Ref. [9], the lower bounds of $g_{S,T}$ are actually a better indicator of the final $\epsilon_{S,T}$ bounds than the errors $\delta g_{S,T}$. It is thus technically more accurate to say that a future determination of $\epsilon_{S,T}$ from a measurement of b_n at the level of 10^{-3} will be dominated by the experimental error as long as $g_S^{min} > 0.64$ and $g_T^{min} > 0.84$.

It is possible to identify twelve effective operators that generate a tree-level contribution to nuclear and neutron β decay, either through a modification of the W boson vertex to fermions or introducing a new four-fermion interaction. It is then possible to relate the Wilson coefficients of both theories, i.e. $\epsilon_i = f(\alpha_j)$ and likewise for $\tilde{\epsilon}_i$. These matching conditions, which can be found in Ref. [10], allow us to understand the implications of collider searches for low-energy experiments and vice versa.

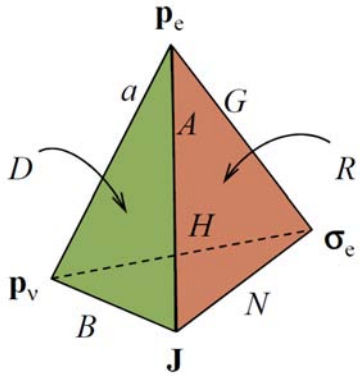

Figure 1 (online color at: www.ann-phys.org) Pictorial representation of the two-fold (edges) and three-fold (sides) correlation coefficients between the kinematic vectors (vertices). Adapted from Ref. [8].

3 Correlations in allowed β decay

The relations between the experimentally accessible angular and energy distributions and the hadronic couplings C_i and C_i' were established in the seminal paper of Jackson, Treiman and Wyld (JTW) for allowed nuclear transitions [17, 20]. Their formalism is also valid for neutron decay when making the appropriate substitutions for the Fermi and Gamow-Teller matrix elements.

The decay rate distributions are expressed in terms of the total energies E_i and the momenta $\mathbf{p}_i$ of the decay products, with $i = e, \nu$ for the β particle and the neutrino respectively, and also the spins $\mathbf{J}$ and $\boldsymbol{\sigma}_e$ of the decaying system and of the β particle. Those distributions include correlation terms which are scalar, pseudo-scalar or mixed products of the kinematic vectors. For example, the angular and energy distribution of the electron and neutrino in the decay of unpolarized nuclei or neutrons has the form [20]

$$\omega(E_e) = \omega_0(E_e)\xi\left(1 + b\frac{m}{E_e} + a\frac{\mathbf{p_e}\cdot\mathbf{p}_\nu}{E_e E_\nu}\right), \tag{9}$$

where the function $\omega_0(E_e)$ includes the phase space factor and the Fermi function, m is the electron mass and the coefficients ξ, b, and a contain the dynamics of the decay. This includes the nuclear matrix elements, M_F and M_{GT}, and the effective couplings C_i and C_i' [17, 20]. Any specific experimental configuration fixes the magnitude of the various correlation terms and then the sensitivity to the coefficients, a, b, etc.

For a quick reference to the most common correlations coefficients, Fig. 1 shows a pictorial representation, in the form of a tetrahedron. The vertices correspond to the kinematic vectors, the edges to the two-fold correlations and the faces to the three-fold correlations.

At leading order in the approximations discussed above, the SM corresponds to $C_V'/C_V = C_A'/C_A = 1$, all other parameters being zero. Deviations of experimental results from the values of the coefficients predicted in the SM would provide an indication for new physics or a departure from the allowed approximation for nuclear decays.

It can easily be seen from the expressions of the coefficients [20] that all of them receive linear NP contributions which are not suppressed to order α except the coefficients a, A and G. Among those, the coefficients that have been accessed experimentally, either directly or in conjunction with other coefficients are: the Fierz interference term b, the neutrino asymmetry parameter B, the polarization-spin correlation N, the β longitudinal polarization from polarized nuclei Q and the triple correlations R and D. These latter are sensitive to a possible relative phase between the couplings arising from time-reversal violation.

Measurements of N and Q require the analysis of the spin of β particles emitted from polarized neutrons or nuclei, what makes such experiments very demanding and challenging.

In most experimental conditions, the measured coefficients receive a linear contribution via the Fierz term of the form

$$\tilde{X} = \frac{X}{1 + b\langle m/E_e\rangle}, \tag{10}$$

where $X = a, A, B$, etc. stands for any of the correlation coefficients and $\langle\rangle$ denotes the weighted average over the observed part of the β energy spectrum. Such a contribution arises for instance in measurements of the $\beta\nu$ angular correlation, a, which is quadratic on the exotic couplings. For $C_i^{(\prime)} \ll 1$, the sensitivity of $\tilde{a}$ to those couplings becomes then dominated by the contribution due to the Fierz term. Under such conditions, the factor $\langle m/E_e\rangle$ becomes an important quantity since it can suppress or en-

hance significantly the NP sensitivity. This factor depends on the transition and the details of the experiment, and is typically in the range $0.2-0.7$ [2].

The contribution of the Fierz term can however adversely affect the sensitivity of other coefficients. For example, for pure Gamow-Teller transitions, which are sensitive to tensor contributions, the b and B coefficients have the form [20]

$$b_{GT} = \pm\gamma \,\mathrm{Re}\left(\frac{C_T + C_T'}{C_A}\right), \tag{11}$$

$$B_{GT} = \lambda_{J'J}\left[\pm 1 + \frac{\gamma m}{E_e}\,\mathrm{Re}\left(\frac{C_T + C_T'}{C_A}\right)\right], \tag{12}$$

where $\lambda_{J'J}$ is a spin factor [17], $\gamma = \sqrt{1-(\alpha Z)^2}$ with Z the atomic number of the daughter nucleus and the upper (lower) sign refers to electron (positron) decay. Following Eq. (10) we have then

$$\tilde{B}_{GT} \approx B_{GT}\left(1 - \frac{m}{E_e} b_{GT}\right) \approx \pm\lambda_{J'J}\,. \tag{13}$$

This shows that the measured coefficient looses then the linear sensitivity to tensor couplings for such transitions. A similar, albeit partial, suppression of sensitivity has been observed for $\tilde{B}$ in neutron decay [9]. These suppressions are due to the fact that B and b have similar (linear) dependence on the exotic couplings.

The sensitivity of B to the couplings actually depends on the initial spin of the transition, on the spin sequence and on the mixing ratio $\rho = C_A M_{GT}/(C_V M_F)$ between the Gamow-Teller and Fermi contributions. Thus the cancellation due to the contribution of b to $\tilde{B}$ observed in pure Gamow-Teller processes does not necessarily happen in all mixed transitions.[4]

In summary, the discussion above shows that the sensitivity of correlation coefficients which are linear in the exotic couplings can strongly be affected by the contribution of the Fierz term. For coefficients that depend quadratically on the couplings, the dominant sensitivity to these couplings will arise from the contribution of the Fierz. For transitions with large end-point energies, the contribution of the Fierz term can however be strongly weaken. We illustrate this quantitatively in the next sections.

[4] It is certainly conceivable to perform simultaneous measurements of ratios of coefficients, like B/a, so that the linear sensitivity to the NP contribution in B is not lost. However, such a measurement has not yet been performed.

4 Constraints from nuclear and neutron β decay

We review here the most stringent constraints on NP from the measurement of energy and angular distributions in nuclear and neutron decays.

The use of the hadronic-level couplings $C_i^{(\prime)}$ of JTW is convenient at this stage because the comparison of sensitivity between different observables and measurements does not require the knowledge of the form factors $g_{V,A,S,T}$. However in the next section we will convert the most precise results to the quark-level notation ϵ_i and $\tilde{\epsilon}_i$ in order to be able to compare the NP sensitivity of these decays with other low- and high-energy observables.

Following the results of Sec. 2.2 we present here the constraints on quantities that can affect linearly the observables, namely: (i) the real part of the vector couplings $(C_V + C_V')$; (ii) the real parts of the scalar and tensor couplings $(C_S + C_S')/C_V$ and $(C_T + C_T')/C_A$; and (iii) the imaginary parts of the scalar and tensor couplings as well as the relative phase between C_V and C_A.

4.1 Limits on real vector couplings

The effect of the NP contribution to the real part of $(C_V + C_V')$ shifts the value of V_{ud} and can be probed through the unitarity test of the CKM matrix.

The most precise determination of V_{ud} comes from the study of super-allowed Fermi transitions [3, 24]. Together with the recent determinations of V_{us} and V_{ub} [26], it offers a very precise test of the CKM unitarity condition

$$|V_{ud}|^2 + |V_{us}|^2 + |V_{ub}|^2 = 1.0001(10) \quad (90\%\ \mathrm{CL})\,, \tag{14}$$

which results in

$$\mathrm{Re}\left(\frac{\overline{C}_V + \overline{C}_V'}{2}\right) = 1.000(1) \quad (90\%\ \mathrm{CL})\,, \tag{15}$$

in perfect agreement with the SM prediction.

4.2 Limits on real scalar and tensor couplings

The most stringent limits on scalar couplings obtained from nuclear and neutron β decays arise from the contribution of the Fierz interference term to the $\mathscr{F}t$-values of super-allowed pure Fermi transitions [24]. The value of the Fierz term extracted from this set reads

$$b_F = -\mathrm{Re}\left(\frac{C_S + C_S'}{C_V}\right) = -0.0022(43) \quad (90\%\ \mathrm{CL})\,, \tag{16}$$

and the constraints are shown by the light blue lines in Fig. 2. The error on this value is determined by the individual errors of the $\mathcal{F}t$-values which are fitted to search for a possible deviation from a constant. The Q_{EC} values in these transitions increase with the mass of the parent nucleus so that transitions in lighter nuclei have a stronger weight in the extraction of b_F due to the $\langle m/E_e \rangle$ factor. The contributions to the error on b_F given in Eq.(16) are then due to the experimental data and to theoretical corrections which have here an important effect. The opportunities for improving the errors of the $\mathcal{F}t$-values have recently been discussed in Ref. [3] in connection with the determination of V_{ud} from pure Fermi transitions for the unitarity test of the CKM matrix.

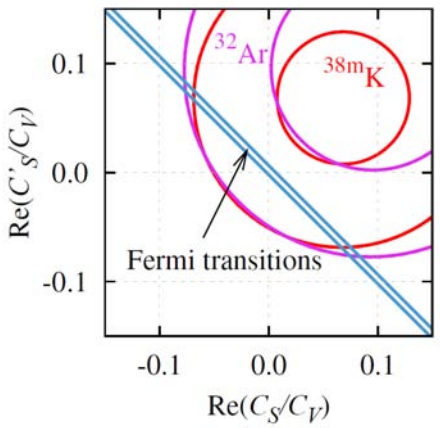

Figure 2 (online color at: www.ann-phys.org) Constraints on real scalar couplings obtained from most precise observables in nuclear β decay. The straight lines are deduced from the Fierz interference term in super-allowed pure Fermi transitions [24]. The circular bounds are deduced from measurements of the $\beta\nu$ angular correlation in ^{38m}K decay [27] (red lines) and in ^{32}Ar [28] decay (purple lines). The limits are calculated at the 90% CL.

The other measured observable providing complementary constraints to those resulting from the $\mathcal{F}t$-values is the $\beta\nu$ angular correlation a. The most precise result obtained so far was in the pure Fermi decay of ^{38m}K. The experiment used the TRIUMF Neutral Atom Trap setup [27] which is a Magneto Optical Trap (MOT) system composed of two traps. The $\beta\nu$ correlation was determined from the shape of the time-of-flight spectra of recoil ions measured in coincidence relative to the β particle. Since ^{38m}K is a positron emitter, the detection of positively charged recoil ions relies on the double or multiple shake-off of electrons following β decay. The statistical precision of the result is 3×10^{-3} and the systematic error is comparable, arising from several instrumental sources [27]. A similar precision has been achieved with an indirect method, by measuring the energy spectrum shape of the delayed proton in the decay of ^{32}Ar [28]. The bounds obtained from these two experiments are shown by the circles in Fig. 2 and are extracted from

$$\tilde{a} = \frac{a}{1 + b\langle m/E_e \rangle} \,. \tag{17}$$

It is interesting to stress that, for each decay, the abscissa, x_C, and ordinate, y_C, of the center of the circles in Fig. 2 are essentially given by $x_C \approx y_C \approx \langle m/E_e \rangle/2$, and that the mean radius of the circular band, R_M, is given by $R_M \approx \langle m/E_e \rangle/\sqrt{2}$. This indicates the importance of the value of the sensitivity factor $\langle m/E_e \rangle$ of the Fierz term, in defining the exclusion plot and hence the interval of allowed values for the exotic couplings.

The value for a possible real scalar coupling obtained from the most recent global analysis [2] including data from experiments in nuclear and neutron decays translates into

$$\mathrm{Re}\left(\frac{C_S + C'_S}{C_V}\right) = 0.0026(42) \qquad (90\%\ \mathrm{CL}), \tag{18}$$

for a three parameters fit with left-handed couplings ($C_S = C'_S$). The fit also includes data from $\mathcal{F}t$-values and the measurement of $\tilde{a}$ in ^{38m}K and ^{32}Ar decays discussed above. Although the compilation of $\mathcal{F}t$-values used in Ref. [2] was not the same than for the value quoted in Eq.(16), the result in Eq. (18) is clearly dominated by the $\mathcal{F}t$-values.

The most stringent limits on tensor couplings arising from single observables is obtained from the ratio between polarizations of β particles emitted from pure Fermi and pure Gamow-Teller transitions P_F/P_{GT}. The longitudinal polarizations are governed by the correlation coefficients G of each decay, and the ratio provides constraints on both scalar and tensor contributions. These experiments were motivated by the search for deviations from maximal parity violation due to the presence of e.g. right-handed currents which would couple through V and A interactions. The polarization ratio P_F/P_{GT} has been measured with high precision by two groups [29–31]. The first experiment compared the longitudinal polarization of positrons from ^{26m}Al and ^{30}P decays using Bhabha scattering in a magnetized foil [29]. The second group detected positrons from ^{10}C and ^{14}O [30, 31] and used the polarimetry technique based on time-resolved spectroscopy of hyperfine positronium decay. Here again, it is the contribution of the Fierz term to G that provides the constraints on exotic couplings deduced from these

experiments. At the 90% CL, the value deduced for the difference between the scalar and tensor terms reads [31]

$$\mathrm{Re}\left(\frac{C_S+C'_S}{C_V}\right)-\mathrm{Re}\left(\frac{C_T+C'_T}{C_A}\right)=0.003(18)\ . \qquad (19)$$

Since the scalar couplings are more severely constrained by the $\mathscr{F}t$-values from pure Fermi transitions, Eq.(16), these experiments provide constraints on the tensor contribution. The limits are shown by the orange straight lines in Fig. 3. It is remarkable that the most stringent limits on tensor couplings from nuclear β decay arise from two experiments that were performed in the 1980's, even though that was not the main motivation of those experiments.

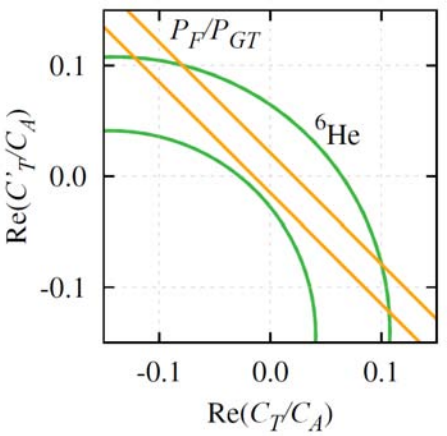

Figure 3 (online color at: www.ann-phys.org) Constraints on real tensor couplings obtained from most precise single observables in nuclear β decay. The straight lines are deduced from the Fierz interference term contributing to the longitudinal polarization of β particles in Fermi and Gamow-Teller transitions [31]. The circular bounds are deduced from the measurement of the $\beta\nu$ angular correlation in ^{6}He decay [32]. All limits are calculated at the 90% CL.

The $\beta\nu$ angular correlation provides also here complementary constraints to those obtained from P_F/P_{GT}. The most precise measurement carried out so far was in the pure Gamow-Teller decay of ^{6}He, fifty years ago [32]. This experiment measured the energy spectrum of the recoil ions in singles with an electromagnetic spectrometer. The relative precision achieved in this measurement was 10^{-2}. The result has been revisited by Glück to include order-α radiative corrections and the effect of induced weak currents to the recoil spectrum [33]. The 90% CL limits obtained from this measurement are shown by the green circles on Fig. 3. It is seen that the (absolute) values of the coordinates (x_C, y_C) of the center of the circles and the mean radius, R_M, of the circular band are here larger than in ^{38m}K decay (Fig. 2), because the sensitivity factor $\langle m/E_e\rangle$ is a factor 1.8 larger. Although the relative error on the measurement of $\tilde{a}$ in ^{6}He decay is a factor of about 2 larger than in ^{38m}K, the width of the circular band is smaller due its larger sensitivity. As expected, the interval for the allowed values of $\mathrm{Re}(C_T+C'_T)/C_A$ from the ^{6}He experiment is dominated by the contribution of the Fierz term to $\tilde{a}$. Moreover, it appears that the sensitivity factors for the measurement of $\tilde{a}$ in ^{6}He and of P_F/P_{GT} in ^{10}C and ^{14}O are the same within 2% [2]. Therefore the ratio between the bounds on $\mathrm{Re}(C_T+C'_T)/C_A$ is provided directly by the ratio between the relative uncertainties of the experimental results.

The value for a possible real tensor coupling as deduced from the global analysis of Ref. [2], for a three parameters fit with left-handed couplings ($C_T = C'_T$), is

$$\mathrm{Re}\left(\frac{C_T+C'_T}{C_A}\right)=0.007(11)\qquad (90\%\ \mathrm{CL})\ . \qquad (20)$$

The error resulting from this fit is somewhat smaller than the one obtained in the measurements of P_F/P_{GT} alone, Eq. (19). This is attributed to the contribution of the Fierz term to the β asymmetry parameter, $\tilde{A}$, in neutron decay which has a significant impact on the global fit. For the data used in Ref. [2], the sensitivity to the Fierz term through the factor $\langle m/E_e\rangle$ is about 2 times larger for the $\tilde{A}$ coefficient in neutron decay than for P_F/P_{GT} [2].

Measurements of other correlations do not provide more stringent limits compared to those presented above. As already mentioned, the coefficients which are linear in the real parts of exotic couplings and that have been measured are B, Q and N.

The coefficient B has been measured in ^{37}K [34] and in neutron decay [35,36]. As discussed in Sec. 3, the sensitivity of $\tilde{B}$ to exotic couplings can be strongly suppressed due to the contribution of the Fierz term. These experiments were however motivated by the search for right-handed currents with vector and axial-vector couplings.

The same goal motivated measurements of the longitudinal polarization of β particles emitted from polarized nuclei, which is dominated by the Q coefficient and contains also a small contribution of N [37]. The measurements were carried out in ^{107}In [38] and ^{12}N [39,40]. Since these are relative measurements, the contribution of the Fierz term cancels and the remaining sensitivity to exotic left-handed couplings is strongly suppressed.

Finally, the N coefficient has been measured in neutron decay [41] as a control parameter of a polarimeter

dedicated to the measurement of the triple correlation R. The achieved experimental error combined with the small value of N under the conditions of that experiment do not provide significantly improved constraints on scalar or tensor couplings.

Absolute measurements of the β asymmetry parameter, A, have recently been performed in Gamow-Teller decays with the explicit purpose to probe tensor couplings via the Fierz term [42, 43]. The experiments used the low-temperature nuclear orientation technique in the decays of ^{114}In [42] and ^{60}Co [43]. These transitions have a relatively low end point energies and hence large sensitivity to the Fierz term. However, the allowed Gamow-Teller matrix element is strongly reduced in ^{60}Co decay. The SM value of the asymmetry parameter has therefore a theoretical uncertainty which is of the same order of magnitude than the experimental error [43] due to the contribution of recoil corrections. The total relative uncertainties achieved were respectively 1.4% and 2.0% at 1σ for ^{114}In and ^{60}Co and do not significantly improve the limits obtained from P_F/P_{GT}.

In neutron decay, a global analysis of data has been performed in order to assess the sensitivity to exotic couplings [44]. It appears that, since the ratio g_A/g_V has to be determined from the same data, the constraints are less stringent than those obtained from the global fit including nuclear data [2]. A similar conclusion was recently obtained in the analysis of $\tilde{a}$, $\tilde{A}$, and $\tilde{B}$, in neutron decay [45]. It is to note that in the global fit of Ref. [2], the determination of the ratio g_A/g_V results essentially from the comparison between the $\mathcal{F}t$-value from pure Fermi transitions and the neutron lifetime so that all correlation in neutron decay, and in particular A serve to constraint exotic couplings.

To summarize, we have shown that the most stringent limits obtained on the real scalar and tensor couplings result solely from the contribution of the Fierz term to the observables. This applies to the total decay rate through the $\mathcal{F}t$-values, to the $\beta\nu$ angular correlation coefficient $\tilde{a}$ in Fermi and Gamow-Teller transitions and to the β particle longitudinal polarization $\tilde{G}$ which enters the ratio P_F/P_{GT}.

4.3 Limits on imaginary couplings

The presence of imaginary phases between the couplings is related to the violation under time-reversal [20]. In nuclear and neutron decays, searches for time-reversal violation have traditionally been focused on the D and R triple correlation coefficients (Fig. 1).

Since the $\beta\nu$ angular correlation depends quadratically on the NP couplings, it is also sensitive to possible imaginary parts in them. Considering that measurements of the $\mathcal{F}t$-values in Fermi transitions and of the polarization ratio P_F/P_{GT}, provide stringent constraints on the Fierz terms associated respectively with scalar, and tensor couplings, Eqs. (16) and (19), it is possible to extract constraints on the imaginary parts from the $\beta\nu$ correlation measurements, by neglecting here the contributions of the Fierz terms.

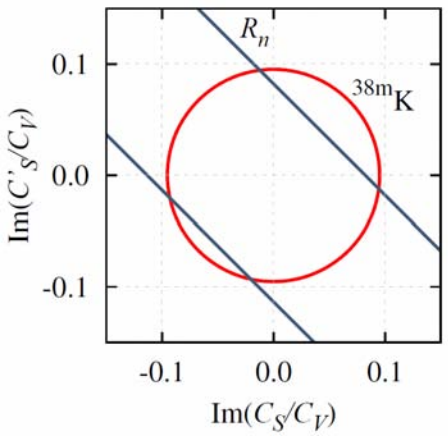

Figure 4 (online color at: www.ann-phys.org) Constraints on imaginary scalar couplings obtained from most precise single experiments in nuclear and neutron decays. The straight lines are deduced from the triple correlation measurement in neutron decay [41]. The circular bound is deduced from the measurement of the $\beta\nu$ angular correlation in ^{38m}K decay [27]. The limits are calculated at the 90% CL.

Figure 4 shows the constraints on imaginary scalar couplings extracted from the $\beta\nu$ angular correlation in ^{38m}K decay [27] and from the measurement of the triple correlation coefficient, R, in neutron decay [41]. The determination of this coefficient requires the measurement of the transverse polarization of β particles emitted perpendicular to the neutron spin. The experiment was performed using a polarized cold neutron beam and the transverse electron polarization was analyzed from the asymmetry in Mott scattering at backward angles using a thin lead foil. The total absolute error reached in this measurement is $\delta R_n = 1.3\%$, generating the following 90% CL constraint

$$\mathrm{Im}\left(\frac{C_S + C'_S}{C_V}\right) - 1.5\,\mathrm{Im}\left(\frac{C_T + C'_T}{C_A}\right) = -(1.8 \pm 5.9) \times 10^{-2}\,.$$

(21)

Using the stronger constraint on the tensor contribution obtained from the measurement of R in ^{8}Li decay (see below), we obtain the limit on the imaginary part of the scalar interaction shown in Fig. 4.

Notice that the quadratic dependence of the $\beta\nu$ angular correlation provides here a competitive constraint. The region allowed by the ^{38m}K result (disk inside the red circle) has been somewhat reduced by the constraint obtained from the new measurement of the triple correlation in neutron decay.

The constraints on the imaginary tensor couplings are shown in Fig. 5. They are extracted from the $\beta\nu$ angular correlation in ^{6}He decay [32] and from the measurement of the triple correlation coefficient R in ^{8}Li decay [46]. This measurement used polarized ^{8}Li nuclei produced by polarization transfer reactions from a vector-polarized deuteron beam on a ^{7}Li target. The target was cooled close to liquid helium temperatures in order to achieve long relaxation times. The transverse polarization of the decay electrons was also deduced here from the Mott scattering asymmetry at backward angles using a lead foil as analyzer. The absolute precision reached in this measurement was $\delta R(^8\text{Li}) = 2.2\times10^{-3}$ and the result has been corrected for the effects of final state interactions, $R_{FSI} = 0.7(1)\times10^{-3}$. The 90% CL value of the imaginary part of tensor couplings obtained from this measurement reads

$$\text{Im}\left(\frac{C_T + C_T'}{C_A}\right) = (0.27 \pm 1.08)\times10^{-2}\,. \tag{22}$$

The situation for the constraints on tensor couplings, Fig. 5, is quite different from the scalar couplings exclusion plot. The strongest constraints are those arising from the measurement of R, which has an uncertainty a factor of 6 smaller than in neutron decay.

The measurement of the D triple correlation coefficient requires the use of mixed transitions and the determination of the neutrino momentum through the observation of the recoil. In nuclear β decay, the D coefficient has been measured in ^{19}Ne decay. The combined result from all runs provided the value $D(^{19}\text{Ne}) = (1\pm6)\times10^{-4}$ [47]. The D coefficient has also been measured by two groups in neutron decay [48,49]. The most recent and precise result is $D_n = (-0.9\pm2.1)\times10^{-4}$ [49] and provides the following 90% CL bounds for a possible phase between the vector and axial couplings

$$\text{Im}(C_V C_A^*) = (-2.1\pm8.0)\times10^{-4}\,. \tag{23}$$

This completes the review of the current status of the six couplings left in the approximation introduced in Sec. 2.1, that affect linearly the observables.

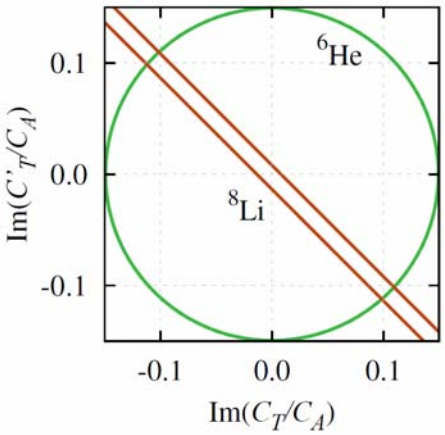

Figure 5 (online color at: www.ann-phys.org) Constraints on imaginary tensor couplings obtained from most precise single experiments in nuclear β decay. The straight lines are deduced from the triple correlation measurement in ^{8}Li decay [46]. The circular bound is deduced from the measurement of the $\beta\nu$ angular correlation in ^{6}He decay [32]. The limits are calculated at the 90% CL.

5 Comparison with other low- and high-energy experiments

5.1 CP-conserving vector/axial couplings

As explained in Sec. 2.1, the linear effects produced by CP-conserving vector and axial-vector interactions, which are represented by $\epsilon_{L,R}$ and $\tilde{\epsilon}_{L,R}$ can be re-expressed as an overall shift in the effective Lagrangian and an unobservable shift in the axial-vector form factor g_A. The only observable effect is then a NP contribution to V_{ud} that can be probed through the test of the unitarity condition of the CKM matrix.

The value obtained in Eq.(15) translates into the following strong bound

$$|\text{Re}(\epsilon_L + \epsilon_R)| < 0.5\times10^{-3} \qquad (90\%\ \text{CL})\,, \tag{24}$$

where once again we have neglected $\mathcal{O}(\epsilon_i,\tilde{\epsilon}_i)^2$ contributions. In the high-energy effective theory, this bound corresponds to an effective NP scale of 11 TeV that represents a more stringent bound than those from LEP and LHC analysis on the same effective interactions [10, 50].

Given a specific NP model this stringent bound translates in severe constraints on the masses and couplings of the new particles, as explicitly shown in various (mostly supersymmetric) extensions of the SM during the last decades [51–56].

5.2 CP-conserving scalar and tensor couplings

The rest of non-standard interactions can be probed by measuring normalized angular and energy distributions, as described in Sec. 4.

For scalar interactions, the most stringent bound comes from the determination of the Fierz term in super-allowed Fermi decays given in Eq.(16). This translates into

$$-1.0\times10^{-3} < g_S\,\mathrm{Re}(\epsilon_S) < 3.2\times10^{-3} \qquad (90\%\ \mathrm{CL})\,, \qquad (25)$$

represented in Fig. 6 with a horizontal green band.

In the case of tensor interactions, we saw in Sec. 4.2 that the best bound from nuclear β decays arises from measurements of the ratio P_F/P_{GT} of longitudinal polarization of positrons emitted in the decay of pure Fermi and pure Gamow-Teller transitions [29,31]. These experiments are sensitive to the difference between Fierz terms and generate the following 90% CL bound

$$-2.6\times10^{-3} < \frac{g_S}{3}\,\mathrm{Re}(\epsilon_S) + g_T\,\mathrm{Re}(\epsilon_T) < 3.2\times10^{-3}\,. \qquad (26)$$

This is represented in Fig. 6 by the wide red diagonal band. The contribution of other observables in nuclear and neutron decays that can possible improve this limit require a global fit as presented in Ref. [2].

More stringent bounds on tensor interactions can be obtained from the analysis of the Dalitz plot of the radiative pion decay $\pi^+ \to e^+\nu_e\gamma$ done by the PIBETA collaboration [57][5]

$$-1.1\times10^{-3} < \mathrm{Re}(\epsilon_T) < 1.4\times10^{-3} \qquad (90\%\ \mathrm{CL})\,, \qquad (27)$$

represented in Fig. 6 by the vertical yellow band.

Another promising process to probe both scalar and tensor interactions is the measurement of the Fierz term in neutron decay [9]. The purple area in Fig. 6 shows the impact of future determinations of this parameter with a sensitivity at the level of $|\delta b| \le 10^{-3}$. It will offer the most stringent bound on tensor interactions, after taking into account the strong bounds existing on b_{F}, Eq. (16).

Finally it is worth mentioning that, although not shown in Fig. 6, the ratio $\mathrm{R}_\pi = \Gamma(\pi\to e\nu)/\Gamma(\pi\to\mu\nu)$ is also a very powerful probe of scalar and tensor interactions since they generate radiatively a pseudo-scalar interaction [59]. More details can be found in Refs. [9, 10].

[5] For the associated hadronic form factor we use $f_T = 0.24(4)$, obtained in Ref. [58], using a large-N_c-inspired resonance-saturation model.

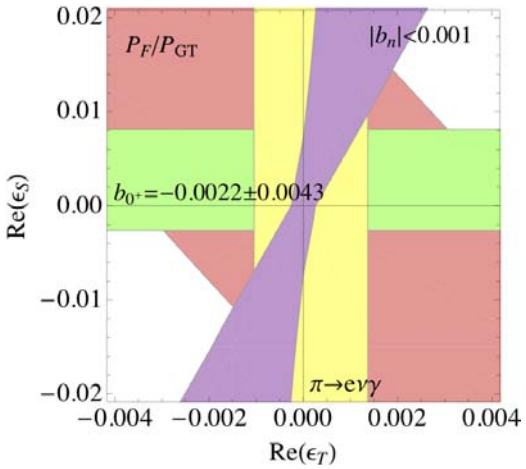

Figure 6 (online color at: www.ann-phys.org) 90% CL limits on the scalar and tensor NP couplings $\mathrm{Re}(\epsilon_{S,T})$ from super-allowed nuclear decays [24] (green), radiative pion decay [57] (yellow) and measurements of the ratio P_F/P_{GT} [29,31] (red), along with the expected bound from future measurements of the Fierz term b in neutron decay (purple).

5.3 CP-violating interactions

The three CP-violating phases with a linear effect on the nuclear β decay observables are represented in the quark-level effective Lagrangian by the imaginary parts of the coefficients $\epsilon_{R,S,T}$. They parameterize the relative phase between the purely vector interaction in the hadronic bilinear and axial-vector, scalar and tensor interactions, respectively.

The 90% CL bounds on the imaginary parts of scalar and tensor interactions obtained from measurements of the R parameter in neutron and in ^{8}Li decays were given in Eqs.(21) and (22). They can be trivially re-expressed as

$$g_S\,\mathrm{Im}(\epsilon_S) + 4.7\,g_T\,\mathrm{Im}(\epsilon_T) = -(0.9\pm3.0)\times10^{-2} \qquad (28)$$

$$g_T\,\mathrm{Im}(\epsilon_T) = -(0.4\pm1.7)\times10^{-3}\,. \qquad (29)$$

Using the recent lattice QCD determination of the form factors $g_{S,T}$ [9] we obtain the bounds shown in Fig 7.

Likewise, the bound on the relative phase between C_V and C_A given in Eq.(23) from the measurement of the D correlation coefficient in neutron decay [49] can be casted in the quark-level language as

$$\mathrm{Im}(\epsilon_R) = -(1.1\pm4.0)\times10^{-4} \qquad (90\%\ \mathrm{CL})\,. \qquad (30)$$

It is worth mentioning that additional T-odd correlations with potential NP sensitivity can be constructed in the radiative β decay of nuclei and neutron, as shown in Refs. [60,61].

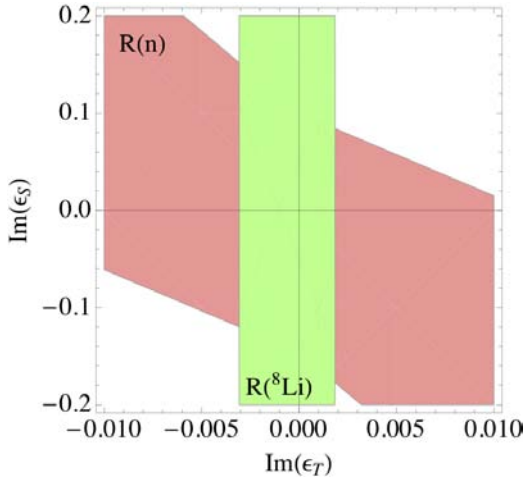

Figure 7 (online color at: www.ann-phys.org) 90% CL limits on the CP-violating scalar and tensor NP couplings $\mathrm{Im}(\epsilon_{S,T})$ from measurements of the triple correlation R in neutron decay [41] (diagonal maroon band) and ^{8}Li [46] (vertical green band). Notice that both ϵ_S and ϵ_T scales are different than in Fig. 6.

Like for the CP-conserving coefficients, the ratio $R_\pi = \Gamma(\pi \to e\nu)/\Gamma(\pi \to \mu\nu)$ offers strong constraints on $\mathrm{Im}(\epsilon_{S,T})$ since they generate radiatively a non-zero $\mathrm{Im}(\epsilon_P)$ [11].

Using the high-energy effective Lagrangian of Eq.(8), it is possible to show that the same $SU(2)_L \times U(1)_Y$ invariant effective operators that generate at low-energy the coefficients $\epsilon_{R,S,T}$ also generate contributions to different EDMs [62], which generates much stronger bounds than those given in Eqs.(28)-(30). In fact, the indirect limit on the D coefficient from the current neutron EDM bound is of the order 10^{-7} [62], whereas for the R coefficient the current Thallium EDM bound implies an indirect bound at the level of 10^{-8} [63]. These bounds from EDMs could be avoided assuming an almost complete cancellation with other effective operators contributing to the EDMs. Although such a scenario is very unnatural from a purely EFT point of view, in a specific NP model the different Wilson coefficients are related to the more fundamental coupling constants and masses and such a cancellation could occur in a less unnatural way. In this sense, direct bounds from β decays complement EDM experiments in the search of new sources of CP-violation. Moreover, this comparison with EDM relies on the use of the high-energy effective Lagrangian of Eq.(8), that in turn relies on some assumptions about the structure of the underlying NP.

We can see that the situation is very different from the CP-conserving coefficients, where direct limits from β decays are very competitive and for some interactions they actually offer the best bound.

5.4 Limits from the LHC

If the new particles are too heavy to be produced on-shell at the LHC we can connect collider searches with low-energy experiments in an elegant model-independent way using the high-energy effective Lagrangian of Eq. (8) to analyze collider data. The natural channel to study at the LHC is the search for electrons and missing transverse energy (MET), $pp \to e + \mathrm{MET} + X$, since the underlying partonic process is the same as in β decay ($\bar{u}d \to e\bar{\nu}$) and so we expect it to be sensitive to the same kind of NP.

Using the matching conditions between Wilson coefficients of the low- and high-energy effective Lagrangians [9, 10] it is possible to express collider observables in terms of the coefficients of the low-energy effective theory, ϵ_i and $\tilde{\epsilon}_i$. In particular the cross-section $\sigma(pp \to e + \mathrm{MET} + X)$ with transverse mass higher than $\overline{m}_T$ takes the following form[6]:

$$\begin{aligned}\sigma(m_T > \overline{m}_T) = \sigma_W \left[\left| 1 + \epsilon_L^{(\nu)} \right|^2 + |\tilde{\epsilon}_L|^2 + |\epsilon_R|^2 \right] \\ -2\sigma_{WL}\,\mathrm{Re}\left(\epsilon_L^{(c)} + \epsilon_L^{(c)}\epsilon_L^{(\nu)\,*}\right) + \sigma_R \left[|\tilde{\epsilon}_R|^2 + |\epsilon_L^{(c)}|^2 \right] \\ +\sigma_S \left[|\epsilon_S|^2 + |\tilde{\epsilon}_S|^2 + |\epsilon_P|^2 + |\tilde{\epsilon}_P|^2 \right] + \sigma_T \left[|\epsilon_T|^2 + |\tilde{\epsilon}_T|^2 \right],\end{aligned} \tag{31}$$

where $\sigma_W(\overline{m}_T)$ represents the SM contribution and $\sigma_{WL,R,S,T}(\overline{m}_T)$ are new functions, which explicit form can be found in Ref. [10]. The crucial feature is that they are several orders of magnitude larger than the SM contribution, which compensates for the smallness of the NP couplings and makes possible to put significant bounds on them from these searches. On the other hand, the lack of such an enhancement makes this search not very sensitive to $\epsilon_L^{(\nu)}$, $\tilde{\epsilon}_L$ and ϵ_R.

The most recent search for electrons and missing transverse energy in the final state was done by the CMS collaboration using 20 fb^{-1} of data recorded at $\sqrt{s} = 8$ TeV [65]. In this analysis they found one single event with a transverse mass above 1.5 TeV, to be compared with the SM expectation of 1.99 ± 0.27 events. This absence of an excess of high-m_T events in this channel can be translated into bounds on the different NP couplings using Eq. (31), as shown in Fig. 8 for scalar and tensor couplings.

[6] Notice that high-energy searches probe separately the vertex correction $\epsilon_L^{(\nu)}$ and contact $\epsilon_L^{(c)}$ contributions to the coupling ϵ_L, defined in Ref. [10].

Assuming that only one operator at a time is present we obtain the following 90% CL bounds

$$|\epsilon_{S,P}|, |\tilde{\epsilon}_{S,P}| < 5.8 \times 10^{-3} , \quad (32)$$

$$|\epsilon_T|, |\tilde{\epsilon}_T| < 1.3 \times 10^{-3} , \quad (33)$$

$$|\tilde{\epsilon}_R|, |\mathrm{Im}\, \epsilon_L^{(c)}| < 2.2 \times 10^{-3} , \quad (34)$$

$$\mathrm{Re}\, \epsilon_L^{(c)} \in (-1.1, 4.5) \times 10^{-3} . \quad (35)$$

Table 1 Summary of 90% CL bounds (in units of 10^{-2}) on the non-standard couplings $\tilde{\epsilon}_i$ from low- and high-energy searches.

	$\lvert\tilde{\epsilon}_L\rvert$	$\lvert\tilde{\epsilon}_R\rvert$	$\lvert\tilde{\epsilon}_P\rvert$	$\lvert\tilde{\epsilon}_S\rvert$	$\lvert\tilde{\epsilon}_T\rvert$
Low energy [2, 10]	6	6	0.03	14	3.0
LHC (this work)	-	0.2	0.6	0.6	0.1

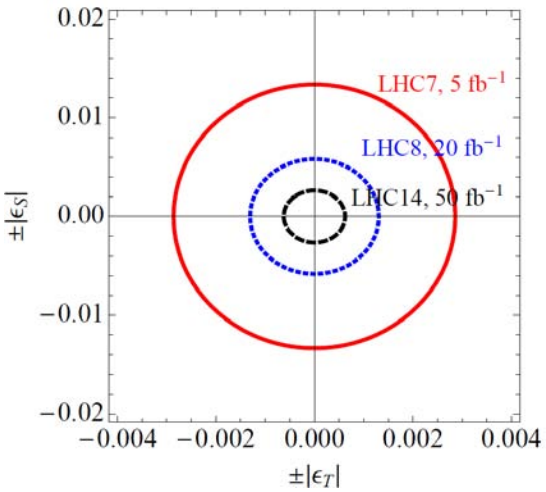

Figure 8 (online color at: www.ann-phys.org) The red solid (blue dotted) line gives the 90% C.L. limits on the scalar and tensor NP couplings $|\epsilon_{S,T}|$ obtained with 5 fb^{-1} (20 fb^{-1}) of data recorded at $\sqrt{s}$ = 7 TeV (8 TeV) by the CMS collaboration in the $pp \to e + \mathrm{MET} + X$ channel [64, 65]. The black dashed line gives an estimated future bound obtained with higher luminosity and energy.

The bounds presented in Figs. 6 and 8 show an interesting competition between low- and high-energy searches looking for new CP-conserving scalar and tensor interactions involving LH neutrinos. On the other hand, interactions involving RH neutrinos are more strongly constrained by the LHC, as shown in Table 1.

In the case of non-standard (axial-)vector interactions with LH neutrinos, the combination $\mathrm{Re}(\epsilon_L + \epsilon_R)$ is strongly constrained by CKM unitarity tests, as shown in Eq. (24), but the orthogonal combination $\mathrm{Re}(\epsilon_L - \epsilon_R)$ cannot be probed by β decay experiments. Although current LHC searches cannot improve the CKM unitarity limit, they are sensitive to the contact interaction part of ϵ_L providing in this way complementary information. For (axial-)vector interactions with RH neutrinos, we see from Table 1 that the LHC dominates the search in the case of $\tilde{\epsilon}_R$, whereas the bounds obtained on $\tilde{\epsilon}_L$ from nuclear β decays are the most competitive, even if they are above the per-cent level.

Finally, for the pseudoscalar couplings ϵ_P and $\tilde{\epsilon}_P$ the ratio $R_\pi = \Gamma(\pi \to e\nu)/\Gamma(\pi \to \mu\nu)$ represents by far the best probe, providing bounds of order 10^{-4} [10].

All in all, we see that only the combination of both low- and high-energy searches can give us a complete picture of non-standard charged current interactions.

Needless to say, this interplay becomes much more interesting if a non-zero result is obtained for one of the Wilson coefficients, either in the low-energy experiments or in collider searches. This was explained in Ref. [9], where it was shown that a hypothetical scalar resonance found at the LHC in the $pp \to e^\pm + \mathrm{MET} + X$ channel would imply a lower bound in the value of $|\epsilon_S|$ that should then be confirmed in nuclear and neutron decay experiments.

6 Experimental activities

Detailed accounts of new results and ongoing activities have been provided in several recent reviews [2, 4–8]. In this section we focus on current experiments or projects aiming at improving present limits on exotic couplings for both the real and imaginary parts. The purpose is to review the anticipated precision goals of such efforts in order to confront them with the current most precise limits and with the estimated reach at the LHC.

Searches for real exotic couplings are mainly focused on measurements of the $\beta\nu$ angular correlation and of the Fierz term. As pointed out in Sec. 4.2, recent measurements of the β asymmetry parameter in nuclei [42, 43] have a rather moderate impact in constraining exotic couplings compared to measurements of the longitudinal polarization ratio, P_F/P_{GT}. New measurements of the β asymmetry parameter in mirror nuclei are primarily motivated by the determination of the Gamow-Teller to Fermi mixing ratios, ρ [66]. In neutron decay, such measurements make possible the precise determination of the weak axial vector coupling [67] and provide competitive

constraints on exotic couplings when they are combined with neutron lifetime measurements and with data from nuclear decays [2, 44, 68].

6.1 The $\beta\nu$ angular correlation, a

As already indicated, the information about the angular correlation between the β particle and the neutrino is contained in the momentum spectrum of the recoiling daughter nucleus. This correlation can be obtained by detecting the recoiling nuclei either in singles or in coincidence with the β particles.

Current efforts aiming at improving the precision on the scalar couplings in Fermi transitions are based on experiments using Penning and Paul traps.

A new measurement of a has recently been carried out in the β decay of ^{35}Ar at the Grand Accélérateur National d'Ions Lourds (GANIL), Caen [69]. The ions were stored in a transparent Paul trap (LPCTrap) [70] and the $\beta\nu$ correlation was deduced from the time-of-flight spectrum of ^{35}Cl recoils detected in coincidence with the β particles. The statistical precision reached in this measurement is $\delta a_F = 2\times10^{-3}$ [69] and the study of systematic effects is currently under way.

Another experiment aiming at meassuring a in ^{35}Ar decay is the Weak Interaction Trap for CHarged particles spectrometer (WITCH) at ISOLDE-CERN [71]. The setup includes two Penning traps located in the same magnetic field. The first trap serves for cleaning and preparation of the ion cloud and the second to store the ions during their decay. In the WITCH spectrometer, the energy spectrum of the recoil ions is measured in singles using a magnetic spectrometer which contains several electrostatic retardation electrodes. The operation of this type of spectrometer is complicated by the possible presence of local Penning traps, where ions or electrons can be confined. This is caused by the electromagnetic field configuration inside the system and by secondary ionization processes. Such effects require the operation of the spectrometer under ultra-high vacuum conditions. The detection of positively charged recoil ions from singly charged trapped ions relies on the single or multiple shake-off process of the bound electrons. A first measurement of a recoil spectrum from stored $^{124}In^{+}$ ions has been reported [72]. The precision goal of this experiment is to reach the level of $\delta a \approx 5\times10^{-3}$ [71][7].

A new experimental setup (TAMUTRAP) based on a Penning trap is currently under preparation at Texas A&M University [73]. The experimental program of TAMUTRAP includes measurements of a in a set of super-allowed pure Fermi transitions with isospin $T = 2$, which are β-delayed proton emitters, like ^{32}Ar decay. The measuring principle relies on the the broadening of the delayed proton energy spectrum, which is affected by the correlation between the β particle and the neutrino [28]. The Penning trap setup employs an optimized length-to-radius ratio in the electrode structure providing a 90 mm large inner radius [73].

In order to calculate the level of precision required in a measurement of $\tilde{a}_F$ from a pure Fermi transition, such as to compete with the direct extraction of the Fierz term from the $\mathcal{F}t$-values in super-allowed pure Fermi transitions, Eq. (16), we refer once again to the linear sensitivity of $\tilde{a}$ to scalar interactions through the contribution of the Fierz term, Eq.(17). This leads to

$$\left|\frac{\delta\tilde{a}_F}{\tilde{a}_F}\right| \approx |\delta b_F|\left\langle\frac{m}{E}\right\rangle . \tag{36}$$

Taking δb_F at 1σ from Eq. (16) and assuming $\langle m/E\rangle \sim 0.2$ as an estimate, Eq. (36) gives $|\delta\tilde{a}_F/\tilde{a}_F| \sim 0.5\times10^{-3}$. This is an order of magnitude smaller than the current level of precision in ^{38m}K [27] and ^{32}Ar [28] and the expected reach of ongoing experiments.

The fact that the constraints on tensor couplings are considerably weaker than those on scalar ones (Figs. 2 and 3) has motivated a number of new experiments for precision measurements in Gamow-Teller transitions, most of them focused on the measurement of the $\beta\nu$ correlation coefficient in the decay of ^{6}He.

A measurement of a in the β decay of ^{6}He has also been carried out at GANIL by the Caen group [74] using the transparent Paul trap [70]. Since this measurement records the position and energy of the β particle and the position and time-of-flight of the ^{6}Li recoils detected in coincidence with the β particles, the kinematics is over determined allowing the construction of the neutrino invariant mass [75] and enabling the control of background and instrumental effects. Three data production runs have been completed with this setup including a measurement of the shake-off probability of the singly bound electron in the recoiling ions following β decay [76]. A relative statistical error of 2% has been obtained from the analysis of the first run [74] with a systematic error of comparable

[7] The projections of the future experimental precision goals do not always specify the statistical CL. Unless explicitly stated otherwise, it is assumed that the quoted experimental errors and the projected precision goals are at 1σ.

size. Since no limit on tensor couplings has been quoted in Ref. [74] we review here this result in order to further stress the sensitivity to the linear contributions of the exotic couplings via the Fierz term. The experimental result from Ref. [74] reads $\tilde{a} = -0.334(10)$ where the statistical and systematic errors have been added in quadrature. For a Gamow-Teller transition, the expression of b in Eq. (17) is given in Eq. (11). Assuming first that the sensitivity to tensor couplings arises only via the Fierz term, we then set $a \approx a_{SM} \approx -1/3$. The value of the term $\langle m/E_e \rangle$ under the conditions of that experiment is $\langle m/E_e \rangle = 0.20$ [8]. Assuming $C_T = C_T'$, the limit obtained from this measurement is then

$$|C_T/C_A| < 0.13 \qquad \text{(90\% CL, first run LPCTrap)}. \tag{37}$$

If, in contrast, the contribution of the Fierz term is ignored, the limit extracted from the quadratic contribution to a would be $|C_T/C_A| < 0.23$ what is a factor of about 2 weaker. We see that, even if the sensitivity to the Fierz term is here only $\langle m/E_e \rangle = 0.20$, it remains nevertheless dominant in the extraction of constraints on exotic couplings from the expression of $\tilde{a}$. A new measurement has been carried out with the LPCTrap at GANIL, resulting in a relative statistical precision $\delta a/a = 4.5 \times 10^{-3}$ at 1σ [69]. Assuming that the final systematic error will be of comparable magnitude than the statistical one, the result will provide the following bound

$$\left|\mathrm{Re}\left(\frac{C_T + C_T'}{C_A}\right)\right| \lesssim 0.052 \qquad \text{(90\% CL, projected LPCTrap)}\,. \tag{38}$$

This will finally improve the fifty-year old measurement of a in ^{6}He decay [32], but will still be a factor of 2.5 away from the current limit obtained from P_F/P_{GT}, Eq. (19).

A high intensity gaseous source of ^{6}He has been developed at the Center for Experimental Nuclear Physics and Astrophysics (CENPA) in Seattle [77]. The measured extracted rate of atomic ^{6}He available at a low background experimental area was about 10^9 atoms/s. The source has been used for a high precision measurement of the ^{6}He half-life [78], with the atoms confined in a cylindrical storage volume. The physics plans include a measurement of a and of the Fierz interference term [77]. The measurement of a will be performed with atoms confined in a MOT [79] and by detecting the β particles in coincidence with the recoil ions. The goal of this project is to reach the precision level of 1% in a first phase and reach an ultimate precision of 0.1% after possible improvements of the setup [79]. Such a total precision would entail the following bound on tensor interactions

$$\left|\mathrm{Re}\left(\frac{C_T + C_T'}{C_A}\right)\right| \lesssim 0.0082 \qquad \text{(90\% CL, projected CENPA)}\,. \tag{39}$$

This would improve the bound from nuclear and neutron decays, Eq. (20), by a factor of about 2. The current bound from radiative pion decay given in Eq. (27) would still be slightly stronger though.

An electrostatic ion beam trap is currently being built at the Weizmann Institute of Science, in Rehovot [80]. The program around this trap includes a measurement of a in ^{6}He decay. The ions will be trapped by mirror potentials, and the ^{6}Li recoil ions and the β particles will be detected in coincidence in a field free region [80]. The project envisages to take advantage of the high yields of radioactive nuclei that will become available at the Soreq Applied Research Accelerator Facility [85].

The β-α-α correlation from ^{8}Li decay has since long been known to offer an attractive scheme in order to circumvent the detection of the recoil nucleus [81] although early results were not selective enough to distinguish between different interaction types. After establishing that the decay was dominated by a Gamow-Teller transition, a first limit on a possible tensor contribution has been provided [82] from the measurement of the α particle momenta. An additional advantage of this correlation in ^{8}Li decay is that, when the α and β particles are detected along the same direction, the sensitivity to the quadratic contributions of the tensor interaction is enhanced by a factor of 3 [82] as compared to a direct measurement of a in a Gamow-Teller transition. This decay has recently been reconsidered at Argonne National Laboratory using ions stored in a longitudinal Paul trap [83]. The α and β particles are detected in coincidence and the shape of the α particle energy shift distribution is analyzed. The experiment has obtained a first result [84] corresponding to a limit $|C_T/C_A|^2 < 0.026$ at 90% CL. It is expected that, with an upgraded detection system, the limit on $|C_T/C_A|^2$ can be improved by an order of magnitude [84]. This would then result in a limit on the tensor couplings a factor of about 2 larger than given in Eq.(38). Note that, since the β particle end-point energy is rather large in ^{8}Li decay (16.1 MeV) the sensitivity to the Fierz term via the factor $\langle m/E_e \rangle$ is 3.3 times smaller than in ^{6}He decay.

[8] For the purpose followed here, the value of $\langle 1/E_e \rangle = \langle 1/(T_e + m_e) \rangle$ was extracted from the spectrum of the measured kinetic energy, T_e, without deconvoluting the detector response function.

Several experiments are currently ongoing aiming at improved measurements of a in neutron decay [86–88]. Such efforts are primarily motivated by the extraction of the ratio g_A/g_V using another observable than the β asymmetry parameter, A, in order to determine the V_{ud} matrix element from the neutron lifetime. The anticipated precision goals on $\delta a/a$ of these experiments are of <1% for aCORN [87] <0.5% for aSPECT [86] and 0.1% for Nab [88]. Significant improvements in precision are also expected to be achieved with the PERC spectrometer [89] in the measurement of several correlation parameters. It is anticipated that the sensitivity goal is of about 10^{-5} for those correlations not involving polarized neutrons.

In summary, the most precise experiments in Fermi transitions have reached a level of of few 10^{-3} at 1σ for the measurements of a [27,28]. Comparable levels of precision are currently being reached by new measurements [69] or have been anticipated by ongoing projects [71]. It appears challenging that the new round of measurements of a would be able to improve the bounds on scalar couplings set by the Fierz term extracted from the $\mathscr{F}t$-values in pure Fermi transitions, Eq. (16). However, this constraint has a stronger dependence to theoretical uncertainties related to nuclear structure and radiative corrections than those obtained from correlation coefficients. Since for pure Fermi and pure Gamow-Teller transitions the nuclear matrix elements cancel to first order in the correlation coefficients, it is expected that nuclear effects manifest themselves at the level of induced weak currents. This leaves significant room for improvements in precision for measurements of correlation coefficients.

For pure Gamow-Teller transitions, considering the number of ongoing experiments in ^{6}He, ^{8}Li and neutron decays and the anticipated precision goals on a longer time scale [79, 88], it is expected that the next round of measurements of a could reach a precision at the 0.1% level. This should have a significant impact to further constraint possible tensor contributions.

6.2 The Fierz interference term, b

The Fierz term can be accessed directly by measurements of the shape of the β energy spectrum. Such measurements are very challenging, in particular because of instrumental difficulties associated with the detection of β particles at low energies such as backscattering, outscattering, detector dead-layers, noise, etc.

The physics program of the CENPA group around the high intensity ^{6}He source includes a measurement of b in ^{6}He decay [77]. The technical details of the detection system to be used for such a measurement and the sensitivity level of the experiment have not yet been anticipated.

The problems associated with the scattering of β particles in matter and the limited precision of available data on low-energy electron scattering that is required for precise Monte-Carlo simulations, have motivated the development of a new and compact β spectrometer (miniBETA) by groups from Krakow and Leuven [90]. The system is based on an ultra-light multi-wire drift chamber combined with energy sensitive detectors. Precision measurements of the shape of β energy spectra for transitions with relatively low endpoint energies are being considered [91].

The Fierz term has never been measured in neutron decay and there are several projects aiming a direct determination from the shape of the β energy spectrum.

The Nab collaboration will use a cold neutron beam at the Fundamental Neutron Physics Beamline of the Spallation Neutron Source in Oak Ridge [88]. The setup uses a field-expansion magnetic spectrometer that confines electrons and protons toward segmented Si detectors. The anticipated precision goal for the direct measurement of b is $\delta b = 3\times10^{-3}$ [88] and is aimed to provide an independent limit on exotic tensor couplings.

The UCNb experiment at Los Alamos National Laboratory [92] uses ultra-cold neutrons confined in a 4π box made of plastic scintillators. This experiment aims a precision of $\delta b \approx 10^{-3}$ [92].

The PERC experiment also includes a measurement of b in the scientific program [93]. The setup will use a cold neutron beam and a long super-conducting channel where neutrons decay.

6.3 Time-reversal violating correlations

A new measurement of the time-reversal violating triple correlation coefficient R has been carried out in ^{8}Li decay at ISAC-TRIUMF [94]. The nuclear polarization is obtained by collinear laser optical pumping of a low-energy beam which is then ionized an implanted on a Pt foil. The β particle transverse polarization is analyzed by Mott scattering on a lead foil and the particles are tracked using planar wire chambers. The precision goal of this experiment is to reach the level of final state interactions which, as already indicated, are at 10^{-4} level for this decay [46].

7 Summary and Outlook

We have reviewed the status of the searches for physics beyond the SM by precision measurements in nuclear and

neutron β decays. For the description of such processes at the quark-level, we have used a model-independent EFT approach, assuming that the NP would emerge at much higher energies, not only compared to those available in β decays but also those currently accessed or projected to be accessed at the LHC. An attractive feature of this approach is that it provides a unified framework to describe the effects of NP in nuclear, neutron and pion decays as well as in collider physics.

It was shown that only three CP-conserving and three CP-violating NP couplings can contribute linearly to the observables in β decay, and so only those couplings can be strongly probed with precision experiments at low energies.

We have then review the constrains on these six couplings from precise measurements in nuclear and neutron decays, using the hadron-level coefficients. Except for the $\mathcal{F}t$-values deduced from pure Fermi transitions, which combines results from a large set of experiments and for several nuclear transitions, we have selected the most precise results from single experiments. A more detailed analysis would require a new global fit of all currently available data. When analyzing the sensitivity of the most stringent constraints on scalar and tensor couplings provided by measurements of correlations or decay rates, we found that the only relevant parameter for all constraints is the Fierz interference term. This term is linear in the couplings and contribute to the measured correlations in most experimental conditions, offering then the dominant sensitivity to those couplings.

With the most precise results, we have then moved to a quark-level description in order to first compare with results obtained from other semi-leptonic processes but then also with results obtained from measurements at the LHC. This illustrates the benefit of the EFT approach for the sensitivity comparison between different hadronic probes, such as pions, nucleons, and nuclei. For the CP-conserving coefficients, direct limits from β decay appear to be very competitive. Next we discussed the interplay with results from the LHC and we stressed the complementary of precision measurements in β decay as probes of new physics. An interesting competition with results from the LHC arises since the effective scale probed by low energy experiments overlaps with the LHC reach. The most attractive scenario of such interplay would be that in which a non-zero result would be observed for an exotic effective coupling either at low energies or in the collider searches. If a new particle were found at the LHC, experiments in β decays will play an important role in disentangling the properties of the NP dynamics. We also presented the projected sensitivities to be reached at LHC which are important to orient new precision goals for measurements at low energies.

We have finally reviewed the current experimental efforts looking for signatures of NP in measurements of correlations or spectrum shapes in nuclear and neutron decays. The purpose was to project the sensitivity level of those efforts and confront them with the future LHC reach. We have stressed again the importance of the Fierz term in those searches and gave simple quantitative illustrations in the measurement of a in Fermi and Gamow-Teller transitions. Although recent measurements of the β asymmetry parameter A in Gamow-Teller transitions have explicitly relied on the sole contribution of the Fierz term in the search for tensor interactions, the role this term does not appear to have been generally incorporated for the optimization of current experiments and for the design of new projects.

The sensitivity goal imposed by future LHC reach is very challenging but possibly within reach by next generation experiments, where precisions at the level of 10^{-3} or below are needed on the Fierz term. For the comparison with the SM predictions of the measured observables, accurate theoretical calculations are fundamental. These require the inclusion of radiative corrections and recoil order effects and, whenever necessary, of nuclear structure corrections. The errors on these corrections set the next theoretical limit of sensitivity for future measurements and leave still a large window for improvements for experiments measuring correlations or spectrum shapes in nuclear and neutron decays.

Acknowledgements. We are grateful to H. Abele, V. Cirigliano, X. Fléchard, V. Gudkov, E. Liénard, K. Minamisono, N. Severijns, M. Sternberg, S. Tulin and F. Wauters for stimulating discussions and for correspondence. This work was supported in part by the U.S. National Science Foundation under grant number PHY-11-02511, the DOE contract DE-FG02-08ER41531 and the Wisconsin Alumni Research Foundation.

Key words. Nuclear beta decay, weak interactions, tests of the standard model, searches for exotic couplings.

References

[1] S. Weinberg, J. Phys. Conf. Ser. **196**, 012002 (2009).
[2] N. Severijns, M. Beck, and O. Naviliat-Cuncic, Rev. Mod. Phys. **78**, 991 (2006).
[3] I.S. Towner, and J.C. Hardy, Rep. Prog. Phys. **73**, 046301 (2010).
[4] N. Severijns, and O. Naviliat-Cuncic, Annu. Rev. Nucl. Part. Sci. **61**, 23 (2011).

[5] N. Severijns, and O. Naviliat-Cuncic, Phys. Scr. **T152**, 014018 (2013).
[6] H. Abele, Prog. Part. Nucl. Phys. **60**, 1 (2008).
[7] J. Nico, J. Phys. G: Nucl. Part. Phys. **36**, 104001 (2009).
[8] D. Dubbers, and M.G. Schmidt, Rev. Mod. Phys. **83**, 1111 (2011).
[9] T. Bhattacharya, V. Cirigliano, S. D. Cohen, A. Filipuzzi, M. Gonzalez-Alonso, M.L. Graesser, R. Gupta, and H.-W. Lin, Phys. Rev. D **85**, 054512 (2012).
[10] V. Cirigliano, M. Gonzalez-Alonso, and M.L. Graesser, J. High Energ. Phys. **1302**, 046 (2013).
[11] V. Cirigliano, S. Gardner, and B. Holstein, 2013, in preparation.
[12] S. Ando, H.W. Fearing, V.P. Gudkov, K. Kubodera, F. Myhrer, S. Nakamura, and T. Sato, Phys. Lett. B **595**, 250 (2004).
[13] A. Czarnecki, W.J. Marciano, and A. Sirlin, Phys. Rev. D **70**, 093006 (2004).
[14] S. Profumo, M. J. Ramsey-Musolf and S. Tulin, Phys. Rev. D **75**, 075017 (2007).
[15] P. Herczeg, Prog. Part. Nucl. Phys. **46**, 413 (2001).
[16] T.D. Lee, and C.N. Yang, Phys. Rev. **104**, 254 (1956).
[17] J.D. Jackson, S.B. Treiman, and H.W. Wyld Jr., Phys. Rev. **106**, 517 (1957).
[18] V. Gudkov, G.L. Greene, and J.R. Calarco, Phys. Rev. C **73**, 035501 (2006).
[19] S. Gardner and C. Zhang, Phys. Rev. Lett. **86**, 5666 (2001).
[20] J.D. Jackson, S.B. Treiman, and H.W. Wyld Jr., Nucl. Phys. **4**, 206 (1957).
[21] J.R. Green, J.W. Negele, A.V. Pochinsky, S.N. Syritsyn, M. Engelhardt, and S. Krieg, Phys. Rev. D **86**, 114509 (2012).
[22] L. Grenacs, Ann. Rev. Nucl. Part. Sci. **35**, 455 (1985).
[23] B.R. Holstein, Rev. Mod. Phys. **46**, 789 (1974); Erratum, Rev. Mod. Phys. **48**, 673 (1976).
[24] J.C. Hardy, and I.S. Towner, Phys. Rev. C **79**, 055502 (2009).
[25] C.N. Leung, S.T. Love, and S. Rao, Z. Phys. C **31**, 433 (1986).
[26] M. Moulson, arXiv:1301.3046 [hep-ex] (2013). W. Buchmuller, and D. Wyler, Nucl. Phys. B **268**, 621 (1986).
[27] A. Gorelov, et al., Phys. Rev. Lett. **94**, 142501 (2005).
[28] E. Adelberger, et al., Phys. Rev. Lett. **83**, 1299 (1999); Phys. Rev. Lett. **83**, 3101 (1999).
[29] V.A. Wichers, T.R. Hageman, J. van Klinken, and H. Wilschut, Phys. Rev. Lett. **58**, 1821 (1987).
[30] A.S. Carnoy, J. Deutsch, T.A. Girard, and R. Prieels, Phys. Rev. Lett. **65**, 3249 (1990).
[31] A.S. Carnoy, J. Deutsch, T.A. Girard, and R. Prieels, Phys. Rev. C **43**, 2825 (1991).
[32] C.H. Johnson, F. Pleasonton, and T.A. Carlson, Phys. Rev. **132**, 1149 (1963).
[33] F. Glück, Nucl. Phys. A **628**, 493 (1998).
[34] D. Melconian, J.A. Behr, D. Ashery, O. Aviv, P.G. Bricault, M. Dombsky, S. Fostner, A. Gorelov, S. Gu, V. Hanemaayer, K.P. Jackson, M.R. Pearson, and I. Vollrath, Phys. Lett. B **649**, 370 (2007).
[35] A.P. Serebrov, I.A. Kuznetsov, I.V. Stepanenko, A.V. Aldushchenkov, M.S. Lasakov, Yu.A. Mostovoĭ, B.G. Erozolimskiĭ, M.S. Dewey, F.E. Wietfeldt, O. Zimmer, and H. Börner, J. Exp. Theo Phys. **86**, 1074 (1998).
[36] M. Schumann, T. Soldner, M. Deissenroth, F. Glück, J. Krempel, M. Kreuz, B. Maĺrkisch, D. Mund, A. Petoukhov, and H. Abele, Phys. Rev. Lett. **99**, 191803 (2007).
[37] P.A. Quin, and T.A. Girard, Phys. Lett. B **229**, 29 (1989).
[38] N. Severijns, J. Deutsch, F. Gimeno-Nogues, B.H. King, I. Pepe, R. Prieels, P.A. Quin, J. Camps, P. De Moor, P. Schuurmans, W. Vanderpoorten, L. Vanneste, J. Wouters, M. Allet, O. Naviliat-Cuncic, and B. R. Holstein, Phys. Rev. Lett. **70**, 4047 (1993); Erratum, Phys. Rev. Lett. **73**, 611 (1994).
[39] M. Allet M, K. Bodek, J. Camps, J. Deutsch, M. Ferro-Luzzi, F. Gimeno-Nogues, J. Govaerts, J. Lang, R. Müller, S. Navert, O. Naviliat-Cuncic, I. Pepe, R. Prieels, P. Quin, N. Severijns, J. Sromicki, E. Stephan, E. Thomas, and J. Zejma, Phys. Lett. B **383**, 139 (1996).
[40] E. Thomas, R. Prieels, M. Allet, K. Bodek, J. Camps, J. Deutsch, F. Gimeno-Nogues, J. Govaerts, J. Lang, O. Naviliat-Cuncic, I. Pepe, P. Quin, N. Severijns, and J. Sromicki, Nucl. Phys. A **694**, 559 (2001).
[41] A. Kozela, G. Ban, A. Bialek, K. Bodek, P. Gorel, K. Kirch, St. Kistryn, O. Naviliat-Cuncic, N. Severijns, E. Stephan, and J. Zejma, Phys. Rev. C **85**, 045501 (2012).
[42] F. Wauters, V. De Leebeeck, I. Kraev, M. Tandecki, E. Traykov, S. Van Gorp, N. Severijns, and D. Zákoucký, Phys. Rev. C **80**, 062501(R) (2009).
[43] F. Wauters, I. Kraev, D. Zákoucký, M. Beck, M. Breitenfeldt, V. De Leebeeck, V.V. Golovko, V.Yu. Kozlov, T. Phalet, S. Roccia, G. Soti, M. Tandecki, I.S. Towner, E. Traykov, S. Van Gorp, and N. Severijns, Phys. Rev. C **82**, 055502 (2010).
[44] G. Konrad, W. Heil, S. Baessler, D. Počanić, and F. Glück, in *Physics Beyond The Standard Models of Particles, Cosmology and Astrophysics*, Proc. 5th Int. Conf. *Beyond 2010*, Cape Town; H.V. Klapdor-Kleingrothaus, I.V. Krivosheina, R. Viollier eds., World Scientific, Singapore, pp. 660-672 (2011).
[45] J. Holeczek, M. Ochman, E. Stephan, and M. Zralek arXiv:1303.5295v1 [nucl-ex] (2013).
[46] Huber R, J. Lang, S. Navert, J. Sromicki, K. Bodek, St. Kistryn, J. Zejma, O. Naviliat-Cuncic, E. Stephan, and W. Haeberli, Phys. Rev. Lett. **90**, 202301 (2003).
[47] F.P. Calaprice, Hyperfine Interact. **22** 83 (1985).
[48] T. Soldner, L. Beck, C. Plonka, K. Schreckenbach, O. Zimmer, Phys. Lett. B **581**, 49 (2004).
[49] T.E. Chupp, R.L. Cooper, K.P. Coulter, S.J. Freedman, B.K. Fujikawa, A. García, G.L. Jones, H.P. Mumm, J.S. Nico, A.K. Thompson, C.A. Trull, F.E. Wietfeldt,

and J.F. Wilkerson, Phys. Rev. C **86**, 035505 (2012).
[50] V. Cirigliano, J. Jenkins, and M. Gonzalez-Alonso, Nucl. Phys. B **830**, 95 (2010).
[51] R. Barbieri, C. Bouchiat, A. Georges and P. Le Doussal, Phys. Lett. B **156**, 348 (1985).
[52] W. J. Marciano and A. Sirlin, Phys. Rev. D **35**, 1672 (1987).
[53] K. Hagiwara, S. Matsumoto and Y. Yamada, Phys. Rev. Lett. **75**, 3605 (1995) [hep-ph/9507419].
[54] A. Kurylov and M. J. Ramsey-Musolf, Phys. Rev. Lett. **88**, 071804 (2002).
[55] W. J. Marciano, PoS KAON , 003 (2008).
[56] S. Bauman, J. Erler and M. Ramsey-Musolf, arXiv:1204.0035 [hep-ph].
[57] M. Bychkov, et al., Phys. Rev. Lett. **103**, 051802 (2009).
[58] V. Mateu, and J. Portoles, Eur. Phys. J. C **52**, 325 (2007).
[59] B.A. Campbell, and D.W. Maybury, Nucl. Phys. B **709**, 419 (2005).
[60] S. Gardner and D. He, arXiv:1302.1862 [hep-ph] (2013).
[61] S. Gardner and D. He, Phys. Rev. D **86**, 016003 (2012).
[62] J. Ng, and S. Tulin, Phys. Rev. D, **85**, 033001 (2012).
[63] S. Tulin, Winter Workshop on Electric Dipole Moments, February 2013.
[64] S. Chatrchyan *et al.* [CMS Collaboration], J. High Energ. Phys. **1208**, 023 (2012).
[65] V. Khachatryan *et al.* [CMS Collaboration], CERN Report number CMS-PAS-EXO-12-060, (2013).
[66] O. Naviliat-Cuncic, in Proc. of the CKM 2012, The 7th Int. Workshop on the CKM Unitarity Triangle, arXiv:1301.4153v1 [nucl-ex].
[67] D. Mund, B. Märkisch, M. Deissenroth, J. Krempel, M. Schumann, H. Abele, A. Petoukhov, T. Soldner, Phys. Rev. Lett. **110**, 172502 (2013).
[68] F. Wauters, A. García, R. Hong, arXiv:1306.2608v1 [nucl-ex].
[69] G. Ban, X. Fléchard, E. Liénard, G. Ban, D. Durand, and O. Naviliat-Cuncic, Ann. Phys. (2013), this issue; DOI: 10.1002/andp.201300043
[70] D. Rodriguez, A. Méry, G. Ban, J. Brégeault, G. Darius, D. Durand, X. Fléchard, M. Herbane, M. Labalme, E. Liénard, F. Mauger, Y. Merrer, O. Naviliat-Cuncic, J.C. Thomas, and C. Vandamme, Nucl. Instrum. Meth. A **565**, 876 (2006).
[71] M. Beck, F. Ames, D. Beck, G. Bollen, B. Delauré, V.V. Golovko, V.Yu. Kozlov, I.S. Kraev, A. Lindroth, T. Phalet, W. Quint, P. Schuurmans, N. Severijns, B. Vereecke, and S. Versyck, Nucl. Instrum. Meth. A **503**, 567 (2003).
[72] M. Beck, S. Coeck, V.Yu. Kozlov, M. Breitenfeldt, P. Delahaye, P. Friedag, F. Glück, M. Herbane, A. Herlert, I.S. Kraev, J. Mader, M. Tandecki, S. Van Gorp, F. Wauters, Ch. Weinheimer, F. Wenander, N. Severijns, and the ISOLDE Collaboration, Eur, Phys. J. A **47**, 45 (2011).
[73] M. Mehlman, P.D. Shidling, S. Behling, L.C. Clark, B. Fenker, D. Melconian, to appear in Nucl. Instrum. Meth. A , (2013).
[74] X. Fléchard, Ph. Velten, E. Liénard, A. Méry, D. Rodríguez, G. Ban, D. Durand, F. Mauger, O. Naviliat-Cuncic, and J.C. Thomas, J. Phys. G: Nucl. Part. Phys. **38**, 055101 (2011).
[75] X. Fléchard, E. Liénard, A. Méry, D. Rodríguez, G. Ban, D. Durand, F. Duval, M. Herbane, M. Labalme, F. Mauger, O. Naviliat-Cuncic, J.C. Thomas, and Ph. Velten, Phys. Rev. Lett. **101**, 212504 (2008).
[76] C. Couratin, Ph. Velten, X. Fléchard, E. Liénard, G. Ban, A. Cassimi, P. Delahaye, D. Durand, D. Hennecart, F. Mauger, A. Méry, O. Naviliat-Cuncic, Z. Patyk, D. Rodríguez, K. Siegień-Iwaniuk, and J.C. Thomas, Phys. Rev. Let. **108**, 243201 (2012).
[77] A. Knecht, D.W. Zumwalt, B.G. Delbridge, A. García, G.C. Harper, R. Hong, P. Müller, A.S.C. Palmer, R.G.H. Robertson, H.E. Swanson, S. Utsuno, D.I. Will, W. Williams, and C. Wrede, Nucl. Instrum. Meth. A **660**, 43 (2011).
[78] A. Knecht, R. Hong, D.W. Zumwalt, B.G. Delbridge, A. García, P. Müller, H.E. Swanson, I.S. Towner, S. Utsuno, W. Williams, and C. Wrede, Phys. Rev. C **86**, 035506 (2012).
[79] A. Knecht, Z.T. Alexander, Y. Bagdasarova, T.M. Cope, B.G. Delbridge, X. Fléchard, A. García, R. Hong, E. Liénard, P. Mueller, O. Naviliat-Cuncic, A.S.C. Palmer, R.G.H. Robertson, D.W. Storm, H.E. Swanson, S. Utsuno, F. Wauters, W. Williams, C. Wrede, and D.W. Zumwalt, arXiv:1208.6433v2 [nucl-ex] (2012).
[80] O. Aviv, S. Vaintraub, T. Hirsh, A. Dhal, M.L. Rappaport, D. Melnik, O. Heber, D. Schwalm, D. Zajfman, K. Blaum, and M. Hass, J. Phys.: Conf. Ser. **337**, 012020 (2012).
[81] R.F. Christy, E.R. Cohen, W.A. Fowler, C.C. Lauritsen, and T. Lauritsen, Phys. Rev. **72**, 698 (1947).
[82] C.A. Barnes, W.A. Fowler, H.B. Greenstein, C.C. Lauritsen, and T. Lauritsen, Phys. Rev. Lett. **1**, 328 (1958).
[83] N.D. Scielzo, G. Li, M.G. Sternberg, G. Savard, P.F. Bertone, F. Buchinger, S. Caldwell, J.A. Clark, J. Crawford, C.M. Deibel, J. Fallis, J.P. Greene, S. Gulick, A.A. Hecht, D. Lascar, J.K.P. Lee, A.F. Levand, M. Pedretti, R.E. Segel, H. Sharma, K.S. Sharma, I. Tanihata, J. Van Schelt, R.M. Yee, and B.J. Zabransky, Nucl. Instrum. Meth. A **681**, 94 (2012).
[84] G. Li, R. Segel, N.D. Scielzo, P.F. Bertone, F. Buchinger, S. Caldwell, A. Chaudhuri, J.A. Clark, J.E. Crawford, C.M. Deibel, J. Fallis, S. Gulick, G. Gwinner, D. Lascar, A.F. Levand, M. Pedretti, G. Savard, K.S. Sharma, M.G. Sternberg, T. Sun, J. Van Schelt, R.M. Yee, and B.J. Zabransky, Phys. Rev. Lett. **110**, 092502 (2013).
[85] T. Hirsh, D. Berkovits, M. Hass, P. Jardin, A. Pichard, M.L. Rappaport, Y. Shachar, and I. Silverman, J. Phys.: Conf. Ser. **337**, 012010 (2012).

[86] M. Simson, F. Ayala Guardia, S. Baessler, M. Borg, F. Gück, W. Heil, I. Konorov, G. Konrad, R. Muñoz Horta, K.K.H. Leung, Yu. Sobolev, T. Soldner, H-F. Wirth, and O. Zimmer, Nucl. Instrum. Meth. A **611**, 203 (2009).
[87] F.E. Wietfeldt, J. Byrne, B. Collett, M.S. Dewey, G.L. Jones, A. Komives, A. Laptev, J.S. Nico, G. Noid, E.J. Stephenson, I. Stern, C. Trull, B.G. Yerozolimsky, Nucl. Instrum. Meth. A **611**, 207 (2009).
[88] D. Počanić, et al., [Nab Collaboration], Nucl. Instrum. Meth. A **611**, 211 (2009).
[89] D. Dubbers, H. Abele, S. Baessler, B. Märkisch, M. Schumann, T. Soldner, O. Zimmer, Nucl. Instrum. Meth. A **596**, 238 (2008).
[90] K. Lojek, K. Bodek, and M. Kuzniak, Nucl. Instrum. Meth. A **611**, 284 (2009).
[91] N. Severijns, private communication (2013).
[92] K.P. Hickerson, PhD thesis, California Institute of Technology (2013) unpublished.
[93] G. Konrad, et al., [PERC Collaboration], J. Phys. Conf. Ser. **340**, 012048 (2012).
[94] J. Murata, H. Baba, J.A. Behr, M. Hata, Y. Hirayama, M. Ikeda, D. Kameda, H. Kawamura, R. Kishi, C.D.P. Levy, Y. Nakaya, K. Ninomiya, M. Nitta, N. Ogawa, J. Onishi, R. Openshaw, M. Pearson, E. Seitaibashi, Y. Totsuka, T. Toyoda, M. Uchida, J. of Phys.: Conf. Ser. **312**, 102011 (2011).

WILEY ONLINE LIBRARY
Early View publication on wileyonlinelibrary.com
(issue and page numbers not yet assigned;
citable using Digital Object Identifier – DOI)

Ann. Phys. (Berlin), 1–16 (2013) / DOI 10.1002/andp.201300052

annalen der physik

Review Article

Electron *g*-factor determinations in Penning traps

Sven Sturm[1,*], *Günter Werth*[2], *and Klaus Blaum*[1]

Received 13 March 2013, revised 22 May 2013, accepted 22 May 2013
Published online 1 July 2013

The magnetic moment of the electron, expressed by the *g*-factor in units of the Bohr magneton, is a key quantity in the theory of quantum electrodynamics (QED). Experiments using single particles confined in Penning traps have provided very precise values of the *g*-factor for the free electron as well as the electron bound in hydrogen-like ions. In this paper the status of these experiments is reviewed. The results allow testing calculations of higher order Feynman diagrams. Comparison of experimental and theoretical results for free and bound particles show no discrepancy within the limits of error, thus representing to date the most sensitive test of QED. Moreover, the *g*-factor provides a unique access to fundamental constants, as e.g. the electron mass or the fine structure constant.

1 Introduction

The magnetic moment associated with the spin of a particle or an atom has played a central role in the development of atomic theory and quantum electrodynamics. The concept of the spin quantum number in units of $\frac{\hbar}{2}$ introduced by Goudsmit and Uhlenbeck in 1925 [1] and the observation of the quantization of the associated magnetic moment by Stern and Gerlach in 1922 [2] led to the understanding of the anomalous Zeeman effect and the fine structure splitting of spectral lines. Dirac [3] showed that the spin is a purely relativistic effect and that the electron's magnetic moment is the Bohr magneton $\mu_B = e\hbar/2m$. A dimensionless quantity g scales the magnetic moment μ of any particle with spin s in units of μ_B:

$$\mu = g\mu_B s. \tag{1}$$

From the Dirac equation follows that $g = 2$ for the free electron. For an atom with orbital angular momentum L, a total Spin S, and total angular momentum J the g-factor can be expressed by the Landé formula

$$g = 1 + \frac{J(J+1) + S(S+1) - L(L+1)}{2J(J+1)}. \tag{2}$$

Numerous measurements of magnetic moments of neutral atoms have been performed using the Rabi-technique [4]: A Stern-Gerlach force acting on an atomic beam in an inhomogeneous magnetic field separates different spin states in space. Transitions between different Zeeman substates are induced in a homogeneous magnetic field region and are monitored by a deflection in a second inhomogeneous B-field. With the knowledge of the magnetic field strength the g-factor can be derived. A particularly interesting result from measurements on atomic hydrogen was the fact that the g-factor of the electron deviates from the Dirac value of 2 by about 1 part in a thousand. This result, together with the discovery of the $2S_{1/2} - 2P_{1/2}$ Lamb shift in hydrogen [5], triggered the development of the theory of quantum electrodynamics (QED), which describes the electromagnetic interaction by exchange of virtual photons. The explanation of the deviation of g from 2 by an additional term [6]

$$g = 2(1 + \alpha/2\pi), \tag{3}$$

with the fine structure constant $\alpha = (1/4\pi\epsilon_0)(e^2/\hbar c)$, was one of the first successes of the new theory. Increasing experimental accuracy required higher order calculations. The comparison of experimental and theoretical results on the g-factor of the electron still represents to date the most stringent test of QED theory [7, 8]. This is particularly true for the electron in free space or bound in simple atomic systems, while in complex atoms relativistic effects can not be calculated sufficiently accurately.

* Corresponding author E-mail: sven.sturm@mpi-hd.mpg.de
[1] Max-Planck-Institut für Kernphysik, Saupfercheckweg 1, 69117 Heidelberg
[2] Institut für Physik, Johannes Gutenberg-Universität Mainz, Staudingerweg 7, 55128 Mainz

Soon after the Stern-Gerlach experiment it was proven by different authors that the technique used in their experiment can not be applied to charged particles [9, 10]. This was circumvented by Dehmelt [11] who coined the term "continuous Stern-Gerlach effect": A charged particle, suspended in a Penning ion trap with superimposed inhomogeneous magnetic field experiences a force acting on the magnetic moment of the particle. The sign of this force depends on the spin direction. It adds to the trapping force of the electric field of the Penning trap and leads to a spin dependence of the particles oscillation frequency which serves to monitor induced spin flips. In the experiments to determine the g-factor of a trapped particle spin flips are induced by a microwave field at the Larmor precession frequency $\nu_L = g\mu_B B/h$. All cases of interest so far dealt with particles where $J = S = \frac{1}{2}$. The magnetic field strength is calibrated by the cyclotron frequency $\nu_c = qB/(2\pi M)$ of the particle with charge q and mass M. The g-factor is then determined by the ratio of the two measured frequencies and the charge-to-mass ratio of the electron to the particle under investigation:

$$g = 2\frac{\nu_L}{\nu_C}\frac{qm}{eM}. \tag{4}$$

In this article we summarize the present status of our knowledge of the electrons g-factor. It serves as test of quantum electrodynamics for free and bound electrons and as test of fundamental symmetries under charge, space, and time reversal. All relevant experiments are performed on charged particles confined in Penning ion traps. Therefore we start our discussion with a brief description of this device and related techniques for single particle operation.

2 The Penning trap

In the ideal Penning trap [12, 13], a homogeneous magnetic field is superimposed to an electrostatic quadrupole potential. In good approximation this potential can be created by a ring electrode and two endcaps of hyperbolical shape as shown in Fig. 1. A voltage U_0 applied between the ring and endcaps creates a potential

$$\Phi = U_0\frac{x^2 + y^2 - 2z^2}{r_0^2 + 2z_0^2}. \tag{5}$$

r_0 is the ring radius and $2z_0$ the minimal distance between the endcaps. The square dependence of the potential on the coordinates leads to linear forces on a

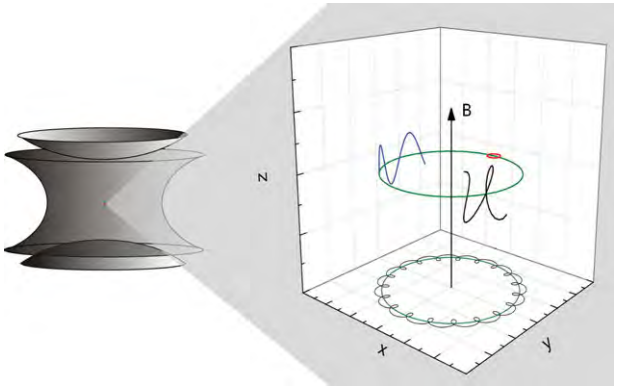

Figure 1 Hyperbolical Penning trap and trajectory of a single charged particle. For details see text.

charged particle inside the device. While axial confinement is provided by a properly chosen sign of U_0, the radial force leads to particle loss. This is circumvented by a magnetic field B oriented along the z-axis of the trap. The equations of motion of a single particle of charge q and mass M in the Penning trap can be solved analytically. The result is a superposition of three uncoupled harmonic oscillations, the axial, the perturbed cyclotron, and the magnetron motion with respective frequencies ν_z, ν_+, and ν_-:

$$\nu_z = \frac{1}{2\pi}\sqrt{\frac{qU_0}{Md^2}} \tag{6}$$

$$\nu_\pm = \frac{\nu_c}{2} \pm \sqrt{\frac{\nu_c^2}{4} - \frac{\nu_z^2}{2}}. \tag{7}$$

Here, $d^2 = (z_0^2 + r_0^2/2)/2$ is a geometrical factor that describes the dimension of the trap. Some useful relations between these frequencies are:

$$\nu_+ + \nu_- = \nu_c \qquad 2\nu_+\nu_- = \nu_z^2 \qquad \nu_+^2 + \nu_-^2 + \nu_z^2 = \nu_c^2.$$

The latter equation is known as "invariance theorem" [14]. It holds also when the trap potential deviates from the ideal form by a tilt of the magnetic field direction with respect to the trap's axis or by an ellipticity of the trap's electrodes, while the individual frequencies are shifted.

Typically we have a hierarchy of frequencies $\nu_+ \gg \nu_z \gg \nu_-$. A stability criterion follows from requirement that the expression in Eq. (7) has to evaluate to a real number: $\nu_c^2 > 2\nu_z^2$ or equivalently $U_0 < \frac{qB^2}{2Md^2}$.

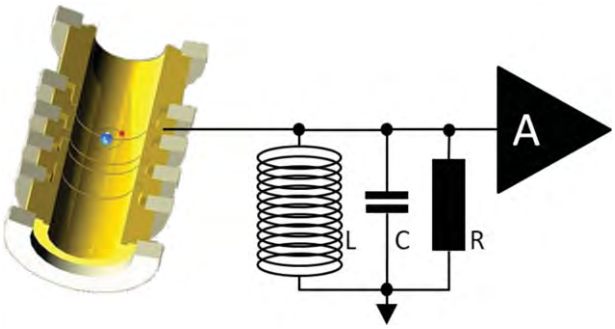

Figure 2 Schematic of single particle detection in a cylindrical Penning trap. The trap is represented by five cylindrical electrodes. The resonator is a parallel tank circuit consisting of an inductance L, an effective resistance R_p and a parasitic capacitance C_p. The signal is coupled to a cryogenic amplifier.

2.1 Trapped particle detection

Trapped particles can be detected both destructively and non-destructively. For the destructive detection they are extracted from the trap and counted in a particle detector. This method is being used successfully in precision mass spectrometry using Penning traps [15, 16]. Non-destructive detection can be realized either by laser-induced fluorescence when the particle has a suitable [17] energy level scheme, or by the image currents induced in the trap electrodes by the ion's oscillation [18–21]. Since this method is applied in all experiments discussed below, we will exclusively consider it here.

We take the axial motion as example. The induced image charge in the endcap electrodes generates a current between any two electrodes. An inductance L, which connects one electrode to ground as shown in Fig. 2, forms a resonant circuit together with a parasitic capacitance C and the effective damping resistance R_p. The current through the circuit increases the noise amplitude across the impedance at the ion's oscillation frequency. When the thermal noise of the impedance is kept sufficiently small by cooling to low temperatures, a Fourier analysis of the noise spectrum exhibits a maximum at the ion's oscillation frequency. Ideally, the amplifier exerts negligible back-action onto the resonant circuit. In practice, recent developments have yielded amplifier systems that cut down the undesired noise current leaking from the primary transistor stage largely and which feature a noise voltage of only 400 pV/$\sqrt{\text{Hz}}$. Combined with superconducting tank circuits, which can reach Q-values in excess of 80,000, equivalent to a parallel resistance of more than $R_p > 1\ G\Omega$ [22, 23], these amplifiers allow to sample the thermal noise of the tank circuit with excellent signal-to-noise ratio.

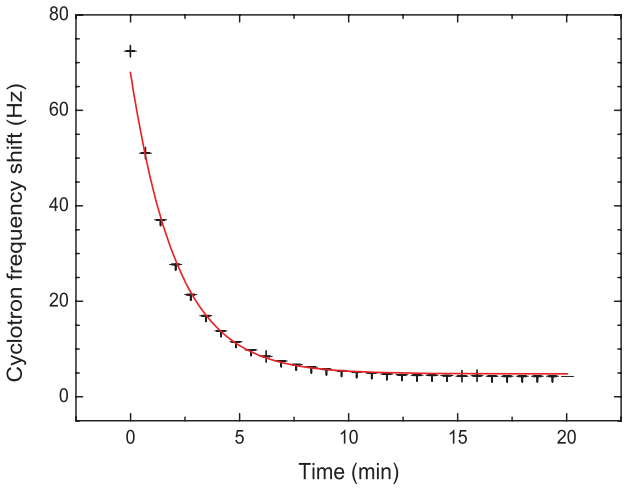

Figure 3 Exponential energy loss of the perturbed cyclotron oscillation by resistive cooling monitored by the decreasing magnetic field seen by the ion when it moves closer to the trap center. The solid line is an exponential fit to the cyclotron frequency evolution.

2.2 Ion cooling

The detection circuit serves also for ion cooling: When the ion's oscillation frequency is kept continuously in resonance with the circuit by adjustment of the trapping voltage the induced image currents raise the circuit's temperature. The excess energy is dissipated to the environment until thermal equilibrium between the ion and the circuit is reached. The time constant τ for exponential energy loss is given by [12]

$$\tau = \frac{MD^2}{\text{Re}(Z(\omega))\, q^2} \tag{8}$$

where $Z(\omega)$ is the impedance of the circuit and D is the effective electrode distance of the pick-up electrode. Figure 3 shows an example of cyclotron mode cooling of a single $^{28}Si^{13+}$ ion.

The presence of the trapped ion is then monitored by a minimum in the Fourier transform. This can be understood when we consider that the equivalent circuit of the oscillating ion is a series resonance circuit [18]. Since there is very little damping of the ion oscillation the quality factor of this circuit is very high. The series resonance shortcuts the thermal noise at the ion's oscillation frequency. Figure 4 shows a signal from a single trapped $^{28}Si^{13+}$ ion in thermal equilibrium with the detection circuit at 4 K. In a similar way the perturbed cyclotron oscillation can be detected when the traps ring electrode is divided into two segments and the detection circuit attached between the segments.

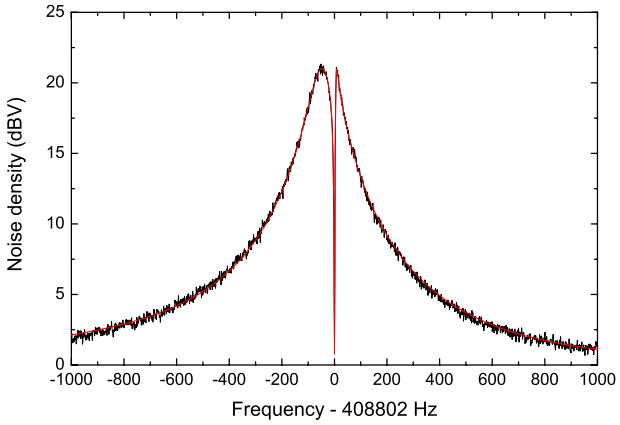

Figure 4 Axial signal from a single trapped $^{28}Si^{13+}$ ion in thermal equilibrium with a high quality detection circuit at a temperature of 4 K. The solid line is a least-squares fit to Eq. (9).

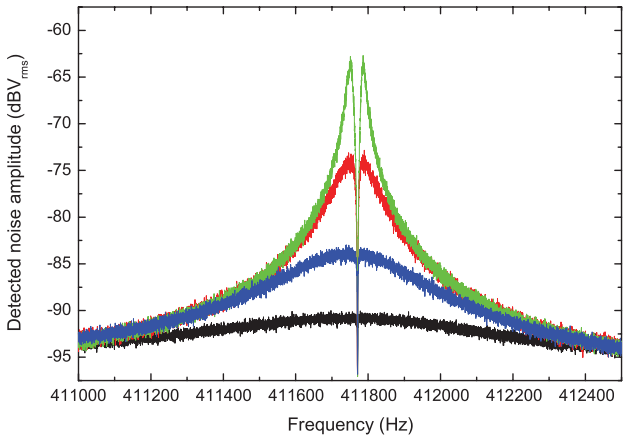

Figure 5 Detected noise amplitude of the tank circuit for various feedback strengths. The effective temperature of tank circuit is varied by more than a factor of 30.

Provided that the effective voltage noise of the cryogenic amplifier is significantly lower than the thermal noise of the tank circuit, it is possible to cool the ion below the temperature of the environment. To this end, part of the detected noise is suitably phase-shifted and fed back to the resonator, canceling a fraction of the thermal noise (see figure 5) [24]. As a result, both the effective resistance as well as the effective noise of the resonator can be adjusted arbitrarily, within the limits of the available signal-to-noise ratio. With this active noise feedback technique, sub-Kelvin temperatures can be reached [22].

2.3 Measurement of the oscillation frequencies

The dip in the noise spectrum of the axial resonator as shown in Fig. 4 is used to measure the axial oscillation frequency. The shape of the noise spectrum is proportional to the real part $Re(Z)$ of the impedance given by the superposition of the response function of the equivalent series circuit of the ion superimposed to the noise spectrum of the detection circuit:

$$Re(Z) = \frac{R_p(\omega l_p - \frac{1}{\omega c_p})^2}{R_p^2 + (\omega l_p - \frac{1}{\omega c_p})^2}, \tag{9}$$

with $l_p = mD^2/q^2$ and $c_p = (1/m\omega_z^2)(q^2/D^2)$ being the respective equivalent inductance and capacitance of the particle oscillating at ω_z. R_p is the effective resistance of the circuit at the resonance frequency ω_0, linked to its quality factor Q by $R_p = \omega_0 L Q$.

The width of the ion's axial resonance is determined by the coupling to the detection circuit and the harmonicity of the trap potential. It is given by [12]

$$\Delta\nu_z(N) = \frac{N}{2\pi}\frac{1}{\tau_z} = \frac{N}{2\pi}\frac{R_p}{m}\frac{q^2}{D^2} \tag{10}$$

and can be used as a measure of the number N of trapped particles [25]. The statistical uncertainty of the ion's axial oscillation frequency is of the order of a few 10 mHz in a total frequency of several 100 kHz in case of highly charged atomic ions.

As stated above, the perturbed cyclotron frequency can in principle be measured in a similar way when a high quality tuned circuit is attached between two segments of the ring electrode. Since tuning of the magnetic field to a value at which the cyclotron frequency matches the resonance of the circuit is difficult, the cyclotron detector can be fine-tuned with a varactor [26] diode. Alternatively, the perturbed cyclotron oscillation can be excited by a radiofrequency field of the respective frequency. This leads to an excess noise in the detector circuit, as shown in Fig. 6. Although the statistical uncertainty is only in the 10^{-10} range, the required oscillation amplitude causes a systematic shift of the line center when the magnetic field is not perfectly homogeneous and eventually from the relativistic mass increase. This problem can be circumvented when one couples the cyclotron mode to the axial one by an additional *rf* field at the difference frequency $\nu_{coupl} = \nu_+ - \nu_z$. The coupling [27] leads to a modulation of the axial oscillation amplitude with a frequency Ω, which depends on the amplitude of the coupling field:

$$\begin{aligned} z(t) &= z_0 \cos(\Omega t + \varphi)\sin(\omega_z t) \\ &= \frac{1}{2} z_0 \left[\sin(\omega_z + \Omega)t + \sin(\omega_z - \Omega)t\right]. \end{aligned} \tag{11}$$

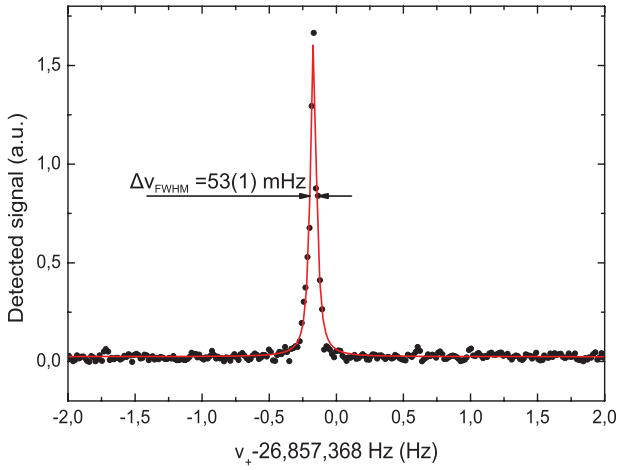

Figure 6 Fourier transform of the center part of the noise spectrum of a tuned circuit attached between two segments of a split ring electrode showing the increased noise amplitude at the perturbed cyclotron frequency of a single $^{28}Si^{13+}$ ion in a *B*-field of 3.76 T.

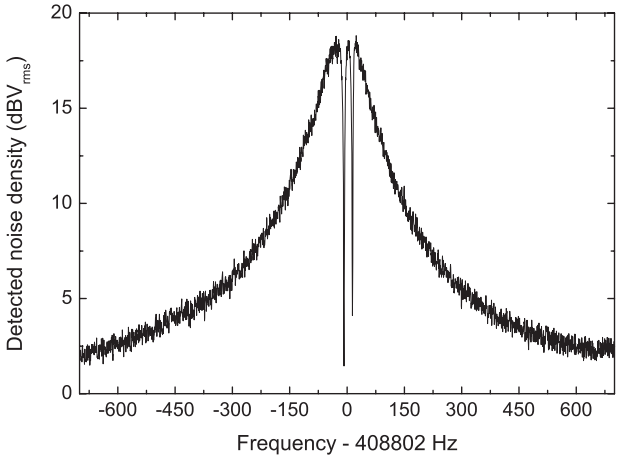

Figure 7 Split of the axial resonance. The double-dip structure is the result of the dressing of the axial mode with the cyclotron mode, using a radiofrequency excitation close to the sum frequency $\nu_+ + \nu_z$. From the frequencies of these two features, combined with the undressed axial and the coupling frequency, the cyclotron frequency can be deduced.

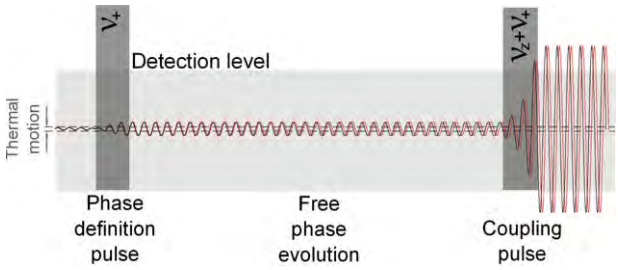

Figure 8 Timing sequence for phase sensitive measurement of the perturbed cyclotron frequency. The two wavetrains depict the evolution of the oscillation amplitude and phase during the measurement for two ions with slightly different cyclotron frequencies. The phase of the cyclotron motion is read indirectly via the phase of the axial motion after the coupling pulse.

It describes a symmetric splitting of the axial motion into two frequencies with a difference of 2Ω. In case of non-resonant coupling, i.e. when the coupling frequency is detuned by a frequency δ relative to the sideband frequency, the frequency components are given by

$$\omega_{r,l} = \omega_z - \delta/2 \pm \left[\delta^2 + A^2\right]^{1/2}, \tag{12}$$

where A is a measure in units of frequency for the strength of the coupling field amplitude. This behavior is in analogy to the avoided crossing of a near-resonantly driven quantum-mechanical two-level system [27]. Figure 7 shows the splitting of the motional frequency into two components. From a measurement of the split and unsplit frequencies the size of the detuning and thus the perturbed cyclotron frequency can be obtained. Similarly the magnetron frequency can be obtained through coupling to the axial motion.

The accuracy of the frequency measurements depends on a number of factors: The width of the axial resonance is determined by the coupling strength to the attached detection circuit, on the stability of the trapping voltage during the sampling time, and on the degree to which anharmonicities of the trap potential can be canceled.

The influence of voltage variations during the sampling time of the axial oscillation can be significantly reduced by detecting the cyclotron frequency directly rather than through the dressed axial frequencies. Simultaneously, the cyclotron energy can be kept small when using a novel method which allows to detect the phase of the cyclotron motion at energies below the detection threshold [28, 29]. The cyclotron oscillation is excited by a pulse, followed by a free oscillation period during which the phase evolves freely. After a given time the cyclotron oscillation is coupled to the axial one by a short pulse at their sum frequency. This pulse can be used to imprint the original phase of the cyclotron motion on the resulting axial motion, which then can be detected. Figure 8 illustrates the timing sequence. Because of the high signal amplitude this method reduces the time needed for the cyclotron measurement by more than one order of magnitude, reducing the uncertainty from instabilities of trap parameters tremendously. It has been applied recently in an experiment on $^{28}Si^{13+}$ [30].

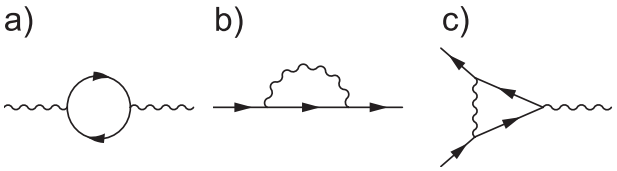

Figure 9 Basic Feynman diagrams. (a) vacuum polarization, (b) self energy, (c) vertex correction

The accuracy of the perturbed cyclotron frequency is of greatest importance for the precise determination of the free particle's cyclotron frequency as required for calibration of the magnetic field. Using the method mentioned above typical statistical uncertainties of a single measurement are in the 10^{-10} range. This requires, however, a temporal stability of the magnetic field in the same order of magnitude. Superconducting magnets as used in all *g*-factor experiments show variations of the magnetic field B of about $\delta B/B \simeq 10^{-9}$ per hour. Temperature and pressure stabilization can improve on this by more than one order of magnitude [31]. In any case it is mandatory to perform the frequency measurements as fast as possible in order to reduce uncertainties.

3 Theoretical background

3.1 The free electron/positron

The theory of quantum electrodynamics is based on the exchange of virtual photons between particles and fields. It can be represented by Feynman diagrams. The basic diagrams are shown in Fig. 9. From these one can construct higher orders by repetitive application. The evaluation of these diagrams for an electron in a magnetic field leads to a deviation of the *g*-factor from the Dirac value $g = 2$. The theory enables us to calculate the deviation as finite radiative corrections. The result can be represented by a series expansion with the fine structure constant as expansion parameter:

$$g/2 = 1 + C_2(\alpha/\pi) + C_4(\alpha/\pi)^2 + C_6(\alpha/\pi)^3 + C_8(\alpha/\pi)^4 + C_{10}(\alpha/\pi)^5 + ... \quad (13)$$

Each of the expansion coefficients C_n corresponds to the evaluation of a number of Feynman diagrams with n lepton-photon vertices. The number of contributing diagrams grows rapidly with the loop order, making calculation of the highest-order terms $n \geq 10$ a *tour de force*. Additionally, small contributions a_{hadronic} and a_{weak} from hadronic and weak interaction contribute to the *g*-factor. The most recent values of the coefficients C_n, taken from [32] are

$$\begin{aligned} C_2 &= 1/2 \\ C_4 &= -0.32847896557919378... \\ C_6 &= 1.181234016827\,(19) \\ C_8 &= -1.9144\,(35) \\ C_{10} &= 0.0\,(3.8) \\ a_{\text{hadronic}} &= 1.671\,(19) \cdot 10^{-12} \\ a_{\text{weak}} &= 0.030\,(1) \cdot 10^{-12}. \end{aligned} \quad (14)$$

The coefficients C_2, C_4 and C_6 have been calculated analytically while the values for C_8 [33] and C_{10} [34] have been obtained by numerical methods. a_{hadronic} has also been obtained by T. Kinoshita and M. Nio [34].

The most precise value of α, $\alpha^{-1} = 137.035\ 999\ 037\ (91)$, obtained largely independent of QED theory arises from photon recoil measurements [35] leading to a theoretical value for the *g*-factor anomaly $a_e = (g-2)/2$:

$$a_e(\text{theo}) = 0.001\,159\,652\,181\,13(84). \quad (15)$$

3.2 The single bound electron

For a single electron, bound to an atomic nucleus of charge Z, additional effects contribute to the *g*-factor. The Dirac equation in the Coulomb potential of a point-like nucleus of infinite mass can be solved analytically and leads to a *g*-factor [36]

$$g = \frac{2\left(1 + 2\sqrt{1-(Z\alpha)^2}\right)}{3}. \quad (16)$$

The fractional changes in g range from 10^{-7} for light nuclei to 10^{-3} for the heaviest ones.

The strong electric field which the electron experiences at the distance of the Bohr radius from the nucleus is by many orders of magnitude larger than available in any laboratory and needs modifications of the formalism of QED in order to account for such an environment. The corresponding Feynman graphs of first order in α, taking care of the binding potential, are shown in Figure 10. Formally, a similar expansion series as in the free electron case can be used for calculation. The coefficients C_i^b, however, now depend on Z:

$$g/2 = 1 + C_2^b[Z\alpha]\,(Z\alpha/\pi) + C_4^b[Z\alpha]\,(Z\alpha/\pi)^2 + C_6^b[Z\alpha]\,(Z\alpha/\pi)^3 + ... \quad (17)$$

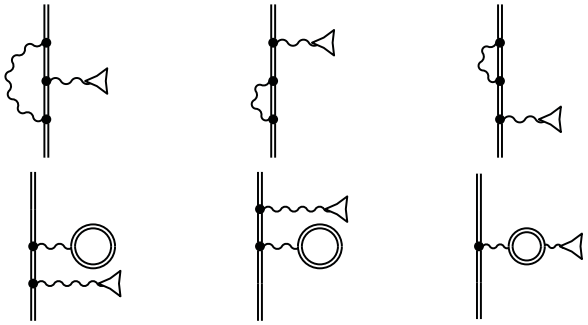

Figure 10 Feynman diagrams in first order in α for the bound electron. The double lines indicate bound states [37].

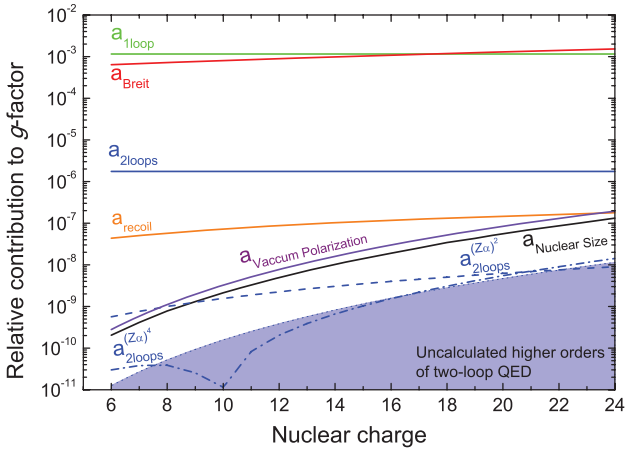

Figure 11 QED, nuclear size and recoil contributions to the g-factor bound in hydrogen-like ions for low numbers of the nuclear charge [40].

The new expansion parameter $(Z\alpha)$ is, at least for large Z, no longer small compared to unity and many more orders would have to be calculated in order to match the precision obtained in the free electron case. A summary of calculations of expansion coefficients and their results is given in [38].

More reasonable is a non-perturbative approach. The electron propagator as derived from the Dirac equation includes the full interaction with the binding potential of the nucleus in all orders of the parameter $(Z\alpha)$. The complex expression of the propagator, however, inhibits an analytical solution and requires numerical evaluation. So far, only the diagrams of first loop order have been evaluated in with this propagator, whereas the second order diagrams have been evaluated only in an expansion in orders of $(Z\alpha)$. The uncertainty arising from uncalculated contributions of higher order in the nuclear binding potential dominates the theoretical error budget.

In addition to the QED modification, nuclear size and structure as well as recoil corrections add to the g-factor. They have been calculated by several groups with uncertainties ranging from 10^{-12} for low-Z ions up to 10^{-5} for hydrogen-like uranium [39, 41, 42]. Figure 11 illustrates the size of all contributions for low numbers of the nuclear charge Z. Table 1 presents the complete theoretical results for selected examples which have been subject to experimental investigations.

4 Experiments

4.1 The free electron/positron

The first trap experiments to determine the g-factor of the free electron were performed at the University of Bonn in 1968 and 1969 [48, 49]. A cloud of about 10^5 electrons was used which were spin polarized by spin exchange collisions with a polarized sodium beam passing through the trap. For detection of microwave induced spin flips inelastic collisions with the sodium atoms were used. The small spin dependence of the inelastic collision cross section led to a modification of the

Table 1 Complete theoretical results for selected examples which have been subject to experimental investigations.

Contribution	$^{12}C^{5+}$ [43]	$^{16}O^{7+}$ [43]	$^{28}Si^{13+}$ [30]
Dirac Value	+1.998 721 354 39 (1)	+1.997 726 003 06 (2)	+1.993 023 571 6
Free QED	+0.002 319 304 37 (1)	+0.002 319 304 37 (1)	+0.002 319 304 37 (1)
Bound-state QED	+0.000 000 843 40 (3)	+0.000 001 594 38 (11)	+0.000 005 855 8 (17)
Finite nuclear size	+0.000 000 000 41	+0.000 000 001 55 (1)	+0.000 000 020 5
Nuclear recoil	+0.000 000 087 62	+0.000 000 116 97	+0.000 000 205 1 (1)
Theory total	+2.001 041 590 18 (3)	+2.000 047 020 32 (11)	+1.995 348 958 0 (17)

energy distribution of the electron cloud which was analyzed. The accuracy of these experiments was limited to $1.5 \cdot 10^{-8}$ in the *g*-factor by instabilities in the electron cloud produced by the Coulomb interaction between the electrons as well as by trap imperfections. Much higher precision was obtained in a series of experiments at the University of Washington using a single electron confined in a Penning trap. The trap used hyperbolical contours for ring and endcaps with compensation electrodes in between to minimize trap imperfections.

The key element to detect induced spin transitions was the development of the "continuous Stern-Gerlach effect" by H. Dehmelt [50]: When the magnetic field of the Penning trap is made inhomogeneous, the trapped particle having the magnetic moment μ_z experiences a force in the axial direction $F = \nabla(\mu_z B_z)$. This force adds or subtracts to the electric trapping force, depending on the spin direction and leads to a change in the axial oscillation frequency. This can be measured and serves to determine the spin orientation.

When the magnetic field inhomogeneity is symmetric around the trap center, e.g. by introducing a ferromagnetic ring in the center plane of the trap as shown in Figure 12, the magnetic field can be expanded in a series around the origin and reads in first order in the axial direction:

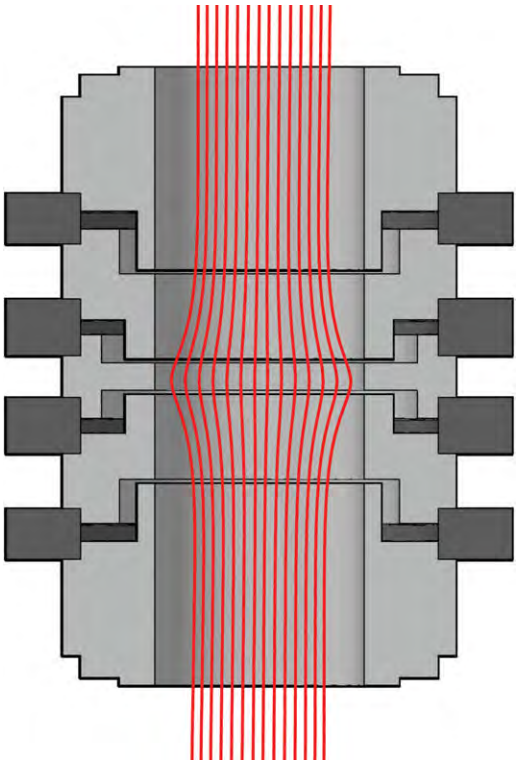

Figure 12 Magnetic field lines of a Penning trap when the ring electrodes is made from ferromagnetic material.

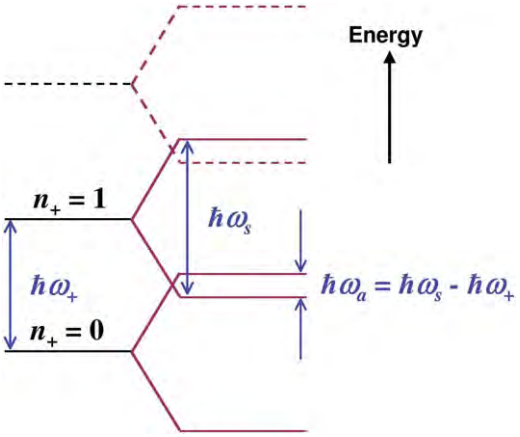

Figure 13 Lowest energy states of the perturbed cyclotron mode of an electron including the two spin states in a magnetic field.

$$B_z = B_0 + B_2 z^2. \tag{18}$$

In this case the difference in the axial frequency for the two spin directions is given by

$$\Delta\omega_z = \frac{2 B_2 \mu_z}{M\omega_z} \tag{19}$$

where M is the particles mass. In the case of the Washington experiment on free electrons one obtains with $B_2 = 120\,\mu\mathrm{T/mm}^2$ and $\omega_z \simeq 2\pi \cdot 60$ MHz a value of $\Delta\omega_z \simeq 2\pi \cdot 1$ Hz. In order to measure such a small frequency difference the trap parameters need to be extremely stable.

Spin flips were induced by microwaves around the Larmor precession frequency $\omega_L = g\mu_B B/\hbar$ (nominally 160 GHz at $B_z = 5$ T) introduced into the apparatus and the number of axial frequency jumps were recorded. These have a maximum around ω_L. B_z is calibrated by the cyclotron frequency of the electron $\omega_c = e/m\,B_z$ and the *g*-factor is determined through $g = 2\omega_L/\omega_c$.

A significant gain in precision was obtained by driving the so-called anomaly frequency $\omega_a = \omega_L - \omega_c$ at which the spin direction and the cyclotron energy are changed simultaneously, see Fig. 13.

The experiment was performed on electrons as well as on positrons, yielding for the *g*-factor anomaly *a*, defined as $a = (g-2)/2$, the values [51]:

$$a(e^-) = 1\,159\,652\,188.4(4.3) \cdot 10^{-12} \tag{20}$$

$$a(e^+) = 1\,159\,652\,187.9(4.3) \cdot 10^{-12}. \tag{21}$$

The main limitations in accuracy arose from the asymmetry of the line shape of the anomaly resonance due to the Boltzmann distribution of the electron oscillation amplitudes in the inhomogeneous magnetic field. Moreover shifts of the resonance frequency from the modification of the vacuum field by the trap electrodes were difficult to calculate considering the hyperbolic electrodes as a microwave cavity.

The experiment was significantly improved by G. Gabrielse and coworkers at Harvard who replaced the hyperbolical trap by a cylindrical one. Considering the trap as a microwave cavity this allowed better calculation of the electric field distribution and reduced the uncertainty arising from cavity shifts. Most important, however, was the reduction of the environmental temperature to below 100 mK. The electron loses energy from its cyclotron oscillation by synchrotron radiation. It has been shown that at equilibrium with the environment only the lowest quantum state of the motion is occupied [52]. Then any ambiguity from the Boltzmann distribution of the cyclotron mode energy is removed and the linewidth is significantly reduced. The most recent result of the experiment for the g-factor anomaly a is [53]

$$a = 1\,159\,652\,180.73\,(28) \cdot 10^{-12}. \tag{22}$$

This is in very good agreement to the theoretical value

$$a_{\text{theo}} = 1\,159\,652\,181.13\,(84) \cdot 10^{-12}. \tag{23}$$

mentioned above.

4.2 The electron bound in hydrogenlike ions

4.2.1 The cylindrical Penning trap

Experiments to determine the g-factor of the electron bound in hydrogen-like ions have been performed at the University of Mainz [63–65]. They follow similar principles as for the free electron's g-factor outlined in 3.1. However, in these experiments the precision of the determined g-factor would not benefit from a measurement of the anomaly frequency due to the large mismatch of the ion's cyclotron frequency and the electron's spin precession frequency. In order to compensate for that, a number of significant modifications have been introduced to meet the requirements for high-precision measurements on these systems.

The trap used in these experiments is a cylindrical five electrode trap [59], consisting of a central ring electrode, two endcaps, and guard electrodes placed between them (Fig. 14). The potential inside this trap with a voltage U applied between ring and endcaps [61] can be described

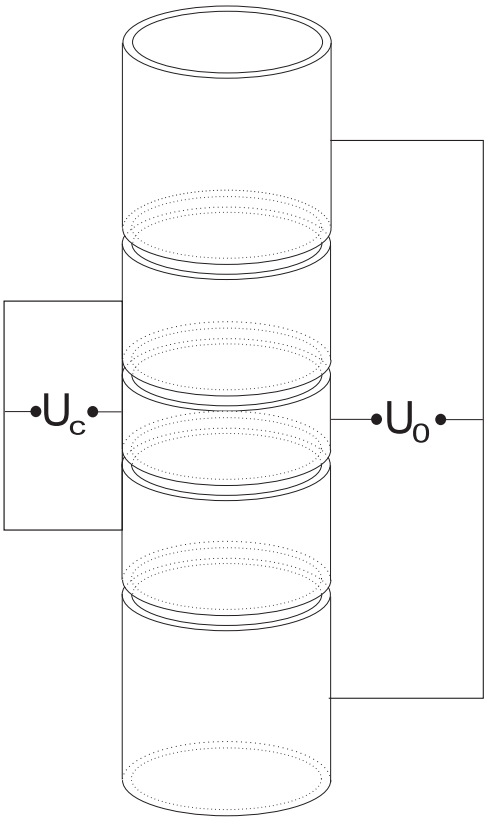

Figure 14 Cylindrical Penning trap with a set of compensation electrodes. In order to minimize electrostatic field anharmonicities, a voltage $U_c = T\,U_0$ is applied to these electrodes.

by a series expansion in which only even terms are nonzero because of the inherent rotational and mirror symmetry of the device.

$$\Phi(r,\theta) = \sum_{k\ \text{even}} C_k^{\text{el}} r^k P_k(\cos\theta) \tag{24}$$

Terms with $k > 2$ exhibit an undesired dependence of the ion's oscillation frequency on its amplitude. Thus it is of utmost importance to minimize those terms to avoid systematic frequency shifts. A rigorous calculation of the resulting frequency corrections was carried out by different authors [13, 59]. Using two additional electrodes placed between the ring and endcaps allows the application of an additional voltage U_c to these correction electrodes. In general it will be possible to choose a voltage $U_c \equiv TU_0$ such that $C_4^{\text{el}} = 0$. The dimensionless quantity T is called the tuning ratio. Moreover, in the process of trap optimization it is very convenient to make $C_2^{\text{el}} = C_2^{\text{el}}(U_0)$ independent of the correction voltage U_c and thus the tuning ratio T. Using the Green's function of conducting cylinders, it is possible to calculate the coefficients C_k^{el} for a given set of electrode dimensions.

After freely choosing the trap radius, it is generally possible to make $C_4^{el} = C_6^{el} = 0$ and simultaneously $\partial C_2^{el}/\partial U_c = 0$ by adjusting the ring- and correction electrode lengths and the tuning ratio T. The resulting trap configuration is called compensated and orthogonal [61].

The trap used for the experiments on the highly charged ions has an identical inner diameter of 7 mm for all electrodes. The central ring, the correction electrodes, and the endcaps have a length of 0.92 mm, 2.85 mm, and 6.8 mm, respectively, with gaps of 0.14 mm in between. The magnetic field is 3.76 T and we apply typically 7.5 V between ring and endcaps. For these parameters a single $^{28}Si^{13+}$ ion has (nominal) oscillation frequencies $\nu_+ = 27$ MHz, $\nu_z = 700$ kHz, and $\nu_- = 9$ kHz.

4.2.2 Triple-trap configuration

The detection of the bound electron's spin direction requires the use of an inhomogeneous magnetic field as outlined in 4.1. The inhomogeneity is provided when the central ring electrode is made from ferromagnetic material. We use nickel and obtain a magnetic field inhomogeneity of 10 mT/mm^2. Thermal fluctuations of the ion's oscillation amplitude in the inhomogeneous field [12] will lead to broadening and asymmetric line shapes of the motional as well as of the spin precession resonances and thus limit the precision of the *g*-factor determination. In order to circumvent this limitation we added a second trap with identical dimensions but without ferromagnetic material. We call the first trap, used to analyze the bound electrons spin direction, "Analysis Trap" (AT), and the second one "Precision Trap" (PT). The two traps are separated by five transport electrodes with a total length of 2 cm. By variation of the voltages applied to these electrodes the ion can be moved between the two traps.

A third trap, consisting of three electrodes, is added for charge breeding of the highly charged ion under investigation in an EBIT-like manner [62]. A sketch of this triple-trap configuration is shown in Fig. 15, a more detailed description is given in [56].

The triple trap and the attached electronics for ion detection is located in a sealed copper housing at the center of a superconducting magnet. The box is in thermal contact to a liquid helium bath. The low temperature serves for a vacuum below 10^{-16} mbar by cryopumping. This leads to a virtual absence of charge exchange collisions which would limit the availability of the ion under investigation. In fact storage times of many months have been obtained for single hydrogenlike ions up to $^{28}Si^{13+}$. The low temperature reduces also the thermal noise of the

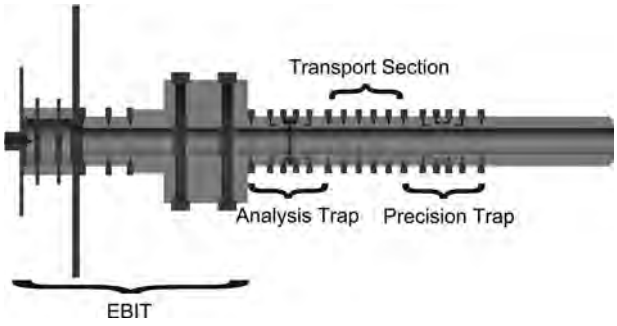

Figure 15 Sketch of the triple trap setup. The dark gray color indicates the ferromagnetic ring electrode of the AT. For details see text.

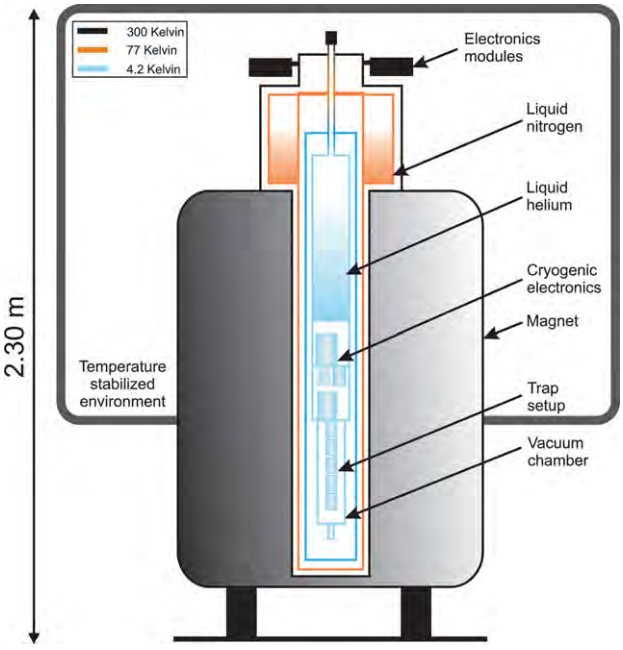

Figure 16 Sketch of the experimental setup, including the superconducting magnet, the cryogenic dewar vessel to cool the sealed vacuum chamber containing the triple trap and the cryogenic electronics.

amplifiers allowing single ion detection with a very good signal-to-noise ratio as demonstrated in Figures 4 and 6. Figure 16 shows the complete setup.

4.3 Experimental procedure

After preparation and cooling of a single ion its spin direction is determined in the AT as described in 4.1. Owing to the significantly higher mass of the ion compared to the free electron, the strength of the magnetic bottle has to be increased by more than two orders of magnitude in order to produce an appreciable shift of the axial frequency with the spin-state. In the triple-trap

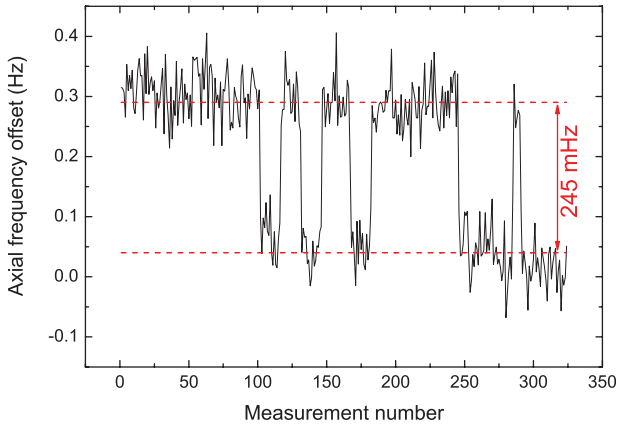

Figure 17 Axial frequency jumps upon microwave induced spin flips in the Analysis Trap.

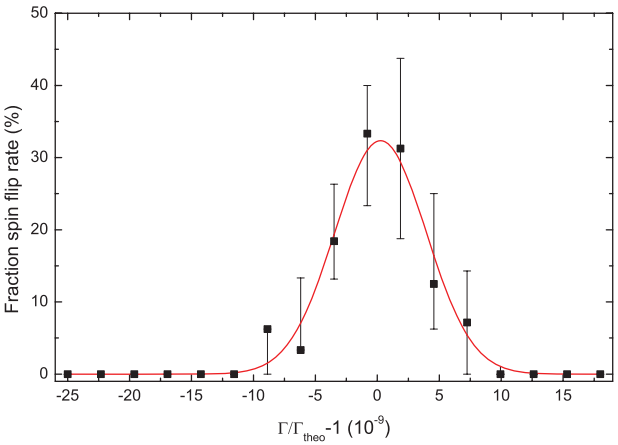

Figure 18 Example of the measured spin flip rate vs. different microwave frequencies, plotted here as the ratio $\Gamma \equiv (\nu_{MW}/\nu_C)$. The lineshape model is fitted directly to the observed events with a maximum-likelihood method. Only to guide the eye the events are binned in this plot. The FWHM of the resonance is $6 \cdot 10^{-9}$ and the statistical uncertainty of the resonance center is $7 \cdot 10^{-10}$.

configuration the nickel ring electrode of the Analysis Trap serves to produce an inhomogeneity of $B_2 = 10\ \mathrm{mT/mm^2}$. This leads for the case of $^{28}Si^{13+}$ to a difference in the axial oscillation frequency of 240 mHz in 411 kHz for the two spin directions. The detection of such small frequency differences produced by an induced spin flip requires an extremely stable voltage source and a superb constancy of the motional amplitudes. Figure 17 demonstrates that the observed frequency jumps are consistent with the expectation and can be unambiguously distinguished from noise.

After preparation in the AT the ion is transportet to the PT where a microwave field is used to induce spin flips during a given period of typically 90 s. It is transported back to the AT and by the same procedure as described above it is determined whether a spin flip has taken place. This sequence is repeated many times with variation of the microwave frequency near the expected Larmor resonance frequency of (nominally) 105 GHz. Simultaneously with the attempts to induce spin flips the cyclotron frequency is measured. The number of successful spin flips vs. the microwave frequency gives a resonance curve as shown Figure 18. We plot the ratio Γ of the microwave frequency and the cyclotron frequency as abcissa. Γ is independent of magnetic field fluctuations in first order. The g-factor is determined from the center frequency ν_L of this resonance using the cyclotron frequency ν_C for B-field calibration. With $h\nu_L = g\mu_B B$ and $h\nu_C = q\,B/M$ we get

$$g = 2\frac{\nu_L}{\nu_C}\frac{q}{e}\frac{m_e}{M} = 2\Gamma_0\frac{q}{e}\frac{m_e}{M}. \tag{25}$$

From Eq. (25) we obtain the g-factor of the bound electron taking the mass of the electron and of the ion under investigation from the literature.

Table 2 Experimental and theoretical g-factors for different hydrogen-like ions. The first error for g_{exp} is the combined statistical and systematical uncertainty, the second one is the uncertainty of the electron mass taking its value at the time of the measurement.

Ion	g_{exp}	g_{th}	$\mathrm{Ref_{exp}}$	$\mathrm{Ref_{th}}$
$^{12}C^{5+}$	2.001 041 596 4 (10)(44)	2.001 041 590 52 (11)	[63]	
$^{16}O^{7+}$	2.000 047 025 4 (15)(44)	2.000 047 021 28 (35)	[64]	see table 1
$^{28}Si^{13+}$	1.995 348 959 10 (9) (80)	1.995 348 958 0 (17)	[30]	

4.4 Results

Experiments have been performed on 3 different hydrogen-like ions, $^{12}C^{5+}$ [63], $^{16}O^{7+}$ [64], and $^{28}Si^{13+}$ [65]. The results are listed in Table 2. The experimental values for the measured frequency ratio $\Gamma_0 = \nu_L/\nu_C$ are subject to systematical shifts and uncertainties. They are dominated by a shift of the perturbed cyclotron frequency from image charges induced in the trap electrodes by the oscillating ion. A calculation for a cylindrical trap geometry [30] yields

$$\frac{\delta\nu_+}{\nu_+} = \frac{1}{4\pi\epsilon_0}\frac{M}{2a^3B^2} \tag{26}$$

where a is the radius of the ring electrode. It changes ν_+ by $6.6 \cdot 10^{-10}$ for $^{28}Si^{13+}$ with an estimated uncertainty of 5% of this value. Taking the slits between the

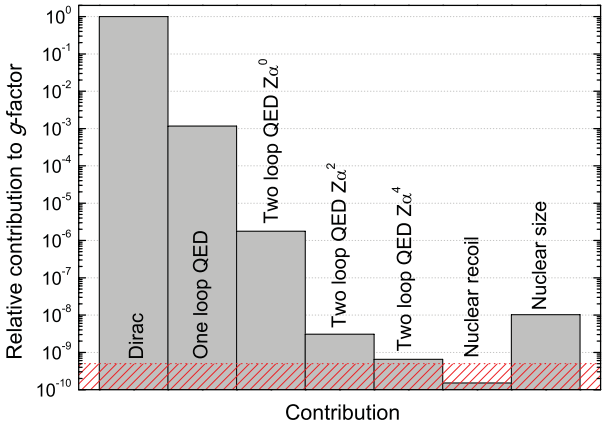

Figure 19 Size of different contributions to the g-factor of the electron bound in hydrogen-like $^{28}Si^{13+}$. The experimental uncertainty is indicated by the dotted line (data from [28]).

individual electrodes into account decreases this correction by about 10% Other potential shifts such as line asymmetries caused by the residual magnetic field inhomogeneity in the precision trap or relativistic shifts have been considered and found to be much smaller. The final results are listed in Table 2. They all agree with the theoretical predictions.

The importance of the results as test of BS-QED calculations is illustrated in Figure 19 where sizes of different contributions are plotted and compared to the experimentally achieved uncertainty for the case of $^{28}Si^{13+}$. Here, the 2-loop contributions of order $(Z\alpha)^4$ become visible for the first time. An upper bound of even higher orders in $(Z\alpha)$, $g_{2L}^{(ho)}$, can be extracted using the tabulated value of the mean squares radius of ^{28}Si for the calculation of the nuclear size correction, leading to $g_{2L}^{(ho)} = 0.71\,(1.1)\cdot 10^{-9}$ [65].

An extension of these experiments to lithiumlike systems introduces the relativistic interaction of the valence electron with the 1s core. A comparison of the prediction with the experimentally determined value then yields a stringent test of the quantumelectrodynamical calculations in the three electron system [66]. Provided that the theoretical evaluation can appropriately account for the three electron interaction, the g-factor of the valence electron can be used to extract information about the size and the structure of the nucleus, which is an important prerequisite for the interpretation of results in heavy, hydrogenlike ions.

5 Determination of fundamental constants

As seen from Table 2, the uncertainties in $g_{\rm exp}$ and $g_{\rm th}$ in case of C^{5+} and O^{7+} are dominated by the finite knowledge of the electron mass. Trust in the experimental and the theoretical values for the g-factor as well as in the determination of the respective ion masses allows adjusting the electron mass in order to have agreement between both results. Using the available data of the theory at the time of the measurements it has led to an electron mass (in atomic units) of [67]

$$m = 5.485\,799\,084\,6\,(22)\cdot 10^{-4}\,u. \tag{27}$$

This is a factor of 6 more precise than the previous most accurate value based on comparison of the cyclotron frequencies of both particles in a Penning trap [68]. Higher accuracy in the electron mass using future g-factor determinations is at hand since by now the theoretical values for C^{5+} and O^{7+} have reduced error bars by calculation of higher order BS-QED contributions [43] and technical progress in the g-factor experiment have been successfully tested in case of Si^{13+}. We expect a reduction of the present error bar in m_e by at least one order of magnitude.

The presently achieved uncertainty and prospects for future improvements may also allow for a determination of the fine structure constant α. The largest α-dependent contribution to the bound electron g-factor comes from the solution of the Dirac equation as given in Eq. (16). Assuming that all other contributions are small and sufficiently well tested, an uncertainty δg in the g-factor determination will lead to an uncertainty $\delta\alpha$ in the fine structure constant of

$$\frac{\delta\alpha}{\alpha} \approx \frac{1}{(Z\alpha)^2}\delta g. \tag{28}$$

This might indicate to use a hydrogen-like system with high Z in order to achieve the highest accuracy. However, as evident from Figure 11 the nuclear size and structure corrections increase rapidly in the high-Z region and their accurate theoretical calculations is very difficult. To this end, Shabaev *et al.* [69] have pointed out that by a comparison of g-factors in H- and B-like ions in high-Z systems the nuclear structure corrections can be determined with sufficient accuracy making a precise determination of α possible, provided that the theoretical prediction of the g-factor of the B-like system can be pushed to accuracies comparable to the H-like system.

The presently most accurate values of the fine structure constant α come from the g-factor of the free electron [53] and from photon recoil measurements [35] which have quoted uncertainties of 0.8 ppb and 2.4 ppb, respectively. In order to achieve a similar uncertainty by g-factor measurements of bound electron systems the experimentally required precision in case of Pb^{81+} is of the order of $8\cdot 10^{-11}$. This is within reach using

technical improvements which are being developed in our laboratory. However, to improve the theoretical prediction of the g-factors of both H- and B-like heavy ions is a considerable challenge.

6 Implications for fundamental symmetries

CPT invariance implies that the magnetic moments of particles and antiparticles are identical. This has been confirmed to 2 parts in 10^{-12} in a comparison of the g-factors of electron and positron [51].

A similar test in a hadronic system may be performed by the g-factors of proton and antiproton. The magnetic moment of the proton is presently known to $1 \cdot 10^{-8}$ [70]. Using similar experimental methods as described for hydrogen-like ions for g-factor determination of the proton an improvement by more than one order of magnitude seems possible. The small size of the proton's magnetic moment, however, makes it technically more challenging. Experiments are under way at the University of Mainz [71] and at Harvard University [72], as well as at CERN for the antiproton [73, 74]. Both have very recently produced first data and an improvement of the relative precision to the anticipated 10^{-9} is foreseeable for the close future. First single spinflips of a single proton have been observed by both teams [75, 76].

A future extension of these experiments to antiprotons will require injection of low-energy antiprotons from an accelerator, similar as performed in antihydrogen experiments at CERN. It is planned to have a low-energy antiproton facility at GSI/Darmstadt [77] where such experiments may be performed.

7 Nuclear physics implications

Assuming that the BS-QED contributions to the g-factor of hydrogen-like ions are tested with sufficient accuracy the remaining uncertainty concerns the nuclear size and structure effects. Their calculation requires the knowledge of the root-mean-square nuclear radius $\langle r^2 \rangle^{1/2}$. A comparison of the experimental and theoretical g-factor can then be used to determine $\langle r^2 \rangle^{1/2}$. This has been tested in $^{28}Si^{13+}$ [28]. Although the result of $\langle r^2 \rangle^{1/2} = 3.18\ (15)$ fm is much less accurate than the value obtained from scattering experiments, $\langle r^2 \rangle^{1/2} = 3.1223\ (24)$ fm [78], it can be considered as proof-of-principle to demonstrate the possibility of nuclear radius determination. Even more detailed insight into the structure of the nucleus becomes accessible through the detailed calculations of nuclear shape effects on the g-factor of hydrogen-like ions, which have been performed recently [42].

8 Future experiments

The method of g-factor determination described above can in principle be applied to any charged particle without loss of accuracy. Since the bound-state QED contributions as well as the nuclear size and structure corrections increase with the nuclear charge it is obvious that high-Z hydrogen-like ions will provide a more sensitive test of the corresponding calculations. This calls for theoretical consideration of higher order BS-QED terms. Experimentally a limitation of the present setup is given by the fact that the production of high-Z ions by electron-impact ionization requires electron energies of many keV, which represents a technical problem. Thus injection of ions from outside will be required. Corresponding experiments are planned at the heavy ion facility GSI where highly charged ions up to hydrogen-like uranium are produced and confined in a storage ring at high energies. It is planned to extract these ions, slow them down and inject then into a Penning trap for further investigation. A description of this HITRAP project can be found in [79].

Apart from hydrogen-like ions the investigation of lithium-like ions is of interest. As pointed out by Shabaev *et al.* [80] the difference of the g-factors in a H- and Li-like isotope reduces the uncertainty in the nuclear structure contribution and the BS-QED part can be tested more rigorously. However, the relativistic interaction of the valence electron with the 1s core plays a role. A comparison of the prediction [81, 82] with the experimentally determined value then yields a stringent test of the quantum-electrodynamic calculations in the three electron system [66]. Provided that the theoretical evaluation can appropriately account for the three electron interaction, the g-factor of the valence electron can be used to extract important information about the size and the structure of the nucleus, which is an important prerequisite for the interpretation of results in heavy, hydrogen-like ions.

The experiments so far are restricted to isotopes without nuclear spin I. When applied to odd isotopes having a nuclear magnetic moment the method described in this article can be applied to determine the g_F-factor

$$g_F = g_S \frac{F(F+1) - I(I+1) + S(S+1)}{2F(F+1)} + g_I \frac{F(F+1) + I(I+1) - S(S+1)}{2F(F+1)} \tag{29}$$

The g_S-factor can be taken from even isotopes since the isotopic dependence is small [83]. Then the nuclear g_I-factor can be extracted. The shielding of the nuclear magnetic moment has been calculated including relativistic, nuclear, and QED effects [84]. Comparison of the g_I-factors in H-like ions with those obtained from neutral atoms or singly charged ions would test for the first time calculations of diamagnetic shielding factors in multi-electron systems. This would resolve discrepancies between different calculations of this quantity appearing in the literature [85].

An alternative method of *g*-factor determinations in high-Z hydrogen-like ion has been proposed by W. Quint *et al.* [86]. The hyperfine splitting of several of those systems is in the optical region allowing laser induced transitions. In the magnetic field of a Penning trap the electronic and nuclear *g*-factors as well as the hyperfine coupling constants can be derived from the transition frequencies.

Acknowledgement. This work was supported by the Max-Planck Society, the Helmholtz Alliance HA216/EMMI and by the EU (ERC Grant No. 290870 - MEFUCO).

Key words. *g*-factor, Penning trap, highly charged ions, quantum electrodynamics.

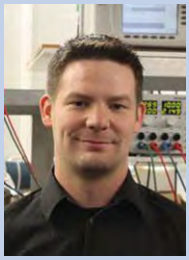

Sven Sturm has worked at ISOLDE/CERN for his diploma thesis. He then joined the group of Klaus Blaum at the University of Mainz, where he performed the g-factor experiment for highly-charged ions. After graduating in 2012, he moved to the Max-Planck Institute for Nuclear Physics in Heidelberg as a group leader where he is currently setting up a next-generation g-factor experiment.

Günter Werth graduated in 1969 at the University in Bonn. After a postdoctoral stay at the NASA Goddard Space Flight Center from 1972–1973 he returned to Germany for his habilitation. As professor at the University of Mainz he led a group for precision measurements in traps and pioneered amongst others the g-factor determination of highly-charged ions. He retired in 2004.

Klaus Blaum graduated in 2000 at the University in Mainz. After a postdoctoral position at GSI, Darmstadt, he went to CERN to lead the ISOLTRAP experiment. In 2004 he became head of a Helmholtz Research Group in Mainz. Since 2007 he is director at the Max-Planck Institute for Nuclear Physics in Heidelberg and head of the Cooled and Stored Ions Division. His main research focus is on precision measurements of atomic and nuclear ground state properties as well as tests of fundamental symmetries using Penning traps.

References

[1] G. E. Uhlenbeck and S. Goudsmit, Naturwissenschaften **13**, 953 (1925).
[2] W. Gerlach and O. Stern, Z. Phys. **9**, 349 and 353 (1922).
[3] P. A. M. Dirac, Proc. R. Soc. Lond. A **117**, (778), 610 (1928).
[4] I. Rabi *et al.*, Phys. Rev. **53**, 318 (1938).
[5] W. W. Lamb and R. C. Retherford, Phys. Rev. **79**, 549 (1950).
[6] J. Schwinger, Phys. Rev. **73**, 416 (1948).
[7] G. Gabrielse *et al.*, Phys. Rev. Lett. **97**, 030802 (2006).
[8] G. Gabrielse *et al.*, Phys. Rev. Lett. **99**, 039902(E) (2007).
[9] N. Bohr in: Collected Works of Niels Bohr, Vol. 6: Foundations of Quantum Physics I (1926-1932), edited by J. Kalckar (North-Holland, Amsterdam, 1985), p. 333.
[10] W. Pauli in: Handbuch der Physik, Bd.5, edited by S. Flügge (Springer, Berlin, Göttingen and Heidelberg, 1958), p. 167.
[11] H. Dehmelt, Proc. Natl. Acad. Sci. USA. Vol. 83, pp. 3074–3077, May 1986.
[12] L. S. Brown and G. Gabrielse, Rev. Mod. Phys. **58**, 233–311 (1986).
[13] F. G. Major, V. Gheorghe, and G. Werth, Charged Particle Traps, (Springer, Heidelberg, 2005).
[14] L. S. Brown and G. Gabrielse, Phys. Rev. A **25**, 2423 (1982).
[15] K. Blaum, Phys. Rep. **425**, 1 (2006).
[16] K. Blaum, Yu. N. Novikov, and G. Werth, Contemp. Phys. **51**, 149 (2010).
[17] R. Ifflaender and G. Werth, Metrologia **13**, 167–170 (1977).
[18] D. J. Wineland and H. Dehmelt, J. Appl. Phys. **46**, 919–930 (1975).
[19] W. M. Itano *et al.*, Physica Scripta. **T59**, 106–120, (1995).
[20] S. R. Jefferts *et al.*, Rev. Sci. Instr. **64**, 737 (1993).

[21] J. Ketelaer *et al.*, Eur. Phys. J. **42**, 311 (2009).
[22] S. Sturm, Doctoral dissertation, University of Mainz, Germany (2012).
[23] A. Mooser, Unpublished doctoral dissertation, University of Mainz, Germany.
[24] B. D'Urso *et al.*, Phys. Rev. Lett. **90**, 4 (2003).
[25] X. Feng, M. Charlton, M. Holzscheiter, R. A. Lewis, and Y. Yamazaki, J. Appl. Phys. **79**, 1 (1996).
[26] S. Ulmer *et al.*, Nucl. Instr. Meth. A **705**, 55–60 (2012).
[27] E. Cornell *et al.*, Phys. Rev. A **41**, 312–316 (1990).
[28] S. Sturm, A. Wagner, B. Schabinger, and K. Blaum, Phys. Rev. Lett. **107**, 143003 (2011).
[29] S. Stahl *et al.*, J. Phys. B: At. Mol. Opt. Phys. **38** 297(2005).
[30] S. Sturm, A. Wagner, M. Kretzschmar, W. Quint, G. Werth, and K. Blaum, Phys. Rev. A **87**, 030501 (2013).
[31] R. van Dyck *et al.*, Rev. Sci. Instr. **70**, 1665–1671 (1999).
[32] M. Passera, Phys. Rev. D **75**, 013002 (2007).
[33] T. Aoyama, M. Hayakawa, T. Kinoshita, and M. Nio, Phys. Rev. Lett. **99**, 110406 (2007).
[34] T. Kinoshita and M. Nio, Phys. Rev. D **73**, 013003 (2006).
[35] R. Bouchendira, P. Cladé, S. Guellati-Khélifa, F. Nez, and F. Biraben, Phys. Rev. Lett. **106**, 080801 (2011).
[36] G. Breit, Nature **122**, 649 (1928).
[37] T. Beier, Phys. Rep. **339**, 2 (2000).
[38] P. J. Mohr, B. N. Taylor, and D. B. Newell, Rev. Mod. Phys. **80**, 633 (2006).
[39] V. M. Shabaev and V. Yerokhin, Phys. Rev. Lett. **88**, 091801 (2002).
[40] J. Zatorski, Z. Harman, and C. H. Keitel, priv. comm. (2010).
[41] U. Jentschura, A. Czarnecki, K. Pachucki, and V. A. Yerokhin, Int. J. Mass Spectr. **251**, 102 (2006).
[42] J. Zatorski, N. S. Oreshkina, Ch. Keitel, and Z. Harman, Phys. Rev. Lett. **108**, 063005 (2012).
[43] K. Pachucki, A. Czarnecki, U. Jentschura, and V. A. Yerokhin, Phys. Rev. A **72**, 022108 (2005).
[44] P. F. Winkler, D. Kleppner, T. Myint, and F. G. Walther, Phys. Rev. A **5**, 83 (1972).
[45] T. Pask, D. Barna, A. Dax, R. S. Hayano, M. Hori, D. Horváth, S. Friedreich, B. Juhász, O. Massiczek, N. Ono, A. Sótér, and E. Widmann, Phys. Lett. B **678**, 55 (2009).
[46] R. Bluhm, V. A. Kostelecki, and N. Russell, Phys. Rev. Lett. **79**, 1432 (1997).
[47] R. Bluhm, V. A. Kostelecki, and N. Russell, Phys. Rev. D **57**, 3932 (1998).
[48] G. Graeff, F. G. Major, R. Roeder, and G. Werth, Phys. Rev. Lett. **21**, 340 (1968).
[49] G. Graeff, E. Klempt, and G. Werth, Z. Phys. **5**, 201 (1969).
[50] H. Dehmelt, Proc. Natl. Acad. Sci. USA. Vol. 83, pp. 2291–2294, April 1986.
[51] R. S. van Dyck Jr., H. Dehmelt, and P. Schwinberg, Phys. Rev. Lett. **59**, 26 (1987).
[52] S. Peil and G. Gabrielse, Phys. Rev. Lett. **83**, 1288 (1999).
[53] D. Hanneke, S. Fogwell, and G. Gabrielse, Phys. Rev. Lett. **100**, 120801 (2008).
[54] M. Vogel, J. Alonso, S. Djekic, H.-J. Kluge, W. Quint, S. Stahl, J. Verdú, and G. Werth, Nucl. Instrum. Meth. B **235**, 7 (2005).
[55] K. Blaum, H. Kracke, S. Kreim, A. Mooser, C. Mrozik, W. Quint, C. C. Rodegheri, B. Schabinger, S. Sturm, S. Ulmer, A. Wagner, J. Walz, and G. Werth, J. Phys. B **42**, 154021 (2009).
[56] B. Schabinger, S. Sturm, A. Wagner, J. Alonso, W. Quint, G. Werth, and K. Blaum, Eur. Phys. J. D **66**, 71 (2012).
[57] G. Gabrielse *et al.*, Int. J. Mass Spectrom. Ion Processes **88**, 319–332 (1989).
[58] J. L. Verdú *et al.*, New J. Phys. **10**, 23 (2008).
[59] L. Brown and G. Gabrielse, Rev. Mod. Phys. **58**, 233 (1986).
[60] M. Kretzschmar, Phys. Scr. **46**, 544 (1992).
[61] J. Tan and G. Gabrielse, Appl. Phys. Lett. **55**, 2144 (1989).
[62] J. Alonso, K. Blaum, S. Djekic, H.-J. Kluge, W. Quint, B. Schabinger, S. Stahl, J. Verdú, M. Vogel, and G. Werth, Rev. Sci. Instrum. **77**, 03A901 (2006).
[63] H. Häffner, T. Beier, N. Hermanspahn, H.-J. Kluge, W. Quint, S. Stahl, J. Verdú, and G. Werth, Phys. Rev. Lett. **85**, 5308 (2000).
[64] J. Verdú, S. Djekić, S. Stahl, T. Valenzuela, M. Vogel, G. Werth, T. Beier, H.-J. Kluge, and W. Quint, Phys. Rev. Lett. **92**, 093002 (2004).
[65] S. Sturm, A. Wagner, B. Schabinger, J. Zatorski, Z. Harman, W. Quint, G. Werth, Ch. Keitel, and K. Blaum, Phys. Rev. Lett. **107**, 023002 (2011).
[66] A. Wagner, S. Sturm, F. Köhler, D. A. Glazov, A. V. Volotka, G. Plunien, W. Quint, G. Werth, V. M. Shabaev, and K. Blaum, Phys. Rev. Lett. **110**, 033003 (2013).
[67] P. J. Mohr, B. N. Taylor, and D. B. Newell (2011), "The 2010 CODATA Recommended Values of the Fundamental Physical Constants".
[68] D. L. Farnham, R. S. Van Dyck Jr., and P. B. Schwinberg, Phys. Rev. Lett. **75**, 3598 (1995).
[69] V. M. Shabaev, D. A. Glazov, N. S. Oreshkina, A. V. Volotka, G. Plunien, H.-J. Kluge, and W. Quint, Phys. Rev. Lett. **96**, 253002 (2006).
[70] P. Winkler, D. Kleppner, T. Myint, and F. Walther, Phys. Rev. A **5**, 83 (1972).
[71] S. Ulmer, C. C. Rodegheri, K. Blaum, H. Kracke, A. Mooser, and W. Quint, and J. Walz, Phys. Rev. Lett. **106**, 253001 (2011).
[72] J. DiSciacca and G. Gabrielse, Phys. Rev. Lett. **108**, 153001 (2012).
[73] S. Ulmer, Y. Yamazaki, C. Smorra, K. Blaum, K. Franke, Y. Matsuda, H. Nagahama, W. Quint, J. Walz, A. Mooser G. Schneider, CERN-SPSC-2013-002 / SPSC-TDR-002 (2013).
[74] J. DiSciacca, M. Marshall, K. Marable, G. Gabrielse, S. Ettenauer, E. Tardiff, R. Kalra, D. W. Fitzakerley, M. C. George, E. A. Hessels, C. H. Storry, M. Weel, D. Grzonka, W. Oelert, and T. Sefzick, arXiv:1301.6310v2 (2013).

[75] A. Mooser, H. Kracke, K. Blaum, S. A. Bräuninger, K. Franke, C. Leiteritz, W. Quint, C. C. Rodegheri, S. Ulmer, and J. Walz, accepted for publication in Phys. Rev. Lett. (2013).
[76] J. DiSciacca, M. Marshall, K. Marable, and G. Gabrielse, accepted for publication in Phys. Rev. Lett. (2013).
[77] E. Widmann, Acta Physica Polonica B **41**, 2, (2010).
[78] I. Angeli, At. Data Nucl. Data Tables **87**, 185 (2004).
[79] H.-J. Kluge, T. Beier, K. Blaum, L. Dahl, S. Eliseev, F. Herfurth, B. Hofmann, O. Kester, S. Koszudowski, C. Kozhuharov, G. Maero, W. Nörtershäuser, J. Pfister, W. Quint, U. Ratzinger, A. Schempp, R. Schuch, Th. Stöhlker, R. C. Thompson, M. Vogel, G. Vorobjev, D. F. A. Winters, and G. Werth, Adv. Quantum Chem. **53**, 83 (2008).
[80] V. M. Shabaev, D. A. Glazov, M. B. Shabaeva, V. A. Yerokhin, G. Plunien, and G. Soff, Phys. Rev. A **65**, 062104 (2002).
[81] D. A. Glazov, V. M. Shabaev, I. I. Tupitsyn, A. V. Volotka, V. A. Yerokhin, G. Plunien, and G. Soff, Phys. Rev. A **70**, 062104 (2004).
[82] D. A. Glazov, A. V. Volotka, V. M. Shabaev, I. I. Tupitsyn, and G. Plunien, Phys. Lett. A **357**, 330 (2006).
[83] T. Beier, I. Lindgren, H. Persson, S. Salomonson, P. Sunnergreen, H. Häffner, and N. Hermanspahn, Phys. Rev. A **62**, 032510 (2000).
[84] V. A. Yerokhin, K. Pachucki, Z. Harman, and C. H. Keitel, Phys. Rev. Lett. **107**, 043004 (2011).
[85] M. Gustavsson and A.-M. Martensson-Pendrill, Phys. Rev. A **58**, 3611 (1998).
[86] W. Quint, D. L. Moskovkhin, V. M. Shabaev, and M. Vogel, Phys. Rev. A **78**, 032517 (2008).

WILEY ONLINE LIBRARY

Early View publication on wileyonlinelibrary.com
(issue and page numbers not yet assigned;
citable using Digital Object Identifier – DOI)

Ann. Phys. (Berlin), 1–10 (2013) / DOI 10.1002/andp.201300079

annalen der physik

Review Article

Progress in quantum electrodynamics theory of highly charged ions

A. V. Volotka[1,2,*], *D. A. Glazov*[2], *G. Plunien*[1], *and V. M. Shabaev*[2]

Received 4 April 2013, revised 27 May 2013, accepted 3 June 2013
Published online 9 July 2013

Recent progress in quantum electrodynamics (QED) calculations of highly charged ions is reviewed. The theoretical predictions for the binding energies, the hyperfine splittings, and the g factors are presented and compared with available experimental data. Special attention is paid to tests of bound-state QED at strong field regime. Future prospects for tests of QED at the strongest electric and magnetic fields as well as for determination of the fine structure constant and the nuclear magnetic moments with heavy ions are discussed.

1 Introduction

Quantum electrodynamics (QED), being the relativistic quantum field theory of the electromagnetic force, describes all phenomena associated with electrically charged particles. Despite the mathematical complexity and difficulties caused by the occurrence of infrared and ultraviolet divergences, it has a great success in describing and predicting experimental results. For a long period of time quantum electrodynamics was mainly tested with light atomic systems: hydrogen, helium, positronium, and muonium. In these systems the QED effects are evaluated employing the expansion in two small parameters α and αZ (α is the fine structure constant and Z is the nuclear charge number) and, therefore, are tested to the leading order(s) in these parameters.

Another scenario for tests of QED has appeared in experiments with highly charged ions. Heavy few-electron ions provide unique micro-laboratories for probing QED effects in the strongest electromagnetic fields accessible at present for experimental study [1, 2]. For example, at the surface of a uranium nucleus the electric field strength amounts to $|E| \simeq 2 \times 10^{19}$ V/cm, which is six orders of magnitude higher than the maximum electric field strength in a petawatt laser pulse. The magnetic field strength of the $^{209}Bi^{83}$ nucleus magnetic moment at the nuclear surface is about 10^9 T, which is several orders of magnitude higher than the field of the most powerful magnets. In this regime, high-precision QED calculations become more complicated, since the consideration should be primarily relativistic. In particular, it means that the parameter αZ cannot be utilized as an expansion parameter and, therefore, the calculations must be performed to all orders in αZ. This requires developments of nonperturbative QED methods, which are suitable for the description of highly charged ions.

In this paper we review the current status of the QED calculations of the spectroscopic properties of highly charged ions: energy levels, hyperfine splitting, and g factor values. The relativistic units $\hbar = c = m_e = 1$ are used throughout the paper.

2 Binding energy

A systematic description of highly charged ions in the framework of QED starts with the one-electron Dirac equation

$$[-i\boldsymbol{\alpha}\cdot\boldsymbol{\nabla} + \beta + V(\mathbf{r})]\,\psi(\mathbf{r}) = E\psi(\mathbf{r}), \tag{1}$$

where $V(\mathbf{r})$ is assumed to be the potential of the nucleus. Another choice of $V(\mathbf{r})$ is an effective local potential, which contains, besides the interaction with the nucleus, an approximate treatment of the interelectronic interaction. Solving the Dirac equation (1), one takes into account the interaction of the electron with the Coulomb field of the nucleus to all orders in αZ. The interaction between the electron–positron and electromagnetic fields, which leads to the radiative and

* Corresponding author E-mail: andrey.volotka@tu-dresden.de
[1] Institut für Theoretische Physik, Technische Universität Dresden, Mommsenstraße 13, 01062 Dresden, Germany
[2] Department of Physics, St. Petersburg State University, Oulianovskaya 1, Petrodvorets, 198504 St. Petersburg, Russia

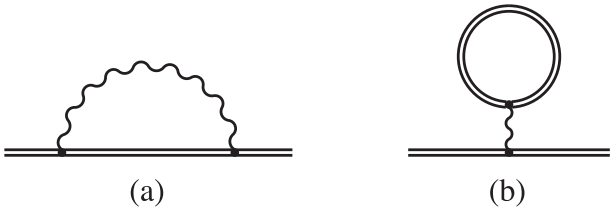

Figure 1 Feynman diagrams representing the self-energy (a) and vacuum-polarization (b) radiative corrections. The wavy line indicates the photon propagator and the double line denotes an electron propagating in the Coulomb field.

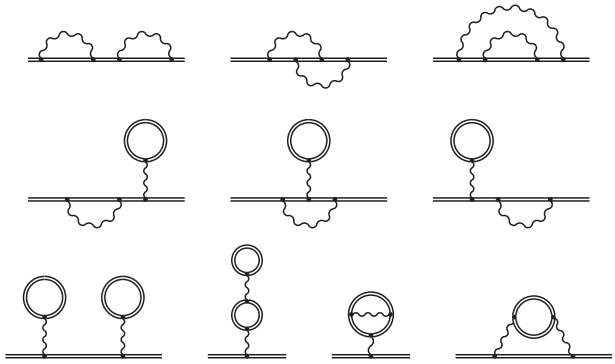

Figure 2 Feynman diagrams representing the second-order one-electron radiative corrections.

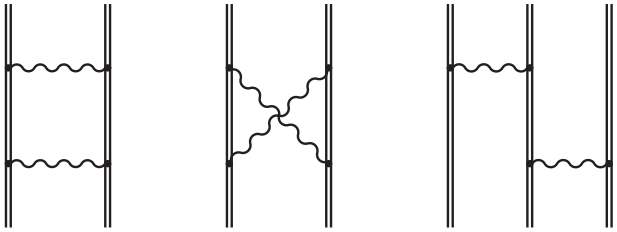

Figure 3 Feynman diagrams representing the second-order interelectronic-interaction corrections.

interelectronic-interaction corrections, is treated by the QED perturbation theory. The formulation of QED, in which the nucleus is treated as a classical source of the Coulomb field, is known as the Furry picture of quantum electrodynamics.

For a point-like nucleus, the solution of the Dirac equation is known analytically, while for a finite-size nucleus this can be done either numerically (see, e.g., Ref. [3]) or analytically (Ref. [4]). The difference between the energies for the extended and the point-nucleus models is known as the finite-nuclear-size correction.

The radiative corrections of the first order in α are described by the Feynman diagrams depicted in Fig. 1. These are so-called self-energy (a) and vacuum-polarization (b) diagrams. In these diagrams, the double solid line indicates an electron propagating in the Coulomb field of the nucleus, while the wavy line corresponds to a virtual photon. In contrast to light atomic systems, in highly charged ions these diagrams have to be calculated to all orders in αZ. The nonperturbative evaluation of the self-energy correction was first performed by Desiderio and Johnson [5] employing the method proposed by Brown, Langer, and Schaefer [6]. Later, Mohr [7] developed a much more accurate and powerful method, which allowed him to carry out a high-precision evaluation of this correction in a wide range of Z values. The most accurate calculations of the self energy to all orders in αZ were performed in Refs. [8–11] for the point-like nucleus case and in Refs. [12, 13] for the extended nucleus case. The first nonperturbative calculations of the vacuum-polarization diagram were made by Soff and Mohr [14] and by Manakov, Nekipelov, and Fainshtein [15]. The most accurate results were obtained in Refs. [16, 17]. The second-order (two-loop) one-electron radiative corrections are defined by the diagrams depicted in Fig. 2. The complete nonperturbative calculations of these diagrams represent an extremely difficult task. Recent crucial developments in this respect were made in Refs. [18–20], where the complete set of the two-loop self-energy diagrams (the first three diagrams in Fig. 2) were rigorously evaluated. At present, only the last two diagrams in Fig. 2, being known only in the lowest order in αZ (see Ref. [21] and references therein), remain uncalculated to all orders in αZ.

For few-electron ions, besides the one-electron radiative corrections, one has to take into account the interelectronic-interaction corrections. These corrections are suppressed by the parameter $1/Z$. For high-Z ions this parameter becomes comparable with the fine structure constant α, which characterizes the radiative corrections. The unperturbed many-electron wave functions are constructed within the jj-coupling scheme. The jj-coupling states are the eigenstates of the relativistic Hamiltonian of noninteracting electrons, which is the sum of one-electron Dirac Hamiltonians (1). For the high-Z regime, it is natural to employ the jj coupling instead of the Russell–Saunders- or the LS-coupling schemes, which become exact in the nonrelativistic limit. The calculations of the first-order interelectronic-interaction contributions are rather simple, while the second-order diagrams depicted in Fig. 3 are much more complicated. The first problem, which occurs in the treatment of these corrections, is the derivation of the formal expressions that are required for their numerical calculations. The most elaborate approach, which enables a rather simple derivation of the desired

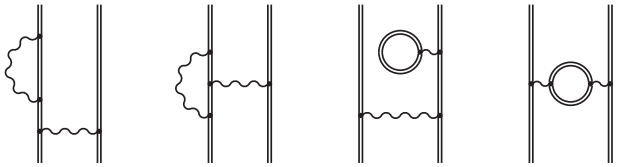

Figure 4 Feynman diagrams representing the self-energy and vacuum-polarization screening corrections.

expressions and is applicable not only for a single state but also for degenerate and quasidegenerate states, is the two-time Green's function method. This method was developed in Refs. [22, 23] and described in detail in Ref. [24]. The complete QED calculation of the second-order (two-photon) exchange diagrams for the ground state of He-like ions was first performed by Blundell *et al.* [25] and by Lindgren *et al.* [26]. In the QED formulation the exact photon propagators are employed, which allows one to perform the calculations to all orders in αZ and obtain the gauge-invariant results in each order of the perturbation theory. In the Breit approximation, which is frequently used in the many-body perturbation theory (MBPT) or configuration-interaction (CI) calculations, the photon propagator is treated approximately. This makes the Breit approximation valid only up to few lowest orders in αZ. As a result, the MBPT calculations of the two-photon exchange corrections to the energy levels give the exact values only for the α^2 and $\alpha^2(\alpha Z)^2$ terms. The contributions beyond the Breit approximation are referred to as the many-electron QED terms. Other many-electron QED contributions come from the combination of the radiative and interelectronic-interaction parts. They are known as the screened self-energy and screened vacuum-polarization contributions and depicted in Fig. 4. The rigorous calculations of the many-electron QED diagrams were performed in Refs. [27–30] for He-like ions and in Refs. [31–38] for Li-like ions.

So far we considered the Furry picture, where the nucleus is assumed to be a source of the external Coulomb field. Beyond this approximation one has to account for the finite nucleus mass and the intrinsic nuclear dynamics, that lead to the nuclear recoil and nuclear polarization effects. In contrast to the nonrelativistic theory, where the recoil effect for a hydrogen-like atom can easily be taken into account by using the electron reduced mass, the full relativistic theory of the recoil effect can be formulated only in the framework of QED. The complete relativistic formula for the recoil effect to first order in m_e/M (M is the nucleus mass) and to all orders in αZ was first derived in Ref. [39] (see also Ref. [40] and references therein) and numerically evaluated in Ref. [41].

The contributions discussed above can be precisely calculated order by order. However, this is not the case for the nuclear polarization corrections, which, due to the phenomenological description of the nucleon–nucleon interaction, set the ultimate accuracy limit up to which the QED corrections can be tested in highly charged ions. The energy shift due to this effect was evaluated by Plunien *et al.* [42, 43] and by Nefiodov *et al.* [44].

Finally, let us turn to the comparison with the experimental results. A precision of about 10^{-2} was obtained in the measurement of the ground state Lamb shift in the one-electron uranium ion [45]. This provides a test of QED effects on the level of about 2%. The most accurate measurements of the binding energy in highly charged heavy ions were performed with Li-like ions [46–48]. The $2p_{1/2}$–$2s$ transition energy in $^{238}U^{89+}$ was measured to be 280.645(15) eV [48]. The total theoretical value for this transition energy, 280.71(10) eV [49], agrees well with the experimental result. Comparing the first- and second-order QED contributions with the total theoretical uncertainty, we find that the present status of the theory and experiment for Li-like uranium provides a test of QED on a 0.2% level to first order in α and on a 6% level to second order in α.

3 Hyperfine structure

In case of a nonzero nuclear spin I, the atomic electron interacts also with the magnetic field induced by the nuclear magnetic moment $\mu = g_I I \mu_N$. Here g_I is the nuclear g factor and μ_N is the nuclear magneton. This interaction splits the energy levels into the hyperfine structure sublevels which correspond to different values of the total angular momentum of the ion $\mathbf{F} = \mathbf{I} + \mathbf{J}$, where J is the total angular momentum of the electrons. Investigations of the hyperfine structure in highly charged ions are of particular interest since the electrons experience not only the strong electric Coulomb field but also the strong magnetic field. This provides a unique possibility for tests of QED in the strongest electric and magnetic fields.

Accurate measurements of the ground-state hyperfine splitting in heavy H-like ions: ^{209}Bi, ^{165}Ho, ^{185}Re, ^{187}Re, ^{207}Pb, ^{203}Tl, and ^{205}Tl [50–54] have triggered a great interest in the theory of this effect. The ground-state hyperfine splitting in H-like ions can be represented in the form

$$\Delta E^{(1s)} = \Delta E^{(1s)}_{\rm Dirac}(1 - \epsilon^{(1s)}) + \Delta E^{(1s)}_{\rm QED}\,, \qquad (2)$$

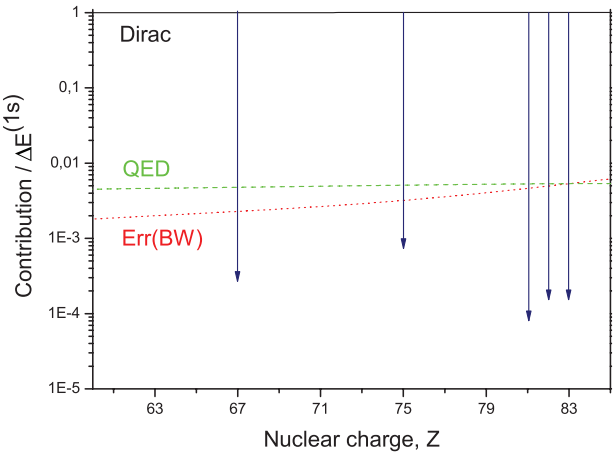

Figure 5 The relative contributions to the ground-state hyperfine splitting in H-like ions: the Dirac value, the QED correction, and the uncertainty of the BW effect. The vertical lines with arrows represent the accuracy of the existing experimental results [50–54].

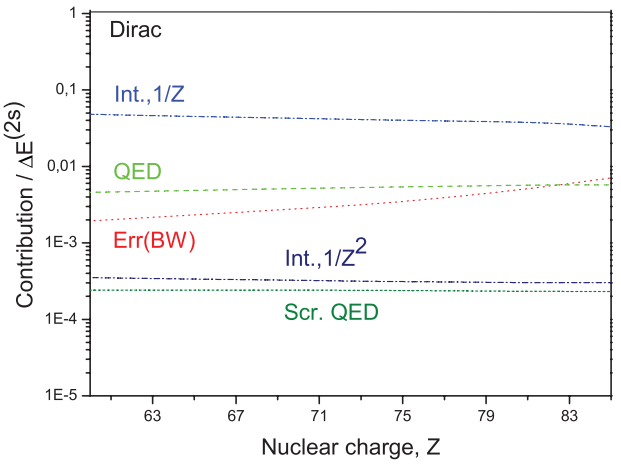

Figure 6 The relative contributions to the ground-state hyperfine splitting in Li-like ions: the Dirac value, the one-electron QED, the interelectronic-interaction, and the screened QED corrections, together with the uncertainty of the BW effect.

where $\Delta E^{(1s)}_{\rm Dirac}$ is the relativistic (Dirac) value of the $1s$ hyperfine splitting, which also contains the nuclear charge distribution correction, $\epsilon^{(1s)}$ represents the nuclear magnetization distribution correction, the so-called Bohr–Weisskopf (BW) effect, and $\Delta E^{(1s)}_{\rm QED}$ stands for the radiative correction. The radiative correction was evaluated independently by several groups [55–62] and the results are found in a good agreement with each other. The theoretical uncertainty is mainly determined by the BW effect, which is very sensitive to the nuclear model employed in the calculation. In Fig. 5 the relative contributions of the Dirac value, the QED correction, and the uncertainty of the BW effect evaluated within the single-particle nuclear model [58] are presented. As one can see from the figure, the uncertainty of the nuclear magnetization distribution correction strongly masks the QED contribution. Accordingly, the direct identification of the QED effects on the hyperfine splitting in heavy H-like ions appeared to be unfeasible.

In this context, it was proposed to consider a specific difference of the ground-state hyperfine splitting values in H- and Li-like ions [63]:

$$\Delta' E = \Delta E^{(2s)} - \xi \Delta E^{(1s)} , \tag{3}$$

where the parameter ξ is chosen to cancel the Bohr–Weisskopf correction. The parameter ξ can be calculated to a rather high accuracy, because it is determined mainly by the behavior of the electron wave function at the atomic scale and, therefore, almost independent of the nuclear structure. The ground-state hyperfine splitting in Li-like ions $\Delta E^{(2s)}$ is conveniently written in the form:

$$\Delta E^{(2s)} = \Delta E^{(2s)}_{\rm Dirac}(1-\epsilon^{(2s)}) + \Delta E^{(2s)}_{\rm QED} + \Delta E_{\rm int}(1-\epsilon^{(\rm int)}) + \Delta E_{\rm SQED} . \tag{4}$$

Here $\Delta E^{(2s)}_{\rm Dirac}$ is the one-electron relativistic value of the $2s$ hyperfine splitting, $\epsilon^{(2s)}$ and $\epsilon^{(\rm int)}$ denote the BW corrections to the leading and the interelectronic-interaction terms, respectively, and $\Delta E^{(2s)}_{\rm QED}$, $\Delta E_{\rm int}$, and $\Delta E_{\rm SQED}$ represent the one-electron QED, the interelectronic-interaction, and the screened QED corrections. In Fig. 6 we display the Z-dependence of the corresponding contributions for the hyperfine splitting in Li-like ions. According to this figure, as in the case of H-like ions, the uncertainty of the BW correction masks the QED contributions. But this uncertainty can be substantially reduced in $\Delta' E$ defined by Eq. (3). The relative contributions of the individual terms to the specific difference $\Delta' E$ are presented in Fig. 7. As one can see from the figure, the remaining uncertainty of the BW effect is two orders of magnitude smaller than the screened QED or two-photon exchange corrections. Thereby, the stringent tests of QED in combination with the strong electric and magnetic fields can be achieved by studying the specific difference of the hyperfine splitting values in H- and Li-like ions.

As was mentioned above, to date there exist several accurate measurements of the hyperfine splitting in H-like ions. But this is not the case for Li-like ions. The first measurement of the hyperfine splitting in Li-like ^{209}Bi was made in Ref. [64]. However, since this was an indirect measurement, its uncertainty is rather large. After more

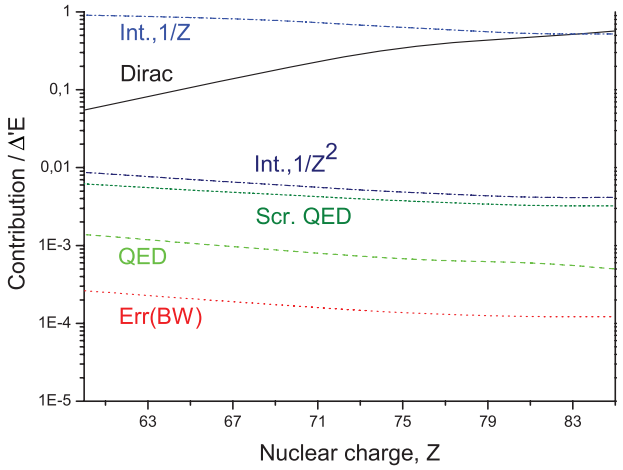

Figure 7 The relative contributions to the specific difference of the ground-state hyperfine splitting values in H- and Li-like ions: the Dirac value, the one-electron QED, the interelectronic-interaction, and the screened QED corrections, together with the remaining uncertainty of the BW effect.

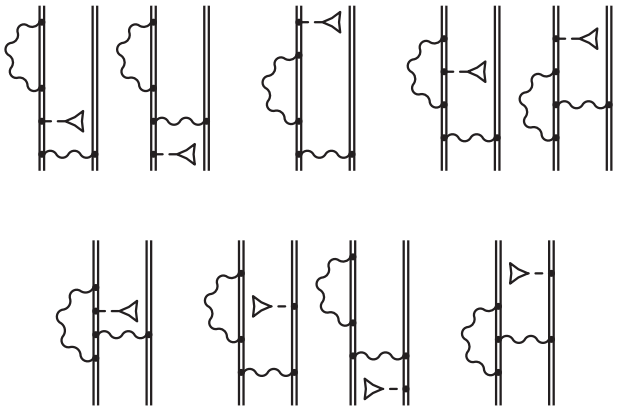

Figure 8 Feynman diagrams representing the screened self-energy corrections in the presence of an external potential. The dashed line terminated with the triangle denotes the interaction with the magnetic field.

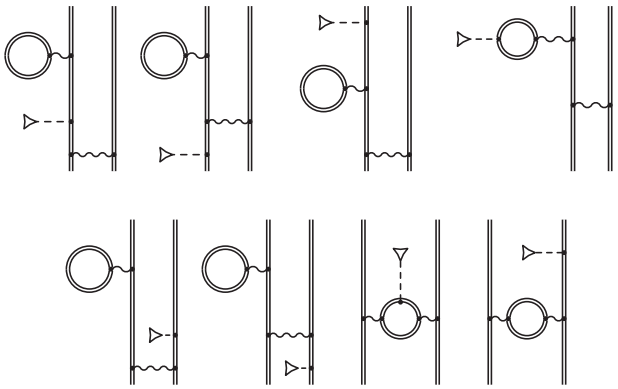

Figure 9 Feynman diagrams representing the screened vacuum-polarization corrections in the presence of an external potential.

than a decade of search, this transition line has been observed in a laser spectroscopy experiment at GSI [65]. It is expected that at the HITRAP facility at GSI the experimental accuracy will be improved by several orders of magnitude approaching the relative uncertainty of several parts in 10^{-7} [66, 67].

Achievement of the required theoretical accuracy for the specific hyperfine splitting difference for H- and Li-like heavy ions demands the rigorous evaluation of various QED and interelectronic-interaction effects. Since the influence of the one-electron QED corrections is considerably reduced in the difference, the total value of $\Delta' E$ is essentially determined by the screened QED and interelectronic-interaction corrections. These contributions correspond to the third-order terms in the QED perturbation theory expansion. The generic types of the screened self-energy and vacuum-polarization diagrams are presented in Figs. 8 and 9. Each diagram contains three parts: self-energy or vacuum-polarization loops, interelectronic interaction, and the vertex with an additional magnetic potential. As an external potential we employ the hyperfine interaction or the Zeeman interaction potentials. Taking into account the permutations of the one-electron states in these diagrams, one obtains 36 screened self-energy and 32 screened vacuum-polarization contributions, respectively.

The screened self-energy contribution has been calculated rigorously within the systematic QED approach in Refs. [68, 69]. This calculation represents an essential advance beyond the local screening potential approximation employed in the previous works [62, 70–74]. The screened vacuum-polarization contribution has been evaluated in the free-loop approximation in Refs. [68, 69], and later the major part of the diagrams has been calculated to all orders in αZ [75]. Presently, only the last two diagrams in Fig. 9 remain uncalculated to all orders in αZ.

The rigorous calculations of the interelectronic-interaction terms are performed within the $1/Z$ perturbation expansion. The one-photon exchange correction corresponding to the first order in $1/Z$ was evaluated rigorously in Ref. [76]. Until recently, the rigorous calculation of the two-photon exchange diagrams (Fig. 10) remained a challenge for theory. In Refs. [62, 77, 78], the contributions of the second and higher orders in $1/Z$ have been calculated within the Breit approximation employing the MBPT and CI methods. Recently, the

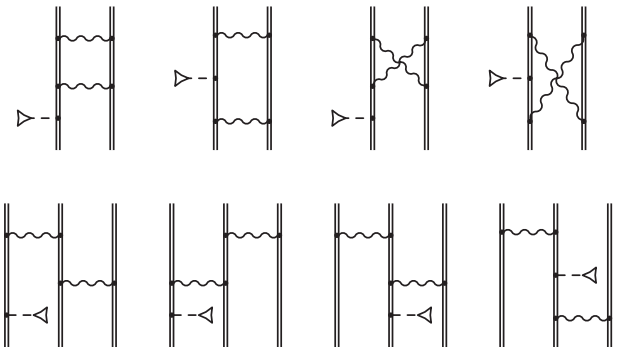

Figure 10 Feynman diagrams representing the two-photon exchange corrections in the presence of an external potential.

Table 1 Individual contributions to the specific difference $\Delta' E$ for ^{209}Bi in meV.

Effect	$\xi \Delta E^{(1s)}$	$\Delta E^{(2s)}$	$\Delta' E$
Dirac value	876.638	844.829	−31.809
QED	−5.088	−5.052	0.036
Interel. interaction			
$\sim 1/Z$		−29.995	−29.995
$\sim 1/Z^2$		0.258	0.258
$\sim 1/Z^{3+}$		−0.003(3)	−0.003(3)
Screened QED		0.193(2)	0.193(2)
Total			−61.320(4)(5)

evaluation of the two-photon exchange diagrams has been performed rigorously to all orders in αZ Ref. [79].

The current status of the specific difference of the hyperfine splitting values of H- and Li-like Bi is presented in Table 1. In this case, the cancellation of the BW effect appears at $\xi = 0.16886$, while the specific difference amounts to 61.320(4)(5) meV. The first uncertainty originates from the uncalculated parts of the screened vacuum-polarization contributions. The second uncertainty comes from the nuclear magnetic moment ($\mu = 4.1106(2)\mu_N$ [80]), the nuclear polarization corrections [81], and other nuclear effects, which are not completely canceled in the specific difference. Thus, the theoretical accuracy achieved for the specific difference allows one to test the many-electron QED effects at the level of a few percent, provided the hyperfine splittings in H- and Li-like bismuth are measured with a relative accuracy of about 10^{-6}. When the QED corrections are be tested and found to be valid, the comparison between the theoretical and experimental values for H- and Li-like ions will enable the determination of the nuclear magnetic moments and their volume distribution.

4 *g* factor

In a homogeneous magnetic field the energy levels split according to the projection of the ion's angular momentum on the field direction. For a weak magnetic field strength B, such a splitting is known as the Zeeman splitting. For a spinless nucleus this splitting can be written in the form

$$\Delta E(B) = g M_J \mu_B B\,, \tag{5}$$

where μ_B is the Bohr magneton, M_J is the projection of the angular momentum on the field direction, and the g factor is a dimensionless quantity characterizing the energy shift.

In recent years, a spectacular progress was made in the experimental and theoretical investigations of the bound-electron g factor. High-precision measurements of the ground-state g factor of H-like carbon [82] and oxygen [83] and the related theoretical calculations provided determination of the electron mass with an accuracy which is four times better than that of the previously accepted value. Recently, highly accurate measurements have been performed for the g factor of H-like $^{28}Si^{13+}$ [84, 85] with a statistical uncertainty significantly smaller than the uncertainty coming from the electron mass value. To date, these experiments provide the most stringent test of the one-electron QED corrections in the presence of a magnetic field. Accurate measurement of the g factor of Li-like $^{28}Si^{11+}$ has been recently accomplished Ref. [86]. High-precision measurements are also anticipated for B-like $^{40}Ar^{13+}$ and $^{40}Ca^{15+}$ [87, 88]. The investigations of the g factor of few-electron ions provide an access to the many-electron QED corrections. Extensions of these investigations to high-Z ions will provide a great opportunity to probe the magnetic sector of QED at a strong Coulomb field.

The ground-state g factors of H- and Li-like ions are conveniently written in the form:

$$g^{(1s)} = g^{(1s)}_{\rm Dirac} + \Delta g^{(1s)}_{\rm QED} + \Delta g^{(1s)}_{\rm nucl}\,, \tag{6}$$

$$g^{(2s)} = g^{(2s)}_{\rm Dirac} + \Delta g^{(2s)}_{\rm QED} + \Delta g_{\rm int} + \Delta g_{\rm SQED} + \Delta g^{(2s)}_{\rm nucl}\,, \tag{7}$$

where $g^{(1s)}_{\rm Dirac}$ and $g^{(2s)}_{\rm Dirac}$ are the one-electron relativistic values of the $1s$ and $2s$ g factors for the point-charge nucleus, $\Delta g^{(1s)}_{\rm QED}$ and $\Delta g^{(2s)}_{\rm QED}$ are the one-electron QED corrections, $\Delta g^{(1s)}_{\rm nucl}$ and $\Delta g^{(2s)}_{\rm nucl}$ incorporate the

nuclear-size, nuclear-recoil, and nuclear-polarization corrections, and $\Delta g_{\rm int}$ and $\Delta g_{\rm SQED}$ denote the interelectronic-interaction and screened QED contributions, respectively. Evaluations of the values $g^{(1s)}_{\rm Dirac}$ and $g^{(2s)}_{\rm Dirac}$ cause no problem. The one-electron QED corrections are evaluated employing the perturbation theory in the parameter α. The first-order QED corrections were addressed in Refs. [89–98], while the second-order corrections were evaluated within the αZ expansion in Refs. [99–101]. The nuclear effects on the g factor have also been investigated: the nuclear-size correction was derived analytically in Ref. [102], the nuclear-deformation correction was calculated in Ref. [103], the recoil contribution to first order in m_e/M and to all orders in αZ was derived in Ref. [104] and numerically evaluated in Ref. [105], and the nuclear-polarization correction was investigated in Ref. [106]. For Li-like ions, besides the one-electron corrections, one has to take into account the screened radiative and interelectronic-interaction corrections, which are defined by diagrams similar to those for the hyperfine splitting (Figs. 8, 9, and 10). For low-Z ions, the screened radiative corrections were obtained employing the perturbation theory to the leading orders in αZ in Refs. [94, 107]. For middle-Z ions, the screening effect was evaluated by introducing the effective screening potential in the QED calculations to all orders in αZ [70]. For high-Z ions, the most accurate results for the screened radiative corrections have been obtained rigorously within the systematic QED approach [68, 69]. The one-photon exchange diagrams, which represent the interelectronic-interaction corrections of the first order in $1/Z$, were evaluated in the framework of QED in Ref. [108]. Recently, the two-photon exchange diagrams have been rigorously evaluated for the case of Li-like $^{28}Si^{11+}$ [86]. The individual contributions to the g factor of Li-like silicon are presented in Table 2. As one can see, the total theoretical value is in excellent agreement with the experimental one. It confirms the interelectronic-interaction effects at the level of 10^{-4} and, in particular, the two-photon exchange contribution is probed on a 1% level.

Table 2 Individual contributions to the ground-state g factor of Li-like $^{28}Si^{11+}$.

Effect	$^{28}Si^{11+}$
Dirac value	1.998 254 751
Finite nuclear size	0.000 000 003
QED, $\sim \alpha$	0.002 324 044 (3)
QED, $\sim \alpha^{2+}$	−0.000 003 517 (1)
Interelectronic interaction, $\sim 1/Z$	0.000 321 592
Interelectronic interaction, $\sim 1/Z^2$	−0.000 006 876 (1)
Interelectronic interaction, $\sim 1/Z^{3+}$	0.000 000 085 (22)
Screened QED	−0.000 000 212 (46)
Nuclear recoil	0.000 000 039 (1)
Total	2.000 889 909 (51)
Experiment [86]	2.000 889 889 9 (21)

Table 3 Individual contributions to the ground-state g factors of $^{208}Pb^{81+}$ and $^{208}Pb^{79+}$.

Effect	$^{208}Pb^{81+}$	$^{208}Pb^{79+}$
Dirac value	1.734 947 023	1.932 002 904
Nuclear size	0.000 452 9(8)	0.000 078 58 (13)
Free QED		
$\sim \alpha$	0.002 322 819	0.002 322 819
$\sim \alpha^2$ and higher orders	−0.000 003 515	−0.000 003 515
Bound-state QED		
$\sim \alpha$	0.000 561 50 (2)	0.000 088 9 (1)
$\sim \alpha^2$ and higher orders	−0.000 000 2 (6)	−0.000 000 1 (5)
Interelectronic interaction		0.002 140 7 (27)
Screened QED		−0.000 001 8 (2)
Nuclear recoil	0.000 001 723	0.000 000 25 (35)
Nuclear polarization	−0.000 000 2 (1)	−0.000 000 04 (2)
Total	1.738 282 0 (10)	1.936 628 7 (28)

Table 3 presents the individual contributions to the ground-state g factors of H- and Li-like lead. Here we split the QED corrections into the free and bound-state QED parts. The free QED terms corresponding to the anomalous magnetic moment of the free electron are known through the order α^5 [109] and do not depend on the nuclear charge Z. The bound-state QED terms reflect the binding effects on the QED corrections and rapidly increase with the nuclear charge. However, as one can see from Table 3, the theoretical uncertainties due to the nuclear-size effect become comparable with the bound-state QED corrections of second order in α. This strongly restricts the tests of bound-state QED in such investigations. In Ref. [108], it was shown that the uncertainty due to the nuclear effects can be significantly reduced in a

specific difference of the g factors of H- and Li-like ions with the same nucleus, similar to the difference of the hyperfine splitting values (see Eq. (3)). Therefore, studying this difference, the QED effects can be investigated to a much higher accuracy than in the separate investigations with H- or Li-like ions.

Besides a test of QED, investigations of the g factors of highly charged ions can provide a possibility for an independent determination of the fine structure constant from the bound-state QED at the high-Z regime [110]. For this purpose it was proposed to consider a specific difference of the g factors of H- and B-like ions of the same spinless isotope in the lead region. It was found that in the case of lead this specific difference can be calculated to an accuracy of about 10^{-10}. Together with the corresponding experimental results for the g factors of H- and B-like lead, this may lead to a determination of α to a precision comparable to one obtained from the free-electron g factor [109].

For ions with nonzero nuclear spin I the energy shift depends not only on the electronic g factor but also on the nuclear g factor $g_I = \mu/(\mu_N I)$. The energy level structure depends on the ratio between the Zeeman and the hyperfine splitting values. For weak magnetic fields, the Zeeman interaction can be treated perturbatively and the hyperfine structure sublevels split into the Zeeman patterns. If the Zeeman splitting is comparable to the hyperfine splitting, the energy level structure is described by the Breit–Rabi formula. Theoretical and experimental investigations of these splittings can provide determinations of the nuclear magnetic moments on the 10^{-6} accuracy level. The case of a weak magnetic field was investigated in Refs. [111–114], while the corrections to the Breit–Rabi formula were evaluated in Refs. [115, 116].

5 Conclusion

In this paper we have reviewed the present status of the QED calculations of highly charged ions. The comparison between the theoretical results and the corresponding experimental data shows that at present the best test of QED at strong electric fields has been achieved in the investigations of the binding energies. For the case of Li-like uranium the $2p_{1/2}$–$2s$ transition energy provides a test of bound-state QED on a 0.2% accuracy level to first order in α and on a 6% accuracy level to second order in α. The Bohr–Weisskopf effect restricts the direct identification of the QED effects on the hyperfine splitting in heavy H-like ions. It was shown instead that the theoretical uncertainty can be significantly reduced in a specific difference of the hyperfine splitting values of H- and Li-like ions with the same nucleus. Thus, the investigations of the hyperfine splitting in heavy H- and Li-like ions of the same isotope provide a unique opportunity for tests of the bound-state QED in combination with the strong electric and magnetic fields. The theoretical accuracy achieved for the specific difference between the hyperfine splitting values in H- and Li-like bismuth allows us to identify the many-electron QED effects at the level of a few percent. The present experimental and theoretical investigations of the bound-electron g factor provide the stringent tests of the magnetic sector of bound-state QED. The one-electron QED corrections to the bound-electron g factor have been probed by direct measurements with H-like carbon, oxygen, and silicon, while the measurement of the g factor of Li-like silicon yields the most stringent test of the many-electron QED effects in presence of a magnetic field. Extensions of these measurements to high-Z ions and to ions with nonzero nuclear spin can serve for independent determinations of the fine structure constant and the nuclear magnetic moments.

Acknowledgements. The investigations reported in this paper were supported by the DFG (Grant No. VO 1707/1-2), GSI, RFBR (Grant Nos. 12-02-31803 and 13-02-00630), and the Ministry of Education and Science of the Russian Federation (Grant No. 8420). D.A.G. acknowledges financial support by the FAIR – Russia Research Center and by the "Dynasty" foundation.

Key words. Quantum electrodynamics, highly charged ions, binding energy, hyperfine structure, g factor.

References

[1] P. J. Mohr, G. Plunien, and G. Soff Phys. Rep. **293**, 227 (1998).
[2] T. Beier, Phys. Rep. **339**, 79 (2000).
[3] T. Franosch and G. Soff, Z. Phys. D **18**, 219 (1991).
[4] V. M. Shabaev, J. Phys. B **26**, 1103 (1993).
[5] A. M. Desiderio and W. R. Johnson, Phys. Rev. A **3**, 1267 (1971).
[6] G. E. Brown, J. S. Langer, and G. W. Schaefer, Proc. R. Soc. Lond. A **251**, 92 (1959).
[7] P. J. Mohr, Ann. Phys. (N.Y.) **88**, 26 (1974); **88**, 52 (1974).
[8] P. J. Mohr, Phys. Rev. A **46**, 4421 (1992).
[9] P. Indelicato and P. J. Mohr, Phys. Rev. A **58**, 165 (1998).
[10] U. D. Jentschura, P. J. Mohr, and G. Soff, Phys. Rev. A **63**, 042512 (2001).

[11] V. A. Yerokhin, K. Pachucki, and V. M. Shabaev, Phys. Rev. A **72**, 042502 (2005).
[12] P. J. Mohr and G. Soff, Phys. Rev. Lett. **70**, 158 (1993).
[13] V. A. Yerokhin, Phys. Rev. A **83**, 012507 (2011).
[14] G. Soff and P. J. Mohr, Phys. Rev. A **38**, 5066 (1988).
[15] N. L. Manakov, A. A. Nekipelov, and A. G. Fainshtein Zh. Eksp. Teor. Fiz. **95**, 1167 (1989) [Sov. Phys. JETP **68**, 673 (1989)].
[16] H. Persson, I. Lindgren, S. Salomonson, and P. Sunnergren, Phys. Rev. A **48**, 2772 (1993).
[17] J. Sapirstein and K. T. Cheng, Phys. Rev. A **68**, 042111 (2003).
[18] V. A. Yerokhin, P. Indelicato, and V. M. Shabaev, Phys. Rev. Lett. **91**, 073001 (2003).
[19] V. A. Yerokhin, P. Indelicato, and V. M. Shabaev, Phys. Rev. Lett. **97**, 253004 (2006).
[20] V. A. Yerokhin, Phys. Rev. A **80**, 040501(R) (2009).
[21] V. A. Yerokhin, P. Indelicato, and V. M. Shabaev, Phys. Rev. A **77**, 062510 (2008).
[22] V. M. Shabaev, Izv. Vuz. Fiz. **33**, 43 (1990) [Sov. Phys. J. **33**, 660 (1990)].
[23] V. M. Shabaev, Teor. Mat. Fiz. **82**, 83 (1990) [Theor. Math. Phys. **82**, 57 (1990)].
[24] V. M. Shabaev, Phys. Rep. **356**, 119 (2002).
[25] S. A. Blundell, P. J. Mohr, W. R. Johnson, and J. Sapirstein, Phys. Rev. A **48**, 2615 (1993).
[26] I. Lindgren, H. Persson, S. Salomonson, and L. Labzowsky, Phys. Rev. A **51**, 1167 (1995).
[27] H. Persson, S. Salomonson, P. Sunnergren, and I. Lindgren, Phys. Rev. Lett. **76**, 204 (1996).
[28] A. N. Artemyev, V. M. Shabaev, and V. A. Yerokhin, Phys. Rev. A **56**, 3529 (1997).
[29] V. A. Yerokhin, A. N. Artemyev, and V. M. Shabaev, Phys. Lett. A **234**, 361 (1997).
[30] A. N. Artemyev, V. M. Shabaev, V. A. Yerokhin, G. Plunien, and G. Soff, Phys. Rev. A **71**, 062104 (2005).
[31] A. N. Artemyev, T. Beier, G. Plunien, V. M. Shabaev, G. Soff, and V. A. Yerokhin, Phys. Rev. A **60**, 45 (1999).
[32] V. A. Yerokhin, A. N. Artemyev, T. Beier, G. Plunien, V. M. Shabaev, and G. Soff, Phys. Rev. A **60**, 3522 (1999).
[33] V. A. Yerokhin, A. N. Artemyev, V. M. Shabaev, M. M. Sysak, O. M. Zherebtsov, and G. Soff, Phys. Rev. Lett. **85**, 4699 (2000).
[34] J. Sapirstein and K. T. Cheng, Phys. Rev. A **64**, 022502 (2001).
[35] O. Y. Andreev, L. N. Labzowsky, G. Plunien, and G. Soff, Phys. Rev. A **67**, 012503 (2003).
[36] A. N. Artemyev, V. M. Shabaev, M. M. Sysak, V. A. Yerokhin, T. Beier, G. Plunien, and G. Soff, Phys. Rev. A **67**, 062506 (2003).
[37] Y. S. Kozhedub, A. V. Volotka, A. N. Artemyev, D. A. Glazov, G. Plunien, V. M. Shabaev, I. I. Tupitsyn, and T. Stöhlker, Phys. Rev. A **81**, 042513 (2010).
[38] J. Sapirstein and K. T. Cheng, Phys. Rev. A **83**, 012504 (2011).
[39] V. M. Shabaev, Theor. Math. Phys. **63**, 588 (1985).
[40] V. M. Shabaev, Phys. Rev. A **57**, 59 (1998).
[41] A. N. Artemyev, V. M. Shabaev, and V. A. Yerokhin, Phys. Rev. A **52**, 1884 (1995).
[42] G. Plunien, B. Müller, W. Greiner, and G. Soff, Phys. Rev. A **43**, 5853 (1991).
[43] G. Plunien and G. Soff, Phys. Rev. A **51**, 1119 (1995).
[44] A. V. Nefiodov, L. N. Labzowsky, G. Plunien, and G. Soff, Phys. Lett. A **222**, 227 (1996).
[45] A. Gumberidze, T. Stöhlker, D. Banaś, K. Beckert, P. Beller, H. F. Beyer, F. Bosch, S. Hagmann, C. Kozhuharov, D. Liesen, F. Nolden, X. Ma, P. H. Mokler, M. Steck, D. Sierpowski, and S. Tashenov, Phys. Rev. Lett. **94**, 223001 (2005).
[46] J. Schweppe, A. Belkacem, L. Blumenfeld, N. Claytor, B. Feinberg, H. Gould, V. E. Kostroun, L. Levy, S. Misawa, J. R. Mowat, and M. H. Prior, Phys. Rev. Lett. **66**, 1434 (1991).
[47] C. Brandau, C. Kozhuharov, A. Müller, W. Shi, S. Shippers, T. Bartsch, S. Böhm, C. Böhme, A. Hoffknecht, H. Knopp, N. Grün, W. Sheid, T. Steih, F. Bosch, B. Franzke, P. H. Mokler, F. Nolden, M. Steck, T. Stöhlker, and Z. Stachura, Phys. Rev. Lett. **91**, 073202 (2003).
[48] P. Beiersdorfer, H. Chen, D. B. Thorn, and E. Träbert, Phys. Rev. Lett. **95**, 233003 (2005).
[49] Y. S. Kozhedub, O. V. Andreev, V. M. Shabaev, I. I. Tupitsyn, C. Brandau, C. Kozhuharov, G. Plunien, and T. Stöhlker, Phys. Rev. A **77**, 032501 (2008).
[50] I. Klaft, S. Borneis, T. Engel, B. Fricke, R. Grieser, G. Huber, T. Kühl, D. Marx, R. Neumann, S. Schröder, P. Seelig, and L. Völker, Phys. Rev. Lett. **73**, 2425 (1994).
[51] J. R. Crespo López-Urrutia, P. Beiersdorfer, D. W. Savin, and K. Widmann, Phys. Rev. Lett. **77**, 826 (1996).
[52] J. R. Crespo López-Urrutia, P. Beiersdorfer, K. Widmann, B. B. Birkett, A. M. Mårtensson-Pendrill, and M. G. H. Gustavsson, Phys. Rev. A **57**, 879 (1998).
[53] P. Seelig, S. Borneis, A. Dax, T. Engel, S. Faber, M. Gerlach, C. Holbrow, G. Huber, T. Kühl, D. Marx, K. Meier, P. Merz, W. Quint, F. Schmitt, M. Tomaselli, L. Völker, H. Winter, M. Würtz, K. Beckert, B. Franzke, F. Nolden, H. Reich, M. Steck, and T. Winkler, Phys. Rev. Lett. **81**, 4824 (1998).
[54] P. Beiersdorfer, S. B. Utter, K. L. Wong, J. R. Crespo López-Urrutia, J. A. Britten, H. Chen, C. L. Harris, R. S. Thoe, D. B. Thorn, E. Träbert, M. G. H. Gustavsson, C. Forssén, and A. M. Mårtensson-Pendrill, Phys. Rev. A **64**, 032506 (2001).
[55] S. M. Schneider, W. Greiner, and G. Soff, Phys. Rev. A **50**, 118 (1994).
[56] H. Persson, S. M. Schneider, W. Greiner, G. Soff, and I. Lindgren, Phys. Rev. Lett. **76**, 1433 (1996).
[57] S. A. Blundell, K. T. Cheng, and J. Sapirstein, Phys. Rev. Lett. **78**, 4914 (1997).
[58] V. M. Shabaev, M. Tomaselli, T. Kühl, A. N. Artemyev, and V. A. Yerokhin, Phys. Rev. A **56**, 252 (1997).
[59] P. Sunnergren, H. Persson, S. Salomonson, S. M. Schneider, I. Lindgren, and G. Soff, Phys. Rev. A **58**, 1055 (1998).
[60] A. N. Artemyev, V. M. Shabaev, G. Plunien, G. Soff, and V. A. Yerokhin, Phys. Rev. A **63**, 062504 (2001).
[61] V. A. Yerokhin and V. M. Shabaev, Phys. Rev. A **64**, 012506 (2001).

[62] J. Sapirstein and K. T. Cheng, Phys. Rev. A **63**, 032506 (2001).
[63] V. M. Shabaev, A. N. Artemyev, V. A. Yerokhin, O. M. Zherebtsov, and G. Soff, Phys. Rev. Lett. **86**, 3959 (2001).
[64] P. Beiersdorfer, A. L. Osterheld, J. H. Scofield, J. R. Crespo López-Urrutia, and K. Widmann, Phys. Rev. Lett. **80**, 3022 (1998).
[65] W. Nörtershäuser *et al.*, Phys. Scr. **T154**, in press (2013).
[66] M. Vogel and W. Quint, Phys. Rep. **490**, 1 (2010).
[67] W. Nörtershäuser, Hyperfine Interact. **199**, 131 (2011).
[68] A. V. Volotka, D. A. Glazov, V. M. Shabaev, I. I. Tupitsyn, and G. Plunien, Phys. Rev. Lett. **103**, 033005 (2009).
[69] D. A. Glazov, A. V. Volotka, V. M. Shabaev, I. I. Tupitsyn, and G. Plunien, Phys. Rev. A **81**, 062112 (2010).
[70] D. A. Glazov, A. V. Volotka, V. M. Shabaev, I. I. Tupitsyn, and G. Plunien, Phys. Lett. A **357**, 330 (2006).
[71] N. S. Oreshkina, A. V. Volotka, D. A. Glazov, I. I. Tupitsyn, V. M. Shabaev, and G. Plunien, Opt. Spektrosk. **102**, 889 [Opt. Spectrosc. **102**, 815] (2007).
[72] Y. S. Kozhedub, D. A. Glazov, A. N. Artemyev, N. S. Oreshkina, V. M. Shabaev, I. I. Tupitsyn, A. V. Volotka, and G. Plunien, Phys. Rev. A **76**, 012511 (2007).
[73] N. S. Oreshkina, D. A. Glazov, A. V. Volotka, V. M. Shabaev, I. I. Tupitsyn, and G. Plunien, Phys. Lett. A **372**, 675 (2008).
[74] A. V. Volotka, D. A. Glazov, I. I. Tupitsyn, N. S. Oreshkina, G. Plunien, and V. M. Shabaev, Phys. Rev. A **78**, 062507 (2008).
[75] O. V. Andreev, D. A. Glazov, A. V. Volotka, V. M. Shabaev, and G. Plunien, Phys. Rev. A **85**, 022510 (2012).
[76] V. M. Shabaev, M. B. Shabaeva, I. I. Tupitsyn, V. A. Yerokhin, A. N. Artemyev, T. Kühl, M. Tomaselli, and O. M. Zherebtsov, Phys. Rev. A **57**, 149 (1998); **58**, 1610 (1998).
[77] S. Boucard and P. Indelicato, Eur. Phys. J. D **8**, 59 (2000).
[78] O. M. Zherebtsov and V. M. Shabaev, Can. J. Phys. **78**, 701 (2000).
[79] A. V. Volotka, D. A. Glazov, O. V. Andreev, V. M. Shabaev, I. I. Tupitsyn, and G. Plunien, Phys. Rev. Lett. **108**, 073001 (2012).
[80] N. J. Stone, At. Data Nucl. Data Tables **90**, 75 (2005).
[81] A. V. Nefiodov, G. Plunien, and G. Soff, Phys. Lett. B **552**, 35 (2003).
[82] H. Häffner, T. Beier, N. Hermanspahn, H. J. Kluge, W. Quint, S. Stahl, J. Verdú, and G. Werth, Phys. Rev. Lett. **85**, 5308 (2000).
[83] J. Verdú, S. Djekić, S. Stahl, T. Valenzuela, M. Vogel, G. Werth, T. Beier, H. J. Kluge, and W. Quint, Phys. Rev. Lett. **92**, 093002 (2004).
[84] S. Sturm, A. Wagner, B. Schabinger, J. Zatorski, Z. Harman, W. Quint, G. Werth, C. H. Keitel, and K. Blaum, Phys. Rev. Lett. **107**, 023002 (2011).
[85] S. Sturm, A. Wagner, M. Kretzschmar, W. Quint, G. Werth, and K. Blaum, Phys. Rev. A **87**, 030501(R) (2013).
[86] A. Wagner, S. Sturm, F. Köhler, D. A. Glazov, A. V. Volotka, G. Plunien, W. Quint, G. Werth, V. M. Shabaev, and K. Blaum, Phys. Rev. Lett. **110**, 033003 (2013).
[87] D. von Lindenfels, N. P. M. Brantjes, G. Birkl, W. Quint, V. M. Shabaev, and M. Vogel, Can. J. Phys. **89**, 79 (2011).
[88] D. von Lindenfels, M. Wiesel, D. A. Glazov, A. V. Volotka, M. M. Sokolov, V. M. Shabaev, G. Plunien, W. Quint, G. Birkl, A. Martin, and M. Vogel, Phys. Rev. A **87**, 023412 (2013).
[89] S. A. Blundell, K. T. Cheng, and J. Sapirstein, Phys. Rev. A **55**, 1857 (1997).
[90] H. Persson, S. Salomonson, P. Sunnergren, and I. Lindgren, Phys. Rev. A **56**, R2499 (1997).
[91] T. Beier, I. Lindgren, H. Persson, S. Salomonson, P. Sunnergren, H. Häffner, and N. Hermanspahn, Phys. Rev. A **62**, 032510 (2000).
[92] S. G. Karshenboim, V. G. Ivanov, and V. M. Shabaev, Can. J. Phys. **79**, 81 (2001); Zh. Eksp. Teor. Fiz. **120**, 546 (2001) [Sov. Phys. JETP **93**, 477 (2001)].
[93] V. A. Yerokhin, P. Indelicato, and V. M. Shabaev, Phys. Rev. Lett. **89**, 143001 (2002).
[94] D. A. Glazov, V. M. Shabaev, I. I. Tupitsyn, A. V. Volotka, V. A. Yerokhin, G. Plunien, and G. Soff, Phys. Rev. A **70**, 062104 (2004).
[95] V. A. Yerokhin, P. Indelicato, and V. M. Shabaev, Phys. Rev. A **69**, 052503 (2004).
[96] R. N. Lee, A. I. Milstein, I. S. Terekhov, and S. G. Karshenboim, Phys. Rev. A **71**, 052501 (2005).
[97] V. A. Yerokhin and U. D. Jentschura, Phys. Rev. Lett. **100**, 163001 (2008).
[98] V. A. Yerokhin and U. D. Jentschura, Phys. Rev. A **81**, 012502 (2010).
[99] K. Pachucki, U. D. Jentschura, and V. A. Yerokhin, Phys. Rev. Lett. **93**, 150401 (2004); **94**, 229902 (2005).
[100] K. Pachucki, A. Czarnecki, U. D. Jentschura, and V. A. Yerokhin, Phys. Rev. A **72**, 022108 (2005).
[101] U. D. Jentschura, Phys. Rev. A **79**, 044501 (2009).
[102] D. A. Glazov and V. M. Shabaev, Phys. Lett. A **297**, 408 (2002).
[103] J. Zatorski, N. S. Oreshkina, C. H. Keitel, and Z. Harman, Phys. Rev. Lett. **108**, 063005 (2012).
[104] V. M. Shabaev, Phys. Rev. A **64**, 052104 (2001).
[105] V. M. Shabaev and V. A. Yerokhin, Phys. Rev. Lett. **88**, 091801 (2002).
[106] A. V. Nefiodov, G. Plunien, and G. Soff, Phys. Rev. Lett. **89**, 081802 (2002).
[107] Z. C. Yan, J. Phys. B **35**, 1885 (2002).
[108] V. M. Shabaev, D. A. Glazov, M. B. Shabaeva, V. A. Yerokhin, G. Plunien, and G. Soff, Phys. Rev. A **65**, 062104 (2002).
[109] T. Aoyama, M. Hayakawa, T. Kinoshita, and M. Nio, Phys. Rev. Lett. **109**, 111807 (2012).

[110] V. M. Shabaev, D. A. Glazov, N. S. Oreshkina, A. V. Volotka, G. Plunien, H. J. Kluge, and W. Quint, Phys. Rev. Lett. **96**, 253002 (2006).
[111] D. L. Moskovkin, N. S. Oreshkina, V. M. Shabaev, T. Beier, G. Plunien, W. Quint, and G. Soff, Phys. Rev. A **70**, 032105 (2004).
[112] D. L. Moskovkin, V. M. Shabaev, and W. Quint, Opt. Spectrosc. **104**, 637 (2008).
[113] V. A. Yerokhin, K. Pachucki, Z. Harman, and C. H. Keitel, Phys. Rev. Lett. **107**, 043004 (2011).
[114] V. A. Yerokhin, K. Pachucki, Z. Harman, and C. H. Keitel, Phys. Rev. A **85**, 022512 (2012).
[115] D. L. Moskovkin and V. M. Shabaev, Phys. Rev. A **73**, 052506 (2006).
[116] D. L. Moskovkin, V. M. Shabaev, and W. Quint, Phys. Rev. A **77**, 063421 (2008).

WILEY ONLINE LIBRARY

Early View publication on wileyonlinelibrary.com
(issue and page numbers not yet assigned;
citable using Digital Object Identifier – DOI)

Ann. Phys. (Berlin), 1–5 (2013) / DOI 10.1002/andp.201300058

annalen der physik

Review Article

Laser spectroscopy of muonic hydrogen

Randolf Pohl[1,], Aldo Antognini[1,2], Fernando D. Amaro[3], François Biraben[4], João M. R. Cardoso[3], Daniel S. Covita[3,5], Andreas Dax[6], Satish Dhawan[6], Marc Diepold[1], Luis M. P. Fernandes[3], Adolf Giesen[7], Andrea L. Gouvea[3], Thomas Graf[7], Theodor W. Hänsch[1,**], Paul Indelicato[4], Lucile Julien[4], Cheng-Yang Kao[8], Paul Knowles[9], José A. M. Lopes[3], Eric-Olivier Le Bigot[4], Yi-Wei Liu[8], Livia Ludhova[9], Cristina M. B. Monteiro[3], Françoise Mulhauser[1,9], Tobias Nebel[1], François Nez[4], Paul Rabinowitz[10], Joaquim M. F. dos Santos[3], Lukas A. Schaller[9], Karsten Schuhmann[2,11], Catherine Schwob[4], David Taqqu[12], João F. C. A. Veloso[5], Jan Vogelsang[1,***], and Franz Kottmann[2]*

Received 15 March 2013, revised 26 April 2013, accepted 30 April 2013
Published online 31 May 2013

Muonic hydrogen (μp) is a very sensitive probe of the proton structure. Laser spectroscopy of two 2S-2P transitions in μp was used to determine both the Lamb shift and the hyperfine splitting of the 2S state in μp. The rms charge radius of the proton, $R_{ch} = 0.84087(39)$ fm, was extracted from the Lamb shift. The Zemach radius of the proton, $R_Z = 1.082(37)$ fm, was obtained from the 2S-hyperfine splitting. This article summarizes the previously published findings.

1 Introduction

The exotic muonic hydrogen atom (μp) is made from a proton and a negative muon. Due to its large mass $m_\mu \approx 200\, m_e$, the muon's Bohr radius is nearly 200 times smaller than the corresponding Bohr radius in (regular) electronic hydrogen (H), causing a $200^3 \approx 10^7$ times increase in the muon's wavefunction overlap with the proton. Sensitivity to nuclear structure corrections is correspondingly increased making laser spectroscopy of μp energy levels a very sensitive probe of e.g. the charge and Zemach radii of the proton.

We have recently determined the 2S-2P energy splitting (Lamb shift) and the 2S hyperfine splitting (HFS) in μp for the first time [1, 2] (see Fig. 1).

2 Method

We have built a novel beam line for negative muons at low-energy (3–6 keV). About 600 μ^- per second enter a 200 mm long hydrogen gas target, filled with 1 hPa H_2 gas at room temperature. Roughly half of the muons stop, in a 200 mm long stop volume, with width and height of 12 mm and 5 mm, respectively.

Before entering the H_2 target, the muons are individually detected in two sets of ultra-thin carbon foils. Electrons ejected from the foils create a signal in plastic scintillators read out by photomultiplier tubes [3]. With efficiencies of 80% and 71% for the two foil detectors, we obtain 330 s^{-1} coincidences, each indicating the arrival of a muon.

Muons slow down in the target gas and are eventually captured by an H_2 molecule. The molecule breaks up and a muonic hydrogen atom μp is formed at a high principal

* Corresponding author E-mail: randolf.pohl@mpq.mpg.de
** also at: Ludwig-Maximilians-University, Munich, Germany.
*** present address: Institut für Physik, Carl von Ossietzky Universität, Oldenburg, Germany.
1 Max-Planck-Institut für Quantenoptik, Garching, Germany
2 Institute for Particle Physics, ETH Zurich, Switzerland
3 Departamento de Física, Universidade de Coimbra, Portugal
4 Laboratoire Kastler Brossel, École Normale Supérieure, CNRS and Université P. et M. Curie, Paris, France
5 I3N, Departamento de Física, Universidade de Aveiro, Portugal
6 Physics Department, Yale University, New Haven, CT, USA
7 Institut für Strahlwerkzeuge, Universität Stuttgart, Germany
8 Physics Department, National Tsing Hua University, Hsinchu, Taiwan
9 Département de Physique, Université de Fribourg, Switzerland
10 Department of Chemistry, Princeton University, Princeton, NJ, USA
11 Dausinger & Giesen GmbH, Stuttgart, Germany
12 Paul Scherrer Institute, Villigen, Switzerland

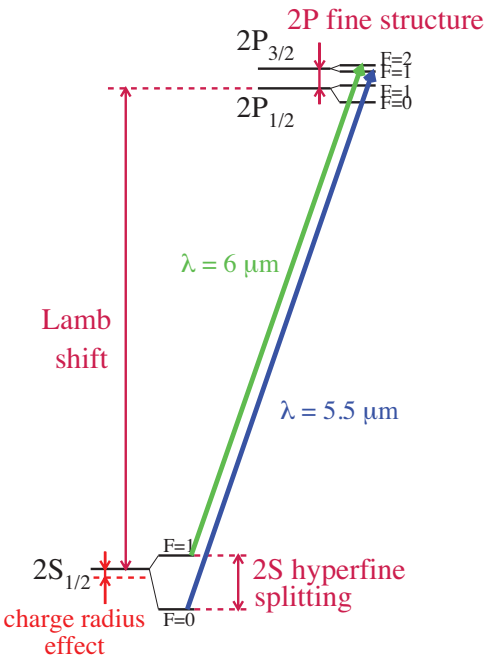

Figure 1 Level scheme of the $n = 2$ states in μp. The Lamb shift is dominated by vacuum polarization which shifts the 2S state below the $2P_{1/2}$ state. There is a 2% contribution of the proton charge radius to the Lamb shift. The 2S hyperfine splitting is affected by the Zemach radius of the proton (not shown).

quantum number $n \approx 14$. Several processes contribute to the deexcitation of the μp atom [4–7]. In the end, about 1% of the stopped muons form μp atoms in the metastable 2S state, whereas the remaining 99% of the muons proceed to the 1S ground state via emission of Lyman x-rays (K_α at 1.9 keV, K_β at 2.2 keV, etc.) [8]. The lifetime of the 2S state is about 1 μs at 1 hPa H_2 gas pressure, limited by collisional deexcitation [9, 10].

Above and below the muon stop volume, two rows of 10 large area avalanche photo diodes (LAAPDs, each with an active area of 14×14 mm^2) are mounted, at a distance of about 8 mm from the muon beam axis. The LAAPDs detect muonic K-x-rays with a time resolution of 35 ns and an energy resolution of 30% (FWHM) [11].

An incoming muon triggers the laser system [12, 13]. It provides 5 ns long pulses of 0.25 mJ energy, tunable from 5.5 μm to 6 μm. A key requirement is a time delay of less than 1 μs (dictated by the lifetime of the μp(2S) state) between the randomly occuring muon trigger and light output. This short delay is accomplished by a cw-pumped, pulsed Yb:YAG oscillator producing pulses at 1030 nm, only 200 ns after a trigger [13]. After amplification and second-harmonic generation, these pulses are used to pump a pulsed Ti:sapphire laser system which is seeded by a cw Ti:sapphire ring laser. The 15 mJ pulse of red light around 708 nm obtained from the Ti:sapphire laser system is then converted to the desired 5.5–6 μm infrared (IR) wavelength by three sequential Stokes shifts in a high-pressure H_2 Raman cell [12]. The wavelength of the IR light is tunable by changing the wavelength of the cw Ti:sapphire laser. The IR wavelength is calibrated with an accuracy of 300 MHz against well-known water vapor absorption lines.

A multipass mirror cavity inside the hydrogen gas target ensures homogeneous illumination of the muon stop volume. On resonance, laser-induced muonic hydrogen 2S-2P transitions are signalled by the observation of K_α x-rays from the subsequent 2P-1S deexcitation.

3 Results

The Lamb shift in μp was determined as 202.3706(23) meV, corresponding to a relative uncertainty $u_r = 11$ ppm. The 2S-HFS was found to be 22.8089(51) meV ($u_r = 224$ ppm).

From the Lamb shift and the 2S-HFS we deduce the proton's rms charge radius

$$R_{ch} = 0.84087\ (26)^{\rm exp}\ (29)^{\rm th}\ {\rm fm} = 0.84087(39)\ {\rm fm} \qquad (1)$$

and the Zemach radius

$$R_Z = 1.082\ (31)^{\rm exp}\ (20)^{\rm th}\ {\rm fm} = 1.082\ (37)\ {\rm fm}, \qquad (2)$$

respectively [2], using up-to-date theory of QED and nuclear structure effects, recently summarized in Ref. [19].

3.1 The charge radius of the proton

The charge radius R_{ch} in Eq. (1) is an order of magnitude more precise than the most recent CODATA-2010 value of $R_{ch}^{\rm CODATA} = 0.8775(51)$ fm [16], but differs by 7 standard deviations (7σ) from it. The CODATA value is obtained from 2 sources, precision spectroscopy in hydrogen (H) and deuterium (D), and elastic electron-proton (e-p) scattering. H/D spectroscopy yields $R_{ch}^{\rm H/D} = 0.8758(77)$ fm [16], and e-p scattering recently performed in Mainz gives $R_{ch}^{\rm Mainz} = 0.879(8)$ fm [17]. Another value recently obtained at Jefferson Lab (JLab) by polarization transfer measurements in e-p scattering is $R_{ch}^{\rm JLab} = 0.875(10)$ fm [18], again in agreement with the other electronic values, but in disagreement with the muonic value.

One should note, however, that analysis of scattering data using dispersion relations has traditionally yielded

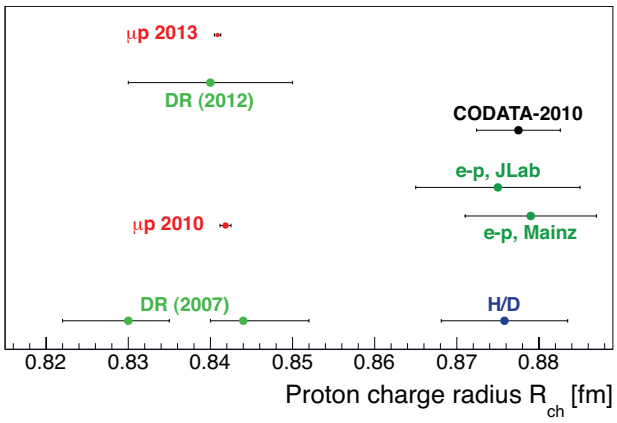

Figure 2 Recent determinations of the rms charge radius of the proton. Muonic hydrogen [1, 2] agrees with dispersion relation (DR) fits [14,15]. Spectroscopy in H and D [16] agree with recent elastic e-p scattering from Mainz [17] and JLab [18]. The CODATA-2010 value [16] is mainly based on H/D and Mainz.

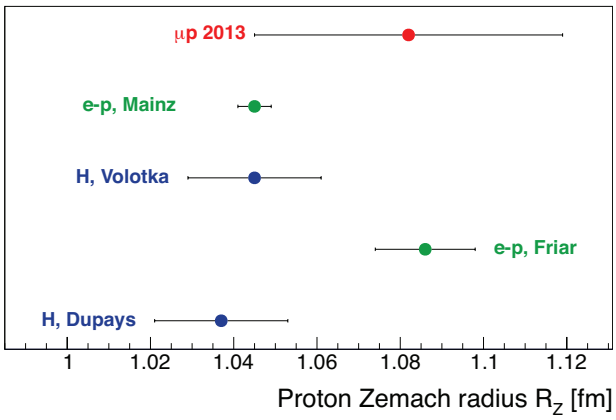

Figure 3 Recent determinations of the proton Zemach radius from H [21, 22], e-p scattering [23, 24] and the 2S HFS in muonic hydrogen [2].

a proton charge radius in agreement with the muonic hydrogen value [14, 20]. Recently, this method has also been applied to the new Mainz data of Ref [17], yielding $R_{ch}^{\mathrm{DR}} = 0.84(1)$ fm [15], again in excellent agreement with the muonic value, albeit with a larger χ^2 of the fit to the data. The situation is depicted in Fig. 2

3.2 The proton radius puzzle

The 7σ discrepancy between the charge radius from muonic hydrogen and the CODATA value has puzzled the physics community for three years now, but no solution has been generally accepted. Briefly, proton charge distributions with bumps or tails have been refuted by e-p scattering data [24]. Molecular effects in muonic hydrogen can also not be responsible for a significant shift of the resonance and therefore of R_{ch} [25]. An unexpectedly large proton polarizability contribution to the Lamb shift in muonic hydrogen [26, 27] seems unlikely [28]. Physics beyond the Standard Model needs delicate fine tuning to evade constraints from many precision measurements [29]. For a recent review see Ref. [30].

3.3 The Zemach radius of the proton

The Zemach radius of the proton, R_Z, enters the description of the hyperfine splitting (HFS) in electronic and muonic hydrogen. The HFS originates from the interaction of the lepton and proton magnetic moments. A convolution of the charge and magnetization distributions appears as a result of the finite magnetic size of the proton and the distortion of the lepton's wave function due to the finite charge distribution of the proton:

$$R_Z = \int \mathrm{d}^3 r\, r \int \mathrm{d}^3 r'\, \rho_{\mathrm{ch}}(|\boldsymbol{r} - \boldsymbol{r}'|)\, \rho_{\mathrm{mag}}(r') = -\frac{4}{\pi}\int_0^\infty \frac{dq}{q^2}\left(G_E(q^2)\, G_M(q^2) - 1\right). \quad (3)$$

Here, $\rho_{\mathrm{ch}}(r)$ and $\rho_{\mathrm{mag}}(r)$ are the (normalized) radial charge and magnetization densities of the proton, respectively. G_E and G_M are the electric and magnetic form factors of the proton.

The Zemach radius from μp is in agreement, but less accurate than the previous values from the HFS in H [21, 22], and e-p scattering [23, 24] (see Fig. 3):

- The 2S-HFS of 5 THz was determined from the *difference* of two Lamb shift transitions at 55 THz and 50 THz. This results already in an increase in (relative) uncertainty by more than an order of magnitude.
- The Zemach radius contributes only 0.7% of the 2S HFS in μp. In contrast, the charge radius effect on the Lamb shift is as large as 2%.

Muonic hydrogen may provide an improved value of the Zemach radius in the future.

The Zemach radius relates the electric and magnetic form factors of the proton (Eq. (3)). A more accurate value of R_Z from muonic hydrogen may therefore be able to resolve the long-standing discrepancy in the measured form factor ratio G_E/G_M between Rosenbluth and polarization transfer measurements [32].

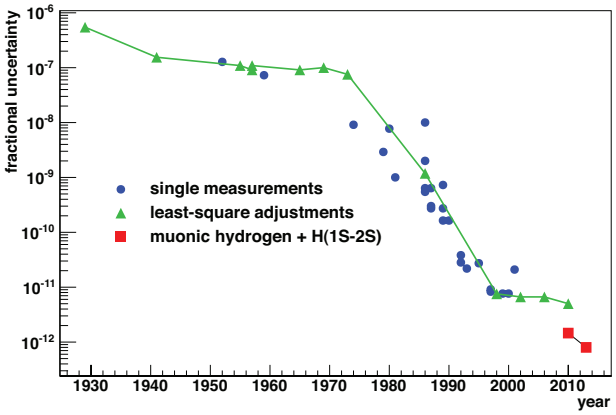

Figure 4 Accuracy of the Rydberg constant over time. The green triangles denote least square adjustments like CODATA [16]. Red squares are the values deduced from the 1S-2S transition frequency in hydrogen [31] using the proton charge radius from muonic hydrogen [1, 2].

3.4 Rydberg constant and the charge radius of the deuteron

Combining the proton charge radius from muonic hydrogen (Eq. (1)) with precision spectroscopy of the 1S-2S transition in hydrogen H [31] and deuterium D [33] yields new, much more accurate values of the Rydberg constant R_∞ and the rms charge radius of the deuteron R_{ch}(d). Both R_∞ and R_{ch}(d) are 7σ away from their respective CODATA-2010 values [16], due to their large correlation (~ 1.0) with the proton charge radius. Therefore, once the proton radius puzzle is solved, new values of R_∞ and R_{ch}(d) emerge.

The 1S-2S transition in H has been measured with an accuracy of 4.2 parts in 10^{15} [31]. When combined with the muonic R_{ch} and QED theory [16], we obtain

$$R_\infty = 3.289\,841\,960\,249\,5\ (10)^{\mathrm{radius}}\ (25)^{\mathrm{QED}} \times 10^{15}\mathrm{Hz/c} \tag{4}$$

which is six times more precise ($u_r = 8 \times 10^{-13}$) than the CODATA-2010 value [16] (Fig. 4). Uncertainties of QED theory in electronic hydrogen H constitute the main uncertainty of 2.5 kHz/c in R_∞. The uncertainty from the proton charge radius is only 1.0 kHz/c.

The isotope shift of the 1S-2S transition in H and D is sensitive to the difference of the squared charge radii of the deuteron and the proton. Both experiment [33] and theory [34] have recently been improved by an order of magnitude. Combined with the muonic proton radius R_{ch} we obtain a deuteron charge radius

$$R_{ch}(\mathrm{d}) = 2.12771\ (22)\ \mathrm{fm}, \tag{5}$$

ten times more precise than the CODATA-2010 value R_{ch}(d) = 2.1424 (25) fm [16].

The Lamb shift in muonic deuterium, performed by our group, may be able to shed some light on the radius puzzle. Nuclear structure corrections to the Lamb shift and hyperfine splitting in muonic deuterium are however large and difficult to calculate [35].

4 Outlook

The proton radius puzzle persists after nearly three years. More data is needed to find its origin. Precision spectroscopy of simple atomic systems may resolve the puzzle [36, 37]. A measurement of the Lamb shift in muonic helium ions is planned for this year [38].

Acknowledgments. We acknowledge support from the European Research Council (ERC) under Starting Grant #279765, the Max–Planck–Society and the Max–Planck–Foundation, the Swiss National Science Foundation (projects 100632 and 138175), the Swiss Academy of Engineering Sciences, the BQR de l'UFR de physique fondamentale et appliquée de l'Université Paris 6, the program PAI Germaine de Staël no.~07819NH du ministère des affaires étrangéres France, and the Fundação para a Ciência e a Tecnologia (Portugal) and FEDER (project PTDC/-FIS/-82006/-2006 and grant SFRH/BPD/46611/2008). P. I. acknowledges support by the ExtreMe Matter Institute, Helmholtz Alliance HA216/EMMI.

Key words. Muonic hydrogen, Proton radius, Charge radius, Zemach radius, Rydberg constant, Proton radius puzzle.

References

[1] R. Pohl, A. Antognini, F. Nez, F. D. Amaro, F. Biraben, J. M. R. Cardoso, D. S. Covita, A. Dax, S. Dhawan, L. M. P. Fernandes, A. Giesen, T. Graf, T. W. Hänsch, P. Indelicato, L. Julien, C. Y. Kao, P. Knowles, E. O. L. Bigot, Y. W. Liu, J. A. M. Lopes, L. Ludhova, C. M. B. Monteiro, F. Mulhauser, T. Nebel, P. Rabinowitz, J. M. F. dos Santos, L. A. Schaller, K. Schuhmann, C. Schwob, D. Taqqu, J. F. C. A. Veloso, and F. Kottmann, Nature **466**, 213 (2010).

[2] A. Antognini, F. Nez, K. Schuhmann, F. D. Amaro, F. Biraben, J. M. R. Cardoso, D. S. Covita, A. Dax, S. Dhawan, M. Diepold, L. M. P. Fernandes, A. Giesen, T. Graf, A. L. Gouvea, T. W. Hänsch, P. Indelicato, L. Julien, C. Y. Kao, P. Knowles, F. Kottmann, E. O. L. Bigot, Y. W. Liu, J. A. M. Lopes, L. Ludhova, C. M. B. Monteiro, F. Mulhauser, T. Nebel, P. Rabinowitz, J. M. F. dos Santos, L. A. Schaller, C. Schwob, D. Taqqu, J. F. C. A.

Veloso, J. Vogelsang, and R. Pohl, Science **339**, 417 (2013).
[3] R. Pohl, A. Antognini, F. Amaro, F. Biraben, J. Cardoso, C. Conde, A. Dax, S. Dhawan, L. Fernandes, T. Hansch, F. Hartmann, V. Hughes, O. Huot, P. Indelicato, L. Julien, P. Knowles, F. Kottmann, Y. W. Liu, L. Ludhova, C. Monteiro, F. Mulhauser, F. Nez, P. Rabinowitz, J. dos Santos, L. Schaller, C. Schwob, D. Taqqu, and J. Veloso, Can. J. Phys. **83**(**4**), 339–349 (2005).
[4] F. Kottmann, H. Daniel, F. J. Hartmann, P. Hauser, C. Maierl, V. E. Markushin, M. Mühlbauer, C. Petitjean, R. Pohl, W. Schott, and D. Taqqu, Hyp. Interact. **119**, 3 (1999).
[5] T. S. Jensen and V. E. Markushin, Eur. Phys. J. D **21**(October), 261–270 (2002).
[6] T. S. Jensen and V. E. Markushin, Eur. Phys. J. D **21**(October), 271–283 (2002).
[7] V. P. Popov and V. N. Pomerantsev, Phys. Rev. A **83**, 032516 (2011).
[8] R. Pohl, Hyp. Interact. **193**, 115–120 (2009).
[9] R. Pohl, H. Daniel, F. J. Hartmann, P. Hauser, Y. W. Liu, F. Kottmann, C. Maierl, V. E. Markushin, M. Mühlbauer, C. Petitjean, W. Schott, and D. Taqqu, Hyp. Interact. **138**, 35–40 (2001).
[10] R. Pohl, H. Daniel, F. J. Hartmann, P. Hauser, F. Kottmann, V. E. Markushin, M. Muhlbauer, C. Petitjean, W. Schott, D. Taqqu, and P. Wojciechowski-Grosshauser, Phys. Rev. Lett. **97**, 193402 (2006).
[11] L. Ludhova, F. D. Amaro, A. Antognini, F. Biraben, J. M. R. Cardoso, C. A. N. Conde, D. S. Covita, A. Dax, S. Dhawan, L. M. P. Fernandes, T. W. Hänsch, V. W. Hughes, O. Huot, P. Indelicato, L. Julien, P. E. Knowles, F. Kottmann, J. A. M. Lopes, Y. W. Liu, C. M. B. Monteiro, F. Mulhauser, F. Nez, R. Pohl, P. Rabinowitz, J. M. F. dos Santos, L. A. Schaller, D. Taqqu, and J. F. C. A. Veloso, Nucl. Inst. Meth. A **540**(**1**), 169–179 (2005).
[12] A. Antognini, F. D. Amaro, F. Biraben, J. M. R. Cardoso, C. A. N. Conde, D. S. Covita, A. Dax, S. Dhawan, L. M. P. Fernandes, T. W. Hänsch, V. . Hughes, O. Huot, P. Indelicato, L. Julien, P. E. Knowles, F. Kottmann, Y. W. Liu, J. A. M. Lopes, L. Ludhova, C. M. B. Monteiro, F. Mulhauser, F. Nez, B. N. Perry, R. Pohl, P. Rabinowitz, J. M. F. dos Santos, L. A. Schaller, C. Schwob, D. Taqqu, and J. F. C. A. Veloso, Opt. Comm. **253**(**4–6**), 362–374 (2005).
[13] A. Antognini, K. Schuhmann, F. D. Amaro, F. Biraben, A. Dax, A. Giesen, T. Graf, T. W. Hänsch, P. Indelicato, L. Julien, K. Cheng-Yang, P. E. Knowles, F. Kottmann, E. Le Bigot, Y. W. Liu, L. Ludhova, N. Moschüring, F. Mulhauser, T. Nebel, F. Nez, P. Rabinowitz, C. Schwob, D. Taqqu, and R. Pohl, IEEE J. Quant. Electr. **45**(**8**), 993–1005 (2009).
[14] M. A. Belushkin, H. W. Hammer, and U. G. Meissner, Phys. Rev. C **75**, 035202 (2007).
[15] I. Lorenz, H. W. Hammer, and U. G. Meissner, Eur. Phys. J. A **48**, 151 (2012).
[16] P. J. Mohr, B. N. Taylor, and D. B. Newell, Rev. Mod. Phys. **84**, 1527 (2012).
[17] J. C. Bernauer, P. Aschenbach, C. Ayerbe Gayoso, R. Böhm, D. Bosnar, L. Debenjak, M. O. Distler, L. Doria, A. Esser, et al., Phys. Rev. Lett. **105**, 242001 (2010).
[18] X. Zhan, K. Allada, D. S. Armstrong, J. Arrington, W. Bertozzi, W. Boeglin, et al., Phys. Lett. B **705**, 59 (2011).
[19] A. Antognini, F. Kottmann, F. Biraben, P. Indelicato, F. Nez, and R. Pohl, Ann. Phys. **331**, 127 (2013).
[20] C. Adamuscin, S. Dubnicka, and A. Z. Dubnickova, Prog. Part. Nucl. Phys. **67**, 479 (2012).
[21] A. Dupays, A. Beswick, B. Lepetit, C. Rizzo, and D. Bakalov, Phys. Rev. A **68**, 052503 (2003).
[22] A. V. Volotka, V. M. Shabaev, G. Plunien, and G. Soff, Eur. Phys. J. D **33**, 23–27 (2005).
[23] J. Friar and I. Sick, Phys. Lett. B **579**, 285 (2004).
[24] M. O. Distler, J. C. Bernauer, and T. Walcher, Phys. Lett. B **696**, 343 (2011).
[25] J. P. Karr and L. Hilico, Phys. Rev. Lett. **109**, 103401 (2012).
[26] G. A. Miller, A. W. Thomas, J. D. Carroll, and J. Rafelski, Phys. Rev. A **84**, 020101(R) (2011).
[27] R. J. Hill and G. Paz, Phys. Rev. Lett. **107**, 160402 (2011).
[28] M. C. Birse and J. A. McGovern, Eur. Phys. J. A **48**, 120 (2012).
[29] C. E. Carlson and B. C. Rislow, Phys. Rev. D **86**, 035013 (2012).
[30] R. Pohl, R. Gilman, G. A. Miller, and K. Pachucki, DOI: 10.1146/annurev-nucl-102212-170627.
[31] C. G. Parthey, A. Matveev, J. Alnis, B. Bernhard, A. Beyer, R. Holzwarth, A. Maistrou, R. Pohl, K. Predehl, T. Udem, T. Wilken, N. Kolachevsky, M. Abgrall, D. Rovera, C. Salomon, P. Laurent, and T. W. Hänsch, Phys. Rev. Lett. **107**, 203001 (2011).
[32] S. J. Brodksy, C. E. Carlson, J. R. Hiller, and D. S. Hwang, Phys. Rev. Lett. **94**, 022001 (2005).
[33] C. G. Parthey, A. Matveev, J. Alnis, R. Pohl, T. Udem, U. D. Jentschura, N. Kolachevsky, and T. W. Hänsch, Phys. Rev. Lett. **104**(June), 233001 (2010).
[34] U. D. Jentschura, A. Matveev, C. G. Parthey, J. Alnis, R. Pohl, T. Udem, N. Kolachevksy, and T. W. Hänsch, Phys. Rev. A **83**, 042505 (2011).
[35] K. Pachucki, Phys. Rev. Lett. **106**, 192007 (2011).
[36] A. Beyer, et al., this issue.
[37] E. Peters, et al., this issue.
[38] A. Antognini, F. Nez, F. D. Amaro, F. Biraben, J. M. R. Cardoso, D. S. Covita, A. Dax, S. Dhawan, L. M. P. Fernandes, A. Giesen, T. Graf, T. W. Hänsch, P. Indelicato, L. Julien, C. Y. Kao, P. Knowles, F. Kottmann, E. O. L. Bigot, Y. W. Liu, J. A. M. Lopes, L. Ludhova, C. M. B. Monteiro, F. Mulhauser, T. Nebel, P. Rabinowitz, J. M. F. dos Santos, L. A. Schaller, K. Schuhmann, C. Schwob, D. Taqqu, J. F. C. A. Veloso, and R. Pohl, Can. J. Phys. **89**, 47 (2010).

WILEY ONLINE LIBRARY

Early View publication on wileyonlinelibrary.com
(issue and page numbers not yet assigned;
citable using Digital Object Identifier – DOI)

Ann. Phys. (Berlin), 1–6 (2013) / DOI 10.1002/andp.201300076

annalen der physik

Original Paper

A new approach to test Lorentz invariance in the weak interaction

H. W. Wilschut, E. A. Dijck, S. Hoekstra, K. Jungmann, S. E. Müller, J. P. Noordmans, C. J. G. Onderwater, C. Pijpker, A. Sytema, R. G. E. Timmermans, K. K. Vos, and L. Willmann*

Received 26 March 2013, revised 10 May 2013, accepted 20 June 2013
Published online DD MM YYYY

Lorentz invariance has been tested rather poorly on the weak interaction in comparison to the electromagnetic interaction. This work discusses which tests on the weak interaction may be relevant. In particular, it considers exploiting the spin degrees of freedom in β decay for testing rotational invariance. The relation between the various phenomenological tests of Lorentz invariance is shown using a new theoretical framework.

Lorentz invariance means that physical laws are invariant under boosts and rotations. There are many experimental tests of Lorentz invariance [1]. Arguably, most tests and the most precise ones have been done on the electromagnetic interaction.

In contrast, very few tests have been made on the weak interaction, even though the Standard Model originated from – and has been shaped by – the details of the weak interaction, i.e. the violation of parity (P) and charge conjugation (C) on the one hand and the violation of the combined CP symmetry on the other. Of course, the importance of Lorentz invariance demands testing it for all interactions. Manifestations of Lorentz invariance violation (LIV) in the weak interaction can be searched for in low-energy experiments, such as in β decay.

Currently, one of the main efforts in fundamental physics is the unification of the Standard Model with General Relativity, in what are mostly referred to as quantum gravity models. Certain models of quantum gravity contain terms which violate Lorentz invariance and CPT symmetry (e.g. [2–6]). Requiring a theory that identifies the appropriate observables, Kostelecký and coworkers have developed a theoretical framework named the "Standard Model Extension" (SME) that contains all the properties of the Standard Model and General Relativity, but additionally contains all possible terms violating Lorentz and CPT symmetry resulting from spontaneous breaking of Lorentz invariance [7]. It also follows from this phenomenological approach that observables for the different interactions are a priori independent. Therefore, it is insufficient to test only the electromagnetic interaction.

We have started an experimental and theoretical program on LIV considering charged currents in the weak interaction, focusing on β decay. A theoretical framework has been formulated that gives guidance to possible experiments [8]. It also shows to what extent experiments can be related. In this theory Lorentz symmetry breaking is implemented by modifying the propagation of the W boson. The theoretical motivation can be found elsewhere [8]. Here we will discuss the relevant results for β-decay experiments. In our experimental work we focus on the spin degree of freedom which was not considered at all before.

The β-decay rate, ignoring Coulomb and induced recoil effects, is given in the Standard Model by [9]

$$\frac{d\Gamma}{\Gamma_0} = 1 + \vec{\beta} \cdot \left[A\frac{\langle \vec{J} \rangle}{J} + G\vec{\sigma} \right], \tag{1}$$

where $\vec{\beta}$ is the velocity of the β particle in units of the velocity of light, $\langle \vec{J} \rangle / J$ describes the direction and degree of nuclear polarization of the parent nucleus, $\vec{\sigma}$ is the spin vector of the β particle, and $\hbar/\Gamma_0$ is the lifetime of the nucleus. A and G are the well-known parity-violating parameters: A is the β asymmetry or "Wu" parameter and G is the longitudinal polarization of the outgoing β particle ($G = \pm 1$ for $\beta^{\mp}$).

If there is a preferred direction in space (i.e. Lorentz symmetry breaking), Eq. (1) will be modified. In that case

* Corresponding author E-mail: wilschut@kvi.nl
Kernfysisch Versneller Instituut, University of Groningen, Zernikelaan 25, 9747 AA Groningen, The Netherlands

we expect it to be of the form

$$\frac{d\Gamma}{\Gamma_0} = 1 + \vec{\beta}\cdot\left[A\frac{\langle\vec{J}\rangle}{J} + \xi_1\hat{n}_1 + G\vec{\sigma}\right] + \xi_2\frac{\langle\vec{J}\rangle}{J}\cdot\hat{n}_2 + \xi_3\vec{\sigma}\cdot\hat{n}_3. \quad (2)$$

Here $\hat{n}_i$ are the preferred directions in space. The directions do not need to be the same for the various observables, as we will show below. The ξ_i are the magnitudes of the Lorentz symmetry breaking terms. Because a measurement of $\vec{\sigma}$ inevitably involves measuring $\vec{\beta}$, it is experimentally logical to first consider ξ_1. Therefore, we will not discuss ξ_3, but we will come back to it later (Eq. (10)). The parameter ξ_1 measures the degree of β-emission anisotropy of non-oriented nuclei, while ξ_2 measures the dependence of the lifetime on orientation. With respect to Eq. (2) two important observations should be made. First, because of the low velocities of the parent nucleus we do not consider modifications of the decay rate due to boosts, i.e. a dependence on absolute velocity. Second, there are more correlations predicted in [8] than the three given in this equation. However, for the experiments we discuss here these suffice.

Concerning the β asymmetry, ξ_1, two measurements were made in the 1970s [10, 11]. Both were made for forbidden decays. The main idea behind these experiments was to test rotational invariance by trying to observe violation of angular momentum conservation. A forbidden decay will be less forbidden by the extent that angular momentum is not conserved, thereby enhancing the violating signal. By measuring the decay rate in various directions and correlating it with the Earth's rotation, deviations from isotropy were searched for. To reach high precision, the whole setup including source and detector needed to be rotated. No deviations were found with a dependence of $\cos(\omega t)$ up to a level of 1.6×10^{-7} for the unique first-forbidden transition in ^{90}Y [10], where ω is the Earth's rotation frequency. The second experiment considered a second-forbidden transition in ^{99}Tc [11] and reached a limit of 3×10^{-5}. It remains to be seen what these values mean in an underlying theory. The results of these early works are currently being evaluated [12] within the context of our theoretical work [8]. Some preliminary conclusions will be discussed below.

In our experimental work we consider a polarization-dependent lifetime, parameterized by $\xi_2\hat{n}_2$, for which no experimental information is available as yet [14]. It requires a sample of radioactive nuclei with oriented spin, for which the lifetime must be measured. We have searched for methods where these two tasks could be efficiently done. We found a class of nuclei that allows one to measure the polarization independently of the lifetime. We show in Fig. 1 the details for ^{20}Na as an example of such nuclei. The nuclear polarization is measured from the asymmetry parameter A, while the lifetime is given by the γ-decay rate. The γ-rays depopulate an excited nuclear state fed by the β decay.

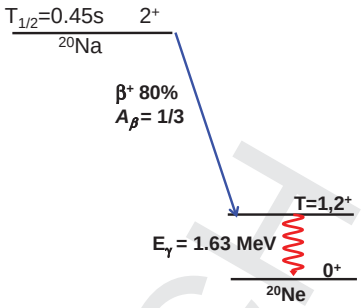

Figure 1 Relevant part of the decay scheme of ^{20}Na.

The degree of polarization is P and the direction of polarization is defined as $P\vec{j} = \langle\vec{J}\rangle/J$, where $\vec{j}$ is a unit vector in the direction of $\vec{J}$. Measuring the difference of decay rates $R_\beta^{\uparrow,\downarrow}$ between β particles emitted parallel ($\uparrow$) and antiparallel ($\downarrow$) to $\vec{J}$, one determines P by

$$P = \frac{1}{AK}\frac{R_\beta^\uparrow - R_\beta^\downarrow}{R_\beta^\uparrow + R_\beta^\downarrow}, \quad (3)$$

where K is the analyzing power of the experimental setup. With P one can extract ξ_2 by measuring the γ-decay rates for the two polarization directions:

$$\xi_2(\vec{j}\cdot\hat{n}_2) = \frac{1}{P}\frac{R_\gamma^\uparrow - R_\gamma^\downarrow}{R_\gamma^\uparrow + R_\gamma^\downarrow} = \frac{1}{P}\frac{\tau^\downarrow - \tau^\uparrow}{\tau^\uparrow + \tau^\downarrow}. \quad (4)$$

To be independent of possible changes in the sample sizes for the two spin directions, one may choose to determine the lifetimes of the sample instead of the decay rates, as noted in the last equality. We assume that the electromagnetic and strong interaction do not break Lorentz symmetry. Note also that the angular distribution of photons may depend on the degree of polarization but not on its sign.

Evaluating Eq. (4) from the γ-decay rates has the advantage that systematic errors due to variations in the polarization are mostly eliminated. Using the β-particle yield, this would lead to errors mimicking LIV.

A generic setup is shown in Fig. 2 which measures simultaneously the asymmetry in β and γ emission from a sample where the polarization can be efficiently reversed. Many of the systematic errors can be eliminated with high precision in this highly symmetric setup [16]. Although there are many isotopes that can be studied

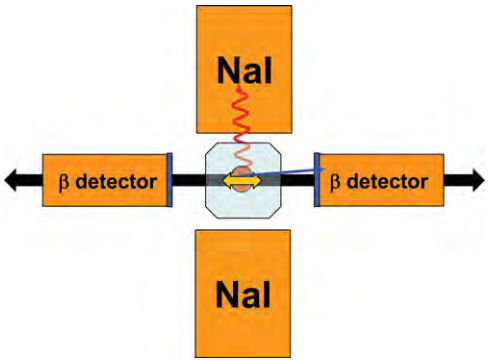

Figure 2 Generic setup to measure rotational invariance violation in spin-polarized nuclei. The yellow arrow indicates the polarization directions of the radioactive sample. The complete setup needs to be oriented in the laboratory, symbolically indicated by the black arrow, to probe specific "preferred" directions as discussed with reference to Fig. 3.

with the strategy described above, the requirement of polarization and the demand of a high source strength restrict the choice of isotope.

The direction of polarization, $\vec{j}$, should be chosen in the context of systematic errors. For example, choosing the polarization parallel to the Earth's rotation axis would result in an asymmetry of the γ yield independent of the time of day. In contrast, orienting $\vec{j}$ in the east–west direction means the asymmetry would show as a sinusoidal dependence around zero with the pattern reversing sign every half rotation of the Earth. Two cases are shown in Fig. 3 for a hypothetical "preferred direction": a polarization in the east and west directions and one in the up and down directions, i.e. perpendicular to the Earth's surface. In the latter case the asymmetry would have an offset from zero and the sinusoidal dependence would be shifted with respect to the east–west case.

It appears that the east–west configuration has to be preferred with respect to systematic errors, because a constant offset is difficult to discriminate from a systematic bias. However, in this east–west configuration, no signal would be observed if $\hat{n}_2$ is parallel to the Earth's rotation axis. Therefore, more than one orientation of the setup of Fig. 2 should be considered.

Measuring ξ_2 requires a highly active sample that can be polarized. Our laboratory has an intense solid-state laser for efficient trapping of radioactive ^{21}Na in a magneto-optical trap [17]. This laser can also be used for polarizing large samples of any Na isotope. Polarizing the sample in a buffer gas avoids the loss mechanisms associated with capturing ions, and neutralizing them for atomic trapping, and hence the buffer gas method is preferred. The decay scheme shown in Fig. 1 is applicable to ^{20}Na, ^{24}Na, ^{25}Na, ^{26}Na, and ^{27}Na. Of these, ^{20}Na, ^{26}Na, and ^{27}Na are useful in our setup (see below), but only ^{20}Na can be produced in excess of 10^6 particles per second at our facility; for this reason, ^{20}Na was selected for this study.

In this experiment we look for a change in the decay rate of the allowed β decay of ^{20}Na when reversing the orientation of the nuclear spin $\vec{J}$ via optical pumping. ^{20}Na is produced via the ^{20}Ne(p,n)^{20}Na reaction by colliding a ^{20}Ne beam with hydrogen in a gas target [18].

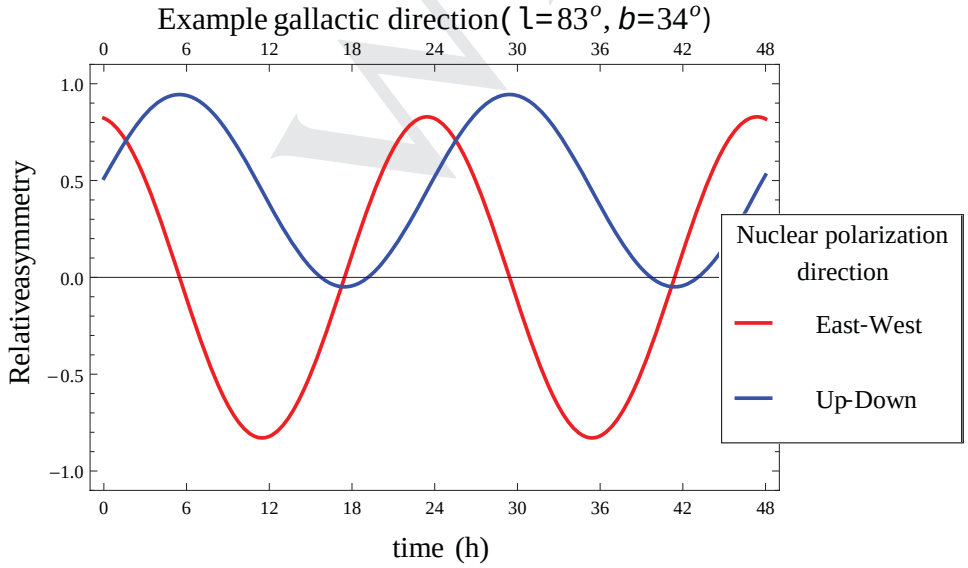

Figure 3 Example of lifetime asymmetry as a function of time for two polarization directions with an arbitrarily chosen "preferred direction" as indicated.

The resulting isotopes pass through the TRIμP isotope separator facility to obtain a ^{20}Na beam which is stopped in a buffer gas cell filled with up to 8 atm of neon gas.

Adjustable aluminum degrader foils in the beamline allow one to position the beam's stopping distribution in the center of the gas cell. The neon buffer gas is cleaned with a cryo-trap filled with liquid nitrogen and a gas purifier cartridge. A heatable dispenser with natural sodium is mounted inside the buffer gas cell. The use of the dispenser proved to be essential. The natural sodium binds residual chemically active contaminants in the gas that would otherwise bind radioactive sodium, making it unavailable for polarization.

The ^{20}Na atoms stopped in the center of the buffer gas cell are optically pumped into a "stretched" state in which the electronic and nuclear spins are both aligned along the direction of the magnetic holding field provided by Helmholtz coils. To achieve this, a circularly polarized laser beam with a wavelength of 589 nm is sent through the buffer gas cell. Remotely operated beam blockers allow one to switch the polarization of the laser light going through the cell. Depending on the helicity of the light that enters the buffer gas cell, the atoms will be pumped into a state with the spins aligned or antialigned to the direction of the magnetic field. The polarization is measured from β^+ rates as shown in Fig. 4 using Eq. (3). For better control of systematic errors we operate the setup in three short cycles of 4 s, one for each spin polarization direction and one with the laser beam off. Within each cycle the beam is on and off for 2 s. A maximum polarization of about 50% is obtained. The polarization decreases when the beam is off, presumably due to the drift of particles out of the volume covered by the laser. For this reason a short lifetime is advantageous; the half-life of ^{20}Na is 448 ms. These and other factors playing a role in the experimental method will not be discussed further here, but in a forthcoming publication [13].

Figure 4 shows also the measured γ rates. When the sample is polarized, a small enhancement of the γ emission can be observed, which is independent of the sign of the polarization. This is due to the quadrupole emission pattern of the γ-rays following the β decay of the polarized parent nucleus. Of course this signal may not depend on the sign of the polarization. A first set of data for up–down polarization has been analyzed and the results will be available soon [13]. In this dataset the precision is at a level of 10^{-3}.

In the following we give some details of the theoretical work that we use to give more physical meaning to the experimental observations. Indeed, to have limits on $\xi_i \hat{n}_i$ without being able to relate them to each other or to some underlying theory is not satisfactory. For this reason a version of the SME was formulated applicable for weak decays. We use an extension wherein the W propagator is modified. Such a specific choice, of course, cannot cover all theoretical possibilities, but it can be well motivated and is most appropriate for β decay. This theoretical work is discussed elsewhere [8]. Here, we restrict the discussion to the results of this theoretical exploration, in particular for the parameters $\xi_i \hat{n}_i$.

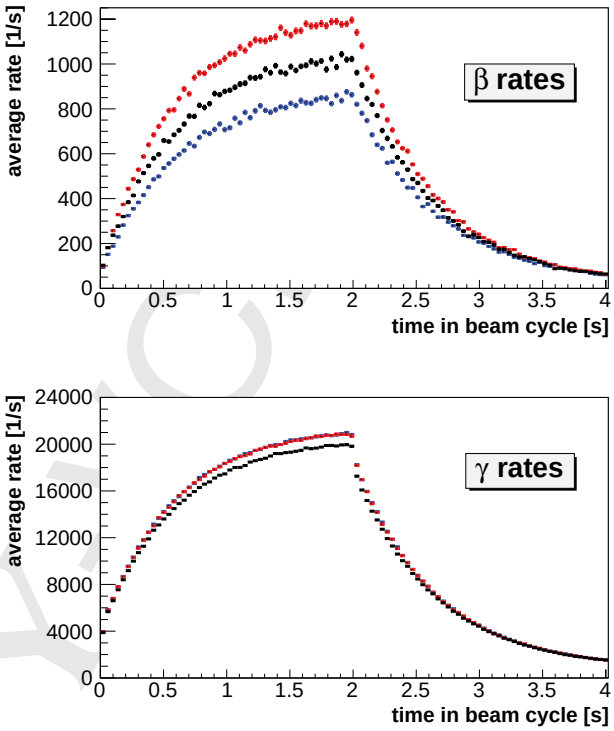

Figure 4 β (top) and γ (bottom) rates measured with laser polarization in two directions (indicated by red and blue data points, the latter mostly covered by the former) and without laser (black data points). The periods with beam on and off are 2 s.

The Lorentz-violating W propagator at low energies that we use is given by

$$\left\langle W^{\mu+}(p)\, W^{\nu-}(-p)\right\rangle = \frac{-i(g^{\mu\nu}+\chi^{\mu\nu})}{M_W^2}, \tag{5}$$

where $g^{\mu\nu}$ is the Minkowski metric and $\chi^{\mu\nu}$ is a general Lorentz-violating (complex, possibly momentum-dependent) tensor. Neglecting the dependence on boosts, i.e. assuming that the velocities of the parent nuclei are small with respect to the "preferred frame", we find that the parameter for the anisotropy of the emission direction is given by

$$\xi_1 \hat{n}_1^l = 2\chi_{\mathrm{r}}^{0l} \tag{6}$$

for Fermi transitions, while for Gamow–Teller transitions it is given by

$$\xi_1 \hat{n}_1^l = \frac{2}{3}\left(\chi_{\rm r}^{l0} + \epsilon^{lmk}\chi_{\rm i}^{mk}\right). \tag{7}$$

Here the subscript r (i) refers to the real (imaginary) part of χ; the notation is such that, for example, the right-hand side of Eq. (7) has the x component $\frac{2}{3}(\chi_{\rm r}^{10} + \chi_{\rm i}^{23} - \chi_{\rm i}^{32})$.

Thus, a striking result of this theory is that there is no single "preferred direction". It differs for Fermi and Gamow–Teller transitions, but it is also different for other observables. How $\xi_1\hat{n}_1$ depends on $\chi^{\mu\nu}$ for forbidden β decays is currently being evaluated. An enhancement for a nucleus with atomic number Z and radius R can be expected of the order of $\alpha Z/R \approx 0.3Z$, i.e. an order of magnitude larger than the LIV effect in allowed decays [12]. The underlying idea of Refs. [10, 11] that angular momentum may not be conserved in the weak interaction can thus be made quantitative in the present theory. The theory also shows that searching for LIV in second-forbidden reactions as in [11] gives no further enhancement over first-forbidden decays.

Gamow–Teller transitions allow one to explore most of the parameter space contained in χ, in particular when measuring β-spin correlations as a function of direction. The full expression is given elsewhere [8]. The parameter ξ_2, which gives the dependence on spin orientation, is relatively simple:

$$\xi_2 \hat{n}_2^l = A\epsilon^{lmk}\chi_{\rm i}^{mk}, \tag{8}$$

where A is the Standard Model β-asymmetry parameter. In terms of the generic measurement of ξ_2 and thus also for the experiment on ^{20}Na described here, one finds that

$$j^l\epsilon^{lmk}\chi_{\rm i}^{mk} = \frac{R_\beta^\uparrow + R_\beta^\downarrow}{R_\beta^\uparrow - R_\beta^\downarrow}\frac{R_\gamma^\uparrow - R_\gamma^\downarrow}{R_\gamma^\uparrow + R_\gamma^\downarrow}. \tag{9}$$

This may suggest that the experimental method just consists of measuring the rates in the detectors shown in Fig. 2. However, in particular for a short-lived sample, one would need to guarantee that conditions during the two polarization periods are identical.

For completeness we note that in our theory, for any allowed transition,

$$\xi_3 \hat{n}_3 = \mp\sqrt{(1-(\alpha Z)^2)(1-\beta^2)}\,\xi_1\hat{n}_1, \tag{10}$$

where $\mp$ refers to the case of $\beta^\mp$ decay. Measuring the β polarization with high efficiency is not possible. Moreover, $\Delta G/G \approx -\xi_3\hat{n}_3/G < \xi_1\hat{n}_1$. In this respect nothing is gained over measuring the β-emission direction only.

Of course, our theory need not be restricted to β decay but can be evaluated for any weak interaction involving the W boson. In this respect it is interesting to note that the KLOE collaboration has measured the lifetime of K_S mesons as function of the kaon emission direction with respect to the dipole anisotropy of the cosmic microwave background [21]. We find [22] that their search for anisotropy is complementary to β decay; however, to gain the maximal information on $\chi^{\mu\nu}$ a reanalysis of their data would be required.

In summary, we have identified, in the context of experimental searches for physics beyond the Standard Model, an important class of tests for Lorentz symmetry breaking in the weak interaction. These tests can be made in experiments exploiting the properties of β decay. First experiments testing the isotropy of the decay rate relative to the spin orientation of the parent nucleus in absolute space have been made.

A theoretical framework that considers modification of the W propagator has been developed. The theory has a rich structure, for example, showing that there need not be a single preferred direction for LIV. It allows one to put the various experimental tests of LIV in β decay in context, for example, by relating them to the SME, but also by showing their complementarity character. It also relates β and non-leptonic weak decays. Part of this theoretical program has been completed.

Acknowledgments. This research was supported by the Stichting voor Fundamenteel Onderzoek der Materie (FOM) under Programmes 104 and 114, and FOM projectruimte 08PR2636-1.

Key words. Lorentz invariance violation, weak interaction, Standard Model Extension, β decay, non-leptonic decay.

References

[1] V. A. Kostelecký and N. Russell, Rev. Mod. Phys. **83**, 11 (2011); and arXiv:0801.0287 [hep-ph].
[2] V. A. Kostelecký and S. Samuel, Phys. Rev. D **39**, 683 (1989).
[3] V. A. Kostelecký and R. Potting, Phys. Lett. B **381**, 89 (1996).
[4] J. R. Ellis, N. E. Mavromatos, and D. V. Nanopoulos, arXiv:gr-qc/9909085.
[5] C. P. Burgess, J. M. Cline, E. Filotas, J. Matias, and G. D. Moore, J. High Energy Phys. **03**, 043 (2002).
[6] R. Gambini and J. Pullin, Phys. Rev. D **59**, 124021 (1999).
[7] D. Colladay and V. A. Kostelecký, Phys. Rev. D **58**, 116002 (1998) .
[8] J. P. Noordmans, H. W. Wilschut, and R. G. E. Timmermans, arXiv:1302.2730.

[9] J. D. Jackson, S. B. Treiman, and H. W. Wyld Jr., Nucl. Phys. **4**, 206 (1957). The SM also has terms with $\vec{J}\cdot\vec{\sigma}$ and $(\vec{\beta}\cdot\vec{\sigma})(\vec{\beta}\cdot\vec{J})$, corresponding to the N and Q correlation coefficients, respectively. These are not discussed here, they are included in [8].
[10] R. Newman and S. Wiesner, Phys. Rev. D **14**, 1 (1976).
[11] J. D. Ullman, Phys. Rev. D **17**, 1750 (1978).
[12] J. P. Noordmans, H. W. Wilschut, and R. G. E. Timmermans, in preparation.
[13] S. E. Müller *et al.*, in preparation.
[14] A. Kozela *et al.*, in: Proceedings of the 5th Meeting on CPT and Lorentz Symmetry, Bloomington, Indiana, USA, 28 June–2 July 2010, pp. 174–178. As a by-product of measuring the R correlation parameter in the decay of the neutron, an analysis along the lines of Eq. (2) was done leading to limits of the order of 10^{-2}. See also [8] for comments.
[15] D. Colladay and V. A. Kostelecký, Phys. Lett. B **511**, 209 (2001).
[16] N. P. M. Brantjes *et al.*, Nucl. Instrum. Meth. A **664**, 49 (2012).
[17] H. W. Wilschut *et al.*, Nucl. Phys. A **844**, 143c (2010).
[18] E. Traykov *et al.*, Nucl. Instrum. Meth. A **572**, 580 (2007).
[19] S. Agostinelli *et al.*, Nucl. Instrum. Meth. A **506**, 250 (2003).
[20] J. Allison *et al.*, IEEE Trans. Nucl. Sci. **53**, 270 (2006).
[21] F. Ambrosino *et al.*, Eur. Phys. J. C **71**, 1604 (2011).
[22] K. Vos, J. P. Noordmans, H. W. Wilschut, and R. G. E. Timmermans, in preparation.

Query

Q1: Author: **References 15 (Colladay and Kosteleck), 19 (Agostinelli et al.), and 20 (Allison et al.) do not appear to be cited in the text. Please check.**

WILEY-BLACKWELL

USING e-ANNOTATION TOOLS FOR ELECTRONIC PROOF CORRECTION

Required software to e-Annotate PDFs: Adobe Acrobat Professional or Adobe Reader (version 8.0 or above). (Note that this document uses screenshots from Adobe Reader X)
The latest version of Acrobat Reader can be downloaded for free at: http://get.adobe.com/reader/

Once you have Acrobat Reader open on your computer, click on the Comment tab at the right of the toolbar:

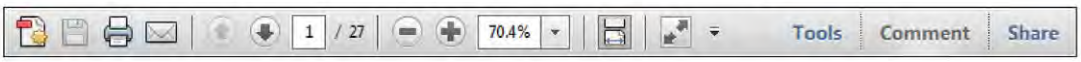

This will open up a panel down the right side of the document. The majority of tools you will use for annotating your proof will be in the Annotations section, pictured opposite. We've picked out some of these tools below:

1. Replace (Ins) Tool – for replacing text.

Strikes a line through text and opens up a text box where replacement text can be entered.

How to use it

- Highlight a word or sentence.
- Click on the Replace (Ins) icon in the Annotations section.
- Type the replacement text into the blue box that appears.

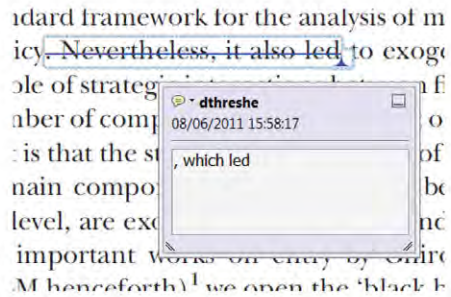

2. Strikethrough (Del) Tool – for deleting text.

Strikes a red line through text that is to be deleted.

How to use it

- Highlight a word or sentence.
- Click on the Strikethrough (Del) icon in the Annotations section.

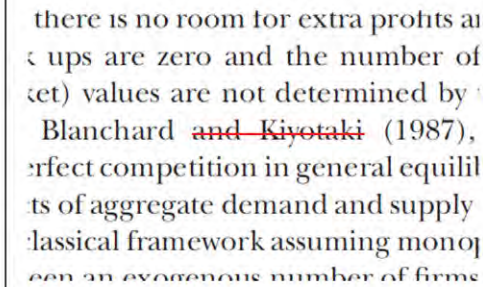

3. Add note to text Tool – for highlighting a section to be changed to bold or italic.

Highlights text in yellow and opens up a text box where comments can be entered.

How to use it

- Highlight the relevant section of text.
- Click on the Add note to text icon in the Annotations section.
- Type instruction on what should be changed regarding the text into the yellow box that appears.

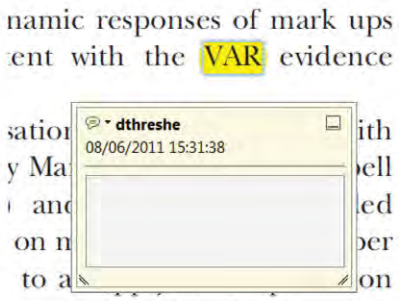

4. Add sticky note Tool – for making notes at specific points in the text.

Marks a point in the proof where a comment needs to be highlighted.

How to use it

- Click on the Add sticky note icon in the Annotations section.
- Click at the point in the proof where the comment should be inserted.
- Type the comment into the yellow box that appears.

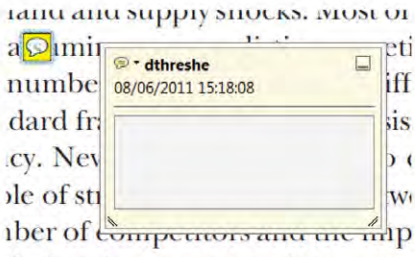

WILEY-BLACKWELL

USING e-ANNOTATION TOOLS FOR ELECTRONIC PROOF CORRECTION

5. Attach File Tool – for inserting large amounts of text or replacement figures.

Inserts an icon linking to the attached file in the appropriate pace in the text.

How to use it

- Click on the Attach File icon in the Annotations section.
- Click on the proof to where you'd like the attached file to be linked.
- Select the file to be attached from your computer or network.
- Select the colour and type of icon that will appear in the proof. Click OK.

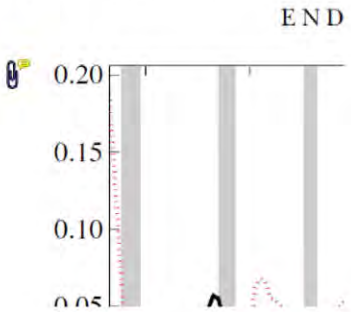

6. Add stamp Tool – for approving a proof if no corrections are required.

Inserts a selected stamp onto an appropriate place in the proof.

How to use it

- Click on the Add stamp icon in the Annotations section.
- Select the stamp you want to use. (The Approved stamp is usually available directly in the menu that appears).
- Click on the proof where you'd like the stamp to appear. (Where a proof is to be approved as it is, this would normally be on the first page).

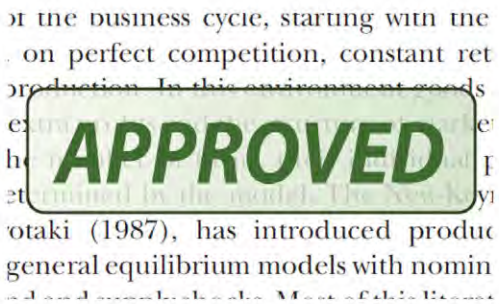

7. Drawing Markups Tools – for drawing shapes, lines and freeform annotations on proofs and commenting on these marks.

Allows shapes, lines and freeform annotations to be drawn on proofs and for comment to be made on these marks..

How to use it

- Click on one of the shapes in the Drawing Markups section.
- Click on the proof at the relevant point and draw the selected shape with the cursor.
- To add a comment to the drawn shape, move the cursor over the shape until an arrowhead appears.
- Double click on the shape and type any text in the red box that appears.

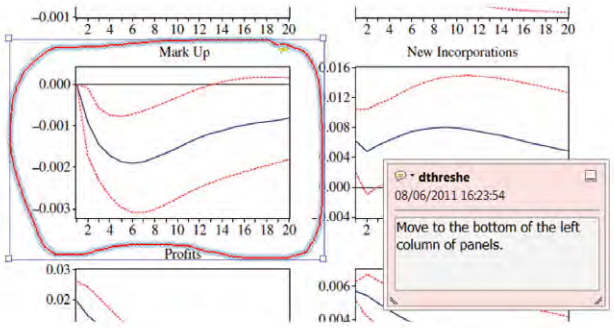

For further information on how to annotate proofs, click on the Help menu to reveal a list of further options:

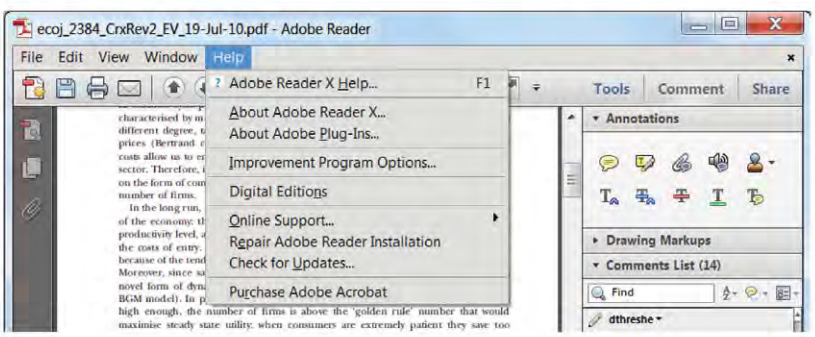

Instructions for Proof Corrections and Orders

annalen der physik

2013

WILEY-VCH Verlag GmbH
& Co. KGaA
Annalen der Physik
Rotherstrasse 21
10245 Berlin
Germany
TEL +49 (0) 30–47 03 13 21
FAX +49 (0) 30–47 03 13 99
E-MAIL ann-phys@wiley.com

WILEY
Publishers Since 1807

Please correct your proofs and return them within 5 days together with the completed reprint order form. The editors reserve the right to publish your article with editors' corrections if your proofs do not arrive in time.

After having received your corrections, your paper will be published online soon in the Wiley Online Library (wileyonlinelibrary.com).
Please keep in mind that reading proofs is your responsibility. Corrections should therefore be clear. We prefer the corrections be made directly within the PDF file (see E-annotations instructions). Alternatively, you may provide us with a list of corrections by e-mail, with the corrections referring to their line number.
Manuscript files are sometimes slightly modified by the production department to follow general presentation rules of the journal.

Note that the quality of the halftone figures is not as high as the final version that will appear in the issue.

Check the enclosed proofs very carefully, paying particular attention to the formulas (including line breakings introduced in production), figures, numerical values, tabulated data and layout of the pages.

A black box (■) or a question at the end of the paper (after the references) signals unclear or missing information that specifically requires **your attention.** Note that the author is liable for damages arising from incorrect statements, including misprints.

The main aim of proofreading is to correct errors that may have occurred during the production process, **and not to modify the content of the paper**. Corrections that may lead to a change in the page layout should be avoided.

Note that sending back a corrected **manuscript** file **is of no use**.

Return the corrected proofs within 5 days by e-mail.

Please do not send your corrections to the typesetter but to the Editorial Office:

E-MAIL ann-phys@wiley.com

Please limit corrections to errors in the text; cost incurred for any further changes or additions will be charged to the author, unless such changes have been agreed upon by the editor.

If your paper contains **color figures**, please fill in the Color Print Authorization and note the further information given on the following pages.

Full color reprints, Customized PDF files, Printed Issues, Color Print, and Cover Posters may be ordered by filling in the accompanying form.

Order Form

annalen der physik

2013

WILEY-VCH Verlag GmbH
& Co. KGaA
AdP Editorial Office
Rotherstrasse 21
10245 Berlin
Germany
TEL +49 (0) 30-47 03 13 21
FAX +49 (0) 30-47 03 13 99
E-MAIL ann-phys@wiley.com

WILEY
Publishers Since 1807

Please complete this form and return it by e-mail or FAX.

Article No.

Author/Title

e-mail address

Required Fields may be filled in using Adobe Reader

Color Print Authorization

Please bill me for

☐ color print figures (total number of color figures)

❒ YES, please print Figs. No. ☐ in color.

❒ NO, please print all color figures in black/white.

Reprints/Issues/PDF Files/Posters

Whole issues, reprints and PDF files (300 dpi) for an unlimited number of printouts are available at the rates given on the next page. Reprints and PDF files can be ordered before *and after* publication of an article. All reprints will be delivered in full color, regardless of black/white printing in the journal.

Reprints

Please send me and bill me for

☐ full color reprints with color cover

☐ full color reprints with personalized color cover

Issues

Please send me and bill me for

☐ entire issues

Customized PDF-Reprint

Please send me and bill me for

❒ a PDF file (300 dpi) for an unlimited number of printouts **with customized color cover sheet.**

The PDF file will be sent to your e-mail address.

Send PDF file to:

Please note that posting of the final published version on the open internet is not permitted. For author rights and re-use options, see the Copyright Transfer Agreement at http://www.wiley.com/go/ctavchglobal.

Cover Posters

Posters are available of all the published covers in two sizes (see attached price list). **Please send me and bill me for**

☐ A2 (42 × 60 cm/17 × 24in) posters

☐ A1 (60 × 84 cm/24 × 33in) posters

Mail reprints and/or issues and/or posters to (no P.O. Boxes):

VAT number:

Information regarding VAT

Please note that from German sales tax point of view, the charge for **Reprints, Issues or Posters** is considered as **"supply of goods"** and therefore, in general, such delivery is a subject to German sales tax. However, this regulation has no impact on customers located outside of the European Union. Deliveries to customers outside the Community are automatically tax-exempt. Deliveries within the Community to institutional customers outside of Germany are exempted from the German tax (VAT) only if the customer provides the supplier with his/her VAT number.

The VAT number (value added tax identification number) is a tax registration number used in the countries of the European Union to identify corporate entities doing business there. It starts with a country code (e.g. FR for France, GB for Great Britain) and follows by numbers.

The charge for **front cover/back cover/inside cover pictures, color figures or frontispieces publications** is considered as **"supply of services"** and therefore it is a subject to German sales tax. However, in case you are an institutional customer outside of Germany, the tax can be waived if you provide us with the VAT number of your company.

Customers outside of the EU may have a VAT number starting with "EU" instead of the country code if they are registered by the EU's tax authorities. In case you do not have a VAT number of EU and you are a taxable person doing business in a country outside EU, then please provide us with a certification from your local tax authorities confirming that you are a taxable person under the local tax law. Please note that the certification needs to confirm that you are a taxable person and you are conducting an economic activity in your country. Certifications which confirm that you are tax-exempt legal body (non-profit organization, public body, school, political party, etc.) in your country cannot be accepted for the German VAT purposes.

Purchase Order No.:

Terms of payment:

❒ Please send an invoice ❒ Cheque is enclosed

❒ **VISA, MasterCard and AMERICAN EXPRESS.**

Please use this link (Credit Card Token Generator) to create a secure Credit Card Token and include this number in the form instead of the credit card data.

https://www.wiley-vch.de/editorial_production/index.php

CREDIT CARD TOKEN NUMBER:

Send invoice to:

Signature _____

Date _____

Please use this form to confirm that you are prepared to pay your contribution.

Please sign and return this page.

You will receive an invoice following the publication of your article in the journal issue.

Price List – Annalen der Physik 2013

Reprints/Issues/PDF-Files/Posters

The prices listed below are valid only for orders received in the course of 2013. Minimum order for reprints is 50 copies. **Reprints can be ordered before *and after* publication of an article. All reprints are delivered with color cover and color figures.** If more than 500 copies are ordered, special prices are available upon request.

Single issues are available to authors at a reduced price.

The prices include mailing and handling charges. All prices are subject to local VAT/sales tax.

Reprints with color cover	Price for orders of (in Euro)					
Size (pages)	50 copies	100 copies	150 copies	200 copies	300 copies	500 copies*
1–4	345	395	425	445	548	752
5–8	490	573	608	636	784	1077
9–12	640	739	786	824	1016	1396
13–16	780	900	958	1004	1237	1701
17–20	930	1070	1138	1196	1489	2022
for every additional 4 pages	147	169	175	188	231	315
for personalized color cover	**190**	**340**	**440**	**650**	**840**	**990**

PDF file (300 dpi, unlimited number of printouts, customized cover sheet)	€ 330
Issues	€ 48 per copy for up to 10 copies.*
Cover Posters • A2 (42 × 60 cm/17 × 24in)	€ 49
• A1 (60 × 84 cm/24 × 33in)	€ 69

*Prices for more copies available on request.

Special offer: If you order 100 or more reprints you will receive a pdf file (300 dpi, unlimited number of printouts, color figures) and an issue for free.

Color figures

If your paper contains **color figures**, please notice that, generally, these figures will appear in color in the online PDF version and all reprints of your article at no cost. This will be indicated by a note "(online color at: www.ann-phys.org)" in the caption. The print version of the figures in the journal hardcopy will be black/white unless the author explicitely requests a color print publication and contributes to the additional printing costs.

	Approximate color print figure charges
First figure	€ 495
Each additional figure	€ 395 Special prices for more color print figures on request

If you wish color figures in print, please answer the **color print authorization** questions on the order form.

Global Network of Optical Magnetometers for Exotic Physics

Novel scheme for exotic physics searches

S. Pustelny[1,2], D. F. Jackson Kimball[3], C. Pankow[4], M. P. Ledbetter[1], P. Wlodarczyk[5], P. Wcislo[2,6], M. Pospelov[7,8], J. Smith[9], J. Read[9], W. Gawlik[2], and D. Budker[1,10]*

We present a novel experimental scheme enabling investigation of transient exotic spin couplings. The scheme is based on synchronous measurements of optical-magnetometer signals of several devices operating in magnetically shielded environments in distant locations ($\gtrsim$ 100 km). Although signatures of such exotic couplings may be present in a signal of the single magnetometer, it would be challenging to extract them from noise. With correlation measurements of signals from the magnetometers, not only the effects can be identified but their nature may also be investigated. The ability of the network to investigate physics beyond the Standard Model is discussed by considering the spin coupling to stable topological defects (e.g. domain walls) of axion-like fields. It is shown that the network consisting of sensitive optical magnetometers is capable to probe an axion-like-field parameter space unconstrained by other experiments.

1 Introduction

Among all magnetometric techniques, optical magnetometry [1,2] presently offers the possibility of the most sensitive magnetic-field measurements [3]. Intrinsic sensitivity of optical magnetometers (OMAGs) to spin dynamics does not limit their application to magnetic-field detection but also enables investigation of other spin interactions, including non-electromagnetic ones (see Ref. [2] and references therein). In particular, OMAGs can be applied to probe couplings between spins and hypothetical fields not predicted by the Standard Model. Such exotic fields are postulated by a variety of theories [4–13]. One manner in which they could manifest themselves on Earth is as transient events. A particular example would be transient coupling of spins to certain constituents of dark matter (DM) and dark energy (DE) [12].

Most experimental DM searches aim at direct detection of some variety of particles that feebly interact with ordinary baryonic matter, e.g., Weakly Interacting Massive Particles (WIMPs) or axions [14]. Until now, however, all the searches have produced only upper limits on the interaction strength between DM and ordinary baryonic matter. Over the years, however, alternative candidates for DM have been proposed. For example, if DM consists of light

* Corresponding author E-mail: pustelny@uj.edu.pl
1 Department of Physics, University of California at Berkeley, Berkeley, California 94720-7300
2 Institute of Physics, Jagiellonian University, Reymonta 4, 30-059 Krakow, Poland
3 Department of Physics, California State UniversityŰEast Bay, Hayward, California 94542-3084, USA
4 Center for Gravitation, Cosmology, and Astrophysics, Department of Physics, University of Wisconsin-Milwaukee, 1900 E. Kenwood Blvd, Milwaukee WI 53211
5 Department of Electronics, AGH University of Science and Technology, Mickiewicza 30, 30-059 Krakow, Poland
6 Current address: Faculty of Physics, Astronomy, and Informatics, Nicolaus Copernicus University, Grudziadzka 5, 87-100 Torun, Poland
7 Department of Physics and Astronomy, University of Victoria, Victoria, British Columbia V8P 1A1, Canada
8 Perimeter Institute for Theoretical Physics, Waterloo, Ontario N2J 2W9, Canada
9 Gravitational-Wave Physics and Astronomy Center, Department of Physics, California State University Fullerton, 800 N State College Blvd., Fullerton CA, 92831
10 Nuclear Science Division, Lawrence Berkeley National Laboratory, Berkeley, California 94720

axions or axion-like particles, it behaves more like a coherent field than a collection of uncorrelated particles [15,16]. In some theoretical scenarios, because the vacuum energy of the axion field is non-zero, the field oscillates at a specific frequency and hence it would not produce static effects on baryonic matter. Such DM scenarios also tend to be generated by stable topological defects [12, 17–23], e.g., an axion-like field with a domain structure [12]. When the Earth crosses one of the domain walls (DWs) separating regions with different vacuum expectation values of the axion-like field, a torque can be exerted on leptonic or baryonic spins. Such a DW-crossing event could lead to transient signal detectable with modern state-of-the-art OMAGs [12]. Based on astronomical constraints, however, one can show that wall-crossing events are rare and brief [12], so the major issue becomes separation of the transient signals induced by the DW crossing from transient signals generated by environmental and technical noise. Reliable rejection of OMAG's transient signals due to other effects requires development of a new approach.

In this paper, we demonstrate the principles of a new technique for detecting transient signals of exotic origin using a global network of synchronized OMAGs (the Global Network of Optical Magnetometers for Exotic physics, GNOME). Although the network may be used for detection of a variety of transient interactions heralding physics beyond the Standard Model, here, for concreteness, we focus our considerations on the transient effects induced by crossing through the DWs of axion-like field. We demonstrate that application of the GNOME enables probing presently unconstrain parameters of the field.

The article is organized as follows. First, a general discussion of OMAGs with a special attention drawn to their most important characteristics relevant for detection of exotic transient events is provided. Next, we review the theory of domain walls of axion-like fields relevant to their detection by the GNOME (Sec. 3). Section 4 discusses a first demonstration experiment using synchronously detected signals of two OMAGs separated by about 9000 km. These two magnetometers form the first elements of the envisioned future GNOME. The principles that form the basis of the GNOME data analysis are outlined in Sec. 5. Finally, the prospects of the GNOME are discussed in Sec. 6 and conclusions are drawn in Sec. 7.

2 Characteristics of OMAGs relevant for the detection of transient effects

Detection of transient events that weakly perturb atomic spins requires OMAGs with specific characteristics. In particular, a suitable device needs to have high enough sensitivity to detect small changes in spin dynamics. Moreover, its response to abrupt changes of spin behavior needs to be suitably fast not to distort or average out the signals, so that their time-domain signature can be reliably understood and compared between different GNOME sites. High sensitivity and high bandwidth, however, may not always be compatible with each other. Typically, high-sensitivity OMAGs also have characteristically slow spin relaxation times, which typically leads to narrower bandwidths, whereas high bandwidth devices typically have faster spin relaxation times, which degrades sensitivity. Below, we discuss fundamental and technical limitations of OMAG sensitivity as well as factors determining the bandwidth of the devices. Discussion of other characteristics of the magnetometers, relevant for detection of transient signals, is also provided.

In OMAGs, detection of magnetic fields occurs in a three-phase process. First, atoms are optically pumped; next, they evolve under the influence of external fields; finally, their quantum state is detected with light [1]. While this scheme allows for the most sensitive measurements of magnetic fields, it also sets a fundamental limit on the sensitivity of OMAGs. The limit results from the quantum nature of photons and atoms and the coupling between them. In the most general form, the fundamental limit of the sensitivity $\delta B_f = \sqrt{\delta B_{at}^2 + \delta B_{ph}^2 + \delta B_{ba}^2}$, where δB_{at} is the magnetic-sensitivity limit due to spin-projection noise (SPN), δB_{ph} is the limit related to photon shot noise, and δB_{ba} is the limit associated with back-action of the probe light on the atoms. The projection noise originates from the Heisenberg uncertainty principle $\delta F_i^2 \delta F_j^2 \geq |\langle [F_i, F_j] \rangle|^2/4 = \hbar^2 \langle F_k \rangle^2/4$, where $F_{i,j,k}$ are three components of the spin $\mathbf{F}$ and [,] denotes the commutator. When this relation become an equality, the SPN-limited magnetic-field sensitivity δB_{at} may be written as [2]

$$\delta B_{at} = \frac{1}{g\mu_B} \sqrt{\frac{1}{N_{at} T_2 \tau}}, \tag{1}$$

where N_{at} is the total number of atoms involved in the light-atom interaction, T_2 is the transverse spin-relaxation time, τ is the duration of the measurement, g is the Landé factor, μ_B is the Bohr magneton, and we use natural units ($\hbar = c = 1$) [2]. Equation (1) reveals two strategies to im-

[1] The phases may either be separated in time or may occur simultaneously.

[2] Although for a minimum uncertainty state, the sensitivity δB_{at} scales as $1/\sqrt{N_{at}}$, for a quantum system with entanglement

prove the sensitivity of OMAGs. The first consists in prolonging the transverse spin-relaxation time T_2, for example, by containing the atoms in a glass cell with antirelaxation coating that preserves spin polarization upon atomic collisions with cell walls or introducing a buffer gas with a low spin-depolarization cross-section into the cell to limit diffusion to the walls. The second approach relies on increasing the number of atoms N_{at}. Both approaches are used in OMAGs and in fact, herein we discuss experimental results obtained with OMAGs exploiting both methods (Sec. 5).

The second contribution δB_{ph} to the fundamental magnetometric sensitivity δB_f is associated with the fluctuation of the number of photons in the light beam used for probing the spins. Due to Poissonian statistics of photons, the intensity and polarization-state of light can only be determined with a finite precision $\propto (\dot{N}_{ph}\tau)^{-1/2}$, where $\dot{N}_{ph}$ is a number of photons of the probe beam hitting detector per unit time. This sets a limit on the precision with which the spin state can be determined and hence the limit on the magnetometric sensitivity. It is important to note, however, that this contribution can be reduced by detuning the probe light frequency away from a resonant optical transition and simultaneously increasing the light intensity. The photon shot-noise limited sensitivity improves due to the increase in $\dot{N}_{ph}$, and the probe light only weakly affects the medium while the state can still be efficiently determined (absorption on an isolated transition scales as $1/\Delta^2$ and dispersion as $1/\Delta$, where Δ is detuning). Hence, the contribution of the photon shot noise to the total magnetometric sensitivity δB_f may be reduced so that $\delta B_{ph} \ll \delta B_{at}$.

The last source of fundamental noise comes from the Stark shift of energy levels induced by quantum fluctuations of light intensity and polarization (back action) [26]; fluctuations of energies of magnetic sublevels introduce uncertainty in spin precession and hence limit magnetometric sensitivity. Yet, there are means of reducing or eliminating backaction [24, 27, 28]. One approach is based on the same principle as used to reduce δB_{ph}, i.e., detuning the probe-light frequency far from any resonant transition [29]. This approach allows reduction of δB_{ba} so that, under optimized conditions, Eq. (1) accurately represents the fundamental sensitivity limit of the magnetic-field measurements with OMAGs ($\delta B_f \approx \delta B_{at}$).

Typically, on top of fundamental noise, there is technical noise δB_t. For example, optical noise may be induced by mechanical vibration of optical elements or air turbulence in the probe-beam optical path. Electronics used in light detection can also contribute to technical noise. With appropriate experimental measures, the influence of the noise on overall magnetometric sensitivity may be reduced but it cannot be completely eliminated. Thus, in many cases, it is a significant (sometimes dominant) contribution to OMAG sensitivity.

A different source of noise originates from uncontrollable magnetic fields. Such fields result in random response of OMAGs thus reduces the sensitivity of an OMAG to non-magnetic interactions affecting the atomic spins. In the case of OMAGs enclosed inside a magnetic shield, a common configuration for precision measurements, uncertainty in spin-dynamics measurements may be introduced by external magnetic fields penetrating into the shield [3], thermal currents induced in the shield material, and instability of the current source used for generating magnetic fields. The noise may be reduced by application of active cancelation of the field outside the shield and/or used of low electric conductivity high magnetic susceptibility shielding materials [4]. Another common approach is to employ comagnetometry techniques, where the magnetic field is measured by multiple species expected to have different couplings to the exotic fields, allowing subtraction or cancelation of magnetic field noise.

Although OMAGs do not have intrinsic $1/f$ noise, existence of technical noise suggests an advantage of detection of optical signals at frequencies higher than $1/f$-"knee". This may be achieved either by modulation of the probe light, i.e., by application of intensity, frequency, or polarization modulation, and phase-sensitive detection of

the scaling could be stronger ($\delta B_{at} \propto 1/N_{at}$). In principle, it should allow for a large improvement in magnetic-field sensitivity of OMAGs. Unfortunately, the entangled states are fragile and rarely improvement of the sensitivity δB_{at} below Eq. (1) is observed [24, 25].

[3] Note that the sensitivity of the magnetometer is at a level of 10^{-15} T/$\sqrt{\text{Hz}}$ or better, while the Earth magnetic field is $\approx 4 \times 10^{-5}$ T. Hence even with a shielding factor of $> 10^6$ for DC fields, the magnetometer is still strongly sensitive to the fluctuation of the external fields.

[4] In order to limit magnetic-field noise due to Johnson currents in the shield, modern magnetic shields have the innermost layer made of ferrite. Although such material has significantly lower magnetic susceptibility than permaloys, in particular, μ-metal, they have orders of magnitude larger resistivity, which suppresses thermal currents in the magnetic-shield layer placed closest to a vapor cell (see Ref. [2] and references therein).

the signal, or by operation of the devices in non-zero magnetic fields $B \gg \hbar/T_2 g\mu_B$. In the latter case, the output signal of the magnetometer is modulated at the Larmor frequency $\omega_L = g\mu_B B/\hbar$ or a multiple thereof, which enables filtering of the low-frequency noise. To detect such higher-frequency signals, however, OMAGs with broad dynamic ranges are required.

Operation at non-zero magnetic fields raises another important issue in magnetic-field detection. Optical magnetometers enable either scalar measurements, where the device response depends on the magnitude of a magnetic field, or vector measurements, where it is determined by specific vector components of the field. However, even scalar magnetometers operating at non-zero magnetic fields become primarily sensitive to the field changes along the dominant component of the field; transverse components of the field add as second-order corrections to the total-field magnitude B. Moreover, modulation of the magnetic field in three spatial directions enables a scalar magnetometer to detect the three vector components of the field [30]. There also exist techniques enabling conversion of a scalar magnetometer into a vector magnetometer without the necessity of applying a modulated magnetic field [31]. The ability to determine not only a magnitude but also the direction of the spin-coupling field may have implications for the envisioned detection of transient effects due to exotic interactions.

Another characteristic of OMAGs, particularly important in detection of transient signals, is bandwidth. For typical OMAGs (see Ref. [2] and references therein), the response of the magnetometer to small field changes is equivalent to a response of a first-order low-pass filter with the time constant T_2 [32]. Hence the natural bandwidth of such OMAGs is given by $(2\pi T_2)^{-1}$, which for shorter measurement times, i.e., $\tau < T_2$, takes the form $(2\pi\tau)^{-1}$. OMAG bandwidth can be broadened by shortening T_2, which can be, for example, accomplished by increasing intensity of the probe light (power broadening). That increase of the magnetometer bandwidth often occurs at the cost of its sensitivity [Eq. (1)]. Therefore, optimized operation of OMAGs requires a compromise between the two quantities. It should be noted, however, that application of quantum nondemolition measurements enables to achieve sensitive magnetic-field measurements at high bandwidth [33, 34].

In order to detect transient spin couplings, the signal characteristics must fall into the detection capabilities of the OMAGs used. Table **??** summarizes characteristics of various OMAGs with potential applicability to the GNOME. Although they differ in various aspects, many of them have the potential to be successfully employed as GNOME sensors.

3 Theoretical background

A specific example of exotic spin coupling that may be detectable with the GNOME is the transit of the Earth through a domain wall (DW) of a light pseudoscalar (axion-like) field [12]. Stable domain structure of axion-like fields is a consequence of certain Standard Model extensions [45–48]. Domains form out of the initially random distribution of the vacuum expectation values of the axion-like field as the Universe expands and cools. In this scenario, DWs separate regions of space with different energy vacua [49]. Importantly, based on astrophysical constraints, only light axion-like fields can build DWs that persist to the present epoch [5].

A detailed theoretical background of the optical detection of wall crossings is presented elsewhere [12]. Here we only briefly review the concept. We start with considering a hypothetical pseudoscalar field $a(\mathbf{r})$ that permeates the Universe and forms a domain structure. As shown in [12], a specific realization of the field existing between neighboring domains with different energy-degenerate vacua (with the DW centered at z=0)

$$a(z) = 4a_0 \arctan[\exp(m_a z)], \tag{2}$$

where a_0 is the characteristic amplitude of the field and m_a is the pseudoscalar-particle mass. Coupling between the axion-like-field gradient ∇a and the spin $\mathbf{F}$ arising during the domain-wall crossing is described by the Hamiltonian [6]

$$H_{\rm DW} = \frac{\mathbf{F}\cdot\nabla a}{F f_{\rm eff}}, \tag{3}$$

where $f_{\rm eff}$ is the effective decay constant in units of energy. $f_{\rm eff}$ depends on the atomic structure of the particles used in a specific OMAG and is a combination of the decay constants of electron ($f_{\rm e}$), proton ($f_{\rm p}$), and nucleon ($f_{\rm n}$). By substituting Eq. (2) into Eq. (3), the Hamiltonian $H_{\rm DW}$ can be expressed using the field parameters m_a and a_0

$$H_{\rm DW} = \frac{2}{f_{\rm eff}} \frac{a_0 m_a \cos\varphi}{\cosh(m_a z)}, \tag{4}$$

where φ is the angle between the spin $\mathbf{F}$ and the field gradient ∇a.

[5] Formation of the wall from QCD-axion field would lead to disastrous cosmological consequences due to the excessive energy stored in the walls.

[6] Note that in general, the higher-order couplings to the spins may be considered (see Ref [12] for further details).

Table 1 Various OMAGs characteristics important for detecting transient signals due to exotic spin couplings. δE_f and δE_d are the fundamental and demonstrated OMAG sensitivities in energy units. The names of the magnetometers indicate the type of the device. HFP is an abbreviation of hexafluorobenzene.

Name	Element(s)/ Compound(s)	δE_f $\left(\mathrm{eV}/\sqrt{\mathrm{Hz}}\right)$	δE $\left(\mathrm{eV}/\sqrt{\mathrm{Hz}}\right)$	T_2 (ms)	Spin coupling	Ref
SERF	K-^{4}He	2.9×10^{-22}	3.1×10^{-21}	100	Total	[3]
μ-SERF	Cs	3.9×10^{-20}	5.8×10^{-20}	5	Total	[35]
NMR-SERF hybrid	pentane-HFB	10^{-23}	3.5×10^{-19}	20000	Nuclear	[36]
NMOR	Rb	5.8×10^{-21}	5.8×10^{-19}	300	Total	[37]
FM/AM NMOR	Rb	4×10^{-20}	1.2×10^{-18}	300	Total	[38–40]
M_x	K, Cs	1.4×10^{-19}	5.8×10^{-19}	300	Total	[41, 42]
μ-M_x	Cs	7.2×10^{-19}	1.4×10^{-18}	0.06	Total	[43]
Hg EDM	Hg	2×10^{-24}	2.5×10^{-22}	100000	Nuclear	[44]

Until now, only lower bounds on the decay constants have been established by astronomical observations ($|f_{\mathrm{e,n,p}}| > 10^9$ GeV). Below we show that the coupling can be further investigated using the GNOME.

The thickness of the DW d is determined by the pseudoscalar-particle mass m_a via

$$d = \frac{2}{m_a}. \tag{5}$$

Consequently, the mass also limits the duration of the transient signal $\Delta t = d/v_\perp$, where $v_\perp$ is the relative speed between the DW and the OMAG. At distances much larger than d, the walls may be characterized by the tension σ, which is the mass/energy per unit area of the DW. In the considered case, it can be written as a function of the field parameters

$$\sigma \approx m_a a_0^2. \tag{6}$$

The tension can be related to the DW energy density ρ_{DW} via $\rho_{\mathrm{DW}} \approx \sigma/L$, where L is the characteristic size of the domain. Importantly, the density ρ_{DW} needs to be smaller than the DM density ρ_{DM} ($\rho_{\mathrm{DM}} \approx 0.4$ GeV/cm^3) or the DE density ρ_{DE} ($\rho_{\mathrm{DE}} \approx 0.4\times10^{-5}$ GeV/cm^3). Determination of the tension also requires knowledge about the characteristic size of the domain L. Since it is not possible to determine L without further assumptions about the specific mechanism of domain-structure formation, here we treat L as a free parameter and constrain it from an experimental perspective, i.e., the experimental feasibility implies that the average time T between two wall crossings should not be longer than 10 years. By taking into account the speed of the solar system relative to the Galactic frame ($v \approx 10^{-3}c$), a DW-crossing event will occur within a time-span of 10 years if the domain size is less than 10^{-2} ly.

By combining Eqs. (4) and (6), one obtains the formula for the effective decay constant f_{eff} at the center of the wall ($z = 0$)

$$f_{\mathrm{eff}} = \frac{2\sqrt{\rho_{\mathrm{DW}} L m_a}}{\delta E}\cos\varphi, \tag{7}$$

where δE is the sensitivity of an OMAG in energy units.

Figure 1 presents the parameter space that can be probed with OMAGs. The shaded region indicates the parameter range that can be realistically probed with the OMAG of a sensitivity of $\approx 3\times10^{-20}$ eV/$\sqrt{\mathrm{Hz}}$ and a characteristic DW-size of 10^{-2} ly. It indicates that detection of axion-like field domain structure with the DM energy density ρ_{DM} is possible with the OMAG. Moreover, with higher sensitivity magnetometers (see Table **??** and discussion in Sec. 6), the parameter space can be further explored enabling probing DWs with the density ρ_{DW}, given by the DE density ρ_{DE} [12].

Being able to detect a single 10-ms duration event in a 10-year time-span requires continuous and robust operation of the magnetometer on a comparable time scale. Figure 2 presents the average time between DW crossings as a function of the decay constant f_{eff} an OMAG with

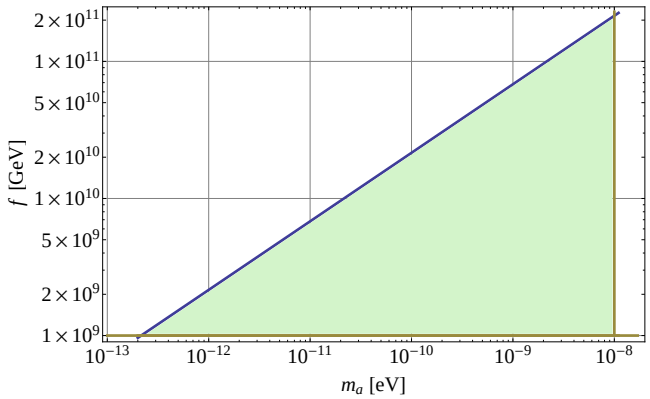

Figure 1 Parameter space of the axion-like field with a domain structure that can be probed with the GNOME (green shaded region). The blue line limits the space due to the sensitivity of applied magnetometers (assumed here to be 2.9×10^{-20} eV/$\sqrt{\text{Hz}}$, which corresponds to a sensitivity of 10^{-15} T/$\sqrt{\text{Hz}}$ of the cesium NMOR magnetometer). The two green lines arise from exiting limits from the astronomical observations [50] (the horizontal line at 10^9 GeV) and the duration of the experiment being less than 10 years (vertical line at 10^{-8} eV). For the plot the DW energy density was assumed to equal the DM energy density ($\rho_{\text{DM}} \approx 0.4$ GeV/cm^3).

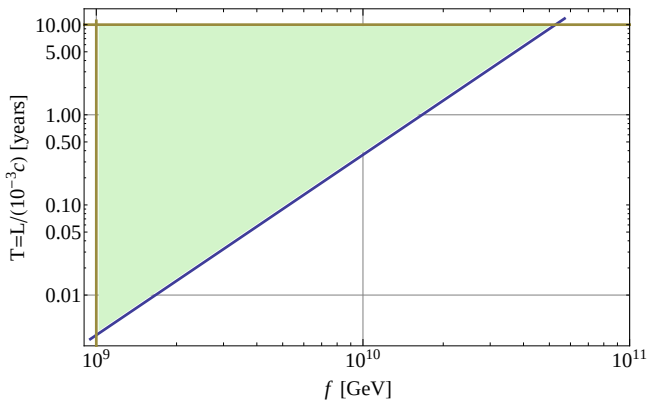

Figure 2 Average time between successive DW crossings T as a function of the effective decay constant f_{eff} (green shaded). The blue line is determined by a magnetometer sensitivity of 2.9×10^{20} eV/$\sqrt{\text{Hz}}$ corresponding to 10 T/$\sqrt{\text{Hz}}$), while the meaning of green lines is the same as in Fig. 1.

a sensitivity equal to 2.9×10^{20} eV/$\sqrt{\text{Hz}}$ (1 fT/$\sqrt{\text{Hz}}$). The results show that the OMAG can probe significant regions of parameter space in as few as three days of continues operation. The accessible parameter space expands rapidly with increasing duration of the measurements.

While, in principle, the parameters of the model can be constrained with a single magnetometer, a particular problem for a search carried out with a single OMAG is the appearance of brief spikes in the OMAG signal related to technical noise or abrupt magnetic field changes. In a single device, rejection of these false-positive signals is difficult. At the same time, coincident measurements between two or more instruments are helpful in rejecting such signals; they provide consistency checks, since a signal would be expected to exist in all instruments whereas environmentally induced events are not typically correlated in the time window required for coincidence. Furthermore, information about a putative event such as its impinging direction can be determined by triangulation if several instruments (at least four) are taking data simultaneously (see discussion in Sec. 6). These features clearly show that synchronous operation of multiple synchronized, geographically separated OMAGs within the proposed GNOME may facilitate searches for such transient signals of astrophysical origin.

4 Experimental apparatus

The concept of the experimental apparatus is shown in Fig. 3. Since detailed descriptions of the two OMAGs used in our experiment may be found elsewhere [38, 51], we only briefly review the most important elements of the devices. Both magnetometers use rubidium vapors as the magneto-optically active medium. In the Kraków magnetometer, the atomic vapor is contained in a paraffin-coated evacuated cylindrical glass cell with volume $\approx$ 3 cm^3. The vapor cell is maintained at about 50°C corresponding to an atomic density of roughly 10^{11} atoms/cm^3. The relaxation rate of the atomic ground state is $2\pi\times$ 30 s^{-1}, which yields a fundamental sensitivity δB_f of ≈ 3 fT/$\sqrt{\text{Hz}}$ (spin-projection limited) [7]. The second magnetometer (Berkeley) exploits a microfabricated vapor cell [52] of a volume of 0.01 cm^3 that is heated up to about 200°C. Operation in the spin-exchange relaxation free regime [53] allows eliminations of relaxation due to spin-exchange collisions, one of the main ground-state polarization-relaxation mechanisms. Application of the technique allows one to obtain a ground-state relaxation rate of about $2\pi\times 400$ s^{-1}, which in combination with 3-4

[7] Note that the demonstrated sensitivity of the magnetometer δB is lower.

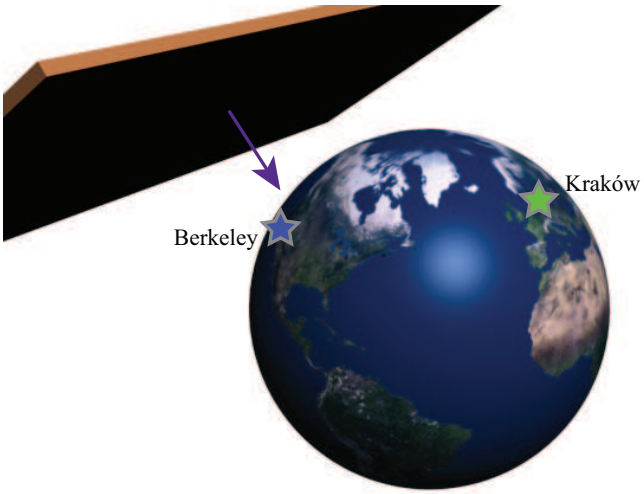

Figure 3 The concept of the synchronized-magnetometer arrangement. OMAGs located at globally separated locations record signals with a time synchronization provided by the GPS. By synchronously detecting and correlating magnetometer signals, transient events of global character may be identified. In particular, correlating signals of at least four devices enables detection of spatiotemporal character of the event. Here, two devices located in Kraków and Berkeley are used to search for transient signals induced by crossing of a DW of an axion-like field.

orders of magnitude higher density yields a similar sensitivity as for the other setup, i.e., about 1 fT/$\sqrt{\text{Hz}}$ [8]. Both magnetometers thus have the capability to detect a DW crossing and probe the parameter space.

Both magnetometers are placed inside multilayer magnetic shields made of μ-metal with the innermost layer made of ferrite [9]. The shields reduce external magnetic fields by a factor larger than 10^6. Inside the shield atoms are subjected to a stable, well-controlled magnetic field generated by a set of three-dimensional magnetic-field coils. In the Kraków magnetometer a field with a magnitude of 10^{-7} T is applied, while at Berkeley the applied-field magnitude is $\approx 5 \times 10^{-8}$ T.

[8] The demonstrated sensitivity of the device δB is roughly 10 fT/$\sqrt{\text{Hz}}$.

[9] While magnetic shields do not screen exotic interactions, their role in searches for transient exotic couplings require more thorough investigations in the future.

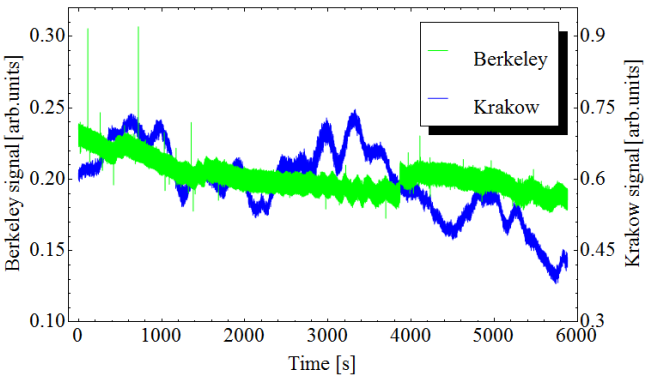

Figure 4 Synchronously detected signals of the two OMAGs located in Kraków and Berkeley. The signal in the Kraków magnetometer was measured at a field of 100 nT, whereas the Berkeley magnetometer operated at 50 nT. The data acquisition rate was 256 samples per second.

The outputs of the magnetometers are acquired using custom-made devices based on Trimble Resolution-T GPS (Global Positioning System) time receivers. The data acquisition devices provides time markers separated by one second with a precision of about 80 ns synchronized with a quartz clock built into the devices. The acquisition devices can record simultaneously signals in four channels with at a rate of 1000 samples/s. Each one-second-long record is stored on a memory card with a header containing information on time, location, etc. Every record is transmitted to the computer (via serial port) where it is binned into groups of 10-1000 records (typically 2-minute long bins are generated). The data are stored with computers located at the respective locations, and every 1-2 hours the information is exchanged between Krakow and Berkeley using File Transfer Protocol (FTP). In this manner, the complete set of data is accessible in either of the locations. The detailed discussion of the GPS-synchronized data-acquisition devices is presented in Ref. [54].

5 Results and Data Analysis

Figure 4 presents magnetometer signals measured synchronously in the two locations (Berkeley, California, USA and Kraków, Poland) over a period of about 1.5 hours. Relative to the mean amplitude of the signal, the long-term drift of the Kraków magnetometer is larger than that of the Berkeley magnetometer. This is most likely attributable to instability of the laser frequency, which

will be addressed in the future by implementation of laser-stabilization techniques. The Berkeley magnetometer signal exhibits short duration ($\lesssim 4$ ms) spikes of relatively large amplitudes not observed in the Kraków signal. Auxiliary tests verified that the noise spikes originated from electronic pick-up, a problem that will be addressed in the future.

In many respects, identification of a DW-crossing event using the GNOME is similar to searches for gravitatio wave bursts with a system of long-baseline laser interferometers [such as the Laser Interferometer Gravitational-Wave Observatory (LIGO), the Virgo detector, GEO 600, and TAMA 300] [55]. Both types of experiments aim to identify and characterize transient signals and search for time-domain correlations between the transient signals from different detectors. Importantly, the field of transient gravitational-wave astronomy has developed a variety of statistical methods to identify brief (duration $\lesssim 1$ s) signals correlated among different detectors but otherwise generic in noisy time series data.

As a proof-of-principle demonstration, we have applied one of the methods upon which such statistical analysis is based, the "excess power" statistic [56], to the synchronous magnetometer data from the Kraków and Berkeley sites. The analysis is carried out as follows. First, an estimation of the power spectral density (PSD) over several continuous, overlapping segments of the data is made for the data from each individual detector. These spectra are updated at regular intervals and combined with previous measurements using a running median exponentially-weighted history (this is a filter that weights contributions to the moving average by a factor that decreases exponentially with the time since the data was acquired). The PSD is then used to whiten the data, ideally, producing a stream of Gaussian distributed, zero-mean, unity variance random variables characterizing the data set. Whitening the data removes correlations between the different variables used to characterize the magnetometer signals. The stream of whitened data is then passed through a bank of band-limited filters producing several channels of filtered data. The filters are Hann windows in the frequency domain, which are themselves whitened with the PSD. The resulting streams are a discrete localization of the energy in the original data stream described by "tiles" having a time-frequency extent bounded by a bandwidth $\Delta\nu_f$ (the bandwidth of the filters) and duration δt. The resulting tile is constructed so as to have N_{DOF} independent degrees of freedom such that $N_{\mathrm{DOF}} = 2\delta\nu_f\delta t$ [57].

The final product is a time/frequency map of tiles describing the whitened signal energy (Fig. 5). Under the conditions of stationarity (the PSD does not fluctuate on the time scale of the estimation process) and Gaussian-

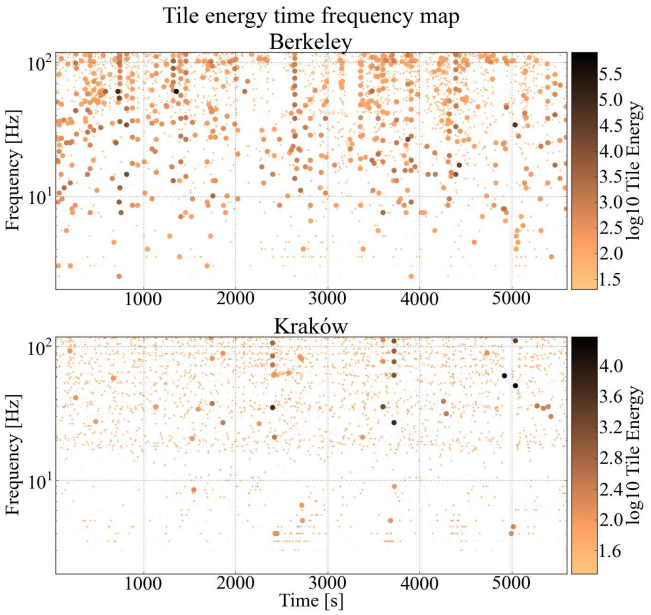

Figure 5 Time-frequency maps of outlying tile energies of the Berkeley (top) and Krakow (bottom) OMAG data. Each dot represents a tile characterized by its power-weighted central time (x-axis), Fourier frequency (y-axis), and tile energy (color and dot size). The large markers indicate tiles with a normalized tile energy greater than 100. Large tile energies are likely caused by discontinuities (which cause short but broadband responses) in the data or environmental influences within the instruments themselves.

ity (the data samples have a distribution matching the Gaussian distribution), the tile energies are distributed as a χ^2 distribution with degrees of freedom as described above. Thus the significance of any tile's energy is well-understood and the statistical probability of outlier tiles can be measured. Correlated transient signals from different magnetometers can be searched for by using the time/frequency tile maps to find overlapping events with related characteristics. Time shifts can be introduced into the data to check for correlated transient events with particular relative delays.

Examination of the time/frequency map of whitened signal energy shown in Fig. 5 reveals that the Kraków instrument produces fewer "loud" transients (associated with high tile energies) than the Berkeley instrument, indicating the that Kraków data more closely follows the signal expected from Gaussian-distributed noise. The loud transients in both instruments are likely due to electromagnetic environmental couplings or technical noise in the instruments themselves (laser light power and frequency noise, etc.). Further investigation is needed to identify the

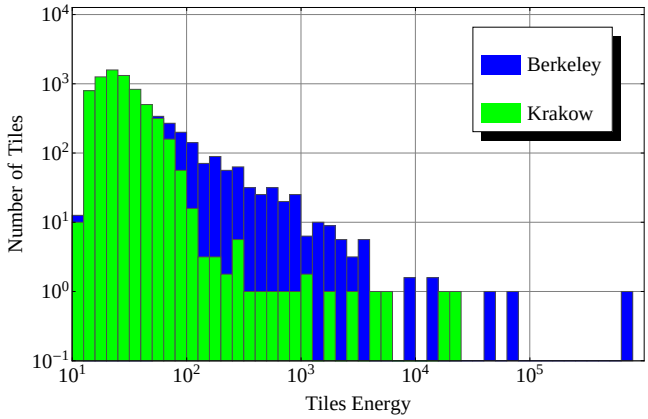

Figure 6 Histogram showing the number of tiles with energy within a specific range for the OMAG data depicted in Figs. 4 and 5.

causes of the loud transients and find appropriate methods to eliminate as many sources of loud transients as possible.

Figure 6 is a histogram of the tile energies from the trigger maps in Fig. 5 with the Berkeley magnetometer signal in blue and the Kraków magnetometer signal in green. One observes a roughly one order-of-magnitude excess of events in the Berkeley magnetometer signal compared to the Kraków signal for tile energies above ~ 100. This indicates problems in the relative quality of the Berkeley data compared to the Kraków data, perhaps a result of environmental noise or technical noise (such as the electronic pick-up noise identified in auxiliary measurements). Such histogram analysis is another useful way to characterize the performance of individual magnetometers in the GNOME.

6 Prospects

Comagnetometry, where the magnetic field is simultaneously measured with multiple atomic species or devices, is a widely used technique in precision measurements searching for anomalous spin-dependent effects. Comagnetometry with different atomic species often takes advantage of the fact that the relative coupling strengths of an exotic field to electrons and nuclei are generally different from the relative coupling strengths of electrons and nuclei to magnetic fields. A particular example of a comagnetometry scheme that will be investigated for possible use as a GNOME sensor is SERF comagnetometer similar to that described in Ref. [58]. In contrast to the devices used in the demonstration experiment described in the present work, an additional noble gas (helium) is introduced into a vapor cell. When the noble gas has nonzero nuclear spin, the alkali and noble gas spins become strongly coupled through spin-exchange collisions [59,60]. This coupling can be represented as the effective magnetic field $\mathbf{B}_{\rm eff}$ experienced by one spin species due to the average magnetization $\mathbf{M}$ of the other, due to enhancement of the alkali valence electron density at the noble gas nucleus,

$$\mathbf{B}_{\rm eff} = \lambda \mathbf{M}, \tag{8}$$

where λ is a parameter determined by the particular properties of the alkali-noble gas spin-exchange [61]. The applied field $\mathbf{B}$ is tuned so that it approximately cancels $\mathbf{B}_{\rm eff}$ experienced by the alkali atoms. The alkali atoms are then in an effective zero-field environment, and because the noble gas magnetization $\mathbf{M}$ adiabatically follows $\mathbf{B}$, transverse components of $\mathbf{B}$ are automatically compensated by $\mathbf{B}_{\rm eff}$ to first order. Such cancelation only occurs for interactions that couple to spins in proportion to their magnetic moments, leaving the SERF comagnetometer sensitive to anomalous spin couplings to electrons and nuclei [59].

The energy resolution of the latest generation of the SERF comagnetometer, employing Rb as the alkali atom and ^{21}Ne as the noble gas, is $\sim 10^{-23}$ eV/$\sqrt{\rm Hz}$ [58]. This new scheme uses hybrid optical pumping of Rb via spin-exchange collisions with low-density, optically pumped K and off-resonant direct optical probing of Rb spins. This approach allows full optimization of both optical pumping and probing. Because of the relatively small gyromagnetic ratio of ^{21}Ne, the Rb-K-^{21}Ne SERF comagnetometer has an order of magnitude better energy resolution for the same level of magnetic-field sensitivity as compared to earlier SERF comagnetometers, and may offer advantages in bandwidth. In the future, we plan to develop and optimize the SERF-based comagnetometer for measurements of exotic transient effects.

Independently from the development of SERF-based comagnetometer, the other magnetometer types will be investigated/developed as potential GNOME sensors. In particular, we envision using sensors that monitor evolution of various types of spins (proton, neutron, electron). This would add another dimension to our investigations by studying influence of exotic coupling to various fundamental particles.

Another important work planned for a future experiment will be correlation of the magnetometer readouts with environmental parameters (e.g., magnetic field outside the shield, temperature, etc.). This is motivated by the fact that despite magnetic shielding, there will inevitably

be some level of transient signals and noise associated with the local environment (and possibly with global effects like the solar wind, changes to the EarthŠs magnetic field, etc.). The environmental-condition data will allow for exclusion/vetoing of data with known systematic issues.

Further step in reducing the influence of magnetic fields on the operation of GNOME is application of Superconducting Quantum Interference Device (SQUID) [62] magnetometers as auxiliary sensors operating next to OMAGs inside the magnetic shields. While the SQUID magnetometers are characterized with magnetometric sensitivity comparable to that of OMAGs, the magnetometers are not sensitive to exotic spin coupling. Thus, they can be used for vetoing false-positive transient signals.

Ultimately, the GNOME will consist of at least five OMAG sensors. Four devices will be used for the detection of a DW and of investigation some of its geometrical properties. Any additional magnetometer would increase the sensitivity of the network. An independent OMAG will serve as cross-check to verify if, based on predicated DW event, a transient signal arises in the magnetometer in a narrow temporal window.

7 Conclusions

In this paper, we presented a new experimental scheme enabling investigations of transient exotic spin couplings. It is based on synchronous operation of globally separated optical magnetometers enclosed inside magnetic shields. Correlation of magnetometers' readouts enables filtering local signals induced by environmental and/or technical noise. Moreover, application of vetoing techniques, e.g., via correlation of optical-magnetometer readouts with signals detected with non-optical magnetic-field sensors, enables suppression of influence of global disturbances of magnetic origins, such as solar wind, fluctuation of the Earth's magnetic field, etc., on the operation of the magnetometers. In such an arrangement, the network becomes primarily sensitive to spin couplings of non-magnetic origins, thus it may be used for searches of physics beyond the Standard Model. A specific example of such searches was discussed here by considering coupling of atomic spins to domain walls of axion-like fields. It was demonstrated that with modern state-of-the-art optical magnetometers probing a significant region of currently unconstrained space of parameters of the fields is feasible. The preliminary results obtained based on synchronous operation of two magnetometers located in Kraków and Berkeley were presented and future plans for the network development were outlined.

Acknowledgements. The authors are thankful to S. Bale, J. Clarke, and M. Zolotorev for useful discussions. S.P. is a scholar of the Polish Ministry of Science and Higher Education within the Mobility Plus Program. D.B. acknowledges the support by the Miller Institute for Basic Research in Science. JRS is supported by NSF Award #0970147. This work has been supported in part by the National Science Foundation under grants: PHY-0969666, PHY-1068875, PHY-0970074 and the "Team" Program of the Foundation for the Polish Science.

Key words. Optical magnetometry, Exotic physics, Dark Matter, Dark Energy, Correlation Measurements

References

[1] D. Budker, and M. V. Romalis, Nat. Phys. **23**, 229 (2007).
[2] D. Budker and D. F. Jackson Kimball (eds.), Optical Magnetometry (Cambridge University Press, Cambridge, 2013).
[3] H. Dang, A. Maloof, and M. V. Romalis, Appl. Phys. Lett. **87**, 151110 (2010).
[4] B. J. Venema, P. K. Majumder, S. K. Lamoreaux, B. R. Heckel, and E. N. Fortson, Phys. Rev. Lett. **68**, 135 (1992).
[5] D. J. Wineland, J. J. Bollinger, D. J. Heinzen, W. M. Itano, and M. G. Raizen, Phys. Rev. Lett. **67**, 1735 (1991).
[6] A. G. Glenday, C. E. Cramer, D. F. Phillips, and R. L. Walsworth, Phys. Rev. Lett. **101**, 261801 (2008).
[7] G. Vasilakis, J. M. Brown, T. W. Kornack, and M. V. Romalis, Phys. Rev. Lett. **103**, 261801 (2009).
[8] C. J. Berglund, L. R. Hunterm, D. Krause, Jr., E. O. Prigge, and M. S. Ronfeldt, Phys. Rev. Lett. **75**, 1879 (1995).
[9] J. M. Brown, S. J. Smullin, T. W. Kornack, and M. V. Romalis, Phys. Rev. Lett. **105**, 151604 (2010).
[10] W. T. Ni, Rep. Prog. Phys. **73**, 056901 (2010).
[11] A. N. Youdin, D. Krause, K. Jagannathan, L. R. Hunter, and S. K. Lamoreaux, Phys. Rev. Lett. **77**, 2170 (1996).
[12] M. Pospelov, S. Pustelny, M. P. Ledbetter, D. F. Jackson Kimball, W. Gawlik, and D. Budker, Phys. Rev. Lett. **110**, 021803 (2013).
[13] M. P. Ledbetter, M. V. Romalis, and D. F. Jackson Kimball, Phys. Rev. Lett. **110**, 040402 (2013).
[14] G. Bertone, D. Hooper, and J. Silk, Phys. Rep. **405**, 279 (2005).
[15] J. Preskill, M. B. Wise, and F. Wilczek Phys. Lett. **B120**, 127 (1983).
[16] M. Dine and M. Fischler, Phys. Lett. **B120**, 137 (1983).
[17] V. Flambaum, S. Lambert, and M. Pospelov, Phys. Rev. D **80**, 105021 (2009).
[18] L. F. Abbott and P. Sikivie Phys. Lett. B **120**, 133 (1983).

[19] M. Pospelov, A. Ritz, and M. B. Voloshin Phys. Rev. D **78**, 115012 (2008).
[20] N. Kaloper and L. Sorbo JCAP **0604**, 007 (2006).
[21] S. M. Carroll, Phys. Rev. Lett. **81**, 3067 (1998).
[22] A. Lue, L,-M. Wang, and M. Kamionkowski Phys. Rev. Lett. **83**, 1506 (1999).
[23] M. Pospelov, A. Ritz, and C. Skordis, Phys. Rev. Lett. **103**, 051302 (2009).
[24] W. Wasilewski, K. Jensen, H. Krauter, J. J. Renema, M. V. Balabas, and E. S. Polzik, Phys. Rev. Lett. **104**, 133601 (2010).
[25] R. J. Sewell, M. Koschorreck, M. Napolitano, D. Dubost, N. Behbood, and M. W. Mitchell, Phys. Rev. Lett. **109**, 253605 (2012).
[26] W. Happer and B. Mathur, Phys. Rev. **163**, 12 (1967).
[27] I. Novikova, A. B. Matsko, V. L. Velichansky, M. O. Scully, and G. R. Welch, Phys. Rev. A **63**, 12 (2001).
[28] G. Vasilakis, V. Shah, and M. V. Romalis, Phys. Rev. Lett. **106**, 143601 (2011).
[29] K. Jensen, V. M. Acosta, J. M. Higbie, M. P. Ledbetter, S. M. Rochester, and D. Budker, Phys. Rev. A **79**, 023406 (2009).
[30] S. J. Seltzer and M. V. Romalis, Appl. Phys. Lett. **85**, 4804 (2004).
[31] S. Pustelny, S. M. Rochester, D. F. Jackson Kimball, V. V. Yashchuk, D. Budker, and W. Gawlik, Phys. Rev. A **74**, 063420 (2006).
[32] P. Wlodarczyk, S. Pustelny, and M. Lipinski, J. Inst. **7**, P07015 (2012).
[33] V. K. Shah, G. Vasilakis, and M. V. Romalis, Phys. Rev. Lett. **104** 013601 (2010).
[34] M. Koschorreck, M. Napolitano, B. Dubost, and M. W. Mitchell, Phys. Rev. Lett. **104**, 093602 (2010).
[35] M. P. Ledbetter, I. M. Savukov, V. M. Acosta, D. Budker, and M. V. Romalis, Phys. Rev. A **77**, 033408 (2008).
[36] M. P. Ledbetter, D. Budker, M. V. Romalis, J. W. Blanchard, and A. Pines, Phys. Rev. Lett. **108**, 243001 (2012).
[37] D. Budker, D. F. Kimball, S. M. Rochester, V. V. Yashchuk, and M. Zolotorev, Phys. Rev. A **62**, 043403 (2000).
[38] S. Pustelny, A. Wojciechowski, M. Gring, M. Kotyrba, J. Zachorowski, and W. Gawlik, J. Appl. Phys. **103**, 063108 (2008).
[39] D. F. Jackson Kimball, L. R. Jacome, S. Guttikonda, E. J. Bahr, and L. F. Chan, J. Appl. Phys. **106**, 063113 (2009).
[40] J. M. Higbie, E. Corsini, and D. Budker, Rev. Sci. Instr. **77**, 113106 (2012).
[41] E. B. Alexandrov, Phys. Scripta **T105**, 27 (2004).
[42] N. Castagna, G. Bison, G. Di Domenico, A. Hofer, P. Knowles, C. Macchione, H. Saudan, and A. Weis, Appl. Phys. B - Lasers O. **96**, 763 (2009).
[43] T. Scholtes, V. Schultze, R. IJseelsteijn, S. Woetzel, and H.-G. Meyer, Phys. Rev. A **84**, 043416 (2011).
[44] M. D. Swallows, T. H. Loftus, W. C. Griffith, B. R. Heckel, and E. N. Fortson, Phys. Rev. A **87**, 012102 (2013).
[45] B. A. Dobrescu and I. Mocioiu, J. High Energy Phys. **11**, 5 (2006).
[46] P. Sikivie, Phys. Rev. Lett. **51**, 1415 (1983).
[47] A. Friedland, H. Murayama, and M. Perelstein, Phys. Rev. D **67**, 043519 (2003).
[48] J. Jaeckel and A. Ringwald, Ann. Rev. Nucl. Part. Sci. **60**, 405 (2010).
[49] P. Sikivie, Phys. Rev. Lett. **48**, 1156 (1982).
[50] G. G. Raffelt, Ann. Rev. Nucl. Part. Sci. **49**, 163 (1999).
[51] M. P. Ledbetter, I. M. Savukov, V. M. Acosta, D. Budker, and M. V. Romalis, Phys. Rev. A **77**, 033408 (2008).
[52] P. D. D. Schwindt, S. Knappe, V. Shah, L. Hollberg, J. Kitching, L. A. Liew, and J. Moreland, Appl. Phys. Lett. **85**, 6409 (2004).
[53] J. C. Allred, R. N. Lyman, T. W. Kornack, and M. V. Romalis, Phys. Rev. Lett. **89**, 130801 (2002).
[54] P. Wlodarczyk, S. Pustelny, and D. Budker - in preparation.
[55] J. Abadie *et al.*, Phys. Rev. D **85**, 122007 (2012).
[56] W. G. Anderson, P. R. Brady, J. D. E. Creighton, and E. E. Flanagan, *An excess power statistic for detection of burst sources of gravitational radiation*, http://arxiv.org/abs/gr-qc/0008066 (2013-02-25).
[57] P. R. Brady, D. Brown, K. Cannon, and E. S. Ray-Majumder, *An excess power statistic for detection of burst sources of gravitational radiation*, https://dcc.ligo.org/DocDB/0088/T1200125/001/power.pdf (2013-02-25).
[58] M. Smiciklas, J. M. Brown, L. W. Cheuk, S. J. Smullin, and M. V. Romalis, Phys. Rev. Lett. **107**, 171604 (2011).
[59] T. W. Kornack and M. V. Romalis, Phys. Rev. Lett. **89**, 253002 (2002).
[60] T. W. Kornack, R. K. Ghosh, and M. V. Romalis, Phys. Rev. Lett. **95**, 230801 (2005).
[61] T. G. Walker, Phys. Rev. A **40**, 4959 (1989).
[62] J. Clarke and A. I. Braginski, The SQUID Handbook (Wiley-VCH, Weinheim, 2004).

WILEY ONLINE LIBRARY

Early View publication on wileyonlinelibrary.com
(issue and page numbers not yet assigned;
citable using Digital Object Identifier – DOI)

Ann. Phys. (Berlin), 1–9 (2013) / DOI 10.1002/andp.201300075

annalen der physik

Original Paper

Precision spectroscopy of the 2S-4P transition in atomic hydrogen on a cryogenic beam of optically excited 2S atoms

Axel Beyer[1,], Janis Alnis[1], Ksenia Khabarova[2], Arthur Matveev[1], Christian G. Parthey[1], Dylan C. Yost[1], Randolf Pohl[1], Thomas Udem[1], Theodor W. Hänsch[1,3], and Nikolai Kolachevsky[1,4]*

Received 25 March 2013, revised 5 May 2013, accepted 13 May 2013
Published online 20 June 2013

Precision spectroscopy of the $2S - 4P_{1/2}$ and $2S - 4P_{3/2}$ transitions in atomic hydrogen is performed with a reproducibility of a few parts in 10^{12}. A cryogenic beam of metastable 2S atoms is obtained by optical excitation, avoiding excessive heating of electron impact excitation used in all previous experiments of this kind. Despite the low temperature of 5.8 K, the first-order Doppler effect is the dominating systematic shift, which is suppressed to a very high degree. The effectiveness of this suppression is verified by employing a time-resolved detection scheme. This experiment should contribute to an improved determination of the Rydberg constant and the proton r.m.s. charge radius.

1 Introduction

Since the publication of a value for the proton r.m.s. charge radius r_p deduced from laser spectroscopy of muonic hydrogen in 2010 [1], the 'proton size puzzle' has been fueling activities in different fields of research. This result of $r_p = 0.84184(67)$ fm is ten times more accurate than any previous determination, but deviates from the CODATA 2010 value $r_p = 0.8775(51)$ fm by seven combined standard deviations [2]. Input data for the CODATA determination come from precision spectroscopy of ordinary hydrogen and deuterium as well as a selection of data obtained from elastic electron-proton scattering. The latter results have been inconclusive in the past. Nevertheless, using the self-consistent hydrogen and deuterium data only, a discrepancy of four standard deviations persists to the muonic value [2]. In a recent publication [3], the muonic hydrogen value has been confirmed and improved ($r_p = 0.84087(39)$ fm), reinforcing the puzzle. The source of the discrepancy remains unclear and possible explanations cover the entire spectrum from undetected systematic effects in different experimental results to physics beyond the Standard Model [5].

Several projects are underway which can give new insight into the proton radius puzzle [5]. The transitions from the metastable 2S state in regular hydrogen contribute with the largest experimental uncertainty. Therefore we want to add an improved measurement of the 2S-4P transition frequency with an uncertainty goal in the low kHz range. When combined with the 1S-2S transition in hydrogen, such a measurement can provide an improved value for the Rydberg constant and a new value of the proton r.m.s. charge radius. Hence we can shed light on the proton radius puzzle and provide input data for an improved test of bound state quantum electrodynamics (QED) in hydrogen.

The theoretical description in terms of QED expresses the atomic energy levels as $R_\infty f(r_p, \alpha, m_e/m_p)$, i.e. as a product of the Rydberg constant R_∞ and a dimensionless function that represents the energies in atomic units. The Rydberg constant ($R_\infty = 10\,973\,731.568\,539(55)\,\mathrm{m}^{-1}$) is needed to convert from atomic units to S.I. units. The somewhat lengthy expression for $f(r_p, \alpha, m_e/m_p)$, is given in detail in reference [2]. Besides the quantum numbers that describe an atomic state, its energy depends on the proton charge radius, the fine structure constant α and the electron-proton mass ratio m_e/m_p. The latter two constants can be obtained by other experiments with sufficient accuracy [2], so that two parameters, R_∞ and r_p are left to describe the hydrogen data.

* Corresponding author E-mail: Axel.Beyer@mpq.mpg.de
[1] Max-Planck-Institute of Quantum Optics, D-85748, Garching, Germany
[2] National Research Institute of Physical, Technical and Radiotechnical Measurements, 141570 Mendeleevo, Russia
[3] Ludwig-Maximilians-Universität, 80799 München, Germany
[4] P.N. Lebedev Physical Institute, 119991 Moscow, Russia

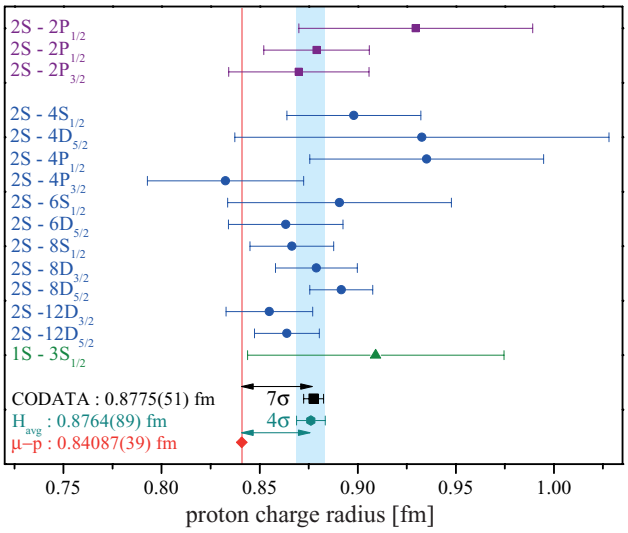

Figure 1 The r.m.s. proton charge radius obtained from precision spectroscopy of atomic hydrogen. Either radio frequency measurements of the 2S-2P Lamb shift (violet) or optical transition frequencies (blue from the 2S and green from the 1S state) are used. To extract the two parameters, the Rydberg constant and the proton charge radius r_p, each of these measurements needs to be combined with another independent measurement, which is the 1S-2S transition frequency here. The analysis reveals the discrepancy between the hydrogen mean value (H_{avg}) and the value determined from laser spectroscopy of muonic hydrogen ($\mu - p$). An even larger inconsistency is obtained when including proton-electron scattering data. This CODATA analysis also uses deuterium data, which have only limited effect on the proton charge radius, because the nucleus is not a proton. A similar picture is obtained when plotting the corresponding results for the Rydberg constant.

Under the assumption that QED calculations correctly describe the energy levels of the hydrogen atom, these two parameters can be obtained by combining at least two measured values (two equations for two unknowns). In doing so the 1S-2S transition frequency is used as a corner stone, because of its low fractional frequency uncertainty of currently 4.2×10^{-15} [6]. The consistency of this data then measures the consistency of QED, provided the experimental input data are correct.

Fig. 1 shows the summary of this analysis. It is found that the hydrogen data by itself are indeed consistent with each other with a reduced chi-square of 0.44. In addition, almost all individual hydrogen measurements are compatible with the muonic hydrogen value for r_p. The average of all hydrogen data, however, differs by 4 standard deviations from the much more precise muonic hydrogen value. It can not be completely excluded that a yet unknown common systematic effect may be the cause of the 'puzzle'. For the 1S-2S transition frequency, this effect needs to be on the level of 4,000 experimental standard deviations to resolve the discrepancy and hence is unlikely. To exclude or uncover a possible systematic effect common within the hydrogen data set with a single precision frequency measurement in addition to the 1S-2S transition frequency, the desired accuracy on the proton charge radius is 1% or below.

Three classes of transitions make use of the metastable 2S state as the lower state. Besides radio frequency measurements of the 2S-2P transitions, two-photon transitions to higher lying S and D states have been used in precision experiments in the past [7]. They offer smaller natural linewidths but suffer from low excitation rates. The large ac Stark shift resulting from the required high excitation light powers is the dominating source of systematic uncertainty. In contrast, the large dipole matrix elements of one-photon transitions to P states have to be traded in for large sensitivity to the first-order Doppler effect. In both cases higher principal quantum numbers n lead to a decrease of the natural linewidth, while the sensitivity to external fields increases. Any choice goes along with a trade off between all these effects, their advantages and drawbacks and in the end, the reliability and accuracy of the various systematic checks is the most critical ingredient for any of them. Our newly developed apparatus to measure the 2S-4P transition frequencies is well adapted to this task.

2 Improvements

The 2S-4P$_{1/2}$ and the 2S-4P$_{3/2}$ transitions have previously been measured relative to the 1S-2S transition with an uncertainty 15 kHz and 10 kHz, respectively, by Berkeland *et al.* [4]. This corresponds to relative uncertainties of 6.4% and 4.8% in r_p. An uncertainty in r_p comparable to the one provided by the aggregate of all electronic hydrogen data in Fig. 1 would be obtained by a measurement of both transitions with a frequency uncertainty of less than 2.5 kHz.

Unlike a two-photon transition driven with counter propagating laser beams, a dipole-allowed one-photon transition transition displays a large first-order Doppler effect. If uncompensated, the 2S-4P transition frequency would be shifted by about 700 MHz for collinear excitation at an average thermal velocity of $v = 350$ m/s ($T = 5$ K). However, as demonstrated by Berkeland *et al.* this Doppler effect can also be greatly reduced by using counter propagating laser beams and excitation perpendicular to the atomic beam axis. Counter propagating beams have been established by retroreflection using a 90° apex angle prism. Experimental difficulties related to

back reflections from the prism front face and a not exactly 90° apex angle had to be overcome in these earlier experiments.

We have advanced the idea used in Ref. [4] and developed an actively stabilized retroreflector (Sec. 3.3). Cleaning the spatial mode profile of the spectroscopy laser by two subsequent single mode fibers and the use of high quality optics provide very small deviation from perfect Gaussian beams. An active stabilization scheme assures high accuracy alignment in the excitation light fields' directions of propagation. For verification of the first-order Doppler shift suppression, we model the system with reasonable upper limits of imperfections and perform experiments with a large set of different effective velocities simultaneously. These velocities can be selected from the Maxwellian distribution by employing a time resolved detection scheme. To remove the faster atoms from the signal, we count signal photons only after the supply of 2S atoms has been discontinued for a time τ. With this test, we can control and correct for the residual Doppler effect and a resulting uncertainty of less than 3 kHz has been demonstrated.

The technique of time-resolved detection is enabled by optical excitation of the 2S state via Doppler-free two photon absorption at 243 nm. Not only does this excitation preserve the atoms' initial thermal velocity, it also allows quickly turning off the stream of 2S atoms via blocking the excitation light. In this context a cryogenic source of atomic hydrogen becomes useful because the tremendous heat up of the atoms accompanied by electron impact excitation is avoided. For the atoms contributing to our spectroscopy signal, mean velocities down to 100 m/s are now accessible, whereas for electron impact excitation typical values are around 4000 m/s.

The laser excitation of the 2S state is part of the setup that has been used for measuring the 1S-2S transition frequency [6]. Operating the same apparatus at room temperature is possible. This increases the average thermal velocity and allows for an additional test for residual Doppler shift.

An additional difficulty with the 2S-4P transitions is the unresolved hyperfine structure of the P states. While the 2S hyperfine structure is resolved, off-resonant excitation may take place shifting the observed resonance frequency. Laser excitation of the 2S state provides an elegant solution to both of these problems by selectively populating the 2S(F=0) hyperfine state only. As the $F = 0 \rightarrow F = 0$ transition is strictly forbidden, only one hyperfine component is driven in the 2S-4P$_{1/2}$ manifold. Likewise, for the 2S-4P$_{3/2}$ transition only the $F = 0 \rightarrow F = 1$ can be excited. Note that these selection rules are valid for any polarization. In contrast, for experiments using electron impact for 2S excitation, exact knowledge of the relative population numbers in the different sublevels and a well defined polarization state of the excitation light are obligatory because of the non-uniform population of the different 2S hyperfine and magnetic sublevels.

Acousto-optic modulators (AOMs) are commonly used for laser frequency scanning and intensity stabilization. A problem which may be overlooked when dealing with broad atomic resonances in a precision spectroscopy experiment is the influence of the AOMs on the spectral purity of the excitation light field. Spectral components which do not coincide with the desired diffraction order may be admixed to the spectroscopy light by different mechanisms: reflections of zero-order diffraction light from the the input and output facets of the AOM crystal, scattered light and diffraction orders that spatially overlap with the desired diffraction order. These components fold into the observed line shape and shift its center in a systematic and reproducible way. The effect is of particular importance if the AOM operating frequency is comparable with the observed linewidth or the line center is to be found with high accuracy. We solved this issue by using an electro-optic modulator (EOM) and polarizing beam splitter combination for laser power stabilization and carefully separating any undesired spectral components brought by the frequency scan AOM from the excitation light. In addition, the spectral purity of the excitation light is controlled by a direct beat note measurement between our narrow linewidth lasers for 1S-2S excitation and 2S-4P spectroscopy (Sec. 3.2) before every day of measurement.

Finally, a new detector for Lyman-γ photons provides a very large solid angle of 80% of 4π with high detection efficiency. Thanks to the high signal levels, the statistical uncertainty, the leading uncertainty contribution in the previous best measurement, could be reduced by approximately one order-of-magnitude and correspondingly the identification and quantification of systematic effects has become significantly simpler.

3 Experimental setup

3.1 Cryogenic source of hydrogen 2S atoms

The apparatus used in our experiment as a cryogenic source of 2S atoms has been described in [6]. Molecular hydrogen is dissociated in a radio frequency discharge running inside an air-cooled sapphire tube at 1 mbar to 2 mbar gas pressure (Fig. 2). The hydrogen flux is reduced by a Teflon capillary and a continuous flow of

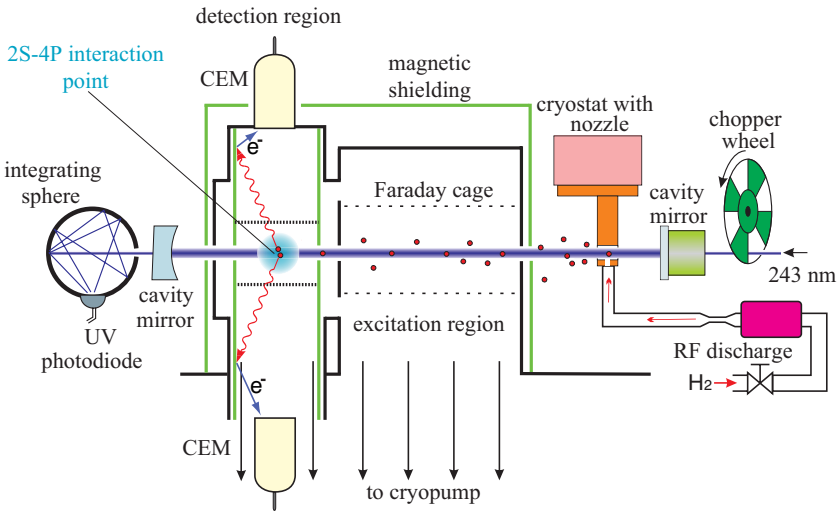

Figure 2 Schematic of the hydrogen beam apparatus (not to scale). The 1S-2S transition is excited by a standing wave light field at 243 nm formed between the cavity mirrors oriented collinearly with the atomic beam that emerges the cooled T-shaped nozzle. The excitation region is shielded against magnetic and electric fields and hosts the 2S-4P spectroscopy laser light at 486 nm which is oriented perpendicular to the plane of drawing and the atomic beam (blue spot). Excitation of the 2S-4P transitions is detected with two channel electron multipliers (CEM) only during dark phases of the chopper wheel (green). The power of the 243 nm is monitored with the help of an integrating sphere and a UV photo-detector.

mixed molecular and atomic hydrogen gas is guided to a T-shaped copper nozzle inside the vacuum chamber. This nozzle can be cooled to 5.8 K with a liquid helium flow cryostat. Hydrogen atoms thermalize inside the nozzle and are emitted from the 2.2 mm diameter nozzle apertures while most of the molecules (hydrogen and other residuals) freeze on the nozzle. The developing layer of frozen molecular hydrogen helps to thermalize the atomic hydrogen. During the course of the experiment the layer of frozen gas grows continuously. When the finesse of the 243 nm enhancement cavity for 1S-2S excitation (Fig. 2) starts decreasing, we interrupt the experiment to heat the nozzle and sublimate the frozen gas.

For collimation of the atomic beam we use two apertures with diameters of 2.4 mm (front) and 2.1 mm (rear) separated by 100 mm. The aperture closer to the nozzle also serves to separate the low vacuum region around the nozzle (10^{-5} mbar) from the high vacuum region (10^{-8} mbar) where 2S atoms are prepared and 2S-4P spectroscopy is performed. Excitation of the 1S-2S transition takes place during the bright phase of a chopper wheel, which switches the 243 nm excitation light at a frequency of 160 Hz (see Fig. 2). For this purpose a standing wave, formed by a linear enhancement cavity with a finesse of 120, oriented collinearly with the atomic beam is employed. The excitation light frequency is tuned to exclusively populate the 2S($F = 0$) hyperfine component and kept on resonance within 170 Hz. Subsequently spectroscopy of the 2S-4P transition is done with a laser at 486 nm that crosses the atomic beam at angles Θ close to 90°.

From previous analyses of the 1S-2S line shape we know that the velocity distribution of the 1S atoms is well described by a Maxwellian with a temperature very close to the set temperature of the nozzle [8]. Their mean velocity is thus a factor 7 lower than at room temperature of 290 K. However, the distribution of the 2S atoms is different because of the interaction-time-dependent excitation rate, which is lower for higher velocity. Nevertheless we can adjust the mean velocity of the 2S state atoms to provide yet another test for the first-order Doppler effect by changing the nozzle temperature. The lower temperature limit (5 K) is given by our liquid helium flow cryostat. The upper useful mean velocity limit (420 m/s at 30 K) is given by the available laser power at 243 nm. The ratio of these 2S atoms mean velocities is then approximately two (see Sec. 5).

3.2 Laser systems

UV laser light near 243 nm is generated with a diode laser system. This system was originally built for measuring the 1S-2S transition frequency and has superior spectral properties [9] which are actually not needed for generating 2S atoms. It consists of a long (24 cm) external

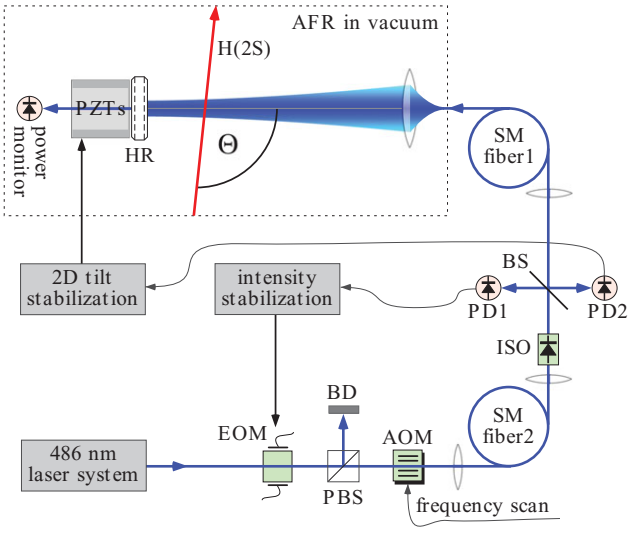

Figure 3 Active fiber-based retroreflector (AFR) with intensity and mirror tilt stabilization scheme. The AFR is amended with laser frequency scanning capabilities though an acousto-optic modulator (AOM) and intensity stabilization using an electro-optic modulator (EOM) and polarizing beam splitter (PBS) combination. SM fiber: optical single mode fiber, BS: non-polarizing beam splitter, HR: high reflectivity ($R = 99.995\%$) piezo transducer controlled mirror, PD: photo diode, BD: beam dump, ISO: optical isolator.

cavity diode master laser at 972 nm that generates 40 mW of output power. The long laser cavity design with an intra-cavity EOM for fast feedback reduces the spectral linewidth of the diode laser and allows suppression of the phase noise typical for diode lasers with shorter external cavities [9]. A tapered amplifier (TA) boosts the power to 2 W which is used with two subsequent frequency doubling stages (SHG) to generate up to 75 mW near 243 nm. To perform spectroscopy of the 2S-4P transitions, we built a copy of the master laser used in the 1S-2S laser system. Similar to the 1S-2S system, its output is first amplified by a TA chip and then doubled in a home-built SHG stage. The phase noise pedestal of this laser has been carefully characterized and found to have a negligible effect on the observed 2S-4P line shape.

Stabilizing both lasers to high finesse cavities made from ultra-low expansion glass (ULE) results in narrow laser linewidths smaller than 1 Hz and fractional frequency drifts of about 2×10^{-16} s^{-1} at 972 nm [10]. The 486 nm laser power of the 2S-4P laser system is stabilized by an EOM and polarizing beam splitter combination (Fig. 3). The laser frequency can be scanned across the atomic resonance by use of a 350 MHz double pass AOM. An Erbium-doped fiber frequency comb with a repetition rate of 250 MHz is used to phase-coherently link the ULE cavity frequencies to an active hydrogen maser which is calibrated via GPS. For our uncertainty goal in the low kHz range, this way of frequency determination is sufficient.

3.3 Active fiber-based retroreflector

Crossing the atomic beam and the laser beam at an angle Θ gives rise to a first-order Doppler shift of $v\cos(\Theta)/\lambda$. For a typical mean velocity of 2S atoms of 270 m/s, the angular deviation from 90° must not be larger than 1.8×10^{-5}rad to suppress this shift to below 10 kHz. Clearly this is not possible with simple alignment procedures, given that the divergences of both the laser and the atomic beam are much larger. Using two perfectly counter propagating laser beams however, causes exactly opposite Doppler shifts that average to zero, irrespective of the shape or divergence of the atomic beam.

While this method gives a large suppression factor, additional measures are required. Taking the laser wavefront curvature into account, it is important to note that the local Doppler shift is given by the projection of the velocity vector onto the normal of the local phase front. The contribution to the two line components are weighted by the local intensity. Therefore in the ideal case the returning laser beam must not only match the spatial intensity distribution of the forward beam but also retrace its phase fronts. This happens when a perfect Gaussian beam is reflected off a perfect mirror placed at its waist oriented along the plane wavefronts there.

To get as close as possible to this ideal situation of a retracing laser beam, an enhancement cavity could be used. However, this cavity would have to be of high finesse to fulfill these requirements. It turns out that the large enhancement of laser power connected with such a cavity requires extremely low input power in order not to saturate the transition and cause significant ac Stark shift. This would in turn prevent generating a high quality error signal to stabilize the cavity. While in principle a far detuned second laser could be used for locking we have instead developed a simpler device which we call active fiber-based retroreflector (AFR).

As sketched in Fig. 3, the light is guided from the laser with a 5 m long single mode fiber to obtain high quality wavefronts. It is then collimated by a high quality lens system with $f = 26$ mm focal distance, that has been specially designed for minimal distortion of the nearly Gaussian-shaped fiber output. Without sufficient quality of the lens system, wavefronts and the radial intensity distribution depend on the propagation length in a different way than the ideal retracing Gaussian beam. After collimation the laser beam crosses the atomic beam at an

angle close to 90° and is reflected back by a high reflectivity mirror (R=99.995%). For continuous alignment, the amount of light coupled back into the fiber is monitored by a photo diode (PD2). The mirror tilt in both directions is adjusted for maximum coupling efficiency by an active stabilization loop utilizing piezo transducers and two modulation frequencies with two lock-in amplifiers. The long focal length provides a large sensitivity to angular misalignment while the resulting beam diameter of $w_0 = 4.5$ mm reduces the time of flight broadening of the observed 2S-4P transition. Tracing the light power coupled back to the fiber during the experiment shows that the angular deviation of the beams is below 10^{-5}rad. The setup is completed with an 350 MHz AOM for scanning the laser frequency, an EOM for laser power stabilization and an optical isolator (ISO) which prevents the light retroreflected by the AFR from penetrating back to the frequency scan part of the scheme (see Fig. 3). Even for perfectly stabilized laser power at PD1 and back reflected power at PD2, parasitic etalon effects due to non-perfect anti reflection coatings could lead to a reproducible, laser frequency dependent variation of the laser power seen by the atoms. Therefore the laser power is monitored behind the high reflecting end mirror (HR) for normalization of the excitation rate.

The above reasoning for a small residual first-order Doppler effect can provide design guidelines for the experimental setup. However, it can not easily provide a strong quantitative upper limit. For example, controlling the maximum back reflection means at most that the returning beam is centered while beam shape distortions that are different for the two propagation directions can not be excluded. Running Monte Carlo simulations, as we did, also provides hints for the most sensitive parameters, but gives quantitative results only for known input parameters. Therefore we do not rely on these estimations but directly measure the residual Doppler effect as detailed in Sec. 5 and remove any velocity dependent effect from our results by extrapolating to zero velocity.

3.4 High efficiency Lyman-γ detector

A substantial improvement in statistics has been achieved in a recent measurement of the absolute 1S-2S transition frequency in our group by a new detector design. This design provides a detection solid angle of almost 4π [11]. For the 2S-4P experiment, the detector design has been advanced and adapted to the special needs of 2S-4P spectroscopy. The detection region is formed by three layers of metal cylinders which are fitted into an aluminum cube and fixed to the titanium box

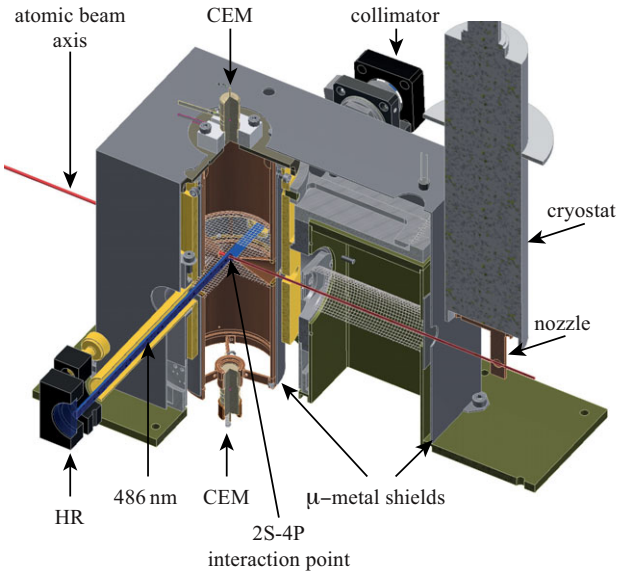

Figure 4 3D view of Lyman-γ detector with almost 4π detection solid angle. Lyman-γ photons emitted from the 2S-4P interaction point impinge on the graphite coated inner detector walls releasing photoelectrons. These can efficently be collected from the large volumes above and below the atomic beam axis by channel electron multipliers (CEMs). The interaction volume is shielded against the electric fields created by the CEMs by grounded meshes and magnetic fields are suppressed by high magnetic permeability material layers (μ-metal shields). The high reflective mirror (HR) and the fiber collimation system (collimator) reside at the ends of 150 mm long brass tubes which keeps all dielectric surfaces far away from the atomic beam.

that houses the 1S-2S excitation region (see Fig. 4). The outer metal cylinder is made from brass and makes the entire assembly rotatable in order to adjust the angle Θ between the atomic beam and the laser beam. Rotation is possible during the experiment by remote control. The high reflectivity mirror and the fiber collimation system of the AFR reside at the ends of two 150 mm long brass tubes that are attached to the brass cylinder and rotate with it. This keeps all dielectric surfaces which may charge up during the experiment due to photo-ionization of hydrogen atoms and scattered UV light far away from the interaction region. The resulting electric fields are efficiently suppressed by the long and narrow grounded metal tubes. All metal surfaces in the detection region are covered with graphite to prevent stray electric fields building up for the same reasons. From a previous characterization, we know that the graphite coating reduces stray electric fields to less than 6 mV/cm, corresponding to a dc Stark effect of less than 100 Hz.

The intermediate cylinder is made from high magnetic permeability material. Together with another layer of the same material in the low vacuum region, it shields the 2S-4P detection region from magnetic fields to a level of less than 1 mG, resulting in a maximum Zeeman shift that is well below 1 kHz. The innermost cylindrical layer of the detector is made from non-magnetic metals. The graphite coated inner walls of copper cylinders above and below the interaction region serve as photocathodes for the detection of Lyman-γ photons emitted upon the rapid decay of the 4P states down to the 1S ground state. Photoelectrons are released from the graphite surfaces when Lyman-γ photons hit it. These electrons can easily be collected from the large detection volume by two channel electron multipliers (CEMs) mounted on top and bottom of the detection region. This way of detection offers a large detection solid angle close to 4π.

Background counts arising from spontaneous decay of the 2S state are suppressed by metal cones surrounding the atomic beam on its way to the atom-light interaction point and afterwards. The electric fields created by the +270 V input voltage on the CEM front faces are shielded from the spectroscopy volume by two grounded meshes fabricated from 30 μm diameter gold-plated tungsten wires. Simulations of the resulting field configuration show that residual fields are negligible. For verification, the 2S lifetime, which rapidly decreases in the presence of electric fields, was compared at CEM input voltages ranging from 0 to 1000 V. No significant effect could be found here or in the difference between the extracted 2S-4P$_{1/2}$ transition frequencies with one and two CEMs switched on. For the final data set, the strength of electric fields influencing the 2S-4P spectroscopy will be characterized by utilizing the strong dependence of the dc Stark effect on the principal quantum number n. It roughly scales like n^7 [12], so that a comparison of the extracted 2S-4P and 2S-6P transition frequencies measured in the same apparatus will set an upper limit on the electric field strength.

4 Time-resolved data acquisition

Spectroscopy of the 2S-4P transition takes place in the second section of the high vacuum region as described above. Only during the dark phases of the chopper wheel, excitation to the 4P state is detected and recorded with its time delay τ, which is the arrival time of a signal photon after the 243 nm laser has been turned off. Statistically independent data sets are obtained simultaneously with the help of a multi-channel scaler for the 100 μs and 200 μs long time intervals $\tau_1 = [10\,\mu\text{s}, 110\,\mu\text{s}], \ldots,$

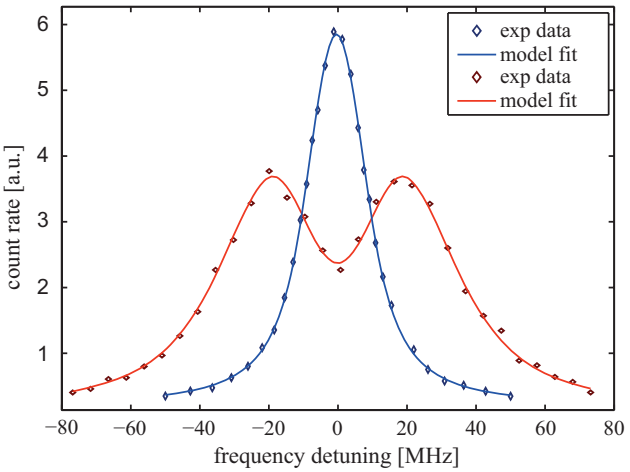

Figure 5 Observed line shapes for the 2S-4P$_{1/2}$ transition frequency at different angles Θ of the counter propagating excitation light fields with respect to the atomic beam. Blue: $\Theta = 90^\circ \pm 0.08^\circ$. Red: $\Theta = 88^\circ \pm 0.5^\circ$. Delay $\tau_1 = [10\,\mu\text{s}, 110\,\mu\text{s}]$.

$\tau_4 = [310\,\mu\text{s}, 410\,\mu\text{s}]$, $\tau_5 = [410\,\mu\text{s}, 610\,\mu\text{s}]$, . . . , $\tau_{14} = [2210\,\mu\text{s}, 2410\,\mu\text{s}]$. The signal is integrated for about 1 s for each recorded data point.

During a scan of the 2S-4P line profile, we record the number of photoelectrons for 30 laser frequency settings (Fig. 5). This takes about 45 s. These frequencies are addressed in random order to avoid possible systematic effects associated with one-directional line scans. In addition, rather than having a fixed set of frequencies to address, we use 30 predefined frequency intervals covering the range of the scan and randomly select one point within each of them for every scan. This reduces the potential influence of the choice of the scan's central frequency.

Two typical line profiles at different angles Θ are shown in Fig. 5. At Θ close to 90°, the two individual line components corresponding to forward and backward waves overlap, while at 88° a splitting of the lines is observable due to the difference in the first-order Doppler effect experienced by atoms excited in each of the beams. Typical observed linewidths close to 90° are on the order of 20 MHz, which corresponds to 1.5 times the natural linewidth of the transition. The additional broadening is mainly caused by the atomic beam divergence and power broadening. The average statistical uncertainty in the line center determination of a single resonance profile amounts to 60 kHz at 5.8 K nozzle temperature.

The number of lines recorded daily varies between 150 and 250, resulting in a statistical uncertainty of the line center of 3 kHz to 5 kHz per day and a statistical uncertainty below 1.5 kHz has been achieved within 8

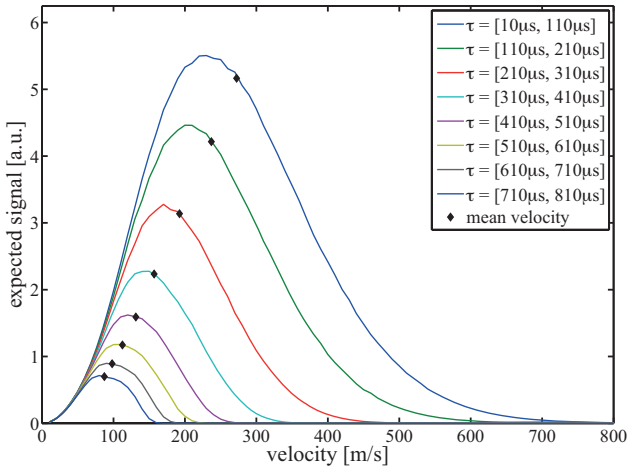

Figure 6 Velocity distributions and mean values of 2S hydrogen atoms contributing to the 2S-4P signal at different detection delay times τ. These results are obtained from a Monte Carlo simulation of the 1S-2S excitation process assuming a Maxwellian velocity flux of 1S atoms at T = 5.8 K emerging from the nozzle.

measurement days. For the final data set, each measurement day may incorporate measurements at different temperatures in order to assure identical experimental conditions and best characterization of the residual first-order Doppler shift.

5 Discussion

The first-order Doppler effect is proportional to the atomic velocity, irrespective of the geometric imperfection that causes it. We exploit this by comparing resonance frequencies extracted for different mean velocities of the 2S atoms. Fig. 6 shows these mean velocities for several detection delays τ. Using all detection delays that have a sufficient signal count rate allows us to vary the mean 2S velocity by a factor of three. Increasing the nozzle temperature from 5.8 K to 30 K delivers a maximum mean velocity of 420 m/s, another factor of two higher than the highest mean velocity at 5.8 K. With these different data sets, an extrapolation to zero velocity eliminating all contributions of the Doppler effect at once is possible and an uncertainty in the low kHz range seems feasible. The second-order Doppler effect, even for our fastest mean velocity class, is reduced by almost two orders of magnitude as compared to the mean velocity in the previous measurement [4] and is also included in the extrapolation.

An additional issue that can cause systematic effects are other closely lying fine and hyperfine components. As shown in Sec. 3.1, we start with a pure 2S($F = 0$) state. However, the excited 4P states decay back to the 2S state with a branching ratio around 12%, some of them to the 2S($F = 1$) state from which they can be re-excited. We simulated the influence of this second excitation on the line center. Due to the low laser power of around 25 μW in our experiment, the estimated shift is only 100 Hz. This also includes the ac Stark effect which is part of the simulation.

An upper level estimation for the line pulling effect by off resonant excitation of the 4P fine structure level complementary to the spectroscopy transition ($4P_{3/2}$ for 2S-$4P_{1/2}$ spectroscopy and vice versa) shows an effect of a few kHz. The same is true for possible line shifts brought by quantum interference effects of the spontaneous decay of different excited states as suggested by Horbatsch and Hessels [13, 14]. A more detailed study of both effects is underway and will be presented in a later publication.

6 Outlook

Using the apparatus presented in this letter we plan to push the uncertainty of the 2S-$4P_{1/2}$ and 2S-$4P_{3/2}$ transitions frequency measurement to the few kHz range. The demonstrated statistical uncertainty allows reaching this target in approximately 10 full measurement days for each of the fine structure sublevels. By reworking the scheme for power stabilization and frequency scan of the spectroscopy laser recently, the spectral purity of the excitation light and data quality have been improved even further. Dominating systematic effects like the Doppler shift, Zeeman and Stark shifts are under control and are within a few kHz uncertainty as well. Line pulling effects, one of the main systematic contributions in the previous measurement have been greatly suppressed by optical excitation of the 2S level. Our target uncertainty corresponds to less than 2% uncertainty of the proton charge radius which promises to be a significant contribution to the proton size puzzle.

A third laser system at 410 nm will be used for the excitation of the 2S-6P transitions. The system is stabilized to a high-finesse ULE cavity and is already fully operating in our lab. In the first step it will be utilized for characterization of stray dc electric fields in our apparatus using the n^7 scaling of the dc Stark effect [12]. After that we plan to perform precision measurements of the 2S-6P as well as 2S-8P and 2S-9P transition frequencies using our cryogenic atomic beam apparatus. The combination of these measurements with the 1S-2S transition can provide an improved value for the Rydberg constant and a new value of the proton r.m.s. charge radius,

facilitating an improved test of bound state QED calculations in atomic hydrogen.

Acknowledgements. The authors thank E. A. Hessels for insightful discussion and F. Biraben for sharing the clear illustration of the proton size puzzle adapted in Fig. 1. J.A. acknowledges support by the Marie Curie Intra European program, N.K. support from RFBR #12-02-01374, R.P. from the European Research Council (ERC) Starting Grant #279765 and T.W.H. from the Max Planck Foundation.

Key words. Precision spectroscopy, atomic hydrogen, Rydberg constant, proton r.m.s charge radius, proton size puzzle.

References

[1] R. Pohl *et al.*, Nature **466**, 213–216 (2010).
[2] P. Mohr *et al.*, Rev. Mod. Phys. **84**, 1527–1605 (2012).
[3] A. Antognini *et al.*, Science **339**, 417–420 (2013).
[4] D. Berkeland *et al.*, Phys. Rev. Lett. **75**, 2470–2473 (1995).
[5] R. Pohl *et al.*, 10.1146/annurev-nucl-102212-170627 (2013)
[6] C. G. Parthey *et al.*, Phys. Rev. Lett. **107**, 203001 (2011).
[7] F. Biraben, Euro. Phys. J. **172**, 109–119 (2009).
[8] A. Huber *et al.*, Phys. Rev. A **59**, 1844–1851 (1999).
[9] N. Kolachevsky *et al.*, Opt. Lett. **36**, 4299–4301 (2011).
[10] J. Alnis *et al.*, Phys. Rev. A **77**, 053809 (2008).
[11] A. Matveev *et al.*, "Precision Measurement of the Hydrogen 1S-2S Frequency via a 920 km Fiber Link", submitted to Phys. Rev. Lett. **110**, 230801 (2013).
[12] H. A. Bethe and E. E. Salpeter, Quantum Mechanics of One- and Two-Electron Atoms, Academic Press, New York (1957).
[13] M. Horbatsch and E. A. Hessels, Phys. Rev. A **82**, 052519 (2010).
[14] M. Horbatsch and E. A. Hessels, Phys. Rev. A **84**, 032508 (2011).

WILEY ONLINE LIBRARY

Early View publication on wileyonlinelibrary.com
(issue and page numbers not yet assigned;
citable using Digital Object Identifier – DOI)

Ann. Phys. (Berlin), 1–8 (2013) / DOI 10.1002/andp.201300038

annalen der physik

Original Paper

Accurate measurements of the Avogadro and Planck constants by counting silicon atoms

Horst Bettin[1], *Kenichi Fujii*[2], *John Man*[3], *Giovanni Mana*[4,*], *Enrico Massa*[4], *and Alain Picard*[5]

Received 28 February 2013, revised 16 May 2013, accepted 21 May 2013
Published online 20 June 2013

Fundamental constants link seemingly different fields of physics and seemingly different quantities and measurement units. Consequently, they are of the utmost interest in metrology and it has been planned to redefine the kilogram by fixing the numerical value of the Planck constant. This paper summarises the methods to measure the ratio between the Planck constant and a mass and reviews the determination of the Avogadro constant by counting the atoms in a silicon crystal highly enriched by the ^{28}Si isotope.

1 Introduction

Since 1889, the international prototype of the kilogram – a mass in a 90% platinum and a 10% iridium alloy – serves as the definition of the unit of mass of the International System of Units (SI): The kilogram definition states that 1 kg is the mass of the international prototype. Therefore, the mass of the international prototype is a *sui generis* type of fundamental constant, which links the SI value of all the quantities related to mass and energy. The international prototype is stored in a vault of the Bureau International des Poids et Mesures, with a number of official copies. Its mass was compared to that of its copies and the national prototypes at intervals of about 40 years; the results show mass-difference evolutions of an average of 50 μg over one hundred years [1]. We might conclude that the value of all the mass- and energy-related quantities, like the electron mass and the Planck constant, is similarly drifting with time, but more prosaically the data might indicate that the prototype is losing contaminants or platinum or iridium. Consequently, a drift of the SI value of the mass- and energy-related fundamental constants would be only apparent.

Since the measurement uncertainty of the related fundamental constants is reaching the uncertainty of mass measurements, this situation is no longer acceptable. Therefore, it is planned to redefine the kilogram by fixing the numerical value of the Planck constant, h [2].

Fundamental constants – for example, the speed of light c in the Einstein equation $E = mc^2$ – are links between seemingly different field of physics and they unify seemingly different concepts and quantities [3]. Accordingly, they are conversion factors between measurement units – in the previous example, the mass and energy units – and are of the utmost interest in metrology. Their measurements – a tour de force of basic metrology, where the useful information is beyond the last digit of the measured value – challenge theoretical models and measurement technologies and set a network of measurement equations on which a universal system of units can be built, which system stems from the most basic concepts of physics. Because of their connection with the mass unit, the Avogadro and Planck constants are in the spotlight.

In 2011, the 24th General Conference on Weights and Measures recommended that the International System of Units will be upgraded in terms of fundamental constants: Four of the base units – the kilogram, ampere, kelvin, and mole – will be redefined in terms of fixed

* Corresponding author E-mail: g.mana@inrim.it

1 PTB – Physikalisch-Technische Bundesanstalt, Bundesallee 100, 38116 Braunschweig, Germany

2 NMIJ – National Metrology Institute of Japan, 1-1-1 Umezono, Tsukuba, Ibaraki 305-8563, Japan

3 NMI – National Measurement Institute, Bradfield Road, Lindfield, NSW 2070, Australia

4 INRIM – Istituto Nazionale di Ricerca Metrologica, str. delle Cacce 91, 10135 Torino, Italy

5 BIPM – Bureau International des Poids et Mesures, Pavillon de Breteuil, 92312 Sèvres Cedex, France

numerical values of the Planck constant, the elementary charge, the Boltzmann constant, and the Avogadro constant. In addition, specific *mises en pratique* will be issued to describe how to realise the units in a practical way. For example, any experiment that is used today to measure the SI value of the Planck constant – hence, necessarily, in terms of the mass of the international prototype – will be reversed to give any mass in terms of an internationally agreed numerical value of the Planck constant.

From a practical viewpoint, it is necessary that the relative realisation uncertainty at 1 kg – which is the same as the uncertainty of the h measurement – does not make the unit dissemination to science and industry worse than what it is today. In addition, it is necessary that the unit redefinition is invisible to most of the users, apart from the metrologists themselves. This requires that the accuracy of the h measurements be at least $2 \times 10^{-8} h$ and that the h value be chosen in such a way that the mass of the international prototype is indistinguishable (when traced back to the new definition) from 1 kg to within the same uncertainty. To this end, the h value will be set to its best estimate calculated by a least-squares adjustment of the measured values of the fundamental constants carried out by the Task Group on Fundamental Constants of the Committee on Data for Science and Technology (CODATA). The last CODATA adjustment was completed in 2010 [4]; the recommended value of the Planck constant is $h = 6.62606957(29) \times 10^{-34}$ J s.

The precision measurements and CODATA least-squares adjustment of the fundamental constants probe nature's work by checking the internal consistency of the network of relationships established by its mathematical description. The energies where the effects of the fundamental interactions are expressed could be out of the reach of any technology, but it may be possible to look for minute effects at accessible energies by measurements of outstanding sensitivity and accuracy. The adjusted constant values are fitted to input data obtained from widely differing experiments and by assuming that a number of interpretative models and measurement equations are valid. Therefore, the least-squares adjustment tests the correctness and consistency of these models and of the relevant measurement technologies.

This paper summaries the methods of measuring the ratio between the Planck constant and a mass; it reviews the watt balance experiment, where the integration of mechanical and electrical measurements allows $h/m(\text{ℜ})$ to be determined ($m(\text{ℜ})$ being the mass of the international prototype of the kilogram). Next is a review of the ^{28}Si experiment, where the Avogadro constant is determined by counting the atoms in a silicon crystal highly enriched by the ^{28}Si isotope. By rewriting the h/m ratio, where m is the mass of a particle or an atom, as $N_A h/M$, where M is the molar mass and N_A the Avogadro constant, the h values obtained from atomic and nuclear physics measurements can be compared with those obtained from the watt balance experiments, which rely on solid state physics. As has happened many times in the past, there is an inconsistency between the h determinations, which indicates that an error was made in at least one of the measurements. Hence, there is room for developments to resolve this discrepancy. The last section looks at the possible weaknesses in counting the silicon atoms. It illustrates the activities necessary to investigate the critical points of the experiment and to stress the N_A measurement and the relevant know-how with a challenging goal to reduce the uncertainty to $1.5 \times 10^{-8} N_A$.

2 The measurements of the Planck constant

The measurement of the Planck constant is going into a new phase. Quantum mechanics shows that the Planck constant links the wavefunction energy E and frequency ν by the Planck equation $E = h\nu$. Consequently, h is the conversion factor between frequency and energy units. Additionally, when quantum mechanics is combined with relativity, h also links the Compton frequency ν_C of a relativistic matter wave (in the reference frame where matter is at rest) to its mass-energy $E = mc^2$. Consequently, by combining the Planck and Einstein equations, we obtain $h\nu_C = mc^2$, which associates a frequency to any mass and shows that h/c^2 is the conversion factor between frequency and mass units.

The measurements of the h/m ratio can be traced back to frequency or wavelength measurements. In principle, h/m could be measured by annihilating an electron-positron pair and determining the frequencies of the emerging photons. However, this frequency is far beyond today's technology; we require a method of scaling it into an accessible range.

A simple example of how this can be done is illustrated by the $h/\Delta m(^{133}\text{Cs}) = c^2/\nu(^{133}\text{Cs})$ equation, where $\Delta m(^{133}\text{Cs})$ is the mass defect between the two hyperfine energy levels that define the second and $\nu(^{133}\text{Cs}) = 9192631770$ Hz by definition. A less simple measurement equation is $h/m(\text{e}) = c\lambda_C(\text{e}) = c\alpha^2/(2R_\infty)$, where $\lambda_C(\text{e}) = c/\nu_C(\text{e}) = \alpha^2/(2R_\infty)$ is the Compton wavelength of the electron and α and R_∞ are the fine structure and Rydberg constants. Since both α and R_∞ are extremely

well measured, $h/m(\mathrm{e})$ can be calculated with a 6.4×10^{-10} relative uncertainty.

Another example is the $h/m(\mathrm{n}) = 3.956033285(287) \times 10^{-7}$ m^2/s ratio, whose measurement was completed in 1998 [5–7]. This experiment relied on the de Broglie equation $m(\mathrm{n})u = h/\lambda$, where both the wavelength λ and the velocity u of monochromatic neutrons were measured. Monochromaticity was obtained by Bragg reflection on a calibrated silicon crystal, whereas the neutron velocity was determined by time-of-flight measurements.

As regards measurements based on atomic masses, the $h/m(\mathrm{X})$ ratio has been determined by measuring the recoil velocity u of ^{133}Cs and ^{87}Rb atoms absorbing or emitting photons in Ramsey-Bordé interferometers [8–11]. The photon momentum h/λ, where λ is the photon wavelength, is balanced by the atomic recoil momentum mu. Conservation of momentum yields $h/m = \lambda u$. The interferometer operation can be also viewed as a measurement of the difference between the proper times of the atoms propagating through the interferometer arms, which is equivalent to measuring a subharmonic of the Compton frequency of the associated matter waves [11].

Measurements based on nuclear physics are possible by determining the wavelengths of the γ photons emitted in the cascades from the capture state to the ground state in the neutron capture reactions [12]

$$\mathrm{n} + {}^{n}\mathrm{X} \rightarrow {}^{n+1}\mathrm{X}^{*} \rightarrow {}^{n+1}\mathrm{X} + \sum \gamma, \tag{1}$$

where, for instance, X is either ^{32}S or ^{28}Si, and

$$\mathrm{n} + \mathrm{H} \rightarrow \mathrm{D}^{*} \rightarrow \mathrm{D} + \gamma_{\mathrm{D}^{*}\rightarrow\mathrm{D}}. \tag{2}$$

The $h/m(^{12}\mathrm{C})$ determination is based on the fact that the daughter isotope is lighter than its parents and that the mass defect can be measured by determining the wavelengths of the γ rays emitted in the decay of the capture state to the ground state. Wavelengths are determined by a double crystal diffractometer in terms of the calibrated lattice parameter of the diffracting crystals. The measurement compares the total energy of the emitted γ photons to the mass defect between the capture and ground states. With some algebra, the comparison can be written as

$$\frac{h}{m_{\mathrm{u}}} = \frac{\left[A_r({}^{n}\mathrm{X}) + A_r(\mathrm{H}) - A_r({}^{n+1}\mathrm{X}) - A_r(\mathrm{D})\right]c^2}{\sum \nu_{n+1\mathrm{X}^{*}\rightarrow n+1\mathrm{X}} - \nu_{\mathrm{D}^{*}\rightarrow\mathrm{D}}}, \tag{3}$$

where A_r is the relative atomic mass, $m_{\mathrm{u}} = m(^{12}\mathrm{C})$ is atomic mass constant, and $\nu = c/\lambda$ are the γ-ray frequencies. The measurements of the relative atomic masses are carried out by comparing the cyclotron frequencies of the relevant ions confined in a Penning trap [13].

A direct way of measuring the h/m ratio, where m is a macroscopic mass, is by a watt balance [14, 15].

This experiment compares, virtually, electrical and mechanical powers equivalent to the power required to move a mass m with a uniform vertical velocity u against the Earth's gravity g. The comparison is carried out in two steps. In the first step, a balance is used to compare the weight mg with the force BLI generated by the interaction between the electrical current I in a coil of wire of length L placed in a magnetic flux density B. The measurement of I is based on the Josephson and quantum Hall effects. Hence, $I = U/R = n_1 n_2 \nu e/2$, where $U = n_1 h\nu/(2e)$, $R = h/(n_2 e^2)$, e is the elementary charge, ν is the frequency of the microwave irradiating the Josephson device, and n_1 and n_2 are integers. In the second step, the coil is moved with velocity u and the induced electromotive force, $\mathscr{E} = BLu$, is measured. The measurement of $\mathscr{E}$ is based again on the Josephson effect, that is, $\mathscr{E} = n_3 h\nu/(2e)$, where n_3 is an integer. Eventually, by eliminating the geometrical factor BL,

$$\frac{h}{m} = \frac{4gu}{n_1 n_2 n_3 \nu^2}. \tag{4}$$

All the quantities on the right-hand side of (4) can be measured with uncertainties small enough to yield $h/m(\mathfrak{K})$, where $m(\mathfrak{K})$ is the mass of the international prototype, with a relative uncertainty of less than 1×10^{-8}, but, in practice, there are a number of additional uncertainties due, for example, to the alignments, unwanted motions, parasitic forces and torques, which must be reduced to the same small level.

3 The measurement of the Avogadro constant

3.1 Counting Si atoms

A way to determine h is by counting the atoms in 1 kg single-crystal spheres (see Fig. 1) that are highly enriched with the ^{28}Si isotope. Nowadays, this corresponds to determining the Avogadro constant. Since the relative atomic masses are extremely well measured, given measured values of N_{A} and $h/m(\mathrm{X})$, by rewriting

$$\frac{h}{m(\mathrm{X})} = \frac{N_{\mathrm{A}} h}{M(\mathrm{X})}, \tag{5}$$

where $M(\mathrm{X}) = A(\mathrm{X})\,M_u$ is the mean molar mass of the crystal, $A(\mathrm{X})$ is the mass of the X isotope relative to

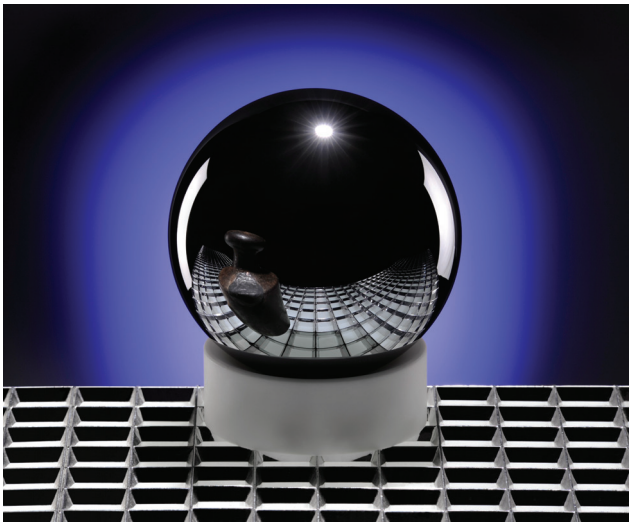

Figure 1 An old mass standard mirroring in a ^{28}Si sphere.

^{12}C, and $M_u = 12$ g/mol is the molar mass constant, the Planck constant can be determined as well.

3.2 Measurement equation

Atoms are counted by exploiting their ordered arrangement in crystals; crystallisation makes the lattice parameter accessible to macroscopic measurements, thus avoiding single atom counting. Provided the crystal and the unit cell volumes are measured and the number of atoms per unit cell is known, the counting requires their ratio to be calculated as

$$N_A = \frac{nMV}{ma^3}, \tag{6}$$

where $n = 8$ is the number of atoms per cubic unit cell, $MV/m \approx 12.06$ cm^3/mol is the molar volume, $M \approx 27.977$ g/mol is the molar mass, $V \approx 431$ cm^3 and $m \approx 1$ kg are the crystal macroscopic volume and mass, $a^3 \approx 0.160$ nm^3 is the unit cell volume, and $a \approx 543$ pm is the lattice parameter. The measurement uses silicon crystals highly enriched with the ^{28}Si isotope because, owing to the demands of modern electronics, they can be grown as high-purity, large, and quasi-perfect single crystals. Enrichment enables isotope dilution mass spectroscopy to be applied in determining the molar mass of the ^{28}Si spheres with unprecedented accuracy, bypassing the limitations of determining the isotopic composition of natural silicon.

The following sections will outline how the spheres' isotopic composition and chemical purity, molar mass, mass, volume, and lattice parameter were determined and their surfaces were geometrically, chemically, and physically characterised on the atomic scale.

3.3 Molar mass

Silicon occurs in three isotopes – ^{28}Si, ^{29}Si, and ^{30}Si. Therefore, a molar mass measurement to within a $10^{-8}\,M$ accuracy requires that the fractions of the minority isotopes ^{29}Si and ^{30}Si – about 0.05 and 0.03, respectively – are determined to within a relative accuracy better than 10^{-5}. However, insuperable difficulties have impaired the efforts to achieve this accuracy. To get around the problem, the Central Design Bureau of Machine Building in St. Petersburg (Russia) enriched a considerable amount of SiF_4 gas to more than 99.995% $^{28}SiF_4$. Subsequently, the Institute of Chemistry of High-Purity Substances of the Russian Academy of Sciences converted the enriched gas into SiH_4 and grew a polycrystal. Eventually, a 5 kg ^{28}Si crystal was grown and purified by the Leibniz-Institut für Kristallzüchtung (Berlin, Germany). Since, in an enriched ^{28}Si crystal, the minority isotopes contribute to the molar mass only through very small corrective terms, measurements of the minority isotope fractions having a 10^{-2} relative uncertainty are sufficient [16]. Accurate molar mass measurements were thus possible by using a combination of isotope dilution mass spectrometry and high resolution inductively coupled plasma mass spectrometry [17, 18].

3.4 Volume

Two 1 kg spheres were carved from the enriched ^{28}Si crystal. The spherical shape was selected because it has no edges that might get damaged, because its volume can be calculated from diameter measurements, and because accurate geometric, chemical, and physical characterisations of the whole surface are possible. To weigh the spheres against the international prototype of the kilogram, their mass is 1 kg to within some ten milligrams. The sphere diameters – 93.7 mm – are measured by optical interferometry. In order to obtain a 10^{-8} relative accuracy in the volume determination, the mean diameter must be measured to a range of 0.3 nm, that is, to within an atom spacing. Such high accuracy requires sub-nanometre surface roughness and a quasi-perfect spherical shape. Eventually, the sphere volumes were determined to within a $2.9 \times 10^{-8}\,V$ uncertainty [19, 20].

3.5 Lattice parameter

X-ray interferometry is the technology that has enabled measurement of the lattice parameter. An X-ray interferometer consists of three Si crystals so cut that the {220} planes are orthogonal to the crystal surfaces. X-rays from a 17 keV Mo Kα source are split by the first crystal and recombined via two transmission crystals by the third, called the analyser. When the analyser is moved in a direction orthogonal to the {220} planes, a periodic intensity variation of the transmitted and diffracted X-rays is observed, the period being the diffracting-plane spacing. The analyser embeds front and rear mirrors, so that its displacement and rotations can be measured by an optical interferometer. The measurement equation is $d_{220} = m\lambda/(2n)$, where $d_{220} \approx 192$ pm is the spacing of the {220} planes, n is the number of X-ray fringes in a displacement of m optical fringes having a period $\lambda/2 \approx 316$ nm, and the lattice parameter is obtained by $a = \sqrt{8}d_{220}$. To ensure the interferometer calibration, the laser source operates in single mode and its frequency is stabilised against that of a transition of the $^{127}I_2$ molecule. To eliminate the adverse influence of the refractive index of air and to achieve millikelvin temperature uniformity and stability, the experiment is carried out in a thermovacuum chamber. Continuous developments led to a measurement accuracy of 3.5 nm/m [21].

3.6 Mass

The BIPM, the PTB and the NMIJ carried out state-of-the-art comparisons between the masses of the ^{28}Si spheres and Pt-Ir standards in air and under vacuum with a combined standard uncertainty of less than 5 μg. The mass of each sphere was determined by taking into account the traceability to the international prototype of the kilogram and the correlations among the 17 Pt-Ir standards used directly or indirectly in the comparisons [22].

The surface of silicon is covered with a thin layer of silicon dioxide. The sphere surface was characterised from the chemical and physical viewpoints by X-ray reflectometry, X-ray photoelectron spectroscopy, X-ray fluorescence, near-edge X-ray absorption fine structure spectroscopy, and spectroscopic ellipsometry to determine contamination, stoichiometry, mass, and thickness of the oxide layer with a spatial resolution of 1 mm^2 [23].

The crystal must be free from imperfections and chemically pure. Consequently, it was purified by the float-zone technique and the pulling speed was so chosen in order to reduce the self-interstitial concentration. The crystal is dislocation free and, to apply the relevant corrections, the concentrations of carbon, oxygen, and boron atoms and vacancies were measured by infrared and positron lifetime spectroscopies [24]. Since, in determining the molar mass, consideration is given only to the Si atoms, the sphere masses were corrected for the mass of the surface layer and the bulk point defects, contaminants – mainly carbon, oxygen, and boron – and vacancies. In this way, the mass of an equivalent naked sphere having one Si atom at each lattice site was obtained.

3.7 Results

The N_A values determined by using each of the two ^{28}Si spheres differ only by $37(35) \times 10^{-9} N_A$. The average of these values, $N_A = 6.02214082(18) \times 10^{23}$ mol^{-1}, has a relative standard uncertainty of 3.0×10^{-8} and is the most accurate input datum for the determination of the Planck constant.

4 Outlooks

Three h measurements have so far achieved accuracies close to that required to make the kilogram redefinition possible: Two watt balance experiments – at the National Institute of Standards and Technology (NIST) [25] and the National Research Council of Canada (NRC) [26] – and an Si-atom count experiment carried out by the International Avogadro Coordination (IAC) [27, 28]. However, as shown in Fig. 2, there are inconsistencies between the values measured in these experiments: their spread, up to $2.6(7) \times 10^{-7} h$, is larger than the combined standard uncertainty. This indicates errors in at least one of the measurements; work is in progress to understand what this error is and to remedy it.

As regards the determination of N_A, the next paragraphs list the possible weaknesses and the activities necessary to investigate them experimentally. The long-term objective is to reach a $10^{-8} N_A$ measurement uncertainty; this stress test is expected to bring to light mistakes and hidden assumptions and to exclude or identify and then eliminate them.

Temperature is a critical factor. Since the volumetric thermal expansion of Si is about 7.7×10^{-9} mK^{-1}, the temperature measurements of the spheres and X-ray interferometer crystals – which are used for the volume and lattice parameter determinations – require sub-mK accuracies. Luckily, measurements of thermodynamic temperature are not required, but it is necessary that the sphere and unit cell volumes refer to the same

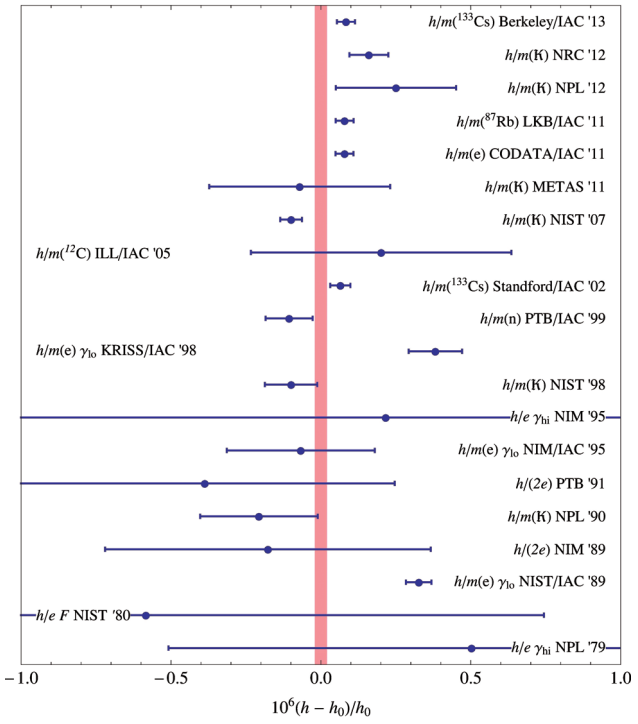

Figure 2 Comparison of the determinations of the Planck constant – data are from [2] and [11]. The reference is the CODATA 2010 value, $h_0 = 6.62606957(29) \times 10^{-34}$ J s. The error bars indicate the standard deviations. The values labelled by IAC combine N_A and h/m measurements; consequently, the seemingly good agreement of some of them is due to correlation. The pink bar indicates the $\pm 2 \times 10^{-8} h$ uncertainty required to make possible a kilogram redefinition based on a conventionally agreed value of h.

temperature. Therefore, only the difference between the practical temperature scales used to extrapolate the volume and lattice parameter measurements to 20 °C must be identified. The thermal gradients in the relevant experimental set-ups must be investigated as well, both experimentally and by finite element modelling.

The total impurities within the ^{28}Si crystal must not exceed a few nanograms per gram; if higher, the relevant mass fractions must be quantified and the measured N_A value must be corrected. There is a general consensus that the contamination by most of the elements is significantly smaller than 10^{-9} parts of an Si atom. In order to gain a direct evidence of purity, an analytical method based on neutron activation is being developed to exclude trace contaminations [29].

Microdefects in dislocation-free Si crystals are related to both vacancies and self-interstitial atoms. The defect type is controlled by the ratio ζ between the growth rate and the thermal gradient at the crystal-melt interface. The vacancy-related defects are formed if $\zeta < 1.6(4)$ mm^{2}min^{-1}K^{-1} (vacancy mode), whereas the self-interstitial related defects are formed if $\zeta > 1.6(4)$ mm^{2}min^{-1}K^{-1} (self-interstitial mode) [30, 31]. This rule comes from the competition of the point-defect fluxes from the crystal-melt interface into the bulk. The ^{28}Si crystal used to determine N_A was grown in vacancy mode. Depending on a number of factors, vacancies react in various ways and become trapped in various forms during the cooling of the crystal – primarily forming voids and complexes with oxygen and nitrogen. It is probably safe to say that when the crystal has reached room temperature there are no free vacancies at all. Since the number density of Si is 5×10^{22} cm^{-3}, in order to achieve a measurement uncertainty of $10^{-8} N_A$, the maximum total vacancy concentration – in any form or combination of forms – must be below 5×10^{14} cm^{-3}, if not, there is a difficult problem. The total vacancy concentration in melt-grown Si crystals varies from zero – if the crystal is grown in interstitial mode – to a few times 10^{14} cm^{-3}; in general, there is a radial dependence of the vacancy concentration, too. It is expected that the ^{28}Si crystal contains roughly 3×10^{14} cm^{-3} total vacancies [32, 33].

A residual stress exists in silicon surfaces, even if the underlying bulk crystal is stress-free. When the surface relaxes, it strains the underlying crystal, makes the lattice parameters of the X-ray interferometer and spheres different, and jeopardises the atom count – which is based on the atomic spacing as measured in the interferometer crystals. Numerical techniques are being developed for first-principle characterisation of both the stress and strain fields of silicon surfaces with atomistic resolution, as well as for the combination of surface stress with the continuum elasticity theory. The experimental determination of the surface stress is a challenge; the design of a variable thickness interferometer is under way to work out a lattice parameter measurement, so that there is a visible effect of the surface stress [34].

When the measurement accuracy approaches 1 nm/m, wavefront distortions are a major problem of dimensional metrology by optical interferometry. At this level of uncertainty, the relation $\lambda = c/\nu$ (the symbols having the usual meanings) is valid only for a plane wave. In reality, some energy disperses outside the region in which it would be expected to remain in plane wave propagation. This effect is known as diffraction and is connected with the wave nature of light. As a result, wavefronts bend and their spacing varies from one point to another and is different from the wavelength of a plane wave. In the case of integrated signals, the analysis of the operation of two-beam interferometers proves that the relevant correction – within the limit of a small difference

between the lengths of the paths through the interferometer arms – is proportional to the principal widths of the angular spectrum of the illuminating beam, no matter how aberrated it could be [35]. These widths – which, in the case of Gaussian beams coincide with the principal divergences – can be measured by making use of the inherent ability of a converging lens to perform two-dimensional Fourier transforms.

This result, provided that the impulse-domain width is measured to within a sufficient accuracy, is central to the lattice parameter measurement, but it does not apply to wavefront waviness originating inside the interferometer or to position-sensitive measurements. In this case, the wavefront evolution with beam propagation makes the locally detected phases different from those that would be expected from a geometrical wavefront translation [36]. This phenomenon plays a particular role in the reconstruction of the sphere topography. In fact, the roundness errors are not mapped one-to-one into the phase-profile ridges of the measured wavefront, but, in principle, they evolve from the sphere surface – where they are imprinted on the wavefront – to the detector – where they are observed.

Whilst this evolution is believed to be small, a good estimate of the difference between the ridges of the phase profile at the detection plane and the roundness errors is still missing. Therefore, the Leibniz-Institut für Oberflächenmodifizierung (Leipzig, Germany) is developing technologies based on ultra-precision ion beam figuring and plasma jet machining to smooth the surface topography. A metallic contamination (by copper and nickel silicides) was detected on the sphere surfaces, which increased the measurement uncertainty because of an influence on the optical constants and mass of the oxide layer. The surface contamination, together with the roundness errors, was a major factor limiting the accuracy of the N_A measurement.

5 Conclusions

The awaited revision of the SI assigns an exact value to the Planck constant; hence, the kilogram will be traced back to the second through the values of h, c, and $\nu(^{133}\mathrm{Cs})$. Macroscopic masses can be related to h via the watt balance experiment. Atomic masses are related to the Planck constant via the measurement of the $h/m(\mathrm{X})$ quotient; the link to macroscopic masses can be made by silicon spheres of known composition, volume, and lattice parameter. The number of atoms in such spheres is $N_{Si} = 8V/a^3$ and, since the binding energy – about 5 eV per Si atom – is negligible, the sphere mass is $m_{Si} = N_{Si}M(\mathrm{Si})/N_A$, where $M(\mathrm{Si})$ is the sphere molar mass. Corrections must be made due to the mass of the surface oxide – which must be characterised as regards the thickness and composition – and the defects of the sphere lattice.

An immediate fallout of the h and N_A measurements is the possibility of monitoring the stability of the international prototype of the kilogram by using ^{28}Si or natural Si spheres, whose mass evolution is traced by monitoring the geometrical, physical, and chemical changes of their surfaces. These measurements play a role in science, too. They allow the consistency of our understanding of nature to be investigated by checking the identity of the values measured at different energies, from meV (solid state physics) to eV (atomic physics and optical spectroscopy) to MeV (nuclear physics).

Acknowledgments. This work was jointly funded by the European Metrology Research Programme (EMRP) participating countries within the European Association of National Metrology Institutes (EURAMET) and the European Union.

Key words. Metrology, precision measurements, Planck constant, Avogadro constant, kilogram, silicon.

References

[1] G. Girard, Metrologia **31**(4), 317–336 (1994).
[2] G. Mana and E. Massa, Rivista del Nuovo Cimento **35**(7), 353–388 (2012).
[3] J. M. Lévy-Leblond, Rivista del Nuovo Cimento **7**(2), 187–214 (1977).
[4] P. J. Mohr, B. N. Taylor, and D. B. Newell, Rev. Mod. Phys. **84**(Oct-Dec), 1527–1605 (2012).
[5] E. Kruger, W. Nistler, and W. Weirauch, Metrologia **32**(2), 117–128 (1995).
[6] E. Kruger, W. Nistler, and W. Weirauch, Metrologia **35**(3), 203–209 (1998).
[7] E. Kruger, W. Nistler, and W. Weirauch, Metrologia **36**(2), 147–148 (1999).
[8] A. Wicht, J. M. Hensley, E. Sarajlic, and S. Chu, Physica Scripta **2002**(T102), 82 (2002).
[9] M. Cadoret, E. de Mirandes, P. Cladé, S. Guellati-Khélifa, C. Schwob, F. Nez, L. Julien, and F. Biraben, Phys. Rev. Lett. **101**(Dec), 230801 (2008).
[10] R. Bouchendira, P. Cladé, S. Guellati-Khélifa, F. Nez, and F. Biraben, Phys. Rev. Lett. **106**(Feb), 080801 (2011).
[11] S. Y. Lan, P. C. Kuan, B. Estey, D. English, J. M. Brown, M. A. Hohensee, and H. Mueller, Science **339**(6119), 554–557 (2013).
[12] S. Rainville, J. K. Thompson, E. G. Myers, J. M. Brown, M. S. Dewey, E. G. Kessler, R. D. Deslattes, H. G.

Borner, M. Jentschel, P. Mutti, and D. E. Pritchard, Nature **438**(7071), 1096–1097 (2005).
[13] K. Blaum, Physics Reports **425**(1), 1–78 (2006).
[14] I. A. Robinson, Metrologia **49**(1), 113–156 (2012).
[15] R. Steiner, Reports on Progress in Physics **76**(1), 016101 (2013).
[16] G. Mana, E. Massa, S. Valkiers, and G. D. Willenberg, International Journal of Mass Spectrometry **289**(1), 6–10 (2010).
[17] G. Mana, O. Rienitz, and A. Pramann, Metrologia **47**(4), 460–463 (2010).
[18] A. Pramann, O. Rienitz, D. Schiel, J. Schlote, B. Guettler, and S. Valkiers, Metrologia **48**(2), S20–S25 (2011).
[19] G. Bartl, H. Bettin, M. Krystek, T. Mai, A. Nicolaus, and A. Peter, Metrologia **48**(2), S96–S103 (2011).
[20] N. Kuramoto, K. Fujii, and K. Yamazawa, Metrologia **48**(2), S83–S95 (2011).
[21] E. Massa, G. Mana, U. Kuetgens, and L. Ferroglio, Metrologia **48**(2), S37–S43 (2011).
[22] A. Picard, P. Barat, M. Borys, M. Firlus, and S. Mizushima, Metrologia **48**(2), S112–S119 (2011).
[23] I. Busch, Y. Azuma, H. Bettin, L. Cibik, P. Fuchs, K. Fujii, M. Krumrey, U. Kuetgens, N. Kuramoto, and S. Mizushima, Metrologia **48**(2), S62–S82 (2011).
[24] S. Zakel, S. Wundrack, H. Niemann, O. Rienitz, and D. Schiel, Metrologia **48**(2), S14–S19 (2011).
[25] R. L. Steiner, E. R. Williams, D. B. Newell, and R. M. Liu, Metrologia **42**(5), 431–441 (2005).
[26] A. G. Steele, J. Meija, C. A. Sanchez, L. Yang, B. M. Wood, R. E. Sturgeon, Z. Mester, and A. D. Inglis, Metrologia **49**(1), L8–L10 (2012).
[27] B. Andreas, Y. Azuma, G. Bartl, P. Becker, H. Bettin, M. Borys, I. Busch, M. Gray, P. Fuchs, K. Fujii, H. Fujimoto, E. Kessler, M. Krumrey, U. Kuetgens, N. Kuramoto, G. Mana, P. Manson, E. Massa, S. Mizushima, A. Nicolaus, A. Picard, A. Pramann, O. Rienitz, D. Schiel, S. Valkiers, and A. Waseda, Phys. Rev. Lett. **106**(Jan), 030801 (2011).
[28] B. Andreas, Y. Azuma, G. Bartl, P. Becker, H. Bettin, M. Borys, I. Busch, P. Fuchs, K. Fujii, H. Fujimoto, E. Kessler, M. Krumrey, U. Kuetgens, N. Kuramoto, G. Mana, E. Massa, S. Mizushima, A. Nicolaus, A. Picard, A. Pramann, O. Rienitz, D. Schiel, S. Valkiers, A. Waseda, and S. Zakel, Metrologia **48**, S1–S13 (2011).
[29] G. D'Agostino, L. Bergamaschi, L. Giordani, G. Mana, E. Massa, and M. Oddone, Metrologia **49**(6), 696–701 (2012).
[30] V. Voronkov and R. Falster, Journal of Crystal Growth **194**(1), 76–88 (1998).
[31] R. Falster, V. Voronkov, and F. Quast, Physica Status Solidi (b) **222**(1), 219–244 (2000).
[32] J. Gebauer, F. Rudolf, A. Polity, R. Krause-Rehberg, J. Martin, and P. Becker, Applied Physics A **68**(4), 411–416 (1999).
[33] J. Martin, H. Bettin, U. Kuetgens, D. Schiel, and P. Becker, IEEE Transactions on Instrumentation and Measurement **48**(2), 216–220 (1999), 1998 Conference on Precision Electromagnetic Measurements (CPEM 98), Washington, D.C., Jul 06-10, 1998.
[34] C. Sasso, D. Quagliotti, E. Massa, G. Mana, and U. Kuetgens, Metrologia, submitted.
[35] A. Bergamin, G. Cavagnero, L. Cordiali, and G. Mana, European Physical Journal D **5**(3), 433–440 (1999).
[36] B. Andreas, L. Ferroglio, K. Fujii, N. Kuramoto, and G. Mana, Metrologia **48**(2), S104–S111 (2011).

The interconversion of the radial motional modes of an ion in a Penning trap mass spectrometer by $4n$-polar external radio frequency fields ($n = 1, 2, 3, 4$)

Martin Kretzschmar*

Institut für Physik, Johannes-Gutenberg-Universität, 55099 Mainz, Germany

March 21, 2013

to be submitted to Annalen der Physik

Abstract

In Penning trap mass spectrometry the masses of stable or radioactive nuclides are determined by measuring their free cyclotron frequency $\nu_c = qB/(2\pi m)$ via the resonant conversion of the magnetron into the cyclotron motional mode, which is induced by the interaction with some external radio-frequency field. Conventionally one uses a quadrupolar field with frequency $\nu_{\rm rf} \approx \nu_c$, in a few experiments octupolar fields with frequency $\nu_{\rm rf} \approx 2\nu_c$ have been employed. With octupolar rf-fields the mass resolution could be improved by more than an order of magnitude as compared to the result obtainable by use of a quadrupolar field with the same pulse duration. This result raises the question what one might expect from using 12-polar rf-fields with frequency $\nu_{\rm rf} \approx 3\nu_c$ or even 16-polar rf-fields with frequency $\nu_{\rm rf} \approx 4\nu_c$.

In this paper we generalize the successful theoretical models describing the interconversion of the radial modes by quadrupolar and octupolar rf-fields to models for general $4n$-polar fields. As proposed in earlier work the complex amplitudes of the cyclotron and magnetron oscillators are used as dynamical variables and the Hamiltonian equations of motion are reformulated in terms of Bloch vector components. The resulting non-linear differential equations are amenable to numerical solution so that the interconversion of the radial motional modes as induced by $4n$-polar ($n \geq 2$) can be studied numerically.

We present results on excitation functions (conversion at the exact resonance frequency) and their dependence on the initial phases of the external rf-field and of the complex oscillator amplitudes as well as detailed results on the phase-averaged conversion line shapes and their FWHM resonance widths. The non-linear resonances seen for octupolar, 12-polar, and 16-polar excitation show remarkable similarities and are quite distinct from the (linear) quadrupolar case. The most important observation is the decrease of the widths of the conversion resonance measured at the point of maximum conversion. Using the dimensionless detuning parameter $\Delta = \frac{1}{n}(\nu_{\rm rf} - n\nu_c)\tau$, where τ is the duration of the rf-pulse for the conversion, we estimate a decrease of the conversion resonance width by a factor of 2×10^3 as we pass from the quadrupolar ($n = 1$) to the 16-polar ($n = 4$) case. For the latter case the conversion landscape is essentially flat with the exception of a thin vertical sheet rising at the exact resonance frequency.

Whether or not the theoretically possible gain in mass resolution can be realized by future experiments remains to be seen. Fluctuations of the experimental environment and lack of control of all initial parameters of the ion will probably be liable for only partial fulfillment of the hopes raised by our theoretical model calculation.

Keywords: Penning trap mass spectrometry; Mass resolution; Ion cyclotron resonance; Octupolar excitation; Interconversion of radial motional modes; Conversion line shapes;

PACS: 07.75.+h (mass spectrometers); 21.10.Dr (binding energies and masses), 37.10.Ty (ion trapping), 37.10.Vz (mechanical effects of light on atoms, molecules, and ions), 82.80.Qx (ion cyclotron resonance mass spectrometry), 82.80.Rt (time-of-flight mass spectrometry)

-

*email: Martin.Kretzschmar@uni-mainz.de

1 Introduction

Penning trap mass spectrometry is presently the most powerful experimental technique to obtain the masses of stable and radioactive nuclides with highest precision. These mass values are important not only for nuclear and astrophysical research, but also for progress on a number of fundamental problems [1, 2, 3, 4]. Novel ideas leading to further improvement of the measurement procedures and to ever greater accuracy of the obtained data are very high on the agenda.

Many experiments use the "Ion Cyclotron Resonance-Time of Flight" (ICR-ToF) method to determine the ion mass m by measuring the ion's free cyclotron frequency $\nu_c = qB/(2\pi m)$, where q is the ion's charge and B is the magnetic field intensity in the Penning trap [5, 6, 7, 8]. Single ions are prepared in a motional state with a large magnetron radius and a cyclotron radius that is as small as possible. The magnetron motion is then converted into cyclotron motion by a pulse of radio-frequency (rf) radiation with frequency $\nu_{\rm rf} \approx \nu_c$ with predetermined amplitude and pulse duration. The energy of the ion now resides in the cyclotron mode and can be determined by a time-of-flight measurement. The conversion of the magnetron into the cyclotron motional mode is for quadrupolar rf-fields resonant at the free cyclotron frequency ν_c of the ion. The exact resonance position is obtained by the time-of-flight measurement of the ion energy as a function of the detuning of the rf-radiation.

The accuracy and mass resolution of the ICR-ToF technique has been analyzed by Bollen [9] and other authors [4, 8, 10]. The mass resolving power $\mathcal{R} = m/\Delta m$, where Δm is determined by the FWHM of the resonance peak, is estimated to be proportional to the resonance frequency $\nu_{\rm rf}$. Assuming the resonance width to be given by the Fourier limit and denoting the pulse duration by $\tau_{\rm rf}$ we have

$$\mathcal{R} = \frac{m}{\Delta m} = \frac{\nu_{\rm rf}}{\Delta \nu_{\rm rf}} \approx \nu_{\rm rf} \cdot \tau_{\rm rf}. \qquad (1)$$

Thus using higher harmonics of the free cyclotron frequency $n\,\nu_c$ $(n = 2, 3, 4)$ to convert magnetron into cyclotron motion one expects an increase of resolving power by a factor of n as compared to conversion by a conventional quadrupolar rf-field at the frequency ν_c and with the same pulse duration.

First experiments to explore for the purposes of mass spectrometry the feasibility of excitation by octupolar rf-fields with frequency $\nu_{\rm rf} \approx 2\nu_c$ have been performed by Ringle et al. [11], Eliseev et al. [12], and Breitenfeld et al. [13]. Surprisingly it was found that the gain in resolving power was much larger than the expected factor of 2. A later experiment by Eliseev et al. [14] confirmed this observation, resulting in a resolving power of $\mathcal{R} \approx 2 \cdot 10^7$, which exceeds that of the quadrupolar technique by more than a factor of 10. Obviously the Fourier limit (1) overestimates the resonance width considerably, a deeper theoretical understanding of the conversion line shape due to $4n$-polar $(n \geq 2)$ rf-fields becomes necessary. In particular it will be of great interest to find out whether or not an excitation of the ion motion by 12-polar or 16-polar rf-fields will lead to even greater gains in accuracy and mass resolution.

In two earlier studies we have developed a theoretical model for excitation of the ion motion by octupolar fields. Our model uses the complex amplitudes of the cyclotron and magnetron oscillators as its basic dynamical variables. The first paper [15], focusing on fundamental questions, starts from a quantum mechanical formulation of the problem and shows that the complex oscillator amplitudes arise in a natural way when one makes the transition from the quantum theory to the classical theory. They occur as expectation values of the annihilation operators for the quanta of the cyclotron and magnetron oscillators, calculated for quasi-classical coherent states corresponding to the classical motional parameters [16]. The second paper [17] aims to simplify the presentation by staying as much as possible within the realm of classical mechanics, using the Poisson bracket formalism to obtain the basic equations of motion. For both studies the concept of the Bloch vector is quite important, because it allows the non-linearity in the equations for the interconversion of the radial motional modes by octupolar excitation to be reduced to a tractable degree. The non-linearity of the equations for the octupolar case represents a fundamental difference to the familiar quadrupolar case which is governed by linear equations.

The present paper generalizes these theoretical considerations to excitation of the ion motion by $4n$-polar rf-fields, with special attention on $n = 2, 3, 4$. The model Hamiltonians and corresponding equations of motion for $n = 3, 4$ are non-linear to an even higher degree than for the octupolar case, but can be studied at least numerically. The cases $n = 2, 3, 4$ exhibit many similarities. Of greatest interest are, of course, the calculated line shapes for the resonant interconversion of the radial motional modes, displayed in Figs. 5, 9, and 13 for $n = 2, 3$ and 4. It is seen that another two orders of magnitude in accuracy and mass resolution might be gained by using 16-polar instead of octupolar excitation.

The paper is structured as follows: In the next section the complex oscillator amplitudes for the ideal Penning trap are introduced and some examples are given for their use. In Section 3 we analyze external radio-frequency fields and explain how the interaction term responsible for the interconversion of the cyclotron and magnetron motional modes is isolated. In Section 4 the concept of a Bloch vector is introduced and motivated. A collection of basic formulas relating to Poisson brackets in general and to the components of the Bloch vector and its bracket relations in particular can be found in the Appendix. The new concept is then used in Section 5 to reformulate the Hamiltonian and the equations of motion in terms of Bloch vector components. Finally in Section 6 these theoretical developments are exploited to gain information about the interconversion of the radial motional modes due to excitation by octupolar, 12-polar, and 16-polar external radio-frequency fields. Results are presented on excitation functions, their phase-dependence, and on phase-averaged conversion line shapes.

2 Complex oscillator amplitudes for ion motion in a Penning trap

The ion motion in an ideal Penning trap can be analyzed in terms of three oscillators, the cyclotron, magnetron, and axial oscillators with the frequencies $\nu_+ = \omega_+/(2\pi)$ (modified cyclotron frequency), $\nu_- = \omega_-/(2\pi)$ (magnetron frequency), and $\nu_z = \omega_z/(2\pi)$ (axial frequency), respectively [18]. These frequencies are related to each other by

$$\left.\begin{array}{l}\omega_+ = \frac{1}{2}(\omega_c + \omega_1)\\ \omega_- = \frac{1}{2}(\omega_c - \omega_1)\end{array}\right\} \quad \text{with } \omega_1 = \sqrt{\omega_c^2 - 2\omega_z^2}\,. \tag{2}$$

The Hamiltonian of the ideal Penning trap can be written as

$$H_0 = \hbar\omega_+\alpha_+^*(t)\alpha_+(t) - \hbar\omega_-\alpha_-^*(t)\alpha_-(t) + \hbar\omega_z\alpha_z^*(t)\alpha_z(t), \tag{3}$$

where the $\alpha_j(t)$ ($j = +, -, z$) are the "complex oscillator amplitudes" of the three oscillators. The asterisk denotes complex conjugation. These complex functions are obtained from the quantized version of the theory by taking the expectation value of the annihilation operator $\hat{a}_j(t)$ for quanta of oscillator j with respect to a quasi-classical coherent state $|\alpha\rangle = |\alpha_+, \alpha_-, \alpha_z\rangle$ [16],

$$\alpha_j(t) = \langle\alpha|\hat{a}_j(t)|\alpha\rangle. \tag{4}$$

This origin fixes the normalization of the complex oscillator amplitudes, which is important for the validity of Eq. (3) and of the Poisson bracket relation

$$\{\alpha_j, \alpha_{j'}^*\} = (i\hbar)^{-1}\delta_{jj'} \quad (j, j' = +, -, z). \tag{5}$$

For more details see the Appendix. The complex oscillator amplitudes are the eigen-amplitudes of the three oscillators describing the ion motion in the Penning trap. They satisfy the relations

$$\alpha_+(t) = e^{-i\omega_+ t}\alpha_+(0) \quad \text{with } \omega_+ = \tfrac{1}{2}(\omega_c + \omega_1), \tag{6}$$

$$\alpha_-(t) = e^{+i\omega_- t}\alpha_-(0) \quad \text{with } \omega_- = \tfrac{1}{2}(\omega_c - \omega_1), \tag{7}$$

$$\alpha_z(t) = e^{-i\omega_z t}\alpha_z(0). \tag{8}$$

Using the classical Poisson bracket formalism (see Appendix), in particular the Eq. (107) and the bracket relation (5) the equations of motion for the complex oscillator amplitudes can be written as

$$\frac{\mathrm{d}}{\mathrm{d}t}\alpha_j(t) = \dot{\alpha}_j(t) = \{\alpha_j(t), H_0\} = -i\epsilon_j\omega_j\alpha_j(t) \tag{9}$$

with $\epsilon_+ = \epsilon_z = +1$, $\epsilon_- = -1$.

The focus of interest in this paper lies on the interconversion of the radial (i.e. cyclotron and magnetron) motional modes by external rf-fields. For this topic the axial oscillator is of no relevance and will be ignored in the discussions and equations which are to follow.

For the radial modes the Cartesian canonical momenta are given by [19]

$$p_x = m\dot{x} - \tfrac{1}{2}m\omega_c\, y\,, \tag{10}$$

$$p_y = m\dot{y} + \tfrac{1}{2}m\omega_c\, x\,. \tag{11}$$

The complex oscillator amplitudes can be expressed in terms of Cartesian coordinates and their conjugate canonical momenta by

$$\alpha_+(t) = \frac{1}{\sqrt{2\hbar}}\left(\frac{\sqrt{m\omega_1}}{2}(x + iy) + \frac{i}{\sqrt{m\omega_1}}(p_x + ip_y)\right), \tag{12}$$

$$\alpha_-(t) = \frac{1}{\sqrt{2\hbar}}\left(\frac{\sqrt{m\omega_1}}{2}(x - iy) + \frac{i}{\sqrt{m\omega_1}}(p_x - ip_y)\right). \tag{13}$$

Inverting these relations we find

$$x = \sqrt{\frac{\hbar}{2m\omega_1}}\left(\alpha_+ + \alpha_+^* + \alpha_- + \alpha_-^*\right), \tag{14}$$

$$y = -i\sqrt{\frac{\hbar}{2m\omega_1}}\left(\alpha_+ - \alpha_+^* - \alpha_- + \alpha_-^*\right), \tag{15}$$

or combined into the single equation

$$x + iy = \sqrt{\frac{\hbar}{2m\omega_1}}\left(\alpha_+ + \alpha_-^*\right). \tag{16}$$

The radial motion in the ideal Penning trap is described in Cartesian coordinates by [19]

$$u(t) = x(t) + iy(t) = R_+\, e^{-i(\omega_+ t + \chi_+)} + R_-\, e^{-i(\omega_- t + \chi_-)}, \tag{17}$$

where R_+ and R_- denote the cyclotron and magnetron radii of the ion motion, and where χ_+ and χ_- are the initial phases of the oscillators at time $t = 0$. Combining the Eqs. (16) and (17) we obtain the relation between the radii and the complex oscillator amplitudes $\alpha_\pm$,

$$R_\pm(t) = \sqrt{\frac{2\hbar}{m\omega_1}}|\alpha_\pm(t)|\,. \tag{18}$$

3 External radio-frequency fields

The ion motion in a Penning trap can be manipulated in a multitude of ways by radiation pulses due to external radio-frequency (rf) fields with specifically chosen pulse duration and frequency. These fields are introduced into the trap via the ring-, correction-, and end-electrodes. The potential U of a single-frequency field can be factorized into a space-dependent and a time-dependent part since retardation effects are negligible,

$$U(x, y, z, t) = \cos(\Phi_{\mathrm{rf}}(t))\, U_{\mathrm{rf}}(x, y, z), \tag{19}$$

where $\Phi_{\mathrm{rf}}(t) = \omega_{\mathrm{rf}}t + \chi_{\mathrm{rf}}$ is the phase of the rf-field. As the field is sourcefree in the trap interior the potential must satisfy there the Laplace equation $\Delta U_{\mathrm{rf}} = 0$. Near the trap center, the region of our interest, solutions of the Laplace equation can be expanded in terms of spherical harmonics $r^\ell Y_\ell^m(\theta, \phi)$, which provide a complete set of solutions. Replacing spherical coordinates by Cartesian coordinates the spherical harmonics become so-called harmonic polynomials $P_{\ell m}(x, y, z)$. The external rf-field can then be expanded in the form

$$U_{\mathrm{rf}}(x, y, z) = \sum_{\ell=0}^{\infty}\sum_{m=-\ell}^{+\ell} c_{\ell m}P_{\ell m}(x, y, z) \tag{20}$$

with coefficients $c_{\ell m}$ that are determined by the way in which the external rf-voltages are applied to the electrode segments.

At the focus of interest is in this paper the interconversion of the cyclotron and magnetron motional modes, without participation of the axial mode. This process is brought about by the part of the external rf-field that does not depend on z. Thus in the general expansion of Eq. (20) we must look for harmonic potentials that are independent of z. For each ℓ there are only two such polynomials, $(x+iy)^\ell + (x-iy)^\ell$ and $(x+iy)^\ell - (x-iy)^\ell$. The two polynomials can be made equivalent to each other with a suitable choice of the phase $\chi_{\rm rf}$ of the external rf-field. It is therefore sufficient to concentrate on the harmonic polynomials

$$\begin{aligned} P_\ell(x,y) &= \frac{1}{2}[(x+iy)^\ell + (x-iy)^\ell] \\ &= \sum_{j=0}^{[\ell/2]} (-1)^j \binom{\ell}{2j} x^{\ell-2j} y^{2j}, \end{aligned} \tag{21}$$

where $[\ell/2]$ denotes the integer part of ℓ. Examples are

$$P_2(x,y) = x^2 - y^2\,, \tag{22}$$
$$P_4(x,y) = x^4 - 6x^2y^2 + y^4\,, \tag{23}$$
$$P_6(x,y) = x^6 - 15x^4y^2 + 15x^2y^4 - y^6\,, \tag{24}$$
$$P_8(x,y) = x^8 - 28x^6y^2 + 70x^4y^4 - 28x^2y^6 + y^8\,. \tag{25}$$

The theoretical framework developed in [17] uses instead of Cartesian coordinates and momenta the complex amplitudes $\alpha_\pm(t)$ of the Penning trap oscillators as its dynamical variables. This requires that the potential (20) must be expressed in terms of these amplitudes. Inserting Eq. (16) into (21) we obtain for $n = 1, 2, 3, ...$

$$P_{2n}(\alpha_+, \alpha_+^*, \alpha_-, \alpha_-^*) \tag{26}$$
$$= \left(\frac{\hbar}{2m\omega_1}\right)^n \cdot \frac{1}{2}\left[\left(\alpha_+ + \alpha_-^*\right)^{2n} + \left(\alpha_- + \alpha_+^*\right)^{2n}\right] \tag{27}$$

Next we expand this expression into pairs of complex conjugate monomials in the complex amplitudes $\alpha_\pm(t)$ and $\alpha_\pm^*(t)$. As explained in more detail in [17], in the quantized version of the theory creation and annihilation operators for the oscillator quanta, $\hat{a}_\pm^\dagger(t)$ and $\hat{a}_\pm(t)$ respectively, take the place of the complex oscillator amplitudes $\alpha_\pm^*(t)$ and $\alpha_\pm(t)$. The potential (27) is seen to drive a number of different physical processes, most of them will change the number of excitation quanta in the system. For each n only one term in the expansion will preserve the number of oscillator quanta $\hat{N}_{\rm tot} = \hat{a}_+^\dagger(t)\hat{a}_+(t) + \hat{a}_-^\dagger(t)\hat{a}_-(t)$ in the system, namely the pair of conjugate monomials associated with the creation of n cyclotron quanta with simultaneous annihilation of n magnetron quanta, and vice versa. Choosing the frequency of the rf-field $\omega_{\rm rf} \approx n(\omega_+ + \omega_-) = n\omega_c$ this term will become dominant and drive the interconversion.

Returning to the classical description in terms of complex oscillator amplitudes we wish to construct an effective interaction Hamiltonian that can be used to set up equations of motion for the ions experiencing the external rf-field. From Eq. (27) we keep

$$P_{2n}(\alpha_+, \alpha_+^*, \alpha_-, \alpha_-^*)$$
$$= \left(\frac{\hbar}{2m\omega_1}\right)^n \cdot \frac{1}{2}\binom{2n}{n}\left[\left(\alpha_+^*\alpha_-\right)^n + \left(\alpha_-^*\alpha_+\right)^n\right] + \dots \tag{28}$$

This expression is combined with Eq. (19). Further simplification by the 'resonating wave approximation' [20, 21] drops the counter-rotating terms and restricts the applicability of interaction to the vicinity of the resonance frequency $\omega_{\rm rf} \approx n(\omega_+ + \omega_-) = n\omega_c$. Our final result is

$$\begin{aligned} H_{\rm eff}^{(n)}(t) &= \hbar g \Big[e^{-i\Phi_{\rm rf}(t)} \left(\alpha_+^*(t)\alpha_-(t)\right)^n \\ &\qquad + e^{+i\Phi_{\rm rf}(t)} \left(\alpha_-^*(t)\alpha_+(t)\right)^n\Big], \end{aligned} \tag{29}$$

where $\Phi_{\rm rf}(t) = \omega_{\rm rf}t + \chi_{\rm rf}$ is the phase of the external rf-field and where the coupling parameter g with physical dimension s^{-1} collects all constants and coefficients that are encountered during the derivation.

Combining the Hamiltonian of the ideal Penning trap Eq. (3) with the effective interaction (29) to a total Hamiltonian

$$H^{(n)}(t) = H_0 + H_{\rm eff}^{(n)}(t) \tag{30}$$

we can use the Poisson bracket relations (106) and (108) to set up equations of motion for the complex oscillator amplitudes,

$$\begin{aligned} \frac{\mathrm{d}}{\mathrm{d}t}\,\alpha_\pm(t) &= \dot{\alpha}_\pm(t) = \{\alpha_\pm(t)\,,\, H^{(n)}(t)\} \\ &= \mp i\omega_\pm\alpha_\pm(t) + \left\{\alpha_\pm(t)\,,\, H_{\rm eff}^{(n)}(t)\right\}. \end{aligned} \tag{31}$$

Unfortunately, for $n \geq 2$ these equations are highly nonlinear and can not readily be solved. On the other hand, for the interpretation of ICR-ToF measurements a knowledge of the ion trajectories is not really required. Instead the quantity that is actually measured is the energy residing in the cyclotron motional mode after the termination of the rf-pulse, assuming an almost pure magnetron motional state as initial state. This energy is measured by

$$n_+(\tau) = \frac{R_+^2(\tau)}{R_+^2(0) + R_-^2(0)} = \frac{\alpha_+^*(\tau)\alpha_+(\tau)}{\alpha_+^*(0)\alpha_+(0) + \alpha_-^*(0)\alpha_-(0)}, \tag{32}$$

where τ denotes the pulse duration. This quantity requires knowledge not of the amplitudes $\alpha_\pm(t)$themselves, but of their bilinear products.

4 The Bloch vector

With reference to the interconversion of the motional modes in a Penning trap the concept of the Bloch vector was introduced in [22]. The components of the Bloch vector are in the quantum version bilinear products of the creation and annihilation operators of the oscillator modes, in the classical version bilinear products of the complex oscillator

amplitudes and their complex conjugate amplitudes. For the classical case the basic definition is

$$T_1(t) = \frac{\hbar}{2}\left(\alpha_+^*(t)\alpha_-(t) + \alpha_-^*(t)\alpha_+(t)\right), \quad (33)$$

$$T_2(t) = \frac{\hbar}{2i}\left(\alpha_+^*(t)\alpha_-(t) - \alpha_-^*(t)\alpha_+(t)\right), \quad (34)$$

$$T_3(t) = \frac{\hbar}{2}\left(\alpha_+^*(t)\alpha_+(t) - \alpha_-^*(t)\alpha_-(t)\right), \quad (35)$$

together with

$$T_0 = \frac{\hbar}{2}\left(\alpha_+^*(t)\alpha_+(t) + \alpha_-^*(t)\alpha_-(t)\right). \quad (36)$$

The scalar $T_0(t)$ commutes with the Hamiltonian (30),

$$\{T_0(t)\,,\, H_0 + H_{\rm eff}^{(n)}(t)\} = 0\,, \quad (37)$$

therefore T_0 is a conserved quantity and thus independent of time.

The identity Eq. (115)

$$T_0^2 = T_1^2(t) + T_2^2(t) + T_3^2(t) \quad (38)$$

tells us that the tip of the Bloch vector describes a path on the surface of the "Bloch sphere" of radius T_0 as the ion motion evolves with time. Each point on the Bloch sphere represents a possible motional state of the ion. In particular the North pole ($T_1 = T_2 = 0$, $T_3 = T_0$) corresponds to a pure cyclotron motional state, while the South pole ($T_1 = T_2 = 0$, $T_3 = -T_0$) corresponds to a pure magnetron motional state. During a conversion process starting with an almost pure magnetron state the tip of the Bloch vector will start out in the immediate vicinity of the South pole and then wander along a certain path into the neighbourhood of the North pole.

The concept of the Bloch vector was very helpful in elucidating the formal analogies between quadrupolar excitation in a Penning trap on the one hand and nuclear magnetic resonance on the other hand for the purpose of implementing Ramsey's idea of separated oscillatory fields for Penning trap mass spectrometry [25, 26]. Also in the study of the excitation of the ion motion by $4n$-polar rf-fields the transcription of the equations to the Bloch vector formalism will reduce the degree of nonlinearity by a factor of 2.

The quantity n_+, which is measured in ICR-ToF experiments, is conveniently expressed in terms of Bloch vector components,

$$n_+(\tau) = \frac{\alpha_+^*(\tau)\alpha_+(\tau)}{\alpha_+^*(0)\alpha_+(0) + \alpha_-^*(0)\alpha_-(0)} = \frac{T_0 + T_3}{2T_0}. \quad (39)$$

For this reason there is no need to calculate the complex oscillator amplitudes themselves, solutions for the Bloch vector components are sufficient to compute the 'degree of conversion' $n_+(\tau)$.

5 The interconversion of the radial modes by $4n$-polar fields

5.1 Hamiltonian formulation

In Section 3 the effective interaction for the interconversion of the radial modes by a $4n$-polar external field was obtained in Eq. (29). We note that this interaction term as well as the Hamiltonian H_0, Eq. (3), can be rewritten in terms of the components of the Bloch vector, resulting in the new Hamiltonian

$$\begin{aligned} H^{(n)}(t) &= H_0 + H_{\rm eff}^{(n)}(t) \\ &= \omega_1 T_0(t) + \omega_c T_3(t) \\ &\quad + \frac{g}{\hbar^{n-1}}\left(e^{-i\Phi_{\rm rf}(t)}T_+^n(t) + e^{+i\Phi_{\rm rf}(t)}T_-^n(t)\right) \end{aligned} \quad (40)$$

with $T_\pm(t) = T_1(t) \pm iT_2(t)$ (see Eqs. (112) and (113)).

By this reformulation of the Hamiltonian we are enabled to use the components of the Bloch vector as our dynamical variables, at the same time we have reduced the degree of non-linearity from $2n$ to n. In the octupolar case ($n = 2$) analytical solutions of the equations of motion become possible.

5.2 Equations of motion

Using Eq. (108) the Hamiltonian $H^{(n)}(t)$ generates the equations of motion for the Bloch vector components,

$$\frac{\rm d}{{\rm d}t}T_+(t) = i\omega_c T_+(t) - i\frac{2gn}{\hbar^{n-1}}e^{+i\Phi_{\rm rf}(t)}\,T_-^{n-1}(t)\,T_3(t), \quad (41)$$

$$\frac{\rm d}{{\rm d}t}T_-(t) = -i\omega_c T_+(t) + i\frac{2gn}{\hbar^{n-1}}e^{-i\Phi_{\rm rf}(t)}\,T_+^{n-1}(t)\,T_3(t), \quad (42)$$

$$\frac{\rm d}{{\rm d}t}T_3(t) = -i\frac{gn}{\hbar^{n-1}}\left(e^{-i\Phi_{\rm rf}(t)}T_+^n(t) - e^{+i\Phi_{\rm rf}(t)}T_-^n(t)\right). \quad (43)$$

In order to eliminate the explicit time-dependence of the right hand sides we transform the Bloch vector to a reference frame rotating with the frequency of the rf-field. We define

$$T'_\pm(t) = e^{\mp(i/n)\Phi_{\rm rf}(t)}T_\pm(t), \quad T'_3(t) = T_3(t), \quad T'_0 = T_0. \quad (44)$$

With

$$\frac{\rm d}{{\rm d}t}T'_\pm(t) = \mp i\frac{\omega_{\rm rf}}{n}T'_\pm(t) + e^{\mp(i/n)\Phi_{\rm rf}(t)}\frac{\rm d}{{\rm d}t}T_\pm(t) \quad (45)$$

the equations of motion for the transformed Bloch vector become

$$\frac{\rm d}{{\rm d}t}T'_+(t) = -i\delta\cdot T'_+(t) - i\frac{2gn}{\hbar^{n-1}}\cdot T_-'^{\,n-1}(t)\,T'_3(t), \quad (46)$$

$$\frac{\rm d}{{\rm d}t}T'_-(t) = +i\delta\cdot T'_-(t) + i\frac{2gn}{\hbar^{n-1}}\cdot T_+'^{\,n-1}(t)\,T'_3(t), \quad (47)$$

$$\frac{\rm d}{{\rm d}t}T'_3(t) = -i\frac{gn}{\hbar^{n-1}}\left(T_+'^{\,n}(t) - T_-'^{\,n}(t)\right). \quad (48)$$

For Cartesian components these equations take the form

$$\frac{\rm d}{{\rm d}t}T'_1(t) = \delta\cdot T'_2(t) - \frac{2gn}{\hbar^{n-1}}\cdot Q_{n-1}\big(T'_1(t), T'_2(t)\big)\cdot T'_3(t), \quad (49)$$

$$\frac{\rm d}{{\rm d}t}T'_2(t) = -\delta\cdot T'_1(t) - \frac{2gn}{\hbar^{n-1}}\cdot P_{n-1}\big(T'_1(t), T'_2(t)\big)\cdot T'_3(t), \quad (50)$$

$$\frac{\rm d}{{\rm d}t}T'_3(t) = \frac{2gn}{\hbar^{n-1}}\cdot Q_n\big(T'_1(t), T'_2(t)\big), \quad (51)$$

where $P_n(T'_1, T'_2)$ and $Q_n(T'_1, T'_2)$ are the polynomials defined in Eqs. (120) and (121).

Since T_0' is conserved we can introduce a normalized Bloch vector with components $X_i = T_i'/T_0'$, satisfying

$$X_1^2 + X_2^2 + X_3^2 = 1. \tag{52}$$

We define a dimensionless evolution parameter θ and a dimensionless detuning parameter η by

$$\theta = t \cdot 2gn \cdot (T_0/\hbar)^{n-1}, \qquad \eta = \frac{\delta}{2gn(T_0/\hbar)^{n-1}}. \tag{53}$$

Denoting the differentiation with respect to θ by $\mathrm{d}X_i/\mathrm{d}t = \dot{X}_i$, we obtain the final form of the equations of motion for the normalized Bloch vector describing the interconversion of the radial modes by $4n$-polar external rf-fields,

$$\dot{X}_1(\theta) = \eta X_2(\theta) - Q_{n-1}\Big(X_1(\theta), X_2(\theta)\Big) \cdot X_3(\theta), \tag{54}$$

$$\dot{X}_2(\theta) = -\eta X_1(\theta) - P_{n-1}\Big(X_1(\theta), X_2(\theta)\Big) \cdot X_3(\theta), \tag{55}$$

$$\dot{X}_3(\theta) = Q_n\Big(X_1(\theta), X_2(\theta)\Big). \tag{56}$$

Using Eq. (123) we see that

$$\dot{X}_1(\theta) \cdot X_1(\theta) + \dot{X}_2(\theta) \cdot X_2(\theta) + \dot{X}_3(\theta) \cdot X_3(\theta) = 0 \tag{57}$$

holds as required by Eq. (52).

In the quadrupolar case ($n = 1$) we have $P_0 = 1$ and $Q_0 = 0$ so that the Eqs. (54) - (56) are linear. The pure cyclotron motional state and the pure magnetron motional state with $(X_1(0), X_2(0), X_3(0)) = (0, 0, \pm 1)$, respectively, are possible initial states. However, for $n \geq 2$ the equations are nonlinear of degree n because the polynomials P_n and Q_n are homogeneous of degree n. As a consequence the pure magnetron and cyclotron states become stationary states with $(\dot{X}_1, \dot{X}_2, \dot{X}_3) = (0, 0, 0)$ and can not be used as starting states for a conversion process. Thus for conversion by octupolar or higher external rf-fields to work a magnetron initial state can not be pure, but requires a small non-vanishing component of cyclotron motion ($\kappa = R_+(0)/R_-(0) \neq 0$).

5.3 Setup for numerical solution

The linear equations for the quadrupolar case can be solved by standard methods. For the octupolar case an analytic solution in terms of Jacobi elliptic functions has been obtained in [24]. However for $n \geq 3$ the Eqs. (54) - (56) can only be treated numerically due to their high degree of non-linearity. Because the norm of the Bloch vector is conserved, Eq. (52), a polar representation of the equations becomes possible. With the new variables $\vartheta(\theta)$ and $\varphi(\theta)$, defined by

$$X_1(\theta) = \sin\vartheta(\theta) \cdot \cos\varphi(\theta), \tag{58}$$

$$X_1(\theta) = \sin\vartheta(\theta) \cdot \sin\varphi(\theta), \tag{59}$$

$$X_1(\theta) = \cos\vartheta(\theta), \tag{60}$$

the Eqs. (54) - (56) can be replaced for $n \geq 2$ by the equivalent equations

$$\dot{\vartheta}(\theta) = -\sin^{n-1}\vartheta(\theta) \cdot \sin(n\varphi(\theta)), \tag{61}$$

$$\dot{\varphi}(\theta) = -\eta - \cos\vartheta(\theta) \cdot \sin^{n-2}\vartheta(\theta) \cdot \cos(n\varphi(\theta)). \tag{62}$$

Here we have used

$$\dot{X}_1(\theta) = \dot{\vartheta}(\theta)\cos\vartheta(\theta)\cos\varphi(\theta) - \dot{\varphi}\sin\vartheta(\theta)\sin\varphi(\theta), \tag{63}$$

$$\dot{X}_2(\theta) = \dot{\vartheta}(\theta)\cos\vartheta(\theta)\sin\varphi(\theta) + \dot{\varphi}\sin\vartheta(\theta)\cos\varphi(\theta), \tag{64}$$

$$\dot{X}_3(\theta) = -\dot{\vartheta}(\theta)\sin\vartheta(\theta), \tag{65}$$

and the trigonometrical identities

$$\cos(n\varphi) = P_n(\cos\varphi, \sin\varphi), \tag{66}$$

$$\sin(n\varphi) = Q_n(\cos\varphi, \sin\varphi). \tag{67}$$

To evaluate specific solutions of Eqs. (54) - (56) we need the initial values of the solution at $\theta = 0$. For the complex oscillator amplitudes we have from Eq. (18)

$$\alpha_+(0) = |\alpha_+(0)|\, e^{-i\chi_+} = \sqrt{\frac{m\omega_1}{2\hbar}} R_+(0)\, e^{-i\chi_+}, \tag{68}$$

$$\alpha_-(0) = |\alpha_-(0)|\, e^{+i\chi_-} = \sqrt{\frac{m\omega_1}{2\hbar}} R_-(0)\, e^{+i\chi_-}. \tag{69}$$

These relations imply together with Eqs. (112), (113), and (44) for the components of the Bloch vector

$$T_\pm'(0) = e^{\mp(i/n)\chi_{\mathrm{rf}}} T_\pm(0) = \frac{m\omega_1}{2} \cdot R_+(0) R_-(0)\, e^{\pm i\chi/n}, \tag{70}$$

$$T_3'(0) = T_3(0) = \frac{m\omega_1}{2} \cdot \frac{1}{2}\left(R_+^2(0) - R_-^2(0)\right), \tag{71}$$

with

$$\chi = n(\chi_+ + \chi_-) - \chi_{\mathrm{rf}}. \tag{72}$$

The phases χ_+, χ_-, and χ_{rf} always occur in this combination. In order to parametrize the initial values of the normalized Bloch vector we define the ratio of the initial radii

$$\kappa = R_+(0)/R_-(0). \tag{73}$$

We obtain with Eqs. (70) and (71)

$$X_1(0) = \frac{2\kappa}{1+\kappa^2}\cos(\chi/n), \tag{74}$$

$$X_2(0) = \frac{2\kappa}{1+\kappa^2}\sin(\chi/n), \tag{75}$$

$$X_3(0) = \frac{\kappa^2 - 1}{\kappa^2 + 1}. \tag{76}$$

Finally for the polar representation we find from Eqs. (58) - (60)

$$\vartheta(0) = \arccos X_3(0) = \arccos\left(-1 + \frac{2\kappa^2}{1+\kappa^2}\right), \tag{77}$$

$$\varphi(0) = \arctan(X_2(0)/X_1(0)) = \chi/n. \tag{78}$$

Thus for given values of the phase χ and of the ratio κ the initial values for the equations of motion in the polar representation are known. The equations can now be solved numerically for any specified value of the detuning parameter η. The figures of the next section were computed with short programs in Mathematica code.

6 Results on excitation functions and conversion line shapes

6.1 Introductory remarks

In this section we present selected results of our numerical calculations ranging from quadrupolar to 16-polar excitation. We have studied the "excitation functions" $n_+(\theta,\eta,\chi,\kappa)\big|_{\eta=0}$ describing the degree of conversion at the exact resonance frequency ($\eta = 0$) as function of the evolution parameter θ for given fixed values of the phase χ and of the ratio of initial radii $\kappa = R_+(0)/R_-(0)$. Because presently the most experiments can not control the phase $\chi = \chi_{\rm rf} - 2(\chi_+ + \chi_-)$ we have calculated also phase-averaged excitation functions

$$\overline{n}_+(\theta,\kappa) = \frac{1}{2\pi}\int_0^{2\pi} \mathrm{d}\chi \cdot n_+(\theta,\eta,\chi,\kappa)\big|_{\eta=0}\,, \tag{79}$$

assuming a uniform probability distribution for the phase χ.

Of greatest relevance for the experiment are results on theoretically expected "conversion line shapes", describing for a given value of the evolution parameter θ and for given values of χ and κ the dependence of the degree of conversion n_+ on the detuning of the $4n$-polar rf-field. The detuning can be parametrized either by η (see Eq. (53)) or by

$$\Delta = \eta\cdot\theta/(2\pi) = \delta\tau = \frac{1}{n}(\nu_{\rm rf} - n\nu_c)\tau\,, \tag{80}$$

where τ is the duration of the rf-pulse. We have calculated "phase-averaged conversion landscapes", which are for a given fixed value of $\kappa = R_+(0)/R_-(0)$ surfaces $\overline{n}_+(\theta,\eta,\kappa)$ or $\overline{n}_+(\theta,\Delta,\kappa)$ over the 2-dimensional (θ,η)- or (θ,Δ)-planes. At each point of the surface an average over the uncontrolled phase χ has been taken.

Phase-averaged conversion line shapes are obtained as cuts at constant θ through the phase-averaged conversion landscapes. All line shapes are presented as functions of Δ because this parameter has more immediate relevance for the experiment.

All calculations in this paper have used for the ratio of initial radii the value $\kappa = R_+(0)/R_-(0) = 0.03$. This value roughly corresponds to actual experimental conditions as in Ref. [12]. In so far the results presented in this section have only model character. For realistic predictions the ratio κ must be varied also. More generally one could take the average over an assumed distribution of κ-values, but this distribution can vary from one to the other experiment depending on the preparation of the initial state of the ions.

6.2 Quadrupolar excitation ($n = 1$)

For quadrupolar excitation Eqs. (54) - (56) reduce to

$$\begin{pmatrix}\dot X_1(\theta)\\ \dot X_2(\theta)\\ \dot X_3(\theta)\end{pmatrix} = \begin{pmatrix}0 & \eta & 0\\ -\eta & 0 & -1\\ 0 & 1 & 0\end{pmatrix}\begin{pmatrix}X_1(\theta)\\ X_2(\theta)\\ X_3(\theta)\end{pmatrix}\,, \tag{81}$$

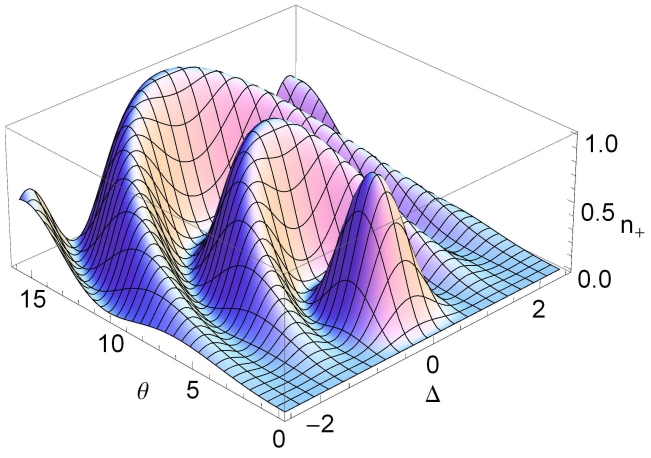

Figure 1: Conversion of the pure magnetron mode into the cyclotron mode by quadrupolar excitation. The plot shows the surface $n_+(\theta,\Delta)$ (Eq. (86)), where $\theta = 2gt$ is the dimensionless evolution parameter and where the dimensionless detuning parameter is $\Delta = (\nu_{\rm rf} - \nu_c)\tau = \eta\theta/(2\pi)$. The conversion maximum $n_+ = 1$ is reached for $\Delta = 0$ and $\theta = \pi, 3\pi, \ldots$.

while the polar representation can not be used due to the singularity in Eq. (62). Eq. (81) is a system of linear differential equations that can be solved by exponentiation. The solution is

$$\begin{pmatrix}X_1(\theta)\\ X_2(\theta)\\ X_3(\theta)\end{pmatrix} = \mathcal{M}'(\theta,\eta)\cdot\begin{pmatrix}X_1(0)\\ X_2(0)\\ X_3(0)\end{pmatrix} \tag{82}$$

with

$$\mathcal{M}'(\theta,\eta) = \sum_{j=0}^{\infty}\frac{\theta^j}{j!}\begin{pmatrix}0 & \eta & 0\\ -\eta & 0 & -1\\ 0 & 1 & 0\end{pmatrix}^j\,. \tag{83}$$

For details of the calculation of the matrix $\mathcal{M}'(\theta,\eta)$ we refer the reader to [25], Eqs. (67) - (70). Here we quote only the result for $\mathcal{M}'_{33}$,

$$\mathcal{M}'_{33}(\theta,\eta) = 1 + \frac{1}{1+\eta^2}\left(\cos\left(\theta\sqrt{1+\eta^2}\right) - 1\right). \tag{84}$$

Mass spectrometric experiments prepare the ions (ideally) in a state of pure magnetron motion. This corresponds to initial values of the normalized Bloch vector $X_1(0) = X_2(0) = 0$, $X_3(0) = -1$. The motional state of the ion is then converted by a pulse of quadrupolar radiation into a state cyclotron and magnetron motion. The experiment measures the degree of conversion $n_+(\theta,\eta) = N_+/N_{\rm tot}$, i.e. the fraction of the total number of motional quanta that are cyclotron quanta, in dependence on θ (pulse duration and amplitude) and η (detuning),

$$\begin{aligned} n_+(\theta,\eta) &= 0.5(1 + X_3(\theta,\eta)) = 0.5(1 + \mathcal{M}'_{33}(\theta,\eta)X_3(0))\\ &= \frac{1}{1+\eta^2}\,\sin^2\left(\frac{\theta}{2}\sqrt{1+\eta^2}\right). \end{aligned} \tag{85}$$

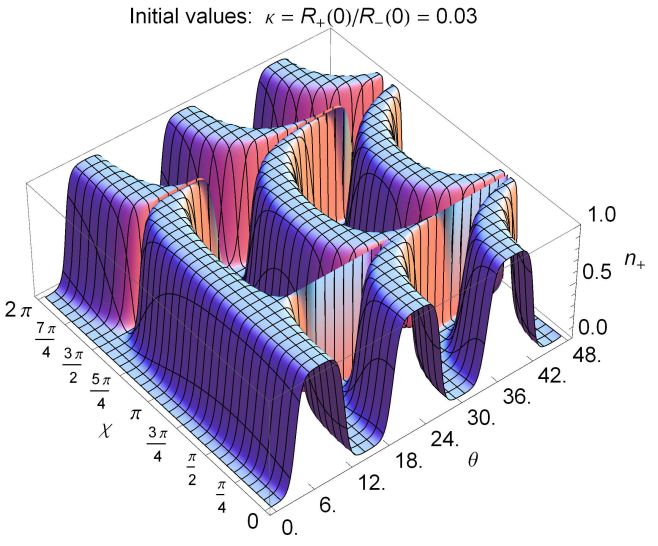

Figure 2: The surface $n_+(\theta,\eta,\chi,\kappa)\big|_{\eta=0,\kappa=0.03}$ is composed of the octupolar excitation functions obtained by varying the phase over the interval $0 \le \chi \le 2\pi$. For given χ and κ excitation functions are periodic functions of the evolution parameter θ. The period varies with χ and becomes infinite for $\chi = \pi/2$ and $\chi = 3\pi/2$. The figure assumes $\kappa = R_+(0)/R_-(0) = 0.03$.

In terms of the detuning parameter Δ we have

$$n_+(\theta,\Delta) = \frac{\theta^2 \sin^2(\sqrt{\theta^2+4\pi^2\Delta^2}/2)}{\theta^2+4\pi^2\Delta^2}. \qquad (86)$$

This function has been plotted in Fig. 1 as a surface over the $\theta\Delta$-plane. It represents the conversion landscape for quadrupolar excitation with a pure magnetron motional state as initial state for the ions. The first conversion peak occurs at at $(\theta,\Delta) = (\pi,0)$. A cut through the surface along the line $\theta = \pi$ results in the familiar conversion line shape for quadrupolar excitation

Note that there is no dependence on the phase χ. This is a special property of the pure magnetron initial state. When we admit a cyclotron component in the initial state, i.e. a non-vanishing value of $\kappa = R_+(0)/R_-(0)$, then the degree of conversion $n_+(\theta,\Delta,\chi,\kappa)$ is phase-dependent and averaging over the phase becomes necessary. A more detailed discussion is found in [23].

6.3 Octupolar excitation ($n = 2$)

For octupolar excitation Eqs. (54) - (56) reduce to

$$\dot{X}_1(\theta) = \eta X_2(\theta) - X_2(\theta)\cdot X_3(\theta), \qquad (87)$$
$$\dot{X}_2(\theta) = -\eta X_1(\theta) - X_1(\theta)\cdot X_3(\theta), \qquad (88)$$
$$\dot{X}_3(\theta) = 2X_1(\theta)\cdot X_2(\theta). \qquad (89)$$

As explained above for non-stationary solutions to these equations the initial predominantly magnetron motional state must contain a small non-vanishing cyclotron component. We have chosen for all our numerical calculations

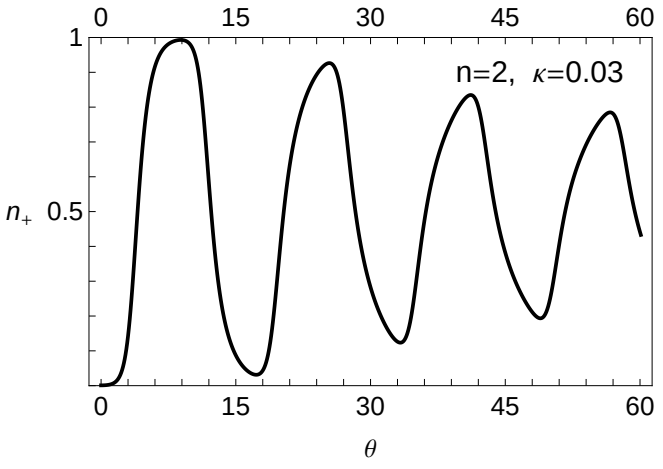

Figure 3: Octupolar excitation functions averaged over the phase χ. The figure assumes a uniform weight distribution over the interval $0 \le \chi \le 2\pi$ and is calculated for $\kappa = R_+(0)/R_-(0) = 0.03$.

the ratio of initial radii to be $\kappa = R_+(0)/R_-(0) = 0.03$. In the polar representation the equations (87) - (89) are equivalent to

$$\dot{\vartheta}(\theta) = -\sin\vartheta(\theta)\,\sin 2\varphi(\theta)\,, \qquad (90)$$
$$\dot{\varphi}(\theta) = -\eta - \cos\vartheta(\theta)\,\cos 2\varphi(\theta)\,. \qquad (91)$$

We have investigated first the phase-dependence of the excitation function $n_+(\theta,\Delta,\chi,\kappa)\big|_{\eta=0,\,\kappa=0.03}$. Contrary to quadrupolar excitation we find for octupolar excitation an intricate dependence on the phase, which is displayed in Fig. 2 by plotting the surface n_+ over the $(\theta\Delta)$-plane. For constant phase χ excitation functions are seen to be periodic, but the period itself depends on χ. For the two values $\chi = \pi/2$ and $\chi = 3\pi/2$ the period of the excitation function becomes infinite. As a function of θ the excitation function for $\chi = \pi/2$ approaches the maximum value 1 and remains there, while for $\chi = 3\pi/2$ it vanishes asymptotically. The analytical solution for the octupolar excitation functions [24] in terms of Jacobi elliptical functions gives insight into this behaviour: For the exceptional values of the phase the 'modulus' k of the elliptic function equals one and the function degenerates to a hyperbolic tangent function.

Unfortunately the phase χ is difficult to control in experiments. Therefore it makes sense to average the excitation function over all possible values of the phase, assuming a uniform distribution over the interval $0 \le \chi \le 2\pi$. The result of this calculation is shown in Fig. 3. We note that the first conversion maximum is reached when the value of the evolution parameter is $\theta \approx 9.5$ to 10. We also note that the phase-averaged excitation function is not strictly periodic, but exhibits some damping. This is explained by the fact that the excitation functions for different χ, although they start out at $\theta = 0$ from the same initial value, get increasingly out of step due to their differences in the period.

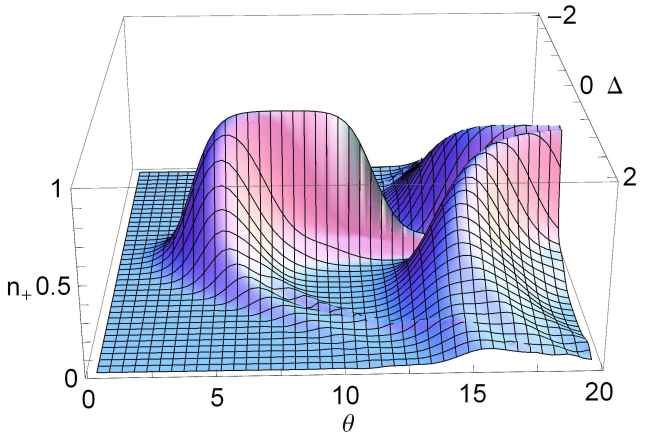

Figure 4: Landscape for the conversion of magnetron into cyclotron motion by octupolar excitation. The figure displays the phase-averaged 'degree of conversion' $\overline{n}_+(\theta, \Delta, \kappa)$ as a function of the evolution parameter θ and the detuning parameter Δ. The ratio of the initial radii is $\kappa = R_+(0)/R_-(0) = 0.03$.

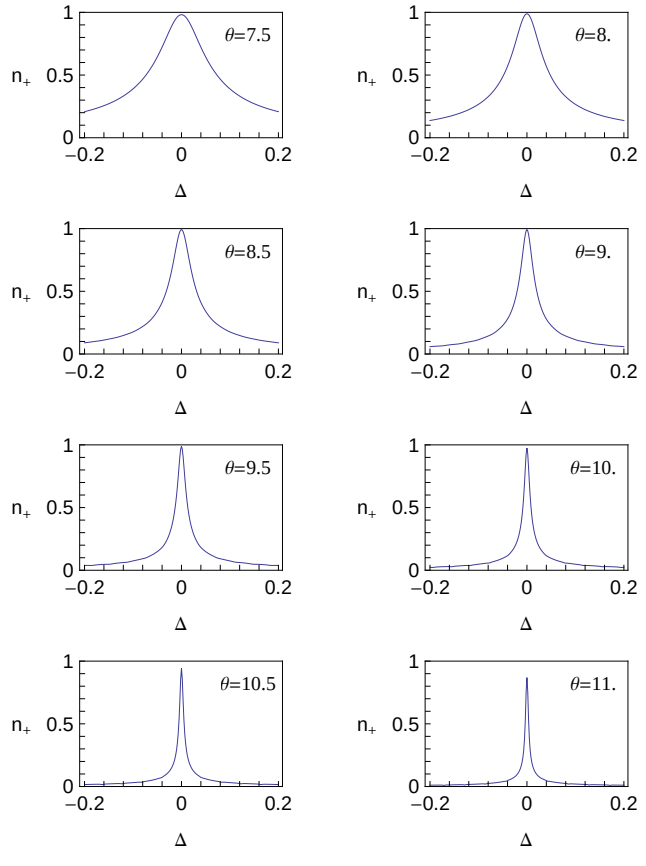

Figure 5: Phase-averaged line shapes for the conversion of magnetron into cyclotron motion by octupolar excitation for various values of the evolution parameter, $8.5 \leq \theta \leq 11$. The detuning parameter is $\Delta = \eta \cdot \theta/(2\pi) = \frac{1}{2}(\nu_{\rm rf} - 2\nu_c)\tau$, where τ is the duration of the rf-pulse. The assumes $\kappa = R_+(0)/R_-(0) = 0.03$.

The most interesting aspect for mass spectrometry is, of course, the dependence of the conversion results on the detuning of the octupolar rf-field, described in terms of one of the dimensionless detuning parameters η or $\Delta = \eta \cdot \theta/(2\pi) = \frac{1}{2}(\nu_{\rm rf} - 2\nu_c)\tau$, where τ is the duration of the rf-pulse. In order to get an overview of the situation we have plotted in Fig. 4 the phase-averaged 'degree of conversion' $\overline{n}_+(\theta, \Delta, \kappa)$ as a surface over the $(\theta\Delta)$-plane, assuming $\kappa = 0.03$. This surface will be called the octupolar conversion landscape. For each point of the surface n_+ has been averaged over the interval $0 \leq \chi \leq 2\pi$. Conversion line shapes are cuts through this surface along lines of constant θ.

The surface is completely different from the conversion landscape for quadrupolar excitation in Fig. 1. Let us now consider the evolution of the conversion line shapes as the dimensionless parameter θ increases from zero to 20. The rise of the conversion signal n_+ follows the curve shown in Fig. 3, at $\theta = 3$ it is still small, but distinctly different from zero, it reaches its full height for $\theta \approx 9.5$. The conversion lines start out for smaller θ as broad signals with a width of approximately 2, but beyond $\theta = 5$ they begin to shrink, with the appearance of a very narrow, needle-like structure on top of a broad pedestal. As we come to the range $\theta = 7$ to 10 the pedestal disappears and only an extremely narrow signal is left over. This signal dies out very fast beyond $\theta = 11$.

This evolution of the conversion signal is illustrated in more detail in Fig. 5, showing the evolution of the conversion signal between $\theta = 7.5$ and $\theta = 11$. While we have complete conversion of the initial almost ($\kappa = 0.03$) pure magnetron motion for most of this range of θ the width of the conversion signal shrinks considerably. Just before the decrease of the signal sets in, at $\theta = 10$ we observe a width (FWHM) of approximately 0.02, i.e. a signal more narrow by a factor of 40 than the corresponding signal for quadrupolar excitation (FWHM = 0.8).

In closing this discussion we remind the reader that all specific numbers depend on the assumed ratio of initial radii $\kappa = R_+(0)/R_-(0) = 0.03$. For a different value, say $\kappa = 0.01$, the picture would be qualitatively the same, but with slightly different numerical results. Ideally one ought to know a probability distribution for κ and calculate the average over this distribution.

6.4 12-polar excitation ($n = 3$)

For 12-polar excitation Eqs. (54) - (56) reduce to

$$\dot{X}_1(\theta) = \eta X_2(\theta) - 2X_1(\theta) \cdot X_2(\theta) \cdot X_3(\theta), \quad (92)$$

$$\dot{X}_2(\theta) = -\eta X_1(\theta) - \Big(X_1^2(\theta) - X_2^2(\theta)\Big) \cdot X_3(\theta), \quad (93)$$

$$\dot{X}_3(\theta) = 3X_1^2(\theta) \cdot X_2(\theta) - X_2^3(\theta). \quad (94)$$

In the polar representation these equations are equivalent to

$$\dot{\vartheta}(\theta) = -\sin^2\vartheta(\theta)\,\sin 3\varphi(\theta)\,, \quad (95)$$

$$\dot{\varphi}(\theta) = -\eta - \cos\vartheta(\theta)\,\sin\vartheta(\theta)\,\cos 3\varphi(\theta)\,. \quad (96)$$

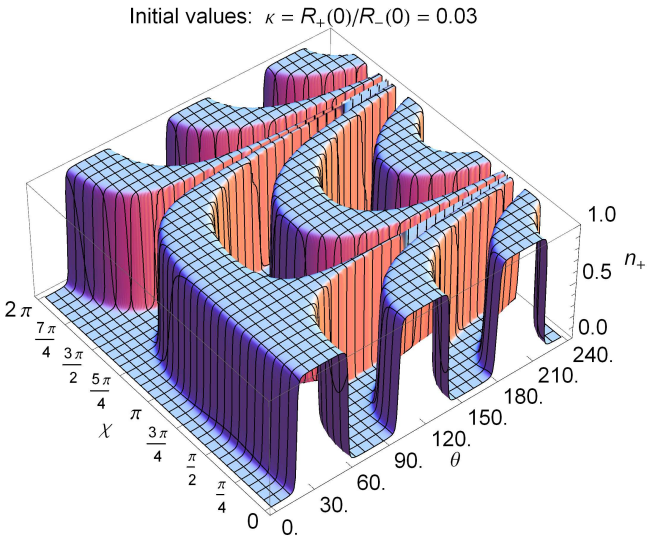

Figure 6: The surface $n_+(\theta,\eta,\chi,\kappa)\big|_{\eta=0,\kappa=0.03}$ is composed of the 12-polar excitation functions obtained by varying the phase over the interval $0 \le \chi \le 2\pi$. For given χ and κ excitation functions are periodic functions of the evolution parameter θ. The period varies with χ and becomes infinite for $\chi = \pi/2$ and $\chi = 3\pi/2$. The figure assumes $\kappa = R_+(0)/R_-(0) = 0.03$.

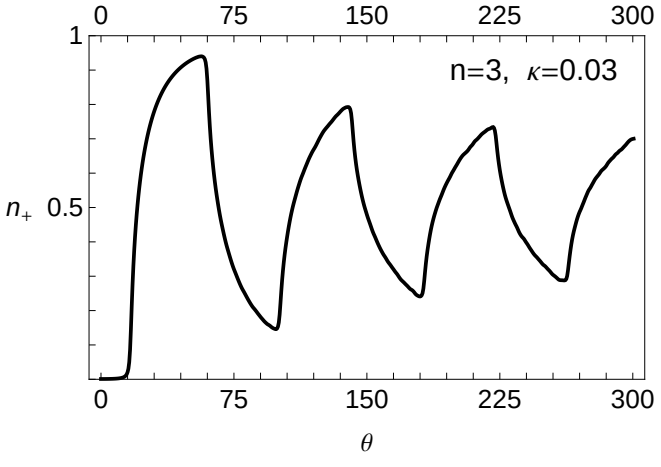

Figure 7: 12-polar excitation functions averaged over the phase χ. The figure assumes a uniform weight distribution over the interval $0 \le \chi \le 2\pi$ and is calculated for $\kappa = R_+(0)/R_-(0) = 0.03$.

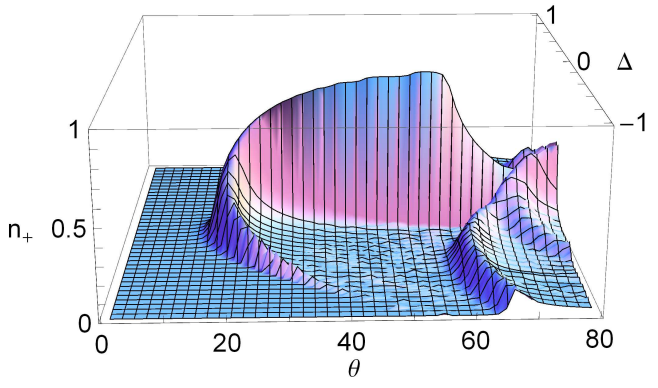

Figure 8: Landscape for the conversion of magnetron into cyclotron motion by 12-polar excitation. The figure displays the phase-averaged 'degree of conversion' $\overline{n}_+(\theta,\Delta,\kappa)$ as a function of the evolution parameter θ and the detuning parameter Δ. The ratio of the initial radii was chosen as $\kappa = R_+(0)/R_-(0) = 0.03$.

No analytical solutions for these equations are known. The numerical solution of the Eqs. (95) and (96) with given initial values proceeds as in the octupolar case using a Mathematica code. Again the first objective is to calculate the excitation functions and to study their dependence on the phase χ. The results are plotted in Fig. 6 as a surface $n_+(\theta,\eta,\chi,\kappa)\big|_{\eta=0,\kappa=0.03}$ over the $(\theta\chi)$-plane. Comparing the figure with the corresponding one for the octupolar case we notice strong similarities. For a given value of χ the excitation function is periodic, but the wave form has changed from sinus-like to a more rectangular shape. Again the values $\chi = \pi/2$ and $\chi = 3\pi/2$ are singular in the sense that the period of the excitation function becomes infinite, the degree of conversion n_+ is approaching asymptotically the values one and zero, respectively. The figure is stretched over a much larger range of θ.

As in the octupolar case we have calculated a phase-averaged excitation function $\overline{n}_+(\theta,\Delta,\kappa)\big|_{\Delta=0}$. The first conversion maximum occurs at $\theta \approx 58$. We see again the damping of the oscillations due to the phase-dependence of the period of the excitation function.

The conversion landscape for 12-polar excitation has been plotted in Fig. 8 for the range $0 \le \theta \le 80$ of the evolution parameter as a surface $\overline{n}_+(\theta,\Delta,\kappa)$ over the $(\theta\Delta)$-plane. At each point of the surface the degree of conversion has been averaged over all phases $0 \le \chi \le 2\pi$. We vary θ from 0 to 80 to study the evolution of the conversion process. As seen in Fig. 7 conversion sets in at $\theta \approx 12$ with a rather broad conversion line. It follows a fast increase of the degree of conversion. Beyond $\theta = 18$ the conversion lines begin to change their shape from a broad structure into a narrow needle-like peak sitting atop of a broad pedestal. The degree of conversion reaches values up 0.9, but not the maximum value 1.0 corresponding to pure cyclotron motion. As in the octupolar case we observe a shrinking of the

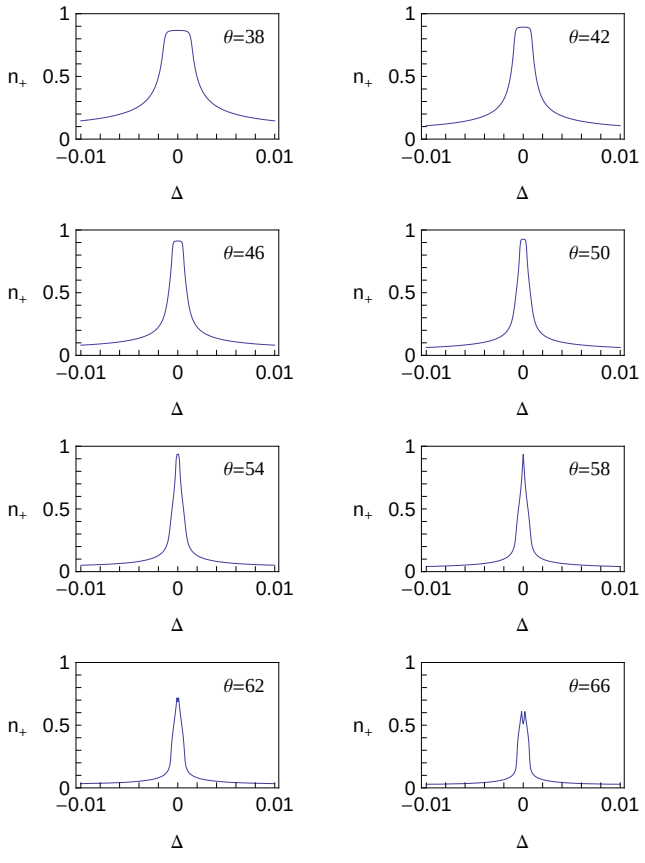

Figure 9: Phase-averaged line shapes for the conversion of magnetron into cyclotron motion by 12-polar excitation for various values of the evolution parameter, $42 \leq \theta \leq 62$. The detuning parameter is $\Delta = \eta \cdot \theta/(2\pi) = \frac{1}{3}(\nu_{\rm rf} - 3\nu_c)\tau$, where τ is the duration of the rf-pulse. The figure is calculated with $\kappa = R_+(0)/R_-(0) = 0.03$.

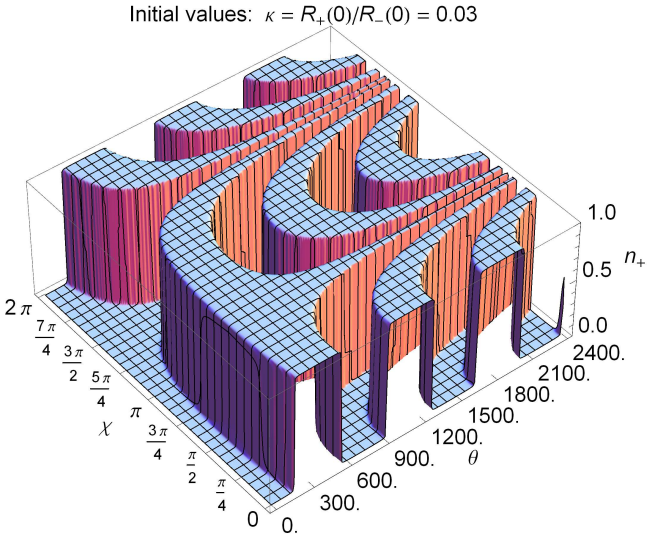

Figure 10: The surface $n_+(\theta, \Delta, \chi, \kappa)\big|_{\Delta=0,\kappa=0.03}$ is composed of the 16-polar excitation functions obtained by varying the phase over the interval $0 \leq \chi \leq 2\pi$. For given χ and κ excitation functions are periodic functions of the evolution parameter θ. The period varies with χ and becomes infinite for $\chi = \pi/2$ and $\chi = 3\pi/2$. The figure assumes $\kappa = R_+(0)/R_-(0) = 0.03$.

width of the needle-like peak at the resonance frequency as we move along the sharp ridge toward the point of maximum conversion (approximately at $\theta = 58$) and from there toward the steep decrease beyond $\theta = 60$.

We have studied the shrinking width of the conversion signal in greater detail in Fig. 9. There we show the evolution of the conversion line width over the range $38 \leq \theta \leq 66$. Note that the scale of the dimensionless detuning parameter Δ runs from -0.01 to +0.01 as compared to Fig. 5 for the octupolar case, where the scale of Δ ran from -0.2 to +0.2. At the point of maximum conversion, $\theta \approx 58$, we estimate the width (FWHM) of the conversion line to be 0.001, which is, compared to the line width obtained in the octupolar case, smaller by a factor of 20, compared to the quadrupolar case smaller by a factor of 800.

6.5 16-polar excitation ($n = 4$)

In view of the results obtained in the two preceding subsections it is tempting to go one step further and take a closer look at the conversion of the radial modes by interaction

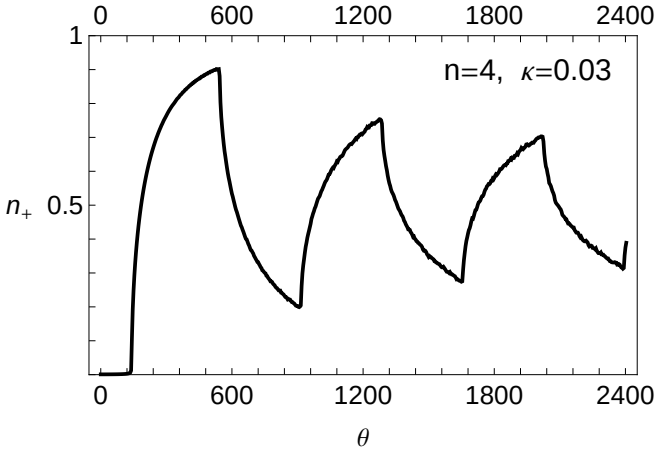

Figure 11: 16-polar excitation functions averaged over the phase χ. The figure assumes a uniform weight distribution over the interval $0 \leq \chi \leq 2\pi$ and is calculated for $\kappa = R_+(0)/R_-(0) = 0.03$.

with 16-polar rf-fields. In this case Eqs. (54) - (56) reduce to

$$\dot{X}_1(\theta) = \eta X_2(\theta) - \Big(3X_1^2(\theta)X_2(\theta) - X_2^3(\theta)\Big) \cdot X_3(\theta), \quad (97)$$

$$\dot{X}_2(\theta) = -\eta X_1(\theta) - \Big(X_1^3(\theta) - 3X_1(\theta)X_2^2(\theta)\Big) \cdot X_3(\theta), \quad (98)$$

$$\dot{X}_3(\theta) = 4X_1(\theta) \cdot X_2(\theta) \cdot \Big(X_1^2(\theta) - X_2^2(\theta)\Big). \quad (99)$$

In the polar representation these equations are equivalent to

$$\dot{\vartheta}(\theta) = -\sin^3\vartheta(\theta)\,\sin 4\varphi(\theta)\,, \quad (100)$$

$$\dot{\varphi}(\theta) = -\eta - \cos\vartheta(\theta)\,\sin^2\vartheta(\theta)\,\cos 4\varphi(\theta)\,. \quad (101)$$

No analytical solutions are known for either set of differential equations. We shall evaluate Eqs. (100) and (101) numerically using a Mathematica code.

As in the previous sections we begin by studying the surface $n_+(\theta,\Delta,\chi,\kappa)\big|_{\Delta=0,\kappa=0.03}$ which combines the excitation functions for all values of the phase in the interval $0 \le \chi \le 2\pi$. The surface is displayed in Fig. 10. The structure of the surface is similar to what we found in the octupolar and 12-polar cases: The period of the excitation functions becomes infinite for $\chi = \pi/2$ and $\chi = 3\pi/2$ and is quite long in the vicinity of the singular phase values. The shape of the excitation functions has become even more rectangular than in the 12-polar case. The figure is stretched over a much larger range of values of the evolution parameter, $0 \le \theta \le 2400$. Assuming a uniform distribution of phase values we have calculated the phase-averaged excitation function $\overline{n}_+(\theta,\Delta,\kappa)\big|_{\kappa=0.03}$ and and have plotted it in Fig. 11. The first conversion maximum occurs at $\theta \approx 540$. The degree of conversion at the maximum is only $n_+ = 0.9$, we have not reached full conversion into a pure cyclotron state ($n_+ = 1$).

The conversion landscape is shown in Fig. 12 as a surface $\overline{n}_+(\theta,\Delta,\kappa)\big|_{\kappa=0.03}$. Comparing it with the corresponding graphs for octupolar and 12-polar excitation we notice that the off-resonance features, which were quite prominent in the octupolar case, have almost died out, so that only a very prominent and very thin wall exactly at the resonance frequency is left over.

Some conversion line shapes as cuts through the conversion landscape along lines of constant θ are displayed in Fig. 13. Note the scale of the detuning parameter Δ which runs from -0.005 to +0.005. At the conversion maximum ($\theta = 540$) we have a width (FWHM) of the conversion line of only 4×10^{-4}, so that compared to the quadrupolar case the width of the conversion line is reduced by a factor 2×10^3.

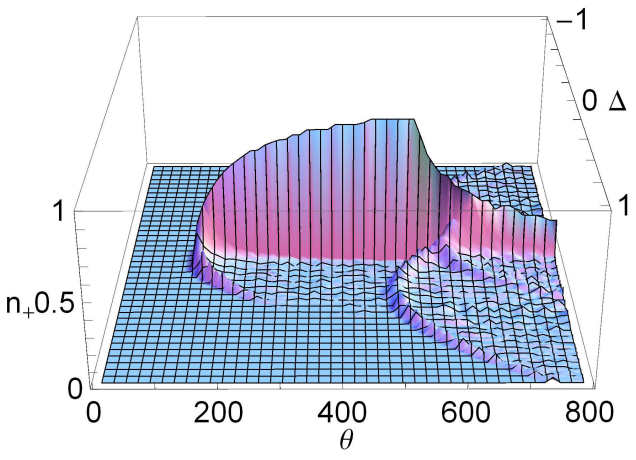

Figure 12: Landscape for the conversion of magnetron into cyclotron motion by 16-polar excitation. The figure displays the phase-averaged 'degree of conversion' $\overline{n}_+(\theta,\Delta,\kappa)$ as a function of the evolution parameter θ and the detuning parameter Δ. For the ratio of the initial radii we assumed $\kappa = R_+(0)/R_-(0) = 0.03$.

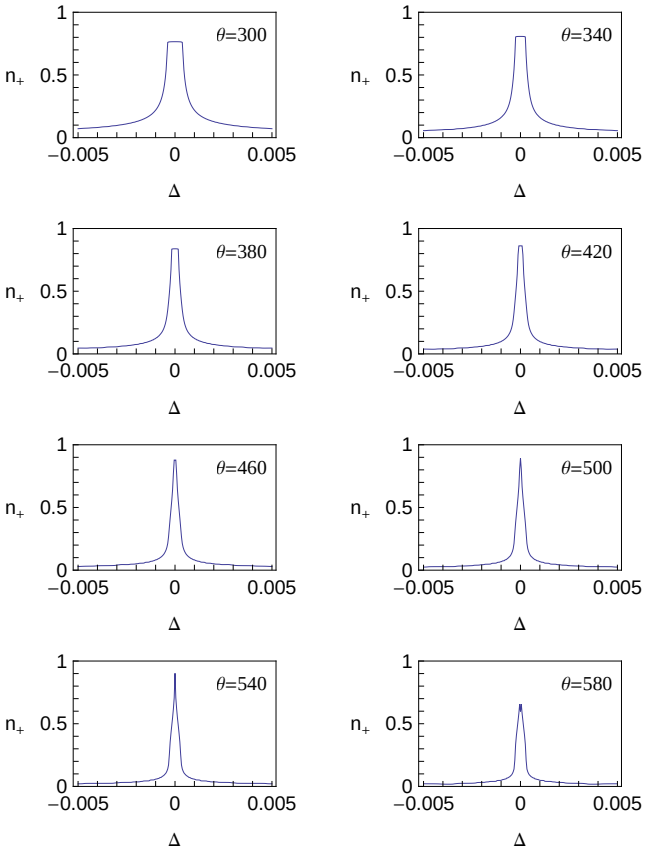

Figure 13: Phase-averaged line shapes for the conversion of magnetron into cyclotron motion by 16-polar excitation for various values of the evolution parameter, $300 \le \theta \le 580$. The detuning parameter is $\Delta = \eta \cdot \theta/(2\pi) = \frac{1}{4}(\nu_{\rm rf} - 4\nu_c)\tau$, where τ is the duration of the rf-pulse. The ratio of the initial radii is assumed to be $\kappa = R_+(0)/R_-(0) = 0.03$.

7 Summary and conclusions

In this paper we have generalized the model for the interconversion of the radial motional modes of a trapped ion by interaction with external quadrupolar or octupolar rf-fields to interconversion by general $4n$-polar rf-fields ($n \ge 3$). The complex amplitudes of the cyclotron and magnetron

oscillators were used as dynamical variables and the Hamiltonian equations of motion were reformulated in terms of Bloch vector components. A set of non-linear differential equations for the "degree of conversion" $n_+(\theta, \eta, \chi, \kappa)$ was obtained and studied numerically as function of the dimensionless "evolution parameter θ" of the dimensionless "detuning parameters" η or $\Delta = \frac{1}{n}(\nu_{\rm rf} - n\nu_c)\tau$, the phase χ, and the ratio of the initial radii $\kappa = R_+(0)/R_-(0)$.

We have obtained results on excitation functions (for conversion at the exact resonance frequency) and their dependence on θ and the phase χ, on phase-averaged excitation functions, "phase-averaged conversion landscapes", i.e. surfaces showing, after averaging over the phase χ, the degree of conversion in dependence on the evolution parameter θ and on the detuning of the rf-field, described by η or Δ, as well as detailed results on the phase-averaged conversion line shapes and their FWHM resonance widths. The non-linear resonances seen for octupolar, 12-polar, and 16-polar excitation show remarkable similarities and are quite distinct from the (linear) quadrupolar case. While for quadrupolar excitation some conversion occurs off resonance, this occurs much less for octupolar excitation, we have much narrower line widths. For 12-polar and 16-polar excitation conversion is almost exclusively restricted to the exact resonance frequency. The conversion landscapes are essentially flat with the exception of a thin vertical wall rising vertically at the exact resonance frequency.

The most important observation is the decrease of the widths of the conversion resonance measured at the point of maximum conversion. Using the dimensionless detuning parameter $\Delta = \frac{1}{n}(\nu_{\rm rf} - n\nu_c)\tau$, where τ is the duration of the rf-pulse for the conversion, we estimate a decrease of the conversion resonance width by a factor of 2×10^3 as we pass from the quadrupolar ($n = 1$) to the 16-polar ($n = 4$) case. A decrease of the resonance width by more than one order of magnitude has already been experimentally observed when we compare excitation by quadrupolar and by octupolar excitation with the same pulse duration [14]. The results obtained in this paper let us expect further substantial gains in mass resolution for future experiments using 12-polar or 16-polar rf-fields to excite the conversion resonance.

Whether or not the theoretically possible gain in mass resolution can be implemented remains to be seen. Fluctuations of the magnetic field, the temperature, and other parameters of the experimental environment as well as an insufficient control of all initial parameters of the ion will probably be serious obstacles for the full realization of the hopes raised by our theoretical model calculation.

A Appendix

A.1 Poisson brackets

Consider a physical system described by a Hamiltonian $H(q, p, t)$, where $q = (q_1, \ldots, q_s)$ and $p = (p_1, \ldots, p_s)$ are the canonical coordinates and momenta, respectively. The Poisson bracket of two physical quantities $A(q, p)$, $B(q, p)$ is defined as [27]

$$\{A(q,p), B(q,p)\} = \sum_j \left(\frac{\partial A}{\partial q_j} \cdot \frac{\partial B}{\partial p_j} - \frac{\partial B}{\partial q_j} \cdot \frac{\partial A}{\partial p_j} \right). \quad (102)$$

A close relation between the classical Poisson bracket $\{A, B\}$ and the commutator of the corresponding quantum mechanical operators $\hat{A}$, $\hat{B}$ is expressed by Dirac's quantization principle [28]

$$\hat{A}\hat{B} - \hat{B}\hat{A} = [\hat{A}, \hat{B}] = i\hbar\{A, B\}. \quad (103)$$

The canonical coordinates and momenta satisfy the fundamental bracket relations

$$\{q_j, p_{j'}\} = \delta_{jj'}, \quad \{q_j, q_{j'}\} = \{p_j, p_{j'}\} = 0, \quad (104)$$

where $\delta_{jj'}$ is the Kronecker symbol.

In this paper we use "complex oscillator amplitudes" $\alpha_+(t)$ and $\alpha_-(t)$ as our dynamical variables. These are non-canonical variables in the sense that they are complex functions and that no canonically conjugate momenta are defined. Nevertheless these variables can be incorporated into the canonical formalism through their relation to standard canonical coordinates and momenta $q_\pm$, $p_\pm$,

$$\alpha_\pm = \frac{1}{\sqrt{2\hbar}}(q_\pm + ip_\pm), \;\; \alpha_\pm^* = \frac{1}{\sqrt{2\hbar}}(q_\pm - ip_\pm), \quad (105)$$

The canonical coordinates and momenta $q_\pm$, $p_\pm$ are obtained from the Cartesian coordinates x, y and their conjugate canonical momenta p_x, p_y (see Eqs. (10) and (11)) by a canonical transformation, the details of which are found in [19], Eq. (6.1).

Eq. (105) relates Poisson brackets of the complex oscillator amplitudes α_j to the canonical formalism, one obtains

$$\{\alpha_j, \alpha_{j'}^*\} \;=\; (i\hbar)^{-1}\delta_{jj'} \quad (j, j' = +, -). \quad (106)$$

The equation of motion of some physical quantity $A(q, p, t)$ is obtained in terms of Poisson brackets as [27]

$$\frac{\mathrm{d}}{\mathrm{d}t}A(q,p,t) \;=\; \frac{\partial}{\partial t}A(q,p,t) + \{A(q,p,t), H(q,p,t)\}. \quad (107)$$

The partial derivative $\partial A/\partial t$ refers to explicit time dependence of A, if applicable. In particular for complex oscillator amplitudes we can write the equation of motion as

$$\frac{\mathrm{d}}{\mathrm{d}t}\alpha_j(t) \;=\; \frac{\partial}{\partial t}\alpha_j(t) + \{\alpha_j(t), H(\alpha, \alpha^*, t)\}. \quad (108)$$

A.2 The Bloch vector

The 3-component Bloch vector can be defined in terms of its Cartesian components (T_1, T_2, T_3),

$$T_1 \;=\; \tfrac{\hbar}{2}\left(\alpha_+^*\alpha_- + \alpha_-^*\alpha_+\right), \quad (109)$$

$$T_2 \;=\; \tfrac{\hbar}{2i}\left(\alpha_+^*\alpha_- - \alpha_-^*\alpha_+\right), \quad (110)$$

$$T_3 \;=\; \tfrac{\hbar}{2}\left(\alpha_+^*\alpha_+ - \alpha_-^*\alpha_-\right), \quad (111)$$

or in terms of its spherical components (T_+, T_-, T_3), where

$$T_+ = \hbar\alpha_+^*\alpha_- = T_1 + iT_2, \quad (112)$$
$$T_- = \hbar\alpha_-^*\alpha_+ = T_1 - iT_2. \quad (113)$$

In addition we define a 'scalar' quantity

$$T_0 = \frac{\hbar}{2}\left(\alpha_+^*\alpha_+ + \alpha_-^*\alpha_-\right). \quad (114)$$

We have the relation

$$T_0^2 = T_1^2 + T_2^2 + T_3^2 = T_+T_- + T_3^2. \quad (115)$$

The components of the Bloch vector satisfy the following Poisson bracket relations:

$$\{T_1, T_2\} = T_3, \quad \{T_2, T_3\} = T_1, \quad \{T_3, T_1\} = T_2, \quad (116)$$
$$\{T_+, T_-\} = -i \cdot 2T_3, \quad \{T_3, T_\pm\} = \mp iT_\pm. \quad (117)$$

The scalar T_0 commutes with all components T_j $(j = 1, 2, 3, +, -)$ of the Bloch vector.

Powers of $T_\pm$ can be expressed by polynomials in T_1, T_2 as follows:

$$T_\pm^n = (T_1 \pm iT_2)^n = \sum_{j=1}^{n} (\pm i)^{n-j} \binom{n}{j} T_1^j T_2^{n-j} \quad (118)$$
$$= P_n(T_1, T_2) \pm iQ_n(T_1, T_2) \quad (119)$$

where $P_0 = 1$, $Q_0 = 0$, and for $n \geq 1$

$$P_n(T_1, T_2) = \sum_{j=0}^{[n/2]} (-1)^j \binom{n}{2j} T_1^{n-2j} T_2^{2j}, \quad (120)$$

$$Q_n(T_1, T_2) = \sum_{j=0}^{[(n-1)/2]} (-1)^j \binom{n}{2j+1} T_1^{n-2j-1} T_2^{2j+1} \quad (121)$$

Here the symbol $[a]$ denotes the integer part of a. We also have the recursion formulas

$$P_n(T_1, T_2) = T_1 P_{n-1}(T_1, T_2) - T_2 Q_{n-1}(T_1, T_2), \quad (122)$$
$$Q_n(T_1, T_2) = T_1 Q_{n-1}(T_1, T_2) + T_2 P_{n-1}(T_1, T_2). \quad (123)$$

Examples are

$$P_1 = T_1, \qquad Q_1 = T_2, \quad (124)$$
$$P_2 = T_1^2 - T_2^2, \qquad Q_2 = 2T_1T_2, \quad (125)$$
$$P_3 = T_1^3 - 3T_1T_2^2, \qquad Q_3 = 3T_1^2T_2 - T_2^3, \quad (126)$$
$$P_4 = T_1^4 - 6T_1^2T_2^2 + T_2^4, \qquad Q_4 = 4T_1^3T_2 - 4T_1T_2^3. \quad (127)$$

References

[1] H.-J. Kluge: *High-accuracy mass spectrometry for fundamental studies* European Journal of Mass Spectrometry **16** (2010), 269 - 282.

[2] K. Blaum, Yu. N. Novikov, and G. Werth: *Penning traps as a versatile tool for precise experiments in fundamental physics*, Contemporary Physics **51** (2010), 149 - 175.

[3] R. G. E. Timmermans, *Low energy precision tests of electroweak theory*, p. 1 - 30 in Lecture Notes in Physics, Vol. 749 (Editors K.Blaum and F.Herfurth), Springer-Verlag, 2008.

[4] K. Blaum, J. Dilling, and W. Nörtershäuser: *Precision atomic physics techniques for nuclear physics with radioactive beams*, Physica Scripta **T 152** (2013), 014017 (32pp).

[5] G. Gräff, H. Kalinowsky, J. Traut, *A direct determination of the proton electron mass ratio*, Zeitschrift für Physik **A 297** (1980), 35 - 39.

[6] G. Bollen, R. B. Moore, G. Savard, and H. Stolzenberg: *The accuracy of heavy-ion mass measurements using time of flight - ion cyclotron resonance in a Penning trap*, J. Appl. Phys. **68** (1990), 4355 - 4374.

[7] M. Koenig, G. Bollen, H.-J. Kluge, T. Otto, J. Szerypo: *Quadrupole excitation of stored ion motion at the true cyclotron frequency*, Int. J. Mass Spectrom. Ion Process **142** (1995), 95 - 116.

[8] K. Blaum: *High-accuracy mass spectrometry with stored ions*, Physics Reports **425** (2006), 1 - 78.

[9] G.Bollen: *Mass measurements of short-lived nuclides with ion traps*, Nuclear Physics **A 693** (2001), 3 - 18.

[10] A.T.Gallant, M.Brodeur, T.Brunner, U.Chowdhury, S.Ettenauer, V.V.Simon, E.Mané, M.C.Simon, C.Andreoiu, P.Delheij, G.Gwinner, M.R.Pearson, R.Ringle, and J.Dilling: *Highly charged ions in Penning traps: A new tool for resolving low-lying isomeric states*, Physical Review **C 85** (2012), 044311(7p).

[11] R. Ringle, G. Bollen, P. Schury, S. Schwarz, and T. Sun: *Octupolar excitation of ion motion in a Penning trap - A study performed at LEBIT*, Int. J. Mass Spectrom. **262** (2006), 33 - 44.

[12] S. Eliseev, M. Block, A. Chaudhuri, F. Herfurth, H.-J. Kluge, A. Martin, C. Rauth, and G. Vorobjev: *Octupolar excitation of ions stored in a Penning trap mass spectrometer - A study performed at SHIPTRAP*, Int. J. Mass Spectrom. **262** (2006), 45 - 50.

[13] M. Breitenfeld, F. Ziegler, A. Herlert, G. Marx, and L. Schweikhard: *Simultaneous monitoring of the radial modes of the ion motion and their manipulation in Penning traps by FT-ICR mass spectrometry*, Int. J. Mass Spectrom. **263** (2007), 94 - 100.

[14] S. Eliseev, C. Roux, K. Blaum, M. Block, C. Droese, F. Herfurth, M. Kretzschmar, M. I. Krivoruchenko, E. Minaya Ramirez, Yu. N. Novikov, L. Schweikhard, V. M. Shabaev, F. Šimkovic, I. I. Tupitsyn, K. Zuber, and N. A. Zubova: *Octupolar-excitation Penning-trap mass spectrometry for Q-value measurement of double-electron capture in ^{164}Er*, Phys. Rev. Lett. **107** (2011), 152501(5).

[15] M. Kretzschmar: *Octupolar excitation of ion motion in a Penning trap: A theoretical study*, submitted to Int. J. Mass Spectrom.

[16] M. O. Scully and M. S. Zubairy:,*Quantum Optics*, Cambridge University Press, Cambridge UK, 1997.

[17] M. Kretzschmar: *Theoretical investigations of different excitation modes for Penning trap mass spectrometry*, submitted to Int. J. Mass Spectrom.

[18] L. S. Brown and G. Gabrielse: *Geonium theory: Physics of a single electron or ion in a Penning trap*, Rev. Mod. Phys. **58** (1986), 233 - 311.

[19] M. Kretzschmar: *Particle motion in a Penning trap*, Eur. J. Phys. **12** (1991), 240 - 248.

[20] S. Haroche and J.-M. Raimond: *Exploring the Quantum: Atoms, Cavities, and Photons*, Oxford University Press, 2006.

[21] J. C. Garrison and R. Y. Chiao: *Quantum Optics*, Oxford University Press, 2008.

[22] M. Kretzschmar: *A quantum mechanical model of Rabi oscillations between two interacting harmonic oscillator modes and the interconversion of modes in a Penning trap*, in *Trapped Charged Particles and Fundamental Physics*, AIP Conf. Proc. Vol. 457, ed. by Daniel H. E. Dubin and Dieter Schneider, The American Institute of Physics (1999), p. 242 - 251.

[23] M. Kretzschmar: *On the phase dependence of the interconversion of the motional modes in a Penning trap by quadrupolar excitation*, Int. J. Mass Spectrom. **309** (2012), 30 - 38.

[24] M. Kretzschmar: *Octupolar Excitation of ion motion in a Penning trap: The analytical solution*, to be submitted to Int. J. Mass Spectrom.

[25] M. Kretzschmar: *The Ramsey method in high-precision mass spectrometry with Penning traps: Theoretical foundations*, Int. J. Mass Spektrom. **264** (2007), 122 - 145.

[26] S. George, S. Baruah, B. Blanck, K. Blaum, M. Breitenfeld, U. Hager, F. Herfurth, A. Herlert, A. Kellerbauer, H.-J. Kluge, M. Kretzschmar, D. Lunney, R. Savreux, S. Schwarz, L. Schweikhard, and C. Yazidjian: *Ramsey method of separated oscillatory fields for high-precision Penning trap mass spectrometry*, Phys. Rev. Lett. **98** (2007), 162501(4).

[27] H. Goldstein: *Classical Mechanics*, Addison-Wesley Publ. Co., Cambridge MA, USA, 1950.

[28] P. A. M. Dirac: *The Principles of Quantum Mechanics* (4th Ed.), Clarendon Press, Oxford, 1958.

WILEY ONLINE LIBRARY

Early View publication on wileyonlinelibrary.com
(issue and page numbers not yet assigned;
citable using Digital Object Identifier – DOI)

Ann. Phys. (Berlin), 1–13 (2013) / DOI 10.1002/andp.201300056

annalen der physik

Original Paper

Penning-trap mass spectrometry and neutrino physics

Sergey Eliseev[1,*], *Yuri N. Novikov*[2,3], *and Klaus Blaum*[1]

Received 15 March 2013, revised 19 May 2013, accepted 27 May 2013
Published online 27 June 2013

Rapidly developing neutrino physics has found in Penning-trap mass spectrometry a staunch ally in investigating a variety of fundamental problems. The most familiar are the absolute neutrino mass, possible existence of resonant neutrinoless double-electron capture and of keV-sterile neutrinos, and investigation of neutrino oscillations. This article is a brief review of the latest achievements and future perspectives of Penning-trap mass spectrometry in the exploration of these problems with a focus on electron capture and double electron capture processes.

1 Introduction

Over the last decades Penning-trap mass spectrometry (PT-MS) has become an important player in the field of fundamental physics [1, 2]. High precision and sensitivity of the Penning-trap technique in mass and magnetic-moment measurements on particles and nuclides along with very accurate theoretical calculations underlie the plethora of new physics results obtained with PT-MS. This technique has been widely used to test the Standard Model (SM) – an integrated theory of "truly" elementary particles, the "building blocks" of nature -, which describes all processes in nature ruled by three of the four known fundamental forces. The interest of PT-MS here are fundamental constants, a test of quantum-electrodynamics and chromodynamics, the CPT-invariance theorem and neutrino physics [3]. Experiments with PT-MS are performed on particles which are almost at rest and thus can be tagged as an "ultra-low energy" approach in contrast to ultra-high energy experiments performed, e.g., at particle accelerators. Both ultra-low and ultra-high energy approaches are highly complementary and may provide a complete picture of the properties of matter in nature. Fig. 1 illustrates this complementarity in the fundamental physics research.

The triumphal procession of the SM throughout the decades has been recently interupted by a striking discovery which demonstrates that neutrinos are massive. At present, the increasing search for new physics beyond the SM in many respects is associated with neutrinos. Remarkably, the neutrino itself is still a "terra incognita" in fundamental physics. Its many basic properties are still entirely unknown. The following list shows some open problems:

- What can one say about the absolute scale of the neutrino masses?
- Is the neutrino a Majorana or Dirac particle and is the total lepton number violated?
- Is the CP symmetry violated in the lepton sector?
- Are there sterile neutrinos and how many neutrino generations exist?
- Are there right-handed heavy neutrinos (see-saw mechanism)?
- How does the entire curve of the neutrinos' flavour oscillations look like?

Obviously, joint efforts of various experimental and theoretical approaches are required to look into these problems [4]. In this context, PT-MS assists the development of the low energy approach in neutrino physics. Low energy neutrinos (with less than a few MeV kinetic energy) can have a solar origin, be produced in nuclear reactors, or emitted from artificial radioactive sources. Geo-neutrinos from the depth of the Earth also fall in this small energy range.

This article briefly reviews the latest achievements and future perspectives of PT-MS in the field of neutrino physics with the focus on the investigation of electron-capture transitions.

* Corresponding author E-mail: sergey.eliseev@mpi-hd.mpg.de
[1] Max-Planck-Institut für Kernphysik, Heidelberg, Germany
[2] Petersburg Nuclear Physics Institute, St. Petersburg, Russia
[3] Department of Physics, St. Petersburg State University, Russia

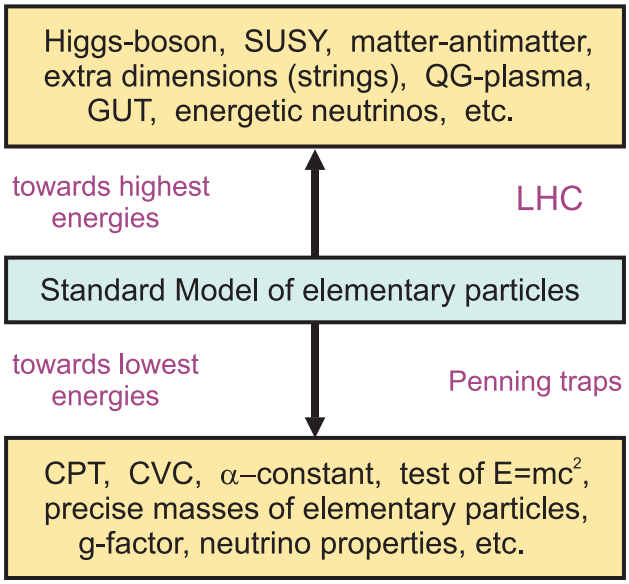

Figure 1 Diagram of different energy approaches in the fundamental exploration of the Standard Model and its extension. The ultra-high energy approach (up to TeV-region) is symbolized by LHC, whereas the ultra-low energy approach (atoms near at rest) can be explored by PT-MS.

2 What does PT-MS provide for neutrino physics?

The most suitable process to investigate the neutrino properties in the low energy domain are nuclear beta transformations accompanied by an emission of neutrinos. The total energy Q_ν carried away by the emitted neutrinos is defined by the beta-transformation energy. In beta and double-beta decays the antineutrinos should share energy with the emitted electrons and thus have a continuous spectrum, whereas in electron and double-electron captures the total neutrino energy is constant because of a two-body character of the capture processes. Thus, electron (ϵ) and double-electron ($\epsilon\epsilon$) captures are more attractive than beta and double-beta decays for the investigation of neutrino properties since the neutrino energy can be directly derived from the transformation energy. In the following we will mainly consider electron and double-electron-capture processes. The uncertainty of the Q_ν determination is thus defined by the uncertainty of the Q_ϵ and $Q_{\epsilon\epsilon}$ determination, i.e. by the uncertainty of the atomic mass difference of parent and daughter nuclides. PT-MS is at present the most suitable technique to precisely measure atomic masses.

The required precision of the mass-difference determination depends on the neutrino property under investigation:

- Determination of the absolute neutrino mass on the level of better than 1 eV from the analysis of the microcalorimetric spectrum of some electron-capture transformations [5, 6] requires an independent measurement of the transformation Q_ϵ-values with a similar uncertainty. These microcalorimetric measurements of the neutrino mass are complementary to the experiments on the determination of the antineutrino mass from the beta decay of tritium [7] and ^{187}Re [5]. Details are given in section 4.
- In the search for keV-sterile neutrinos the ratio of the capture probabilities from different electron orbits in electron capture should be bolometrically measured. This ratio contains the Q_ϵ-value of the process, which must be determined with an uncertainty of below 100 eV. This topic is covered in section 5.
- Neutrino oscillometry has a goal to measure the neutrino oscillation length (a length of the neutrino flavor changes) in a single experiment. The neutrino oscillation length is linked to the neutrino energy, and consequently, to the mass difference of the electron-capture nuclide pair. As described in section 6 it requires the precision of the Q_ϵ-values in the range of 10–100 eV.
- For the neutrinoless double-electron-capture exploration the uncertainty of the $Q_{\epsilon\epsilon}$-values of certain transitions on the level of 10–100 eV seems quite reasonable presently, because similar values are typically attributed to the widths of the intermediate states in the double-electron capture, which governs the resonance enhancement of this process. Details can be found in section 7.

To conclude, PT-MS should provide very accurate measurements of decay energies Q in the range of 0.1 to 100 eV. The achievement of the below-eV uncertainties requires a new generation of Penning traps.

3 Principle of Penning-trap mass spectrometry

A determination of the Q-value of a certain transition, i.e. the mass difference $Q/c^2 = M_i - M_f$ of the initial and final states of the transition, is performed in PT-MS by measuring the cyclotron frequencies of the initial and final ionic states of the transition in a strong static homogeneous magnetic field B. The cyclotron frequency of a charged particle with the mass M and charge state q is given by

$$\nu_c = \frac{1}{2\pi} \cdot \frac{q}{M} \cdot B. \tag{1}$$

In order to push the uncertainty of the Q-value determination down to sub-eV level, the ion must be confined to a well-localized volume within the homogeneous magnetic field for at least some seconds. This is achieved by a superposition of a static three-dimensional quadrupole electric field on the magnetic field such that an electrostatic potential well along the magnetic field lines is created. Such a configuration of fields is called a Penning trap. An exhaustive overview on the theory of the Penning trap can be found in [8].

The presence of the electrostatic quadrupole field modifies the pure ion's cyclotron motion to three independent trap motions: modified cyclotron, magnetron and axial motions with the frequencies ν_+, ν_- and ν_z, respectively. Although none of these frequencies are simple functions of the ion's mass, the invariance theorem [9] gives a simple relation between the pure cyclotron and the trap frequencies:

$$\nu_c^2 = \nu_+^2 + \nu_-^2 + \nu_z^2. \tag{2}$$

In Penning-trap mass spectrometry of radioactive nuclides the cyclotron frequency ν_c is determined from

$$\nu_c = \nu_+ + \nu_-. \tag{3}$$

This expression holds for traps employed in high-precision Penning-trap mass spectrometry. There are two methods in use to measure the cyclotron frequency: (1) via detection of the image current induced by the ion's motion in the resonant tank circuit attached to the trap (FT-ICR method) [10] and (2) with the so-called Time-of-Flight Ion-Cyclotron-Resonance technique (ToF-ICR) from the measurement of the time of flight of the ion through the strong gradient of the magnetic field [11]. The ToF-ICR method is routinely employed at online Penning-trap mass spectrometers for measuring the masses of short-lived nuclides with typical relative uncertainty of above 1ppb [1, 2]. The FT-ICR method is used or is planned to be used to measure the cyclotron frequency ν_c with ultimate relative uncertainty of below 0.01 ppb at such ultra-precision Penning-trap mass spectrometers as the FSU-trap [12], the THe-Trap [13] and PENTATRAP [14, 15].

4 Neutrino mass

To date, only an upper limit for the absolute antineutrino mass has been obtained on the level of 2 eV from the tritium β^--decay [16], whereas for the neutrino mass the limit is stuck at the level of 225 eV from the measurements of ^{163}Ho inner bremsstrahlung spectrum [17]. The new projects KATRIN [7], MARE [5], ECHo [6], and groups in Ref. [18, 19] aim to push these limits to the level of well below 1 eV. In these projects the neutrino mass will be derived from the analysis of the electron spectra of the corresponding decay. The input parameters in this analysis are the end point of the spectra and the Q_β-values of the decays. The determination of the Q_β-value of tritium β^--decay is planned to be performed with two Penning-trap mass spectrometers, the FSU-trap [12] and THe-trap [13]. These measurements are under preparation. The direct measurements of the Q_β-value of the β^--decay of ^{187}Re and the Q_ϵ of the electron capture in ^{163}Ho will be performed with PENTATRAP [14, 15].

The best candidate for neutrino mass measurements should have the smallest possible decay energy in order to provide the highest relative contribution of the neutrino rest mass to the total neutrino energy Q_ν. There are only two relevant candidates in the β^--decay sector: tritium and ^{187}Re. Recently, another candidate has been found, ^{115}In. It has the smallest decay energy of Q_β = 0.155 (10) keV [20] to an excited state of ^{115}Sn [21]. This value is the smallest one ever determined. However, the intensity of this decay branch is vanishingly small (10^{-4} %). Therefore, the analysis of the continuous spectrum of this β^--decay transition with very small decay energy is not straightforward. Note that the energy of this β^--decay has been determined by very precise PT-MS measurements of the mass-difference of ^{115}In and ^{115}Sn ground states [22, 23]. Another possible but still not observed β^--transition with low Q-value, namely β^- decay of ^{135}Cs to the second excited state in ^{135}Ba, was noted in Ref. [24] with expected Q-value of 0.5(11) keV. A measurement of the mass difference between ^{135}Cs and ^{135}Ba by PT-MS is required.

Meanwhile, the variety of possible candidates for neutrino mass determination can be in principle larger in the orbital electron capture sector because the neutrino energy depends on the difference $Q_\epsilon - B_i$, where B_i is the binding energy of the captured i-orbital electron. As the capture can happen from different atomic states the neutrino energy is also different, and thus a variety of suitable transitions can be found for the neutrino-mass determination. A suitable transition must fulfill two criteria: $Q_\epsilon - B_i$ and Q_ϵ must be as small as possible in order to provide the largest impact of the neutrino rest mass on the monochromatic-spectrum shape. Thus, a suitable candidate must be looked for in electron-capture transitions with $Q_\epsilon < 100$ keV. As shown in Ref. [25] the Q_ϵ-values of many potential candidates are known with by far insufficient precision to be able to assess their suitability for the neutrino mass determination. To shed light on this issue Q_ϵ-value measurements with conventional Penning traps can be carried

out with a keV-uncertainty to find a suitable candidate for the future neutrino mass determination. One of such cases, ^{194}Hg $\rightarrow$ ^{194}Au, has been tested at the ISOLTRAP-facility [25] by independent measurements of the absolute masses of mother and daughter nuclides.

The experiment scheme was very typical for direct mass measurements of radioactive nuclides with PT-MS [1]. ^{194}Hg and ^{194}Au-ions were produced in a fragmentation reaction of 1.4-GeV protons impinged on a thick uranium carbide target. Reaction products ionized either in a hot plasma ion source (^{194}Hg) or in a laser ion source RILIS (^{194}Au) were delivered as a 60 keV continuous ion beam to the GPS ISOLDE separator and forwarded to the ISOLTRAP experiment. There, the ion beam was first stopped, cooled, and bunched in a linear radio-frequency quadrupole (RFQ). The ion bunch was then transported to the first, cylindrically shaped Penning trap for the removal of isobaric contaminants (mass resolution of up to $m/\Delta m = 10^5$) that were still present after the mass selection with the ISOLDE separator. The masses of ^{194}Hg and ^{194}Au-ions were determined by measuring their cyclotron frequency $\nu_c(^{194}\mathrm{Hg}^+)$ and $\nu_c(^{194}\mathrm{Au}^+)$, respectively, in the second, hyperbolical Penning trap with the ToF-ICR technique. The magnetic field was calibrated by measuring the cyclotron frequencies $\nu_c(^{197}\mathrm{Au}^+)$ and $\nu_c(^{133}\mathrm{Cs}^+)$ of ^{197}Au and ^{133}Cs-ions with well known mass, respectively.

The mass difference has been determined from the equation which contains a ratio of the measured cyclotron frequencies:

$$Q_\epsilon = \left[m\left(^{133}\mathrm{Cs}\right) - m_e\right] \cdot \frac{\nu_c\left(^{133}\mathrm{Cs}^+\right)}{\nu_c\left(^{194}\mathrm{Hg}^+\right)} - \left[m\left(^{197}\mathrm{Au}\right) - m_e\right] \cdot \frac{\nu_c\left(^{197}\mathrm{Au}^+\right)}{\nu_c\left(^{194}\mathrm{Au}^+\right)}. \quad (4)$$

The obtained value of $Q_\epsilon = 29(4)$ keV [25] strongly deviates from the mass value of 69(14) keV [26] evaluated before the ISOLTRAP-measurements. Figure 2 illustrates a very peculiar scheme for the decay of He-like ions of ^{194}Hg. Since the new Q_ϵ is much smaller than the binding energy of the K-electron ($B_K = 80.7$ keV), the K-electron capture is energetically forbidden, and hence $^{194}\mathrm{Hg}^{79+,78+}$ ions become β-stable. However, they can undergo double-electron capture and alpha-decay.

The determined Q_ϵ-value of the electron capture in ^{194}Hg is by one order of magnitude larger than that of the electron capture in ^{163}Ho. Therefore, from the energy point of view this nuclide is less favourable than ^{163}Ho for the neutrino absolute mass determination. However, the final decision on the most suitable candidate will be made by cryogenic microcalorimetry [6, 18].

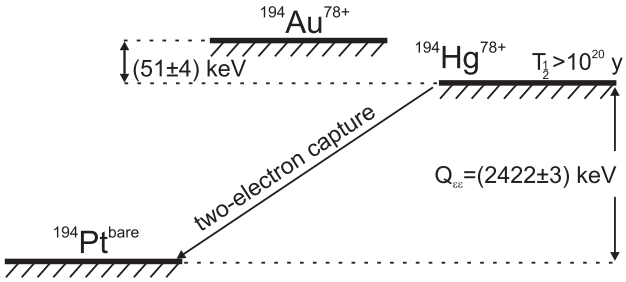

Figure 2 (Updated figure from [25]) The decay scheme for He-like charged Hg-atom derived from the Q_ϵ of [25]. As can be seen this state is nearly stable, whereas the neutral state is radioactive ($T_{1/2} = 4570$ y).

5 Search for keV-scale sterile neutrinos in electron capture

The discovery of sterile neutrinos would be a "beyond SM physics" event [27]. Last explorations of the decay and reactor antineutrino anomalies [28, 29] as well as the analysis of the short baseline neutrino oscillation anomalies (see, e.g., [30]) hint at a possible existence of sterile neutrinos. Current estimations for the light sterile neutrino mass are on the level of 1 eV [31, 32]. However, there are no conceptual restrictions for a very broad mass range of sterile neutrinos. Neutrinos with keV-masses can be attributed to Warm Dark Matter (WDM) [27], whereas much heavier MeV-neutrinos can be observed in π- and K-decays [33]. GeV-neutrinos can be responsible for the baryon asymmetry in the Universe [34].

The neutrino electron flavor state can be considered as a mixture of the active neutrino and the sterile neutrino mass eigenstates with the corresponding unitary mixing matrix. Since all the masses of active neutrinos are much smaller than the mass of the sterile one, we can consider on the keV scale a simplified version of a mixing of one active mass eigenstate with $m_i \ll 1$ eV and one sterile neutrino mass eigenstate with m_s on the keV-scale:

$$|\nu_e> = cos\theta|\nu_i> + sin\theta|\nu_s>, \quad (5)$$

where θ is the mixing angle between the active ν_i and sterile ν_s state. Thus $sin^2\theta = U^2_{e4}$ accounts for the contribution of sterile neutrinos in the probability of corresponding processes.

Cosmology sets the upper limit on the mixing angle on the level of $sin\theta = 10^{-4}$ (see, e.g., [35]) if keV-sterile neutrinos are considered candidates for WDM. However, this and all other mixing angle values yielded by cosmology are strongly model dependent. Up to date, no direct indication for sterile neutrinos from the cosmic

observations has been found. Therefore, an independent discovery of keV sterile neutrinos in terrestrial laboratory experiments is of utmost importance for the research on WDM. An overview of different approaches employed in the search for keV sterile neutrinos is given in Ref. [36]. A suggestion to use the tritium and ^{187}Re β^- decays for the search for a kink in the continuous β^--spectrum which should manifest the contribution of sterile neutrinos was made in Ref. [37]. Meanwhile, the re-analysis of the data of Mainz [38] and Troitsk [39] measurements with tritium has revealed no contribution of sterile neutrinos with mass values of 2-200 eV to the differential β^--spectra. The upper limit of this contribution is estimated as $U^2_{e4} \approx 10^{-2}$ for the $m_s \approx$100 eV in Ref. [39].

The orbital electron capture sector provides another approach for the search for keV sterile neutrinos. There are some advantages compared to β^--decay and the main of them is a discrete spectrum of the atomic de-excitation following the capture process instead of the continuous β^--decay spectrum. This discrete spectrum can be measured by means of cryogenic microcalorimetry [5,6], which embodies all atomic de-excitations (characteristic X-rays, Auger and Coster-Kronig electrons, etc.) following the electron vacancy occupation. The ratio of partial capture probabilities depends on the neutrino rest mass and Q_ϵ-value. Independent precise measurements of Q_ϵ-value must be provided by PT-MS.

The probability to capture an electron by a nucleus from the i atomic orbit taking into account the contribution from the sterile neutrinos can be written as

$$\lambda_i = \frac{G^2}{4\pi^2} \cdot C_i \cdot \left[\left(1 - U^2_{e4}\right) \cdot |q_i| \cdot Q_i + U^2_{e4} \cdot |q_{si}| \cdot Q_i\right], \qquad (6)$$

where G is the weak coupling constant. The form-factor for the allowed transition is $C_i = |M|^2 \cdot |\psi_i|^2$, M is the nuclear matrix element, $|\psi_i|^2$ is the electron density in the nucleus (atomic wave-function)[1], $|q_i| = \sqrt{Q_i^2 - m^2}$ and $Q_i = Q_\epsilon - B_i$ are the momentum and the total active neutrino energy, respectively, m is the active neutrino mass, which can be considered negligibly small on the keV scale of the sterile neutrino mass m_s. Energy values in Eq. (6) are given in ($m_e c^2$) units.

The ratios of the experimental probabilities λ_i/λ_j from different atomic orbits i and j can be determined from the areas under the peaks in the calorimetric spectrum, whereas the theoretical ratios (i.e. without the sterile neutrino contribution) can be precisely calculated [40] taking into account the cancellation of the nuclear matrix elements in the probability ratios. The ratio with and without the sterile neutrinos is as follows:

$$\alpha_{ij} \equiv \frac{\lambda_i/\lambda_j}{(\lambda_i/\lambda_j)_{act}} = \frac{1 - U^2_{e4} + U^2_{e4} \cdot \sqrt{1 - \left(\frac{m_s}{Q_\epsilon - B_i}\right)^2}}{1 - U^2_{e4} + U^2_{e4} \cdot \sqrt{1 - \left(\frac{m_s}{Q_\epsilon - B_j}\right)^2}}. \qquad (7)$$

Here, i and j stand for different combinations of allowed orbits K,L,M, etc.; the active neutrino is assumed massless. As can be seen from Eq. (7), the sensitivity to U^2_{e4} depends on the ratio of the sterile neutrino mass m_s to the difference $Q_\epsilon - B$, and on the accuracy of the determined values of α_{ij}. Thus, the knowledge of the Q_ϵ-value with a low uncertainty is mandatory.

The accuracy of the α_{ij}-determination depends on the precision of the i/j-probability ratios for the spectra with and without the contribution from the sterile neutrinos. The areas under experimental peaks can have a good precision dependent on the statistics, whereas the precision for theoretically calculated $(\lambda_i/\lambda_j)_{act}$ depends on the accuracy of i/j electron wave function ratio and precision of atomic mass difference Q_ϵ. The ratio for the K/L electron wave functions squared can be calculated with a precision of $5 \cdot 10^{-3}$. A similar relative precision for Q_ϵ is needed for some specific regions of $m_s \approx Q - B$. At present, this can only be provided by PT-MS. Thus, α_{KL} can be determined with a relative uncertainty of 10^{-2}. Provided sterile neutrinos exist, such an approach allows determining the sterile neutrino contribution on the 10^{-2}-level for a chosen sterile neutrino mass range which is specific for each electron-capture transition. A list of relevant candidates contains electron-capture transitions in ^{157}Tb, ^{163}Ho, ^{179}Ta, ^{193}Pt, ^{202}Pb, ^{205}Pb and ^{235}Np.

6 Neutrino oscillometry

A global analysis of the neutrino data [41], which incorporates the results of various neutrino experiments all over the world, opens the possibility for a quantitative comparison of the oscillation lengths L_{ij} with the neutrino energy E_ν. These parameters are linked by the following relation [42]:

$$L_{ij}[m] \equiv \frac{2.48 \cdot E_\nu[MeV]}{\left|\Delta m^2_{ij}\right|[eV^2]}. \qquad (8)$$

Assuming $\left|\Delta m^2_{13}\right| = 2.5 \cdot 10^{-3}$ eV^2 [41], one obtains $L_{13}[m] \approx E_\nu[keV]$. For $\left|\Delta m^2_{14}\right| = 1$ eV^2 $L_{14}[m] \approx 0.0025 \cdot E_\nu[keV]$. To confirm these relations independent

[1] We do not consider here the higher order effects which can be neglected on the keV scale of interest in this work. See for details, e.g., [40].

measurements of L_{ij} and E_ν must be performed. The oscillation lengths can be determined by means of neutrino oscillometry with monochromatic neutrinos [43], whereas the neutrino energy can be accurately and reliably measured by PT-MS.

In all previous neutrino experiments used for the global analysis the oscillation length L_{13} has been much larger than the size of detectors. For neutrinos with energies much higher than 1 MeV, the length L_{13} is much longer than one kilometer. Obviously, it was unrealistic to have a detector of such a size. Hence, all experiments which aim at neutrino oscillations have so far considered just a single or at most a two-point measurement instead of the full oscillation curve. However, if the neutrino energy is much smaller than 1 MeV and the neutrinos are monoenergetic, then the oscillation pattern can be within the dimensions of a realistically sized detector. The single oscillation curve can be scanned by a point-by-point detection of the recoil electron events which are mainly sensitive to the electron-neutrino flavor. This neutrino oscillometry (the term was given in Ref. [43,44]) can be used for the eV- sterile neutrino identification and measurement of the length L_{14}. As the oscillation lengths L_{13} and L_{14} are disentangled, the 100 m long liquid scintillator detector LENA [45] can be used for a concurrent determination of these lengths as well as mixing angles θ_{13} and θ_{14} (the length L_{14} and the mixing angle θ_{14} are associated with the existence of sterile neutrinos). The liquid scintillator neutrino detector LENA will be able to resolve a signal with space resolution of 20 cm [45], which could allow a precise determination of L_{14} on the level of a few times 10^{-4}, provided a neutrino source with 5 MCi intensity is used and many periods of the oscillation curve are fitted. In order to precisely determine the eV-sterile neutrino mass it is desirable to measure the oscillation length and neutrino energy with similar uncertainties. The most relevant candidates for neutrino oscillometry are electron-capture transitions in ^{37}Ar, ^{51}Cr, ^{75}Se, ^{113}Sn, ^{145}Sm, and ^{169}Yb [44]. At present, their Q_ϵ-values are known from indirect mass measurements and hence direct and unambiguous precise mass measurements with PT-MS on a 100 eV-level are required. These nuclides can be produced at reactors and accelerators.

7 Neutrinoless double-electron capture

The fact of massiveness of neutrinos raises the question whether neutrinos and antineutrinos are different (Dirac) or identical (Majorana) particles. At present, the only practical way to unambiguously answer this question consists in the observation of the neutrinoless double-beta transformations: (1) double-β^- emission ($0\nu\beta^-\beta^-$), (2) double-positron emission ($0\nu\beta^+\beta^+$), (3) one electron capture with one-positron emission ($0\nu\epsilon\beta^+$), or (4) double-electron capture ($0\nu\epsilon\epsilon$). These neutrinoless transformations are possible only if neutrinos are Majorana particles that in turn implies a violation of the total-lepton-number conservation. Since these neutrinoless processes are not allowed in the SM, their observation will thus manifest new physics beyond this fundamental paradigm.

The most probable process among all neutrinoless transformations was thought to be neutrinoless double-β^- decay ($0\nu\beta^-\beta^-$) with an emission of two electrons. Over the last decades about 20 large-scale projects [46] have been proposed for a search for this phenomenon. In these experiments [47] a monoenergetic peak is searched for in the sum-kinetic-energy spectrum of the two emitted electrons at the location which corresponds to the Q-value of the transition. PT-MS has provided these experiments with precise measurements of the Q-values of the used double-β^--decay transitions [48–56]. The complexity of these projects are conditioned by the required extraordinary sensitivity to neutrinoless double-β^- decay, whose rate is expected to be on the level of a few decay events/(ton yr) [57]. This demands a source/detector of a very large size placed underground as deeply as possible. Though there is still some room for improvements in sensitivity by current methods [58, 59], a further breakthrough can be made only by invention of new alternative methods.

The inverse process, neutrinoless double-electron capture [60], can be considered such an alternative [61]. This process was long kept in the shadow because of its expected smaller transition probability. But in some cases the probability of this process can be resonantly enhanced by many orders of magnitude and hence becomes comparable to that of neutrinoless double-beta decay. Althougth, the possibility for a resonant enhancement of the process was already known long ago [62–64], the search for a resonantly enhanced transition was hampered by not sufficiently precise knowledge of the $Q_{\epsilon\epsilon}$-values of possible candidate-transitions [65]. Tremendous progress in high-precision Penning-trap mass spectrometry in the last decade [1, 2] has provided a necessary base for a determination of atomic masses and mass differences with sufficient accuracy and thus stimulated an experimental campaign for a search for resonantly enhanced neutrinoless double-electron-capture transitions.

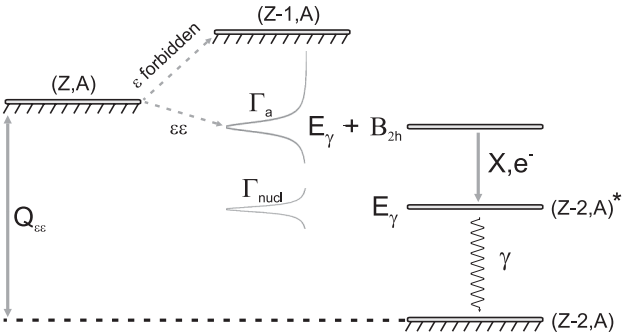

Figure 3 (from [61]) Energy diagram for double-electron capture between two neutral atoms of isobaric nuclides (with the same mass number A). The intermediate nuclide (Z-1,A) can energetically not be populated. The atomic level de-excitation (by X-rays and Auger and other electrons) and nuclear de-excitation by gamma-ray are shown. Γ_a and Γ_{nucl} are atomic and nuclear level widths, respectively, and $\Gamma_a \gg \Gamma_{nucl}$.

7.1 Formalism of neutrinoless double-electron capture

In double-electron-capture process a nuclide captures two electrons from its atomic shells. The intermediate atomic state has two holes in the atomic shell, which are occupied by outer electrons with subsequent photon and electron emission. The energy balance is shown in Fig. 3 and is given by

$$\begin{aligned} Q_{\epsilon\epsilon} &= [M(Z, A) - M(Z-2, A)] \cdot c^2 \\ &= Q_{\nu\nu} + B_{2h} + E_\gamma, \end{aligned} \tag{9}$$

where $Q_{\epsilon\epsilon} <$ a few MeV is the atomic mass difference between (Z,A) and (Z-2,A) nuclides. $Q_{\nu\nu}$ is the total energy of the two neutrinos if they are emitted. B_{2h} is the (positive) energy of the double-electron hole in the atomic shell in the daughter nuclide, and E_γ is the gamma-decay energy of de-excitation of the daughter nucleus. We ignore a negligibly small recoil energy of the nucleus in Eq. (9).

The two-neutrino mode of double-electron capture is an ordinary second order weak interaction process similar to double-β^- decay with emission of two neutrinos [66]. If neutrinos are Majorana particles, then the neutrino emitted from the single capture process in the first step will be reabsorbed by the virtual intermediate state in the second step giving rise to the second capture process without emission of neutrinos. Fig. 4 shows two diagrams corresponding to the two-neutrino (a) and neutrinoless (b) transitions, respectively. In fact, the intermediate state of the double-electron-capture transition has a two-electron hole in its atomic shell and hence is unstable. It means that its energy having a certain

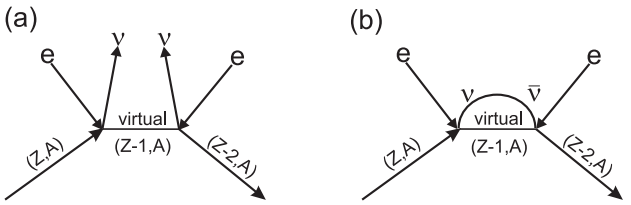

Figure 4 Schematic illustration of double-electron capture: (a) two-neutrino mode and (b) neutrinoless mode.

width is not exactly defined. It results in the non-zero probability for overlapping the energies of the intermediate and initial states that provides the resonance conditions. The probability of neutrinoless double-electron capture can be written as [64]:

$$\begin{aligned} \lambda_{0\nu\epsilon\epsilon} &= C \cdot |M_{0\nu\epsilon\epsilon}|^2 \cdot |m_{\epsilon\epsilon}|^2 \\ &\quad \cdot P_{0\nu\epsilon\epsilon} \cdot \frac{\Gamma_{2h}}{(Q_{\epsilon\epsilon} - B_{2h} - E_\gamma)^2 + \left(\frac{\Gamma_{2h}}{4}\right)^2}, \end{aligned} \tag{10}$$

where $M_{0\nu\epsilon\epsilon}$ is the nuclear matrix element of the transition, $m_{\epsilon\epsilon}$ is the effective Majorana neutrino mass in eV, $P_{0\nu\epsilon\epsilon}$ is the square product of the wave functions of the captured electrons, Γ_{2h} is the total width of the final transition state and C is a transition-specific constant. A complete degeneracy of the initial and intermediate atomic states takes place when

$$\Delta = \left| Q_{\epsilon\epsilon} - B_{2h} - E_\gamma \right| \approx \Gamma_{2h} < 100 \text{ eV}, \tag{11}$$

where Δ is called a degeneracy factor of the transition. Thus, in order to estimate the probability of neutrinoless double-electron capture normalized to $|m_{\epsilon\epsilon}| = 1$ eV one must calculate $P_{0\nu\epsilon\epsilon}$, $M_{0\nu\epsilon\epsilon}$, Γ_{2h} and B_{2h}. $Q_{\epsilon\epsilon}$ must be measured on the level of 100 eV. In a recent measurement compaign performed with PT-MS [61] the $Q_{\epsilon\epsilon}$-values of almost all potential candidates have been determined with sufficient uncertainty. In the following subsection this measurement compaign is described in detail.

7.2 Search for resonant neutrinoless double-electron-capture transitions

Four groups have contributed to the measurements of the Q-values of potentially resonantly enhanced transitions: SHIPTRAP [67–73], JYFLTRAP [74–76], TRIGATRAP [77] and the FSU Penning trap [12]. Since the majority of the Q-values have been measured with SHIPTRAP, the experiments on the determination of the Q-values are described here by the example of this mass spectrometer.

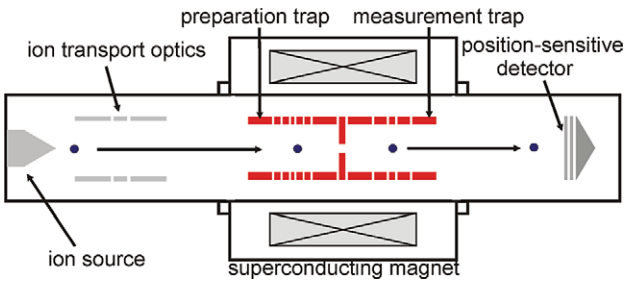

Figure 5 "Off-line" SHIPTRAP used for the $Q_{\epsilon\epsilon}$-value measurements of potential resonantly enhanced neutrinoless double-electron-capture transitions.

The SHIPTRAP facility is located at GSI Darmstadt with the aim for direct high-precision mass measurements of short-lived heavy and superheavy nuclides. A detailed description of the whole project and its achievements can be found in [78]. Here, only part of the facility, for short "off-line SHIPTRAP", relevant to the measurements of the Q-values is presented (Figure 5). It consists of a station with ion sources for production of singly charged ions from neutral species in various chemical forms, and the heart of the system – the Penning-trap mass spectrometer. Singly charged ions produced from neutral species in various chemical forms with electron-impact or laser-ablation ion sources are transported by means of electrostatic electrodes and Einzel lenses towards the Penning-trap mass spectrometer, which has two cylindrical Penning traps – the preparation trap (PT) and measurement trap (MT). The PT serves for separating the ions of interest from unwanted ions by employing the mass-selective buffer gas cooling technique [79]. Thus, only the nuclide of certain mass can be allowed to pass into the MT. In the MT a measurement of the cyclotron frequency of the chosen nuclide takes place via the ToF-ICR technique.

The Q-value of the transition under consideration is determined by measuring the ratio of the cyclotron frequencies of the initial and final nuclides. A few-days' measurement campaign results in a determination of the frequency ratio with the required uncertainty of about 10^{-9}, which corresponds to the uncertainty of the $Q_{\epsilon\epsilon}$-value of about 100 eV.

Nuclides which can undergo double-electron capture [65] can be sorted into two groups: transitions to nuclear (1) ground and (2) excited states, respectively. Each group has its pros and cons for the future search for neutrinoless double-electron capture.

The transitions to nuclear ground states are the most attractive for several reasons. First, these are transitions between nuclear ground states with spin and parity of 0^+. The nuclear matrix elements of such transitions are the largest and unlike transitions to nuclear excited states can be calculated quite reliably [61, 80]. Furthermore, for such transitions the capture of two orbital K-electrons is allowed if $Q_{\epsilon\epsilon} > B_{2h}$. The probability for K-electrons to be found in the nucleus is the highest among all orbital electrons. These two factors make such transitions the most probable and even only partial resonant enhancement of them can still result in capture rates which can be observed with modern detection means. In addition, in the case of even partial resonant enhancement the capture rate of the two-neutrino branch, which plagues the experiments for a search for neutrinoless processes, is negligible compared to neutrinoless double-electron capture. Nevertheless, despite all these obvious virtues, the transitions to nuclear excited states were favored till recently. The argument was the absence of the signature for the occurrence of ground-to-ground states transitions. Thanks to rapid progress in the development of cryogenic microcalorimetry [5, 6] it has become feasible to detect the total energy of the de-excitation of the atomic shell of the final nuclide. The total de-excitation energy should be equal to the $Q_{\epsilon\epsilon}$-value of the transition, if it is neutrinoless, and its measurement is the signature for the occurrence of neutrinoless double-electron capture.

In order to define the most promising transition to start with, the half-lives of all known transitions (Figure 6) with an assumed nuclear matrix element of 2.5 and an effective Majorana neutrino mass of 1 eV were estimated. The values of the masses of the initial and final states and binding energies of captured electrons were taken from [26] and [81], respectively. The neutrinoless double-electron capture in ^{152}Gd, ^{164}Er and ^{180}W were considered the only potential candidates for the search for neutrinoless double-electron capture. For these transitions the nuclear matrix elements $M_{0\nu\epsilon\epsilon}$ and binding energies of the two-electron holes B_{2h} were calculated (Table 1) [80]. Together with the precisely measured $Q_{\epsilon\epsilon}$-values [67, 68, 72] it allowed the estimation of the minimal and maximal half-lives of these transitions (Table 1). The minimal and maximal half-life are the half-lives of the transition corresponding to the degeneracy factors which are by three-sigma experimental error smaller and larger, respectively, than the measured Δ(new). Although for none of these transitions the requirement of the full degeneracy is fulfilled, the degeneracy factor Δ of ^{152}Gd$\rightarrow^{152}$Sm is smaller than 1 keV and thus neutrinoless double-electron capture in ^{152}Gd can be tagged as resonantly enhanced with the minimal half-life of 10^{26} years normalized to the effective Majorana neutrino mass of 1 eV. Note that the calculation

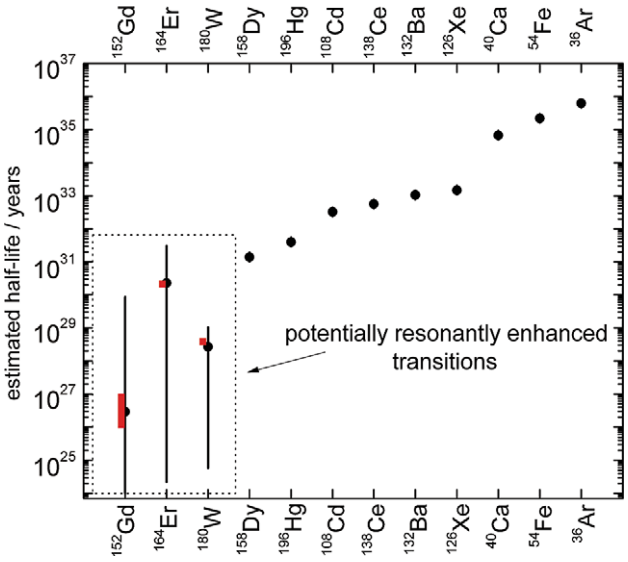

Figure 6 (from [61]) Estimated half-lives of all possible neutrinoless double-electron transitions between nuclear ground states. The $Q_{\epsilon\epsilon}$ and B_{2h}-values were taken from [26] and [81], respectively. For the calculation the nuclear matrix element of 2.5 and effective Majorana neutrino mass of 1 eV were assumed. The minimal and maximal half-lives of the neutrinoless double-electron transitions in ^{152}Gd, ^{164}Er and ^{180}W from the new data of [67, 68, 72] are presented by the red rectangles. They are calculated in Ref. [80] and given in Table 1.

Table 1 Parameters of neutrinoless double-electron-capture transitions to nuclear ground states adressed by PT-MS. The nuclear matrix elements $M_{0\nu\epsilon\epsilon}$ are taken from Ref. [80]. The minimal (min.$T_{1/2}$) and maximal (max.$T_{1/2}$) half-life are the half-lives of the transition corresponding to the degeneracy factors which are by three-sigma experimental error smaller and larger, respectively, than the measured Δ(new).

$0\nu2EC$-transition	^{152}Gd $\rightarrow$ ^{152}Sm	^{164}Er $\rightarrow$ ^{164}Dy	^{180}W $\rightarrow$ ^{180}Hf
reference	[67]	[68]	[72]
electron orbitals	KL_1	L_1L_1	KK
$Q_{\epsilon\epsilon}$(old)/keV	54.6(35)	23.3(39)	144.4(45)
Δ(old)/keV	−0.27(350)	5.05(390)	12.4(45)
$Q_{\epsilon\epsilon}$(new)/keV	55.70(18)	25.07(12)	143.20(27)
Δ(new)/keV	0.83(18)	6.82(12)	11.24(27)
$M_{0\nu\epsilon\epsilon}$	2.7−3.2	2.3−2.6	1.8−2
min. $T_{1/2}$ / y	$1 \cdot 10^{26}$	$2 \cdot 10^{30}$	$3 \cdot 10^{28}$
max. $T_{1/2}$ / y	$1 \cdot 10^{27}$	$2 \cdot 10^{30}$	$4 \cdot 10^{28}$

of the mentioned nuclear matrix elements performed in Ref. [82] with an advanced energy density functional method yields substantially smaller values compared to those from [80].

In contrast to the transitions to nuclear ground states, the calculation of the nuclear matrix elements for the transitions to nuclear excited states are much more complicated and hence performed with larger uncertainty. In addition, very often the assignment of the correct spin and parity to the transition cannot be made unambiguously. This makes such transitions less favourable for the quantitative determination of the capture rates. Nevertheless, the virtue of such transitions are, first, the gamma-rays from the de-excitation of the nuclear excited state which are a signature for the neutrinoless double-electron-capture occurrence and, second, the possibility for such transitions to proceed to a variety of nuclear excited states with different spins and parities and thus for a multiple resonance phenomenon. The observation of the transitions to nuclear excited states with different spins and parities allows for the investigation of different mechanisms which can mediate neutrinoless double-electron capture [83]. A complete list of the transitions to nuclear excited states adressed by PT-MS can be found in Ref. [61]. The measurements of their $Q_{\epsilon\epsilon}$-values have yielded that only neutrinoless double-electron capture in ^{156}Dy can at present be considered a promising case to look into. In ^{156}Dy a multiple-resonance phenomenon has been discovered [70] (Figure 7). Here, the transitions to four nuclear excited states are resonantly enhanced. The transition to the nuclear excited state with energy 2003.749(5) keV, though fully resonantly enhanced ($\Delta = (40\pm100)$ eV), is hardly observable due to a spin state $I_f = 2^+$ and a capture of M- and N-electrons. The half-life of the transition to the nuclear excited state with energy 1946.375(6) keV and spin 1^- is expected to be well larger than 10^{30} years due to a small magnitude of the nuclear matrix element. For the remaining two transitions the minimal and maximal half-lives normalized to the effective Majorana neutrino mass of 1 eV have been calculated. For the calculation of the half-lives (Table 2) the value of 2.5 was taken, which approximately corresponds to the nuclear matrix elements for the ground-state-to-ground-state transitions. The real magnitude of the nuclear matrix elements, which has still to be calculated, may substantially be smaller than 2.5. The transition to the nuclear excited state with an energy of 1988.5(2) keV and a spin of 0^+ is fully resonantly enhanced within three-sigma experimental error (see Table 2) and thus its capture rate can become comparable to the decay rates

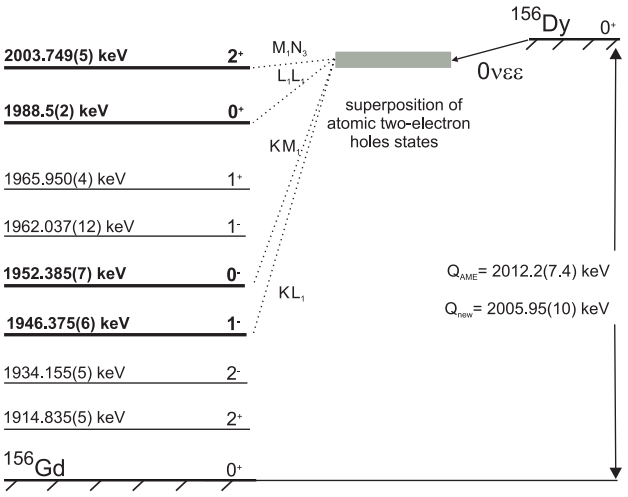

Figure 7 (from [70]) The scheme of neutrinoless double-electron capture in ^{156}Dy. Shown are only the nuclear excited states in ^{156}Gd with spin $I_f \leq 2$ [84], to which a resonantly enhanced $0\nu\epsilon\epsilon$ can result in a half-life which is short enough for a realistic search for neutrinoless double-electron capture. The $0\nu\epsilon\epsilon$-transitions to the nuclear excited states marked with thick lines are resonantly enhanced as has been found by PT-MS.

Table 2 Estimated min. and max. half-lives of the two most promising resonantly enhanced neutrinoless double-electron-capture transitions in ^{156}Dy to nuclear excited states with energy E_γ.

E_γ/keV	min. $T_{1/2}$/y	max. $T_{1/2}$/y
1988.5(2)	$3 \cdot 10^{24}$	$3 \cdot 10^{29}$
1952.385(7)	$3 \cdot 10^{28}$	$8 \cdot 10^{28}$

of neutrinoless double-beta transitions. In order to make a certain statement on the suitability of this transition for the search for neutrinoless double-electron capture, the nuclear excitation energy has to be measured by at least a factor of 4 more accurately than the present uncertainty [84] and the nuclear matrix element has to be calculated.

The half-lives presented in Table 2 are calculated in assumption of the "mass mechanism" underlying neutrinoless double-electron capture. The calculation of the total capture rates must take into account the other mediating mechanisms [83]. The transitions can, e.g., also occur in the presence of right-handed currents with amplitude essentially independent of the neutrino mass or can be caused by an exchange of heavy particles. Also light sterile neutrinos if they exist can increase the value of the effective Majorana neutrino mass. In general, several contributions to the total transition amplitude can add coherently, allowing for interference effects, resulting in a much shorter total half-life of neutrinoless double-electron capture in ^{156}Dy than the estimates given in Table 2.

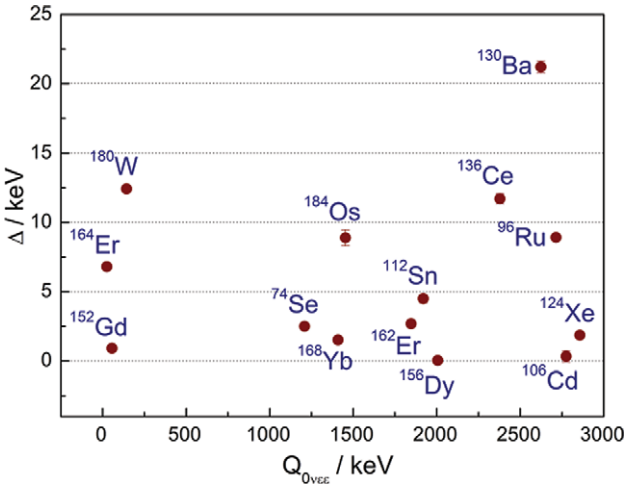

Figure 8 Degeneracy factors Δ of all $0\nu\epsilon\epsilon$-transitions with $\Delta < 25$ keV adressed by PT-MS [61] (the error bars are within the circles).

7.3 Merits and demerits in searching for $0\nu\epsilon\epsilon$-transitions. Double beta-transformations in the isobaric chains

The degeneracy factors of all $0\nu\epsilon\epsilon$-transitions with $\Delta < 25$ keV adressed by PT-MS are collected in Figure 8. The resonant enhancement, which can reach many orders of magnitude, strongly depends only on the degeneracy factor Δ and does not depend on the absolute values of the excited level energy of the daughter nucleus and the binding energy of the captured electrons. In the case of full resonant enhancement the half-lives of even the $0\nu\epsilon\epsilon$-transitions with small nuclear matrix elements due to angular momentum change can be still comparable to those of $0\nu\beta\beta$-transitions. This feature of neutrinoless double-electron capture offers a number of advantages for this process in the neutrino exploration compared to neutrinoless double-β^- decay [57]. They are

– a variety of excited nuclear states with different low spin values and different parities in one nuclide to which the double-electron-capture transition can be resonantly enhanced resulting in relatively short partial half-lives,

– a possibility to test the existence of right-handed lepton current by observing transitions to nuclear excited states with negative parity [83],
– no essential background from the two-neutrino mode in the monochromatic spectrum of the neutrinoless mode.

Meanwhile, there are some disadvantages in exploration of neutrinoless double-electron capture:

– a small abundance ratio for neutron-deficient stable nuclides which can be planned to use for the large scale long term experiment,
– an appearance of the α-decay channel in heavy nuclides which can create significant background.

Thus, the exploration of $0\nu\epsilon\epsilon$ and $0\nu\beta\beta$-processes must complement each other. There is a natural link which connects these processes via a common daughter nuclide in mass isobaric triplets of type (Z-2,A) $\rightarrow$ (Z,A) $\leftarrow$ (Z+2,A), where the arrows to the right and left mean double-β^- decay and double-electron capture, respectively. Only four such triplets are known in nature. They are ^{96}Zr $\rightarrow$ ^{96}Mo $\leftarrow$ ^{96}Ru, ^{124}Sn $\rightarrow$ ^{124}Te $\leftarrow$ ^{124}Xe, ^{130}Te $\rightarrow$ ^{130}Xe $\leftarrow$ ^{130}Ba and ^{136}Xe $\rightarrow$ ^{136}Ba $\leftarrow$ ^{136}Ce. These triplets have common daughter nuclides in the middle: ^{96}Mo, ^{124}Te, ^{130}Xe and ^{136}Ba. This can have a positive synergetic impact on the accuracy of the calculation of the nuclear matrix elements within the same isobaric mass chain. Even between the different triplets the interdependence of nuclear physics structure can be used. Transitions in the triplets with mass numbers of A=124, 130, 136 contain the isotopes of the same elements: Te, Xe and Ba. The nuclide ^{136}Xe in the chain has the "magic" neutron number N=82 and thus could be easy processed theoretically. The three out of four isobaric triplets have been adressed by the PT-MS. Results are presented in Ref. [73]. Only for the neutrinoless double-electron capture in ^{124}Xe a partial resonance has been identified with $\Delta = 1.86(15)$ keV with the estimated half-life of about 10^{28} years [73]. Thus, ^{124}Sn $\rightarrow$ ^{124}Te $\leftarrow$ ^{124}Xe triplet can be considered to be interesting to investigate with the next generation of neutrino detectors [45].

8 Conclusion

Neutrino physics is a rapidly growing field of fundamental science. Neutrinos are probably ones of the most mysterious particles whose many properties are still unknown. Fortunately, nature provides a wide scope of possibilities to explore neutrinos with different flavors and energies from very energetic of the galactic origin to "hand-made" neutrinos with very small energies. The latter actually is a cradle of neutrino physics whose discovery potential can be revealed with invention of novel experimental approaches. One of them is high-precision Penning-trap mass spectrometry whose adoption to the neutrino-physics goals began a few years ago. This technique provides neutrino physics with precise Q-values of the investigated reactions.

Experiments for the determination of the neutrino mass assisted by PT-MS aim at the determination of the neutrino mass on a sub-eV level. For this, novel ultra high-precision Penning-trap mass spectrometers are currently in preparation.

The present generation of Penning-trap mass spectrometers has already played the major role in the determination of the most suitable neutrinoless double electron-capture transition for future large-scale experiments aimed to clarify the Majorana or Dirac nature of neutrinos.

It has been recently realized that the role of PT-MS in neutrino oscillometry and in the search for keV-sterile neutrinos can be very significant.

The list of mentioned problems which can be assisted by PT-MS is by far not complete. Tremendous developement of PT-MS and rapidly expanding neutrino physics are promising a deeper involvement of PT-MS in the field of neutrino physics in the future.

Acknowledgement. The financial support by the Max-Planck Society, the EU (ERC Grant Agreement No. 290870 - MEFUCO), and from the Alliance Program of the Helmholtz Association (HA216/EMMI) is acknowledged.

Key words. Penning-trap mass spectrometry, neutrinos, neutrino mass, neutrino oscillometry, sterile neutrinos, neutrinoless double-electron capture.

References

[1] K. Blaum, Phys. Rep. **425**, 1–78 (2006).
[2] K. Blaum, J. Dilling, and W. Nörtershäuser, Phys. Scr. **T152**, 014017(32pp) (2013).
[3] K. Blaum, Y. Novikov, and G. Werth, Contemp. Phys. **51**, 149–175 (2010).
[4] P. Hernández, arXiv:1010.4131[hep-ph] (2010).
[5] M. Galeazzi, F. Gatti, M. Lusignoli, A. Nucciotti, S. Ragazzi, and M. Gomes, arXiv:1202.4763[physics.ins-det] (2012).
[6] P. O. Ranitzsch, J. P. Porst, S. Kempf, C. Pies, S. Schäfer, D. Hengstler, A. Fleischmann, C. Enss, and

L. Gastaldo, J. Low Temp. Phys. **167**, 1004–1014 (2012).
[7] G. Drexlin, V. Hannen, S. Mertens, and C. Weinheimer, Advances in High Energy Phys. **2013**, 293986(39pp) (2013).
[8] L. Brown and G. Gabrielse, Rev. Mod. Phys. **58**, 233–311 (1986).
[9] L. Brown and G. Gabrielse, Phys. Rev. A **25**, 2423–2425 (1982).
[10] H. Dehmelt and F. Walls, Phys. Rev. Lett. **21**, 127–131 (1968).
[11] G. Gräff, H. Kalinowsky, and J. Traut, Z. Phys. A **297**, 35–39 (1980).
[12] B. Mount, M. Redshaw, and E. Myers, Hyperfine Interact. **199**, 327–335 (2011).
[13] C. Diehl, K. Blaum, M. Höcker, J. Ketter, D. Pinegar, S. Streubel, and R. V. D. Jr., Hyperfine Interact. **199**, 291–300 (2011).
[14] J. Repp et al., Appl. Phys. B **107**, 983–996 (2012).
[15] C. Roux et al., Appl. Phys. B **107**, 997–1005 (2012).
[16] E. Otten and C. Weinheimer, Rep. Prog. Phys. **71**, 086201(36pp) (2008).
[17] P. Springer, C. Bennett, and P. Baisden, Phys. Rev. A **35**, 679–689 (1987).
[18] A. Nucciotti, Nucl. Phys. B Proc. Suppl. **229–232**, 155–159 (2012).
[19] J. P. Porst, L. Gastaldo, P. Ranitzsch, F. von Seggern, A. Kirsch, S. Kempf, C. Pies, S. Schäfer, A. Fleischmann, and C. Enss, Nucl. Phys. B Proc. Suppl. **229–232**, 446 (2012).
[20] J. Blachot, Nucl. Data Sheets **113**, 2391–2535 (2012).
[21] C. Cattadori, M. D. Deo, M. Laubenstein, L. Pandola, and V. Tretyak, Nucl. Phys. A **748**, 333–347 (2005).
[22] J. Wieslander et al., Phys. Rev. Lett. **103**, 122501(4pp) (2009).
[23] B. Mount, M. Redshaw, and E. Myers, Phys. Rev. Lett. **103**, 122502(4pp) (2009).
[24] M. Mustonen and J. Suhonen, Phys. Lett. B **703**, 370 (2011).
[25] S. Eliseev et al., Phys. Lett. B **693**, 426–429 (2010).
[26] G. Audi, O. Bersillon, J. Blachot, and A. Wapstra, Nucl. Phys. A **729**, 3–128 (2003).
[27] M. Lindner, Presentation at the NOW-2012 workshop, September 9-16, Italy (2012) (2012).
[28] C. Giunti and M. Laveder, Phys. Rev. D **82**, 053005(14pp) (2010).
[29] G. Mention, M. Fechner, T. Lasserre, T. Mueller, D. Lhuillier, M. Cribier, and A. Letourneau, Phys. Rev. D **83**, 073006(20pp) (2011).
[30] K. Abazajan et al., arXiv:1204.5379[hep-ph] (2012).
[31] C. Giunti, Presentation at the νTurn-2012 workshop, May 8-10, Italy (2012) (2012).
[32] J. Kopp, M. Maltoni, and T. Schwetz, Phys. Rev. Lett. **107**, 091801(5pp) (2011).
[33] L. Lello and D. Boyanovsky, arXiv:1208.5559[hep-ph] (2012).
[34] S. Gninenko, D. Gorbunov, and M. Shaposhnikov, arXiv:1301.5516[hep-ph] (2013).
[35] A. Kusenko, Phys. Rep. **481**, 1–28 (2009).
[36] F. Bezrukov and M. Shaposhnikov, Phys. Rev. D **75**, 053005(6pp) (2007).
[37] H. de Vega, O. Moreno, E. M. de Guerra, M. R. Medrano, and N. Sanchez, arXiv:1109.3452[hep-ph] (2012).
[38] C. Kraus, A. Singer, K. Valerius, and C. Weinheimer, arXiv:1210.4194[hep-ex] (2012).
[39] A. Belesev, A. Berlev, E. Geraskin, A. Golubev, N. Likhovid, A. Nozik, V. Pantuev, V. Parfenov, and A. Skasyrskaya, arXiv:1211.7193[hep-ex] (2012).
[40] W. Bambynek, H. Behrens, M. Chen, B. Crasemann, M. Fitzpatrick, K. Ledingham, H. Genz, M. Mutterer, and R. Intemann, Rev. Mod. Phys. **49**, 77–221 (1977).
[41] G. Fogli, E. Lisi, A. Marrone, D. Montanino, A. Palazzo, and A. Rotunno, arXiv:1205.5254[hep-ph] (2012).
[42] J. Beringer et al., Phys. Rev. D **86**, 010001 (2012).
[43] J. Vergados and Y. Novikov, Nucl. Phys. B **839**, 1–20 (2010).
[44] Y. Novikov et al., arXiv:1110.2983 [physics.ins-det] (2011).
[45] M. Wurm et al., Astropart. Phys. **35**, 685–732 (2012).
[46] S. Elliot, arXiv:1203.1070 [nucl-ex] (2012).
[47] K. Zuber, J. Phys. G: Nucl. Part. Phys. **39**, 124009(12pp) (2012).
[48] G. Douysset, I. Bergström, M. Björkhage, C. Carlberg, and T. Fritioff, Phys. Rev. Lett. **86**, 4259 (2001).
[49] B. Mount, M. Redshaw, and E. Myers, Phys. Rev. C **81**, 032501(R) (2010).
[50] S. Rahaman et al., Phys. Lett. B **662**, 111 (2008).
[51] M. Redshaw, B. Mount, E. Myers, and F. A. III, Phys. Rev. Lett. **102**, 212502 (2009).
[52] N. Scielzo et al., Phys. Rev. C. **80**, 025501 (2009).
[53] M. Redshaw, E. Wingfield, J. McDaniel, and E. Myers, Phys. Rev. Lett. **98**, 053003 (2007).
[54] V. Kolhinen, T. Eronen, D. Gorelov, J. Hakala, A. Jokinen, A. Kankainen, J. Rissanen, J. Suhonen, and J. Äystö, Phys. Lett. B **697**, 116 (2011).
[55] D. Lincoln, J. Holt, G. Bollen, M. Brodeur, S. Bustabad, J. Engel, S. Novario, M. Redshaw, R. Ringle, and S. Schwarz, Phys. Rev. Lett. **110**, 012501 (2013).
[56] M. Redshaw, G. Bollen, M. Brodeur, S. Bustabad, D. Lincoln, S. Novario, R. Ringle, and S. Schwarz, Phys. Rev. Lett. **110**, 012501 (2013).
[57] F. A. III, S. Elliot, and J. Engel, Rev. Mod. Phys. **80**, 481–516 (2008).
[58] J. Gomez-Cadenas, J. Martin-Albo, M. Mezzetto, F. Monrabal, and M. Sorel, arXiv:1109.5515 [hep-ex] (2012).
[59] A. Barabash, J. Phys. G: Nucl. Part. Phys. **39**, 085103(8pp) (2012).
[60] R. Winter, Phys. Rev. **100**, 142–144 (1955).
[61] S. Eliseev, Y. Novikov, and K. Blaum, J. Phys. G: Nucl. Part. Phys. **39**, 124003(21pp) (2012).
[62] H. Georgi, S. Glashow, and S. Nussinov, Nucl. Phys. B **193**, 297–316 (1981).
[63] M. Voloshin, G. Mitsel'makher, and R. Eramzhyan, JETP Lett. **35**, 656–659 (1982).
[64] G. Bernabeu, A. Rujula, and C. Jarlskog, Nucl. Phys. B **223**, 15–28 (1983).

[65] V. Tretyak and Y. Zdesenko, At. Data and Nucl. Data Tables **80**, 83–116 (2002).
[66] J. Vergados, H. Ejiri, and F. Šimkovic, Rep. Progr. Phys. **75**, 106301(52pp) (2012).
[67] S. Eliseev et al., Phys. Rev. Lett. **106**, 052504(4pp) (2011).
[68] S. Eliseev et al., Phys. Rev. Lett. **107**, 152501(5pp) (2011).
[69] S. Eliseev, D. Nesterenko, K. Blaum, M. Block, C. Droese, F. Herfurth, E. M. Ramirez, Y. Novikov, L. Schweikhard, and K. Zuber, Phys. Rev. C **83**, 038501(3pp) (2011).
[70] S. Eliseev et al., Phys. Rev. C **84**, 012501(R)(4pp) (2011).
[71] M. Goncharov, K. Blaum, M. Block, C. Droese, S. Eliseev, F. Herfurth, E. M. Ramirez, Y. N. Novikov, L. Schweikhard, and K. Zuber, Phys. Rev. C **84**, 028501(3pp) (2011).
[72] C. Droese et al., Nucl. Phys. A **875**, 1–7 (2012).
[73] D. Nesterenko et al., Phys. Rev. C **86**, 044313(8pp) (2012).
[74] S. Rahaman, V. V. Elomaa, T. Eronen, J. Hakala, A. Jokinen, A. Kankainen, J. Rissanen, J. Suhonen, C. Weber, and J. Äystö, Phys. Rev. Lett. **103**, 042501(4pp) (2009).
[75] V. Kolhinen, V. V. Elomaa, T. Eronen, J. Hakala, A. Jokinen, M. Kortelainen, J. Suhonen, and J. Äystö, Phys. Lett. B **684**, 17–21 (2010).
[76] V. Kolhinen, T. Eronen, D. Gorelov, J. Hakala, A. Jokinen, A. Kankainen, J. Rissanen, J. Suhonen, and J. Äystö, Phys. Lett. B **697**, 116–120 (2011).
[77] C. Smorra et al., Phys. Rev. C **86**, 044604(5pp) (2012).
[78] M. Block et al., Eur. Phys. J. D **45**, 39–45 (2007).
[79] G. Savard, S. Becker, G. Bollen, H. J. Kluge, R. Moore, T. Otto, L. Schweikhard, H. Stolzenberg, and U. Wiess, Phys. Lett. A **158**, 247–252 (1991).
[80] D. L. Fang, K. Blaum, S. Eliseev, A. Faessler, M. Krivoruchenko, V. Rodin, and F. Šimkovic, Phys. Rev. C **85**, 035503(6pp) (2012).
[81] F. Larkins, At. Data and Nucl. Data Tables **20**, 311–387 (1977).
[82] T. Rodriguez and G. Martinez-Pinedo, Phys. Rev. C **85**, 044310(6pp) (2012).
[83] J. Vergados, Phys. Rev. C **84**, 044328(7pp) (2011).
[84] Center for Nuclear Studies, Department of Physics, The George Washington University. Data Analysis Center: http://www.nndc.bnl.gov; Status on February 2013.

WILEY ONLINE LIBRARY

Early View publication on wileyonlinelibrary.com
(issue and page numbers not yet assigned;
citable using Digital Object Identifier – DOI)

Ann. Phys. (Berlin), 1–10 (2013) / DOI 10.1002/andp.201300074

annalen der physik

Original Paper

MICROSCOPE – fabricating test masses for an in-orbit test of the equivalence principle

Daniel Hagedorn[1,*], *Heinz-Peter Heyne*[1], *Stephan Metschke*[1], *Uwe Langner*[1], *Sven Grüner*[1], *Frank Löffler*[1], *Vincent Lebat*[1], *Manuel Rodrigues*[2], *and Pierre Touboul*[3]

Received 25 March 2013, revised 21 May 2013, accepted 24 June 2013
Published online DD MM YYYY

The MICROSCOPE space mission is to test in 2016 the Weak Equivalence Principle (WEP) with an accuracy of 10^{-15}. This fundamental physics mission should provide answers to the basic question of the universality of free-falling bodies in a uniform gravity field. During 18 months, the mission should improve the current ground experiments by at least two orders of magnitude. The payload is composed of two electrostatic differential space accelerometers that exhibit a resolution of 2×10^{-12} m s^{-2} Hz$^{-1/2}$. By measuring the difference of acceleration between two concentric test masses at the orbital frequency, a possible WEP violation signal is extracted from the measurement where the gravity gradient effect dominates by a factor of one hundred.

This paper addresses the scientific objective of the space mission and describes how the performance drives the specification. A particular focus is made on the work jointly performed by ONERA and PTB to fulfil the fabricating requirements.

1 The weak equivalence principle test motivation

The WEP states that gravity acts on all bodies placed in a uniform gravitational field in the same way and that the acceleration is independent of the mass or composition of the body. In other words, acceleration cannot be distinguished from gravity for "free-falling objects". On this principle, Einstein founded the gravitation theory, i.e. General Relativity.

Nevertheless, some theoretical developments [1] point to a possible range of EP violation [10^{-14}–10^{-21}] as a consequence of the coupling between matter and the string dilaton, one of the promising candidates for an alternative theory of gravitation. A test of 10^{-15}, as foreseen for MICROSCOPE, is of major interest to differentiate between the alternative candidates.

To achieve this challenge, the geometry of the core parts of the accelerometers, i.e. the electrodes and the test masses, must be machined with an accuracy of a few micrometers in order to guarantee the fine electrostatic operation of the instrument and a maximum in-orbit test-mass centering displacement of 20 μm. With the help of the in-orbit calibration process, the test-mass centering is afterwards computed with 0.1 μm accuracy in order to subtract the effect of the Earth's gravity, which is a well-known gradient from the acceleration data. Thus, the performance of the mission relies dramatically on the machining and precise metrology of the parts of the sensor core and particularly on the test masses.

In the best ground test [2] a torsion pendulum was operated by the EötWash group. Test masses made of copper, aluminum, silica, titanium or beryllium were used. To cope with perturbation signals in the laboratory, the authors placed the test masses on turntables in order to modulate the signal to a higher frequency, helping also to reject part of the long-term drift or of the stochastic errors. The best achieved accuracy of this experiment is $(0.3 \pm 1.8) \times 10^{-13}$ with Be and Ti test masses. Besides statistical errors, the main source of disturbance originates in time variations of gravity gradients and thermal noise. For the former, it depends mainly on the environment: seismic and human activities, building stability, gravity gradients from nearby hills, etc. Optimistic

* Corresponding author E-mails: daniel.hagedorn@ptb.de
[1] Physikalisch-Technische Bundesanstalt (PTB), Bundesallee 100 D-38116, Braunschweig, Germany
[2] Office National d'Etudes et de Recherches Aérospatiales (ONERA), 29 avenue de la Division Leclerc 92320, Châtillon, France
[3] ONERA, Chemin de la Hunière, BP 80100, 91123 PALAISEAU CEDEX Palaiseau, France

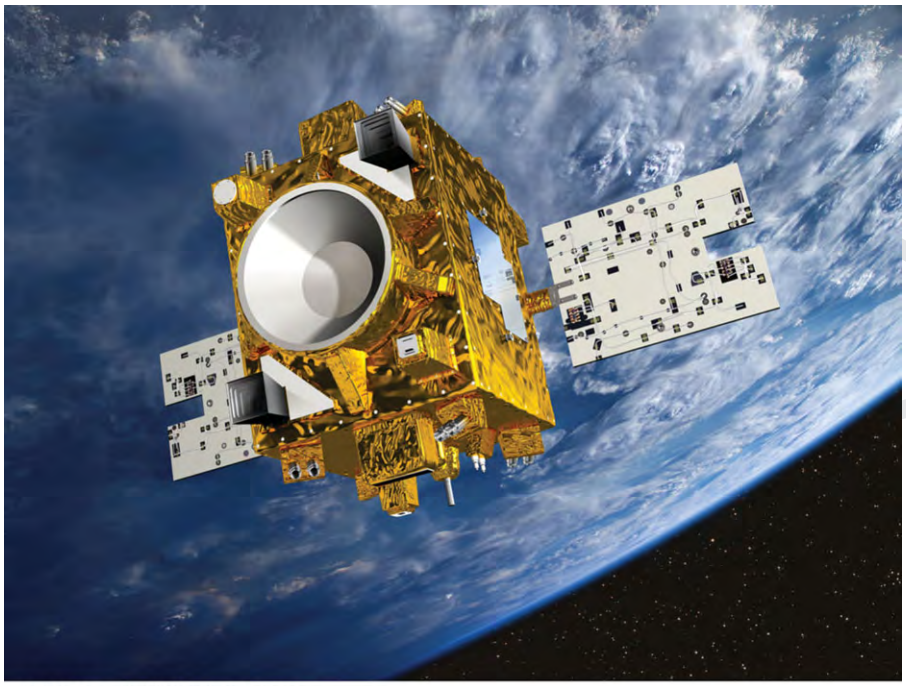

Q2 **Figure 1** An artist's view of the MICROSCOPE satellite (courtesy of CNES).

projections for improving the sensitivity suggest one order of magnitude within 5 years.

2 The MICROSCOPE mission and performance drivers

The MICROSCOPE (Micro-Satellite à traînée Compensée pour l'Observation du Principe d'Equivalence) mission is a European space fundamental physics experiment led by the French Space Agency, CNES, with a satellite launch in 2016. Proposed by the Observatoire de la Cote d'Azur and ONERA [3] in the frame of the CNES Myriad microsatellite programme, MICROSCOPE takes advantage of the best technologies currently available to perform the WEP test in space with an accuracy of at least 10^{-15} [4]. Performing the WEP test in space allows limiting all gravitational disturbances due to seismic noise or human activity. The residual gravity disturbance remaining due to the satellite thermal expansion has been estimated to be less than 2–10^{-16} m s^{-2} and is thus compatible with the mission objectives. Moreover, one can take advantage of long measurement periods with the 18-month mission leading to about 1200 useful orbits for the benefit of the rejection of stochastic disturbances.

At the core of the MICROSCOPE satellite, the payload is composed of two differential electrostatic space accelerometers. Each of the accelerometers contains one pair of test masses. The first instrument serves to test the WEP (outer test mass TiAl6V4, inner test mass PtRh10), while results from the second one (both PtRh10) are to help to eliminate systematic errors as no violation signal is obviously expected for the same material.

3 Measurement equation and performance objective

For an ideal test of the EP one would use two spherical test masses with identical radii and a perfectly homogeneous density distribution located at the same point. As such, a configuration cannot be realized in an actual experimental setup, test masses in the form of hollow cylinders have been selected. For technical reasons, additional features are required as described below. However, the shape has been optimized to obtain the same value of the inertia matrix along the three axes, as is the case for the sphere. Indeed, a difference of inertia values induces a defect in the angular measurement output of the accelerometer that does not purely depend on angular acceleration.

In the MICROSCOPE project, in each accelerometer, two hollow cylinders, aligned as concentrically as possible, are orbiting in the Earth's gravity field.

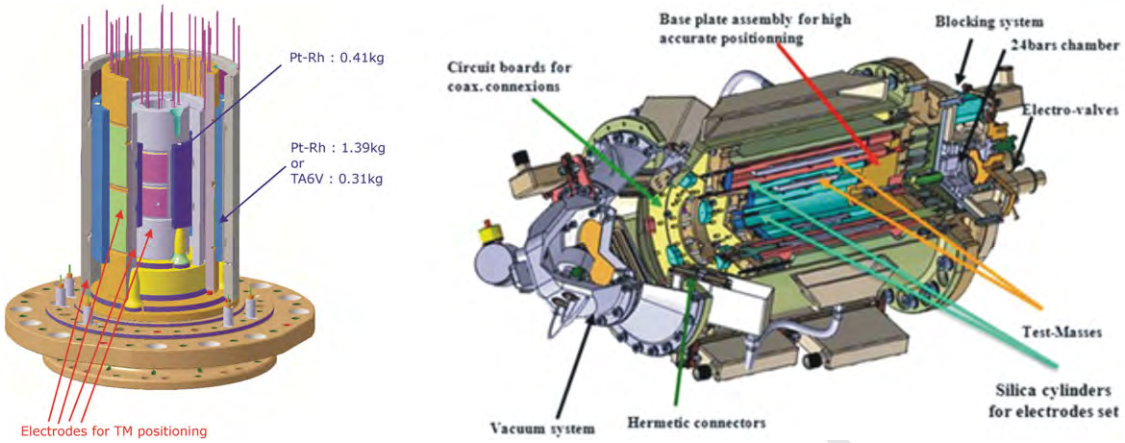

Figure 2 Left: Test masses surrounded by the electrodes. Right: Cut-off of the sensor unit with its sensor core, the blocking mechanism for in-orbit test-mass release, the vacuum system.

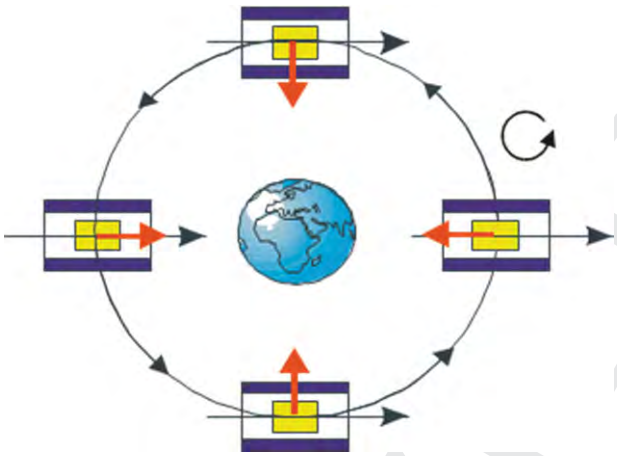

Figure 3 Orbital motion of MICROSCOPE: measurement frame in black, gravitational field in red.

Electrostatic fields maintain both test masses motionlessly with respect to the surrounding sensing electrodes. By finely measuring the difference of the electrostatic forces needed to maintain the two bodies in a motionless state, one can deduce whether both test masses are being accelerated equivalently or not. To take advantage of the accelerometer performance, the satellite is maintained in an inertial pointing mode or slowly rotated about the axis normal to the orbital plane, see Fig. 3. The Earth's gravity field is then projected either along the measurement axis at the orbital frequency or at the satellite rotation frequency in addition to the orbital frequency. More details of the satellite and the instrument description are provided in ref.4.

The requirements concerning the accuracy of the test-mass geometry can be deduced as follows. In a perfect free fall, the test-mass acceleration is expressed by Newton's law:

$$m_{Ik}\overrightarrow{\Gamma_{\mathrm{App},k}} = m_{Gk}\vec{g}\,(O_k)\,,$$

where m_{Ik} is the inertial mass of the body placed in O_k and $\overrightarrow{\Gamma_{\mathrm{App},k}}$ is its acceleration.

In a uniform gravity field, the force exerted on the mass is $m_{Gk}\vec{g}\,(O_k)$, g expressing the gravity field and m_{Gk} the gravitational mass of the body. The WEP implies: $m_{Ik} = m_{Gk}$ and $\overrightarrow{\Gamma_{\mathrm{App},k}} = \vec{g}\,(O_k)$.

In the MICROSCOPE experiment, the test masses are submitted to electrostatic forces $\vec{F}el_k$ which maintain the bodies motionlessly with respect to the satellite that in turn is submitted to nongravitational forces (drag, radiation pressure) $\vec{F}ext$ and to thruster actuations $\vec{F}th$. O_{sat} describes the center of gravity of the satellite.

The applied acceleration to the mass k in the test-mass reference frame is expressed by:

$$\overrightarrow{\Gamma_{\mathrm{App},k}} = \frac{\vec{F}el_k}{m_{Ik}} = \frac{M_{\mathrm{Gsat}}}{M_{\mathrm{Isat}}}\vec{g}\,(O_{\mathrm{sat}}) - (1+\delta_k)\,\vec{g}\,(O_k) + R_{\mathrm{In,COR}}\left(\overrightarrow{O_{sat}O_k}\right) - \frac{\vec{F}\,pa_k}{m_{Ik}} + \frac{\vec{F}ext}{M_{\mathrm{Isat}}} + \frac{\vec{F}th}{M_{\mathrm{Isat}}}.$$

The term $\frac{\vec{F}\,pa_k}{m_{Ik}}$ expresses the contribution of the internal parasitic forces applied to each mass k.

The term $\frac{m_{Gk}}{m_{Ik}} = 1+\delta_k$ expresses the ratio of the gravitational mass to the inertial mass, which is different from unity if the EP is violated and depending on the test-mass material [1]. The gravitational mass M_{Gsat} and the inertial mass M_{Isat} of the satellite are also considered.

The term $R_{\mathrm{In,COR}}\left(\overrightarrow{O_{\mathrm{sat}}O_k}\right)$ stands for the inertia and the Coriolis accelerations in the satellite frame due to

the satellite attitude motion. If the test-mass electrostatic control is sufficiently stiff, the residual relative motion can be neglected and the inertia effect is simply expressed by: $\dot{\vec{\Omega}} \wedge \overrightarrow{O_{\rm sat}O_k} + \vec{\Omega} \wedge (\vec{\Omega} \wedge \overrightarrow{O_{\rm sat}O_k})$, where $\vec{\Omega}$ represents the angular velocities of the satellite with respect to the inertial reference frame.

Finally, the expression of the differential acceleration applied on the two test bodies (i) and (j) is given by:

$$\begin{aligned}\overrightarrow{\Gamma_{{\rm App},i}} - \overrightarrow{\Gamma_{{\rm App},j}} &= \left(\delta_j - \delta_i\right)\vec{g}\left(O_j\right) + (1+\delta_i)\,[T]\,\overrightarrow{O_iO_j} \\ &\quad - R_{\rm In,COR}\left(\overrightarrow{O_iO_j}\right) - \frac{\vec{F}\,pa_i}{m_{Ii}} + \frac{\vec{F}\,pa_j}{m_{Ij}} \\ &= \overrightarrow{\Gamma_{{\rm app},i}} - \overrightarrow{\Gamma_{{\rm app},j}} - \frac{\vec{F}\,pa_i}{m_{Ii}} + \frac{\vec{F}\,pa_j}{m_{Ij}}\end{aligned}$$

.

O_iO_j is the distance between the two bodies.

$[T]$ is a linear approximation of the gravity field variations:

$$\vec{g}\left(O_j\right) - \vec{g}\left(O_i\right) = [T]\,\overrightarrow{O_iO_j} + {\rm O}(T2).$$

The second-order gravity development terms $T2$ are very small indeed, leading to an acceleration residual smaller than 2×10^{-17} m s^{-2}.

$\left(\delta_j - \delta_i\right)\vec{g}\left(O_j\right)$ represents the violation signal of the EP if it exists.

At the 700 km-altitude of the microsatellite, the Earth's gravity has a value of 7.96 m s^{-2}. In order to detect a potential EP violation at 10^{-15}, it is necessary to measure a difference of acceleration as small as $\left(\delta_j - \delta_i\right)\vec{g}\left(O_j\right) = 7.96 \times 10^{-15}$ m s^{-2} at the EP test frequency. This is the objective of accuracy of the differential accelerometer: all sources of error are evaluated and their contributions to the global accuracy are summarized hereafter [4].

4 Centering requirements

$$(1+\delta_i)\,[T]\,\overrightarrow{O_iO_j} \approx [T]\,\overrightarrow{O_iO_j}$$

represents the effect of the Earth's gravity gradient, because the test-mass alignment cannot be perfectly concentric. The components of $[T]$ have amplitudes of less than 5×10^{-9} m s^{-2}/m at the measurement frequency (i.e. the orbital frequency with an inertial pointing satellite). Hence, the test-mass centering accuracy must be specified to 0.1 μm along the two directions of the orbital plane that are affected by the Earth's monopole term. This specification cannot be achieved with any technology available.

Fortunately, the Earth's gravity is very well known, an achievement of the space missions GRACE and GOCE [5]. By evaluating the effect of the Earth's gravity gradient at twice the orbital frequency, the off-centering is calibrated in the orbital plane and its effect at orbital frequency can thus be subtracted.

The application of this in-orbit procedure [4] allows the relaxation of the requirement of the test-mass centering during integration to 20 μm. This specification must include the following error contributors:

- the electrostatic biasing;
- the machining limitations; and
- the accuracy of the mounting process (integration).

The former is due to electronics offsets of the position sensor that are wrongly interpreted by the servoloop accelerometer as a test-mass displacement. This contribution is easily measured on the ground through the electronics characterisation and has been optimized in terms of value and stability, its overall contribution being less than 0.2 μm.

The second contributor to the off-centering is caused by deviations from the optimal geometry of the sensor core that modifies the electrostatic field between the sensor electrodes made of gold-coated silica and the test masses. The silica parts are obtained by a specific ultrasonic machining process that allows an accuracy of a few micrometers when assisted by laser interferometry as in situ control.

As shown in Fig. 4, the operation of the electrostatic loop will move the mass according to the defects of symmetry of the geometry. When the test mass moves towards the right, the capacitance on the right, $C2$, increases while the capacitance on the left, $C1$, decreases. If the geometry were ideal, $C1$ would equal $C2$ when the test mass was centered. The electrostatic servo loop acts to equalise the two capacitances and thus the test mass remains motionless and centered in the electrode frame (along X in this simple example). If the test mass is shaped as a cone of angle α, the servo loop will again displace the test mass in order to equalise both capacitances. But due to the small slope, $C1$ and $C2$ are not symmetric and the test mass is displaced by δl evaluated in this case to:

$$C1 = C2 \quad \text{when} \quad x = \delta{\rm l} = -\alpha\frac{(L_{\rm PM} - Lel)\,Lel}{2gap}.$$

For the qualification test-mass model, the angle is about 7 μm over the 60-mm length leading to a generated miscentering of 30 μm. To cope with this value, which is too large, the defects on the electrode cylinders, when smartly orientated, can compensate the

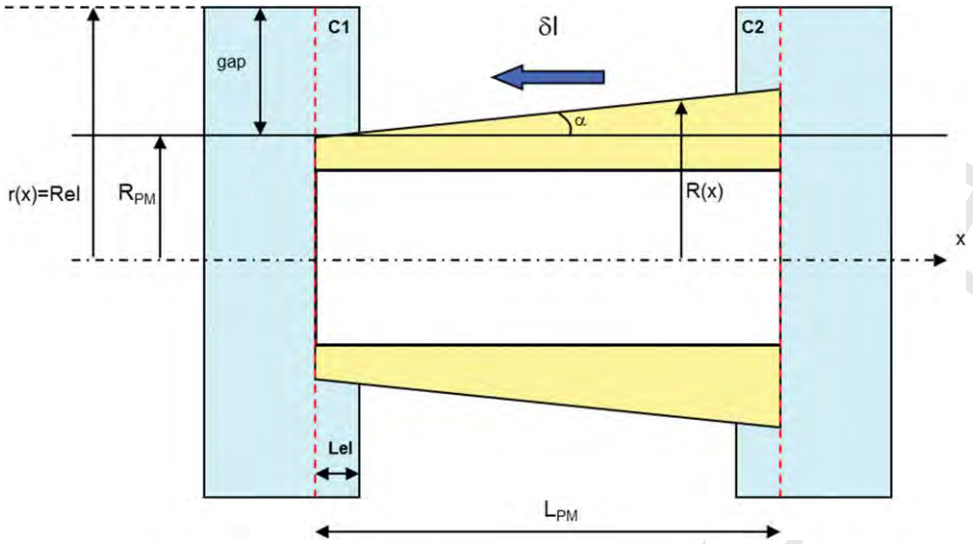

Figure 4 Schema of a TM conicity for the capacitance sensing position of the test-mass TM along *X*.

test-mass defects: fortunately this was the case. For the flight models, the machining procedures have been optimized and this defect has been reduced by one order of magnitude.

For the third contributor, the relative centering of the two concentric test masses relies also on the mounting procedure of the overall core that accurate machining and permanent metrology enable to guarantee an accuracy of a few micrometers.

5 Acceleration disturbances in the measurement

$-\frac{\vec{F}pa_i}{m_{Ii}} + \frac{\vec{F}pa_j}{m_{Ij}}$ represents the difference of the parasitic acceleration applied on the two test masses: stochastic accelerations and systematic tone errors at the EP measurement frequency must be considered.

As the orbital motion can be maintained very stably because of the drag-free satellite, one can take advantage of very long steady periods of integration in order to reduce the stochastic noises to a level of a few 10^{-15} m s^{-2}. The instrument's major source of noise, the mechanical residual damping of the test mass, is of the order of 2 $\times 10^{-12}$ m s^{-2} Hz$^{-1/2}$. Integrating over 120 orbits ($\sim 7\times 10^5$ s) reduces this contribution to 2.4 $\times 10^{-15}$ m s^{-2} at the EP measurement frequency.

$R_{\mathrm{In,COR}}\left(\overrightarrow{O_{\mathrm{sat}}O_k}\right)$ represents the effect of the satellite angular velocity or angular acceleration. This term can only be controlled by the satellite attitude system [4]. The accelerations along the 6 degrees of freedom are fortunately provided by the instrument itself, and the satellite-pointing system nullifies the angular acceleration measured by the 6-axis accelerometers. Nevertheless, the angular and linear axes of the measurement depend on the test-mass shape and inertia. Thus, the requirements of the test-mass geometry are deduced.

6 Developing the test masses: test mass description

Each hollow cylinder test mass for the MICROSCOPE differential accelerometer has four flat areas at the outer shell and six precision countersinks at each face. The flat areas are used to control the test-mass rotation, while the countersinks serve as seats for the blocking mechanism that clamps the test masses during launch.

The large PtRh10 and TiAl6V4 test masses are 69.395 mm in outer diameter, 60.800 mm in inner diameter, and have a length of 79.830 mm – tolerance: 3 μm and below. The small PtRh10 test masses are 34.400 mm in outer diameter, 30.800 mm in inner diameter, and have a length of 43.332 mm – tolerance: 3 μm and below.

TiAl6V4 is used in aeronautics and motorsports due to its machinability and form stability in the range of less than 10 μm. However, to achieve and maintain form and dimension tolerances of less than 5 μm, a multi-stage heat treatment and special low-force turning parameters have to be applied. PtRh10 is a soft and ductile material and therefore not ideal for turning. Only a small window of cutting parameter space (turning speed, feed, amount of lubricant sprayed at the tool) and the use of polycrystalline diamonds lead to an acceptable surface quality.

However, because of the overall geometrical complexity of the test masses with stringent requirements on shape, sizes and center of gravity, and due to the fact that each surface is referenced to all connecting surfaces, turning is the technology of choice for the manufacturing of all test masses [6].

7 Developing the test masses: the need for high-precision in situ measurement

Any form of mechanical machining is subject to tool wear. In standard applications a mean time before tool wear-out or failure is determined, by which time the tool has to be replaced. In the case of the fabrication of the MICROSCOPE test masses, this approach is not applicable, because even small defects or extraordinary wear of the cutting tool due to surface anomalies like hard rhodium clusters embedded in softer platinum surroundings may lead to a significant form deviation or even damage to the test-mass surface beyond any repair. This is, of course, especially valid at the end of the fabrication, when all dimension, form and surface roughness parameters have to be achieved with one last and final cut.

In order to gain the information necessary for the correction and, of course, the determination of the final form and dimensions, high-precision in situ measuring equipment has to be installed inside the BENZINGER *TNI* precision fabrication station. As the fabrication tools use the same frame as the measuring equipment, two distinct adjustment steps are necessary.

First, certified ring and plug gauges (the outer and inner diameters of which, respectively, are identical to those of the final test masses and whose cylindricity is within the specifications of the test masses, as well) are placed at the exact position the test mass will be mounted at during fabrication. The diameter is determined by contact measurement (using a Renishaw OMP 400 high accuracy touch probe and SiN balls to minimise adhesion) of several tens of points along the respective diameter and calculating the best fitting circle and its respective diameter. The in situ measurement verification of the inner and outer diameter has to pass a rigorous regime of measurement and repetition measurement. Only if the comparison of all measurements shows a deviation of less than one micrometer, is the adjustment regarded as successful.

Secondly, during test-mass fabrication, along several z-axis positions (the z-axis being the central axis of the adjustment standard/test mass), the inner and outer diameters are measured. Additionally, the distance from the test-mass center, the flatness and the angle of all four flats of the body are measured, too. Hereafter, the adjustment standard is transferred to a coordinate measuring machine (CMM) and measured against calibrated gauges at exactly the same positions. The results are in turn used to adjust the precision fabrication machine. The overall uncertainty budget has been verified to be less than two micrometers. Results above this limit are rejected and the procedures are repeated in total.

Through this approach, the results are traceable to the SI unit of length.

Only the combination of both adjustment procedures guarantees reproducible results. The second step is vital to the success, because both the tool holder and the measuring setup are mounted at the same frame. Thus, defects of the frame itself cannot be detected using the first method only.

Though it may seem that other methods of mechanical engineering like polishing or even electrical discharge machining (EDM) might be advantageous over turning, this is only true for single aspects of the overall fabrication work flow. Polishing, for example, would result in an improved surface roughness, especially of the PtRh10 alloy. Still, other parameters like concentricity or precision of angles with its very low tolerances could not be achieved. Not least the position and depth of the countersinks, especially on the second face, call for an exact knowledge of both the test mass and the tool positions. At a precision fabrication station, the whole manufacturing of the test mass can be achieved in just two clamping positions.

Upon beginning the fabrication, a thread is cut at one end of the hollow cylinder and the raw-mass is screwed against the dead stop of a custom-made brass adapter. In this way the mounting forces are directed almost completely in the z-direction and any unloading of stress after unmounting the finished test mass is reduced to the technical minimum, see Fig. 5.

Whilst clamping the first face, the inner and outer diameter, the four flats at the outer shell, the 45° angle chamfers connecting the faces and the inner and outer shell along with the six countersink are fabricated. The form and aperture of the countersinks are determined by carefully selecting optimal styli, test drilling countersinks using identical materials and drilling parameters, measuring the test countersinks on a specialized CMM (ZEISS F25), and, additionally, allowing for tool wear.

Hereafter, the test mass is unmounted and the thread is removed by means of wire EDM. Then, the test mass is mounted at the precision fabrication station again, this time using an adapted clamping system (Hainbuch

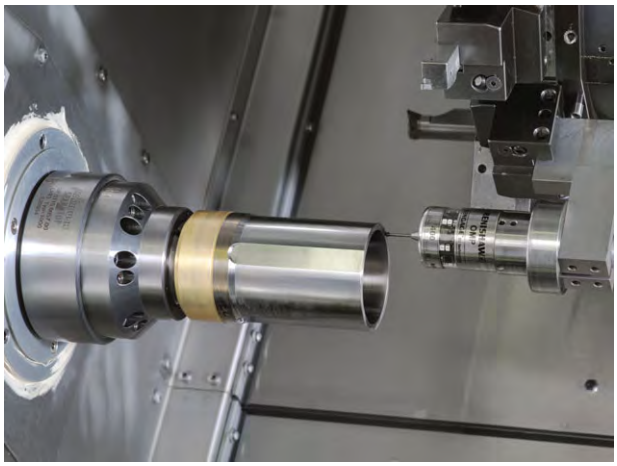

Figure 5 PtRh10 TM mounted at a brass adapter and testing probe inside the precision fabrication station.

Figure 6 One large Ti TM fixed at the measuring stand at the Leitz *reference* 600 CMM.

company), which allows secure clamping, while at the same time not damaging the inner shell's surface.

Once again, the motion control system of the precision fabrication station is adjusted against a calibrated gauge block and then the length, the second face, and the final six countersinks are fabricated.

8 Developing the test masses: measuring the test masses

After fabrication, the test masses undergo extensive measurements. Besides form and dimension measurements [7], density, thermal expansion, and the mass are determined also.

The form and dimension measurements consist of tactile measurements performed using a calibrated Leitz *reference* 600 CMM, see Fig. 6. Basically, for reasons of comparability, measurements are performed at exactly the same positions as they were conducted during fabrication with respect to circumference and the z-axis. To gain a higher resolution, additional measurements were taken between these points and at additional z-positions especially close to the faces. From these results, all necessary features (diameters, length, concentricity, parallelism, planarity of both the flats and the faces, position of countersinks) are determined. Figure 7 shows a photo composition of the inner and the outer test mass.

Tactile measurement has been chosen, since the accuracy of optical methods was found to be inadequate as a result of the roughness of the test-mass surfaces. While for the Ti alloy a surface roughness of about Ra $\approx$ 100 nm was achieved, which would allow the use of optical

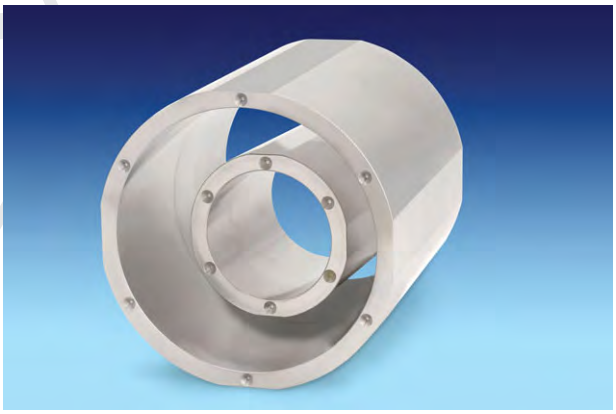

Figure 7 Photo composition of both inner and outer TM.

methods, the surface roughness of the PtRh10 was found to be about a factor of three higher, leading to a significantly larger error budget, when optical measurements were conducted during the development of the fabrication and measuring procedure.

As a rule, before and after the measurement of the test masses, custom-made calibrated gauges with diameters identical to those of the test masses are measured. Then each test mass is measured in four positions: horizontally mounted, inverse horizontally mounted, vertically mounted, and inverse vertically mounted. All measurement results have to comply with the two-micrometer criterion of the overall uncertainty budget.

The countersinks are measured using the ultraprecision CMM ZEISS F25. Here, position, depth, aperture, and the angle of the countersink's central axis with respect to the faces are determined.

All additional measurements (density, thermal expansion, and mass) are performed by PTB's dedicated laboratories.

The density of the test masses is determined by direct measurement of all test masses, apart from the large PtRh10 mass, because it is too heavy for the setup available. An uncertainty of up to 5×10^{-5} can be reached.

A direct measurement of the density distribution to determine the test-masses' multipole moments was considered, but finally rejected due to insufficient resolution. Instead, in addition to the density measurement of the test mass itself, the density of rings, separated from both ends of the test masses, were measured and the respective results were compared. It was found that, in all cases, the measured density was in a band of 1×10^{-4} and, hence, the density distribution was regarded as adequate.

The thermal expansion coefficient is measured in the range from 18 °C to 24 °C with an uncertainty of 10^{-8}. As the space experiment is conducted at about 300 K, this is the range of choice.

Finally, the mass is determined with a precision of below 10^{-7}.

9 Conclusion and outlook

The MICROSCOPE space test of the Weak Equivalence Principle will be launched in 2016 on board a drag-free satellite. The experiment will operate on a polar orbit for about two years. The two differential accelerometers at the core of the experiment each hold two test masses comprising PtRh10 and TiAl6V4 alloys.

The 10^{-15} accuracy of the test, the electrostatic operation of the instrument, the capacitive position sensing of the test masses, as well as the corrections of the mass off-centering, require a demanding geometry. Extensive effort has been carried out to develop the means for both fabrication and measurement of the necessary core components, foremost the silica casing and the test masses. A fabrication precision has been achieved, formerly unreached for these kinds of materials, guaranteeing the necessary in-orbit centering accuracy of 20 μm. The flight models of the test masses were produced according to the precisions established and meet the mission requirements.

Though the experiment is not completed at the time of writing, the community is already discussing a follow-up mission. Several concepts are on the table, not least the development of an orbit-based, superconducting accelerometer, which could improve the experiment's uncertainty down to the 10^{-18} range, but with even more stringent requirements on the test masses.

Acknowledgements. PTB's Scientific Instrumentation Department would like to thank the dedicated PTB Departments of Mass (1.1), Analytics and Thermodynamic State Behaviour of Gases (3.2), Dimensional Nanometrology (5.2), Coordinate Metrology (5.3), and Interferometry on Material Measures (5.4) for their valuable support in metrological characterisation of the test masses. The authors also want to acknowledge the CNES for their support and funding to develop the payload, the national aeronautics and space research center of the Federal Republic of Germany (DLR) for supporting the test-mass material, the Bremen ZARM centrum for their contribution to the qualification and acceptance tests of the payload in free-fall conditions. Part of the work is funded by ONERA and PTB.

Key words. xxxxx.

References

[1] T. Damour and A. M. Polyakov, Nucl. Phys. B **423/3–2** 855–235 (1994).

[2] S. Schlamminger, K.-Y. Choi, T. A. Wagner, J. H. Gundlach, and E. G. Adelberger, Phys. Rev. Lett. **100**, 041101 (2008).

[3] P. Touboul, M. Rodrigues, G. Métris, and B. Tatry, Comptes Rendus de l'Académie des sciences, IV-tome 2-N, 9 (2001).

[4] P. Touboul, G. Métris, V. Lebat, and A. Robert, Class. Quantum Gravity 29 (2012).

[5] P. Touboul, B. Foulon, M. Rodrigues, and J. P. Marque; Aerospace Sci. Technol. **8**, 431–441 (2004).

[6] D. Hagedorn, H.-P. Heyne, H. Reimann, M. Neugebauer, S. Grüner, St. Metschke, and F. Löffler, ISBN **13**: 978-0-9553082-6-0, 29-32, EUSPEN 2009.

[7] O. Jusko, N. Gerwien, D. Hagedorn, F. Härtig, H.-P. Heyne, U. Langner, F. Löffler, St. Metschke, M. Neugebauer, and H. Reimann, Proc. ISPEMI 2010, 6th International Symposium on Precision Engineering Measurements and Instrumentation, 8.-11.8. 2010, Hangzhou, China.

Queries

Q1: Author – **Please check all heading numbers.**
Q2: Author – **Figures 1 and 2 citations are missing. Please suggest.**
Q3: Author – **Please provide keywords.**
Q4: Author – **Volume/page numbers?**

WILEY-BLACKWELL

USING e-ANNOTATION TOOLS FOR ELECTRONIC PROOF CORRECTION

Required software to e-Annotate PDFs: Adobe Acrobat Professional or Adobe Reader (version 8.0 or above). (Note that this document uses screenshots from Adobe Reader X)
The latest version of Acrobat Reader can be downloaded for free at: http://get.adobe.com/reader/

Once you have Acrobat Reader open on your computer, click on the Comment tab at the right of the toolbar:

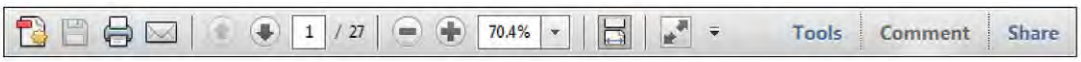

This will open up a panel down the right side of the document. The majority of tools you will use for annotating your proof will be in the Annotations section, pictured opposite. We've picked out some of these tools below:

1. Replace (Ins) Tool – for replacing text.

Strikes a line through text and opens up a text box where replacement text can be entered.

How to use it

- Highlight a word or sentence.
- Click on the Replace (Ins) icon in the Annotations section.
- Type the replacement text into the blue box that appears.

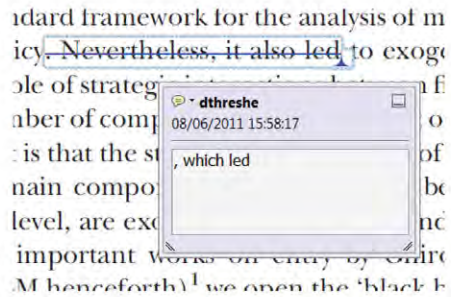

2. Strikethrough (Del) Tool – for deleting text.

Strikes a red line through text that is to be deleted.

How to use it

- Highlight a word or sentence.
- Click on the Strikethrough (Del) icon in the Annotations section.

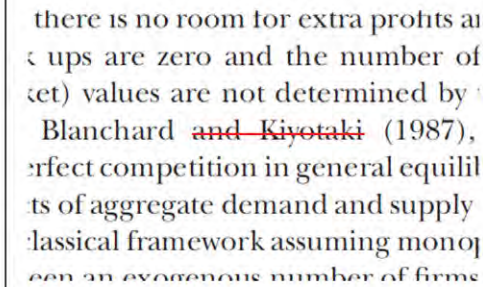

3. Add note to text Tool – for highlighting a section to be changed to bold or italic.

Highlights text in yellow and opens up a text box where comments can be entered.

How to use it

- Highlight the relevant section of text.
- Click on the Add note to text icon in the Annotations section.
- Type instruction on what should be changed regarding the text into the yellow box that appears.

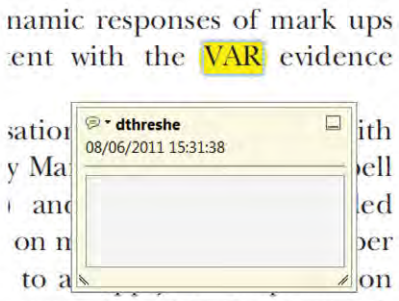

4. Add sticky note Tool – for making notes at specific points in the text.

Marks a point in the proof where a comment needs to be highlighted.

How to use it

- Click on the Add sticky note icon in the Annotations section.
- Click at the point in the proof where the comment should be inserted.
- Type the comment into the yellow box that appears.

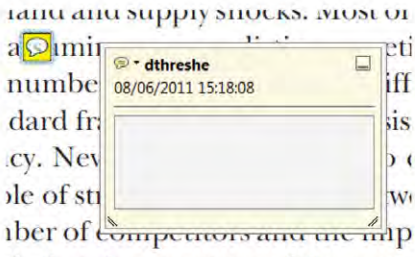

WILEY-BLACKWELL

USING e-ANNOTATION TOOLS FOR ELECTRONIC PROOF CORRECTION

5. Attach File Tool – for inserting large amounts of text or replacement figures.

Inserts an icon linking to the attached file in the appropriate pace in the text.

How to use it

- Click on the Attach File icon in the Annotations section.
- Click on the proof to where you'd like the attached file to be linked.
- Select the file to be attached from your computer or network.
- Select the colour and type of icon that will appear in the proof. Click OK.

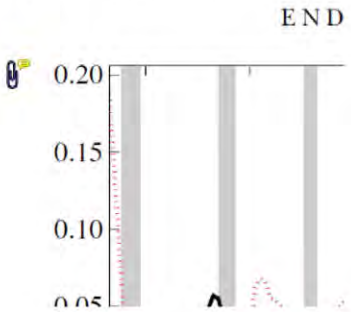

6. Add stamp Tool – for approving a proof if no corrections are required.

Inserts a selected stamp onto an appropriate place in the proof.

How to use it

- Click on the Add stamp icon in the Annotations section.
- Select the stamp you want to use. (The Approved stamp is usually available directly in the menu that appears).
- Click on the proof where you'd like the stamp to appear. (Where a proof is to be approved as it is, this would normally be on the first page).

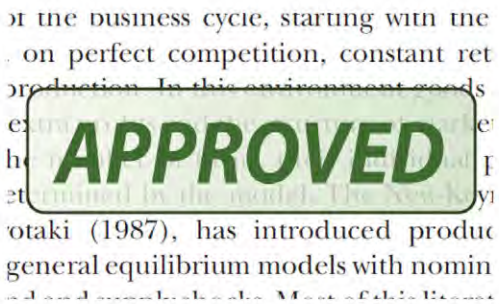

7. Drawing Markups Tools – for drawing shapes, lines and freeform annotations on proofs and commenting on these marks.

Allows shapes, lines and freeform annotations to be drawn on proofs and for comment to be made on these marks..

How to use it

- Click on one of the shapes in the Drawing Markups section.
- Click on the proof at the relevant point and draw the selected shape with the cursor.
- To add a comment to the drawn shape, move the cursor over the shape until an arrowhead appears.
- Double click on the shape and type any text in the red box that appears.

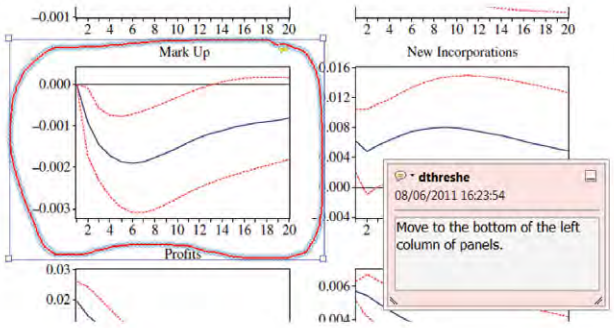

For further information on how to annotate proofs, click on the Help menu to reveal a list of further options:

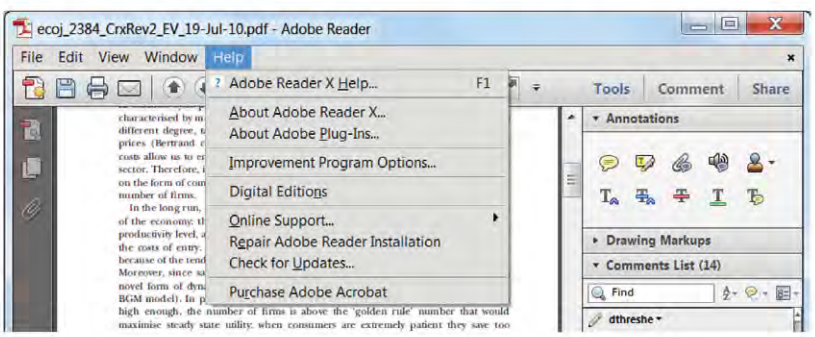

Instructions for Proof Corrections and Orders

annalen der physik

2013

WILEY-VCH Verlag GmbH
& Co. KGaA
Annalen der Physik
Rotherstrasse 21
10245 Berlin
Germany
TEL +49 (0) 30–47 03 13 21
FAX +49 (0) 30–47 03 13 99
E-MAIL ann-phys@wiley.com

WILEY
Publishers Since 1807

Please correct your proofs and return them within 5 days together with the completed reprint order form. The editors reserve the right to publish your article with editors' corrections if your proofs do not arrive in time.

After having received your corrections, your paper will be published online soon in the Wiley Online Library (wileyonlinelibrary.com).
Please keep in mind that reading proofs is your responsibility. Corrections should therefore be clear. We prefer the corrections be made directly within the PDF file (see E-annotations instructions). Alternatively, you may provide us with a list of corrections by e-mail, with the corrections referring to their line number.
Manuscript files are sometimes slightly modified by the production department to follow general presentation rules of the journal.

Note that the quality of the halftone figures is not as high as the final version that will appear in the issue.

Check the enclosed proofs very carefully, paying particular attention to the formulas (including line breakings introduced in production), figures, numerical values, tabulated data and layout of the pages.

A black box (■) or a question at the end of the paper (after the references) signals unclear or missing information that specifically requires **your attention.** Note that the author is liable for damages arising from incorrect statements, including misprints.

The main aim of proofreading is to correct errors that may have occurred during the production process, **and not to modify the content of the paper**. Corrections that may lead to a change in the page layout should be avoided.

Note that sending back a corrected **manuscript** file **is of no use**.

Return the corrected proofs within 5 days by e-mail.

Please do not send your corrections to the typesetter but to the Editorial Office:

E-MAIL ann-phys@wiley.com

Please limit corrections to errors in the text; cost incurred for any further changes or additions will be charged to the author, unless such changes have been agreed upon by the editor.

If your paper contains **color figures**, please fill in the Color Print Authorization and note the further information given on the following pages.

Full color reprints, Customized PDF files, Printed Issues, Color Print, and Cover Posters may be ordered by filling in the accompanying form.

Order Form

annalen der physik

2013

WILEY-VCH Verlag GmbH
& Co. KGaA
AdP Editorial Office
Rotherstrasse 21
10245 Berlin
Germany
TEL +49 (0) 30-47 03 13 21
FAX +49 (0) 30-47 03 13 99
E-MAIL ann-phys@wiley.com

WILEY
Publishers Since 1807

Please complete this form and return it by e-mail or FAX.

Article No.

Author/Title

e-mail address

Required Fields may be filled in using Adobe Reader

Color Print Authorization

Please bill me for

☐ color print figures (total number of color figures)

❒ YES, please print Figs. No. ☐ in color.

❒ NO, please print all color figures in black/white.

Reprints/Issues/PDF Files/Posters

Whole issues, reprints and PDF files (300 dpi) for an unlimited number of printouts are available at the rates given on the next page. Reprints and PDF files can be ordered before *and after* publication of an article. All reprints will be delivered in full color, regardless of black/white printing in the journal.

Reprints

Please send me and bill me for

☐ full color reprints with color cover

☐ full color reprints with personalized color cover

Issues

Please send me and bill me for

☐ entire issues

Customized PDF-Reprint

Please send me and bill me for

❒ a PDF file (300 dpi) for an unlimited number of printouts **with customized color cover sheet.**

The PDF file will be sent to your e-mail address.

Send PDF file to:

Please note that posting of the final published version on the open internet is not permitted. For author rights and re-use options, see the Copyright Transfer Agreement at http://www.wiley.com/go/ctavchglobal.

Cover Posters

Posters are available of all the published covers in two sizes (see attached price list). **Please send me and bill me for**

☐ A2 (42 × 60 cm/17 × 24in) posters

☐ A1 (60 × 84 cm/24 × 33in) posters

Mail reprints and/or issues and/or posters to (no P.O. Boxes):

VAT number:

Information regarding VAT

Please note that from German sales tax point of view, the charge for **Reprints, Issues or Posters** is considered as **"supply of goods"** and therefore, in general, such delivery is a subject to German sales tax. However, this regulation has no impact on customers located outside of the European Union. Deliveries to customers outside the Community are automatically tax-exempt. Deliveries within the Community to institutional customers outside of Germany are exempted from the German tax (VAT) only if the customer provides the supplier with his/her VAT number.

The VAT number (value added tax identification number) is a tax registration number used in the countries of the European Union to identify corporate entities doing business there. It starts with a country code (e.g. FR for France, GB for Great Britain) and follows by numbers.

The charge for **front cover/back cover/inside cover pictures, color figures or frontispieces publications** is considered as **"supply of services"** and therefore it is a subject to German sales tax. However, in case you are an institutional customer outside of Germany, the tax can be waived if you provide us with the VAT number of your company.

Customers outside of the EU may have a VAT number starting with "EU" instead of the country code if they are registered by the EU's tax authorities. In case you do not have a VAT number of EU and you are a taxable person doing business in a country outside EU, then please provide us with a certification from your local tax authorities confirming that you are a taxable person under the local tax law. Please note that the certification needs to confirm that you are a taxable person and you are conducting an economic activity in your country. Certifications which confirm that you are tax-exempt legal body (non-profit organization, public body, school, political party, etc.) in your country cannot be accepted for the German VAT purposes.

Purchase Order No.:

Terms of payment:

❒ Please send an invoice ❒ Cheque is enclosed

❒ **VISA, MasterCard and AMERICAN EXPRESS.**

Please use this link (Credit Card Token Generator) to create a secure Credit Card Token and include this number in the form instead of the credit card data.

https://www.wiley-vch.de/editorial_production/index.php

CREDIT CARD TOKEN NUMBER:

Send invoice to:

Signature _____

Date _____

Please use this form to confirm that you are prepared to pay your contribution.

Please sign and return this page.

You will receive an invoice following the publication of your article in the journal issue.

Price List – Annalen der Physik 2013

Reprints/Issues/PDF-Files/Posters

The prices listed below are valid only for orders received in the course of 2013. Minimum order for reprints is 50 copies. **Reprints can be ordered before *and after* publication of an article. All reprints are delivered with color cover and color figures.** If more than 500 copies are ordered, special prices are available upon request.

Single issues are available to authors at a reduced price.

The prices include mailing and handling charges. All prices are subject to local VAT/sales tax.

Reprints with color cover	Price for orders of (in Euro)					
Size (pages)	50 copies	100 copies	150 copies	200 copies	300 copies	500 copies*
1–4	345	395	425	445	548	752
5–8	490	573	608	636	784	1077
9–12	640	739	786	824	1016	1396
13–16	780	900	958	1004	1237	1701
17–20	930	1070	1138	1196	1489	2022
for every additional 4 pages	147	169	175	188	231	315
for personalized color cover	**190**	**340**	**440**	**650**	**840**	**990**

PDF file (300 dpi, unlimited number of printouts, customized cover sheet)	€ 330
Issues	€ 48 per copy for up to 10 copies.*
Cover Posters • A2 (42 × 60 cm/17 × 24in)	€ 49
• A1 (60 × 84 cm/24 × 33in)	€ 69

*Prices for more copies available on request.

Special offer: If you order 100 or more reprints you will receive a pdf file (300 dpi, unlimited number of printouts, color figures) and an issue for free.

Color figures

If your paper contains **color figures**, please notice that, generally, these figures will appear in color in the online PDF version and all reprints of your article at no cost. This will be indicated by a note "(online color at: www.ann-phys.org)" in the caption. The print version of the figures in the journal hardcopy will be black/white unless the author explicitely requests a color print publication and contributes to the additional printing costs.

	Approximate color print figure charges
First figure	€ 495
Each additional figure	€ 395 Special prices for more color print figures on request

If you wish color figures in print, please answer the **color print authorization** questions on the order form.

A nanonewton force facility to test Newton's law of gravity at micro- and submicrometer distances

Journal:	*Annalen der Physik*
Manuscript ID:	andp.201300057.R3
Wiley - Manuscript type:	Original Paper
Date Submitted by the Author:	01-Jul-2013
Complete List of Authors:	Nesterov, Vladimir; PTB, Buetefisch, Sebastian; PTB, Koenders, Ludger; PTB,
Keywords:	non-Newtonian gravity, Yukawa attractor, Dark energy, Casimir force, short-range gravitational force, nanonewton force facility, microtechnology

A nanonewton force facility to test Newton's law of gravity at micro- and submicrometer distances

Vladimir Nesterov*, Sebastian Buetefisch and Ludger Koenders

Physikalisch-Technische Bundesanstalt (PTB), Bundesallee 100, 38116 Braunschweig, Germany

Key words Dark energy, non-Newtonian gravity force, Casimir force, short-range gravitational forces, nanonewton force facility, microtechnology, Yukawa attractor

PACS 04.80.Cc, 04.80.-y, 95.36.+x

An experiment to test Newton's law of gravity at micro- and submicrometer distances using a nanonewton force facility at PTB and modern microtechnologies is proposed. It is anticipated that the proposed method can advance the search for non-Newtonian gravity forces via an enhanced sensitivity of 10^3 to 10^4 in comparison to current experiments at the micrometer length scale.

1 Introduction

Recent cosmological observations [1-3] have shown that 70 % of the entire mass and energy of the universe is a mysterious "dark energy" with a density $\rho_{vac} \approx 4.6 \cdot 10^{-10}$ J·m^{-3} and a repulsive gravitational effect. This dark energy density corresponds to a length scale $\lambda_d = [(\hbar \cdot c)/(8 \cdot \pi^2 \cdot \rho_{vac})]^{1/4} \approx 30$ μm that may represent a fundamental length scale of gravity [4-6]. The observed gravitational vacuum-energy density is about 10^{120} times smaller than the vacuum zero-point energy density computed according to the standard laws of quantum mechanics. In [7], it was suggested that this huge discrepancy (the "cosmological constant problem") could be solved if the graviton were a "fat object" (with a size comparable to λ_d) which is not influenced by the short-distance physics that dominates the vacuum energy. This scenario implies that the gravitational force would decrease for objects separated by distances $s \leq \lambda_d$. Other scenarios predict the opposite behavior: The extra space dimensions would cause the gravitational force to become stronger for $s \leq R_d$, where R_d is the size of the largest compactified dimension [8]. A number of theories of physics suggest that new physics related to gravity may appear at submillimeter length scales [9-11]. Corrections to Newtonian gravity are generally parameterized according to a Yukawa-type potential [12]. For two point masses m_1 and m_2 separated by a distance r, the gravitational potential energy is modified to

$$V(r) = -G \cdot \frac{m_1 \cdot m_2}{r} \cdot \left[1 + \alpha \cdot e^{-r/\lambda}\right], \quad (1)$$

where α is a dimensionless strength parameter and λ a length scale parameter.

* E-mail: Vladimir.Nesterov@ptb.de

Figure 1 shows the experimental constraints [6, 13-18] on the range of the parameters (α, λ) of the Yukawa form (equation (1)) for short-range gravitational forces. For the minimization of electrostatic and Casimir interactions, a stiff, conducting membrane was placed [6, 13, 19] between two probe masses. This membrane must have a very high stiffness and, at the same time, it must be very thin for testing the gravitational inverse-square law experimentally at the micrometer length scale. A method for the detection of short-range gravitational forces using optically trapped and cooled dielectric micro-spheres was described in [20].

In this paper, we propose an experiment using the nanonewton force facility at PTB to detect the very small exerted forces. The sensing element of this facility acts as one of the probe masses of the experiment – the fixed "detector". The other part consists of the second probe mass – the "attractors" with integrated shielding membranes – the "Yukawa attractor". The Yukawa attractor consists of mono-crystalline silicon which is produced by microtechnical fabrication methods. With this set-up, it is possible to test the gravitational inverse-square law at micro- and sub-micrometer distances. We anticipate that the proposed method can advance the search for non-Newtonian gravity forces via an enhanced sensitivity of 10^4 in comparison to current experiments at the micrometer length scale.

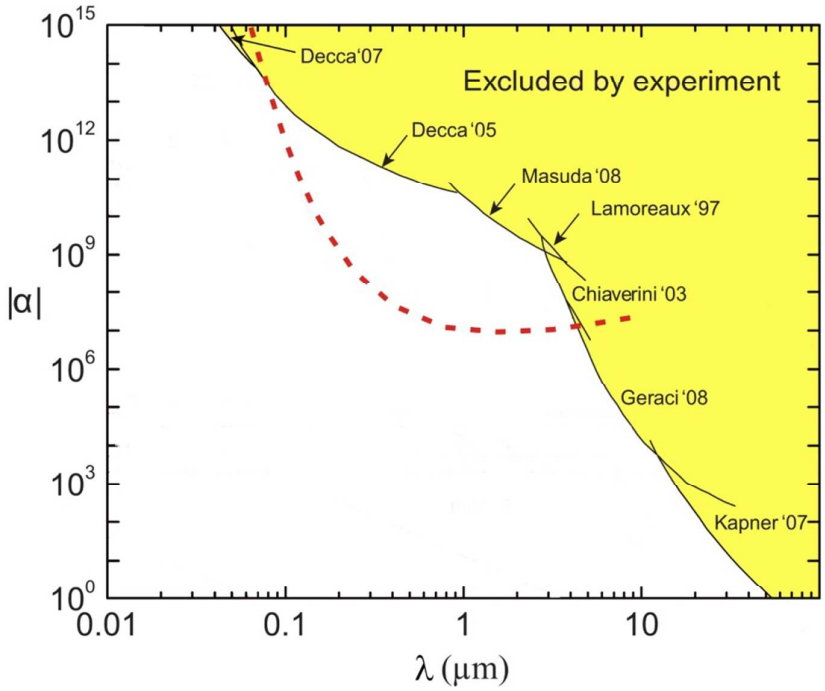

Fig. 1 Experimental constraints [6, 12-18] for short-range forces due to an interaction potential energy of the Yukawa form $V(r) = -G \cdot \frac{m_1 \cdot m_2}{r} \cdot \left[1 + \alpha \cdot e^{-r/\lambda}\right]$. The dashed line denotes the presumable improvement of the results which can be reached by the method proposed here.

2 Estimation of the gravitational force between two thin discs for the interaction potential of the Yukawa form at small distances

For a simplified representation of the analysis, an explicit analytical expression for the estimation of the gravitational force between two thin discs for the interaction potential energy of the Yukawa form $V(r) = -G \cdot \frac{m_1 \cdot m_2}{r} \cdot \left[1 + \alpha \cdot e^{-r/\lambda}\right]$ at small distances was derived. Let us consider two parallel coaxial discs as shown in Fig. 2. Disc 2 creates the gravitational potential *V(A)* in axial point A that can be written as

$$V(A) = -\int_0^{h_2} dx \int_0^R G \cdot \frac{2 \cdot \pi \cdot \rho_2}{r} \cdot \left[1 + \alpha \cdot exp\left(-\frac{r}{\lambda}\right)\right] \cdot y \cdot dy\,, \tag{2}$$

where h_2 is the thickness of disc 2, R is the radius of the discs, and ρ_2 is the density of disc 2.

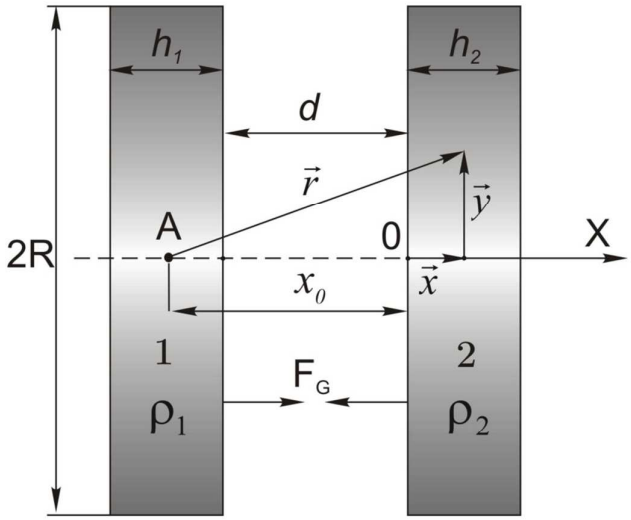

Fig. 2 Configuration for the estimation of the gravitational force between two thin discs for the interaction potential of the Yukawa form $V(r) = -G \cdot \frac{m_1 \cdot m_2}{r} \cdot \left[1 + \alpha \cdot e^{-r/\lambda}\right]$.

Assuming that $(h_1 + h_2 + d) << R$ and $R >> \lambda$, and using then equation (2), the gravitational field strength *g(A)* in the axial point *A* can be estimated by the expression

$$g(A) = \frac{\partial V(A)}{\partial x_0} \approx -B \cdot \left[h_2 + \alpha \cdot \lambda \cdot exp\left(-\frac{x_0}{\lambda}\right) \cdot \left\{1 - exp\left(-\frac{h_2}{\lambda}\right)\right\}\right], \tag{3}$$

where $B = 2 \cdot \pi \cdot \rho_2 \cdot G$.

We discard, in estimation (3), the negligibly small term δg

$$\delta g = B \cdot h_2 \cdot \left(\frac{x_0}{R} + \frac{h_2}{2 \cdot R}\right)\,. \tag{4}$$

Neglecting the edge effect of the gravity at the edges of the discs with the size of approximately λ, the gravitational force F_G acts on each of the discs and can be determined by the integration of equation (3) over the volume of disc 1:

$$F_G \approx S \cdot B \cdot \int_{-(d+h_1)}^{-d} \left[h_2 + \alpha \cdot \lambda \cdot exp(-\tfrac{x_0}{\lambda}) \cdot \left\{1 - exp(-\tfrac{h_2}{\lambda})\right\}\right] \cdot dx_0 \ , \quad (5)$$

where $S = \pi R^2$ is the area of the disc, h_1 is the thickness of disc 1, and d is the distance between the discs, respectively.

Using equation (5), we obtain the following explicit analytical expression for the estimation of the gravitational force F_G acting on each of the discs:

$$F_G = F_N + F_Y \ , \quad (6)$$

$$F_N \approx 2 \cdot \pi \cdot G \cdot \rho_1 \cdot \rho_2 \cdot S \cdot h_1 \cdot h_2 \ , \quad (7)$$

$$F_Y \approx 2 \cdot \pi \cdot G \cdot \rho_1 \cdot \rho_2 \cdot S \cdot \alpha \cdot \lambda^2 \cdot exp\left(-\tfrac{d}{\lambda}\right) \cdot \left[1 - exp\left(-\tfrac{h_1}{\lambda}\right)\right] \cdot \left[1 - exp\left(-\tfrac{h_2}{\lambda}\right)\right], \quad (8)$$

where ρ_1 is the density of disc 1, F_N is the Newtonian force, and F_Y is the Yukawa addition to the Newtonian force, respectively.

3 Measurement method

To measure the Yukawa force at the micrometer length scale λ, an attractor is brought into close range ($d \approx 1$ µm) to the detector (see Fig. 3). Since the Casimir force and the electrostatic forces are by orders of magnitude larger than the Yukawa force, their influence has to be eliminated. Therefore, a metal membrane has to be applied between the attractor and the detector to reduce the influence of the parasitic forces. Fig. 3 shows the principle of the measurement set-up for this experiment. To increase the magnitude of the effect, material of high density – like gold or platinum – should be used for the detector and the attractor. Due to the micrometer length scale λ, it is sufficient to apply a thin layer of gold (platinum) to the attractor and the detector (see Eq. (8)). Since the Yukawa force is proportional to the area S between the detector and the attractor in Eq. (8), it has to be as large as possible, resulting in a macro-object.

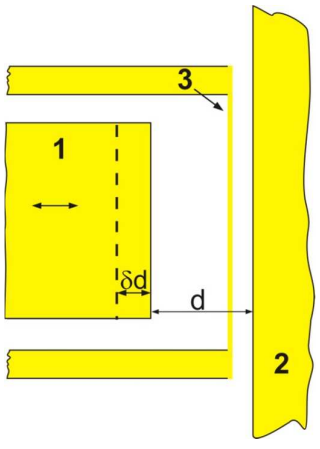

Fig. 3 Principle of the measurement set-up: (1) attractor, (2) detector, (3) shield membrane

For the measurement of the Yukawa force occurring at the detector, a force measurement device with an extremely high resolution is necessary. PTB's nanonewton force facility

fulfills these high requirements. A detailed description of this nanonewton force facility has already been published [21-23].

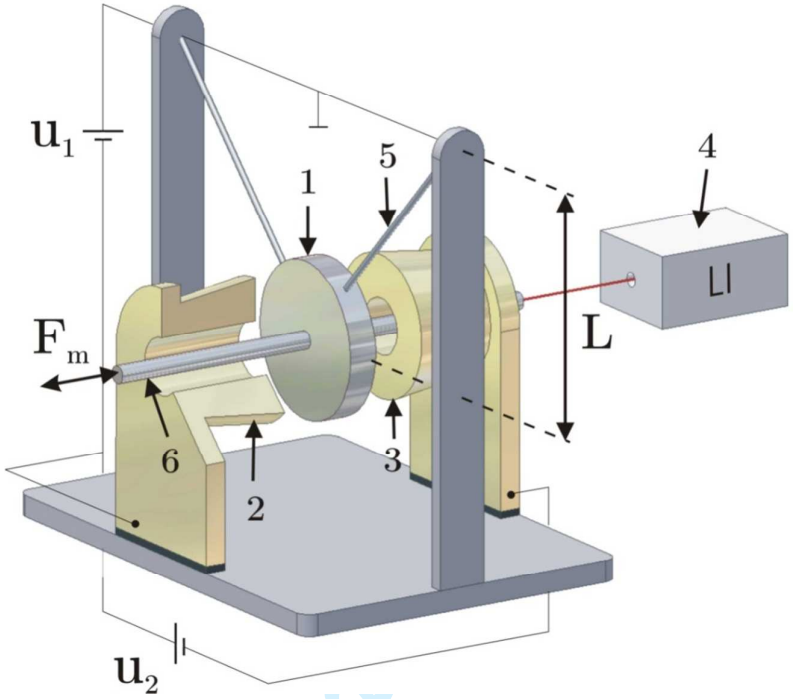

Fig. 4 Functional diagram of the nanonewton force facility at PTB: (1) conductive disc pendulum, (2, 3) outer conductive plates, (4) laser interferometer, (5) pendulum suspension (thin gold-plated tungsten wire), (6) cylindrical probing rod, F_m measuring force

The nanonewton force facility consists of a measuring part and an identical reference part for the reduction of thermal drift and seismic noise. The functional diagram of the measuring part is presented in Fig. 4. Both pendulum devices consist of a conductive disc pendulum (1), arranged between two outer parallel plates (2, 3) which form two parallel plate capacitors. The distance between the disk pendulum (1) and the outer plate (2) is equal to the distance between the disk pendulum (1) and the outer plate (3). This distance is about 100 µm. The gold-plated disc pendulums (radius 15 mm, thickness 2 mm, mass m = 3.97 g) are suspended with two gold-plated tungsten wires (20 µm in thickness and approx. 500 mm in length). A direct voltage $u_2 \approx 4$ V is applied between the disc pendulum and the outer parallel plates to reduce the stiffness of the disc pendulum from 10^{-1} N/m down to 10^{-3} N/m. The deflection of the disc pendulum is detected via a laser interferometer (4). The electrostatic force compensation is realized by means of a servo system (feedback) composed of an interferometer for the deflection measurement (4) and a compensation (feedback) voltage source u_1. The difference between the compensation voltages of the measuring disc pendulum and the reference disc pendulum is used to determine the force F_m. The cylindrical probing rod (6) is attached to disc (1). Due to the electrostatic stiffness reduction and electrostatic deflection compensation of the disc pendulums, the nanonewton force facility allows quasi-static forces to be measured in the range < 10^{-5} N with a force resolution of 10^{-12} N [21, 22]. Note that the disc pendulum (1) and the cylindrical probing pin (6) are macro-objects. In the proposed experiment, the attractor (1) and the membrane (3) (Fig. 3) will be placed next to the

probing rod of the nanonewton force facility which serves as detector (2). Note that the attractor (1) and the membrane (3) form a common structure. Then the attractor will be moved with respect to the detector and the membrane and the variation in the measured force will be recorded. A displacement of the attractor at the distance δd (see Fig. 3) changes only the Yukawa addition to the Newtonian force F_Y (7, 8). From equations (7, 8), it follows that only the Yukawa addition F_Y to the Newtonian force depends on the distance between the discs d. Taking into account equation (4), the condition of the independence of the Newtonian force F_N on d can be written as

$$F_Y \gg F_N \cdot \frac{\delta d}{R} \ . \tag{9}$$

Let us assume that the attractor executes a periodic motion at the distance δd (see Fig. 3). The detector (see Figs. 3, 4) senses the force with a resolution of δF during a measuring time τ. Using (7-9), the dependence between the dimensionless strength parameter α and the length scale parameter λ can be described by the following equation:

$$\alpha = \frac{\delta F \cdot h_1 \cdot h_2 \cdot \sqrt{\frac{\tau}{\tau_m}}}{F_N \cdot \lambda^2 \cdot \left[\exp\left(-\frac{d}{\lambda}\right) - \exp(-\frac{(d+\delta d)}{\lambda})\right] \cdot \left[1-\exp(-\frac{h_1}{\lambda})\right] \cdot \left[1-\exp(-\frac{h_2}{\lambda})\right]}, \tag{10}$$

where τ_m is the total duration of the measurement.

4 Design of the shielded attractors ("Yukawa attractor")

For the proposed experiment, the distance between the detector and the shielded attractor is in the range of approximately λ, which limits the thickness of the membrane in the submicron range. The problem with the set-up shown in Fig. 3 is that because of the limited stiffness of the membrane, a deflection occurs due to the Casimir and electrostatic forces which has a direct influence on the measured force (see Sec. 5). Therefore, the stiffness of the membrane has to be very high to minimize the influence of these parasitic forces. The stiffness of a membrane is defined by its overall dimension, by Young's modulus of the material it is made of, and by its thickness. As described above, the thickness of the membrane is limited to the submicron ranges and Young's modulus is also limited. Therefore, the only parameters for optimization are the lateral dimensions of the membrane. Since the Yukawa force is proportional to the area of the attractor that is exposed to the detector, it has to be as large as possible to obtain a high measurement signal. This requirement is contrary to the fact that the stiffness of a membrane decreases with its lateral dimensions. Therefore, a design is proposed where the attractor is divided into a large number of small attractors, each one of these shielded by a small membrane (Fig. 5). The calculations (see Sec. 5) show that the lateral dimensions of the membrane have to be in the range of some ten microns to provide sufficient stiffness. All attractors and all membranes are connected respectively, resulting in an attractor array and a corresponding membrane array (Yukawa attractor). Attractor array and membrane array are connected via flexural hinges which enable a relative movement. For the

experiment, the membrane array is fixed, whereas the attractor array can be moved relative to the detector.

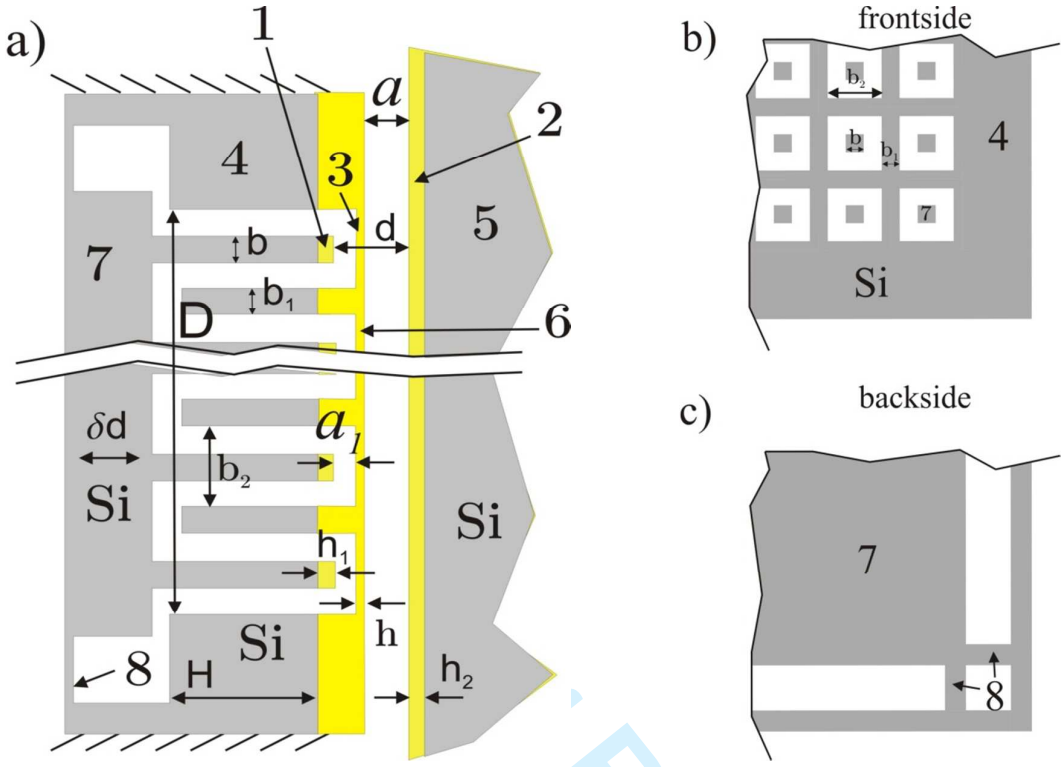

Fig. 5 Schematic view of the shielded attractors (Yukawa attractor): a) cross section of the set-up: (1) attractor, (2) mass enhancement of the detector, (3) shield membrane, (4) membrane array, (5) detector (probing rod of the nanonewton force facility), (7) attractor array, (8) flexural hinges; b) top view of the structure; c) bottom view of the structure

5 Quantitative estimations of the experimental constraints

Figure 6 illustrates the appearance of additional electrostatic and Casimir forces between the membrane and the detector for a certain displacement of the attractor. Electrostatic and Casimir forces between the attractor and the membrane lead to the deflection of the membrane $w(y, z)$ (see Fig. 6). A displacement of the attractor δd leads to an additional deflection of the membrane $\delta w(y, z)$ (see Fig. 6). This additional deflection of the membrane $\delta w(y, z)$ creates additional electrostatic and Casimir forces between the membrane and the detector (disc pendulum or cylindrical probing rod) (see Figs. 3-6). The displacement of the attractor array leads to an additional deflection of the membrane array $\Delta W(y, z)$ (see Fig. 5) and to additional electrostatic and Casimir forces between the membrane array and the detector.

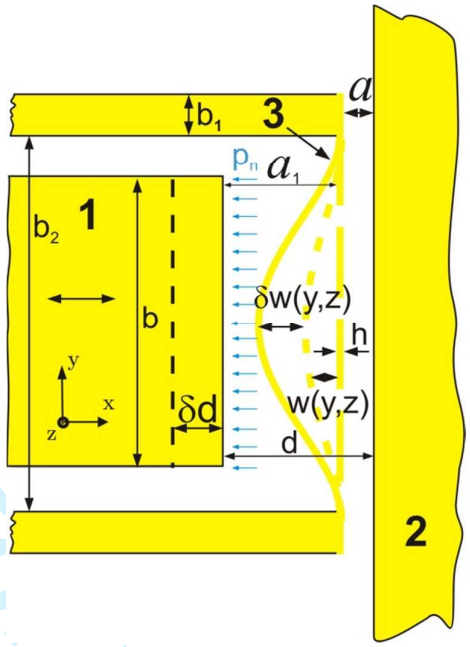

Fig. 6 Configuration for the estimation of the additional electrostatic and Casimir forces between the membrane (3) and the detector (2) for a displacement of the attractor (1).

Let us assume that the surface pressure p_n acts on the membrane (3), with an area $b_2 \times b_2$, from the side of the attractor (1). This pressure can be described by the expression

$$p_n = -\frac{A_n}{a_1^n}\,, \tag{11}$$

where a_1 is the distance between the membrane and the attractor (see Fig. 6) and n is a natural number.

Note that the real pressure p_n is applied to the center of the membrane (3) to an area $b \times b$ equal to the area of the attractor (1) (see Fig. 6). Therefore, these estimations should be regarded as an upper limit.

If n = 2, it corresponds to the electrostatic force pressure [17], with the parameter

$$A_2 = \frac{1}{2}\cdot \varepsilon_0 \cdot \Delta\varphi^2\,, \tag{12}$$

where ε_0 is the vacuum permittivity and $\Delta\varphi$ is the contact potential difference between the surfaces.

If n = 4, it corresponds to the Casimir pressure [17, 24], with the parameter

$$A_4 = \frac{\hbar \cdot c \cdot \pi^2}{240}, \tag{13}$$

where c is the velocity of light and $\hbar$ is Plank's constant.

Let us assume that for the entire surface of the membrane, the pressure p_n is constant. A displacement of the attractor δd ($\delta a_1 = \delta d$) leads to an additional pressure δp_n and an additional deflection of the membrane $\delta w(y, z)$ (see Fig. 6). Using [25, 26], the estimation of the additional deflection of the membrane $\delta w(y, z)$ is given by

$$\delta w(y,z) \approx \frac{3.5 \cdot \delta p_n}{E \cdot h^3 \cdot b_2^4} \cdot \left(z^2 - \frac{b_2^2}{4}\right)^2 \cdot \left(y^2 - \frac{b_2^2}{4}\right)^2, \tag{14}$$

$$\delta p_n = \frac{A_n \cdot n}{a_1^{n+1}} \cdot \delta a_1, \tag{15}$$

where E, h and b_2 are Young's modulus and the thickness and length of the membrane, respectively (see Fig. 6).

Using (14, 15), the additional electrostatic and Casimir pressures $\delta p_n(y, z)$ and forces δF_n between the membrane (3) and the detector (2) (disc pendulum or cylindrical probing rod) (see Figs. 3-6) can be described by the expressions

$$\delta p_n(y,z) \approx \frac{A_n \cdot n}{a^{n+1}} \cdot \delta w(y,z), \tag{16}$$

$$\delta F_n \approx \iint_{-b_2/2}^{b_2/2} \delta p_n(y,z) \cdot dy \cdot dz = \frac{3.5 \cdot A_n^2 \cdot n^2 \cdot b_2^6}{900 \cdot E \cdot h^3 \cdot a_1^{n+1} \cdot a^{n+1}} \cdot \delta d, \tag{17}$$

where a is the distance between the membrane (3) and the detector (2) (see Figs. 5-6).

Since $(a + h + a_1) = d$, it is easy to show that δF_n has a minimum if $a_1 = a$. Assuming that $a_1 = a$ and using (17), the force δF_n can be described by the following equation:

$$\delta F_n \approx \frac{3.5 \cdot A_n^2 \cdot n^2 \cdot b_2^6}{900 \cdot E \cdot h^3 \cdot {a_1}^{2 \cdot n+2}} \cdot \delta d. \tag{18}$$

A displacement of the attractor array δd ($\delta a_1 = \delta d$) leads to an additional pressure Δp_n on the membrane array, resulting in a larger scale deflection of the membrane array $\Delta W(y, z)$ (see Fig. 5). Using [25, 26], the estimation of the additional deflection of the membrane array $\Delta W(y, z)$ is given by

$$\Delta W(y,z) \approx \frac{3.5 \cdot \Delta p_n}{E_{eff} \cdot H^3 \cdot D^4} \cdot \left(z^2 - \frac{D^2}{4}\right)^2 \cdot \left(y^2 - \frac{D^2}{4}\right)^2, \tag{19}$$

$$\Delta p_n = \frac{A_n \cdot b_2^2 \cdot N_0 \cdot n}{D^2 \cdot {a_1}^{n+1}} \cdot \delta a_1, \tag{20}$$

where E_{eff}, H, D and N_0 are the effective Young's modulus, the thickness, the length and the number of the membranes of the membrane array, respectively (see Fig. 5).

The effective Young's modulus E_{eff} can be estimated by the following equation:

$$E_{eff} \approx \frac{E_{Si} \cdot b_1 \cdot (b_1 + b_2)}{b_1^2 + b_1 \cdot b_2 + b_2^2}, \tag{21}$$

where E_{Si} is Young's modulus of silicon.

In analogy to the forces δF_{n} between the membrane and the detector, the additional electrostatic and Casimir forces ΔF_n between the membrane array and the detector (see Fig. 5) can be calculated from the following equation:

$$\Delta F_n \approx \frac{3.5 \cdot A_n^2 \cdot b_2^4 \cdot n^2 \cdot N_0^2 \cdot D^2}{900 \cdot E_{eff} \cdot H^3 \cdot {a_1}^{2 \cdot n+2}} \cdot \delta d\,. \tag{22}$$

With the parameters of this proposed experiment $G = 6.67 \cdot 10^{-11}$ m^3·s^{-2}·kg^{-1}; $\rho_1 = \rho_2 = 19600$ kg·m^{-3}; $h_1 = h_2 = 0.5$ µm; $b = 5$µm; $N_0 = 2.25 \cdot 10^4$; $S = b^2 \cdot N_0 = 56 \cdot 10^{-8}$ m^2; $d = 1.2$ µm; $\delta d = 0.1$ µm; $\delta F = 10^{-12}$ N; $\tau = 20$ s; $\tau_m = 2 \cdot 10^5$ s; $\varepsilon_0 = 8.85$ F·m^{-1}; $\Delta\varphi = 30$ mV; $\hbar = 1.05 \cdot 10^{-34}$ J·s; $c = 3 \cdot 10^8$ m·s^{-1}; $E = 77.2$ GPa; $h = 0.2$ µm; $b_1 = b_2 = 15$ µm; $\delta a_1 = \delta d = 0.1$ µm; $a_1 = a = 0.5$ µm; $H = 400$ µm; $D = (b_1 + b_2)\, N_0^{1/2} = 4.5 \cdot 10^{-3}$ m; $E_{Si} = 168.4$ GPa, the main analytically computed parameters of the proposed experiment are presented in Table 1.

Table 1 The main analytically computed parameters of the proposed experiment

F_N, [N]	A_2, [N]	A_4, [N·m^2]	$\delta F_2 \cdot N_0$, [N]	$\delta F_4 \cdot N_0$, [N]	ΔF_2, [N]	ΔF_4, [N]	E_{eff}, [Pa]
$2.3 \cdot 10^{-20}$	$4 \cdot 10^{-15}$	$1.3 \cdot 10^{-27}$	$0.7 \cdot 10^{-15}$	$4.5 \cdot 10^{-15}$	$1.2 \cdot 10^{-16}$	$7.9 \cdot 10^{-16}$	$1.1 \cdot 10^{11}$

A periodical displacement of the attractor leads to a parasitic force with the amplitude δF_p.

Using (Table 1), this amplitude can be estimated by the following expression:

$$\delta F_p \approx \delta F_2 \cdot N_0 + \delta F_4 \cdot N_0 + \Delta F_2 + \Delta F_4 < 6.1 \cdot 10^{-15}\ \mathrm{N}\,. \tag{23}$$

The achievable resolution of PTB's nanonewton force facility for the amplitude of the periodic force $\delta F_m(f_m)$ (period of oscillation $\tau \approx 20$ s and a frequency of oscillation $f_m = \tau^{-1} \approx 50$ mHz) and the measurement duration τ_m can be estimated by the following expression:

$$\delta F_m(f_m) \approx \delta F \cdot \sqrt{\frac{\tau}{\tau_m}} \approx 10^{-14}\ N, \qquad \delta F_p < \delta F_m(f_m). \tag{24}$$

PTB's nanonewton force facility is housed within a vacuum chamber with a base pressure of $\approx 10^{-5}$ Pa.

Using (10, 24), new experimental constraints are achieved by the proposed experiment. These improved constraints are depicted in Fig. 1 (dashed line) as the dependence between the dimensionless strength parameter α and the length scale λ. The estimations should take the van der Waals forces into account if the distances are less than 100 nm.

6 Fabrication of the shielded attractors (Yukawa attractor)

It is obvious that this kind of structure (Yukawa attractor) can only be manufactured using advanced microtechnology fabrication methods. It is also obvious that the two parts – the attractor array and the membrane array – have to be manufactured in one piece to avoid a very complicated assembly and an adjustment process. The great challenge is to bring about the separation between the attractor array and the framework that carries the membranes. In Fig. 7, a possible process flow for the proposed structure is shown. It is based on mono-crystalline silicone, since it has excellent mechanical properties and since there is a wide range of well-established structuring processes. For the structuring of the functional parts, a dry-etching process was chosen. Using an etching reactor based on inductively coupled plasma (ICP), it is possible to produce nearly perpendicular etching profiles in silicon, going along with very high etching rates. Using this technology, it is even possible to etch through the complete wafer-leaving movable structures with vertical walls [27]. The process [28] used to produce these high-aspect ratios is well established and widely used. To obtain the vertical side walls, the process is split into two phases:

- etching step
- passivation step

The etching step itself is isotropic, resulting in an under-etching of the mask. The anisotropy is achieved by (rapidly) alternating the etching step and the passivation step:

After the first etching step, a shallow groove is obtained. Then, in the second step, the surface of the groove is passivated, disabling further etching. Due to an electric field (bias), the "reactive ions" causing the etching of the material are accelerated perpendicular to the wafer surface. Therefore, the passivation at the bottom of the groove is sputtered away and the etching starts again, but only at the bottom. After a while, the passivation at the sidewalls is also worn off and has to be "refreshed" in a further passivation step. Both steps last for several seconds and are repeated many times, resulting in vertical sidewalls. By varying the parameters (switching time, bias power, ICP power...), the anisotropy of this process can be controlled over a wide range.

To produce the attractor array and the membrane array which are separated from each other, a combination of anisotropic and isotropic etching will be applied. The first part of the etching will be anisotropic (Fig. 7a) and in a certain depth, the etching parameters will be changed, resulting in an isotropic etching behavior. In detail, the change will take place after the last passivation step of the anisotropic etching step. Then the bottom passivation will be sputtered, followed by a step with low bias, resulting in an isotropic etching leading to a "cave-like" etching profile (Fig. 7e). By choosing slightly different lateral dimensions for the attractors

and the membrane supports, the "caves" get into contact under the membrane support and leave a small support under the attractors. In an ongoing (anisotropic) etching step from the back side, the two structures will be separated completely, leaving only some very thin (20 µm) support beams which serve as flexural hinges. In a last step, the shield membrane will be applied using a special process based on vapor deposition. The distance between the attractors and the membrane is ensured by "spacer" structures which were produced prior to the dry-etching steps (Fig.7c). Details of this process will be described in the future.

	a) The base material for the Yukawa attractor is mono-crystalline silicon
	b) Applying of the attractor mass enhancement (gold or other material with high density) by vapor deposition and an ongoing structuring process
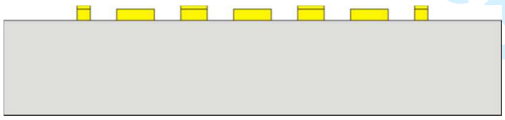	c) Vapor deposition and structuring of gold serving as spacer structures
	d) Masking and dry-etching (anisotropic) of silicon
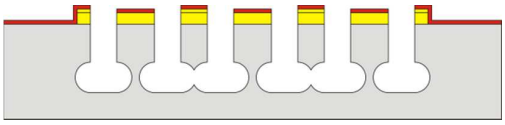	e) Dry-etching (isotropic) resulting in free-standing membrane supports
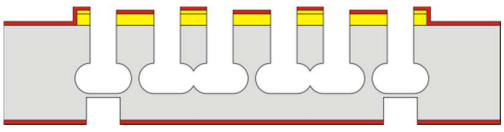	f) Dry-etching of flexural hinges from the back side
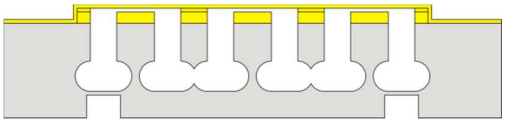	g) Application of the shield membrane by vapor deposition

Fig. 7: Possible process flow for the fabrication of the Yukawa attractor

7 Discussion

The electrostatic force noise might be the most important factor limiting the search for the non-Newtonian gravity. The observed variation of the surface potential of a clean polycrystalline metal [29-34] is most likely due to local changes in the surface crystalline structure. This is referred to as the "patch effect". Patch potentials are also generated and influenced by surface contamination and, in the case of alloys, by variations in the chemical composition. The difference in the average potential of two connected metals is referred to as the "contact potential difference". Typical observed contact potential differences between gold surfaces are in the order of 1 mV to 180 mV [30, 34-38]. The contact potential differences between the gold surfaces without vacuum baking (in the air) reported in [38] ranged from 120 mV to 180 mV. The contact potential differences between the gold surfaces that were baked in an ultrahigh vacuum ranged from -10 mV to 15 mV [30, 35]. The contact potentials and the forces due to contact potentials are measured and compensated relatively easily, as they lead to long-range electrostatic forces which are equivalent to those between the plates of a capacitor. The temporal fluctuations of the surface potential create force noise. The spatial distribution of the surface potential creates a non-trivial dependence of the electrostatic force on the distance between the surfaces [29-32, 34]. The measurements of the surface potential variations, carried out by means of a torsion balance [34], showed that they do not exceed $S^{1/2}(f) \approx 12$ μV·Hz$^{-1/2}$ for an area of 500 mm^2 (at a frequency of $f \approx 1$ mHz). For the 4.5 mm × 4.5 mm square (membrane array) (area ≈ 20 mm^2) used here, the scaling factor 5 = (500 mm^2 / 20 mm^2)$^{1/2}$ is yielded for the surface potential variations. From this, the upper limit 60 μV·Hz$^{-1/2}$ results for the voltage noise $S_V^{1/2}(f)$. The voltage noise $S_V^{1/2}(f) \approx 60$ μV·Hz$^{-1/2}$ between the shield membrane (3) and the detector (2) (see Fig. 5) leads to a force noise PSD (power spectral density) $S_N(f)$. Assuming that the contact potential between the membrane and the detector was measured and compensated to the value $\Delta\varphi_{off} \approx 0.1$ mV, the force noise $S_N^{1/2}(f)$ can be estimated by the expression

$$S_N^{1/2}(f) \approx \frac{\varepsilon_0 \cdot \Delta\varphi_{off} \cdot D^2 \cdot S_V^{1/2}(f)}{a^2} \approx 4 \cdot 10^{-12} \frac{N}{\sqrt{Hz}}, \quad (25)$$

where D = 4.5 mm is the length of the membrane array and a = 0.5 μm is the distance between the membrane (3) and the detector (2) (see Fig. 5).

The force noise $S_N(f_m)$ (at a frequency of $f_m \approx 50$ mHz) is probably considerably less than the force noise $S_N(f)$ (at a frequency of $f \approx 1$ mHz). The parasitic force $\delta F_{pV}(f_m)$ (at a frequency of $f_m \approx 50$ mHz and the measurement duration $\tau_m = 2 \cdot 10^5$ s) can be estimated by the following expression:

$$\delta F_{pV}(f_m) \approx \frac{S_N^{1/2}(f_m)}{\sqrt{\tau_m}} < \frac{S_N^{1/2}(f)}{\sqrt{\tau_m}} \approx 9 \cdot 10^{-15}\ N. \quad (26)$$

This parasitic force $\delta F_{pV}(f_m)$ may exceed the parasitic force δF_p (23) and has therefore to be taken into account.

The functional principle of PTB's nanonewton force facility is based on the electrostatic system for reducing the stiffness and the electrostatic deflection of the disk pendulum (1) (Fig. 4) [21-23, 39, 40]. The voltage noise *S(f)* arises between a conductive disc pendulum and outer conductive plates (Fig. 4). The voltage noise $S^{1/2}(f) \approx 12$ μV·Hz$^{-1/2}$ [34] corresponds to a force noise $S_{Nm}^{1/2}(f) \approx 18$ pN·Hz$^{-1/2}$ (at a frequency of $f \approx 1$ mHz) for the nanonewton force facility at PTB [39, 40] (the surface area of the outer conductive plates (2, 3) (Fig. 4) of the nanonewton force facility ≈ 500 mm^2). The force noise $S_{Nm}(f_m)$ (at a frequency of $f_m \approx 50$ mHz) is probably considerably less than the force noise $S_{Nm}(f)$ (at a frequency of $f \approx 1$ mHz). Taking this force noise into account, the achievable resolution of PTB's nanonewton force facility for the amplitude of the periodic force $\delta F_{Vm}(f_m)$ (at a frequency of $f_m \approx 50$ mHz) and the measurement duration $\tau_m = 2 \cdot 10^5$ s can be estimated by the following expression:

$$\delta F_{Vm}(f_m) \approx \frac{S_{Nm}^{1/2}(f_m)}{\sqrt{\tau_m}} < \frac{S_{Nm}^{1/2}(f)}{\sqrt{\tau_m}} \approx 4 \cdot 10^{-14}\ N. \qquad (27)$$

The sensitivity to voltage ($S_{Nm}^{1/2}(f)/S_V^{1/2}(f)$) and the force resolution $\delta F_{Vm}(f_m)$ of PTB's nanonewton force facility can be easily reduced [21, 22]. The force resolution $\delta F_{Vm}(f_m)$ can be reduced to $\delta F_m(f_m) \approx 10^{-14}$ N, as is needed for the estimation (24). In the proposed experiment the feedback voltage u_1 (Fig. 4) might be about ±1mV.

PTB's nanonewton force facility is housed within a vacuum chamber with a base pressure of ≈ 10^{-5} Pa. Using [33], this pressure must be sufficient to reduce the Brownian force noise caused by molecular collisions in the proposed geometry to 1 pN·Hz$^{-1/2}$. The search for the non-Newtonian gravity at micro- and submicrometer distances requires the investigation of the following parasitic effects:

- the electrostatic force noise at a frequency of $f_m \approx 50$ mHz and submicrometer distance
- non-parallelism of the probe surfaces
- non-ideal shape of the probe surfaces
- Casimir forces
- Brownian force noise caused by residual gas.

8 Conclusion

An explicit analytical expression for the estimation of the gravitational force between two thin discs for the interaction potential of the Yukawa form at small distances has been derived. We propose an experiment to test Newton's law of gravity at micro- and submicrometer distances using a nanonewton force facility at PTB and a structure produced by means of microtechnical fabrication methods ("shielded attractors" or "Yukawa attractor"). It has been demonstrated in a first analysis that the proposed method can advance the search for non-Newtonian gravity forces via an enhanced sensitivity of 10^3 to 10^4 in comparison to the current experiments at the micrometer length scale, although a more thorough analysis of the systematic and statistical errors will be required. The proposed method can be used to investigate the non-Newtonian gravity forces between different materials. The proposed

experiment uses the optimal geometric set-up (two planes) for the measurement of the Yukawa force in the micro- and submicrometer length scale.

References

[1] A. G. Riess *et al.,* Astron . J. **116**, 1009 (1998).

[2] C. L. Bennet *et al.,* Astrophys. J. **148**, 1 (2003).

[3] S. Perlmutter *et al.,* Astrophys. J. **517**, 565 (1999).

[4] S. R. Beane, Gen. Relativ. Gravit. **29**, 945 (1997).

[5] G. Dvali, G. Gabadadze, M. Kolanovic, and F. Nitti, Phys. Rev. D **65**, 024031 (2001).

[6] D. J. Kapner *et al.,* Phys. Rev. Lett. **98**, 021101 (2007).

[7] R. Sundrum, Phys. Rev. D **69**, 044014 (2004).

[8] N. Arkani-Hamed, S. Dimopoulis, and G. R. Dravi, Phys. Lett. B **436**, 257 (1998).

[9] S. Dimopoulos, and G. F. Guidice, Phys. Lett. B **379**, 105 (1996).

[10] L. Antoniadis, S. Dimopoulos, and G. Dvali, Nucl. Phys. B **516**, 70 (1998).

[11] N. Arkani-Hamed, S. Dimopoulis, and G. R. Dravi, Phys. Lett. B **429**, 263 (1998).

[12] E. Fischbach *et al.,* Phys. Rev. Lett. **56**, 3 (1986).

[13] A. A. Geraci *et al.,* Phys. Rev. D **78**, 022002 (2008).

[14] R. C. Decca *et al.,* Phys. Rev. D **75**, 077101 (2007).

[15] R. C. Decca *et al.,* Phys. Rev. Lett. **94**, 240401 (2005).

[16] M. Masuda, and M. Sasaki, Phys. Rev. Lett. **102**, 171101 (2009).

[17] S. K. Lamoreaux, Phys. Rev. Lett. **78**, 5 (1997).

[18] J. Chiaverini *et al.*, Phys. Rev. Lett. **90**, 151101 (2003).

[19] C. D. Hoyle *et al.,* Phys. Rev. D **70**, 042004 (2004).

[20] A. A. Geraci *et al.*, Phys. Rev. Lett. **105**, 101101 (2010).

[21] V. Nesterov, Meas. Sci. Technol. **18**, 360 (2007).

[22] V. Nesterov *et al.,* Metrologia **46**, 277 (2009).

[23] V. Nesterov, Meas. Sci. Technol. **20**, 084012 (2009).

[24] H. B. G. Casimir, Proc. K. Ned. Akad. Wet. **51**, 793 (1948).

[25] S. Timoshenko, Strength of Materials (Princeton, NJ: Van Nostrand-Reinhold, 1955).

[26] S. J. Lekhnitskii, Theory of Elasticity of an Anisotropic Body (San Francisco:Holden-Day, 1963).

[27] S. Bütefisch, Entwicklung von Greifern für die automatisierte Montage hybrider Mikrosysteme, Shaker Verlag (2003), ISBN-10: 3832221948.

[28] W. Menz, J. Mohr: Mikrosystemtechnik für Ingenieure. VCH-Verlag, Weinheim 1997.

[29] C. C. Speake, and C. Trenkel, Phys. Rev. Lett. **90**, 160403 (2003).

[30] S. E. Pollack, S. Schlamminger, and J. H. Gundlach, Phys. Rev. Lett. **101**, 071101(2008).

[31] W. J. Kim *et al.*, Phys. Rev. Lett. **103**, 060401 (2009).

[32] W. J. Kim *et al.,* Phys. Rev. A **81**, 022505 (2010).

[33] R. Dolesi *et al.,* Phys. Rev. D **84**, 063007 (2011).

[34] F. Antonucci *et al.*, Phys. Rev. Lett. **108**, 181101 (2012).

[35] J. B. Camp *et al.,* J. App. Phys. **69**, 7126 (1991).

[36] L. Carbone *et al.*, Phys. Rev. Lett. **91**, 151101 (2003).

[37] N. A. Robertson *et al.*, Classical Quantum Gravity. **23**, 2665 (2006).

[38] J. R. Pratt, and J. A. Kramar, Proc. IMEKO (Rio de Janeiro, 2006).

[39] B. Beckhoff *et al.,* PTB-Mitteilungen **121**, Heft 2, 165 (2011).

[40] http://www.ptb.de/cms/en/fachabteilungen/abt5/fb-51/512-nano-force-metrology/nano-force-standard-facility.html

Table 1 The main analytically computed parameters of the proposed experiment							
F_N, [N]	A_2, [N]	A_4, [N·m^2]	$\delta F_2 \cdot N_0$, [N]	$\delta F_4 \cdot N_0$, [N]	ΔF_2, [N]	ΔF_4, [N]	E_{eff}, [Pa]
$2.3 \cdot 10^{-20}$	$4 \cdot 10^{-15}$	$1.3 \cdot 10^{-27}$	$0.7 \cdot 10^{-15}$	$4.5 \cdot 10^{-15}$	$1.2 \cdot 10^{-16}$	$7.9 \cdot 10^{-16}$	$1.1 \cdot 10^{11}$